The role of MYO9A at the neuromuscular junction

Emily Ann O'Connor

A thesis submitted for the degree of Doctor of Philosophy

Institute of Genetic Medicine

Newcastle University

April 2019

Abstract

Congenital myasthenic syndromes (CMS) are a group of rare, inherited disorders characterised by impaired function of the neuromuscular junction (NMJ). This is due to defects in one of the many proteins associated with the NMJ. Patients with CMS present with fatigable skeletal muscle weakness that can vary in age of onset, severity and muscles affected. In 3 patients with CMS, missense mutations in a gene encoding an unconventional myosin protein, not previously linked to neuromuscular diseases, MYO9A, were identified as likely causing their disorder. Therefore, the aim of this project was to determine whether MYO9A is playing a role at the NMJ and how loss or defective function of this protein may impact signal transmission. This question was addressed using a range of models, including patient fibroblasts converted into neurons, morpholino and CRISPR/Cas9-mediated knockdown zebrafish and a knockout mouse model.

Investigation of the NSC-34 cells led to the finding that the cytoskeleton was affected in the absence of MYO9A, and this impacted on the dynamics of intracellular vesicles and endo/exocytosis. Secretome analysis revealed a downregulation of agrin secretion in MYO9A deficient cells, a protein important for the development and function of the NMJ.

Analysis of NMJs in MYO9A-depleted zebrafish and mice revealed changes in morphology, including smaller nerve terminals and area of endplates. Due to the suitability of zebrafish for drug screening, fish were treated with a synthetic agrin compound. This rescued a number of the defective features identified in the knockdown fish, thus providing a potential mode of action for this form of CMS and an avenue for patient treatment. This study highlights a role for MYO9A at the NMJ, the first unconventional myosin motor protein associated with a neuromuscular disease, thus opening a new avenue of proteins and pathways that may be relevant for a range of disorders.

Acknowledgments

First of all, I would like to thank my supervisors Professor Hanns Lochmüller and Professor Clarke Slater. It has been fantastic working with such inspiring scientists and I greatly appreciate the opportunities you have both given me during my PhD, as well as the unwavering support and intellectual input from you both. I am also very grateful to my other supervisors who have supported this project during my time at Newcastle University, including Dr Andreas Roos, Professor Rita Horvath and Dr Veronika Boczonadi.

I would also like to thank Dr Sally Spendiff for the continued support and rational approach to sorting out my (many) problems in the lab, I look forward greatly to working with you in the future. Dr Juliane Müller, for teaching me everything when I started in the lab and listening to my dilemmas every Friday evening for the last three years, you have been a fantastic friend and colleague.

I am also grateful to many other members of the lab who have made the last three years enjoyable, particularly Dan Cox, Steph Carr, Grace McMacken, Rachel Howarth and everyone ‘upstairs’. Lucy Imber, Vicki Hedley and John Dawson, thank you for always being a slack message away.

To all my fantastic family and friends for supporting me outside of work and reminding me that there is life beyond the lab. In particular, thank you to George Cairns, I would not have finished this without you.

I am very appreciative of the animal facility staff in the zebrafish facility and the advice you have given me over the years. I am also thankful to Neurotune, for providing the NT1654 compound used in this study, Professor Martin Bähler for provision of mice and Vietxuan Phan along with the rest of the Neuromuscular diseases proteomic facility at the Leibniz-Institut for Analytical Science, for the proteomic data analysed in this study.

This work was funded by a studentship from Kindness for Kids and research project grant from AFM-Téléthon.

Table of Contents

List of publications

McMacken, G. M., Spendiff, S., Whittaker, R. G., O'Connor, E., Howarth, R. M., Boczonadi, V., Horvath, R., Slater, C. R., Lochmüller, H., (2019) Salbutamol modifies the neuromuscular junction in a mouse model of ColQ myasthenic syndrome, Hum. Mol. Gen. ddz059.

Phan, V., Cox, D., Cipriani, S., Spendiff, S., Buchkremer, S., O'Connor, E., Horvath, R., Goebel, H. H., Hathazi, D., Lochmuller, H., Straka, T., Rudolf, R., et al. (2019) SIL1 deficiency causes degenerative changes of peripheral nerves and neuromuscular junctions in fish, mice and human. Neurobiol. Dis., 124:218-229.

O'Connor, E., Phan, V., Cordts, I., Cairns, G., Hettwer, S., Cox, D., Lochmüller, H., Roos, A., (2018) MYO9A deficiency in motor neurons is associated with reduced neuromuscular agrin secretion. Hum. Mol. Gen., 27(8):1434–46.

O'Connor, E., Töpf, A., Zahedi, R., Spendiff, S., Cox, D., Roos, A., and Lochmüller, H., (2018) Clinical and research strategies for limb-girdle congenital myasthenic syndromes. Ann. N.Y. Acad. Sci. 1412(1):102-12.

Boyle, K. A., Gutierrez-Mecinas, M., Polgár, E., Mooney, N., O'Connor, E., Furuta, T., Watanabe, M., and Todd., A. J., (2017) A quantitative study of neurochemically defined populations of inhibitory interneurons in the superficial dorsal horn of the mouse spinal cord. Neuroscience 363:120-133.

Editor's choice – O'Connor, E., Töpf, A., Müller, J. S., Cox, D., Evangelista, T., Colomer, J., Abicht, A., Senderek, J., Hasselmann, O., Yaramis, A., Laval, S. H., and Lochmüller, H., (2016) Identification of mutations in the MYO9A gene in patients with congenital myasthenic syndrome. Brain 139(8):2143-53.

Khan, M. M., Lustrino, D., Silveira, W. A., Wild, F., Straka, T., Issop, Y., O'Connor, E., Cox, D., Reischl, M., Marquardt, T., Labeit, D., Labeit, S., et al., (2016), Sympathetic innervation controls homeostasis of neuromuscular junctions in health and disease. PNAS 113(3):746-750.

Table of Figures

Table of Tables

List of abbreviations

aBTx	α-bungarotoxin	Cas9	CRISPR associated protein 9
ACh	Acetylcholine	DAP	Diaminopyridine
AChR	Acetylcholine receptor	dpf	Days post fertilisation
AChE	Acetylcholinesterase	DOK7	Downstream of Tyrosine Kinase 7
ATP	Adenosine triphosphate	DMEM	Dulbecco's modified Eagle medium
AMPAR	Alpha-amino-3-hydroxy-5-methyl-4-isoxazole propionic acid receptor	EMG	Electromyography
ALS	Amyotrophic Lateral sclerosis	EPP	Endplate potential
ANOVA	Analysis of variance	FBS	Fetal bovine serum
bp	Base pair	F-actin	Filamentous actin
BSA	Bovine serum albumin	GEF	GDP/GTP nucleotide exchange factor
C.elegans	Caenorhabditis elegans		
CNS	Central nervous system	gDNA	Genomic DNA
ChAT	Choline Acetyl Transferase	GAP	GTPase activating protein
CHRNE	Cholinergic Receptor Nicotinic Epsilon Subunit	HBSS	Hank's Balanced Salt Solution
		hpf	Hours post fertilisation
CRISPR	Clustered regularly interspaced short palindromic repeats	HA	Human influenza hemagglutinin
		iNPC	Induced neuronal progenitor
CMAP	Compound muscle action potential	KD	Knockdown
		KO	Knockout
CTCF	Corrected total cell fluorescence	LB	Luria broth

LRP4	LDL Receptor Related Protein 4
MACF1	Microtubule Actin Crosslinking Factor 1
mEPP	Miniature endplate potential
MO	Morpholino
MuSK	Muscle-specific kinase
MyHC	Myosin heavy chain
MYO9A	Myosin IXa
NGF	Nerve growth factor
NMJ	Neuromuscular junction
PBST	PBS with 0.1% Tween
PCR	Polymerase chain reaction
PEDF	Pigment epithelium-derived factor
PFA	Paraformaldehyde
QC	Quantal content
qRT-PCR	Quantitative reverse transcriptase PCR
ROCK	Rho-associated protein kinase
SDS	Sodium dodecyl sulfate
SD	Standard deviation
SEM	Standard error of the mean
sgRNA	Single guide RNA
SMA	Spinal Muscular Atrophy
SNARE	Soluble N-ethylmaleimide-sensitive fusion protein attachment protein receptors
STRING	Search Tool for the Retrieval of Interacting Genes/Proteins
SV2	Synaptic Vesicle Protein 2
TBST	TBS + 0.1% tween
TBS	Tris-buffered saline
TrkA	Tropomyosin receptor kinase A
Tyr	Tyrosinase
VaChT	Vesicular acetylcholine transporter

Chapter 1. Introduction

The main aim of this project was to determine whether Myosin IXa (MYO9A) contributes to the development and integrity of the neuromuscular junction (NMJ). Pathological mechanisms that may lead to manifestation of a Congenital Myasthenic Syndrome (CMS) phenotype in patients lacking the functional protein were determined, and thus potential therapeutic targets for new treatments identified.

1.1 The motor nervous system

The cell bodies of skeletal motor neurons reside in the ventral spinal cord, where they receive descending inputs from the brain and direct inputs from the sensory nervous system in order to guide and control all movements of the body. This includes tonic action to maintain posture and position, as well as voluntary movement. The axons of motor neurons exit the spinal cord during prenatal development and travel to their target tissue (muscle for the somatic motor system) where they often branch profusely and innervate multiple muscle fibres. Initially mammalian muscle fibres are contacted by multiple axons, however, during a process of competition this is reduced to a single axon per fibre (Tapia et al., 2012). A motor neuron and its associated muscle fibres are collectively referred to as a motor unit, as shown in Figure 1.1. During movement, motor units are recruited according to size, with progressively larger motor units recruited as the desired force of muscle contraction increases (Mendell, 2005).

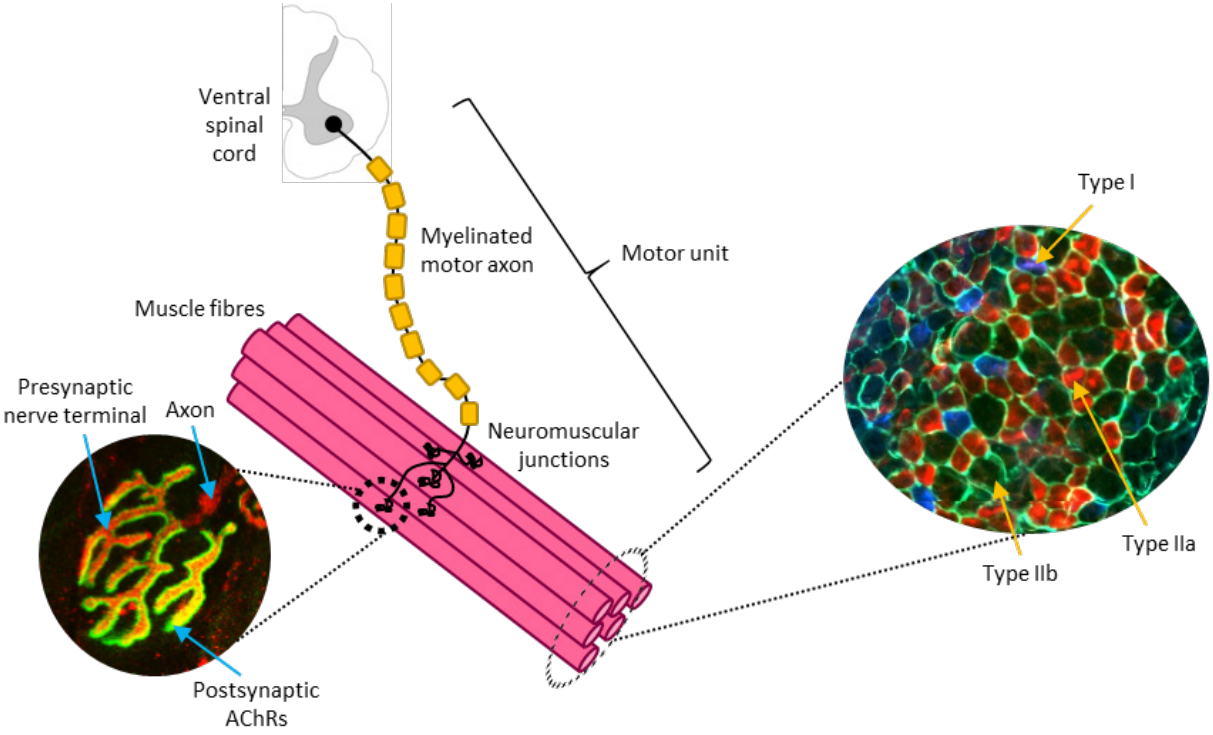

Figure 1.1. Structure of the motor system. Schematic diagram showing a myelinated motor neuron axon originating in the ventral spinal cord, and extending towards a target muscle where it branches and innervates a number of muscle fibres. The collective muscle fibres, neuromuscular junctions and motor axon are termed the motor unit. Individual muscle fibre types can be detected using antibodies against specific isoforms of myosin heavy chain (MyHC): MyHC I = Type I, blue, MyHC IIa = Type IIa, red, MyHC IIb = Type IIb, green and MyHC IIx = Type IIx, not shown. NMJs can be visualised using fluorophore-bound α-bungarotoxin (aBTx) to bind acetylcholine receptors (AChRs, green) and antibodies against neurofilament and synaptophysin for the presynaptic axon and terminal (red), respectively.

Skeletal muscles are composed of many individual fibres that contain repeating functional units (sarcomeres) made up of actin and myosin, necessary for muscle contraction. During development, myoblasts fuse to form multinucleated muscle fibres, with nuclei located in the centre of the fibre. As muscle matures, the nuclei migrate to the cell periphery, and thus internal nuclei can be a marker of regenerating fibres or disease (Folker and Baylies, 2013). Fibres are classified according to their rate of contraction (fast or slow) and the main method for adenosine triphosphate (ATP) production (glycolysis or oxidative phosphorylation). Fibres are classed as: Type I (slow, oxidative), Type IIa (fast, oxidative), Type IIx (fast, glycolytic) or Type IIb (fast, glycolytic, not expressed in human), and they can be identified by the expression of different MyHC isoforms, as shown in Figure 1.1 (Schiaffino and Reggiani, 2011). Muscles are made up of varying combinations of muscle fibre types which convey different functional properties.

Muscle fibre architecture is relatively conserved among vertebrates, even at the level of zebrafish in which fast and slow fibres are present, albeit at different proportions (van Raamsdonk et al., 1978). While muscles in mammals contain different fibre types throughout, in zebrafish a vast collection of fast twitch muscles fibres is surrounded by a single layer of superficial slow twitch fibres to allow for fast, darting movements to take place (van Raamsdonk et al., 1978). Zebrafish also have motor units that are recruited according to the movement required. However, muscle fibres are co-innervated by primary motor neurons with large amplitude outputs, recruited for fast, short bursts of movement, and multiple secondary motor neurons with lower amplitude signals that coordinate slow swimming (Wang and Brehm, 2017, Luna et al., 2015). Thus graded muscle responses in zebrafish can be achieved by the same motor unit, depending on the neural input activated, thus expanding on the recruitment of increased muscle fibres and larger units observed in mammals. The connection between the nerve and muscles in these motor units is termed the NMJ (Figure 1.1).

1.2 Neuromuscular junction

1.2.1 Signal transmission at the NMJ

The NMJ is the site of signal transmission between a motor axon terminal and its target muscle fibre. It is a highly specialised cholinergic tripartite synapse, consisting of the motor axon and muscle fibre, as well as a terminal Schwann cell which surrounds the junction. Initiation of an action potential at the axon hillock adjacent to the motor neuron cell body is caused by descending input from the central nervous system (CNS) or reflex pathway from the sensory nervous system. The action potential is transmitted down the axon which is ensheathed in myelin, produced by Schwann cells, to allow for salutatory conduction to occur (Figure 1.2, step 1). Arrival at the nerve terminal of an action potential leads to membrane depolarisation and subsequent activation of voltage-gated calcium channels (Figure 1.2, step 2). There is an influx of calcium ions that stimulate the fusion of vesicles docked at the presynaptic terminal with the membrane thus releasing their contents into the synaptic cleft (Figure 1.2, step 3). These vesicles contain acetylcholine (ACh), the main neurotransmitter released at the NMJ. ACh is synthesised in the nerve terminal from acetyl coenzyme A and choline, mediated by the enzyme choline acetyl-transferase (ChAT). Availability of choline is a rate limiting step for this process. It is recycled after breakdown of ACh by acetylcholinesterase (AChE) in the synaptic

cleft, and is taken back into the nerve terminal (Figure 1.2, step 8). After synthesis of ACh, the neurotransmitter is packaged into synaptic vesicles by vesicular ACh transporter (VaChT), forming individual ‘quantum’ of transmitter (Taylor and Brown, 1999). Vesicles are transported to the active zone of the nerve terminal, which is the specialised release site. Docking and priming vesicles is a complex process, involving a number of macromolecules at the active zone that interact with the vesicle to manoeuvre it into the site of release, as described in detail by the McMahan laboratory (Harlow et al., 2013, Jung et al., 2018). Action potential-mediated influx of calcium is detected by synaptotagmin which triggers the fast, synchronous fusion of these vesicles to the presynaptic membrane (Brose et al., 1992). This process is thought to be modulated by the active zone protein Bassoon, which has been shown to co-localise with P/Q type (adult subtype) voltage-sensitive calcium channels at the release sites of vesicles (Nishimune et al., 2012). Exocytosis involves a number of proteins associated with the soluble N-ethylmaleimide-sensitive fusion protein attachment protein receptors (SNARE) complex, including syntaxin 1A and SNAP-25. Vesicle-SNARE proteins interact with target-SNAREs on the nerve membrane to initiate release of ACh from the vesicle and into the synaptic cleft. The number of vesicles released after each action potential is termed the ‘quantal content’ (QC), and this tends to increase in line with terminal area (Slater, 2017).

Nicotinic ACh receptors (AChR) are situated on the postsynaptic muscle fibre opposed to the release sites of the nerve terminal to minimise diffusion distance (Fagerlund and Eriksson, 2009). AChRs are anchored in place with a complex arrangement of cytoskeletal components within the cell. Binding of ACh to AChRs leads to the influx of cations into the muscle cell, causing depolarisation (Figure 1.2, step 4/5). Spontaneous release of quanta of neurotransmitter occurs even at rest, and causes miniature endplate potentials (mEPPs) to occur. These small events are graded postsynaptic potentials and they are not sufficient to cause an action potential. Following arrival of a presynaptic action potential and subsequent release of ACh into the cleft, there is a larger postsynaptic depolarisation termed the endplate potential (EPP). If sufficient depolarisation occurs and reaches threshold, an action potential is initiated that propagates along the muscle fibre membrane, causing an increase in intracellular calcium and contraction mediated by a network of actin and myosin filaments (Figure 1.2, step 6/7, Fagerlund and Eriksson, 2009). ACh is rapidly broken down in the cleft by AChE which terminates its action on the muscle fibre (Figure 1.2, step 8). AChE is situated in the synaptic basal lamina, which contains

numerous proteins important for cell adhesion and neuromuscular signalling such as collagens, laminin and agrin.

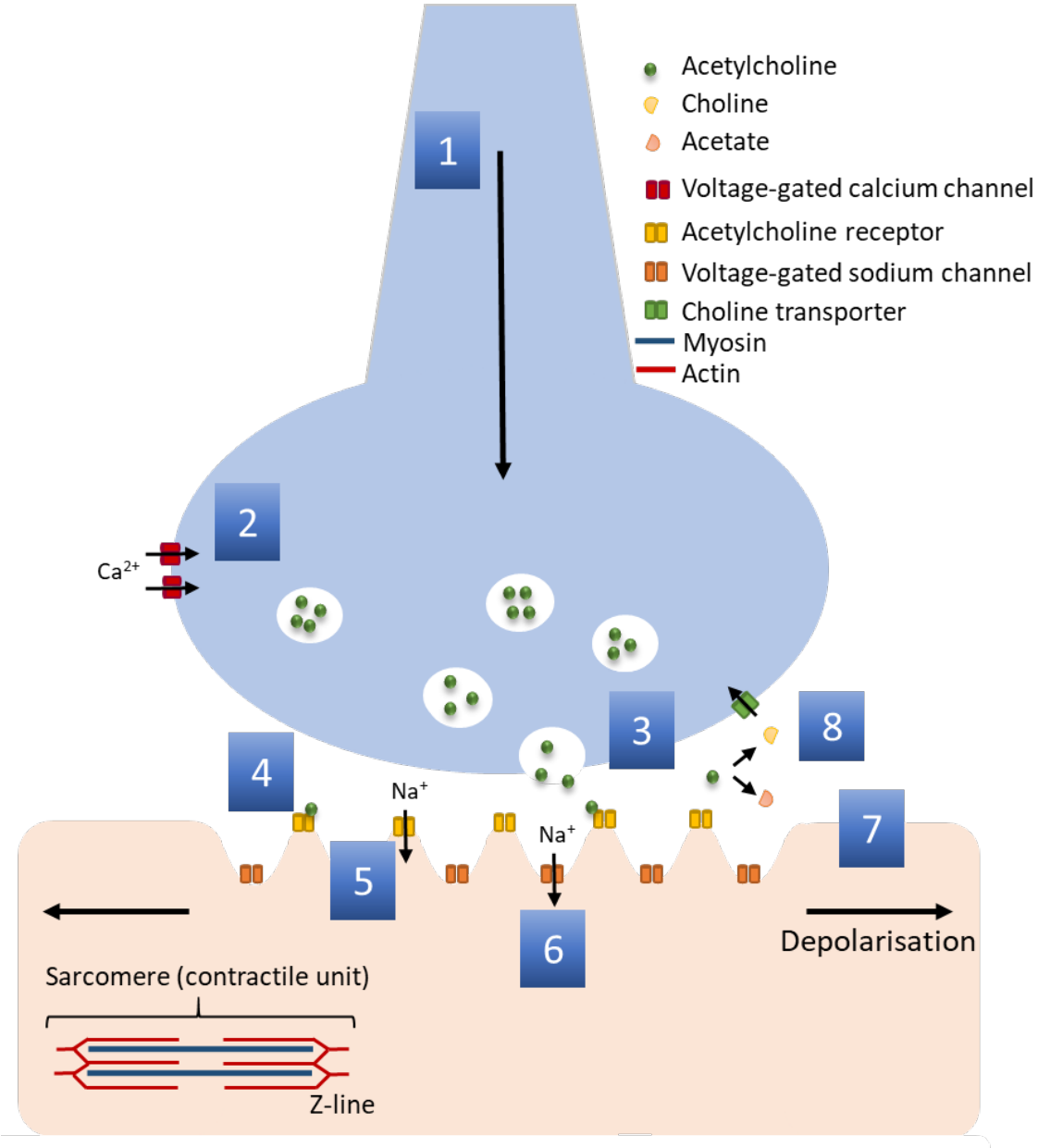

Figure 1.2. Signal transmission at the Neuromuscular Junction: 1) An action potential propagates down the motor axon, reaching the nerve terminal where it depolarises the membrane. 2) Voltage gated calcium channels open and there is an influx of Ca^{2+} into the cell. 3) An increase in intracellular Ca^{2+} initiates fusion of vesicles docked at active zones with the membrane and release of acetylcholine into the synaptic cleft. 4) Acetylcholine diffuses across the cleft and binds to acetylcholine receptors causing a change in pore configuration. 5) Na^{+} passes through the AChR into the postsynaptic muscle cell causing depolarisation of the muscle membrane. 6) Voltage-gated Na^{+} channels open and there is a further influx of ions and leading to the generation of an action potential. 7) The action potential propagates across the muscle membrane leading to muscle fibre contraction (contractile unit shown). 8) The effect of acetylcholine is short-lived as upon detaching from AChRs it is rapidly broken down by acetylcholinesterase in the synaptic cleft and one of its substrates; choline, is recycled back into the nerve terminal.

1.2.2 Development of the NMJ

The main aim of NMJ development is to form a highly efficient and reliable synapse which successfully converts action potentials from the nerve terminal into muscle contractions. This is achieved by complex developmental processes to create a number of pre and postsynaptic specialisations that optimise function and can adapt to physiological stress. These specialisations act to enforce a robust safety factor for signal transmission. The safety factor has been defined as ‘the amount of transmitter released per nerve impulse being greater than that required to trigger an action potential in the muscle fibre’ (Wood and Slater, 2001).

The features important for safety factor maintenance include a number of structures that can be viewed at the ultrastructural level, as indicated in the electron micrographs of Figure 1.3, such as a concentration of vesicles at the nerve terminal, a synaptic cleft containing a basal lamina to anchor a number of important proteins, postsynaptic folds which increase the surface area of the endplate, and an enrichment of receptors, ion channels and structural proteins at the postsynapse represented as dense material on the electron micrographs.

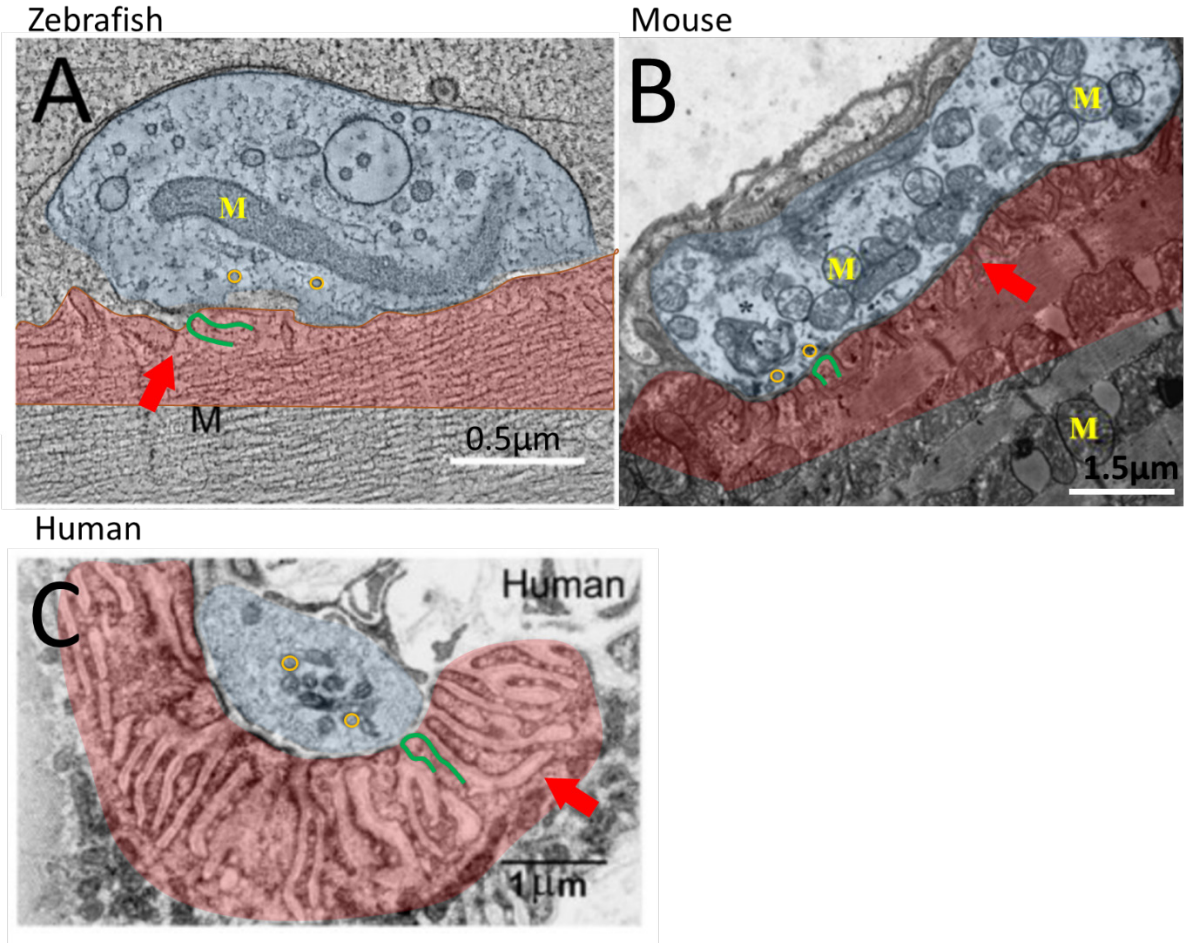

Figure 1.3. Electron micrographs of NMJs from zebrafish, mouse and human. Presynaptic nerve terminals are highlighted in blue and part of the postsynaptic muscle fibre is highlighted in red. Synaptic vesicles can be observed in each case, an example of which is outlined in orange, as well as clear postsynaptic folds in mouse (B) and human (C), as well as potential folds in zebrafish (A), indicated with red arrows. Mitochondria can also be observed (yellow M) and examples of postsynaptic densities lining the folds are shown in green. Images modified from: (Helmprobst et al., 2015, Issop et al., 2018, Slater, 2017).

Zebrafish NMJs, as studied in this project, have also been visualized using electron microscopy (Figure 1.3A). This revealed the presence of extensive synaptic vesicles, presynaptic mitochondria, cytoskeletal components, endosomal structures and vesicles docked at the active zone, connected with filamentous structures that have also been described in mammals (Jung et al., 2018, Helmprobst et al., 2015, Bruses, 2011, Westerfield et al., 1990). At 30 hours post fertilisation (hpf) the presynaptic terminal in zebrafish is large and the synaptic cleft is not well defined, however, by 3 days post fertilisation (dpf) a dense basal lamina structure can be identified and terminals are smaller and well-defined (Drapeau et al., 2001). The synaptic cleft is around 65nm wide in 4-8 dpf zebrafish, falling within the range of 50-100nm found in human junctions (Helmprobst et al., 2015, Slater, 2017). An as yet unclear feature of

zebrafish NMJs is the extent of post-junctional folding, which is extensive in human and mouse NMJs. Furthermore, terminal size and QC holds a positive correlation for most vertebrates, with humans having small terminal sizes and small QCs (20-30), whereas vertebrates such as frogs have large terminals and correspondingly large QCs (over 100) (Slater, 2015). However, in zebrafish measurements of QC and overall terminal size have not been performed in parallel, and thus whether they observe a similar trend is not known. Despite these differences, the gross morphology of zebrafish NMJs is similar to human and the relative ease in which the junctions can be studied and manipulated make them useful models for studying human NMJ diseases, especially those that affect early development.

Much of the current understanding regarding structure and function of NMJs originates from research that has been performed in the mouse, due to the accessibility and availability of tissue, as well as the multitude of murine disease models now available. As mammals they have a closer NMJ structure to humans than zebrafish, bearing more obvious postsynaptic specialisations and clearly defined AChR clusters forming individual endplates (Figure 1.3B). There remain some differences however, in features such as postsynaptic junctional fold lengths which are much longer in humans, terminal size which is smaller in humans and the QC of motor synapses is also smaller in humans than in mice (20-30 in humans vs 50-100 in mouse, Slater, 2015). Overall, however, the process of cholinergic signalling and the main structural components of zebrafish and mouse NMJs are similar to those found in humans and allow comprehensive analysis to be performed which would not otherwise be achievable. The development of such features is discussed in subsequent sections.

1.2.2.1 AChR cluster formation

Development of the NMJ begins prenatally in humans, mice and zebrafish. In mice and zebrafish, NMJ development has been observed to start with a process termed ‘pre-patterning’, in which aneural AChR clusters form over the surface of myotubes in a distinct position along the midline of the muscle and in the absence of any neural input (Yang et al., 2001). While muscles have an intrinsic capacity to form these AChR clusters, further specialisations and mature synapse formation require nervous input. Contact from motor neurons leads to the incorporation of aneural AChR clusters to form neural clusters and thus an immature synapse is formed. The purpose of aneural clusters in pre-patterning has been questioned due to the ability

of zebrafish to establish AChR clusters after developing on a muscle-specific kinase (MuSK)-null background, thus in the absence of aneural receptors (Jing et al., 2009). Furthermore, some NMJs in zebrafish form where aneural clusters were situated, whereas others form on previously unoccupied regions of muscle (Panzer et al., 2005). Nevertheless, in the presence of aneural receptor clusters subsequent release of ACh from the nerve terminal leads to the dispersal of surrounding AChRs and a concentration of receptors just at the NMJ. Localised synthesis of new AChRs also contributes to the receptor density (Sanes and Lichtman, 2001). Mature AChR clusters form directly opposite the ACh-releasing synaptic boutons of the innervating axon. These receptor clusters can be visualised by using a fluorophore-bound neurotoxin: aBTx, which can bind to AChRs (Anderson and Cohen, 1974). In humans, use of such tools reveals NMJs with multiple, distinct, round clusters of AChRs colocalising with terminal boutons. The presynaptic boutons are usually stained with antibodies against synaptophysin in mice and synaptic vesicle protein 2 (SV2) in fish (Panzer et al., 2005, Colasante et al., 1993). Whereas in mice these clusters are less distinct and merge to form a characteristic ‘pretzel’ configuration (Figure 1.4). Fish NMJs are less condensed, with long interconnected boutons forming across the muscle fibre, which is reflected in the spatial distribution of AChR clusters (Slater, 2017). NMJs can grow with developing muscle during postnatal life, achieved by the insertion of new AChRs to maintain a consistent receptor density (Slater, 1982, Balice-Gordon et al., 1990).

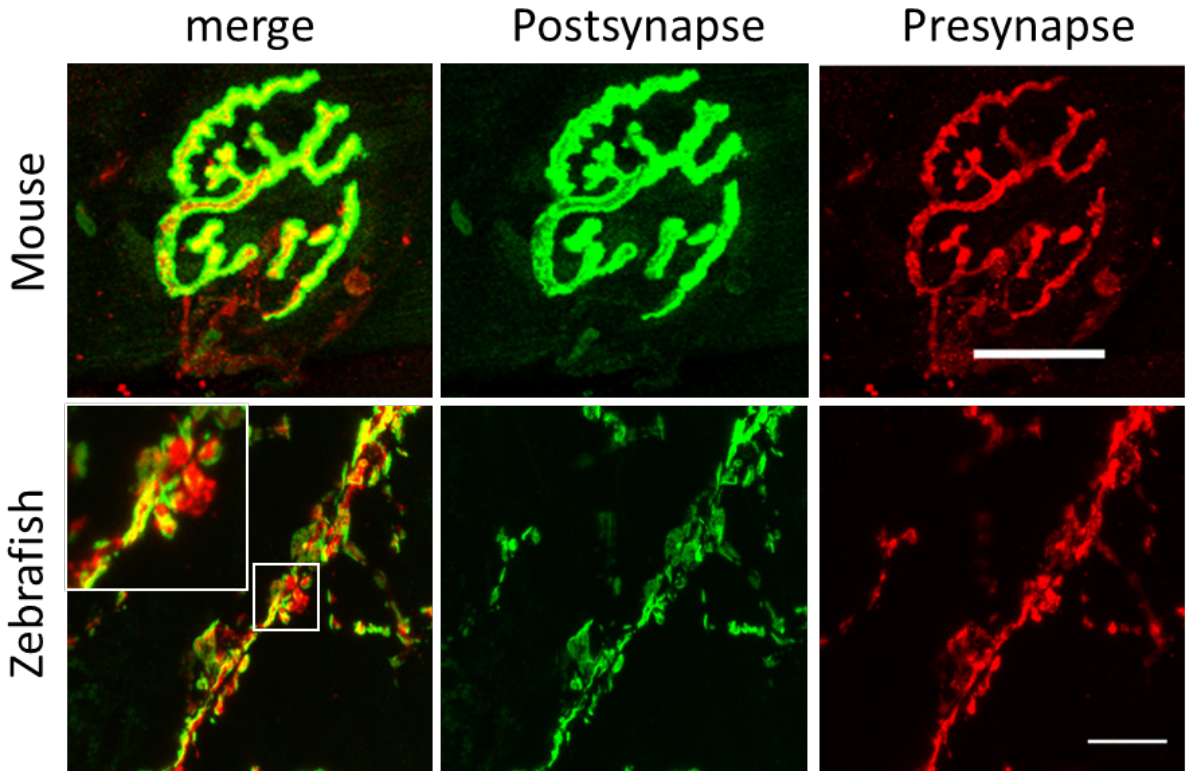

Figure 1.4. Mouse and zebrafish NMJs. Example of characteristic mouse pretzel shaped NMJs (10 months old) and zebrafish (5 dpf) NMJs, white box shows enlarged region. Presynapse stained with antibodies against SV2 (red) in zebrafish and synaptophysin with neurofilament (red) in mice. Postsynaptic acetylcholine receptors are stained with aBTx (green). Mouse scale bar = 25μm, zebrafish = 10μm.

Perhaps one of the most important events in NMJ development is the release of neural agrin, which acts to mediate these clustering events. Agrin is a heparin proteoglycan located in the synaptic basal lamina after it has been released from the nerve. Originally isolated from the electric organ of *Torpedo Californica* (Godfrey et al., 1984), agrin was later found to be present in the nerves, muscles and Schwann cells of mammals (Magill-Solc and McMahan, 1988), however, it has been demonstrated that neural agrin is 1000-fold more adept at inducing AChR clusters than muscle agrin (Gesemann et al., 1995). This key difference has been attributed to the secreted, neural isoform of agrin having an extra 8, 11 or 19 amino acid insert at a 3' splice site termed the z-site (Ruegg and Bixby, 1998, Tintignac et al., 2015). The receptor for agrin is Low Density Lipoprotein Receptor Related Protein 4 (LRP4), found on the muscle membrane in dimers (Kim et al., 2008). LRP4 is bound by MuSK, also present in dimers, and binding of agrin to this complex begins a cascade of events starting with MuSK self-phosphorylation and recruitment of Downstream of Tyrosine Kinase 7 (DOK7) and leading to the stable incorporation of AChRs (Inoue et al., 2009, Okada et al., 2006, Zhang et al., 2011, Bergamin et al., 2010). This

process is very important for NMJ development as mice lacking agrin are not viable and die at birth due to defective NMJ formation (although the presence of aneural receptor clusters is not affected) (Gautam et al., 1996, Lin et al., 2001). MuSK also affects other downstream pathways including the accumulation of rapsyn, which has been shown to cluster AChRs and other NMJ proteins important for synapse function. Concurrently, rapsyn deficient mice have AChRs that are spread out over the muscle fibre rather than concentrated in clusters (Gautam et al., 1995). Zebrafish also express these key proteins, including LRP4, MuSK, agrin and AChR subunits, and loss of such factors in the fish also affects signal transmission, NMJ structure and movement abilities (Kim et al., 2007, Remedio et al., 2016, Zhang and Granato, 2000, Zhang et al., 2004, Zhang et al., 2001, Park et al., 2014). While development of appropriate AChR clusters is a crucial part of NMJ formation, there are numerous other specialisations that take place to complete maturation of the synapse.

1.2.2.2 Innervation of NMJ and presynaptic specialisations

After establishment of the mature innervation pattern, further optimisation of the functional apparatus is required to produce an efficient and reliable synapse, as outlined in Figure 1.5. In the presynaptic nerve terminal active zones form, which are sites optimised for vesicular release of ACh with concentrated presence of exocytotic machinery (Jung et al., 2018). Nerves also start to release agrin and ACh to modulate AChR clustering as described above. There are likely to be many secreted proteins important for cross-talk at the NMJ and co-maturation of pre and postsynaptic regions. Another such group of identified factors is the Wnt family, which have demonstrated importance for concentration of presynaptic vesicles and maintenance of appropriate terminal size. In addition, blocking Wnt secretion is associated with reduced postsynaptic folds. This effect results collectively in impaired neurotransmission in mice (Shen et al., 2018). Similarly, Wnt signalling also plays a role in development of zebrafish NMJs, as Wnt11r is important for AChR pre-patterning and guidance of growth cones to the appropriate muscle region, thus affecting both the pre and postsynapse (Jing et al., 2009).

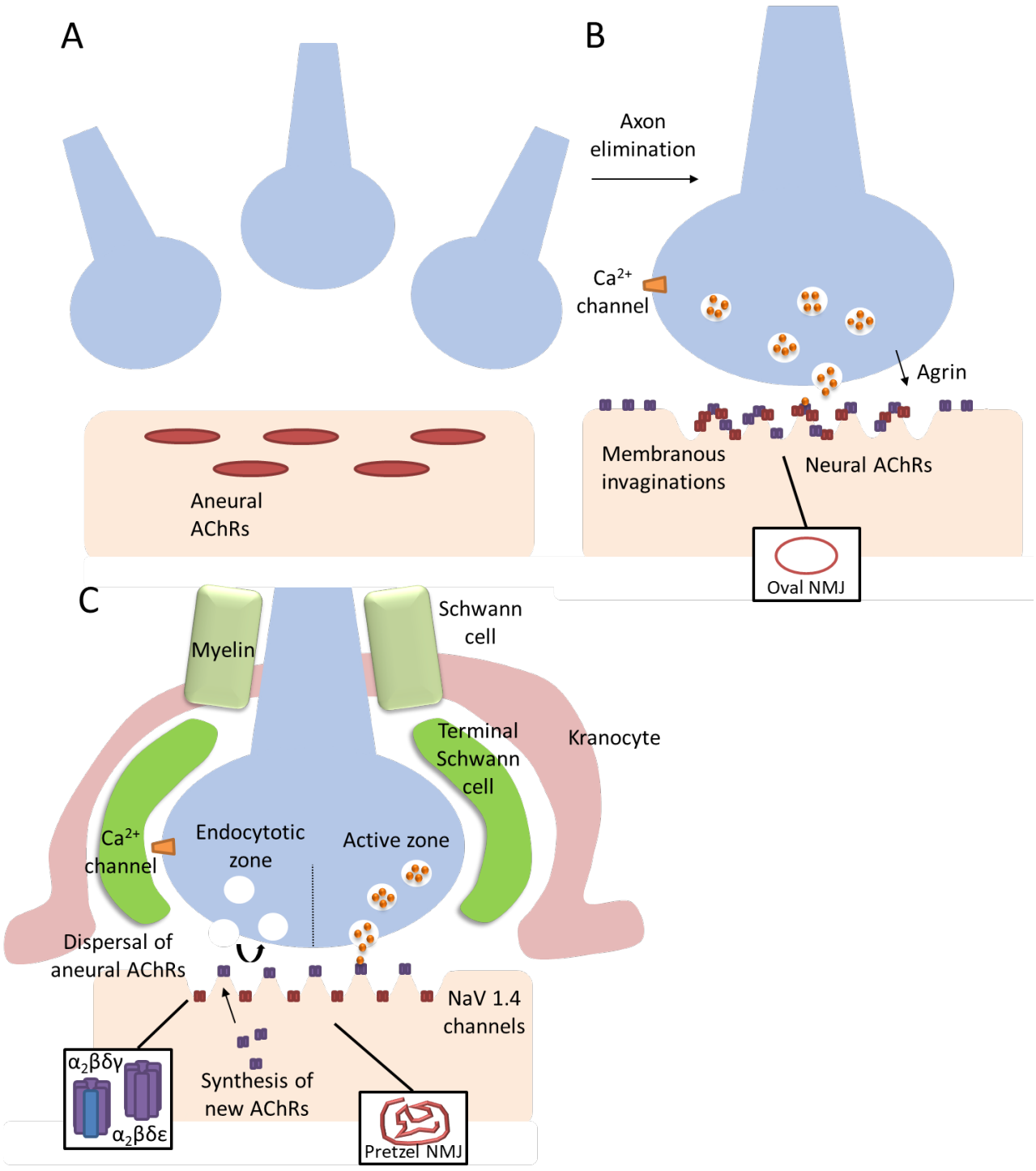

Figure 1.5. Formation and maturation of the neuromuscular junction: A) Motor axons extend from the ventral spinal cord and branch to form many small varicosities that lie in proximity to the muscle fibre. Many axons may innervate a single immature NMJ at this stage in development, competing for sole occupation. On the muscle fibre there are aneural AChRs formed in a pre-patterning process. B) Axons are eliminated during development until only one innervates each muscle fibre, and there is only one NMJ per fibre. Membranous invaginations are also formed to vastly expand the surface area of the muscle endplate and aneaural AChRs are incorporated to form neural clusters in response to the release of neural agrin. The NMJ at this stage takes on an oval conformation that gradually becomes more complex during development. C) The release of ACh from the presynapse causes the dispersal of surrounding aneural AChRs that have not been incorporated. The

presynaptic apparatus also segregates into distinct active zones, from which ACh is released, and endocytotic zones. On the postsynaptic membrane the AChRs and voltage-gated Na^+ channels segregate to the peaks and troughs of the invaginations respectively, to minimise the diffusion distance for ACh from the active zones. The AChRs also demonstrate an alteration in their subunit conformation, replacing the γ subunit for ε, thus forming the adult receptor. During development there is perforation of the AChR clusters, as well as an insertion of new and extrasynaptic receptors that lead to the formation of a pretzel-like postsynaptic structure (in mice). After birth there is also myelination of the motor axons to allow for fast salutatory conduction and terminal Schwann cells encapsulate the nerve terminal providing metabolic support and signalling interactions. Kranocytes also localise to the NMJ, capping the synapse in postnatal development.

Maturation of the NMJ is not complete at birth and continues into early postnatal life, with a series of pre- and postsynaptic changes mediated by numerous factors which facilitate the development of movement. In mice, the innervation pattern of muscle fibres by motor axons alters during early postnatal development, but is complete before birth in humans. Initially there is a rich neural innervation of fibres (Figure 1.5A), followed by significant elimination of axons during a highly dynamic phase of competition that takes place until only one axon per muscle fibre remains, allowing for very specific control of muscles (Gan and Lichtman, 1998, Walsh and Lichtman, 2003). While the NMJ is a cholinergic synapse, recent research has also implicated a role for glutamatergic signalling in the elimination of excess axons, as blockade of glutamate slowed elimination and application of exogenous N-methyl-D-aspartate accelerated the elimination process (Personius et al., 2016). During this stage of maturation it can be observed that the alignment between pre- and postsynaptic apparatus is not perfect, motor axons often project beyond AChR clusters. However, following the pruning process the nerve terminal and postsynaptic region are precisely apposed. The colocalisation of pre and postsynaptic areas can be measured to determine whether any defects in this process have occurred, as misalignment may result in less ACh binding AChRs, thus affecting postsynaptic depolarisation.

Myelination of motor axons by Schwann cells also occurs in early life, facilitating fast salutatory conduction of action potentials. Appearance of terminal Schwann cells is also important for the external environment of the NMJ, with interaction of many growth factors and signalling molecules, muscle fibres and nerves taking place (Figure 1.5C). A fourth cell type is also present at the NMJ, the kranocytes, which cover the terminals during postnatal development and are reactive to physiological changes within the neuromuscular system, such as paralysis (Court et al., 2008).

Further changes to the NMJ occur, with the nerve terminal separating into distinct compartments. The endocytic regions alternate with active sites to allow alignment of ACh releasing regions with receptor rich domains on the crests of folds in the postsynaptic NMJ, which enhances synaptic transmission (Figure 1.5C, Matthews-Bellinger and Salpeter, 1983). The molecular events responsible for these presynaptic maturation steps are not fully understood, however there have been a number of important factors identified. For example, loss of the main subunit present in all synaptic laminins (laminin β2) leads to defective synaptic vesicle clustering, less active zones, a reduction in QC, as well as invasion of terminal Schwann cell processes into the cleft, thus less efficient synaptic signalling (Noakes et al., 1995, Knight et al., 2003).

1.2.2.3 Postsynaptic specialisations

As discussed above, the postsynapse forms folds to extend the surface area of the endplate, thus increasing the amount of membrane in contact with the synaptic region. AChRs become localised at the top of junctional crests. This places the receptors as close to the active zones as possible thus reducing the diffusion distance for ACh across the synaptic cleft (Figure 1.5B). There is also segregation in the folds between AChRs and voltage-gated Na^+ channels, the latter of which become localised to the junctional troughs (Figure 1.5C, Flucher and Daniels, 1989). This has been suggested to provide a route for signal amplification between nerve and muscle, which could explain, for example, why folds are extensive in human NMJs that have relatively small QCs (Slater, 2017). The folds are thus crucial determinants for the safety factor, which could be affected by a reduction in folding, AChR number or localisation, or concentration of Na^+ channels, therefore preventing depolarisation from reaching action potential threshold.

Further specialisations to the postsynapse include changes in AChR subunit composition during synaptic maturation, with the γ-subunit being replaced by the ε-subunit to form the adult receptor (from α2βγδ to α2βδε, Figure 1.5C, Mishina et al., 1986). The change in receptor configuration leads to shorter burst durations but an accompanying increase in Na^+, K^+, and Ca^{2+} conductance (Mishina et al., 1986, Villarroel and Sakmann, 1996). Zebrafish express the same AChR subunits as mammals in their most abundant muscle type, fast muscle. However, on slow muscles it has been postulated that zebrafish express an AChR receptor lacking both ε and γ subunits, containing only α,β and δ (Mongeon et al., 2011). Finally, a recent

role for rapsyn as an E3 ligase has been reported, which confers the ability of this protein to increase AChR subunit neddylation at the NMJ (Li et al., 2016). This was found to stimulate AChR clustering and could be further activated by agrin, thus expanding on the known roles of rapsyn and possible mechanisms by which AChR stability is mediated. While it is clear a number of important changes occur during development to form NMJs, many of these pathways are also crucial for the continued function of this synapse in adult muscle.

1.2.3 Maintenance of the NMJ

Signal transmission at the NMJ is required throughout life for all actions requiring movement of skeletal muscle, therefore maintenance of this synapse after development and maturation is important. During development, AChRs are inserted into the endplate membrane after which they are endocytosed and either targeted for degradation and replacement by a new receptor, or recycled back to the surface. In newly formed synapses this process is rapid, with AChR half-life only around 1 day. In adult synapses this extends significantly to around 10 days, highlighting the increased stability of endplate AChRs in vertebrates following development (Bruneau et al., 2005, Cohen et al., 1990, Yampolsky et al., 2010, Burden, 1977). The purpose for prolonged AChR half-lives has not been fully elucidated, however, it has been suggested that the process of receptor internalisation itself acts as a means to degrade defective AChRs and insert new, fully functional receptors (Yampolsky et al., 2010). Thus any defects in receptor endocytosis, degradation or recycling may affect the density of AChRs and proportion of functional receptors at the postsynapse. Proteins implicated in maintaining balance of inserted/recycling/degrading receptors include those that interact with the cytoskeleton such as Myosin Va, important for recycling of AChRs back to the surface (Roder et al., 2008), and rapsyn which plays a crucial role in AChR stability (Gervasio et al., 2007). Microtubule Actin Crosslinking Factor 1 (MACF1) has also recently been shown to regulate postnatal AChR cluster size in mice, through interaction with the cytoskeleton and rapsyn (Oury et al., 2019). The action of neural agrin is also necessary for the longer-term stability of AChRs in adult synapses, as well as its role in forming receptor aggregations during development (Bezakova et al., 2001, Samuel et al., 2012). Similarly, Agrin's receptor LRP4 is required for NMJ maintenance as knockout from adult mice leads to shortening of junctional folds and less synaptic vesicles, with a corresponding reduction in mEPP frequency and amplitude (Barik et al., 2014). Another component

of the agrin-LRP4 pathway is MuSK, and similarly removal of MuSK from the postnatal synapse leads to loss of AChRs, thus highlighting the continued importance for these proteins throughout life (Hesser et al., 2006).

As well as the contribution of proteins known to be important for NMJ development in maintenance of this synapse, such as agrin and LRP4, a number of other proteins may be involved in NMJ stability in the adult. For example, in the laminin family of proteins laminin β2 is critically important for presynaptic maturation and absence of laminin α5 delays differentiation of the NMJ but its loss does not affect the adult synapse (Nishimune et al., 2012, Noakes et al., 1995). On the other hand, laminin α4 has been shown to have minor effects on developing NMJs but is important for maintaining presynaptic morphology in adult mice (Samuel et al., 2012). Overall, the continued presence, and involvement of new proteins toward the maintenance of NMJ structure and function is required throughout life.

Further to these classical pathways involved in NMJ development and maintenance, recent data has drawn on observations from the early 1900's that sympathetic innervation is also present at the NMJ. Presynaptic vesicle release, muscle contraction force and AChR levels were all found to be modulated by sympathetic innervation, thus highlighting the complexity of NMJ development and function (Khan et al., 2016, Rodrigues et al., 2019). Close association of NMJs with sympathetic neurons has been demonstrated and this increases during postnatal development (Straka et al., 2018). Furthermore, β-2 adrenoceptors partially colocalise with AChRs (Khan et al., 2016). Activation of these adrenoceptors by sympathetic innervation, or application of agonists, causes an elevation of cyclic adenosine monophosphate and a downstream increase in AChR expression at the NMJ (Khan et al., 2016, Legay and Mei, 2017). Therefore, it is apparent that not only innervation from motor neurons is important for functioning of the NMJ. The inherent complexity of NMJ development and maintenance exposes numerous areas in which dysfunction may lead to disease.

1.3 Disorders of the NMJ

The safety factor of the NMJ allows signalling to occur reliably as physiological conditions and demands change. This ensures that neural signalling results in a muscle contraction for that motor unit when required, even during periods of intense exercise. The complex nature of NMJ development and maintenance contributes to the formation of this safety factor, thus defects in any of a number of proteins

involved in this process may affect its efficacy. The safety factor of mammalian NMJs is estimated to be between 2 and 10, indicating that there is at least twice as much neurotransmitter released than required to stimulate a postsynaptic response (Wood and Slater, 2001). Despite this flexibility, an impairment in any part of the pathway between the action potential arriving at the nerve terminal and postsynaptic muscle contraction that reduces the safety factor to below this threshold can affect efficiency of signal transduction and thus cause disease.

Disorders of the NMJ can be caused through genetics, autoimmune diseases or through influence of environmental factors such as toxins. Toxins that affect the NMJ include aBTx, present in snake venom, which binds to the α subunit of the AChR. The relatively irreversible binding of this toxin prevents signalling and leads to paralysis of the muscle (Furman, 2018). However, the use of aBTx bound to a fluorophore is also a valuable tool for the study of NMJs by providing a reliable label for the postsynaptic AChRs as demonstrated in Figure 1.4. Impaired signalling at the NMJ also occurs due to disease, termed the Myasthenic syndromes. These are a group of disorders that manifest with fatigable weakness of the skeletal muscles. Myasthenias are most commonly autoimmune (Myasthenia Gravis), in which patients acquire antibodies against key components of the NMJ such as AChRs or MuSK (Meriggioli and Sanders, 2009). A rare class of genetically determined myasthenias also occurs, termed CMS. CMS are caused by mutations in genes encoding proteins that act to maintain this safety factor and conduct successful NMJ signalling, of which there are now over 30 reported proteins implicated in the disease (Finsterer, 2019, Rodriguez Cruz et al., 2018).

Other diseases that are not considered primarily disorders of the NMJ can also demonstrate impairment of the safety factor as part of their pathology. These include the much more common neurological disorders such as amyotrophic lateral sclerosis (ALS), whereby defective NMJs have been found early in disease progression with features such as reduced synaptic vesicle populations (Cappello and Francolini, 2017). Diseases primarily characterised by myopathic changes can also show impaired NMJ signalling, including Muscular Dystrophies. For example, mouse muscular dystrophy models (*mdx* and *mdx/utrn*$^{-/-}$) exhibit smaller mEPPs and NMJ fragmentation, with a compensatory increase in QC (van der Pijl et al., 2016). Therefore, understanding more about the structural and functional components that are important in the maintenance of the safety factor and thus ability to perform

voluntary muscle movements will have widespread implications for a number of diseases.

1.3.1 Congenital Myasthenic Syndromes

Patients with CMS present with a heterogeneous set of phenotypes, largely dependent on the genetic basis underlying that individual's disorder. The disease is characterised by fatigable skeletal muscle weakness (and sparing of smooth/cardiac muscles), however, even this feature can vary considerably in the muscle affected and severity of weakness. Commonly affected muscles include the proximal and distal limb muscles, bulbar muscles involved in eating and speaking, ocular muscles for eye movements and the respiratory muscles. An effect on the respiratory muscles can cause potentially life threatening episodes of apnoea requiring hospitilisation and ventilation (McMacken et al., 2018b). Age of onset can be as early as *in utero*, manifesting as reduced foetal movements, or mild adult onset of symptoms and anywhere in between, although onset is usually in early childhood (average age 3.6 years Jagtap et al., 2013). Patients may also have other atypical phenotypes such as CNS abnormalities, epilepsy or neuropathy (Finsterer, 2019, Rodriguez Cruz et al., 2018).

1.3.1.1 Clinical diagnosis

A clinical diagnosis of CMS can be suspected based on the presence of muscle weakness, family history of CMS, absence of auto-antibodies for NMJ components and electrophysiological investigations. These include repetitive nerve stimulation and single fibre electromyography (EMG). Repetitive nerve stimulation is a technique in which supramaximal electrical stimulation of a motor neuron is performed to elicit a reliable postsynaptic response in the target muscle, a compound muscle action potential (CMAP). The safety factor of the NMJ ensures a consistent CMAP amplitude in healthy muscle. Therefore, in diseases such as CMS where the safety factor is impaired, the amplitude of the CMAP can vary (Pitt, 2018). This can depend on the location of the defect, although clear distinction between pre and postsynaptic CMS is not always possible. For example, in cases of postsynaptic protein involvement in disease, a decrease in CMAP amplitude can be observed and this is generally considered pathological if the decrement is over 10%. Conversely, in presynaptic CMS there can be a smaller initial CMAP amplitude, followed by an

increment when stimulation frequency increases due to increased terminal calcium levels (McMacken et al., 2018b).

Single-fibre EMG records from fibres within the same motor unit and allows the difference in latency from stimulation to muscle fibre action potential to be observed. Variation in latency is termed jitter and in disorders such as CMS there can be increased jitter or impulse blocking (in which no action potential is elicited) due to impairment of signal transmission from the nerve to muscle (Howard, 2013).

1.3.1.2 Genetic diagnosis

After a clinical diagnosis of CMS is made, a genetic diagnosis is important for understanding which treatments may be applicable for a patient. The phenotypic profile of the patient may provide strong evidence suggesting mutations in a specific established CMS gene, allowing single genes to be sequenced for mutations. For example, if a patient presents with only typical NMJ-associated phenotypes and has ophthalmoplegia, then the most common cause of CMS is due to mutations in the Cholinergic Receptor Nicotinic Epsilon Subunit (*CHRNE)* gene encoding the AChR Ɛ subunit (Rodriguez Cruz et al., 2018). In the case where screening known genes is not successful or there are no clear phenotypic clues, whole exome or genome sequencing can be undertaken to identify novel mutations in known genes, or potentially new candidate genes for CMS (for example; Azuma et al., 2017, Cossins et al., 2013, Logan et al., 2015, O'Connor et al., 2016). This approach is particularly useful when genetic data from parents is also available for analysis.

1.3.1.3 Treatment approaches

Treatment approaches for CMS vary depending on the nature of the NMJ dysfunction, however, a few options are available that can reduce symptoms in a number of patients (Figure 1.6, Thompson et al., 2019). In general, AChE inhibitors, which prolong the presence of ACh at the synaptic cleft, can show benefit if the defective protein is part of the glycosylation network but not part of the LRP4/MuSK pathway. This family of drugs is often administered along with 3,4-Diaminopyridine (DAP) which blocks presynaptic potassium channels thus increasing intracellular calcium and subsequent ACh secretion (Wirtz et al., 2010). Therefore, this drug often shows efficacy in disorders resulting in less stimulation of the AChRs (including presynaptic CMS, Engel, 2007). Sympathomimetic drugs, including the β-2

adrenoceptor agonist Salbutamol, have also shown beneficial effects in CMS patients such as those with mutations in *Dok7, CHRNE* and *MuSK* (Finsterer, 2019). The reason sympathomimetic drugs can provide symptomatic improvement to patients is as yet unknown, although recent efforts have been made to uncover more about the action of these drugs at the NMJ. These include *in vitro* analysis of C2C12 cells demonstrating an increase in AChR cluster number after salbutamol treatment, improvement in zebrafish AChR clustering and motility and beneficial effects to the postsynapse in a CMS mouse model (Clausen et al., 2018, McMacken et al., 2018a, McMacken et al., 2019). AChR open channel blockers, such as Fluoxetine, have variable effects but tend to provide improvements in slow-channel syndrome (characterised by prolonged acetylcholine receptor ion channel activation) cases. Although such compounds can have serious side effects including severe hypotension and serotonergic crisis (Chaouch et al., 2012).

While a number of treatments can be used for CMS, they show variable efficacy and sometimes detrimental effects in different subtypes, as well the presence of a number of associated side-effects (Engel et al., 2015). Therefore, there is a pressing requirement for greater understanding of the genetic defects involved in NMJ transmission disorders, pathways of action and specific effects on the various components of the NMJ, in order to develop more targeted treatments for patients.

1.3.1.4 CMS genes

To date 33 genes have been reported to cause CMS, each encoding proteins that provide structural or functional support to the safety factor of the NMJ (Finsterer, 2019). Proteins are generally classified as presynaptic, synaptic, postsynaptic or part of the glycosylation pathway, as outlined in Figure 1.6.

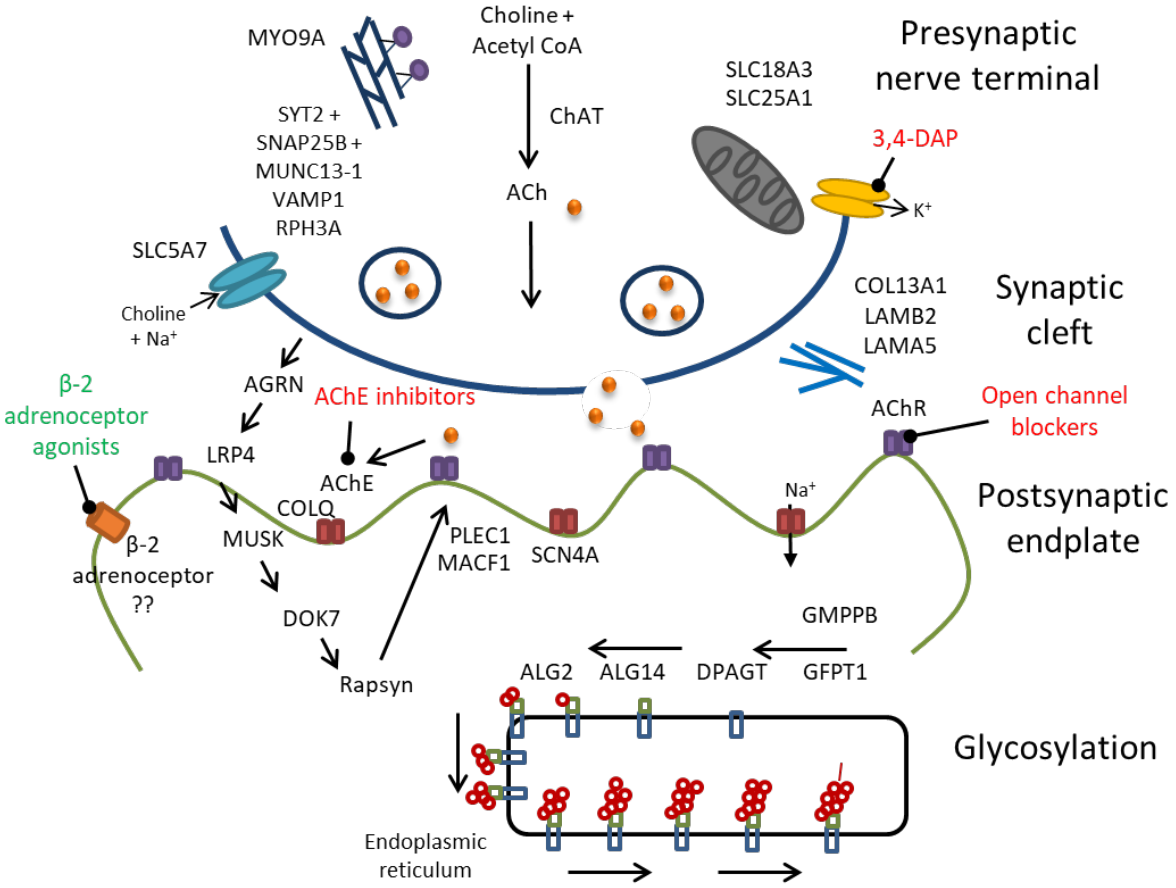

Figure 1.6. Localisation of proteins implicated in CMS at the NMJ. Schematic of pre, synaptic and postsynaptic NMJ displaying localisation and general pathway of reported CMS genes, including the ubiquitously expressed glycosylation proteins. Commonly used classes of drug used to treat CMS are also shown, along with their site of action. The presence of β-2 adrenoceptors and site of agonist action has not been confirmed. Red = antagonist/blocker, green = agonist.

The first identified genetic cause of CMS were mutations in the *CHRNE* gene encoding for the AChR Ɛ subunit (Gomez and Gammack, 1995, Ohno et al., 1995). To this day, defective AChR subunit proteins remain the cause of the most prevalent subtypes of CMS, and genes encoding proteins involved in clustering AChRs and postsynaptic specialisations are also commonly identified with mutations in CMS patients such as *DOK7* and *RAPSN* (Finsterer, 2019). Therefore, the majority of CMS cases are caused by proteins affecting AChR signal transmission at the postsynapse. The most prevalent presynaptic CMS subtype is that due to mutations in *CHAT*, which is the gene encoding for the enzyme (ChAT) responsible for ACh synthesis in the nerve. Other presynaptic genes encode for proteins implicated in ACh vesicle release, which would clearly affect the safety factor of the NMJ by reducing release probability or dynamics (Finsterer, 2019). Within the last decade, mutations in genes encoding ubiquitously expressed glycosylation proteins have been identified and research is ongoing to uncover how proteins with widespread expression manifest

with a primarily neuromuscular pathology (Belaya et al., 2012, Cossins et al., 2013, Selcen et al., 2014, Senderek et al., 2011). Recently, a number of cytoskeletal and structural proteins have also been identified with involvement in CMS, including MYO9A, MACF1, PLEC, COL13A1 and PREPL, highlighting that proteins not directly involved in the transmission of ACh from nerve to muscle may be important (Oury et al., 2019, O'Connor et al., 2016, Logan et al., 2015, Regal et al., 2014, Selcen et al., 2011). An association network of the proteins currently identified as defective in CMS patients is shown in Figure 1.7. Proteins are linked according to evidence suggesting they work toward a common function (rather than physical interaction), as predicted by STRING (Search Tool for the Retrieval of Interacting Genes/Proteins) analysis (Szklarczyk et al., 2019). Groups of proteins that cluster together are highlighted and form the subsets often used to define CMS: ACh synthesis and release, postsynaptic specialisations, postsynaptic transmission and glycosylation. A number of proteins do not fall directly within one of these clusters, but are nevertheless important for pathology as the genetic causes for this group of diseases expands.

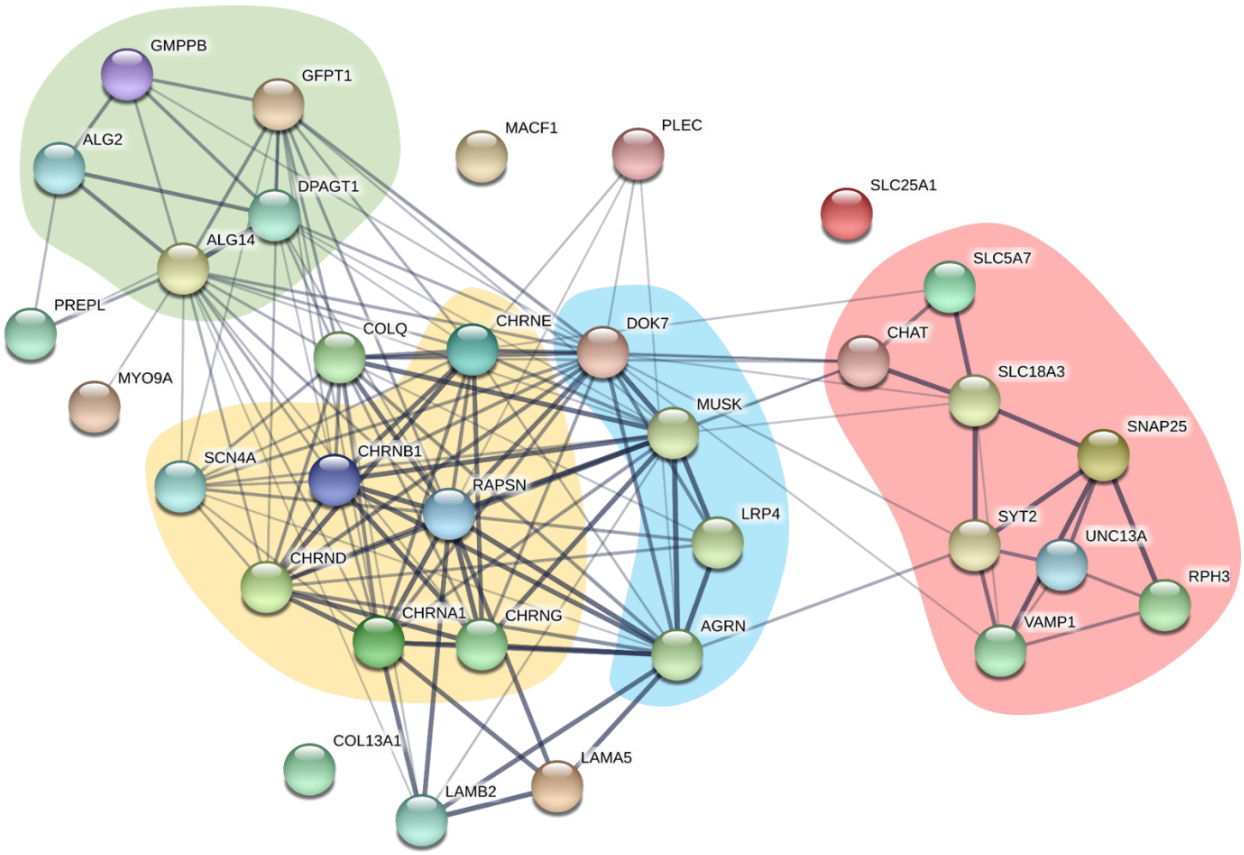

Figure 1.7. Interaction network of proteins implicated in CMS. Proteins that have found to be defective CMS are shown in an association network. Line thickness represents confidence that two proteins work toward a similar function (rather than a physical interaction). Clusters in red represent proteins implicated in ACh synthesis

and release, those in blue are involved in postsynaptic specialisations, yellow proteins are involved in postsynaptic transmission and glycosylation-related proteins are highlighted in green. Data based on text mining, databases, gene fusion, co-expression, co-occurrence, experimental evidence and gene neighborhood data as outlined on STRING v11.0 (**https://string-db.org, last accessed** 29.03.2019).

Despite the advent and increasing use of genetic techniques such as whole exome and whole genome sequencing, between 20-40% of CMS patients remain without a genetic diagnosis indicating there are still further novel causative genes to be identified (Thompson et al., 2019). By expanding the protein association network to include closely related proteins, further insight may be gained regarding potential candidate proteins playing roles in NMJ physiology or disease. In Figure 1.8, proteins predicted to influence the same function as the reported CMS proteins are shown. This highlights a number of presynaptic components that may be implicated in ACh synthesis and release. Roles for ubiquitously expressed or extracellular proteins are being increasingly recognised as important for CMS, and highlighting this, a number of glycosylation and extracellular matrix proteins were also identified. As the genetic landscape for CMS expands, it remains important to investigate novel genes using *in vitro* and *in vivo* models to assist in assigning causality to genetic defects and understanding more about the pathways involved in the disease.

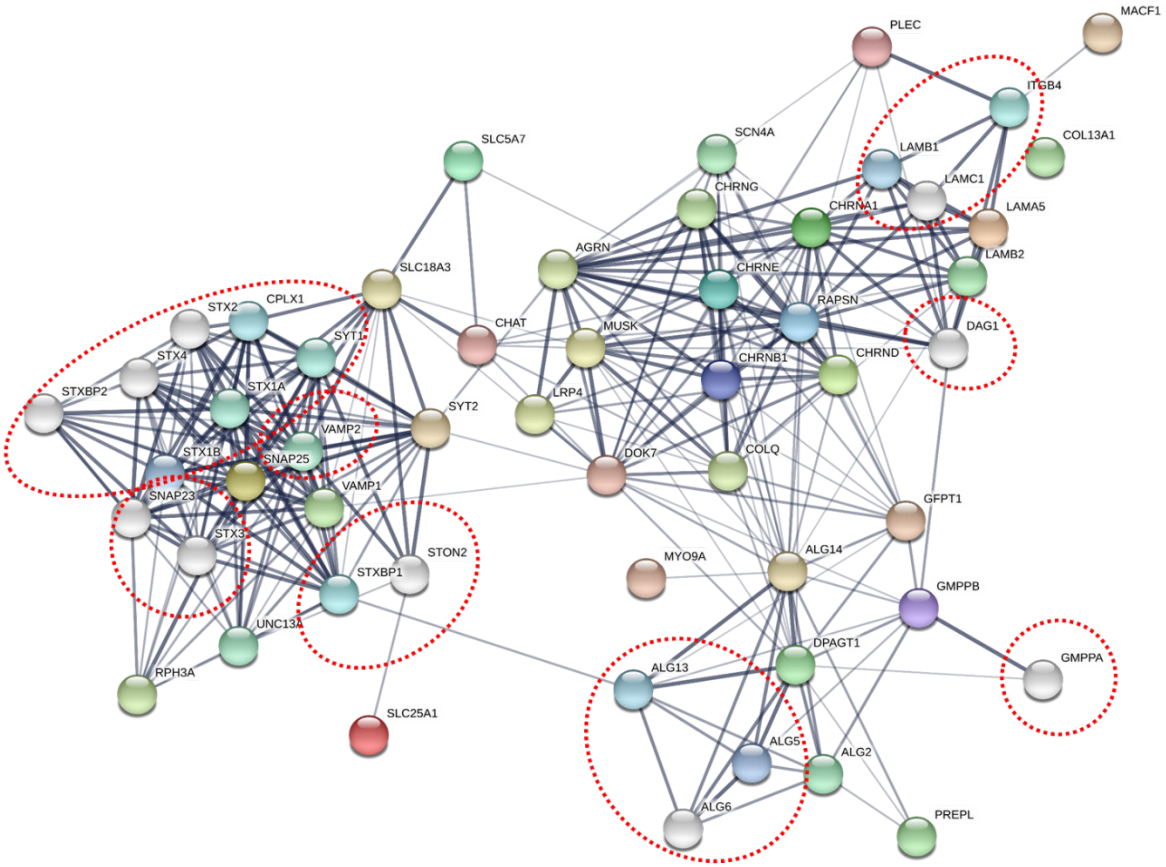

CMS protein cluster	Protein not previously implicated in CMS
Extracellular matrix	ITGB4 LAMC1 LAMB1
AChR clustering and transmission	DAG1
Presynaptic ACh synthesis and release	STXBP1 STX1B STX3 STX1A STX2 STXBP2 STON2 SNAP23 VAMP2 SYT1 CPLX1 STX4
Glycosylation	GMPPA ALG6 ALG5 ALG13

Figure 1.8. Association network of proteins implicated in CMS, including interacting proteins. STRING diagram showing clustering of CMS proteins with interacting proteins included. Line thickness represents confidence that two proteins work toward a similar function (rather than a physical interaction). Red dashed circles encompass proteins not previously associated with CMS and are listed in the table under the heading of the CMS protein cluster they fall within.

1.4 Models used to investigate CMS

Investigation of rare diseases such as CMS are greatly facilitated by the advent of *in vitro* and *in vivo* models. These can be used for investigating molecular mechanisms, modelling patient mutations, functional analysis of movement and NMJ signalling, as well as for trialing drug treatments and novel therapeutic strategies.

1.4.1 Cell models for CMS

A multitude of cell models have been used in CMS research, usually to analyse the effect of a particular patient mutation on protein function. The cell models used in studies of CMS proteins are shown in Figure 1.9. The vast majority of *in vitro* analysis related to CMS is undertaken using the immortal human embryonic kidney cell line HEK293, likely due to the ease of culturing and transfection of these cells making them amenable to screening of multiple patient mutations. Most of the studies using HEK293 cells performed analysis of AChR kinetics, thus demonstrating the benefit of these cells if mutations in genes are expected to affect AChR function. A number of studies also utilised C2C12 cells, an immortilised mouse skeletal muscle cell line. The C2C12 cells are initially myoblasts which can be differentiated into multinucleated myotubes over a period of 5-7 days. The myotubes express the subunits of AChRs and can be stimulated by agrin to form clusters along the surface of the myotubes (Ferns et al., 1996). Therefore, C2C12 cells are particularly suited to analysis of AChR clustering dynamics, which was assessed in 5 of the 7 publications identified. Surprisingly, only 4 studies used neuronal cell-lines, while 7 used the fibroblast-like cell-line: COS. However, the majority of experiments involving COS cells were performed to analyse protein expression and improper splicing due to patient mutations, rather than NMJ-specific functions or pathways.

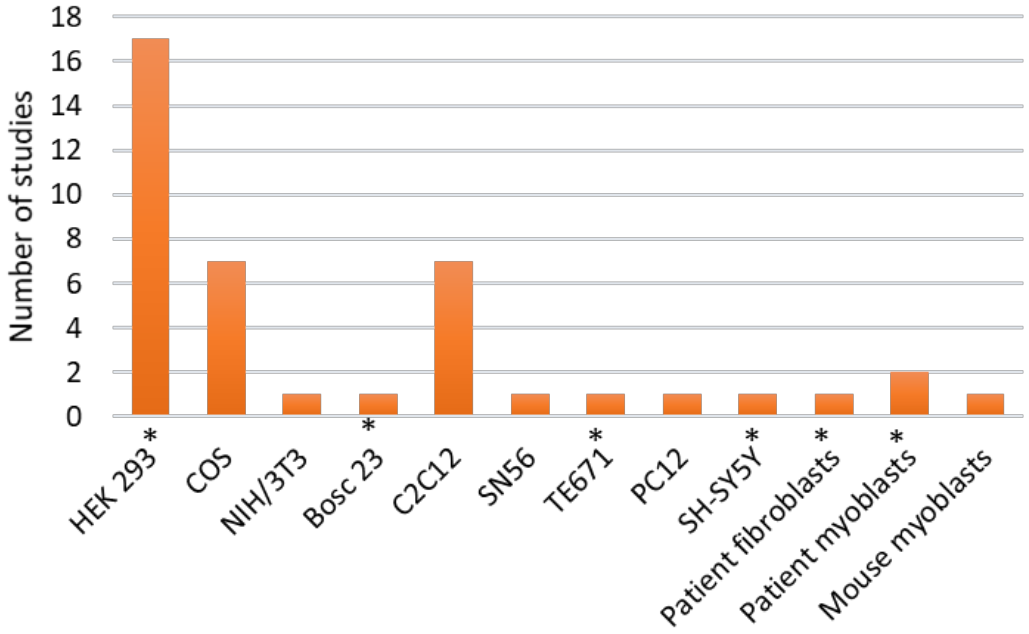

Figure 1.9. Cell models used for studying CMS genes. Graph depicts the number of studies that have used each cell type for study of molecular function of identified CMS genes. Some studies used more than one cell type thus are included in multiple categories, total study number is 38. Only studies explicitly studying the role of the protein in the context of CMS were included. Cell-lines from human sources are denoted with an asterisk.

Analysis of cells from patients can be useful as further genetic manipulation is not required and expression of the variants of interest are present on the genetic background of the patient. However, patient cells are often unavailable. Only 3 publications noted the use of patient cells, however, proteomic analysis revealed that myoblasts/myotubes of humans express almost all of the CMS-related proteins, including all of the AChR subunits and postsynaptic specialisation-associated proteins (O'Connor et al., 2018b). As the use of direct conversion protocols becomes more widespread, the use of patient cells may increase. Obtaining fibroblasts from patients is the least invasive procedure commonly performed for sample collection, but fibroblasts are likely not the ideal model for an NMJ disorder. If they were converted into myoblasts or induced neuronal progenitor cells (iNPCs), then they would be more functionally relevant and would expand the possibilities for performing *in vitro* experiments (Wakao et al., 2017, Meyer et al., 2015). Cell models are valuable for analysing effects of patient mutations on protein expression and ion channel kinetics, and models related to muscle or nerve have further benefits due to the ability to assess integrity of pathways important for NMJ development such as neurite extension in nerves or AChR clustering in muscles.

1.4.2 Zebrafish models of CMS

In order to understand more about the contribution of CMS-related proteins to the functioning of the NMJ, and how defective proteins may cause the disease, animal models are required. Multisystem models, rather than cells, are particularly important for studying CMS disease mechanisms as patients present with a range of phenotypes that affect not only different muscles but also other tissues. Furthermore, a number of CMS-related proteins are expressed ubiquitously, and using animal models may shed light on the selective NMJ pathology related to many of these proteins. *In vivo* studies are also useful in designing and testing novel therapeutic strategies and preparing preclinical data that may support future clinical trials in patients.

There are a number of invertebrate models that have been used to assess proteins associated with CMS, such as *Caenorhabditis elegans* (*C.elegans*) and *Drosophila melanogaster*. For example, an LRP4-null *Drosophila* model revealed a decrease in excitatory synapse number and disruption of active zone structure, and a MuSK-deletion *C.elegans* mutant showed mislocalised AChR subunits, disrupted channel currents and impaired localisation of cholinergic synaptic vesicles (Francis et al., 2005, Mosca et al., 2017, O'Connor et al., 2018b). Use of such models offers many benefits, including their small size, ability to screen many animals rapidly and access to the complete lineage of developing cells in *C.elegans,* allowing cells to be traced through development. Furthermore, many of the proteins involved in molecular events at the NMJ, such as transmitter release machinery, are conserved (Ackermann et al., 2015).

Vertebrates are more commonly used to generate disease models for the NMJ, as they are evolutionarily closer to humans, have cholinergic synapses and those such as zebrafish share many of the benefits observed for invertebrate systems. Zebrafish produce around 200 embryos per pairing (Wilson, 2012), allowing large numbers of fish to be studied. Embryonic development occurs externally in a chorion and zebrafish remain optically transparent in early life allowing gross morphological features to be observed. This includes features such as muscle somite structure and developing neurons and receptor clusters if fluorescent probes are used. Genetic manipulation techniques in zebrafish are now well developed, including the use of transient morpholino(MO)-mediated knockdowns to reduced expression of a protein from the transcriptional level, or CRISPR/Cas9 (Clustered regularly interspaced short

palindromic repeats/CRISPR associated protein 9) to induce genomic deletions or insertions at desired target points (Hwang et al., 2013). Zebrafish also perform a stereotyped set of movements at different time points in development and maturation of nerve and muscle systems are well documented, with many of the same proteins involved as found in humans. Another benefit to using zebrafish for NMJ studies is the ability to perform paired nerve-muscle recordings, in which the cell body of a primary motor neuron can be patch clamped, along with a muscle cell innervated by that neuron (Wen and Brehm, 2005). This provides a powerful system in which to record effects of different genetic manipulations or drug treatments on NMJ signalling. One main difference when considering the use of zebrafish as models for genetic disease is the genome duplication event that teleosts underwent (Meyer and Schartl, 1999). As a result, zebrafish often express more than one orthologue for human genes, and whether they have acquired different functions or have genetic redundancy is unclear. While 70% of human genes have a zebrafish orthologue, it has been reported that 82% of human disease genes are accounted for in the zebrafish genome (Howe et al., 2013), and from a search of the Zebrafish Information Network database (https://zfin.org/) it can be seen that all CMS-associated genes identified to date have at least one orthologue.

The main zebrafish models of CMS are shown in Table 1-1. To date, 14 of the 33 CMS genes have associated zebrafish models that have been used to delineate their role at the NMJ. Others may be available that do not refer to the NMJ. CMS manifests as fatigable muscle weakness in patients, and this can affect the ability to perform motor tasks. In corroboration with this 71% of the models generated also reveal movement defects. Of the remaining 31%, motility wasn't reported for 4 models and was found to be unaffected in only one, highlighting the ability to induce measurable movement changes in zebrafish due to impairments in CMS-related proteins. Tail shape and muscle integrity is affected in less than half of the fish, which corroborates with the majority of patients not displaying myopathic features. Almost all zebrafish that were assessed for pre or postsynaptic defects exhibited abnormalities, supporting the use of this model for studying such effects. Some of the ubiquitously expressed proteins, such as GMPPB and SLC25A1, also influence other tissues such as the CNS and heart. Overall, a number of zebrafish models have been generated that successfully replicate a number of important components of the patient disease phenotype, and these allow further experiments including drug

screens or use of electrophysiology to functionally analyse effects on the NMJ to be performed.

CMS Gene	Genotype	Motility	Tail shape	Motor neuron extension/ branching	AChR clustering	Muscle integrity	Other phenotypes, eg CNS/cardiac	PMID
AGRN	zAgrinLG1 MO and zAgrinLG2 MO						CNS + sensory	17110391
CHAT	baj tf247							18684905, 9007258
CHRNA1	*nic1*$^{twister\ dbn12}$							15128655
CHRNA1	*nic1b107*							2361010, 16249237
CHRND	Sofa potato (sop tj19d)							15201319, 11466415, 9007258
CHRND	Love sofa L28P							25080583
DOK7	zDok-7 MO							20147321
GFPT1	zGfpt1 MO							21310273
GMPPB	zGmppb MO						CNS	23768512
LAMB2	*Soft m272a (softy)*							19736328
LRP4	zLrp4p184							27151977
MUSK	Unplugged mutants*							10769234, 11784083 , 15543140
MUSK	Unplugged MO and SV1 MO							15543140, 29462491
MYO9A	zMyo9aa MO and zMyo9ab MO						Cardiac	27259756, 29462312
RAPSN	*twitch once*$^{(two-/-)}$							9007258, 12151528, 27798141
SLC25A1	zSLC25A1a MO and zSLC25A1b MO						Cardiac + CNS	26870663
SYT2	zSyt2 MO							20643933

Table 1-1. Zebrafish models of CMS. Zebrafish with mutations in genes implicated in CMS, or targeted for knockdown with morpholinos (MO). Genotype is included, and phenotypes correspond to homozygotes when mutant lines are used. Motility refers to any abnormalities in movement reported from chorion movements in early development, through to swimming. Tail shape, if affected, refers to presence of curved tails. Impaired motor neuron extension and branching, as well as any AChR clustering defects (prepatterned or synaptic) are included, along with effects on muscle integrity and somite size. Other phenotypes include presence of cardiac/hindbrain oedemas, eye size, brain abnormalities and sensory defects. Red boxes = affected, green = unaffected and white = not reported. *unptbr307, unptbo81, unptbt187, unptbb72, unptbr160, unptdp253, unpte314b and unpp31CD.

1.4.3 Mouse models of CMS

Mammalian models of human diseases are also important, as the pathways involved in developing and maintaining the NMJ are evolutionarily closer to human than those in fish. Perfect phenocopies of human diseases in mouse models are still unlikely to be achieved due to variations in protein function or genetic redundancy between species, as well as differences in protein homology as outlined in Table 1-2. However, use of mice overcomes the problem of gene duplications present in the zebrafish and thus increases the chance of genes encoding for proteins that have similar functions. Furthermore, mouse CMS-related proteins have a higher sequence homology with human than those found in zebrafish, with 64% of the mouse models analysed in Table 1-2 demonstrating over 90% sequence similarity.

	HOMOLOGY OF MOUSE PROTEIN TO HUMAN PROTEIN				HOMOLOGY OF ZEBRAFISH PROTEIN TO HUMAN PROTEIN			
Protein	Cover %	Identity %	Human isoform	Uniprot accession number	Cover %	Identity %	Human isoform	Uniprot accession number
Agrin	98	80	1	A2ASQ1	99	55	1	B3GQ72
ALG2	100	81	1	Q9DBE8	96	66	1	Q7ZU66
ALG14	92	79	1	Q9D081	90	62	1	Q5XJS2
COLQ	100	90	1	O35348	76	62	3	F1Q7Y1
DOK7	100	85	1	Q18PE0	99	46	4	F1R1E6
DPAGT1	100	94	1	P42867	99	77	1	A2BFS6
GFPT1	100	99	1	P47856	100	91	1	F1QDD9
GMPPB	100	91	1	Q8BTZ7	100	76	1	Q6DBU5
LRP4	100	97	1	Q8VI56	99	78	1	XP017212642
MuSK	100	93	1	Q61006	98	56	1	FL Q5J1R9

Table 1-2. Protein homologies of limb-girdle CMS proteins for mouse and zebrafish as compared with human using the NCBI protein BLAST tool.
Percentage sequence cover and identity is shown, as well as the human isoform the sequence matched with and the Uniprot accession number of the corresponding zebrafish/mouse protein. Modified from O'Connor *et al* (2018b).

Mice are also able to perform more complex behvioural tasks than fish, which can be important when assessing features such as fatigable weakness or muscle strength in functional tests. A number of electrophysiological tests can also be performed in mice, which is of particular importance as morphologically disrupted NMJs may not significantly affect signal transmission, and vice versa. The tests that are often performed include EMG, which is an *in vivo* test whereby CMAPs can be recorded following nervous stimulation, as sometimes used in CMS patients for diagnosis. Due to the nature of the test it can be performed at repeated points to monitor disease progression or response to treatments. *Ex vivo* nerve-muscle preparations can also be subject to physiological analysis, allowing measurement of mEPPs and EPPs

which provides the ability to make estimates of QC, and thus whether a nerve is releasing appropriate amounts of ACh (Webster, 2018). Finally, when testing novel therapeutics, mammalian preclinical models must be used (McElvany, 2009), thus generating robust animal models at an early stage of the research process is desirable so that phenotypes can be well characterised and appropriate outcome measures generated.

There are a large number of mouse models that have been developed for the study of CMS-associated genes as shown in Table 1-3. Only 10 of the 33 genes do not have a corresponding mouse model published in relation to effects on the NMJ or as a CMS disease model (there may be models generated for other purposes). A number of these models have been well-characterised, comprising morphological analysis of NMJs, electrophysiology to assess synapse function and behvioural tests, rendering them useful for future drug testing studies.

Gene	Mouse model	Gene	Mouse model
AGRN	✓	LRP4	✓
ALG14	×	MACF1	✓
ALG2	×	MUNC13–1	✓
CHAT	✓	MUSK	✓
CHRNA1	✓	MYO9A	✓
CHRNB1	✓	PLEC1	✓
CHRND	✓	PREPL	×
CHRNE	✓	RAPSN	✓
CHRNG	✓	RPH3A	×
COL13A1	✓	SCN4A	✓
COLQ	✓	SLC18A3	✓
DOK7	✓	SLC25A1	×
DPAGT1	×	SLC5A7	×
GFPT1	✓	SNAP25	×
GMPPB	×	SYT2	×
LAMA5	✓	VAMP1	✓
LAMB2	✓		

Table 1-3. Mouse models developed for the *in vivo* analysis of the 33 currently recognised CMS genes.Only models in which the NMJ has been analysed are included.

For example, a mouse model of slow channel myasthenia has been generated in which the human AChR εL221F mutation is expressed on an AChRε-null background (Webster et al., 2013). This mouse successfully recapitulates many of the patient symptoms, such as fatigable muscle weakness as demonstrated using the inverted

screen test (where latency to fall is assessed in mice hanging from a wire mesh). The patient mutation *in vitro* causes prolonged AChR channel opening, thus ex *vivo* nerve-muscle preparations were used to analyse the time course of endplate currents, revealing they were similarly prolonged in the mouse model. *In vivo* EMG was also performed, which showed the presence of increased jitter and decrement of CMAPs after a train of stimuli beyond that observed in mice harbouring a wildtype copy of the AChRε subunit. This is also observed in patients. Another phenotypic similarity with patients was observed in morphological analysis of the NMJs, revealing evidence of fragmentation and of degeneration of the postsynaptic folds. The characterisation of this model provided a basis for performing tests using another CMS drug, ephedrine, that had not previously been tested in humans with this subtype of the disease (Webster et al., 2013).

Overall, a combined approach utilising both *in vitro* and *in vivo* models of disease, coupled with analysis of patient material or performance of electrophysiological tests in patients, is likely to yield the most robust information. This would allow molecular targets and pathways to be studied at the cellular level, as well as determining the effect of specific genetic manipulations at the level of the NMJ and in whole systems, thus forming the basis for testing novel therapeutic strategies.

1.5 MYO9A-CMS

1.5.1 Clinical presentation of MYO9A-CMS patients

The finding that a number of ubiquitously expressed proteins can cause impaired function of the NMJ leading to CMS has expanded the search for novel causative genes encoding proteins that may play other roles out with the NMJ. In 2016, mutations in three patients from two unrelated families were identified in an unconventional myosin gene; *MYO9A (O'Connor et al., 2016).* This is a ubiquitously expressed gene that encodes for a protein classed as an actin-based molecular motor, as part of a large family of unconventional myosin proteins. Mutations were identified using whole exome sequencing analysis on a cohort of genetically undiagnosed CMS patients, as part of my MSci research project. The variants in *MYO9A* were first identified in patient 1, who was of German origin and was the first daughter of healthy non-consanguineous parents (Figure 1.11A). After finding these variants, the remaining genetically unsolved cohort were analysed for the presence of any variants in *MYO9A* and two siblings that had consanguineous parents of Kurdish origin were identified (Figure 1.11B,C).

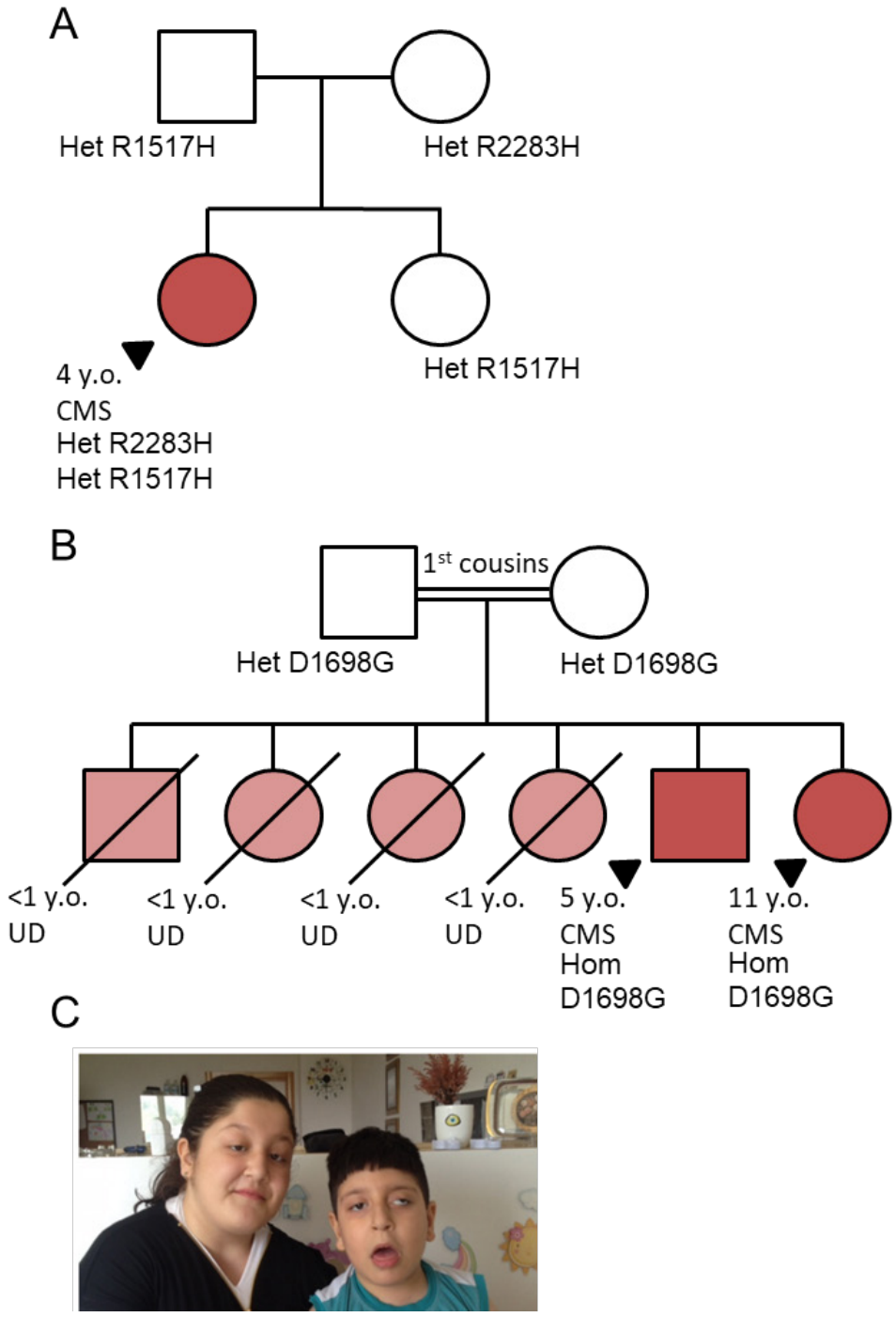

Figure 1.10. MYO9A-CMS patient pedigrees. A. Pedigree for patient 1 (arrow head), including age at last clinical update and compound heterozygous amino-acid changes in MYO9A. The mother, father and unaffected sister all carried one variant. B. Pedigree for patients 2 and 3 (arrow heads), including age at last clinical update and homozygous amino-acid changes in MYO9A. Parents are first degree cousins and both carry the variant in heterozygous form. They had 4 deceased children who died within the first year of life due to CMS-like symptoms but no diagnosis was made. UD = undiagnosed but symptomatic (light red), y.o = years old, hom = homozygous, het = heterozygous, red = CMS diagnosis. C. Patients 2 and 3, indicating presence of bilateral ptosis and ophthalmoplegia; with asymmetric upward deviation of gaze (left eye) in the male patient. Photo from O'Connor *et al* (2016).

Patient 1 presented with a variety of typical CMS symptoms, including proximal and distal skeletal muscle weakness, difficulties with swallowing, ptosis (drooping of the eyelids), episodic apnoea and respiratory failure. Other forms of CMS that display episodic apnoea include CHAT, RAPSN, SLC5A7, fast channel syndrome and SLC18A3 (McMacken et al., 2018b). These symptoms manifested at the neonatal stage and up until the last update at age 4 years, when the patient still relied on feeding with a percutaneous endoscopic gastrostomy. To confirm the diagnosis of suspected CMS, single fibre EMG was performed on the orbicularis oculi muscle. This revealed the presence of abnormal jitter, with 4 abnormal pairs recorded at an average jitter of 75μs, compared to 39.8-54.6μs (95% confidence intervals) reported in orbicularis oculi muscle recordings from healthy 10 year olds (Selvan, 2011). When testing another site of the orbicularis oculi muscle, despite increasing stimulation intensity, unstable potentials were identified. However, testing was ceased due to distress of the infant. As increased jitter can also be a sign of reinnervation (Selvan, 2011), concentric EMG recordings were also performed, revealing normal action potential configurations and no evidence of denervation, thus supporting a CMS diagnosis.

Magnetic resonance imaging of the brain did not reveal any pathological findings, although there may be a slight cognitive delay (not objectively tested). Metabolic testing to rule out other disorders such as muscular dystrophy were negative, covering acylcarnitines in blood, amino acids in serum, creatine kinase and organic acids in urine. The patient exhibited improvements in motor and respiratory function in response to a combination of an anticholinesterase (pyridostigmine) and 3,4-DAP, which are also often effective in CHAT, PREPL, RAPSN and fast channel syndromes, as well as sometimes in agrin-CMS (Engel, 2018).

Patients 2 and 3 also had early symptom onset as they presented in the prenatal period with reduced foetal movements. The parents had previously lost 4 children in the first year of life due to severe CMS-like symptoms. Bilateral ptosis was present from birth in patient 2, and further manifestations appeared after 2 months in the form of generalised hypotonia and difficulty with swallowing. Reaching motor milestones was delayed, with head control only obtained at 12 months, sitting at 3 years and walking with support by 5 years of age, which was the age of last update. Further ocular phenotypes were also present with symmetric multivectorial nystagmus, left eye up-gaze deviation and ophthalmoplegia. Presence of learning difficulties was

found and the ability to speak had not yet been obtained. Treatment with 3,4-DAP and fluoxetine led to respiratory crises, which also occurred during respiratory infection, however improvements were obtained by treatment with pyridostigmine. A diagnosis of CMS was made after single fibre EMG results indicated the presence of increased jitter.

The older sibling, patient 3, was 11 years old at the time of last update. Symptom onset was also early, with bilateral ptosis apparent within the first week after birth, followed by development of generalised hypotonia, difficulties swallowing and controlling head and torso. By 12 months of age patient 3 could sit and at 18 months head control was obtained, followed by the ability to walk unassisted by 30 months. Nystagmus, symmetric ophthalmoplegia and oculomotor apraxia with head tilt were also present. Episodes of respiratory crises also occurred for this patient in periods of respiratory infection. Pryidostigmine treatment improved management of ptosis, swallowing, chewing and breathing in this patient, and in the younger sibling. Brain magnetic resonance imaging did not reveal any abnormalities in patient 3, nor did metabolic testing including creatine kinase in serum, organic acids in urine and amino acids in serum. Repetitive nerve stimulation of the right ala nasi muscle revealed a 22% decrement, supporting the diagnosis of CMS.

1.5.2 MYO9A patient mutations

The variants identified in these three patients were all missense changes in the tail domain of the MYO9A protein, shown in Figure 1.13. Patient 1 has compound heterozygous mutations affecting protein residues: p.R1517H and p.R2283H (rs149046541 and rs142345927, respectively). In both positions an arginine amino acid is exchanged for a histidine, which is exchanging a positively charged amino acid for a neutral one, and due to the unique chemical properties of histidine it does not generally substitute well. Corroborating this, polyphen prediction software predicts p.R1517H to be damaging, and this variant has a minor allele frequency of 0.09% in the ExAC database (a database of 60,706 individuals exomes) not appearing in homozygosity in any subjects (Lek et al., 2016). This variant resides within exon 25 of the main transcript (NM_006901) in a highly conserved region of *MYO9A* (Figure 1.12). This exon is within the tail region, specifically in a coiled-coil domain that is situated between an IQ motif and a C1 zinc-binding domain.

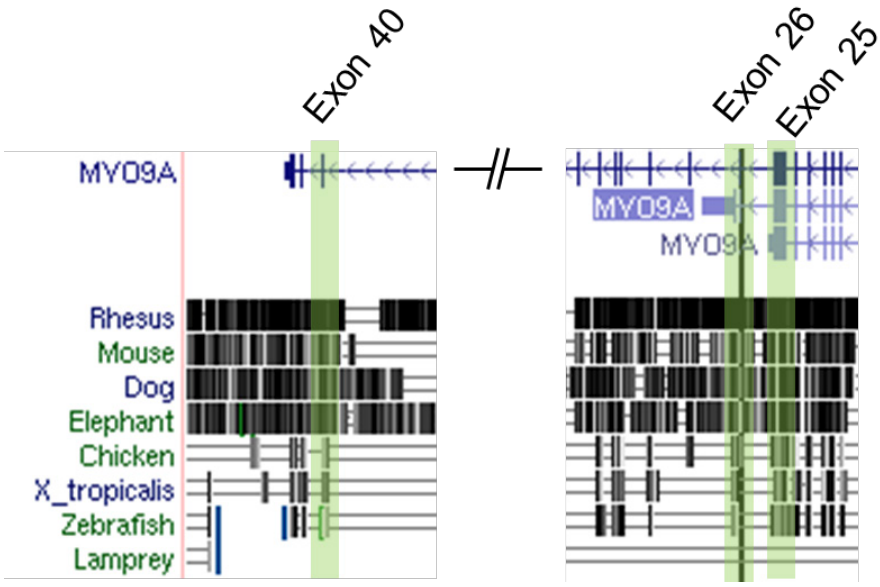

Figure 1.11. Conservation of MYO9A exons in different species. The top sequence in dark blue, denoted by MYO9A, indicates the full isoform of the human protein. Exons of interest are highlighted in green, demonstrating their presence throughout the species shown, except lamprey. Data generated from UCSC genome browser (Kent et al., 2002).

On the other hand, p.R2283H is predicted to be benign using polyphen prediction software, although appears damaging using MutationTaster (O'Connor et al., 2016, Schwarz et al., 2014). P.R2283H has a minor allele frequency of 0.2% in the ExAC database, with 2 homozygotes reported. In the main *MYO9A* transcript, p.R2283H is situated in exon 40 in a relatively well-conserved region. This is also in the tail region of MYO9A, towards the c-terminus and adjacent to the Rho-GTPase domain. It is hypothesised that p.R2283H, due to its benign predicted effect and relatively high minor allele frequency for a rare disease (predicted to occur in homozygosity for 4 in 1,000,000 people), has a rather mild effect on the patient phenotype and only when expressed in conjunction with the rarer p.R1517H is there a sufficiently detrimental effect on protein function.

Patients 2 and 3 had homozygous missense variants in *MYO9A:* p.D1698G (rs150726107). This variant had a minor allele frequency of 0.06% in the ExAC database, with no presence of homozygosity. Parents were both heterozygous for the variant. Exchange of a negatively charged, fairly well conserved aspartate for a small amino acid residue glycine, is predicted to alter splicing of the *MYO9A* (Desmet et al., 2009). The variant is positioned within exon 26 of the main transcript, which is also located between the IQ motif and protein kinase C domain.

Overall, these variants were identified as the likely cause for CMS in these three patients, after considering the rest of the exome data available for each case. The mutations found in these patients could be altering the structure and function of the MYO9A protein, which will be discussed in subsequent sections.

1.5.3 Family of Unconventional Myosins

MYO9A is an unconventional myosin protein. Myosin proteins are a diverse group of actin-based molecular motors, present in almost all eukaryotic cells. They are involved in a multitude of cellular functions including muscle contraction, cell motility, intracellular trafficking, endo- and exocytosis and alterations in cell morphology (Batters and Veigel, 2016). Humans have around 40 genes encoding myosins which can be divided into 12 distinct subfamilies depending on their specific protein domains (Foth et al., 2006). These include the muscle-specific or conventional myosin; myosin II, which is part of the contractile apparatus of muscle cells. The rest of the family constitute the unconventional myosins, a group of myosin motors that have the ability to interact with actin and perform a variety of functions. Myosins all have a catalytic domain of approximately 80 kDa in their N-terminal head region responsible for the hydrolysis of ATP and binding of actin, termed the myosin motor domain (Batters and Veigel, 2016). This confers the ability of myosins to bind actin and processively move along filaments. Each class of myosin also possesses a neck region of varying lengths, containing different numbers of IQ motifs, from 1 in myosin XVI to 6 in myosin IX (Patel et al., 2001, Gorman et al., 1999). This region undergoes small conformational changes which affect the motor domain, with the length of the neck determining how much force can be generated by the head (Batters and Veigel, 2016). Each class has a distinct tail region containing different domains which confer the unique functions of each myosin subset, such as ability to anchor the myosin to cellular compartments or select cargo (Krendel and Mooseker, 2005). Two sets of myosins; myosin III and IX, are able to act as motorised signalling molecules due to the expression of domains with enzymatic activities (Bahler, 2000). The diseases that have been associated with unconventional myosins so far are listed in Table 1-4, highlighting the diversity in function and expression of this protein family.

Unconventional Myosin subtype	Disease association	OMIM identifier
Ie	Glomerulosclerosis	601479
IIIa	Deafness	606808
Va	Griscelli syndrome	160777
Vb	Microvillus inclusion disease	606540
VI	Deafness	600970
VIIa	Deafness, Usher Syndrome	276903
IXa	Congenital Myasthenic Syndrome	604875
XVa	Deafness	602666

Table 1-4. Diseases associated with unconventional myosins as reported on the OMIM database. Unconventional myosin subtype, disease and OMIM identifier included.

With relevance to the NMJ, only two unconventional myosins have been directly implicated in having a role at this synapse, including the identification of MYO9A as potentially causative for a subset of CMS (O'Connor et al., 2016). Myosin Va has also been demonstrated to play a role at the NMJ in mice, where a subsynaptic enrichment of Myosin Va and protein kinase A was found to positively correlate with AChR stability in the dystrophic mdx mouse model (Roder et al., 2008, Roder et al., 2012). A number of myosins have been shown to play roles in the nervous system in general, with functions in neuronal migration, outgrowth, morphogenesis and axonal transport (Brown and Bridgman, 2004). Of potential relevance to the NMJ, several myosins have also been shown to partake in endo- and exocytotic mechanisms, as well as vesicle trafficking in both nerves and other tissues. For example, Myosin X provides a link between the extracellular matrix receptors; integrins, and the necessary cytoskeletal rearrangements that precede axonal elongation in development or following injury in spinal sensory and motor neurons (Plantman et al., 2013). This group of myosins also transports netrin-1 receptors to the peripheral tip of neurites where interactions are important for axonal guidance (Zhu et al., 2007). Myosin VI associates with cortical actin which lies beneath the plasma membrane, and is thought to be the only unconventional myosin to move toward the minus end (rather than plus end) of actin filaments and thus is likely to play a role in endocytosis (Wells et al., 1999). During secretion from cells actin filaments undergo local

reorganisation to facilitate the process. Myosins Ic, Ie, II, Va and VI have been implicated in these final stages of secretion, commonly described as approach, docking, priming and fusion of vesicles (Bond et al., 2011). If an unconventional myosin were to play a similar role at the NMJ it may affect the ability of the synapse to respond to guidance cues, changes in environment, internalisation of ligand-bound receptors and in secretion of proteins from the cell.

1.5.4 MYO9 proteins

1.5.4.1 Protein structure

There are 2 class 9 myosin proteins expressed in humans; MYO9A (chromosome 15, Figure 1.13) and MYO9B (chromosome 19). Both myosins follow the same basic structural composition as other unconventional myosins, containing a force generating motor domain in the head region which binds actin and hydrolyses ATP. This is preceded by an extension that has similarities to a Ras-association domain, however it has been shown not to bind Ras in both MYO9A and MYO9B (Chieregatti et al., 1998, Kalhammer et al., 1997). Unique to this subset of myosins is the presence of a large 100-200 amino acid insertion in the head domain, termed loop 2. This extension contains an IQ motif for binding calmodulin and has been shown to bind actin, allowing this single-headed motor protein to move processively along actin filaments (Elfrink et al., 2014, Saczko-Brack et al., 2016). A further 6 IQ motifs for MYO9A and 4 motifs for MYO9B are present in the neck domain, which can also bind calmodulin. Activity of MYO9B has been shown to be responsive to calcium due to the conformational changes induced by a switch from calcium-free calmodulin to calcium-calmodulin, which inhibit its ATPase activity (Liao et al., 2010) and recently, the ability of MYO9A to bind calcium-calmodulin has also been demonstrated (Li et al., 2017). Both class IX myosins have an extended tail region that contains an atypical C1 domain for which the function is not yet known (typical C1 domains bind diacylglycerol) and a Rho-GTPase activating protein (GAP) domain (Gorman et al., 1999, Bahler et al., 2011). The tail region of MYO9A is longer than MYO9B, containing a sequence predicted to adopt a coiled-coil structure and two alternatively spliced regions (Chieregatti et al., 1998), resulting in a 293 kDa protein for MYO9A as opposed to 243 kDa for MYO9B. The Rho-GAP domains were found to stimulate the GTPase activity of Rho but not Rac (Post et al., 1998, Chieregatti et al., 1998). MYO9A is predicted to possess 20 different protein isoforms that differ in 5’ and 3’ truncations, as well as absence of 16 cassette exons. Of these splice variants only 4

include the tail region bearing the patient mutations, and 2 of these contain all of the identified domains (Thierry-Mieg and Thierry-Mieg, 2006). Tissue specific expression of these different isoforms may provide an explanation for the NMJ-specific phenotype of the patients.

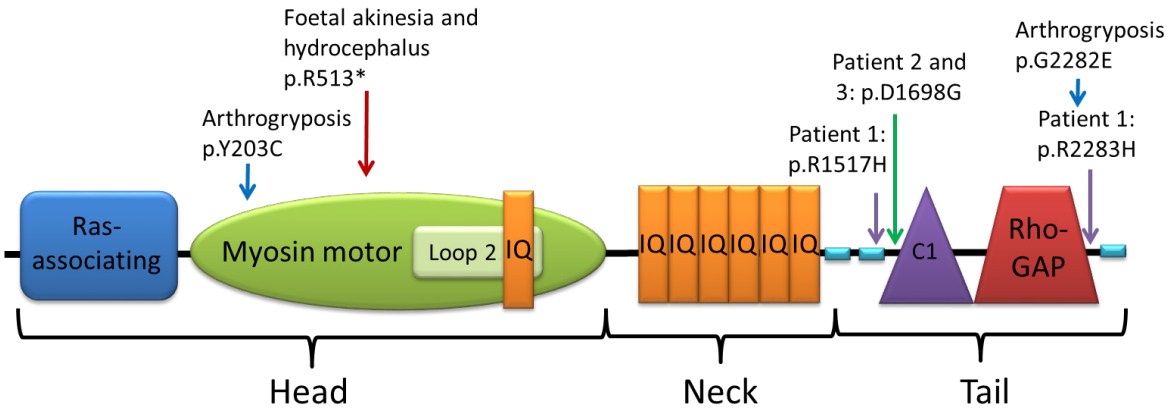

Figure 1.12. Structure of MYO9A. Diagram of MYO9A protein domains identified, including the head region Ras-associating domain and myosin motor domain that contains an extension at loop 2 with an IQ motif. The neck region consists of 6 IQ motifs for binding of calmodulin. The tail region of MYO9A has 3 sequences predicted to adopt a coiled-coil conformation, as well as an atypical C1 domain and Rho-Gap domain. The location of the 3 MYO9A-CMS patient mutations are noted: patient 1 in purple, compound heterozygous, patients 2 and 3 in green, homozygous. The location of reported mutations in an arthrogryposis patient (Bayram et al., 2016) are also included (blue, compound heterozygous), and homozygous mutations in a foetal akinesia patient shown in red (Maddirevula et al., 2019). Modified from: O'Connor *et al* (2016).

MYO9A RNA is expressed ubiquitously, with highest levels present in the testis and peripheral nerves, and to a lesser extent in the muscle and brain (GTEx, https://gtexportal.org/home/gene/MYO9A, last accessed 26.03.19, Chieregatti et al., 1998). As there are a number of different isoforms, expression of specific exons that contain patient mutations were also analysed, revealing that exons 25 (p.R1517H) and 26 (p.D1698G) are predominantly expressed in the testis, nerve, oesophagus muscle and arteries. Exon 40, in which the p.R2283H variant resides, is expressed in the brain, muscles and many other tissues. Considering protein expression levels using the Human Protein Atlas resource, the level of expression is similar across all aforementioned tissues, with the RNA enrichment in the testis absent at the protein level (Uhlen et al., 2015). MYO9B on the other hand is expressed to a higher extent in endocrine tissues, immune cells, muscle, testis and many other tissues at both the protein and RNA level (GTEx, https://gtexportal.org/home/gene/MYO9B, last accessed 26.03.19, Uhlen et al., 2015, Chieregatti et al., 1998).

The human class IX myosin canonical protein sequences are only 57% similar, which includes only 71% coverage of MYO9A, thus highlighting the likely differing roles of the two proteins within this class. Human MYO9A compared to the mouse homolog displays an 88% similarity, covering 100% of the sequence. Zebrafish also display a high degree of homology with human MYO9A, with Myo9aa 63% similar covering 100% of the sequence, and Myo9ab 62% similar covering 82% of the sequence (https://blast.ncbi.nlm.nih.gov/Blast.cgi, last accessed 26.03.19). Overall MYO9A is well conserved, including within the species relevant to this project.

1.5.4.2 Protein function

Consistent with the identification of an active RhoGAP domain in MYO9A, analysis of the MYO9A interactome as generated by the STRING database reveals associations of this unconventional myosin with a range of Rho family proteins (Figure 1.13). This includes RhoA, with which MYO9A has been shown to interact with in numerous studies by negatively regulating its activity (Abouhamed et al., 2009, Omelchenko and Hall, 2012).

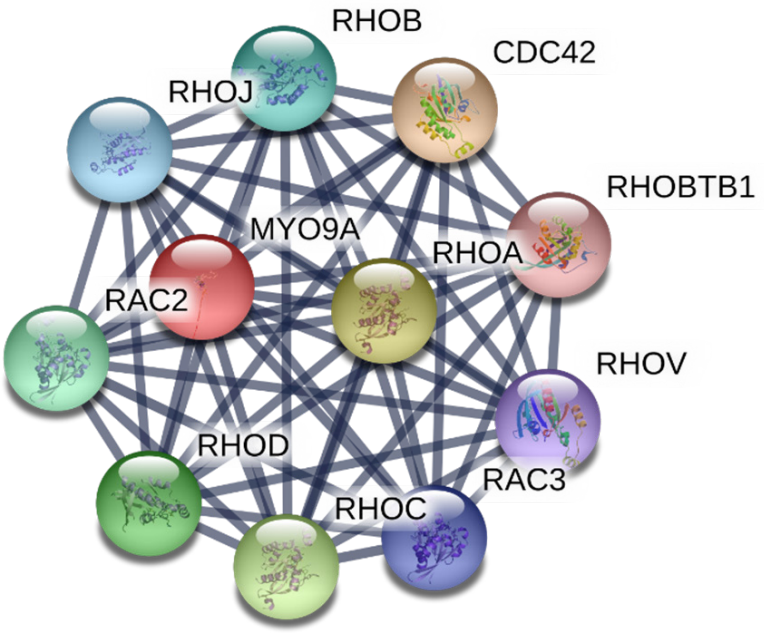

Figure 1.13. String association network for MYO9A. Human MYO9A and associated proteins are shown, linked with lines representing confidence of interaction. Interactions do not necessitate binding but suggest the two proteins work towards the same function, based on experimental evidence, databases, text mining, co-expression, neighbourhood, gene fusion and co-occurrence data, performed using the STRING database (Szklarczyk et al., 2019).

Human MYO9A was originally cloned by Gorman *et al* (1999), performed because it was in a region identified to contain a gene causing the disease Bardet-Biedl syndrome. Despite this, *MYO9A* variants have never been identified in patients with this disease. The previous year, Myr 7, the rat MYO9A homolog, was identified as a protein similar in structure to Myr 5 (MYO9B). Initial analysis revealed Myr 7/MYO9A could activate RhoA, but not Rac1 and only partially CDC42 GTPase activities *in vitro* (Chieregatti et al., 1998). These first observations, coupled with expression studies identifying the protein within the brain, lead to the hypothesis that MYO9A may be important for regulating Rho activity in neurons. It was not until 10 years later that further research emerged suggesting a role for this unconventional myosin protein in brain ependymal epithelial cells that line the ventricles, due to its absence causing hydrocephalus in a mouse model (Table 1-5). This was attributed to altered epithelial cell morphology and cell junctions, but could be attenuated by blocking the Rho-associated protein kinase (ROCK) pathway, a downstream target for RhoA (Abouhamed et al., 2009). Therefore, this demonstrated for the first time *in vivo* that MYO9A activity has functional consequences for the RhoA pathway.

Mouse genotype	Tissue affected	Phenotype	PMID
Myo9a$^{-/-}$	Kidney	Bilateral renal disease, polyuria and low molecular weight proteinuria	26136556
Myo9a$^{-/-}$	Brain (ventricles)	Severe hydrocephalus with stenosis, closure of the ventral caudal 3rd ventricle and the aqueduct	19828736
Myo9a$^{+/-}$	Brain (hippocampus)	Impairment of long term potentiation, synaptic transmission and cognitive function	26834556
Myo9a$^{-/-}$	Gross phenotype	Abnormal gait and small size	19828736

Table 1-5. Phenotypes associated with depletion of MYO9A in mice. Table shows genotype of mice (homozygous or heterozygous knockout) along with associated phenotypes and main tissue investigated. Pubmed IDs are provided (PMID).

The downstream network of RhoA includes a number of proteins with diverse functions. However, one of the main roles is in modulation of the actin cytoskeleton, as well as some microtubule and intermediate filament interactions (Jaffe and Hall, 2005). Through these functions, Rho GTPases such as MYO9A are particularly important for cell migration, polarity, movement and junction formation. This is exemplified by reports highlighting that an absence of MYO9A from bronchial epithelial cells leads to cell scattering based on a loss of local actin cytoskeleton organisation and inability of cells to form new adhesions. The binding of actin filaments could be reinstated by expression of the motor domain in the head,

whereas rescue of cell junction formation required the RhoGAP domain (Omelchenko and Hall, 2012). In further support for a role for MYO9A in regulating RhoA-dependent processes, it has been reported that MYO9A contains a PDZ-binding motif at the c-terminus (p.2540-2550), allowing binding of a viral PDZ-containing protein that brings MYO9A and RhoA into close association allowing MYO9A-mediated inactivation of RhoA. This leads to altered actin cytoskeleton dynamics and allows viral spread between cells (Handa et al., 2013). In two studies performed to identify genes that may contribute to desirable features in farmed animals there was a suggested contribution of MYO9A to abdominal fatness in chickens and muscle mass in pigs. However, no functional work was performed to support these findings and thus mechanisms of action are unclear (Zhang et al., 2012, Liu et al., 2018).

As described, actin dynamics and other unconventional myosins have been shown to play important roles in vesicle secretion from cells. Corroborating this, MYO9A in mouse was shown to localise to cortical actin in kidney tubule cells, where its loss affected endocytosis of ligand bound receptors from the cell surface (Thelen et al., 2015). A previously unreported effect on diaphanous-related formin 1 was also identified, a Rho effector protein that modulates the cytoskeleton and thus is likely a downstream target of the MYO9A/RhoA pathway.

Almost 20 years after initial predictions that MYO9A would play a role in neurons, 2 studies reported effects of MYO9A in the CNS and PNS. The first of these was by Folci *et al* (2016), demonstrating an association of MYO9A with the postsynaptic density of hippocampal neurons from rat, where it binds to the GluA2 subunit of the alpha-amino-3-hydroxy-5-methyl-4-isoxazole propionic acid receptor (AMPAR). Heterozygous knockout of MYO9A from mice impacted on long term potentiation and performance in cognitive tasks as outlined in Table 1-5. While mechanisms for such an effect were not investigated, it was hypothesised that MYO9A affects AMPAR endocytosis and trafficking through both RhoA-mediated and myosin motor-mediated pathways. As a result, its loss leads to a surface build-up of AMPARs and affects synaptic plasticity. The second such study to implicate a role for MYO9A in neurons was based on our observations that 3 patients with CMS harboured variants in *MYO9A* that segregated with the disease, and found MYO9A to localise at the NMJ in mouse, and loss of the protein to impact on NMJ development in zebrafish (O'Connor et al., 2016). Another disease, arthrogryposis, has also been associated with MYO9A mutations, in which compound heterozygous missense variants were

identified in one patient (Bayram et al., 2016). Association of a gene with both arthrogryposis and CMS has occurred previously, as there are overlapping phenotypes. For example, reduced foetal movements due to prenatal NMJ transmission defects sometimes present in CMS and can lead to joint contracture (arthrogryposis) formation (Brownlow et al., 2001, Vajsar et al., 1995). A homozygous nonsense mutation in *MYO9A* was recently reported in an autozygosity study for a foetal akinesia patient, linking in with the report of arthrogryposis, and also with the hydrocephalus phenotype observed in MYO9A KO mice (Maddirevula et al., 2019). The mutation was positioned in the motor domain, the same region in which one of the arthrogryposis variants was located, and thus may explain the severity of the patient's phenotype due to the likely truncation of the protein near the n-terminus. Reflecting this observation, the motor domain of MYO9A has been shown to play an important novel role delineated *in vitro*, in which MYO9A crosslinks actin filaments to form polar structures that may provide support for localised RhoGAP activity, as well as involvement in cell polarity and migration (Saczko-Brack et al., 2016). Further defects due to a role of this myosin in cytoskeleton regulation has been highlighted by the identification of *MYO9A* gene dysregulation in monosomy blastocysts (in which a chromosome is absent, chromosome 15 in this case). Decreased expression of *MYO9A* was hypothesised to affect implantation of monosomy blastocysts in pregnancy due to roles in cytoskeleton modulation and cell junction formation, although no functional data was obtained (McCallie et al., 2016).

With regards to clinical effects of RhoA pathway modulation due to MYO9A, the presence of ANXA2-MYO9A gene fusions were reported to significantly worsen the prognosis of diffuse gastric cancer patients. The gene fusion product maintained the RhoGAP domain of MYO9A and caused its overexpression, subsequently reducing the activity of active RhoA in cells (Yang et al., 2018). Hum-7 is the *C.elegans* homolog of MYO9A/B. Although it only has approximately 20% protein homology with its human counterparts, it contains the main domains. Depletion of Hum-7 increased embryonic lethality, corroborating previous studies suggesting roles for MYO9A in early development (Bayram et al., 2016, Maddirevula et al., 2019, McCallie et al., 2016, O'Connor et al., 2016). Further supporting the role of MYO9A in nervous development, Hum-7, was also found to affect postembryonic axon guidance, causing axon migration defects when knocked down (Wallace et al., 2018).

Overall, a number of recent studies have built on the suggested roles for MYO9A in neuronal function but also broadly in cytoskeletal structure and RhoA pathway modulation. However, the precise role of MYO9A at the NMJ remains to be established. Furthermore, whether such a role is due to interactions with the cytoskeleton and RhoA pathway in particular is not known, or if there is involvement of other pathways. A mechanism by which dysfunction of MYO9A could disrupt the safety factor of the NMJ and lead to impaired signalling resulting in CMS also requires investigation. These questions will be addressed within this thesis, with a particular focus on the roles of MYO9A in morphology and function of the NMJ.

1.6 Aims

The main aim of this project was to determine whether MYO9A contributes to the development and integrity of the NMJ. Pathological mechanisms that may lead to manifestation of a CMS phenotype in patients lacking the functional protein will be determined, and thus potential therapeutic targets for new treatments identified. It is hypothesised that defects in MYO9A cause a presynaptic CMS, due to interactions with the cytoskeleton and RhoA pathway within motor neurons. Each chapter will address a specific aim to investigate this hypothesis.

Chapter 3:

To generate a range of *in vitro* and *in vivo* models appropriate for studying the role of MYO9A at the NMJ, including patient-derived neuronal progenitor cells and knockdown zebrafish.

Chapter 4:

To perform observations of NMJ development in zebrafish, coupled with behavioural testing to assess whether loss of MYO9A affects motor activity and/or synapse morphology. This was accompanied by assessment of patient nerve cells and morphology of adult NMJs in a MYO9A knockout mouse.

Chapter 5:

To assess the effects of MYO9A-depletion or patient mutation on the cytoskeleton and vesicular transport, using cell models as well as zebrafish and mouse tissue.

To determine whether any defects observed were mediated by the interaction of MYO9A with the RhoA/ROCK pathway.

ROCK inhibitor treatment was trialed *in vitro* and *in vivo* and effects on vesicular transport and NMJ development studied.

Chapter 6:

To determine whether loss of MYO9A affects secretion from a nerve cell model, using secretomics.

Identified factors of relevance to the NMJ guided selection and application of novel compounds using the most appropriate model to test for therapeutic potential. Screening of a novel compound was performed including morphological analysis of NMJs and effects on motor behaviours.

Chapter 2. Materials and Methods

2.1 Solutions and buffers

A list of solutions and buffers used in this project is shown below in alphabetical order.

Coomassie Brilliant Blue dye

1% Coomassie

40% ETOH

50% distilled water

10% acetic acid

Destaining buffer 1

47.7% water

10% acetic acid

40% ETOH

2.3% glycerine

Destaining buffer 2

82.8% water

5% acetic acid

10% ETOH

2.3% glycerine

E3 medium

5mM NaCl

0.17mM KCl

0.33mM $MgSO_4$

0.33mM $CaCl_2$

0.01% methylene blue

Fibroblast growth medium

DMEM

15% FBS

FM-Dye staining solution

5µg/ml FM-Dye

HBSS

Freezing medium

NSC-34 cell growth medium

DMEM

10% FBS

100 units/ml penicillin/streptomycin

3 µg/ml puromycin

1xPBS

1x PBS tablet

500ml distilled water

1xPBST

1x PBS tablet

500ml distilled water

0.1% Tween 20

4% PFA in PBS

1xPBS

NaOH pellets

4% PFA

pH adjusted to 7.4

Secretomics lysis buffer

50 mM TrisHCl pH 7.8

150 mM NaCl

1% SDS

1 protease cOmplete mini tablet

1 phosphatase inhibitor PhosSTOP tablet

SH-SY5Y cell growth medium

1:1 DMEM:Ham's F12

10% FBS

TAE buffer

40mM Tris base

30% FBS

60% DMEM

10% dimethylsulfoxide

Immunofluorescence blocking buffer

1x PBS

4% BSA

0.1% Tween 20

Immunofluorescence blocking buffer for zebrafish

1x PBS

5% horse serum

0.1% Tween 20

LB media

10 mg/ml Bacto-tryptone

5 mg/ml yeast extract

10 mg/ml NaCl

2% w/v dextrose (pH 7.4)

LB plates

LB media

15 g/l agar

Lysis buffer

RIPA buffer

Protease cOmplete mini tablet (1 tablet/10ml)

Neuroinduction media

1:1 DMEM:F-12 with 1% GlutaMAX

1x N2 supplement (from 100x stock)

1x B27 supplement (from 50x stock)

10ng/ml Recombinant Human Leukemia Inhibitory Factor

3μM CHIR 99021

2μM SB431542

Neurodifferentiation media

20mM acetic acid

1mM EDTA

1xTBS

50 mM Tris-Cl, pH 7.5

150 mM NaCl

Made up in distilled water

1xTBS-T

1xTBS

0.1% Tween 20

1xTransfer buffer

25 mM Tris

192 mM glycine

20% methanol

Made up in distilled water

1xTris-Glycine running buffer

25 mM Tris

192 mM glycine

0.1% SDS

Made up in distilled water

Western blot blocking buffer

5% BSA

1xTBS

1:1 DMEM:F-12 with 1% GlutaMAX

1x N2 supplement (from 100x stock)

1x B27 supplement (from 50x stock)

300ng/ml cAMP

200µM Vitamin C

10ng/ml BDNF

10ng/ml GDNF

2.2 Standard molecular biology techniques

2.2.1 DNA extraction

The 'Hot Shot' method of DNA extraction was utilised for obtaining genomic DNA (gDNA) from zebrafish embryos (maximum 20 per reaction), adult zebrafish fin clips (<2mm) and mouse tails (<2mm). Lysis reagent (50mM NaOH) was added to each sample until submerged (approx. 50µl for embryos and fin clips and 100µl tail tips). Samples were incubated at 95ºC for 15 mins, with regular vortexing. After cooling samples to 4ºC, 1M Tris-HCL (pH8) neutralisation buffer was applied at a volume of one tenth of the lysis reagent. After mixing, samples were centrifuged at 13000g and stored at -20ºC until use.

2.2.2 RNA extraction

To prepare cells in culture for RNA extraction, cells ($<1x10^5$) were washed 3x in ice-cold phosphate buffered saline (PBS) and scraped into PBS before centrifuging at 250g at 4ºC. Following removal of supernatant, pellets were homogenised by vortexing in lysis buffer and RNA extracted using a Qiagen RNeasy Mini Kit according to the manufacturer's instructions.

To isolate RNA from zebrafish embryos, a combination of TRIzol and Qiagen RNeasy Mini Kit methods was used. Approximately 30 embryos were incubated in 250µl of TRIzol reagent (Invitrogen) and homogenised using a Tissue Rupture, followed by a 5 min incubation at room temperature. Chloroform (50µl, Sigma Aldrich) was added to the lysed samples before centrifuging at 12000g for 15 mins at 4ºC. The upper aqueous phase was placed in a new microcentrifuge tube and combined at a ratio of 1:1 with 70% ethanol. The combined solution was then applied to an RNeasy spin column and the Qiagen RNeasy Mini Kit instructions followed.

Samples were incubated at -80ºC until required, after which purity and concentrations were determined using a NanoDrop 2000 (ThermoFisher Scientific). RNA was considered pure if the 260/280 ratio of absorbance was approximately 2, and 260/230 ratio of absorbance between 2 and 2.2.

2.2.3 Reverse transcription cDNA synthesis

Reverse transcription was performed using the Applied Biosciences High Capacity cDNA reverse transcription kit, according to manufacturer's instructions. Briefly, a 2x master mix was prepared including 2µl 10x reverse transcription buffer, 0.8µl 25x dNTP mix (100mM), 2µl 10x reverse transcription random primers, 1µl Multiscribe reverse transcriptase, 4.2µl nuclease-free water, per reaction. The master mix was combined with the RNA sample (<2µg) at a 1:1 ratio and subject to thermal cycling for 10 mins at 25ºC, 120 mins at 37ºC and 5 mins at 85ºC, before storing at 4ºC.

2.2.4 Polymerase chain reaction

HotStarTaq DNA polymerase kit (Qiagen) was used to perform polymerase chain reactions (PCRs). The final concentration of components in each reaction mix was as follows; 1x PCR buffer, 200µM of each dNTP, 0.1µM forward and reverse primers, 2.5 units HotStarTaq DNA polymerase, 8.825µl distilled water and 1µl DNA, to a total volume of 15µl. Reactions were then subject to thermal cycling, as shown in Table 2-1.

Step	Temperature (ºC)	Time (mins)	Cycles
Initial activation	95	15	1
Denaturation	95	1	25-40 (40 used only for zebrafish reactions)
Annealing	Variable	0.5	
Extension	72	1	
Final Extension	72	10	1
Storage	4	∞	

Table 2-1. Thermal cycling conditions used for PCR reactions with HotStarTaq DNA polymerase.

Gradient PCRs were performed for each new primer set to determine the most effective annealing temperature. Primers shown in Table 2-2.

Primer	Species	Application	Sequence (5'-3')	Annealing temperature (°C)
myo9aa exon 2 Fwd	Zebrafish	Sequencing	ACTATCTACTGCCCTGTCGC	56
myo9aa exon 2 Rev	Zebrafish	Sequencing	GGTAGTCCTCGCTGCTGAAG	56
myo9aa exon 2b Fwd	Zebrafish	Sequencing	TGACTTGCAACCACATCTGC	56
myo9aa exon 2b Rev	Zebrafish	Sequencing	AGGTTATCGATCGGCTGCAG	56
myo9ab exon 1 Fwd	Zebrafish	Sequencing	TCACACTTCTCCTACTCGCG	56
myo9ab exon 1 Rev	Zebrafish	Sequencing	TGGCGAAGTTGATGCAGAAC	56
myo9ab exon 12 Fwd	Zebrafish	Sequencing	CCGTTGTGTGTTTCTCCAGG	56
myo9ab exon 12 Rev	Zebrafish	Sequencing	TCCTCTAGATCTGCCAGTTCC	56
R1517 Fwd	Human	Sequencing	AGAAGGTATCACTGCTCAGGA	55
R1517 Rev	Human	Sequencing	GCCACCAAACACTCTCCAAT	55
D1698G Fwd	Human	Sequencing	AGAGAGGGAAATGCTAGGCC	56
D1698G Rev	Human	Sequencing	CGCTGTGATGTCTCTCTTTGG	56
R2283H Fwd	Human	Sequencing	GACACCACTGACCCACTACA	57

R2283H Rev	Human	Sequencing	GGCAACCGAACTACAACAGG	57
S1971L Fwd	Human	Sequencing	TCTGGAAAAGACGATGAGGC	55
S1971L Rev	Human	Sequencing	GGGATGCTATATTGGGTGGC	55
MYO9A start	Human	Sequencing	AGCTGCTGAGGTGATTGAGT	/
MYO9A mid	Human	Sequencing	TTCCTCTGCTCACTTACCCC	/
MYO9A end	Human	Sequencing	GCAAGTCTGAACCTTCCAGC	/
S1971L Fwd	Human	Mutagenesis	GATGAATATATGAATGAATTCAAGACTTTAGATTGCACAGCCACAAAGGTGCC	63
S1971L Rev	Human	Mutagenesis	GTTTTTGGCACCTTTGTGGCTGTGCAATCTAAAGTCTTGAATTCATTCATATATTCATC	63
R1517 Fwd	Human	Mutagenesis	GAATGAAAAAGAGATGATGGAACAGATTCACCAGCAAACAGATATTTTAGAGAAGGAGC	63
R1517 Rev	Human	Mutagenesis	GCTCCTTCTCTAAAATATCTGTTTGCTGGTGAATCTGTTCCATCATCTCTTTTTCATTC	63
D1698G Fwd	Human	Mutagenesis	CAGTAAAAATCCTCAACTCCATAAAGAAGGTGAACCAGCATGGAAACCTGTGAAGTTAGCTG	63
D1698G Rev	Human	Mutagenesis	CAGCTAACTTCACAGGTTTCCATGCTGGTTCACCTTCTTTATGGAGTTGAGGATTTTTACTG	63
R2283H Fwd	Human	Mutagenesis	GATTCGTAGATCAATGGGAAAGGGGCATATTCGTCGAGGAAACTATCCAGGTC	63
R2283H Rev	Human	Mutagenesis	GACCTGGATAGTTTCCTCGACGAATATGCCCCTTTCCCATTGATCTACGAATC	63

Myo9a Fwd 1	Mouse	Genotyping	GCAGCTAGAGCCGTGAGTC	58
Myo9a Rev	Mouse	Genotyping	TCAGCATCCACATGATGACTC	58
Myo9a Fwd 2	Mouse	Genotyping	ATGTTTGCATGTGTGCAGTGC	58

Table 2-2. Primers used in PCRs and sequencing for human, mouse and zebrafish. Application, sequence and annealing temperature included, except when primers used only for sequencing.

2.2.5 Agarose gel electrophoresis

Agarose gels were poured at a concentration of 1-4% (w/v) agarose (NBS Biologicals, Low EEO) in 1 x TAE buffer (40mM Tris base, 20mM acetic acid and 1mM EDTA) depending on the predicted size of the product. SafeView DNA dye (NBS Biologicals) was added to the gel at a ratio of 1:10 for visualisation of DNA fragments. Samples were combined with 6x blue/orange loading dye and loaded onto the gel submerged in 1x TAE buffer, along with a 100 base pair (bp) DNA ladder (Promega), and ran for 30-45 mins at 90 V. Gels were imaged using a GelDoc-It imager.

2.2.6 DNA sequencing

For sequencing of DNA, PCRs were performed as described in Section 2.1.4 and purified using ExoSAP-IT (Applied Biosystems). ExoSAP-IT was added at a ratio of 5:2 with the PCR reaction and incubated at 37ºC for 15 mins, followed by 15 mins at 80ºC. Purified samples (1ng/µl), along with 2µl primer for sequencing (10µM), were sent to Eurofins Genomics (Germany).

2.2.7 Quantitative RT-PCR

Quantitative reverse transcriptase PCR (qRT-PCR) was performed on cDNA using either PowerSYBR green master mix (Applied Biosystems) or iTaq Universal SYBR Green supermix (Bio-Rad).

Optimisation of annealing temperature was performed for each primer set using standard gradient PCR, primers shown in Table 2-3. Annealing temperature optimisation for *COL1A1, COL3A1, PAX6, SOX1, SOX2, NES* and *GAPDH* primers was performed by the laboratory of Professor Rita Horvath. Appropriate cDNA concentration and reaction efficiency for each primer set (excluding those listed

above) was determined by carrying out a qRT-PCR dilution calibration curve on serial dilutions of stock cDNA.

Primer	Species	Sequence 5'-3'	Annealing temperature (°C)
COL1A1 Fwd	Human	GATTCCCTGGACCTAAAGGTGC	58
COL1A1 Rev	Human	AGCCTCTCCATCTTTGCCAGCA	58
COL3A1 Fwd	Human	CCCTGGATCTCCAGGATA	58
COL3A1 Rev	Human	GTCCGGGTCTACCTGATT	58
PAX6 Fwd	Human	GTGTCCAACGGATGTGTGAG	58
PAX6 Rev	Human	CTAGCCAGGTTGCGAAGAAC	58
SOX1 Fwd	Human	GAGTGGAAGGTCATGTCCGAGG	58
SOX1 Rev	Human	CCTTCTTGAGCAGCGTCTTGGT	58
SOX2 Fwd	Human	GCTACAGCATGATGCAGGACCA	58
SOX2 Rev	Human	TCTGCGAGCTGGTCATGGAGTT	58
NES Fwd	Human	TCAAGATGTCCCTCAGCCTGGA	58
NES Rev	Human	AAGCTGAGGGAAGTCTTGGAGC	58
GAPDH Fwd	Human	GTCTCCTCTGACTTCAACAGCG	58
GAPDH Rev	Human	ACCACCCTGTTGCTGTAGCCAA	58
TBP Fwd	Human	TATAATCCCAAGCGGTTTGC	58
TBP Rev	Human	GCTGGAAAACCCAACTTCTG	58
MYO9A Fwd	Human	AAGGCCTCAAGTACTGGTCC	58
MYO9A Rev	Human	TCAGTGCATCGTGATTTCAGG	58
Myo9a Fwd	Mouse	ATTCTGAGCCGGATTGCTT	60
Myo9a Rev	Mouse	TGTCTTCGTGTCTTGGGAAG	60
Pgk1 Fwd	Mouse	GGAGCGGGTCGTGATGA	60
Pgk1 Rev	Mouse	GCCTTGATCCTTTGGTTGTTTG	60

Table 2-3. Primers for qRT-PCR, including species, sequence and annealing temperature.

Reactions using PowerSYBR green master mix contained: 1x Power SYBR Green PCR Master Mix, 500nM forward/reverse primers, cDNA (variable), nuclease-free water (up to final volume of 20µl). ITaq universal SYBR Green reactions were composed of: 1x iTaq Universal SYBR Green Supermix, 750nM forward/reverse primer, cDNA (variable), nuclease-free water (up to final volume of 20µl).

A CFX96 Touch Real Time detection system (BioRad) was used to perform thermal cycling for the qRT-PCRs (Table 2-4). Melt curves were analysed and qRT-PCR products also subject to gel electrophoresis to confirm the presence of a single amplicon. Data analysis was performed in CFX Manager software, or manually using Excel, applying the delta Ct method.

		Power SYBR Green	ITaq universal SYBR Green	
Step	**Temperature (ºC)**	**Time (mins)**		**Cycles**
Enzyme activation	95	10	3	1
Denaturation	95	0.15	0.10	40
Annealing/Ex-tension	Variable	1	1	
Melt Curve	65-95 with 0.5 increments	0.03/step	0.03/step	1

Table 2-4. Thermal cycling conditions for PowerSYBR Green and iTaq universal SYBR Green reaction mixes for qRT-PCR.

2.2.8 Production of single guide RNAs for CRISPR/Cas9-mediated genome editing

This protocol was modified from Varshney *et al* (2016). Single guide RNAs (sgRNAs) for generating CRISPR/Cas9-mediated knockdown zebrafish were designed using CRISPR scan (http://www.crisprscan.org/, date last accessed February 20, 2019, Moreno-Mateos et al., 2015). Targets were picked that had the highest CRISPRscan score (efficiency score) and no off target effects predicted (Table 2-5). DNA oligonucleotides that included the target region and surrounding T7 promoter sequence and tail sequence were then ordered from Eurofins Genomics, along with a universal bottom strand ultramer (5′AAAAGCACCGACTCGGTGCCACTTTTTCAAGTTGATAACGGACTAGCCTTATTTTAACTTGCTATTTCTAGCTCTAAAAC-3′). Primers were designed to flank the surrounding region of the gene for confirmation of knockdown and also ordered from Eurofins Genomics (Table 2-2).

Gene	Target site sequence	Promoter + sgRNA + universal primer sequence	Off-targets	CRISPRscan efficacy score
myo9aa	AGGAGTTCGGTGGGGAGGAGTGG	taatacgactcactataGGGAGTTCGGTGGGGAGGAGgtttagagctagaa	0	79
myo9aa	GCGCTGGACGGGATAATCGGTGG	taatacgactcactataGGGCTGGACGGGATAATCGGgtttagagctagaa	0	77
myo9ab	GTGTTTCAGATCCTGTCCATTGG	taatacgactcactataGGGTTTCAGATCCTGTCCATgttttagagctagaa	0	69
myo9ab	AGTGCAGACTTGGAGCCCAGCGG	taatacgactcactataGGTGCAGACTTGGAGCCCAGgtttagagctagaa	0	78
Tyr	GGACTGGAGGACTTCTGGGG	taatacgactcactataGGACTGGAGGACTTCTGGGGgtttagagctagaa	0	69

Table 2-5. sgRNA sequences used for CRISPR/Cas9-mediated gene modification in zebrafish. Sequence of target site and target site including promoter and universal binding sequence are shown. Off targets refers to other areas of the genome the sgRNA may bind. The higher the CRISPRscan score (out of 100), the higher the predicted efficacy of that sgRNA.

The sgRNA sequence oligo and universal bottom strand were annealed using the reaction mix described in Table 2-6 and reaction performed in a thermocycler according to steps in Table 2-7.

Component	1x Volume (µl)
5x My Taq Buffer	5
gRNA target oligo (100µM)	2
Universal strand ultramer (100µM)	2
My Taq DNA polymerase	0.2
Nuclease free water	15.8
Total volume	25

Table 2-6. Annealing reaction for sgRNA oligo and universal bottom strand.

Temperature (°C)	Time (mins)
95	5
89	0.25
83	0.25
77	0.25
71	0.25
65	0.25
59	0.25
53	0.25
50	10
72	10
4	∞

Table 2-7. Thermocycler program for annealing of sgRNA and universal bottom strand.

A Qiagen PCR purification kit was then used to purify samples according to manufacturer's instructions. The purified product was used as a template for the MEGAshortscript T7 kit (Invitrogen), set up as shown in Table 2-8, with 8 reactions per sgRNA sequence. This was incubated overnight at 37ºC. The following day, 1µl of TURBO DNase was added to each reaction and incubated at 37ºC for 15 mins.

Component	1x volume (µl)
T7 10x reaction buffer	2
T7 ATP solution	2
T7 CTP solution	2
T7 GTP solution	2
T7 UTP solution	2
Template DNA	8
T7 Enzyme mix	2
Total volume	20

Table 2-8. MEGAshortscript T7 reaction mixture.

The 8 reactions per sgRNA were pooled to increase yield and RNase-free water added to a final volume of 800µl. The pooled samples were then added to a Mirvana spin column (mirVana miRNA isolation kit, ThermoFisher Scientific) and subject to washes to purify the RNA according to manufacturer's instructions. RNA was eluted in 30µl of RNase-free water and concentration/purity assessed using a Nanodrop 2000 (ThermoFisher Scientific), aliquots were stored at -80ºC.

Prior to injection into zebrafish embryos, the sgRNA and Cas9 reaction mix was prepared as outlined in Table 2-9, and heated to 37ºC for 5 mins to improve knockdown efficiency as described by Burger *et al* (2016).

Component	1x volume (µl)
10x Cas9 Buffer (0.2M HEPES, 1M NaCl, 50mM $MgCl_2$, 1mM EDTA)	1
EnGen Cas9 NLS Protein (20µM, NEB, MO646T)	3.58
RNA	3000ng - variable
2M KCL	1.5
0.5% Phenol red	1
RNase-free water	Up to 10
Total volume	10

Table 2-9. Reaction mixture for zebrafish injection with sgRNA and Cas9 protein.

2.3 Tissue culture

2.3.1 Maintenance of cultured cells

Cells were maintained at 37ºC in 5% CO_2 to subconfluence. Fibroblasts were cultured in Dulbecco's modified Eagle medium (DMEM, Gibco), supplemented with 15% fetal bovine serum (FBS, Gibco). NSC-34 cells (control and MYO9A knockdown (KD)) were cultured in DMEM with 10% FBS, 100 units/ml penicillin/streptomycin (Gibco) and 3 µg/ml puromycin (Gibco) to maintain selective pressure. SH-SY5Y cells were maintained in 1:1 DMEM:Ham's F12 (Gibco), supplemented with 10% FBS.

Cells were sub-cultured when reaching 90-100% confluence by washing with PBS followed with application of Trypsin-EDTA (0.05%, Gibco), for 5 mins at 37ºC. In the case of SH-SY5Y cells, medium was also centrifuged at 250g to collect cells in suspension. Dissociation was ceased by addition of 4x volume of DMEM + 10% FBS and cells subject to centrifugation at 250g. The resulting cell pellet was re-suspended in its respective growth medium and plated as required.

Freezing of cells was performed at an early (<5) passage for each cell-type used. Cells were cultured in T75 flasks until 80% confluent, before Trypsin-mediated dissociation was performed as described. Cell pellets were resuspended in 10ml freezing medium, composed of 30% FBS, 60% DMEM and 10% dimethylsulfoxide. Vials containing 1ml (10 per flask) were transferred to a ThermoFisher Scientific Mr Frosty with 100% isopropyl alcohol in a -80°C freezer, to ensure slow cooling. Long-term stocks of cells were transferred to liquid nitrogen storage after 3 days at -80°C.

Thawing of cells was performed rapidly at 37°C before plating in a T25 flask with growth medium. After allowing cells to adhere for 6 hours, medium was changed to new growth medium to remove the dimethylsulfoxide present in freezing medium.

2.3.2 shRNA transfection of NSC-34 cells

Generation, optimisation and transfection of shRNAs for MYO9A knockdown from NSC-34 cells was performed during my Masters project (O'Connor, 2015, University of Glasgow). A new control shRNA knockdown line was generated during this project, using the commercially available control shRNA, expressed within a plasmid containing a puromycin resistance gene (Santa Cruz Biotechnology, 108060). Transfection of the control shRNA was performed using FuGENE HD transfection reagent (Promega). Cells were seeded at the same time as the transfection protocol was performed, as this gave a higher rate of success than when transfecting adhered cells, optimised during my Masters project. A ratio of 1:1.5 plasmid DNA to FuGENE reagent was used. After 12 hours, medium was exchanged for normal growth medium and cells were cultured for a further 36 hours. Growth medium supplemented with 3µg/ml puromycin was then added to the cells and replaced every second day for 14 days. A polyclonal population of knockdown cells was then maintained under selective pressure for performing experiments.

2.3.3 Site-directed mutagenesis of human MYO9A construct and expression in SH-SY5Y cells

In order to analyse the effect of MYO9A-CMS patient mutations *in vitro,* site-directed mutagenesis was used on a human-MYO9A construct and SH-SY5Y cells used to express the resulting plasmids.

A plasmid containing the human MYO9A open reading frame with a c-terminal Human influenza hemagglutinin (HA)-tag was obtained from VectorBuilder, as an E.Coli stock (Figure 2.1). A sterile inoculating loop was used to transfer bacteria from the stock to Luria broth (LB) agar plates containing 100µg/ml of Ampicillin (Sigma Aldrich) before incubating at 37°C overnight. A distinct colony was selected and cultured overnight with vigorous shaking at 37ºC in 3ml LB medium, containing 100µg/ml of Ampicillin. Purification of plasmid DNA was performed using a QIAprep Spin Miniprep Kit (Qiagen) according to manufacturer's instructions. To confirm the presence of the expected *MYO9A* sequence, plasmid DNA was sent for Sanger sequencing (Eurofins Genomics, Germany), using MYO9A start, middle and end primers listed in Table 2-2 to sequence different regions of the insert.

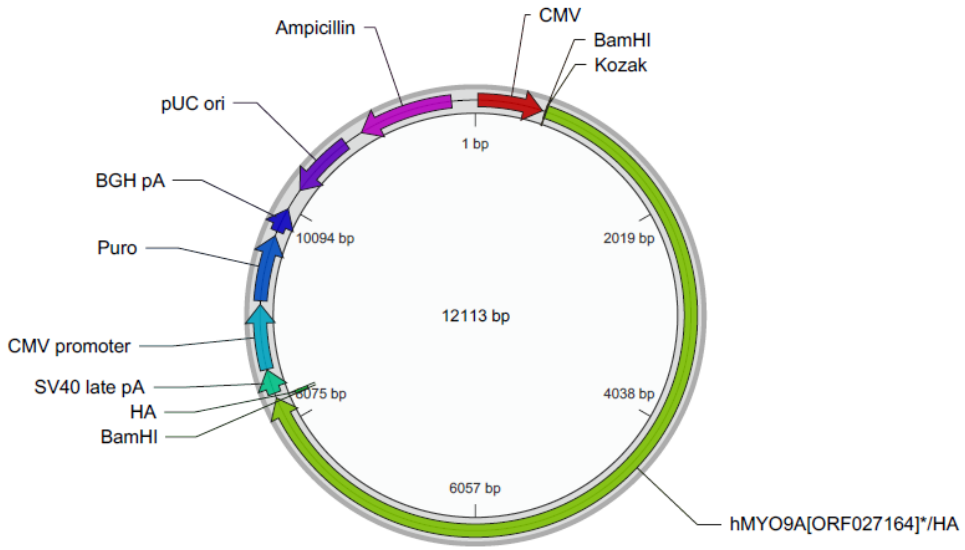

Figure 2.1. Vector map of human MYO9A plasmid. Includes c-terminal HA-tag, cytomegalovirus promoter, puromycin resistance gene, ampicillin resistance gene and BamHI restriction sites.

Following confirmation of the insert, CMS-patient mutations (R1517H, D1698G and R2283H) and a benign polymorphism (S1971L) were inserted into the sequence using a QuikChange XL Site-Directed Mutagenesis Kit according to manufacturer's instructions (Agilent). Briefly, mutagenesis primers were obtained from Eurofins (Table 2-2) and a reaction mixture prepared as shown in Table 2-10 for each primer pair.

Component	Quantity per reaction (µl)
10× reaction buffer	5
Double stranded DNA template	Volume for 10ng
Oligonucleotide primer 1	Volume for 125ng
Oligonucleotide primer 2	Volume for 125ng
dNTP mix	1
QuikSolution	3
ddH20	To final volume of 50
Pfu Turbo DNA polymerase	1 (2.5U/µl)

Table 2-10. Components for QuikChange XL site-directed mutagenesis kit.

The reaction mixes were subject to thermal cycling according to the steps in Table 2-11, followed by cooling on ice for 2 mins. Dpn I restriction enzyme (10U/µl) was then added to each reaction and mixed gently before incubating for 1 hour at 37°C.

Step	Temperature (ºC)	Time	Cycles
1	95	1 min	1
2	95	50 secs	18
	60	50 secs	
	68	1 min/kb of plasmid length = 12 min	
3	68	7	1

Table 2-11. Thermal cycling parameters for the QuikChange XL site-directed mutagenesis kit.

XL10-Gold ultracompetent cells were used for transformations. XL10 cells were thawed on ice and 45µl added to a prechilled 14ml falcon tube, along with 2µl β-ME mix and incubated for 10 mins with regular mixing. Dpn I-treated DNA from each reaction was added to separate aliquots of ultracompetent cells, at 2µl per sample and gently mixed. Reactions were incubated on ice for 30 mins and then cells heat-shocked at 42°C in a water bath for 30 secs. After incubating on ice for 2 mins, 0.5ml of preheated (42°C) NZY$^+$ broth was added to each sample and incubated at 37°C for 1 hour with shaking at 250 rotations per minute. Samples were then applied to LB-ampicillin (100µg/ml) agar plates and incubated overnight at 37°C.

The following day, colonies from each plate were selected as described above, incubated overnight in LB medium containing ampicillin, and subject to purification using a QIAprep Spin Miniprep Kit (Qiagen) according to manufacturer's instructions. To confirm mutagenesis success, PCRs were performed on the plasmid DNA as described in Section 2.1.4, using primers from Table 2-2, before sending for Sanger sequencing (Eurofins Genomics, Germany).

For expression of the human MYO9A constructs (wild-type and with mutations), transfections were performed using Lipofectamine 2000 reagent (ThermoFisher Scientific) in SH-SY5Y cells. Cells were seeded at the time of transfection ($0.3x10^6$ cells/well of a 6-well plate), and the protocol performed as described in Section 2.2.7. A ratio of 1:3 plasmid DNA:Lipofectamine reagent was used. After 6 hours, the medium was changed for growth medium and cells cultured for 24-48 hours before lysing for western blot (Section 2.5), or fixing for immunofluorescence (Section 2.4.3).

2.3.4 Conversion of fibroblasts to iNPCs

A summary of this protocol is shown in Figure 2.2. Fibroblasts from a skin biopsy from suspected MYO9A CMS patient 1 (aged 3 at time of biopsy) were isolated by

EuroBioBank (http://www.eurobiobank.org/) and obtained, along with fibroblasts from a healthy control subject (age 27 at time of biopsy). Ethical approval obtained by the EuroBioBank. MYO9A CMS patient cells were cultured for 2 passages in fibroblast growth medium as described (section 2.2.1). Cells were then dissociated and counted using a haemocytometer, before seeding 75,000 cells/well of a 12-well plate. After 24 hours of culturing in growth medium, the conversion process was initiated. Control cells were converted under the same conditions by Emily McCarthy (Wellcome Trust Centre for Mitochondrial research, Newcastle, Prof. Rita Horvath).

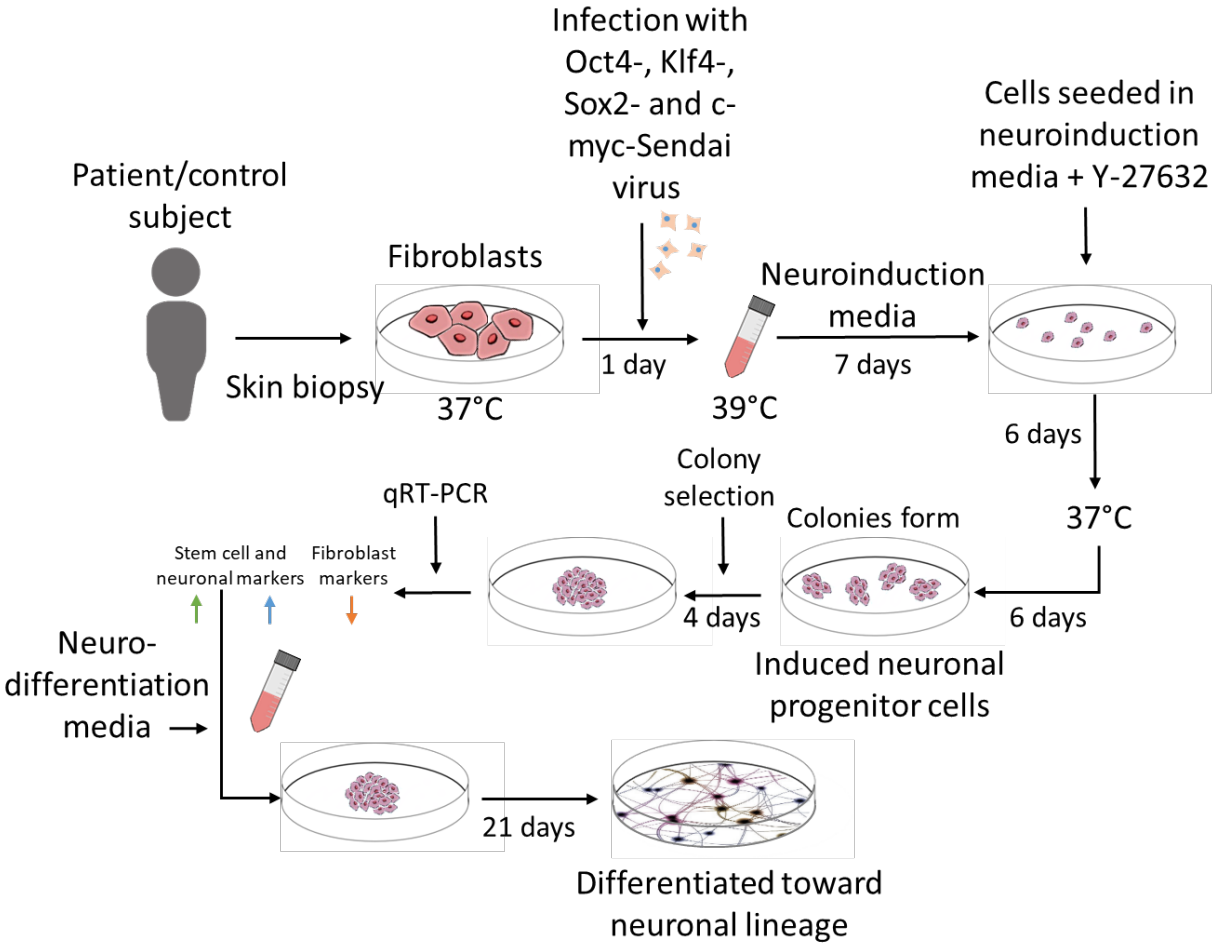

Figure 2.2. Summary of direct conversion protocol for fibroblasts to differentiated iNPCs.

Direct conversions of fibroblasts into a proliferating neural progenitor cell population can be achieved by performing transductions to overexpress transcription factors (Oct4, K1f4, Sox2 and c-myc) using Sendai virus (Meyer et al., 2015). Virus containing each transcription factor were added to the cells with a multiplicity of infection of 3, in growth media and mixed gently. Cells were cultured overnight at

37ºC in the presence of the viruses before application of neuroinduction media, as described in Table 2-12, and subsequent incubation at 39ºC.

Component	Company	Concentration
DMEM/F-12 with GlutaMAX (1%)	Gibco	1:1 with neurobasal
Neurobasal Medium	Gibco	1:1 with DMEM/F-12
100x N-2 Supplement	ThermoFisher Scientific	1x
50x B27 Supplement	ThermoFisher Scientific	1x
Recombinant Human Leukemia Inhibitory Factor	Peprotech	10ng/ml
CHIR 99021	Peprotech	3μM
SB431542	Stemcell technologies	2μM

Table 2-12. Components of neuroinduction media for culturing cells during conversion from fibroblasts to iNPCs.

Neuroinduction media was replaced every second day and stocks of media replaced every 5 days. Laminin-coated 6-well plates were prepared 6 days following transduction by diluting laminin (Gibco natural laminin mouse protein) to 50μg/ml in PBS and incubating overnight at 4ºC. The laminin was then removed from the wells and wells allowed to air dry for 20 mins. Meanwhile, transduced cells were washed once in PBS and then split by incubating cells at 37ºC for 5 mins in Accutase solution (Merck). The same volume of DMEM/F-12 was then added to each well and the sample centrifuged at 180g for 5 mins. The resulting pellet was resuspended in 1.5ml of neuroinduction media, containing 10μM of ROCK inhibitor (Y-27632, Millipore Sigma) and plated onto a laminin-coated well before incubating at 39ºC. Medium was changed every second day and cells were moved to 37ºC 14 days after initial infection. Colonies began to form around day 17 and were large enough to be selected by day 20. Laminin coating of 48-well plates was performed on day 19 post-infection and cell colonies were selected the following day. Selection was performed using a fine pipette tip to scrape each colony from the plate, and then transferring the colony to a well of the 48-well plate containing neuroinduction medium with 10μM Y-27632. Around 20 colonies were selected and grown for 4 days, until approximately 90% confluent. Medium was changed every second day.

Following selection of individual colonies, those that had adhered and expanded were subject to RNA extraction, as described in section 2.1.2, and then cDNA generated for qRT-PCR (Section 2.1.3). Primers for a range of markers were used, as optimised by Prof. Rita Horvath's research group at Newcastle University. These included primers against fibroblast markers; COL1A1 and COL3A1, stem cell markers; SOX1 and SOX2, and neuronal markers; NES and PAX6. House-keeping targets TBP and GAPDH were also included for normalisation of expression, sequences in Table 2-3. Colonies in which fibroblast marker expression was downregulated and both stem cell and neuronal markers were upregulated as compared to the initial fibroblast sample were deemed successfully converted into induced neuronal progenitor cells (iNPCs) and these were expanded for future experimental use and storage. Expansion was performed in neuroinduction media with 10μM Y-27632 at 37ºC on laminin-coated plates, and freezing of iNPCs was achieved by detaching the cells as described above and resuspending the pellet in Recovery Cell Culture Freezing Medium (ThermoFisher Scientific).

2.3.5 Differentiation of iNPCs to neurons

Differentiation of iNPCs towards the neuronal lineage was performed on the most successfully converted iNPC colonies, as deemed by the qRT-PCR results. Cells were seeded onto laminin-coated plates, some containing coverslips if confocal imagining was required after differentiation. Neuroinduction medium was exchanged for neuro-differentiation medium when cells were around 70% confluent, the components of which are described in Table 2-13.

Component	Company	Concentration
DMEM/F-12	Gibco	
100x N-2 Supplement	ThermoFisher Scientific	1x
50x B27 Supplement	ThermoFisher Scientific	1x
cAMP	Millipore Sigma	300ng/ml
Vitamin C	Millipore Sigma	200µM
BDNF	Peprotech	10ng/ml
GDNF	Peprotech	10ng/ml

Table 2-13. Components of neurodifferentiation medium for differentiation of INPCs toward neuronal lineage.

Neuro-differentiation media was replaced every second day for three weeks, at which point cells had developed neurite outgrowths and organised into networks. They also expressed neuronal markers as confirmed by immunofluorescence imaging of Tuj1 and MAP-2 (section 2.4.3, Table 2-14).

Antibody type	Antibody	Source	Concentration for immunofluore-scence	Concentra-tion for western blot
Primary	Mouse monoclonal anti-neurofilament	ThermoFisher Scientific	1:100	1:1000
Primary	Rabbit polyclonal anti-TrkA	Millipore	1:100	
Primary	Rabbit polyclonal anti- ubiquitin	Abcam	1:500	
Primary	Rabbit polyclonal anti-SQSTM1/ P62	Abcam	1:400	
Primary	Rabbit polyclonal anti-β-tubulin	Abcam	1:100	1:500
Primary	Mouse monoclonal anti-β-actin	Millipore Sigma		1:1000
Primary	Mouse monoclonal anti-agrin (D-2)	Santa Cruz	1:100	
Primary	Rabbit polyclonal anti-synaptophysin Ab-4	ThermoFisher Scientific	1:200	
Primary	Mouse anti-SV2	Developmental Studies Hybridoma Bank	1:200	
Primary	Mouse anti-Tuj1	Abcam	1:200	
Primary	Chicken anti-MAP2	Millipore Sigma	1:250	

Primary	Mouse monoclonal anti-HA (12CA5)	Roche	1:100	1:100
Primary	6H1 Mouse monoclonal MHC2x IgGM	Developmental Studies Hybridoma Bank	1:25	
Primary	Mouse monoclonal BA-F8 anti-MHC1 IgG2b	Developmental Studies Hybridoma Bank	1:25	
Primary	Sc-71 Mouse monoclonal MHC2a IgG1	Developmental Studies Hybridoma Bank	1:200	
Primary	BF-F3 Mouse monoclonal MHC2b IgM	Developmental Studies Hybridoma Bank	1:200	
Primary	Rabbit polyclonal anti-laminin IgG	Millipore Sigma	1:750	
Direct	Oregon Green 488 phalloidin	Life Technologies	1:1000	
Direct	Alexa Fluor 594 phalloidin	Life Technologies	1:1000	
Direct	Alexa Fluor 488 α-bungarotoxin conjugate	Life Technologies	1:1000	
Secondary	Alexa Fluor 488 IgG goat anti-rabbit	Life Technologies	1:500	
Secondary	Alexa Fluor 594 IgG goat anti-rabbit	Life Technologies	1:500	

Secondary	Alexa Fluor 594 IgG goat anti-mouse	Life Technologies	1:500	
Secondary	Alexa Fluor 488 IgG goat anti-rabbit	Life Technologies	1:500	
Secondary	Alexa Fluor 350 IgG2b goat anti-mouse	Life Technologies	1:500	
Secondary	Alexa Fluor 594 IgG1 goat anti-mouse	Life Technologies	1:100	
Secondary	Alexa Fluor 488 IgM goat anti-mouse	Life Technologies	1:500	
Secondary	Goat anti-rabbit HRP conjugated	Invitrogen		1:2000
Secondary	Goat anti-mouse HRP conjugated	Invitrogen		1:2000
Secondary	DyLight 680 goat anti-mouse	ThermoFisher Scientific		1:2000
Secondary	DyLight 680 goat anti-rabbit	ThermoFisher Scientific		1:2000
Secondary	DyLight 800 goat anti-mouse	ThermoFisher Scientific		1:2000
Secondary	DyLight 800 goat anti-rabbit	ThermoFisher Scientific		1:2000

Table 2-14. Antibodies used for immunofluorescence and immunoblotting studies, including concentrations.

2.3.6 FM-Dye endo/exocytosis

To look at recycling dynamics in cells depleted for MYO9A, an FM-Dye assay was performed. NSC-34 control and MYO9A-depleted cells were seeded at 0.1 x 10^6 cells per well of 12 well plates containing coverslips and incubated in growth medium at 37ºC overnight. FM 1-43X (ThermoFisher Scientific) working stock (5µg/ml) was made up in ice cold Hank's Balanced Salt Solution (HBSS, Gibco) without magnesium or calcium.

Dye was added to each well of control and knockdown cells in duplicate sequentially to achieve staining times of 1, 3, 6, 9, 12, 15 and 18 mins. After addition of dye to each well, cells were incubated at 37°C. After incubating each well for the appropriate time, cells were washed in ice-cold HBSS 3 times and fixed in 4% paraformaldehyde (PFA) in HBSS for 10 mins on ice. Coverslips were removed from wells and mounted onto slides with mounting medium containing DAPI (Vectashield). Imaging was then performed using a Nikon A1R confocal. Z-stacks were obtained throughout the cells volumes, and 4 separate fields of view were chosen at random for imaging for each cell type/time point. Fluorescence intensity was then measured using ImageJ for at least 36 cells per condition using the corrected total cell fluorescence (CTCF) value to correct for cell size. This is calculated by measuring the area, average fluorescence and integrated density of individual cells, and a mean background fluorescence value taken from 3 regions of each field of view. CTCF was then calculated using the following equation:

CTCF=Integrated density-(area of selected cell x mean fluorescence of background)

In iNPC cells the FM-Dye procedure was carried out using an alternative procedure, whereby high K^+ was used to stimulate exocytosis. INPCs that had been differentiated for 3 weeks were used for this experiment. The staining solution described above was added to each well of control subject or MYO9A-patient neuronal cells and left for 1 min at 37°C. Some cells were fixed at this point. The rest of the cells were subject to a 10 min wash at room temperature with 2 changes of wash solution, before more cells were fixed. For the remaining cells, HBSS with 50mM KCl was added for 5 or 25 mins, before fixation. Cells were then mounted, imaged and analysed as described for NSC-34 cells above.

2.3.7 TrkA receptor transfection

For the two assays requiring expression of a paradigmatic receptor, Tropomyosin receptor kinase A (TrkA), transfections were performed in the same manner using Lipofectamine 2000 as described (O'Connor et al., 2018a). NSC-34 control and MYO9A-depleted cells were split as described in Section 2.2.1 and seeded either onto coverslips within 6-well plates (for the receptor internalisation assay, 0.3 x 10^6 cells/well) or onto µ-Slide 8 well glass bottom chambered coverslips (Ibidi, for live-cell time-lapse imaging, 5x10^4 cells/well). Transfections were performed at the time of seeding cells as this was found to improve efficiency. TrkA-GFP tagged constructs (gift from Dr. Joachim Weis, Aachen) were transfected according to manufacturer's instructions using Lipofectamine 2000 (ThermoFisher Scientific) at a ratio of 1:3 DNA to reagent. Briefly, plasmid DNA was added to opti-MEM reduced serum medium (Gibco) and Lipofectamine reagent combined with opti-MEM, then both incubated at room temperature for 5 mins. Lipofectamine solution was then combined with plasmid DNA solution and mixture incubated at room temperature for 20 mins before adding to cells. Cells were incubated overnight in the transfection reagent and then washed 3 times in PBS before continuing incubation in growth medium until required.

2.3.8 TrkA receptor internalisation tracking

Transfected cells were washed twice with pre-warmed PBS 24 hours after transfection. Cells were then serum starved in serum-free DMEM for 2 hours before application of growth medium containing 50ng/ml of nerve growth factor (NGF, Millipore Sigma) to stimulate internalisation of receptors. This process should be complete by around 15 mins (Cabrera et al., 2015), after which serum- and NGF-free medium was added to the cells to allow recycling of receptors back to the surface. Fixation of cells was performed at different time points within this procedure, including before NGF application and then 0, 10, 30, 60 and 180 mins following NGF addition. Cells were fixed in 1:1 4% PFA in PBS:growth medium at 37°C for 5 mins. Samples were then mounted in ProLong Diamond Antifade Mountant with DAPI (Molecular probes) for confocal imaging. For analysis, 50 cells per time point were imaged and the entire experiment repeated 4 times, giving a total of 200 cells per time point. Cells were individually assessed for the presence of surface or internalised TrkA receptors. Confirmation that the TrkA-GFP plasmid was producing TrkA protein, a set of transfected cells were also stained with an anti-TrkA antibody to look for colocalising signals (Table 2-14).

2.3.9 Protein levels of TrkA

During the receptor internalisation assay described above, it is possible that receptors are being targeted for degradation rather than recycling back to the surface. To account for this, levels of TrkA protein were also assessed throughout the time period of the experiment. Cells were seeded onto 10 cm^2 plates at a density of 4 x 10^6 cells/plate, and transfected as described in section 2.2.7. Cells were lysed before addition of NGF, and then following 0, 60 and 180 mins after application. Lysates were then subject to western blotting as described in section 2.5, using an antibody against TrkA (Table 2-14). This was performed 3 times.

2.3.10 TrkA live-cell trafficking

For tracking of TrkA receptor movements within the cell, time-lapse imaging was performed on control and MYO9A-depleted NSC-34 cells. One day following transfection, cells were either incubated overnight in serum-free medium or in serum-free medium containing 3nM of ROCK inhibitor (InSolution Y-27632, Calbiochem). Control NSC-34 cells were also subject to other treatment conditions for assessing the contribution of a disturbed cytoskeleton to disruption of trafficking dynamics. Treatment of cells with Nocodazole (10μM, Millipore Sigma) was performed in growth medium for 5 hours before imaging cells, and Cytochalasin D (1μg/ml, Millipore Sigma) was also applied in growth medium and cells incubated for 1 hour before imaging.

To visualise nuclei during imaging, NucRed Live 647 ReadyProbes reagent (Invitrogen) was applied to each well (2 drops per ml). Cells were imaged using a Nikon A1R laser scanning confocal microscope over a period of 10 mins per cell, with z-stacks obtained covering the height of the cell. Resulting image series were then analysed using IMARIS (x64 v8.4.0, Bitplane AG). TrkA-positive vesicles were automatically detected using thresholding which was manually edited to ensure appropriate vesicle selection. Following identification of vesicles, the IMARIS software tracked their movement over time and in 3D space to allow speed to be calculated for each point. Over 3 experimental repeats, 10 cells were analysed per condition.

2.4 Zebrafish

2.4.1 Maintenance and strains

Zebrafish were maintained in tanks with fresh water at 28.5°C under the care of facility staff, according to Home Office guidelines (under project number: 70/8038). Fish were housed with a continuous light-dark cycle (14 hours light, 10 hours dark). The strains of zebrafish used in this project are listed in Table 2-15. Euthanasia of fish was achieved by using a 1:1 ratio of fresh system water:4mg/ml tricaine methanesulfonate.

Strain	Genotype	Function	Source
AB	Wild-type		Zebrafish International Resource Center
Golden	slc24a5b1/+	Lack of pigmentation	Zebrafish International Resource Center
Islet-1	Tg[*isl1*:GFP]	Express GFP in cranial motor neurons and Rohon beard sensory cells	Zebrafish International Resource Center

Table 2-15. Strains of zebrafish used, including the effect of each genotype.

2.4.2 Breeding and embryo harvesting

To breed zebrafish for injection of embryos or to generate new lines, males and females were separated the evening before. Breeding tanks with mesh grids to separate the fish were used, with 1 male in the bottom tank and 1 or 2 females in the top tank. Larger tanks were also used, holding up to 6 males and females.

In the morning the water in the tanks was replaced and fish combined for mating. Approximately 20 mins after eggs were laid, they were collected and washed with E3 medium (5mM NaCl, 0.17mM KCl, 0.33mM $MgSO_4$, 0.33mM $CaCl_2$ and 0.01% methylene blue). Embryos were taken for injection if required and then stored in E3 medium at 28.5°C for up to 5 days post fertilisation (dpf). Embryos after this point were culled or moved into nursery tanks for development.

2.4.3 Design and preparation of morpholinos

MOs against the zebrafish MYO9A orthologues, Myo9aa and Myo9ab, were designed and optimised in my Masters project (O'Connor et al., 2016). These MOs were splice blocking and targeted exon 4 and exon 7 of *myo9aa/ab* respectively

(ZV9/danRer7 assembly) and were obtained from Gene Tools LLC (USA). The sequences for MOs used were: *myo9aa*: 5'-CAGCAGGATGAAGTCGTACCTGATT-3' and *myo9ab* 5'-TATGTTGAAGAGTGTTACCGTTGTC-3'. For a negative control, the standard control MO from Gene Tools was utilised, which targets a mutation in human beta-globin, to account for phenotypes associated with the injection process.

To prepare MO stocks for injecting, the 300nmols of lyophilized powder received from Gene Tools LLC was dissolved in Danieau buffer to a concentration of 5mM, this was stored at -20°C. For a working stock solution, the 5mM stock was diluted to 1mM and aliquoted for use in injections. Prior to injecting, the MO working stock was supplemented with 0.05% Phenol red and heated to 65°C for 5 mins, cooled on ice for 1 min and then mixed by gentle vortexing.

2.4.4 Microinjections of MOs and Cas9/gRNA

To perform microinjections, embryos were taken at the one cell stage and all dead or abnormal embryos were removed. Embryos (20-30) were lined up in a petri dish against a microscope slide as shown in Figure 2.3. Glass needles were made from Bo-glass capillaries with filament (Hilgenberg, Germany) using a micropipette puller ((Program P:500, Heat:800, Pull:150, Velocity:100 and Time:150), Flaming/Brown Micropipette Puller, Sutter Instrument Co. Novato, USA). Needles were loaded with 5µl of required solution and placed onto the micromanipulator before attaching to a microinjector (FemtoJet Microinjector, Eppendorf, UK). To obtain the appropriate drop size, settings on the microinjector were kept constant (180hPa injection pressure, 0.1ms Injection time, 18hPa back pressure), and the needle was broken using forceps to change the diameter of the drop (measured using a graticule with 0.01mm units). To calculate the amount of MO injected using this technique, the following calculation was used:

Volume of a sphere= $V = \frac{4}{3}\pi r^3$

d = Diameter of drop on graticule in mm

r = Radius (half of diameter)

1mm^3 = 1µl, therefore Vmm^3=Vµl given per injection

Morpholino molecular weight = MMw

Morpholino working stock concentration = WS in mM

1M= MMw

Therefore $WSmM = \frac{MMw}{\left(\frac{1M}{WS}\right)} g\ in\ 1L$

Convert to ng/nl

$WSmM = \left(\frac{ng}{nl}\right) x\ Vnl$ = amount injected in each drop

After setting up the microinjector (Figure 2.3), the MOs were injected into the yolk sac directly behind the cell between the 1 and 4 cell stage. For generating 'crispant fish', which are the F0 mosaic fish generation, the sgRNA and Cas9 protein were injected directly into the cell at the single cell stage.

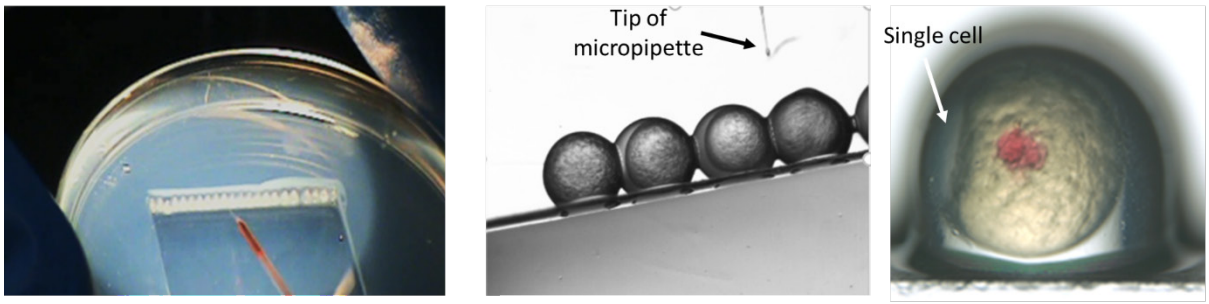

Embryos arranged for injection in petridish

Micropipette containing injection solution controlled by micromanipulator

Example injection of phenol red into yolk sac of one-cell stage embryo

Figure 2.3. Images demonstrating set-up for microinjection of zebrafish embryos. Embryos are positioned in a petridish underneath a light microscope and a micromanipulator used to control entry of a micropipette into the yolk sac or single-cell of embryos. 0.05% phenol red solution can be used to confirm injection success. Images taken from video generated by Dr Alasdair Wood and Dr Juliane Müller (Newcastle University).

Fish were then incubated in petri dishes of up to 50 fish containing E3 medium at 28.5°C for a maximum of 5 days, with dead fish removed daily. For experiments requiring dechorionation, pronase (from Streptomyces griseus, Roche) was added to the zebrafish embryos at a final concentration of 1mg/ml in E3 medium. After approximately 5 mins the chorions were removed and the zebrafish were washed three times with E3 medium. Zebrafish were then left to acclimatise outside of the chorion for at least half an hour before further use.

2.4.5 Genotyping crispants

Crispant zebrafish genotyping was performed on 4 dpf fish. For genotyping, 5 control and 5 fish injected with each of the CRISPR/Cas9 sgRNAs were pooled and gDNA extracted as described in section 2.1.1. PCRs were performed using primers outlined

in Table 2-2, according to the HotStarTaq protocol described in section 2.1.4. PCR products were then ligated into the pGEM-T Easy vector (Promega), by first setting up the reaction shown in Table 2-16.

Component	Amount (µl)
2x Rapid Ligation Buffer, T4 DNA Ligase	5
pGEM-T Easy Vector (50ng)	1
PCR Product	1
T4 DNA Ligase (3 Weiss units/µl)	1
Nuclease free water	2

Table 2-16. Ligation reaction mix for pGEM-T-Easy vector and zebrafish PCR product.

Reactions were incubated overnight at 4°C before analysing the product on an agarose gel to confirm ligation success. Transformations using Top10 chemically competent cells (One Shot TOP10 Chemically Competent E.coli, Life Technologies) were then performed according manufacturer's instructions. Briefly, 1µl of ligation reaction was added directly to a vial of One Shot cells and incubated on ice for 30 mins. After 30 seconds in a 42ºC water bath, samples were incubated on ice for 2 mins and 250µl of warmed S.O.C medium was added. The vial was shaken vigorously for 1 hour at 37ºC. Bacteria from these vials was then cultured overnight at 37ºC on LB agar plates containing 100µg/ml of Ampicillin (Millipore Sigma).

After the formation of individual colonies, 5 from each condition were selected and used for colony PCR. The PCR reaction was prepared using the HotStarTaq protocol as described, and a pipette tip was used to remove the colony from the agar plate and placed in the PCR reaction. Primers for this reaction were M113 standard primers, with annealing temperature set at 57°C and 35 cycles performed. After checking for PCR success on an agarose gel, products were sent for Sanger sequencing using a Eurofins 'PlateSeq Kit for crude PCR products' kit, with the M13 uni (-21) standard primer (5'-TGTAAAACGACGGCCAGT-3').

Sequences were then analysed for the presence of deletions or insertions within the sgRNA target site to confirm the effectiveness of the CRISPR/Cas9 injections.

2.4.6 Generating genetic mutants using CRISPR/Cas9

In this study the F0 mosaic 'crispant' zebrafish were used for experiments. In parallel, attempts were made to generate an adult mutant line. In order to produce the genetic mutant line, crispants injected with all 4 sgRNAs were grown to 3 months in nursery tanks, before being transferred into main tanks ready for breeding. The F0 fish were incrossed and the F1 generation raised to adulthood before being fin clipped to identify zebrafish with the same mutations. Males and females with the same deletions/insertions were incrossed and the F2 generation raised to adulthood, of which 25% should be homozygous for the identified deletion/insertion.

2.4.7 Chorion movements

In early development zebrafish begin to perform spontaneous movements within the chorion. These movements consist of tail turns that involve contraction and swivelling of the tail, and occur from around 18 hpf up until 27hpf. To quantify the number of spontaneous chorion movements performed by the zebrafish, embryos at 24 hpf were recorded using a Leica stereomicroscope mounted with a Chameleon digital camera (CMLN-13s2M). Recordings were made for one minute, and included over 40 zebrafish per condition. The number of full twists performed by each fish was then manually counted from the recordings.

2.4.8 Tactile stimulation assay

At 48 hpf zebrafish are able to respond to tactile stimulation by swimming quickly away by at least one body length. In order to assess this response, zebrafish were first dechorionated at 48 hpf using the aforementioned method (Section 2.3.4) and allowed to acclimatise for around an hour. The tactile response assay was then performed as described in O'Connor *et al* (2018a). Briefly, the fish were placed in a petri dish (one fish at a time) containing fresh E3 medium on top of an illuminated stage and a Canon legria hfr76 camera was held using a clamp 7cm above the dish. A fine pipette was used to touch the zebrafish on the back of the head and the response recorded (camera records at 25 frames per second). Room temperature remained constant at 28°C throughout the experiment.

The videos were imported into Fiji ImageJ as FFmpeg movies and then manually thresholded to allow visualisation of the zebrafish, before converting to a binary image. The Trackmate plugin was then used to measure the movement of the zebrafish, with manual editing of each frame to ensure that only the zebrafish was detected and the movement identified was accurate (Figure 2.4). Values for distance

travelled and average speed were exported, and from this data the initial acceleration could also be calculated.

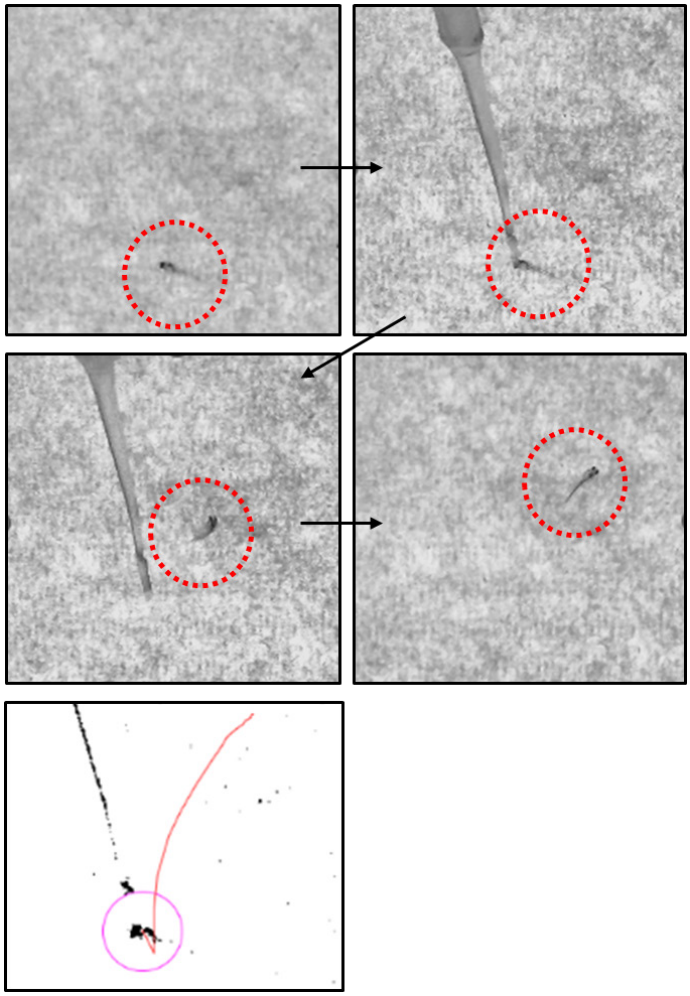

Figure 2.4. Trackmate tracking protocol. Example images from video of the tactile response assay in a control 48 hpf zebrafish, showing the fish in a petridish, a tap on head with pipette tip and subsequent swimming away from stimulus. Fish outlined with red dashed circle. The output from the Trackmate tracking software (ImageJ) is also shown, with the thresholded zebrafish detected in a pink circle and tracked movement shown with a red line.

2.4.9 Acetylcholinesterase assay

To quantify the activity of AChE at different time points of development, a protocol was modified from Teixido *et al* (2013). Zebrafish tails (removed with a scalpel following euthanasia) were pooled at age 1, 2, 3, 4 and 5 dpf (10 per condition and time point). Homogenisation of tissue was performed in 0.5ml of ice cold sodium phosphate buffer (0.1M, pH7.2, with 0.1% v/v Triton x-100), using a Tissue Rupture. Samples were then centrifuged at 10000g for 15 mins at 4ºC, before removing supernatants for the assay. A bicinchoninic acid assay was then used to quantify protein concentration and 10µg of each sample was made up to 30µl in the sodium

phosphate buffer (without Triton). The samples were then added to a 96-well plate in triplicate, along with buffer only blanks. A reaction mix was then added to each well, containing 50mM sodium phosphate buffer (without Triton), 60µl of 0.35mM 5,5′-Dithiobis(2-nitrobenzoic acid, ThermoFisher Scientific) made up in sodium phosphate buffer with 0.1mM EDTA and 18µl of 0.53mM acetylthiocholine iodide (made up in distilled water, Millipore Sigma). A Varioskan LUX plate-reader (ThermoFisher Scientific) was then used to take spectrophotometric readings at 405nm continuously for 10 mins, maintaining a constant temperature of 22ºC. Enzyme activity was then calculated and expressed as nmols of substrate hydrolysed per min per mg of protein.

2.4.10 Treatment with NT1654

The agrin compound NT1654 was used to treat control and Myo9aa/ab-depleted zebrafish. This compound is a 44kDa artificial agrin fragment developed by Neurotune (Switzerland). NT1654 was delivered to the embryos at the same time as MO or CRISPR/Cas9 injection, due to the size being incompatible with water-based diffusion delivery (Pelka et al., 2017). Embryos from the same pair of fish were split into each of the four categories (control, treated control, Myo9aa/ab-depleted, treated Myo9aa/ab-depleted) for each injection session to ensure fair comparisons for survival and development. As there was no previous data regarding NT1654 use in zebrafish, a range of doses were trialled from 0.15ng to 2.4ng per injection droplet and survival rates were assessed at 2 dpf. After selecting the lowest two doses as most appropriate, further fish were treated with these concentrations and subject to movement tests as described in Sections 2.3.7 and 2.3.8 to assess any effects on the control zebrafish. A final concentration of 0.15ng/injection droplet was then selected.

2.4.11 Treatment with fasudil

Fasudil (5mM, Millipore Sigma), a ROCK inhibitor, was used to treat the control and Myo9aa/ab-depleted zebrafish. The zebrafish were housed in 12-well plates, with ten or less fish per well, in E3 medium. A range of concentrations of fasudil were trialled to optimise the dose, from 1nM to 100µM, starting from 7 hpf and final assessments made at 48 hpf. Based on preliminary survival rate data and assessment of chorion movements as described in Section 2.3.7, a concentration of 10µM was used for the study.

Fish were split into 4 treatment groups including control, 10μM fasudil treated control, Myo9aa/ab-depleted and 10μM fasudil treated Myo9aa/ab-depleted. Treatment started at 7 hpf and was continued to 5 dpf, with solution changes daily. NMJ morphology was assessed at 24 hpf, 48 hpf and 5 dpf, as described in section 2.4.9. Chorion movements were also analysed at 24 hpf and the tactile stimulation assay performed at 48 hpf.

2.5 Immunofluorescence and histology

2.5.1 Dissection of mouse tissue

Control and MYO9A KO mice were obtained from the laboratory of Prof. Martin Bähler in Münster, Germany (Table 2 17, Abouhamed et al., 2009). Mice were euthanised by cervical dislocation and the following tissues dissected; gastrocnemius, tibialis anterior, quadriceps, heart, liver, kidney, spleen, diaphragm, intercostal muscles, brain, spinal cord and sciatic nerve.

Animal	Gender	Strain	DOB	Age
Wild type 1	male	Bl6/C57	19.07.16	8months 12 days
Wild type 2	male	Bl6/C57	02.11.16	4months 29 days
Wild type 3	male	Bl6/C57	02.11.16	4months 29 days
Mutant 1	male	Bl6/C57	10.05.16	10months 21 days
Mutant 2	male	Bl6/C57	13.05.16	10months 18 days
Mutant 3	male	Bl6/C57	10.05.16	10months 21 days
Mutant 4	male	Bl6/C57	30.05.16	10months 1 day

Table 2-17. Wildtype and MYO9A KO (mutant) mice used in this study.

2.5.2 Cryosection of mouse muscle

Freshly dissected mouse tissue was submerged in OCT compound in a tissue mould, however, unfortunately isopentane and liquid nitrogen were unavailable for snap freezing. Therefore, samples were frozen slower than desired on dry ice. Samples were shipped to Newcastle University and stored at -80°C until required, at which point they were removed from moulds and mounted on cryostat grids. Sections between 7 and 50μm were cut and mounted on SuperFrost microscope slides (FisherScientific).

2.5.3 Staining of cells

To prepare cells for staining, they were seeded onto coverslips, coverslides or 8-well chamber glass bottom coverslips, and then treated as desired. Cells were fixed as

described in section 2.2.6 and washed 3 times in PBS. If permeabilisation was required, this was achieved using 0.1% Triton X-100 in PBS for 10 mins at room temperature. Following 3 washes in PBS, blocking was performed using 4% bovine serum albumin (BSA) in PBS with 0.1% Tween (PBST) at room temperature for 1 hour. Primary antibodies (Table 2-14) were diluted in 1% BSA in PBST and incubated overnight at 4ºC. Samples were washed 3 times in PBST and then incubated for one hour at room temperature with secondary antibodies diluted in 1% BSA in PBST, as listed in Table 2-14. Following a final 2 washes in PBST and 1 wash in PBS, samples were mounted in ProLong Diamond Antifade Mountant with DAPI (Molecular Probes) or Vectashield fluorescent mounting medium with DAPI (Vector Laboratories).

Cells were imaged using a Nikon A1R confocal microscope using 10x and 20x air objectives as well as 40x, 60x and 100x oil-immersion objectives. For a number of experiments the CTCF value was also calculated using ImageJ as described in section 2.2.6, to provide a means of quantifying differences in protein abundance between samples or over time.

In cells stained with phalloidin and imaged at 40x or 60x objective, the presence or absence of stress fibre-like structures was manually assessed. A directionality plugin on ImageJ was also applied to the same images to determine the orientation of the actin filament network in the cells (http://imagej.net/Directionality; date last accessed November 5, 2017).

2.5.4 Staining of whole zebrafish

Zebrafish were stained at different developmental stages between 24 hpf and 5 dpf. All fish were dechorionated using Pronase if required and then euthanized using the described Tricaine method. Fish were fixed in 4% PFA in PBS overnight at 4ºC. This was followed with a 5 min PBS wash and then a 5 min distilled water wash, before incubating in acetone at -20ºC for 7 mins. Another wash in distilled water was performed, followed by PBST. Fish older than 48 hpf then had Collagenase A (Millipore Sigma, 1mg/ml) treatment for 30 mins, 60 mins or 90 mins for 3, 4 and 5 dpf fish respectively. Collagenase was removed and fish washed 4 times in PBST. Fish of all ages were then blocked in 5% horse serum in PBST for 1 hour at room temperature. Primary antibodies (listed in Table 2-14) were diluted in 5% horse serum in PBST and applied to fish overnight at 4ºC with constant agitation. Fish were

then washed 5 times in PBST for 20 mins each time before incubating at room temperature with secondary antibody for 2 hours, also diluted in 5% BSA in PBST (Table 2-14). Samples were washed 2 times in PBST before leaving to wash overnight at 4ºC with constant agitation, followed by a final PBS wash. Fish were mounted in wells created by tape on microscope slides, in Vectashield fluorescent mounting medium (Vector Laboratories), then sealed to make airtight. Z-stack images encompassing the entire volume of the zebrafish tail were obtained using a 10x and 20x air objective, as well as a 40x oil-immersion objective on a Nikon A1R confocal microscope. Some images for NMJ morphology assessments were also taken on a Zeiss LSM880 Airyscan laser scanning confocal microscope using a 63x water-immersion objective.

2.5.5 Staining of mouse muscle sections for MHC analysis

To stain mouse sections, slides were defrosted and sectioned tissue circled with a PAP pen (Abcam). Slides were soaked for 10 mins in PBS and then fixed in 4% PFA in PBS for 5 mins. After washing 3 times with PBS, tissue was then permeabilised in 0.1% Triton X-100 in PBS for 15 mins, then blocked in 1% normal goat serum in PBS at room temperature for 1 hour. Samples were incubated with primary antibody (Table 2-14) diluted in blocking solution for 1 hour at room temperature. One section was labelled with the following antibodies; anti-MHC1 IgG2b, anti-MHC2a IgG1, anti-MHC2b IgM and anti-laminin IgG, while a serial section was labelled with anti-MHC2x IgGM and anti-laminin IgG. Slides were washed 3 times with PBS and then secondary antibodies (Table 2-14) were applied for 1 hour at room temperature, hidden from light. After washing 3 times in PBS, Vectashield was added for mounting with a coverslip. Imaging tiles were taken to cover the whole muscle section and this was performed using an Axio Imager Z1 fluorescent microscope at 10x and 20x objectives.

2.5.6 Staining of whole mouse muscles

Tissue was fixed in 4% PFA in PBS overnight at 4ºC, before washing 3 times in PBS for storage and shipping back to the UK. Muscles were labelled with aBTx-conjugated with Alexa Fluor 488 (Molecular Probes) for 30 mins at room temperature under constant agitation. Samples were washed for 1 hour in PBS at room temperature with 4 changes of PBS. Ideally the fixation step would have been performed at this point for 1 hour at room temperature but unfortunately this was not possible due to the requirement of transporting tissue back to the UK. Muscles were

then teased into small bundles and cleared of connective tissue using a dissecting microscope before being treated with ethanol for 10 mins at -20ºC and then methanol in the same conditions. Permeabilisation was performed using 0.1% Triton in PBS at room temperature for 15 mins using constant agitation. A PBS wash followed for 2 hours and then blocking was performed with 5% BSA in PBST for 2 hours at room temperature under constant agitation. Primary antibodies were then applied (anti-neurofilament light chain and anti-synaptophysin, Table 2-14) in blocking buffer and samples incubated overnight at 4ºC with constant agitation, and a further 2 hours at room temperature the following day. After washing 5 times for 20 mins each in PBST, secondary antibodies were applied (Table 2-14) in blocking buffer. An overnight PBS wash was then performed at 4ºC and then muscles mounted in Vectashield on slides framed with tape to create a well. Muscles were then imaged using a Nikon A1R confocal microscope with Z-stack images taken to encompass each NMJ identified with 1-3µm step sizes, using a 60x oil-immersion objective.

2.5.7 Haematoxylin and Eosin Staining

Mouse muscle sections were defrosted at room temperature for 30 mins before incubating in Mayer's Hematoxylin (ThermoFisher Scientific) for 1 min. After washing in water until clear, slides were placed in 1% aqueous eosin solution (ThermoFisher Scientific) for 30 secs and washed again in water until clear. Samples were then dehydrated in a series of alcohol solutions; 70% ethanol for 1 min, 90% ethanol for 1 min, 100% ethanol for 1 min, fresh 100% ethanol for 3 min, then slides were cleared with histoclear (NationalDiagnostics, USA) for 5 mins and then fresh histoclear for 2 mins before partially drying and mounting with DPX mounting medium (Merck). Stained sections were imaged using the tiling feature on an Axio Imager Z1 microscope at 20x objective.

2.5.8 NMJ morph protocol

This protocol, developed by Jones *et al* (2016), was used to analyse mouse NMJs (stained with aBTx, synaptophysin and neurofilament) imaged using a confocal microscope to obtain z-stacks. Analysis was performed using FIJI (ImageJ). Briefly, a z-stack image was opened as a maximum intensity projection, then each channel colour (red for presynaptic and green for postsynaptic) was separately subject to manual thresholding. After removing noise, applying a despeckle process and then manually removing any remaining background artefacts the image was converted into binary.

With the presynaptic image the number of axonal inputs was counted when present, and the diameter of axons measured (average taken from minimum, maximum and edge of endplate diameters). After removing the axon from the image, the nerve terminal area and perimeter were measured. To assess branching of the nerve terminal, the binary image was skeletonized and the 'BinaryConnectivity' plugin used to obtain number of terminal branches, branch points and total branch length, giving rise to the average length of branches and a 'complexity' rating.

For the postsynaptic image the same processes as described above were applied to obtain measurements for AChR perimeter and area. Endplate area (total area taken up by AChRs, including gaps), diameter and perimeter were also obtained and a 'compactness' value calculated by dividing the area of the AChRs by the endplate area.

To measure the overlap of the pre and postsynapse and the area of synaptic contact, the original images were used. The colour of the endplate image was inverted, and the images of the nerve terminal and endplate concatenated before producing an average intensity projection and making the image binary. This will show only the unoccupied AChRs. The area of these receptors removed from overall AChR area provides a value for synaptic contact, whereas division by AChR area gives a value for overlap.

Finally, to calculate the number of AChR clusters, average cluster area and 'fragmentation' of NMJs, the original aBTx maximum intensity projected image was segmented using the 'segmented particles' process. The number of clustered segmented particles was then manually counted and used to calculate the average area by dividing with the AChR area, and then 'fragmentation' obtained by subtracting the number of clusters from 1 and then dividing 1 by this value. Muscle fibre measurements were not obtained.

2.5.9 NMJ morphology measurements in zebrafish

In MO-injected fish, the morphology of the NMJs were assessed by observation of overall motor neuron length/branching/AChR staining. To generate a more robust means of assessment that allowed for quantification of morphological features of zebrafish NMJs that could be compared between genotypes and treatment conditions, a set of parameters were established for 24 hpf, 48 hpf and 5 dpf fish and used to assess the crispants (Figure 2.5).

Zebrafish were labelled with an SV2 antibody (motor neurons) and aBTx (AChRs). Z-stacks were obtained on a confocal microscope through the entire depth of the zebrafish tail. Using Fiji (ImageJ), maximum intensity projections were produced and used for subsequent analysis. At 24 hpf, the size of the myotomes was measured, and the presence or absence of a central AChR cluster noted, referred to as the 'choice point'. The distance motor neuron axons had travelled past the choice point was also manually measured, along with total AChR area per myotome. In 48 hpf and 5 dpf fish, size of myotomes were also measured, along with number of presynaptic and postsynaptic clusters per myotome and per 100μm^2. The average size and total area of clusters was also calculated and the number of large clusters with a size over 20μm^2 recorded.

Counts and measurements of clusters were performed by automatic thresholding and conversion of images to binary before using the 'analyse particles' tool in Fiji. The length of the myosepta, displaying AChR-positive staining, was manually measured, along with the innervation by motor neurons, giving a percentage of myoseptal innervation value.

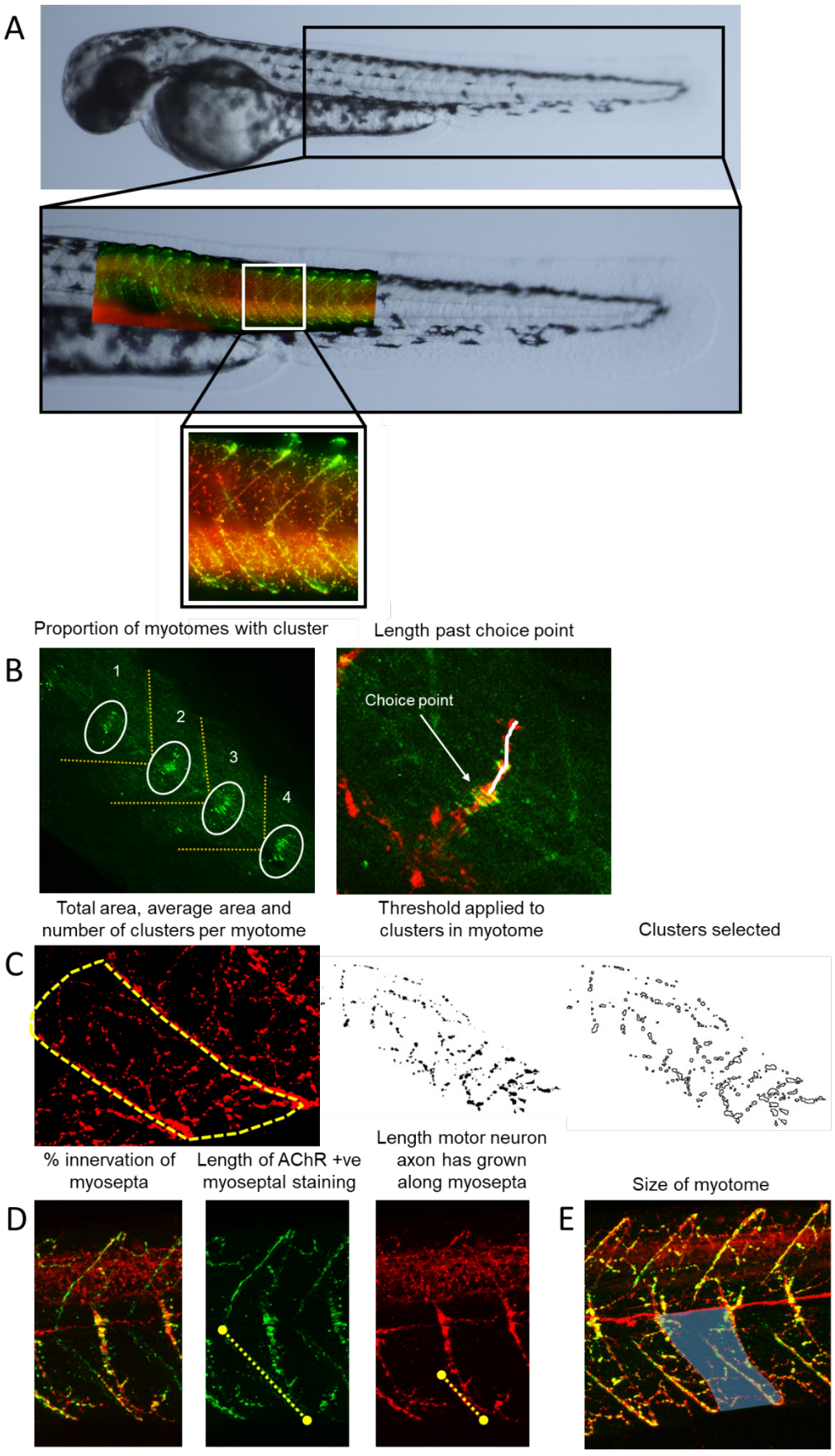

Figure 2.5. NMJ morphology measurements. A. Representative image of whole zebrafish at 72 hpf, with enlarged tail region demonstrating the orientation of the NMJ staining within the tail musculature. B. Example features measured at 24 hpf:

proportion of myotomes with a choice point cluster of AChRs (outlined with a white circle) and length of motor neuron extension past the choice point (white line). C. Total area, average area and number of clusters can be measured per myotome from maximum intensity projections. Following selection of the myotome and thresholding, the distinct clusters are selected and number and area are analysed. D. % innervation of myosepta as calculated from the amount of motor axon growth up the myosepta (red, yellow line) expressed as a percentage of myosepta length (length of aBTx +ve myosepta, green, yellow line). E. Size of myotome measured by outlining individual myotomes as highlighted in blue.

2.5.10 Western blotting

2.5.11 Lysate preparation

To make protein lysates from cultured cells, cells were washed three times in PBS before scraping directly into ice-cold lysis buffer (RIPA buffer with protease inhibitor tablet (Roche)) to generate whole protein extracts. Samples were maintained at 4°C with constant agitation for 30 mins, centrifuged for 20 mins at 1750g at 4°C, then supernatant removed and stored at -80°C. To prepare lysates from zebrafish tissue, embryos were euthanised with Tricaine and washed 3 times in PBS. Mouse tissues that had been stored at -80°C were also used. For both sample types, ice cold lysis buffer was added and homogenisation performed using a TissueRuptor before incubating at 4°C with constant agitation for 2 hours. Samples were then centrifuged for 20 mins at 13000g before discarding the pellet. Samples were then subject to a bicinchoninic acid assay, using serial dilutions of BSA in RIPA buffer as protein standards.

2.5.12 SDS-PAGE and western blotting

To prepare samples for loading onto the gel, they were diluted in RIPA buffer to the same concentration, then 2x Laemmli buffer (Bio-Rad) was added before heating to 95°C for 5 mins. Equal loading of samples was confirmed by Coomassie staining, in which Coomassie Brilliant Blue dye (ThermoFisher Scientific, 1g Coomassie, 400ml ETOH, 500ml water, 100ml acetic acid) was added to the gel for 30 mins at room temperature with constant agitation, then destained for 1 hour in destaining buffer 1 (477.5ml water, 100ml acetic acid, 400ml ETOH and 22.5ml glycerine), followed by another destain in buffer 2 (827.5ml water, 50ml acetic acid, 100ml ETOH and 22.5ml glycerine). The gel was then washed overnight in water before imaging using a LiCor Odyssey CLx Imaging System and protein bands per lane quantified using the CLx imaging software (Image Studio Lite).

For western blotting, adjusted samples were loaded onto hand-cast polyacrylamide gels (6 or 12%), or onto 4-12% Bis-Tris NuPAGE gels (1mm, 26 well, ThermoFisher Scientific), along with a protein ladder (SeeBlue Plus2 pre-stained protein standard or PageRuler Prestained Protein Ladder, ThermoFisher Scientific). Hand-cast gels were run in Tris-Glycine running buffer (3g Tris, 14.4g glycine, 990ml water, 10ml 10% sodium dodecyl sulfate (SDS)). Pre-made gels were run in NuPAGE MES SDS running buffer (ThermoFisher Scientific). Gels were run at 120V for 30 to 100 mins depending on protein size.

After running, gels were transferred using wet transfer or dry transfer. For wet transfer a polyvinylidene difluoride-membrane (Millipore) was soaked in methanol for one minute before assembling the transfer stack. The stack was placed in a tank with transfer buffer (3g Tris, 14.4g glycine, 800ml water and 200ml methanol) and put in an ice box before running at 100V for 1 to 2.5 hours depending on protein size. For dry transfer an iBlot2 blotting system was used according to manufacturer's instructions (ThermoFisher Scientific), using iBlot2 transfer stacks (Regular, midi size, polyvinylidene difluoride-membrane, ThermoFisher Scientific). For most proteins the protocol used was 20V for 1 min, 23V for 4 min then 25V for 2 mins, except for proteins of a molecular weight above 180kDa, for which a transfer of 20V at 10 mins was used. After transfer, membranes were blocked in 5% BSA in tris-buffered saline (TBS) with 0.1% Tween 20 (TBST) for 1 hour at room temperature with constant agitation.

Blocking buffer was washed off using TBST and primary antibodies made up in TBST according to dilutions shown in Table 2-14. Membranes were incubated overnight at 4°C with constant agitation. The following day membranes were washed 3 times in TBST for 5 mins each, before making up secondary antibodies in TBST according to dilutions listed in Table 2-14. Secondary antibody mixtures were applied for 1 hour at room temperature and then membranes washed 3 times in TBST before a final wash in TBS.

Membranes incubated with a secondary antibody conjugated to HRP were visualised using enhanced chemiluminescent substrate (SuperSignal West Femto, Pierce) and imaged on an Amersham Imager 600. Those incubated with fluorescent secondary antibodies were imaged using the Odyssey CLx Imaging System. Analysis of band density was either performed using the CLx image analysis software (Image Studio Lite), or ImageJ FIJI.

2.6 Sample preparation for secretomics

NSC-34 cells (three samples of both wild-type and MYO9A-depleted) were cultured to 80% confluence in 10cm dishes and washed 3 times with PBS. Serum-free growth medium was added for 4 hours, followed by the addition of growth medium supplemented with 10% FBS for 1 hour (pulse). Following 3 washes with PBS, serum-free medium was applied for 3 hours (chase) and then collected and centrifuged for 4 mins at 1750g. The supernatant was combined with 10× ice-cold ultrapure ethanol overnight at -80°C. Samples were then centrifuged at 18000g for 30 mins at 4°C and the pellets dried under laminar hood flow before the addition of SDS lysis buffer (50 mM Tris–HCl pH 7.8, 150 mM NaCl, 1% SDS, 1 protease cOmplete mini tablet and one phosphatase inhibitor PhosSTOP tablet, Roche). Samples were subjected to quantitative mass spectrometry in Leibniz-Institut für Analytische Wissenschaften-ISAS e.V (ISAS), Dortmund by Vietxuan Phan.

Criteria for defining a protein as regulated are: protein commonly quantified in each replicate, identified by at least one unique peptide, an analysis of variance (ANOVA) p-value of <0.05 and an average log 2 ratio of either lower than the down-regulated cut-off (-4.44) or higher than the up-regulated cut-off (4.06).

2.7 Statistical analysis

Statistical analysis was performed using GraphPad Prism software (v5.04 and v8.0.2). Data sets were first tested for normal distribution and from these results either nonparametric (Mann-Whitney test) or parametric tests (unpaired t-test) were applied for comparisons of two data sets. For analysis of 3 or more datasets, one-way ANOVA with Turkey post hoc test or Kruskal-Wallis with Dunn's post hoc test were performed, depending on distribution of data. Outliers were identified and removed according to the ROUT method. Statistical significance was taken as $p < 0.05$. *In vitro* experiments were blinded for image analysis and *in vivo* experiments blinded prior to live recording and for image acquisition.

Chapter 3. Generation and characterisation of models of MYO9A-deficiency

3.1 Introduction

Studying the contribution of a specific protein to the phenotype of a complex disorder affecting many different muscles of the body requires a combination of approaches. A number of cell and animal systems have been utilised in the study of CMS, including immortal cell-lines, patient cells, zebrafish, mice and patient motor point biopsies (O'Connor et al., 2018b, Webster, 2018, Slater et al., 2006).

In vitro models are particularly useful for analysing molecular pathways and biochemical events. This is important for understanding the pathway on which the protein acts to disrupt the safety factor of the NMJ and to assess the pathogenicity of variants identified in patients. The majority of studies in the CMS field have utilised immortal cell-lines such as kidney-derived HEK 293 or fibroblast-derived COS-7 cells (Chapter 1, Section 1.4.1), with the aim of analysing the effect of specific patient mutations on protein localisation, binding, splicing or AChR channel kinetics. C2C12 cells have proven useful for identifying mutations important for AChR clustering (Chapter 1, Section 1.4.1) and the only studies identified in which patient myoblasts were utilised revealed further information regarding the function of GFPT1 (Chen et al., 2015, Dusl et al., 2015).

MYO9A had not previously been associated with normal function or a disease of the neuromuscular system prior to our finding that 3 patients with CMS exhibit variants in *MYO9A* that segregate with the disease (O'Connor et al., 2016). Based on a number of lines of evidence, including the presence of other unconventional myosins at the growth cone of nerves (Yu et al., 2015, Suter et al., 2000), the potential presence of MYO9A at the growth cone in a nerve cell-model (O'Connor et al., 2016), effects of MYO9A-loss on CNS neurons (Folci et al., 2016) and features of the human MYO9A-CMS condition being compatible with a presynaptic disorder, in this study I hypothesised that MYO9A plays a role in the nerve terminal. Therefore, rather than utilise muscle or fibroblast-derived cells, a mouse-derived motor neuron cell line (NSC-34) was used. This model was complemented by derivation of iNPCs from patient-fibroblasts, the first time this has been performed for a CMS patient. This allowed for molecular features and pathways involved in MYO9A-CMS to be assessed.

It is apparent that not only the presence of proteins at the NMJ, but also their correct function and localisation at the synapse, is important for maintaining transmission. For example, the proteins mediating the close apposition of presynaptic active zones with postsynaptic AChRs are essential for maintaining the safety factor (Slater, 2017). Therefore, the use of animal models in which the entire NMJ can be analysed in its native environment is a useful tool for CMS research. A large number of animal models have been generated for studying CMS subtypes, including mice, zebrafish, *Drosophila* and *C.elegans* (Table 3-1), some of which are discussed in O'Connor *et al* (2018b). Invertebrate models and small vertebrates such as zebrafish offer opportunities to study molecular and behavioral defects in well characterised systems over short time periods. For more complex behavioral assays, anatomical analysis and preclinical studies, mice are the model of choice for most CMS studies (Chapter 1, Section 1.4.3).

By exploring a range of techniques and taking advantage of the benefits of each model system, a greater understanding regarding a potential role for MYO9A in function and disease at the NMJ can be obtained.

Gene	Models developed			
	Mouse	Zebrafish	*C.elegans*	*Drosophila*
DOK7	✓	✓	×	×
MUSK	✓	✓	✓	×
LRP4	✓	✓	×	✓
AGRN	✓	✓	✓	×
COLQ	✓	×	×	×
GFPT1	✓	✓	×	×
ALG2	×	×	×	×
ALG14	×	×	×	×
GMPPB	×	✓	×	×
DPAGT1	×	×	×	×

Table 3-1. Animal models developed for the in vivo analysis of the ten currently recognised LG-CMS genes, including mice, zebrafish, *Caenorhabditis elegans* (*C.elegans*) and *Drosophila*. Table from O'Connor *et al* (2018b).

3.2 Aim of chapter

To generate a range of *in vitro* and *in vivo* models appropriate for studying the role of MYO9A at the NMJ, including patient-derived neuronal progenitor cells and knockdown zebrafish.

3.3 MYO9A knockdown NSC-34 cells

Expression of MYO9A was knocked down from NSC-34 cells using shRNA-mediated selective inactivation of MYO9A mRNA. Initially, two different MYO9A shRNAs were trialed for effectiveness, along with a non-targeting control shRNA complementary to the luciferase RNA sequence (O'Connor et al., 2016). This was performed in my MSci project (MSci thesis, University of Glasgow, 2015), however, confirmation of MYO9A knockdown and generation of new control knockdown cells (using a commercially available non-target shRNA) was performed during this PhD project.

3.3.1 Confirmation of knockdown

The selection of one MYO9A shRNA was performed previously, and this shRNA was used to generate a polyclonal population of stable knockdown NSC-34 cells. Control

knockdown cells were similarly generated, using a commercially available non-targeting control shRNA.

To confirm whether the MYO9A shRNA had the desired effect on *Myo9a* expression, and in the absence of a validated MYO9A antibody, qRT-PCR was used. Initially this experiment had been performed using the house-keeping gene encoding β-Actin, however, this was later found to be regulated in cells lacking MYO9A and thus the loss of expression was re-confirmed using an alternative gene: *Pgk1.*

Expression of *Myo9a* in the stable knockdown population was significantly reduced as compared to control knockdown cells (p=0.002, Mann Whitney test, Figure 3.1).

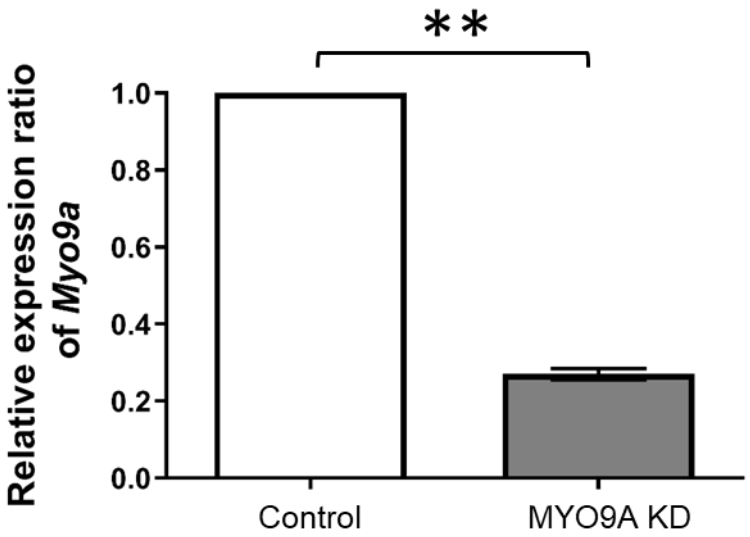

Figure 3.1. qRT-PCR to assess effectiveness of shRNA-mediated knockdown of MYO9A from NSC-34 cells. Expression of *Myo9a* in control and MYO9A KD (knockdown) cells, normalised to *Pgk1* and results expressed for MYO9A KD cells relative to controls. Error bars represent mean of 3 repeats ± standard error of the mean (S.E.M). **p≤0.005, Mann Whitney test.

3.3.2 MYO9A KD cell gross morphology

Control and MYO9A KD cells were cultured and gross morphology assessed. At the light microscope level cells lacking MYO9A appeared larger and flatter, therefore cells were stained with phalloidin to detect filamentous (f)-actin and their morphology studied using confocal microscopy. Nuclear area and cell area of MYO9A KD cells was significantly larger than controls (p≤0.0001, Mann Whitney test, Figure 3.2.A,B,E). Volume of nuclei was not significantly different (p=0.068, Mann Whitney test, Figure 3.2C,E), and height of cells at the tallest point was significantly reduced in MYO9A KDs (p≤0.0001, Mann Whitney test, Figure 3.2D,E).

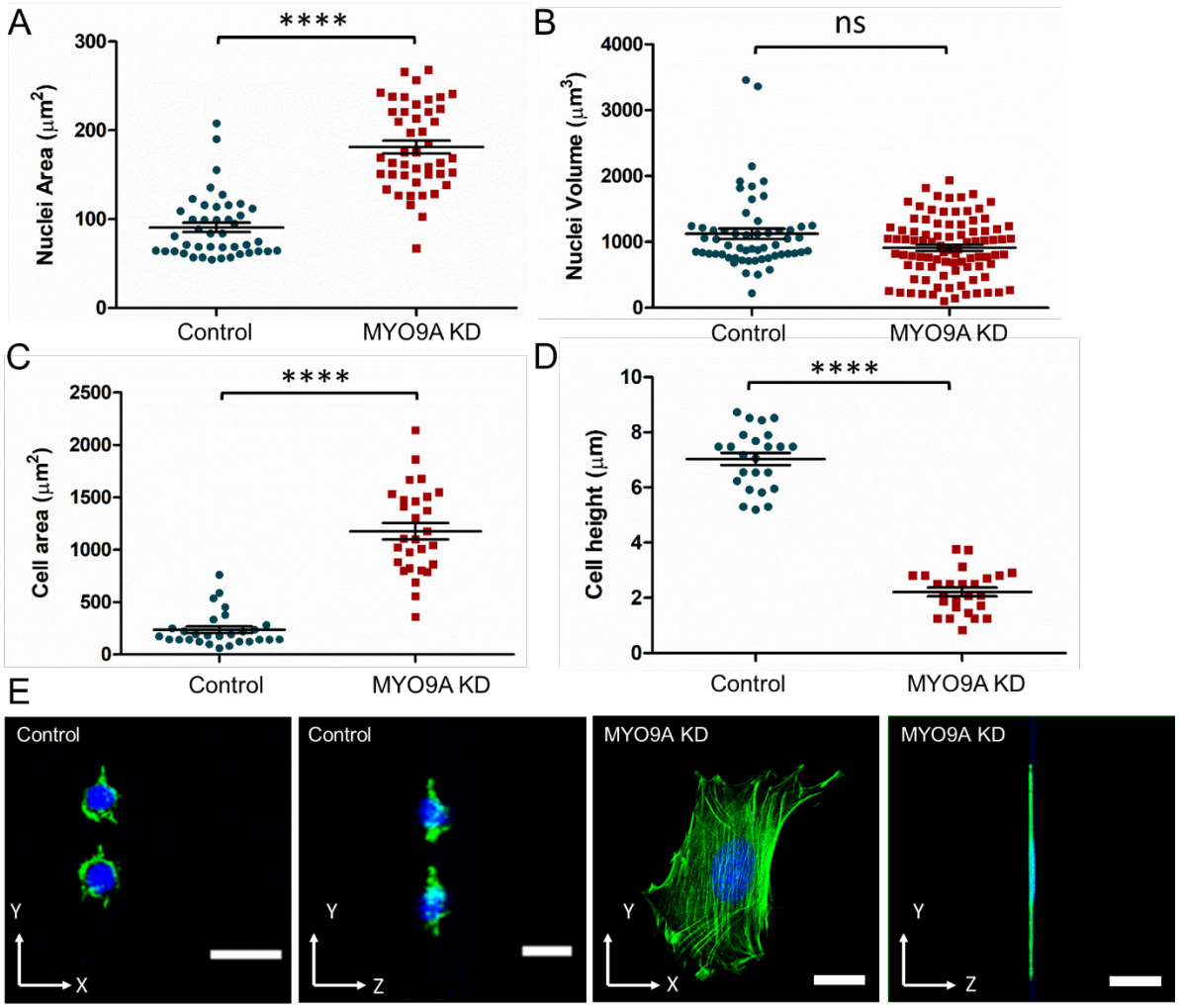

Figure 3.2. Gross morphology of MYO9A KD NSC-34 cells. A. Area (control n=43 and MYO9A KD n=45) and B. Volume of control (n=57) and MYO9A KD (n=90) cell nuclei. C. Area (n=28) and D. Height (n=24) of control and MYO9A KD cells. E. Representative images of control and MYO9A KD cells, nuclei stained with DAPI (blue) and f-actin, used to delineate cell area, stained with fluorophore-conjugated phalloidin (green). Axes of plane in view depicted in bottom left of each image. Scale bar = 20μm. Error bars represent mean ± S.E.M, ns=not significant, ****p<0.0001, Mann Whitney test.

3.4 Patient-derived induced neuronal progenitor cells

3.4.1 Induced neuronal progenitor cell conversion

In order to better replicate the genetic environment of MYO9A-CMS, fibroblasts from a skin biopsy of MYO9A patient 1 (p.R1517H and p.R2283H) were obtained by the MRC Centre for Neuromuscular Diseases Biobank and made available for culture. The levels of *MYO9A* expression in patient fibroblasts compared to a control subject were analysed using qRT-PCR, revealing no significant differences between the levels of *MYO9A* RNA (p=0.519, paired t-test, Figure 3.3). Due to the lack of a validated commercially available MYO9A antibody, levels of protein expression were not quantified.

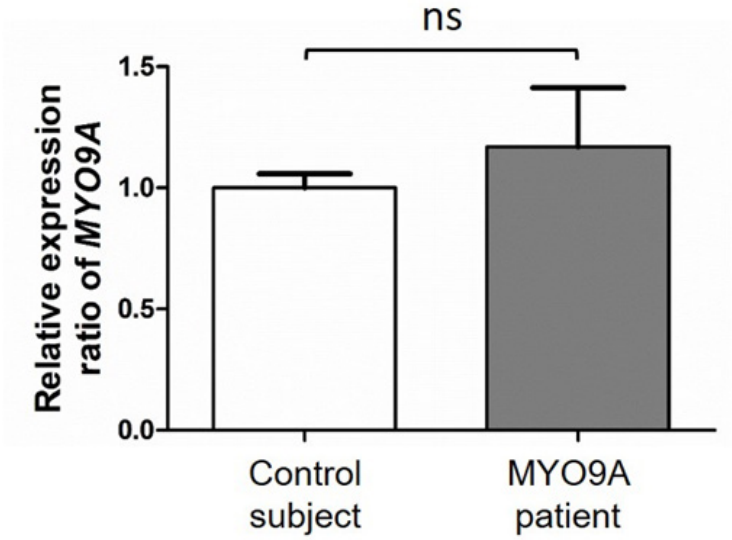

Figure 3.3. qRT-PCR to assess expression of *MYO9A* in control and MYO9A patient fibroblasts. Expression of *MYO9A* in control subject and MYO9A patient fibroblasts, normalised to *TBP* and expressed relative to control. Error bars represent mean of 3 repeats + S.E.M. ns=not significant, paired t-test.

Based on previous data (O'Connor et al., 2016), we hypothesised that MYO9A would play a role in the nerve/nerve terminal, therefore we converted the fibroblasts into neuronal progenitor cells. This was achieved using a direct conversion method in which fibroblasts are infected with Sendai virus to induce expression of transcription factors: Oct4, Klf4, Sox2 and c-myc (Meyer et al., 2015). Fibroblasts were subject to the conversion protocol for up to 20 days, by which time distinct colonies of iNPCs had formed (Figure 3.4). Fibroblasts from a control subject were converted and confirmed as iNPCs by Emily McCarthy, an MRes student (Newcastle University), by using RNA expression of nerve/stem cell markers as described below.

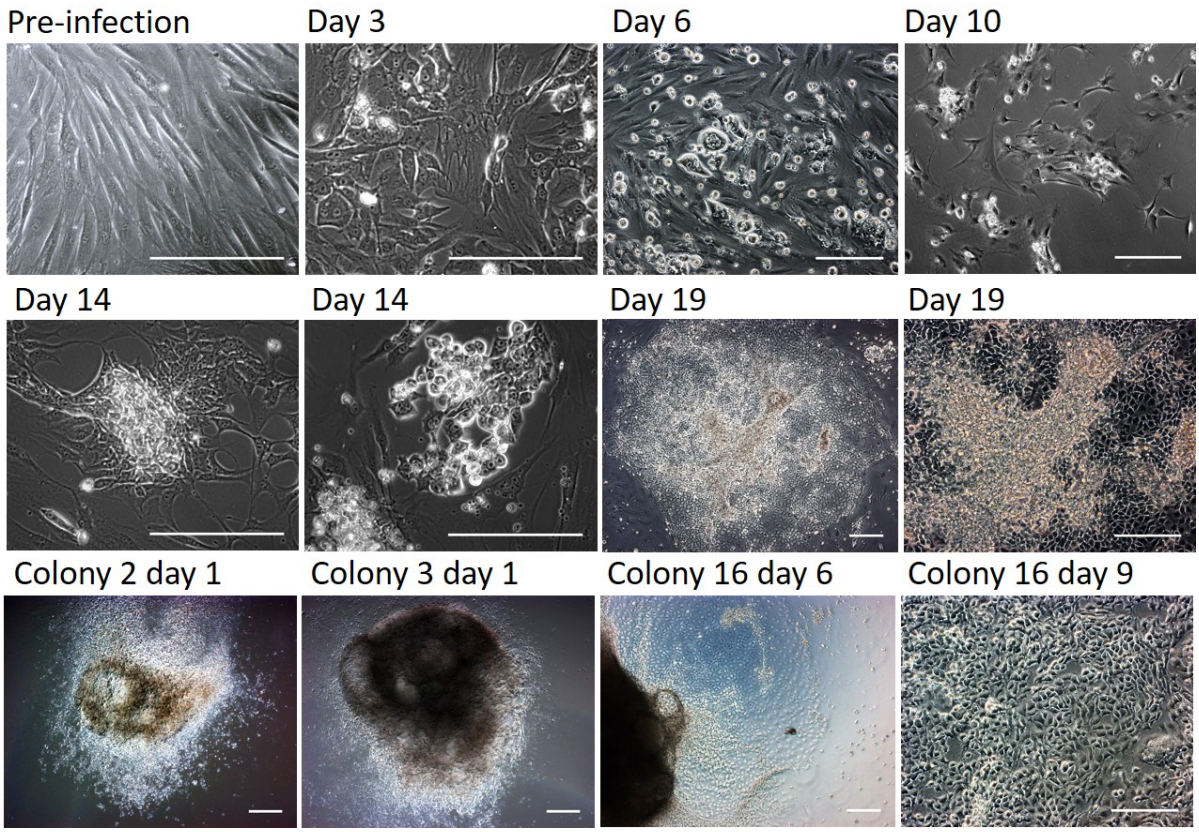

Figure 3.4. Conversion of MYO9A-patient fibroblasts into induced neuronal progenitor cells. MYO9A-CMS patient fibroblasts shown pre-infection, followed by varying time points post-infection. 20 colonies were isolated upon formation of multiple, distinct colonies and expanded for 7 days. Scale bar = 200μm.

A number of colonies were selected and expanded separately. After 1 week, cells were harvested for RNA and qRT-PCR performed to analyse the expression of fibroblast markers (*COL1A1, COL3A1*), neuronal markers (*NES, PAX6*) and stem cell markers *(SOX1, SOX2*). Identification of colonies that have a decrease in fibroblast markers and increase in neuronal and stem cell markers as compared to the initial patient fibroblasts were deemed successful conversions and were maintained for differentiation to the neuronal cell lineage. In total, 20 colonies were assessed, a selection of failed and successful conversions are shown in Figure 3.5. For example, iNPC colonies 11 and 16 have a decrease in *COL1A1* and *COL3A1* expression, but an increase in *SOX1, SOX2, PAX6* and *NES* expression as compared to the fibroblasts they are derived from, thus have successfully undergone the conversion process.

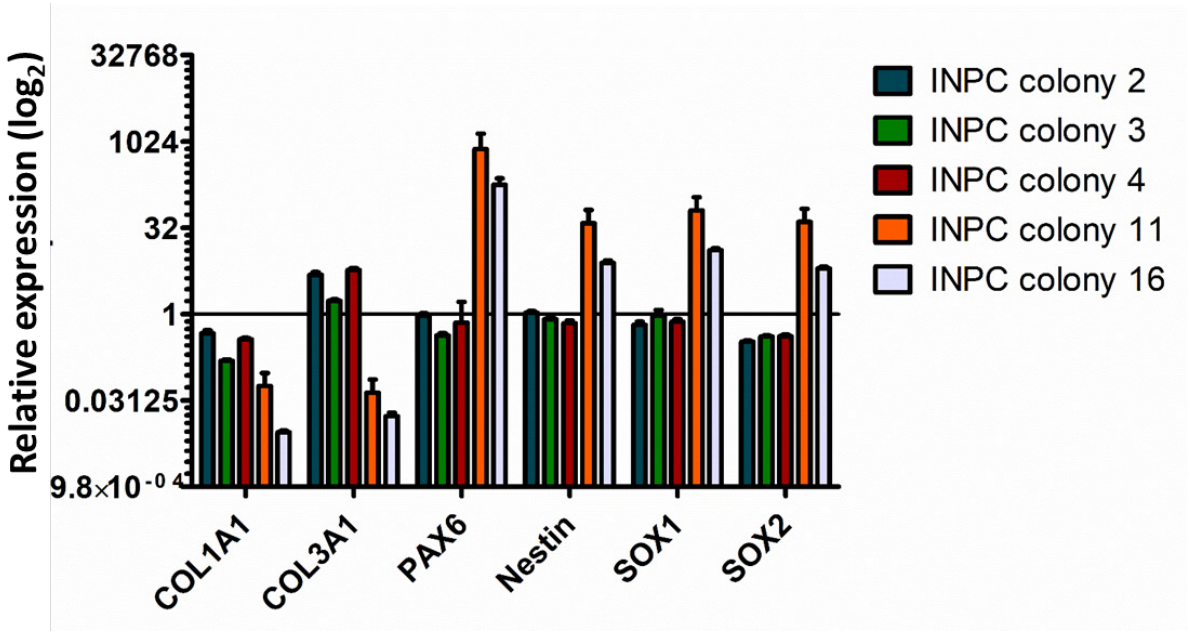

Figure 3.5. Relative expression ratio of induced neuronal progenitor cell colonies as compared to patient fibroblasts. Gene expression of colonies as compared to the original patient fibroblasts (black line) were confirmed using qRT-PCR against a selection of fibroblast, neuronal and stem cell markers. Results shown are normalised to TATA-binding protein and GAPDH, and relative to fibroblast cells. Error bars represent mean + S.E.M. from 3 repeats.

3.4.2 Differentiation of induced neuronal progenitor cells towards neuronal lineage

Following selection of successfully converted colonies, 3 were expanded and subject to 21 days of differentiation as described by Meyer *et al* (2015). Light microscope images at different time points of the differentiation process for control subject and MYO9A patient cells are shown in Figure 3.6. Cells re-arrange into colonies and form a network of connections across the culture plate.

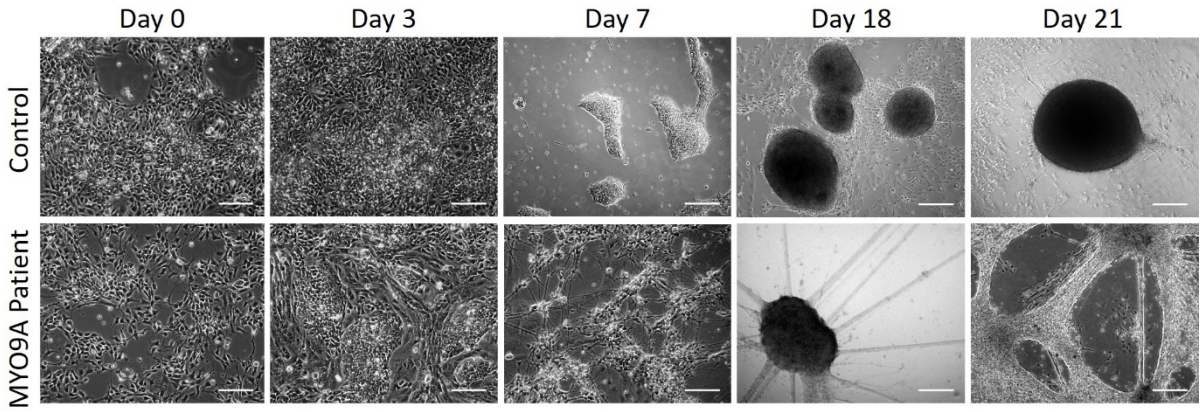

Figure 3.6. Differentiation of control and MYO9A patient INPCs over 21 days. Scale bar = 200μm.

To assess whether cells have differentiated into neurons, cells were then stained with antibodies against Tuj1 (neuron-specific class III beta-tubulin) and MAP2 (expressed in neurons), as shown in Figure 3.7. Both control and patient cells express the neuronal markers and thus have been successfully differentiated.

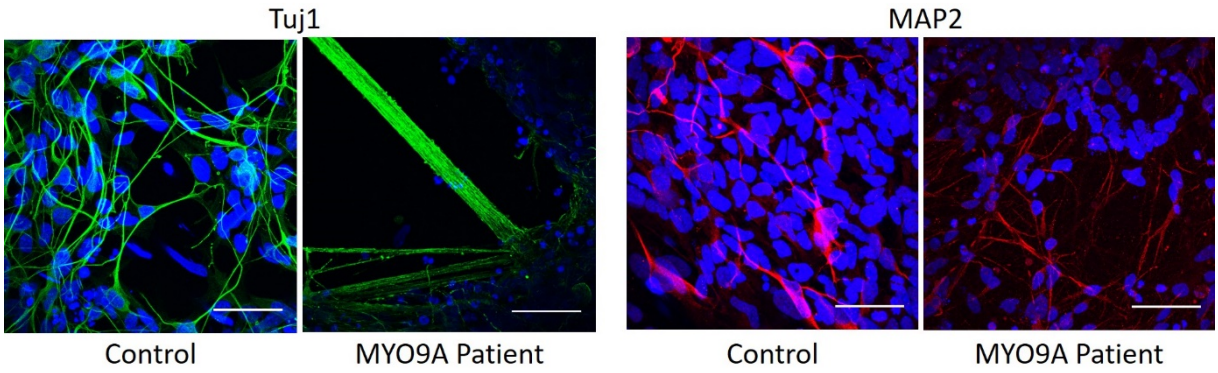

Figure 3.7. Control and MYO9A patient INPCs following neuronal differentiation. Cells were stained for 2 neuronal cell markers: Tuj1 (green) and MAP2 (red). Scale bar = 50μm.

3.4.3 SH-SY5Y cells expressing MYO9A with patient mutations

The levels of MYO9A RNA were not reduced in fibroblasts from one of the patients, therefore an attempt was made to express each of the patient *MYO9A* mutations in SH-SY5Y cells (a neuroblastoma cell-line derived from bone marrow). A vector containing the coding sequence of MYO9A and an HA-tag was obtained from VectorBuilder (https://en.vectorbuilder.com/). Mutagenesis was performed on the sequence to generate 4 further constructs. Of these, 3 had the patient mutations (R1517H, R2283H and D1698G) and 1 contained a predicted benign polymorphism in the same region of *MYO9A* (S1971L). Confirmation of the mutagenesis protocol was obtained by sequencing, as shown in Figure 3.8.

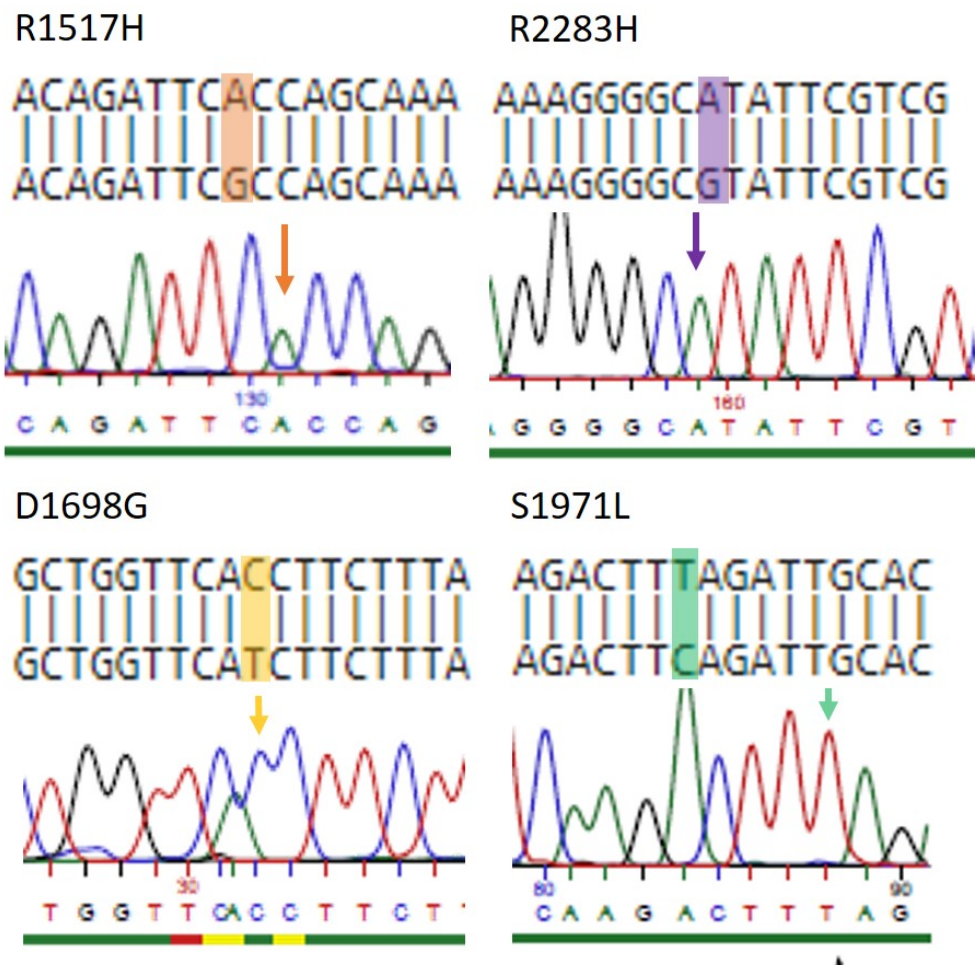

Figure 3.8. Sequencing of mutagenesis constructs. The wildtype *MYO9A* coding sequence was subject to mutagenesis to introduce the 3 patient mutations (R1517H, R2283H and D1698G), as well as a benign polymorphism (S1971L). Sequencing was performed to confirm the mutagenesis was successful (coloured arrows) and aligned with the wildtype sequence to show the base change (highlighted).

SH-SY5Y cells were transiently transfected with each construct and cells harvested for western blot or fixed for imaging. Western blotting was performed with an anti-HA antibody, however, no band around the predicted molecular weight for MYO9A was identified (293 kDa, Uniprot). A number of non-specific bands were also present, including a strong band at 100 kDa (Figure 3.9).

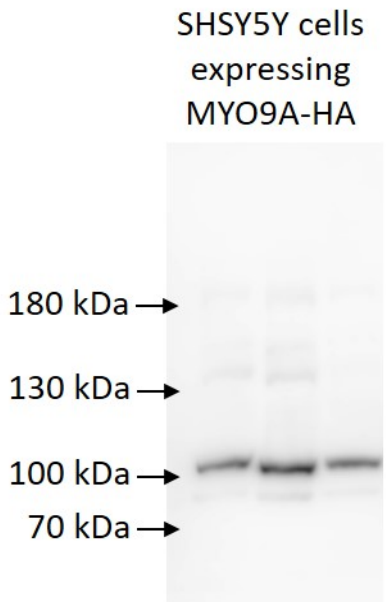

Figure 3.9. SH-SY5Y cells expressing MYO9A-HA. SH-SY5Y cells were transfected with a construct coding for wildtype MYO9A with an HA tag. Anti-HA antibody reveals lack of band at the predicted molecular weight for MYO9A (293 kDa), and the presence of non-specific banding at lower molecular weights. Molecular weight marker positions are shown on the left.

Immunofluorescent staining of SH-SY5Y cells expressing wildtype *MYO9A* and each of the introduced mutations was performed using an anti-HA antibody and phalloidin to label f-actin (Figure 3.10). Localisation of MYO9A was not as expected: either colocalising with f-actin, or at the tips of extending processes. The localisation or cellular compartment containing MYO9A was unclear, and some staining appeared to be outside of the cell, thus raising the question as to what was being detected by the anti-HA antibody. No gross differences in the localisation between wildtype, polymorphism and patient mutation forms of MYO9A were identified.

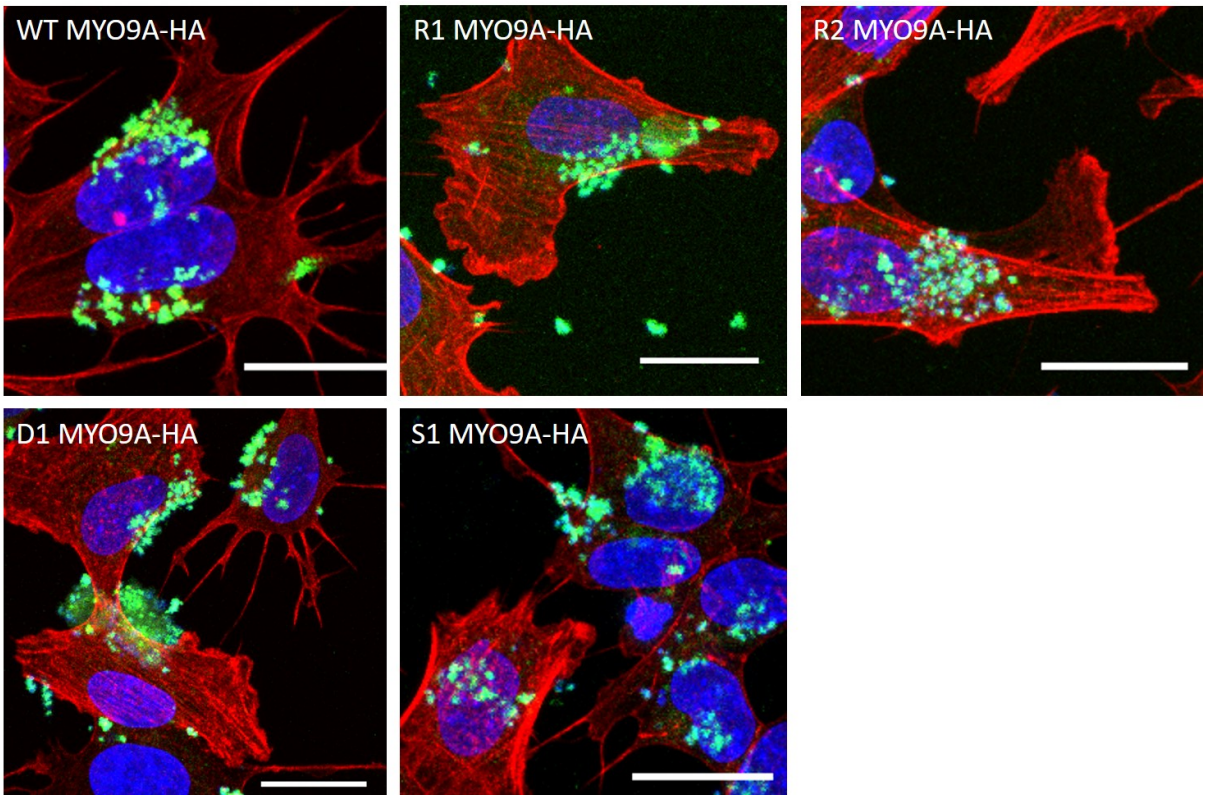

Figure 3.10. Immunofluorescent staining of SH-SY5Y cells expressing *MYO9A.* Cells transfected with a construct containing the coding sequence for wildtype MYO9A and patient/polymorphism variants (R1, R2, D1 and S1). Anti-HA antibody used to identify MYO9A (green) and phalloidin to detect f-actin (red). Scale bar = 20μm.

3.5 MO-mediated Myo9aa/ab knockdown zebrafish

While much can be learnt from *in vitro* models of disease, CMS is a complex disorder affecting NMJ signal transmission, and where MYO9A in particular plays a role is not yet known. Therefore, we utilised zebrafish as an *in vivo* model to allow the study of movement, NMJ development and morphology. The MO model was first generated during my MSci project, however, I have performed comprehensive phenotyping and expanded on preliminary data during this doctoral project.

3.5.1 Gross morphology of knockdown zebrafish

Zebrafish have two orthologues to human *MYO9A: myo9aa/ab* and both have been shown to be expressed during development (O'Connor et al., 2016). Knockdown of Myo9aa/ab by co-injection of MOs in zebrafish produced a pronounced phenotype at 48 hpf including varying degrees of tail curvature and some presence of cardiac oedema (Figure 3.11.A). Survival of fish was assessed daily and dead fish removed. By 48 hpf, twice as many Myo9aa/ab KD fish died as compared to controls (22% and 11% respectively, Figure 3.11.B).

Abnormal phenotypes were already present at 24hpf, by which time the more severely affected embryos had stunted tail growth within the chorion and reduced head size, while mild/moderate zebrafish had shortened tails. The levels of severely affected fish were increased by 9% in the Myo9aa/ab KD fish, and the mild/moderate phenotype present in 45% more of the injected Myo9aa/ab KD population (Figure 3.11.C).

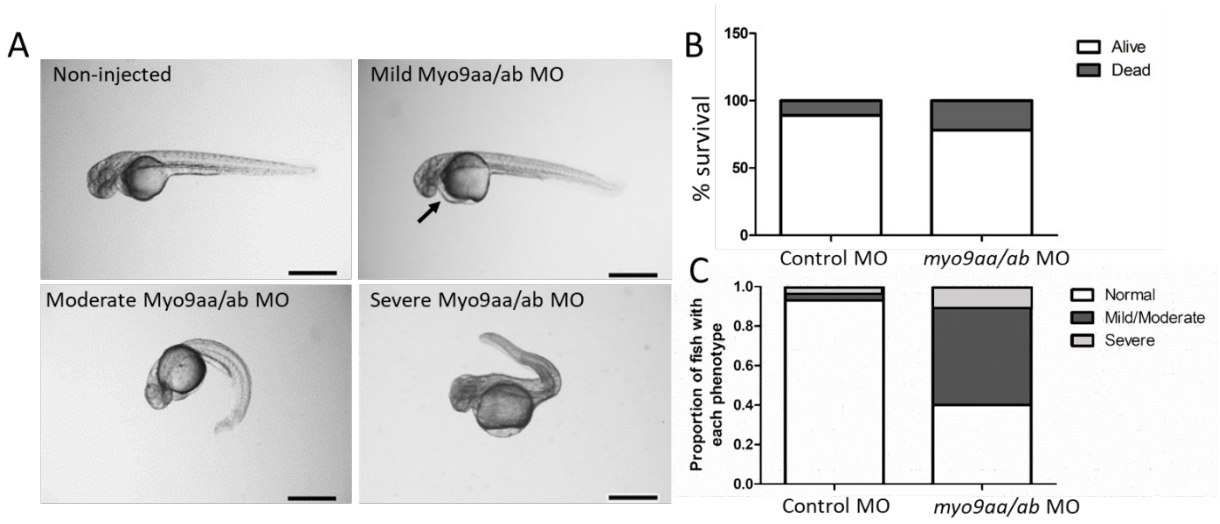

Figure 3.11. Gross morphology of Myo9aa/ab KD zebrafish. A. Phenotype of zebrafish at 48 hpf, with examples of non-injected, mild, moderate and severely affected Myo9aa/ab KD fish shown. Presence of cardiac oedema indicated with black arrow. Scale bar = 200μm, images used in my MSci thesis (University of Glasgow, 2015). B. Survival rate of zebrafish by 48 hpf following injection with a control MO or optimised quantity of Myo9aa/ab MO (n=100). C. Phenotype of fish at 24 hpf, defined as normal, mild/moderate or severe (n>50). MO = morpholino.

3.6 CRISPR/Cas9-mediated *myo9aa/ab* knockout zebrafish

There has been some concern within the scientific community regarding the reliability of MO-mediated knockdowns in zebrafish, largely due to a disparity between phenotypes observed in morphants and genetic mutants generated by techniques such as CRISPR/Cas9 (Kok et al., 2015). To address this issue, the generation of a genetic knockout for *myo9aa/ab* in zebrafish was carried out using CRISPR technology.

3.6.1 Generation of crispants

Four different sgRNAs, two against each gene, with predicted off-target effects of zero, were synthesised and injected into zebrafish at the one-cell stage along with the Cas9 protein.

To confirm the success of the CRISPR/Cas9 injections at inducing deletions/insertions at the predicted genomic locations, sequencing was performed.

A wild-type sequence of *myo9aa* is shown in Figure 3.12, along with a deletion within the target region of *myo9aa* using one of the sgRNAs against exon 2. Successful deletions in *myo9ab* exon 1, and an insertion in *myo9ab* exon 12 are also shown, demonstrating the effectiveness of the selected sgRNAs and injection protocol.

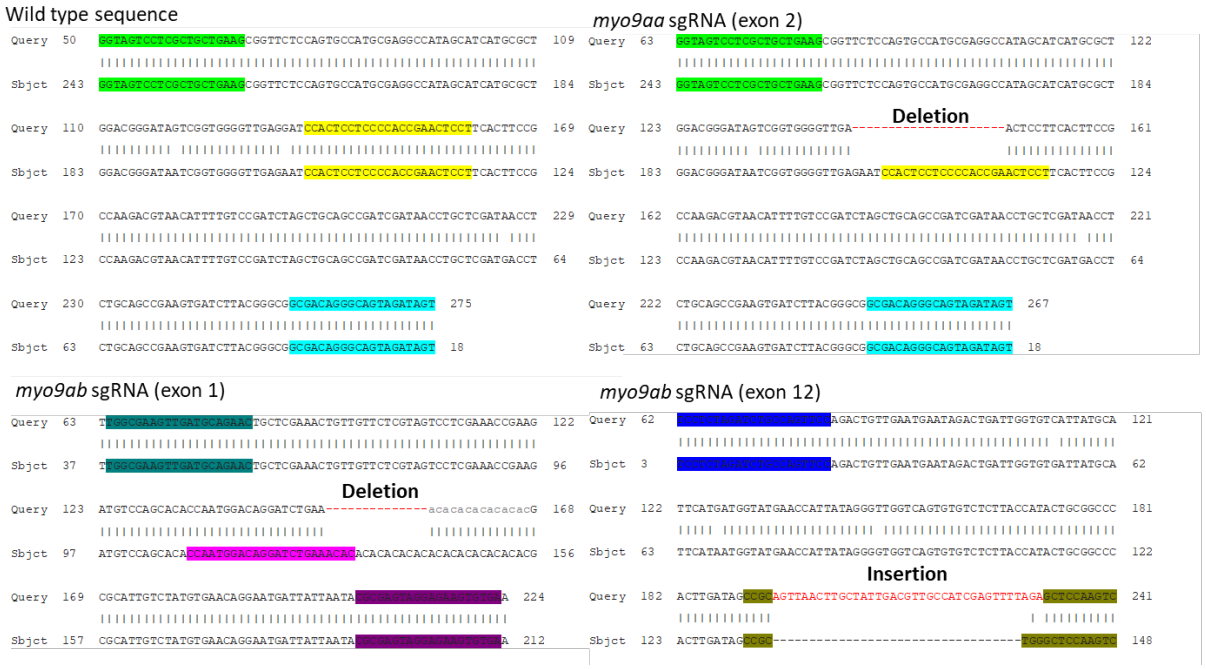

Figure 3.12. Genomic sequence of CRISPR-targeted *myo9aa* and *myo9ab*. The wild-type sequence for *myo9aa* is shown in the first panel, with the presence of a deletion in the target region of the sgRNA for exon 2 (highlighted yellow) shown in the top right. The bottom left panel shows a deletion induced by a sgRNA against exon 1 of *myo9ab* (pink), and in the bottom right panel an insertion can be observed (green) in exon 12 of *myo9ab.* The other highlighted regions show the location of the sequencing primers.

3.6.2 Gross morphology of myo9aa/ab crispants

Similar phenotypes were induced by each *myo9aa/ab* sgRNA, as well as in co-injected fish, as shown in Figure 3.13A. The co-injected crispant groups, as outlined in the methods section, include: 3 sgRNAs (*myo9aa2* + *myo9ab1* + *myo9ab12*) or 4 sgRNAs (*myo9aa2* + *myo9aa2b* +*myo9ab1* + *myo9ab12*). Tyrosinase (Tyr) is a protein involved in pigment formation in the fish, therefore a published sgRNA against *tyr* was included as an injected control (Jao et al., 2013). The lack of pigment confirms the success of CRISPR/Cas9/sgRNA delivery and action. Furthermore, fish injected with *tyr* sgRNA do not have a tail phenotype demonstrating that this is not a result of the CRISPR/Cas9 injection itself.

Severity of the phenotype was ranked at 72 hpf from mild to severe by degree of tail curvature, as outlined in Figure 3.13B. The number of injected fish (3 and 4 sgRNA injected) with each phenotype, expressed as a proportion of controls, is shown in

Figure 3.13B. Fewer normal fish were identified for 3 and 4 sgRNAs as compared to controls. For the 3 sgRNA group, 3-fold more were identified as ‘mild’, whereas injecting 4 sgRNAs resulted in over twice the number of ‘moderate’ fish.

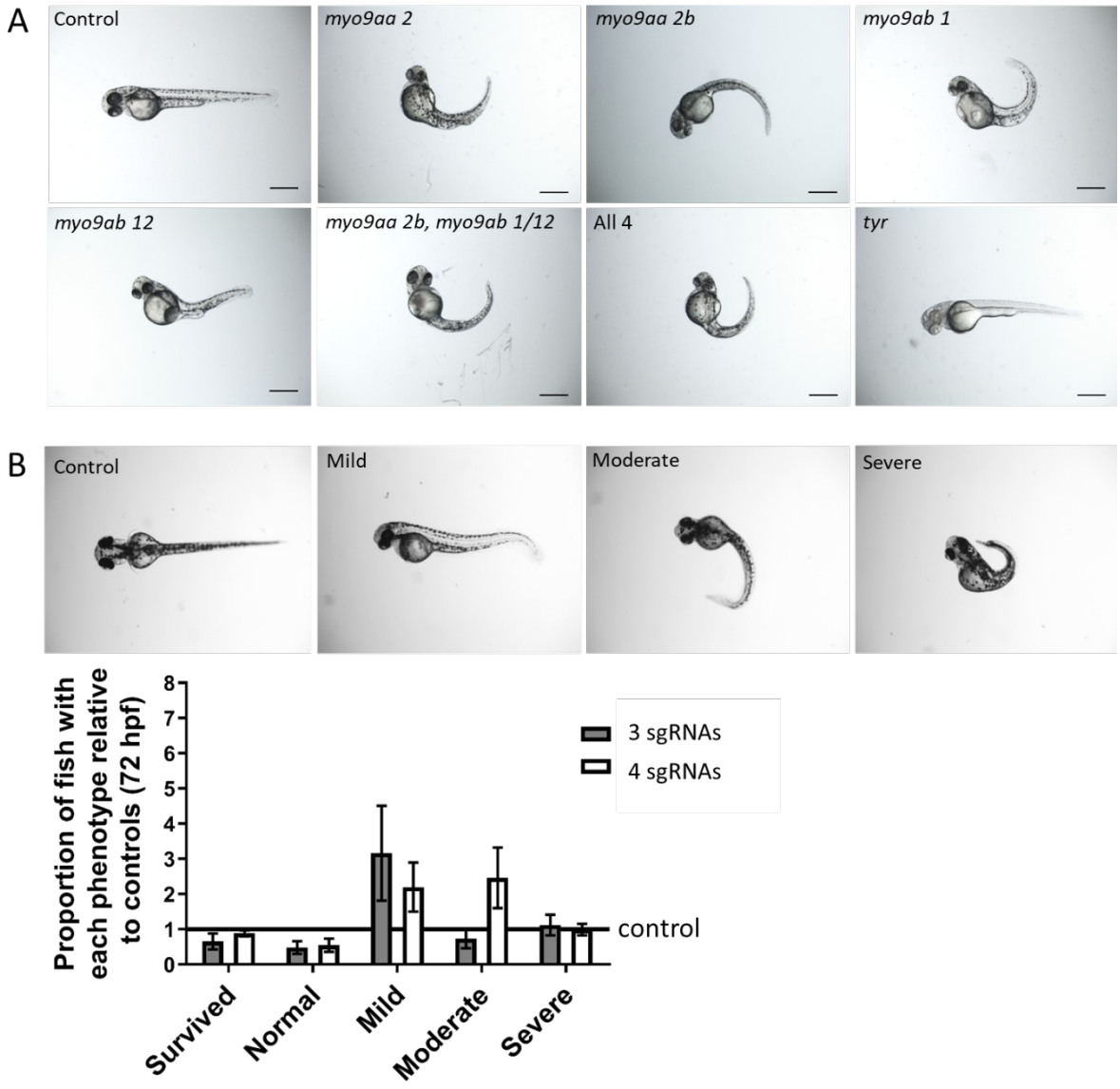

Figure 3.13. Phenotypes of mosaic *myo9aa/ab* knockout zebrafish. A. Representative images of 48 hpf zebrafish injected with sgRNAs (numbers following the gene refer to exon targeted). Combinations of 3 and all 4 sgRNAs were also performed, along with a control against the tyrosinase gene (*tyr*) in which no pigment can be observed confirming knockdown success. Scale bar = 500μm. B. Images showing phenotypic classification of injected zebrafish at 72 hpf, ranging from normal to severe. Graph shows proportion of fish injected with 3 (n = 292) or all 4 (n = 160) sgRNAs as compared to controls (black line, n = 138). Error bars represent mean ± S.E.M.

3.7 MYO9A KO mouse

A MYO9A KO mouse was generated by Prof. Bähler (University of Münster, Abouhamed et al., 2009). This mouse often exhibited hydrocephalus due to a buildup of fluid within the 3rd ventricle of the brain, and has shown defective kidney function, however, skeletal muscle performance and integrity of the neuromuscular synapse had not yet been assessed (Abouhamed et al., 2009, Thelen et al., 2015). To extend our analyses into a mammalian system, tissue from the MYO9A KO mouse was obtained. The genotype of the 4 mutant mice supplied was confirmed using gDNA extracted from tail tips. The wild-type allele was absent from all 4 mutant mice, as shown in Figure 3.14. A product of approximately 700 bp using primers against the mutant allele was present in all of the mutant animals and not in the wild-type, indicating the presence of a large deletion, as predicted product size is 2896 bp.

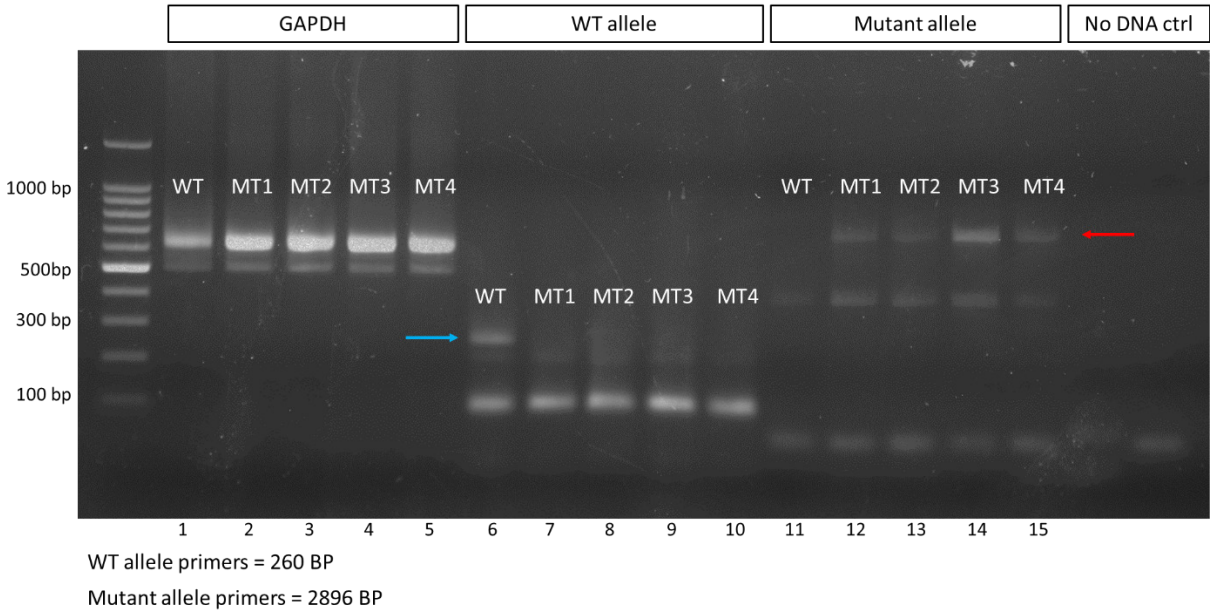

Figure 3.14. Genotyping of Myo9a KO mouse. PCR electrophoresis gel confirming genotype of MYO9A KO mice from gDNA extracted from tail tips. The presence of the wild-type allele (260 bp) is absent from all 4 mutant mice, indicated by the blue arrow. The mutant allele (approx. 700 bp) is present in all 4 mutant mice (red arrow), and not in the wild-type. Primers against *Gapdh* were also used to confirm quality of gDNA. WT = Wildtype, MT= mutant, ctrl = control.

3.8 Discussion

The aim of this chapter was to describe the generation of models of MYO9A-CMS or MYO9A loss that could help achieve the overarching goal of discovering whether MYO9A plays a role at the NMJ. To gain a comprehensive overview, a range of approaches were used as summarised in Table 3-2, including a knockdown cell-line, patient cells, zebrafish models and a MYO9A KO mouse.

Model	Advantages	Disadvantages	Chapter used
MYO9A KD NSC-34 cells	Unlimited supply of material, easy to work with, neuronal cell relevant for NMJ	Knockout rather than patient mutation	5, 6
Patient mutation-expressing SH-SY5Y cells	Expression of patient mutation, neuronal cell	Expression of patient mutations not confirmed, expression of endogenous MYO9A not removed, expression not on genetic background of patient	-
Patient iNPCs	Cells from patient, patient genetic background, neuronal cells relevant for NMJ	Limited supply of tissue, only one patient available	4, 5
Zebrafish Myo9aa/ab MO knockdown	Rapid results, whole organism, study of intact NMJs rather than nerve or muscle cell, behavioural assessment	MOs are transient, two orthologues of human gene, knockout rather than expression of patient mutations, mosaic knockdown	4, 6
Zebrafish *myo9aa/ab* crispant	Not transient, rapid results, whole organism, study of intact NMJs, behavioural assessment	Two orthologues of human gene, knockout rather than expression of patient mutations and mosaic knockdown	4, 5, 6
MYO9A$^{-/-}$ mouse	Mammalian model, NMJs more similar to human, whole organism and ability to study intact NMJs	Behavioural testing was not possible, knockout rather than expression of patient mutations and tissue preparation not optimal	4, 5

Table 3-2. Summary of models generated for study of MYO9A. Table includes model generated, main advantages and disadvantages for studying the role of MYO9A at the NMJ and the chapter where each model is used.

3.8.1 MYO9A KD NSC-34 cells

During my MSci project MYO9A was targeted for stable knockdown from NSC-34 cells, and reduced levels of *MYO9A* expression confirmed by qRT-PCR due to the lack of a commercially available antibody that worked in western blot (O'Connor et al., 2016). Abundance of MYO9A was normalised to β-actin, however, in later experiments the levels of actin identified in western blot and immunofluorescence experiments differed between control and MYO9A KD cells. Therefore, the knockdown of MYO9A was reconfirmed in this study using an alternative housekeeping gene: *Pgk1*. This gene has been shown to be an appropriate reference gene for qRT-PCR in neuronal cells (Boda et al., 2009).

NSC-34 cells were initially selected as an appropriate *in vitro* model to assess the effect of reduced MYO9A levels due to features such as ability to synthesise and release ACh, ability to generate action potentials, presence of important cytoskeletal proteins like neurofilament, as well as the capability of clustering AChRs on cultured myotubes (Cashman et al., 1992). This cell-line has been used to model various neurodegenerative diseases, including ALS (Liu et al., 2002, Rizzardini et al., 2005) and SMA (Acsadi et al., 2009), as well as looking at cellular processes associated with a myosin protein (myosin VI) (Sundaramoorthy et al., 2015). This is the first study to use these cells as an *in vitro* model for CMS and for the analysis of MYO9A-loss on cell structure and function.

Basic morphology assessment of MYO9A KD NSC-34 cells was performed in this chapter, with detailed analysis of pathways and mechanisms of action addressed in subsequent sections of this thesis. The actin cytoskeleton is a major component of cells and regulates cell size and shape (Rottner et al., 2017). MYO9A is an actin-based molecular motor that can also act to cross-link actin filaments, as well as displaying indirect effects on the cytoskeleton as a regulator of RhoA activity (Hall, 1998, Wallace et al., 2018, Saczko-Brack et al., 2016, Omelchenko and Hall, 2012, Chieregatti et al., 1998). Therefore, changes in MYO9A levels may impact on the ability of the actin cytoskeleton to maintain an extensive and complex three-dimensional cell structure. Initial observations of MYO9A KD cells revealed an increase in cell area and a corresponding reduction in height. This likely reflects an overall flattening and spreading out of cells, rather than changes in volume. Similarly, nucleus area was increased in MYO9A KD cells and volume remained the same as control cell nuclei. Actin also attaches to the cell membrane and drives protrusions

such neurite extensions, which have been shown to be affected in cells lacking MYO9A (O'Connor et al., 2016). Other reports of MYO9A-depletion in cell models are conflicting, with loss from 16HBE (human bronchial epithelial) cells leading to rounding of cell bodies (Omelchenko and Hall, 2012) where as in caco-2 (human intestinal) cells there is flattening and thus a larger area of cells (Abouhamed et al., 2009). This could be due to variations in RhoA activity in different cells types (Hall, 1998), However, RhoA activity in nerves has been reported to be associated with cell rounding as opposed to fibroblasts for which RhoA activation causes cell spreading (Guilluy et al., 2011, Kranenburg et al., 1999, Ridley and Hall, 1992). It could also be due to effects of MYO9A on downstream pathways other than those mediated by RhoA.

Alterations in nuclei area in MYO9A KD cells were also observed, which has been suggested to be due to perinuclear stress fibre formation compressing the nuclei (Vishavkarma et al., 2014). Another ubiquitously expressed CMS-related protein, MACF1, interacts with the actin cytoskeleton and has been shown to regulate the shape and position of nuclei in muscles and other cell types (Escobar-Aguirre et al., 2017, Oury et al., 2019, Wang et al., 2015). Therefore, the effect observed due to MYO9A-loss may be influenced by altered actin dynamics but further investigation would be required.

3.8.2 MYO9A-CMS patient cells

The three reported MYO9A-CMS patients carry *MYO9A* missense mutations that are unlikely to cause loss of protein expression to the same extent as the knockdown cells. Therefore, to better replicate the patient condition, fibroblasts from one of the MYO9A-CMS patients were obtained. To quantify the level of *MYO9A* expression, qRT-PCR was performed revealing no significant difference between levels of MYO9A in the patient cells as compared to a healthy control subject. Due to the inability to quantify protein levels in the fibroblasts, the possibility remains that the mutations affect protein folding, stability or degradation. It could also be the case that fibroblasts do not express high levels of *MYO9A,* however, levels of *MYO9A* RNA were not quantified in iNPCs. An investigation of the Human Protein Atlas (https://www.proteinatlas.org, last accessed February 21, 2019, Uhlen et al., 2015) revealed levels of MYO9A in fibroblasts are among the lowest in all expressing tissues (whereas nerve and muscle tissues have higher levels of MYO9A) thus there may not be easily detectable changes in abundance. The levels of RNA often do not

predict protein quantity due to factors such as post-translational modifications and activation of protein degradation pathways. For example, levels of MYO9A RNA in skeletal muscle on the Human Protein Atlas are among the lowest, but protein levels are among the highest. In CMS caused by *SLC18A3* p.Gly360Arg, levels of RNA are unchanged as compared to wild-type, however protein levels are undetectable in the patient (Aran et al., 2017). A larger sample size and an antibody for western blot would have provided better insight into this question, however, fibroblasts were not available from the other patients. In the future, a genetic modification technique such as CRISPR/Cas9 could be used to knockout MYO9A expression from the patient fibroblasts. Cells could then be converted into neurons and results compared with unmodified patient cells to see if results from the patient mutation were similar to loss of MYO9A.

While fibroblasts have been used in many cases to investigate the molecular basis for neuropathic and myopathic diseases, they are more suited to analysis of events that occur in in all cell types such as mitochondrial biogenesis and function (Bartsakoulia et al., 2018, Chaouch et al., 2014, Perez et al., 2017). However, to compare with the knockout NSC-34 cells neurons would be a more appropriate system to allow features such as neurite growth and vesicle release to be assessed. The technique applied here involves converting fibroblasts into iNPCs, a proliferating neuronal stem cell population that are tripotent and can differentiate into neurons, oligodendrocytes and astrocytes (Meyer et al., 2015). To deliver the transcription factors, a non-integrating virus (Sendai) was used, thus avoiding issues such as random genome integration associated with lentiviral vectors (Fusaki et al., 2009). Successful generation of iNPCs was achieved in this project, determined by the up and downregulation of various stem cell, neuron and fibroblast markers. This was further confirmed by the ability of selected colonies to differentiate into neurons that express Tuj1 and MAP2, as described by Meyer *et al* (2015).

3.8.3 SH-SY5Y cells with patient mutations

In an attempt to address the qRT-PCR findings using a different method, and to understand more about the effect of each patient mutation on nerve cells, SH-SY5Y cells were used. Cells were transfected with a *MYO9A* construct containing each of the patient mutations, as well as a predicted benign polymorphism in the same tail region. However, the presence of MYO9A in these cells could not be confirmed by western blot against the HA-tag expressed by the vector. MYO9A is 298 kDa protein

and has been shown to be detectable by immunoblot using an anti-MYO9A antibody generated by the laboratory of Prof. Bähler (Münster, Chieregatti et al., 1998). In this case, however, a strong band was present at 100kDa, the origin of which is unknown. Use of an antibody against MYO9A in NSC-34 cells revealed an enrichment of the protein at growth cones of extending neurites (O'Connor et al., 2016). Immunofluorescence results in the transfected SH-SY5Y cells were inconclusive, as the localisation of MYO9A was not as expected, either in the growth cones or associated with the actin network. The HA-positive staining appeared in some cases to be extracellular, raising the possibility that the culture was contaminated, however mycoplasma testing was negative. As the presence of MYO9A could not be confirmed, these cells were not used in subsequent experiments.

3.8.4 Zebrafish models of MYO9A-deficiency

The NMJ changes significantly during development and there is constant cross-talk between the pre and postsynaptic components, and other associated cell types such as Schwann cells. Therefore, to obtain a more holistic view of MYO9A function at the NMJ, an *in vivo* model was required. Zebrafish develop rapidly and are well suited for studies of the NMJ in first few days of life, due to their optical transparency and well documented time-points of NMJ development. In previous data collected in my MSci project, a MO-mediated knockdown approach was utilised to target Myo9aa/ab in zebrafish and their basic phenotype was assessed (O'Connor et al., 2016).

The zebrafish depleted for Myo9aa/ab exhibited varying degrees of tail curvature, a feature present in other zebrafish models of CMS (Chaouch et al., 2014, Muller et al., 2010, Kim et al., 2007). Curvature of tails can be associated with activation of p53-mediated apoptosis, however, co-injection with a p53 MO did not rescue the tail phenotype, suggesting it is likely related to loss of MYO9A (Langheinrich et al., 2002, Robu et al., 2007, O'Connor et al., 2016). Large injection volumes have also been shown to affect morphology of zebrafish in development including causing tail curvature and reducing survival rates (Schubert et al., 2014). The injection volume used in this study of 4.2nl falls within the recommended range for limiting this effect. This is supported by analysis of survival rates, for which zebrafish injected with a control MO in this study had a survival rate of 89%, as compared with a report that zebrafish injected with water at a 4.2nl volume have a survival rate of 84% (Schubert et al., 2014).

A suggested control for zebrafish morphants is to compare results to a genetic knockdown using a technique such as CRISPR/Cas9 (Stainier et al., 2017). This has further benefits for analysis of NMJ development as MOs are diluted and degrade over the first few days, whereas genetic knockout allows assessment at later time points. Injection of 4 sgRNAs against *myo9aa/ab* along with the Cas9 protein successfully induced deletions and insertions at their target sites as expected, and gave rise to a curved tail phenotype as found in MOs.

Ideally the sgRNA should target the 5' end of the gene, thus increasing the likelihood of producing a truncated protein that is not functional, but not so near the start that an alternative start codon may allow protein production to continue. However, due to the numerous parameters that must be fulfilled to design an effective sgRNA (Sorlien et al., 2018), for *myo9ab* one sgRNA targeted exon 1 and the other exon 12. This was deemed acceptable as *Myo9ab* has 44 exons and thus even targeting exon 12 is likely to significantly impair protein function, especially the tail region which is where the patient mutations reside. This was supported by the presence of a curved tail phenotype in zebrafish injected with the *myo9ab* exon 12 sgRNA alone, however both were injected for experiments to increase the likelihood of knockdown. The sgRNA targets for *myo9aa* were in close proximity to each other in exon 2 (33 bases), therefore co-injection was more likely to induce larger deletions if cutting occurs in both places at a similar time. Thus, injecting both *myo9ab* sgRNAs and either 1 or both *myo9aa* sgRNAs was trialed, revealing a more severe phenotype present in fish injected with all 4 sgRNAs. Co-injection of multiple (up to 5) sgRNAs has been performed elsewhere with no reported toxic effects (Ota et al., 2014), thus this method was used for the rest of the study.

As a control for the CRISPR/Cas9 injections, a sgRNA against the pigment formation gene *Tyr* was used, as previously described (Jao et al., 2013). Injection successfully reduced pigment formation and did not induce the curved tail phenotype associated with the *myo9aa/ab* knockout. Full pigment depletion was often achieved, suggesting a high degree of efficiency. Mutagenesis rates in F0 fish using CRISPR/Cas9 of 75-99% have been reported, thus despite the genetic mosaicism of the zebrafish crispants, they still offer a good model in which to screen for phenotypes. Crispants were initially used while adult knockout lines were generated, however, efforts to make single gene or double gene knockouts were not successful, with no homozygote F2 zebrafish identified.

3.8.5 MYO9A KO mouse

Finally, to apply findings to a mammalian system, tissue from a MYO9A KO mouse generated by the laboratory of Prof. Bähler (University of Münster) was obtained (Abouhamed et al., 2009). As proteomic data has identified the presence of MYO9A in human myoblasts and myotubes, mouse muscle was taken for analysis (O'Connor et al., 2018b). Mouse muscle can offer many insights into pathology, through histological analysis of fibres, immunological staining of various markers including fibre type-specific labels and NMJ morphology. Genotype of the mice was confirmed and thus the model utilised for experiments.

3.8.6 Conclusion

Overall, generation of a variety of models to investigate MYO9A function in nerve cells and at the NMJ was achieved. Using a combination of *in vitro* and *in vivo* approaches in the following chapters, the contribution of this unconventional myosin protein to NMJ development, morphology and function will be explored and potential mechanisms of action investigated.

Chapter 4. Assessment of early NMJ development and adult NMJ morphology in models of MYO9A-depletion

4.1 Introduction

The overall aim of this project was to determine whether MYO9A plays a role at the NMJ, and therefore in the absence of correct function leads to impaired signal transmission that manifests as a CMS. The use of the models generated in the previous chapter form the basis of this investigation, with a range of *in vitro* and *in vivo* approaches applied. The use of zebrafish as a model for CMS will first be discussed, followed by a description of zebrafish development and the functional tests that can be used in the context of NMJ disruption, as well as the benefits associated with NMJ analysis in mouse models.

MYO9A CMS patients present with symptoms early in life. The two Kurdish siblings, previously shown to have mutations in *MYO9A,* presented clinically with a prenatal onset including reduced foetal movements (O'Connor et al., 2016). They also had 4 other siblings that had previously died due to symptoms associated with CMS (hypotonia, feeding difficulties, respiratory failure) within the first year of life (O'Connor et al., 2016). This suggests that MYO9A affects synaptic transmission early in development. Zebrafish are a well-suited model to study early development as they develop externally, with optical clarity allowing visualisation of NMJs. In addition, they perform a well characterised set of movements that appear sequentially such as twists of the tail while in the chorion, response to tactile stimulation after hatching and then free swimming in larval stages (Saint-Amant and Drapeau, 1998). Zebrafish have successfully been used to study other forms of CMS (Muller et al., 2010, Senderek et al., 2011), as well as myopathic and neurological disorders such as muscular dystrophies and spinal muscular atrophy (SMA) (Bassett et al., 2003, Boon et al., 2009, Gupta et al., 2012).

The developmental stages of zebrafish from embryo to larvae are displayed in Figure 4.1. Of particular interest here is the rapid appearance of the tail structure, which is a useful site in which to study neuron extension, AChR clustering and muscle morphology.

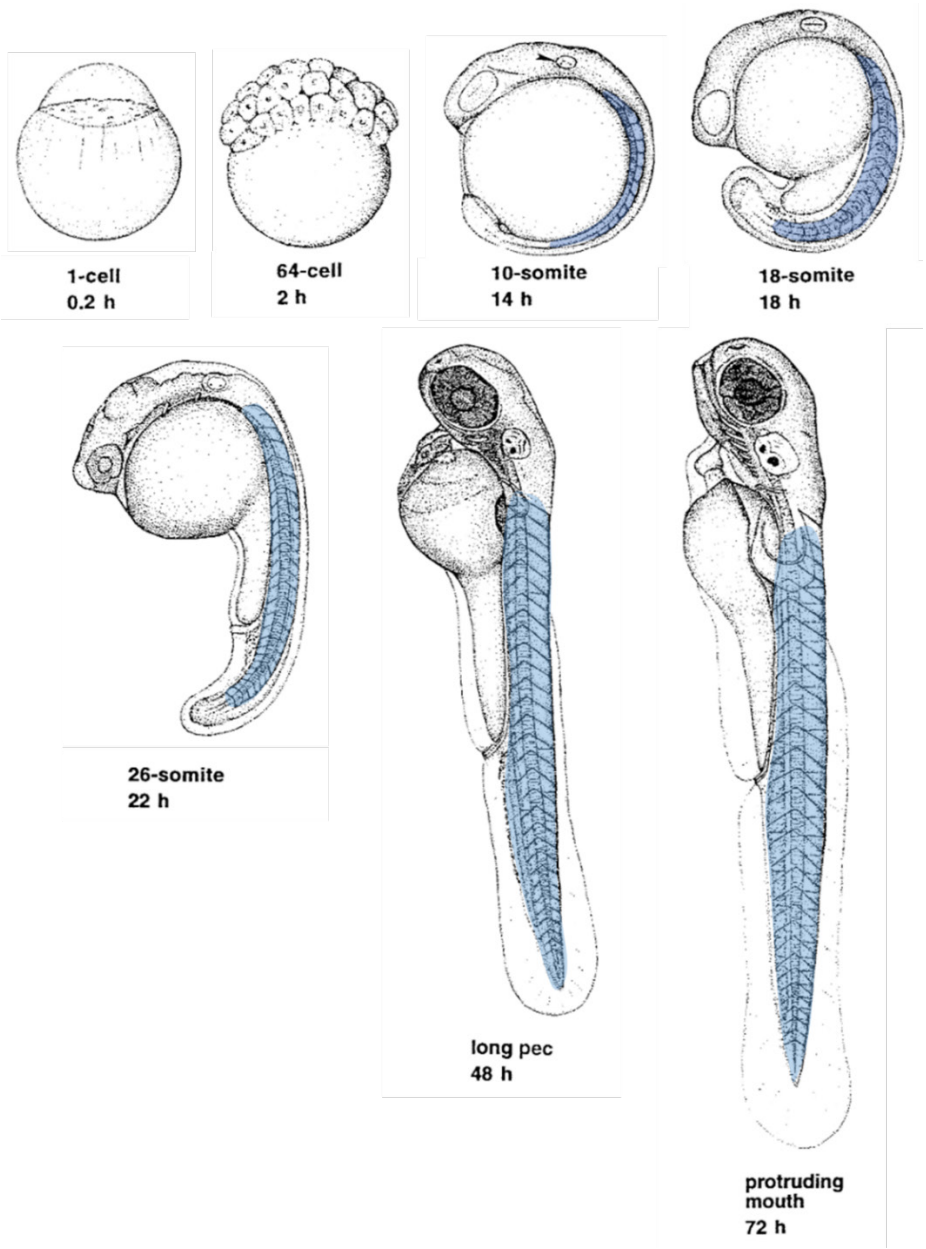

Figure 4.1. Early zebrafish development. Development of zebrafish embryos begins at the one cell stage, in which the cell and adjoining yolk sac are maintained within an egg (chorion). By 2 hpf the 64-cell stage is reached, and by only 14 hours the presence of 10 muscle somites can be observed in the tail (blue). Between 48 and 72 hours post fertilisation the zebrafish hatch from the chorion and the total number of somites is present (30-34). Zebrafish are referred to as larvae by 72 hours. Image modified from Kimmel *et al* (1995).

Innervation of the tail musculature commences during the embryonic stage at around 18 hpf. This begins with the extension of axons from primary motor neurons that have their cell bodies in the ventral spinal cord. There are 3 primary neurons that innervate each muscle somite, the caudal, medial and rostral neurons. These neurons have specific, non-overlapping regions of innervation covering the myotomes (Figure 4.2). The first of the 3 primary neurons to send out an axon from the spinal cord is the caudal motorneuron. Within minutes of this axonal outgrowth

spontaneous muscle twitches can be observed while the zebrafish is still within the chorion, giving rise to spontaneous coiling movements (Saint-Amant and Drapeau, 1998). These movements increase in frequency as the motorneurons continue to develop, peaking at 19 hpf and then slowly declining in frequency until ceasing at 27 hpf. This is the time point at which secondary motorneurons begin to send out axons, which are thought to mediate muscle contractions for slower rhythmic swimming, rather than fast muscle twitches (Myers et al., 1986, Saint-Amant and Drapeau, 1998). During primary motorneuron extension the axons from each of the 3 primary motor neurons travel along a common pathway to the horizontal myoseptum. At this point is a cluster of prepatterned AChRs that are present on muscle pioneer cells (cells that give rise to the earliest muscle cells in the zebrafish, Eisen et al., 1986, Felsenfeld et al., 1991). Here, the axons make a choice (thus this point is referred to as the ‘choice point’) regarding their route of innervation, with axons from each primary motor neuron subset diverging to give rise to the non-overlapping pattern of innervation observed in zebrafish muscle (Figure 4.2). The target choice of these axons can be achieved in the absence of muscle pioneer cells and the cluster of prepatterned AChRs that is formed on them, however, this absence influences formation of appropriate arborisations (Melancon et al., 1997).

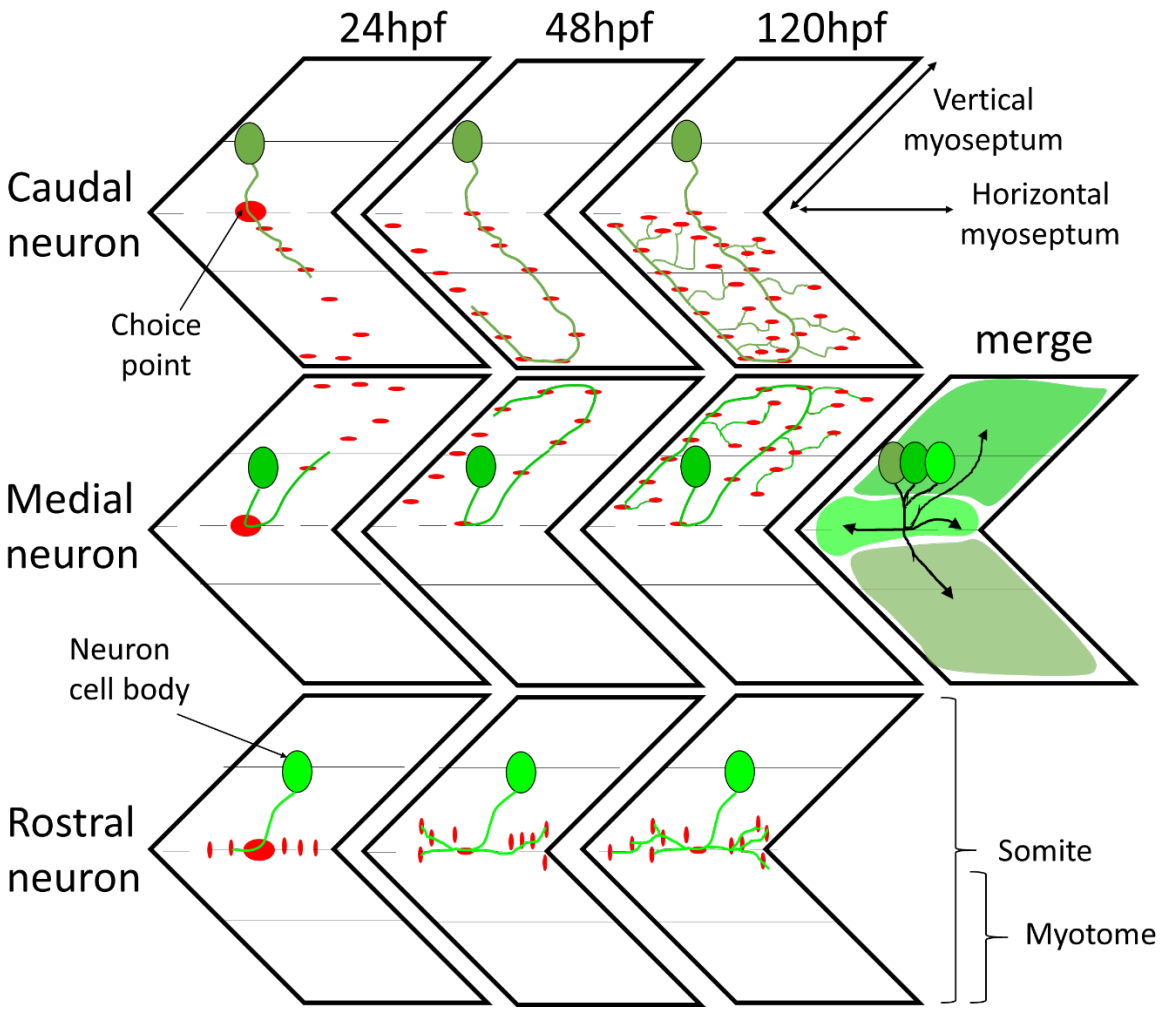

Figure 4.2. Innervation pattern of primary motor neurons in the developing zebrafish tail. Neuronal trajectories of caudal, medial and rostral primary motor neurons shown at 24 hpf, 48 hpf and 120 hpf. A merged image shows the resulting non-overlapping regions of innervation for each primary motor neuron. Red spots = AChRs, large red spot = choice point cluster situated at the horizontal myoseptum.

Embryos begin to respond to touch from 21 hpf if manually removed from the chorion, but do not gain the ability to respond by swimming until the time of secondary motorneuron outgrowth at around 27 hpf. The swimming response increases in frequency until peaking at 36 hpf (Saint-Amant and Drapeau, 1998). As zebrafish naturally hatch from the chorion by 48 hpf, a useful test to assess the movement of the fish can be performed after this time point. This is the touch-evoked response assay in which a tap on the head or tail of the fish causes a rapid swim away from the stimulus (O'Connor et al., 2018a, Saint-Amant and Drapeau, 1998). At this time point it is a particularly useful test as it can be performed on a large number of animals and initial acceleration of the zebrafish is proportional to the force produced by the skeletal muscle, removing the need for securing zebrafish in a force transduction system (Sztal et al., 2016). From 3 dpf zebrafish begin to swim freely

and this behaviour matures over the following days to prepare for capture of prey when zebrafish begin to feed themselves at 6 dpf (Budick and O'Malley, 2000, Buss and Drapeau, 2001). In humans a 6-minute walk test is commonly used to assess functional ability in patients with disorders such as muscular dystrophy, and by analogy with this a 10-minute swim test has also been developed in the 6 dpf zebrafish (Sztal et al., 2016). While this is a useful test to indirectly analyse nerve/muscle performance, it cannot be performed on MO-mediated knockdowns due to the transient nature of the technique. Overall, there are a number of well-defined NMJ and locomotive development features that can be tracked throughout zebrafish embryo and larval stages as summarised in Figure 4.3, providing a useful model in which to study the effects of MYO9A loss.

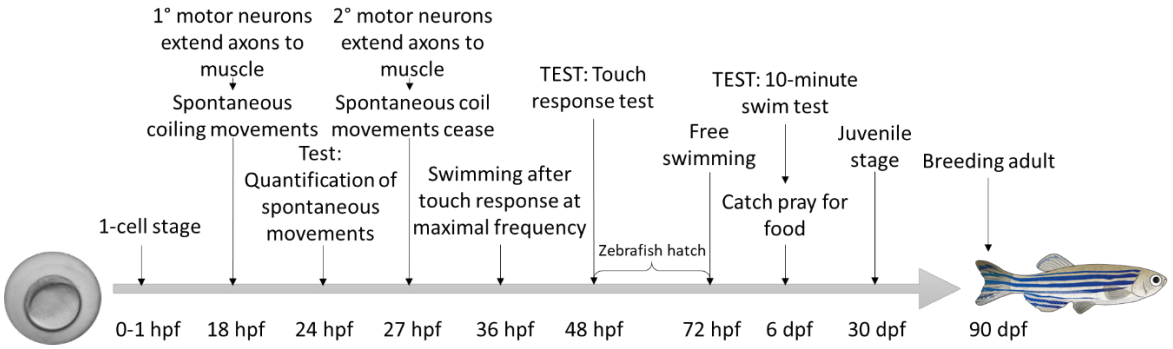

Figure 4.3. Stages of zebrafish development and behavioural tests performed. Timeline shows the main points of zebrafish development important for this study including neuron extension, time that movements are obtained, tests performed at each stage and progression to adult zebrafish. Hpf = hours post fertilisation, dpf = days post fertilisation.

The zebrafish motor system has a number of similarities to the human which make it a useful model to study the NMJ, including similarities of neuron subtypes, region specific innervation, preservation of the dystrophin associated glycoprotein components and similar contractile apparatus (Babin et al., 2014, Egashira et al., 2018). However, it also has some key differences including the presence of gap junctions and innervation of muscle fibres by single primary motor neurons and multiple secondary motor neurons that coordinate different forms of swimming activity (Nguyen et al., 1999, Westerfield et al., 1986). Therefore, it is useful to also include analysis of mammalian NMJs which are evolutionarily closer to human.

Mouse models have been used successfully to study the developing and mature NMJ in response to different genetic manipulations, including CMS models of disease (O'Connor et al., 2018b, Webster, 2018). Key features of NMJ morphology

can be quantified, including AChR area, nerve terminal size, fragmentation and more recently this has been extended by Jones *et al* (2016) to encompass 21 variables giving a comprehensive overview of the structure of NMJs. However, the contribution of any morphological defect toward function requires electrophysiological data and careful interpretation.

Using a combination of approaches to assess the effect of MYO9A deficiency at the NMJ will help to elucidate any contribution of this unconventional myosin protein to cholinergic signal transmission. Furthermore, if characterisation of any models reveal consistent changes, this offers parameters that can be measured following drug screens.

4.2 Aim of chapter

To perform observations of NMJ development in zebrafish, coupled with assessment of patient nerve cells and morphology of adult NMJs in a MYO9A knockout mouse.

Initially analysis of patient cell neurites was performed to determine whether the presence of *MYO9A* mutations affected neurite extension. This was followed by behavioural assessments of zebrafish depleted for Myo9aa/ab accompanied with analysis of NMJ morphology at different time points in development. Finally, mature NMJs in MYO9A KO mouse were assessed and compared to wild-type controls to determine presence of any structural abnormalities.

4.3 Morphology of neurites in vitro

Previous data demonstrated a neurite phenotype in the mouse-derived motor neuron NSC-34 cell-line lacking MYO9A (O'Connor et al., 2016). Neurites were significantly longer in KD cells, and had more primary, secondary and tertiary branches. To assess whether the patient cells also exhibited altered neurite outgrowths, differentiated MYO9A CMS patient iNPCs, generated from fibroblasts (Chapter 3, Section 3.4) were compared to controls in a scratch assay (Al-Ali et al., 2017). A region of cells was removed by scratching with a pipette tip and imaged at ‘Day 0’. Following 3 days of culture the same region was imaged to enable visualization of neurite extension over the scratched area (Figure 4.4A). Measurement of neurites revealed a significant increase in the length of those extending from the MYO9A-CMS patient cells as compared to the control subject ($p \leq 0.0001$, Mann Whitney test). This suggests that patient cells also exhibited a neurite phenotype, as observed in the MYO9A KD NSC-34 cells.

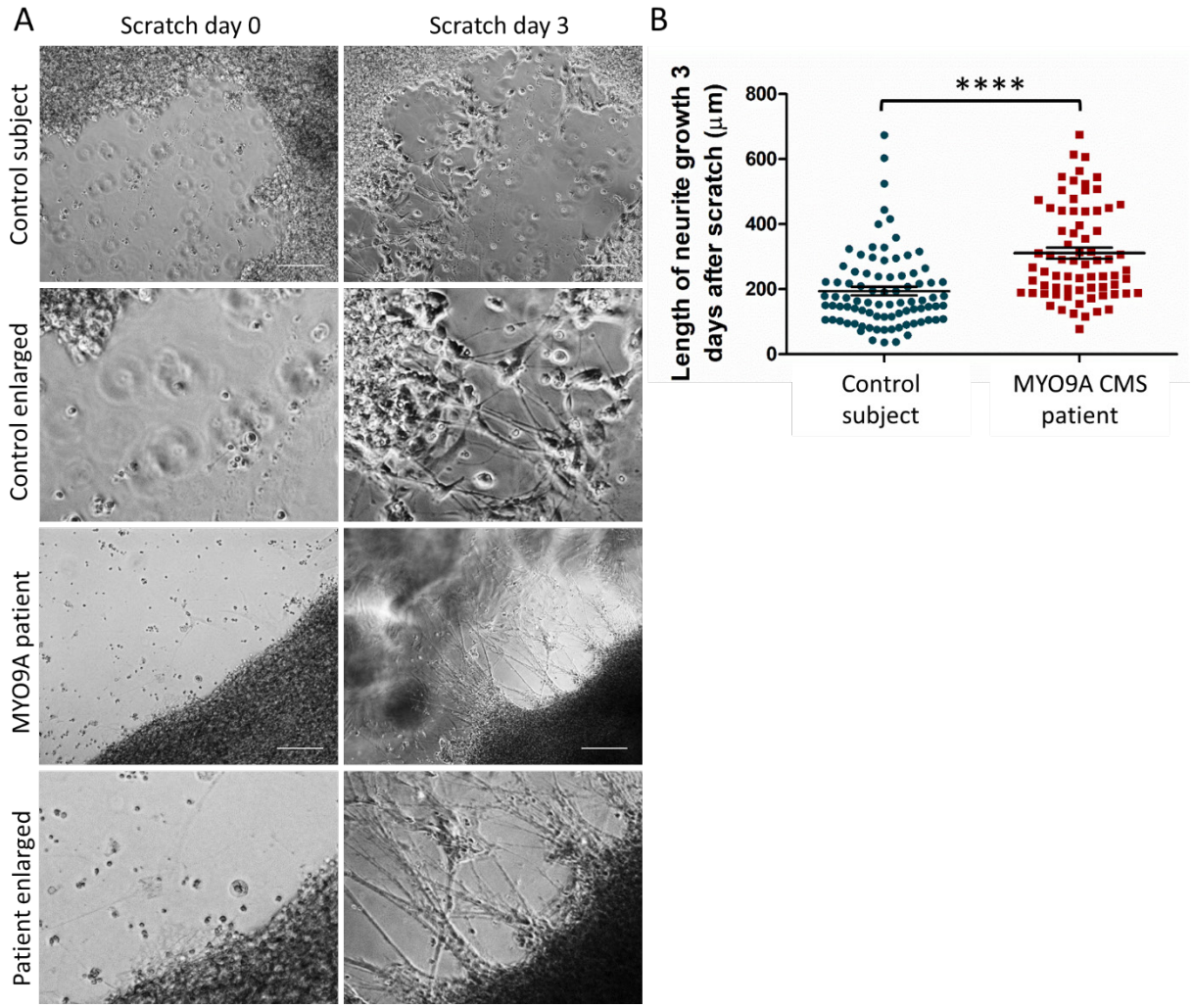

Figure 4.4. Neurite extension in iNPCs following scratch assay. A. Representative images of differentiated control and MYO9A patient iNPCs immediately following a scratch to remove cells in the tissue culture dish, and 3 days after when neurites have started to bridge the gap. Enlarged regions of each image are shown in the lower panel. Scale bars = 200μm. B. Graph showing the length of neurites of control (n=86) and MYO9A patient (n=72) cells 3 days following the scratch. A total of 3 scratches was performed. Error bars = mean ± S.E.M, ****p<0.0001, Mann Whitney test.

4.4 Behavioral assessment of zebrafish models

Zebrafish perform well characterised movements during development at distinct time points. These movements coincide with development of the NMJ, allowing any differences that impact on NMJ signalling to be identified if they manifest as changes in behaviour. As zebrafish have two *MYO9A* orthologues; *myo9aa* and *myo9ab*, sgRNAs targetting both genes were required. Preliminary experiments were performed to determine the most effective combination of sgRNAs using either:

3 sgRNAs - *myo9aa2* + *myo9ab1* + *myo9ab12* sgRNAs

4 sgRNAs - *myo9aa2* + *myo9aa2b* +*myo9ab1* + *myo9ab12* sgRNAs

The preliminary tests performed to determine the combination of sgRNAs to be used for subsequent NMJ analysis consisted of 2 behavioural tests, in which *myo9aa/ab* depleted fish were compared with uninjected controls and *Tyr* sgRNA controls (targets a gene affecting pigmentation). To support results by using an alternative method of depletion and to expand on the observational analysis performed in O'Connor *et al* (2016), Myo9aa/ab MO-mediated knockdown zebrafish were also subject to behavioural assessments.

4.4.1 Chorion movements

Spontaneous movements begin in zebrafish embryos around 17 hpf, and as axon outgrowth progresses across the myotomal surface, the movements increase in frequency until ceasing at 27 hpf (Myers et al., 1986, Saint-Amant and Drapeau, 1998). The spontaneous movements are characterised by a full rotation of the embryo within the chorion, driven by the tail. Results obtained from the Myo9aa/ab MO zebrafish revealed a significant reduction in chorion movements performed at 24 hpf as compared to controls (O'Connor et al., 2016). To reconfirm these results, chorion movements were again assessed in Myo9aa/ab MO fish at 24 hpf (Figure 4.5). Morphants performed significantly fewer chorion rotations as compared to controls (p=0.0031, Mann Whitney test), thus demonstrating the same trend as in our previous study.

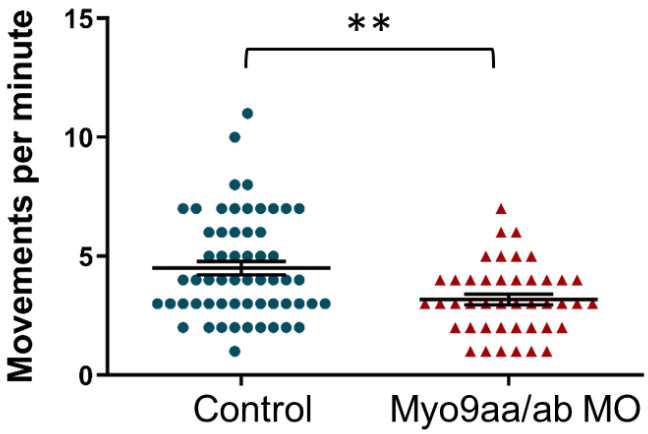

Figure 4.5. Movements performed by zebrafish within the chorion at 24 hpf. Full chorion movements performed in one minute by uninjected (control, n=58) and Myo9aa/ab MO-injected (n=43) zebrafish. MO=morpholino. Error bars = mean ± S.E.M. **p<0.01, Mann Whitney test.

To determine whether depletion of Myo9aa/ab using CRISPR/Cas9 produces a similar lack of movement in early development, zebrafish injected with 3 (*myo9aa2,*

myo9ab1 and *myo9ab12)* or 4 sgRNAs (*myo9aa2, myo9aa2b, myo9ab1* and *myo9ab12*) were subject to chorion movement analysis.

Uninjected (control) and *tyr* (injected control) sgRNA injected zebrafish perform on average 2.4 and 3 rotations per minute, respectively (p=0.095, Mann Whitney test), demonstrating that the injection procedure and CRISPR-mediated knockdown of alternative genes doesn't significantly affect chorion movements (Figure 4.6). *Myo9aa/ab* 3 sgRNA fish move on average 1.2 times per minute which is significantly lower than both controls (p≤0.0001, Mann Whitney test). *Myo9aa/ab* 4 sgRNA zebrafish perform significantly less rotations than 3 sgRNA-injected, as well as the controls, with only 0.3 turns per minute (p≤0.0001, Mann Whitney test (Figure 4.6). Therefore, the 4 sgRNA-injected fish show a more pronounced phenotype, and both MO and CRISPR/Cas9-mediated depletion of Myo9aa/ab affect chorion movements.

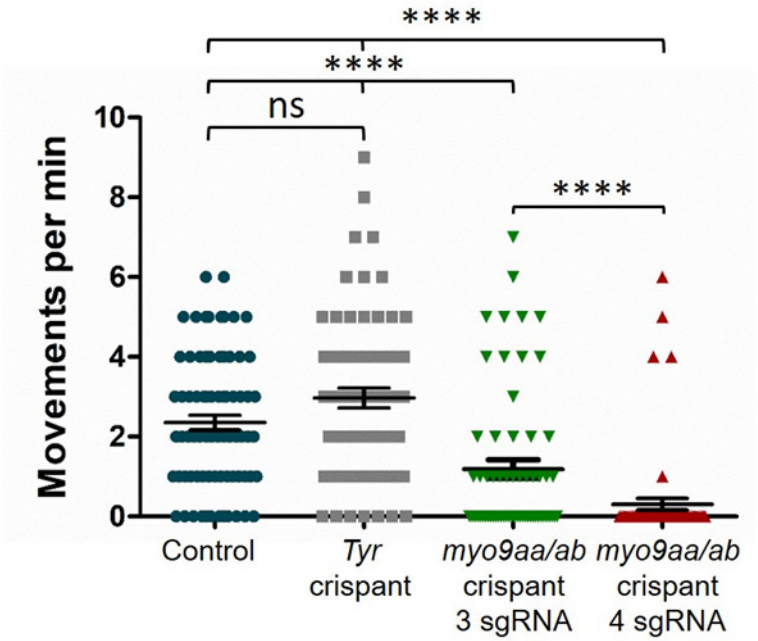

Figure 4.6. Movements performed by zebrafish within the chorion at 24 hpf. Full chorion movements performed in one minute by uninjected (control, n=77), 3 *myo9aa/ab* sgRNA (n=63) and 4 *myo9aa/ab s*gRNA (n=65) injected zebrafish. Tyrosinase (*tyr*) crispant injected control also included (n=68). KD = knockdown, error bars = mean ± S.E.M. ****p<0.0001, ns = not significant, Mann Whitney test.

4.4.2 Tactile stimulation

In the hours that follow the initial outgrowth of secondary motorneurons, the fish gain the ability to perform a touch-evoked swimming response in reaction to contact with a fine pipette tip on the back of the head, referred to here as the tactile stimulation assay (Saint-Amant and Drapeau, 1998, Kimmel et al., 1974). The evoked movement is an escape response which causes a characteristic c-bend movement performed by

the zebrafish, followed by a fast swim away from the stimulus (Saint-Amant and Drapeau, 1998). Initially in my MSci project this was analysed by simple observation of responses (O'Connor et al., 2016), however, the movements performed can be quantitatively analysed using ImageJ software with a TrackMate plugin as described in our recent manuscript (O'Connor et al., 2018a). Therefore, the tactile stimulation assay was performed in the Myo9aa/ab MO zebrafish and the distance travelled, average speed of swimming and initial acceleration were quantified (Figure 4.7).

Myo9aa/ab MO zebrafish moved on average 15.5mm, which was significantly less than controls which travelled 34.6mm after stimulation ($p=0.0001$, Mann Whitney test, Figure 4.7A). Similarly, the controls were able to swim over twice as fast as the Myo9aa/ab MO fish, with an average speed of 19mm/s as opposed to 6.8mm/s, respectively ($p<0.0001$, Mann Whitney test, Figure 4.7B). Initial acceleration, indicative of force of muscle contraction, was also reduced in zebrafish depleted for Myo9aa/ab as compared to controls with averages of 2.9mm/s^2 and 8.1mm/s^2, respectively ($p<0.0001$, Mann Whitney test, Figure 4.7C).

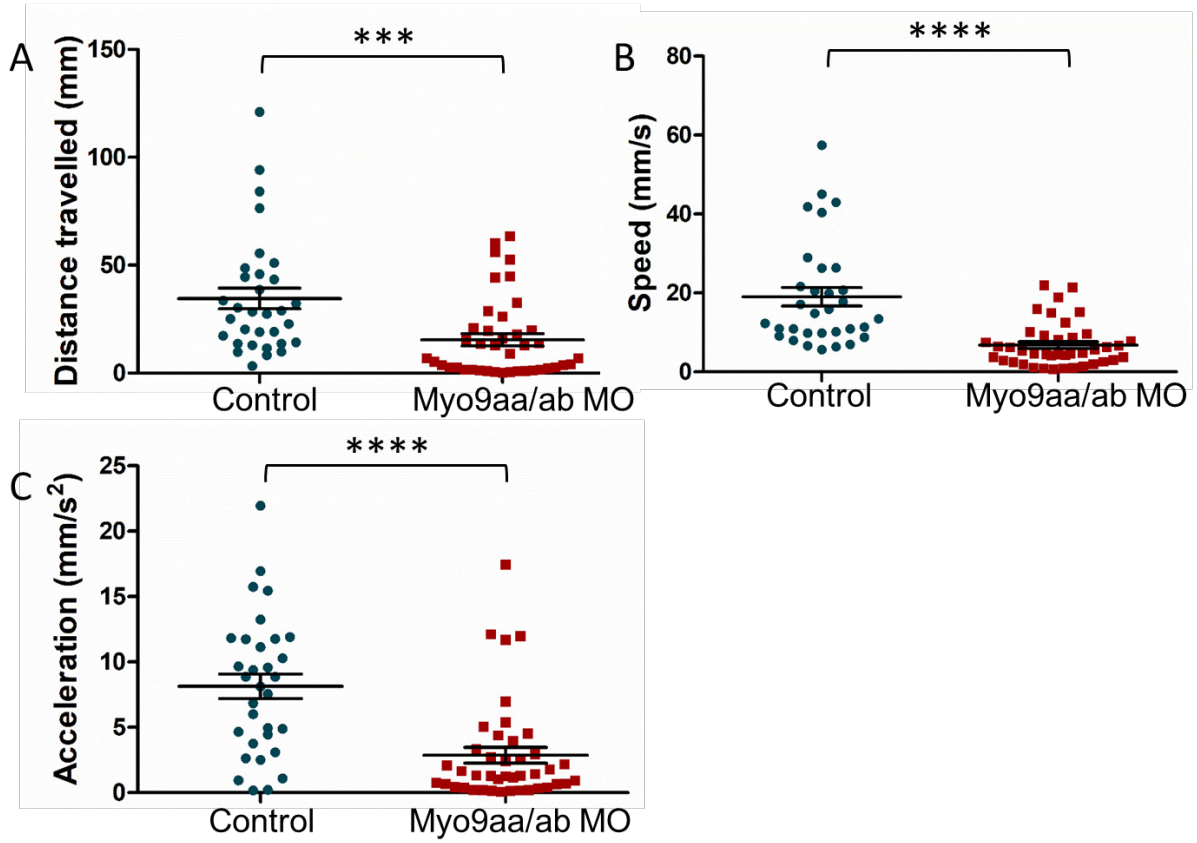

Figure 4.7. Tactile stimulation response of MO-mediated Myo9aa/ab knockdown zebrafish. Uninjected and Myo9aa/ab morphant zebrafish were subject to a tactile stimulation assay at 48 hpf. Distance travelled (A), average speed (B) and initial acceleration (C) of each fish was quantified. Error bars = mean ± S.E.M, control n=32, Myo9aa/ab morphant n=41. ***p≤0.001, ****p<0.0001, Mann Whitney test. MO = morpholino.

This experiment was also performed using CRISPR/Cas9-mediated KD for two main reasons. Firstly, to determine whether CRISPR/Cas9 depletion of Myo9aa/ab produced a similar effect on movement as MO-mediated reduction, and secondly to assist in selecting an effective sgRNA combination for NMJ morphology assessments (Figure 4.8).

There were no significant differences between control (uninjected) and control (*tyr* sgRNA) zebrafish for distance, speed or acceleration (p=0.619, p=0.102, p=0.380 respectively, Mann Whitney test). MYO9A KD 3 sgRNA injected zebrafish travelled significantly less distance than uninjected and *tyr* controls (p=0.011, p=0.093 respectively, Mann Whitney test). They also swam significantly slower than *tyr* controls (p=0.011, Mann Whitney test), but not uninjected controls (p=0.163, Mann Whitney test). Initial acceleration was similarly reduced in comparison to *tyr* controls but not uninjected zebrafish (p=0.201, p=0.100 respectively, Mann Whitney test). The movement response was more severely affected in 4 sgRNA injected zebrafish when

compared to uninjected and *tyr* injected controls, with significant decreases in distance travelled ($p<0.0001$, $p=0.0001$ respectively, Mann Whitney test), speed of movement ($p<0.0001$, Mann Whitney test) and initial acceleration ($p=0.005$, $p=0.002$ respectively, Mann Whitney test).

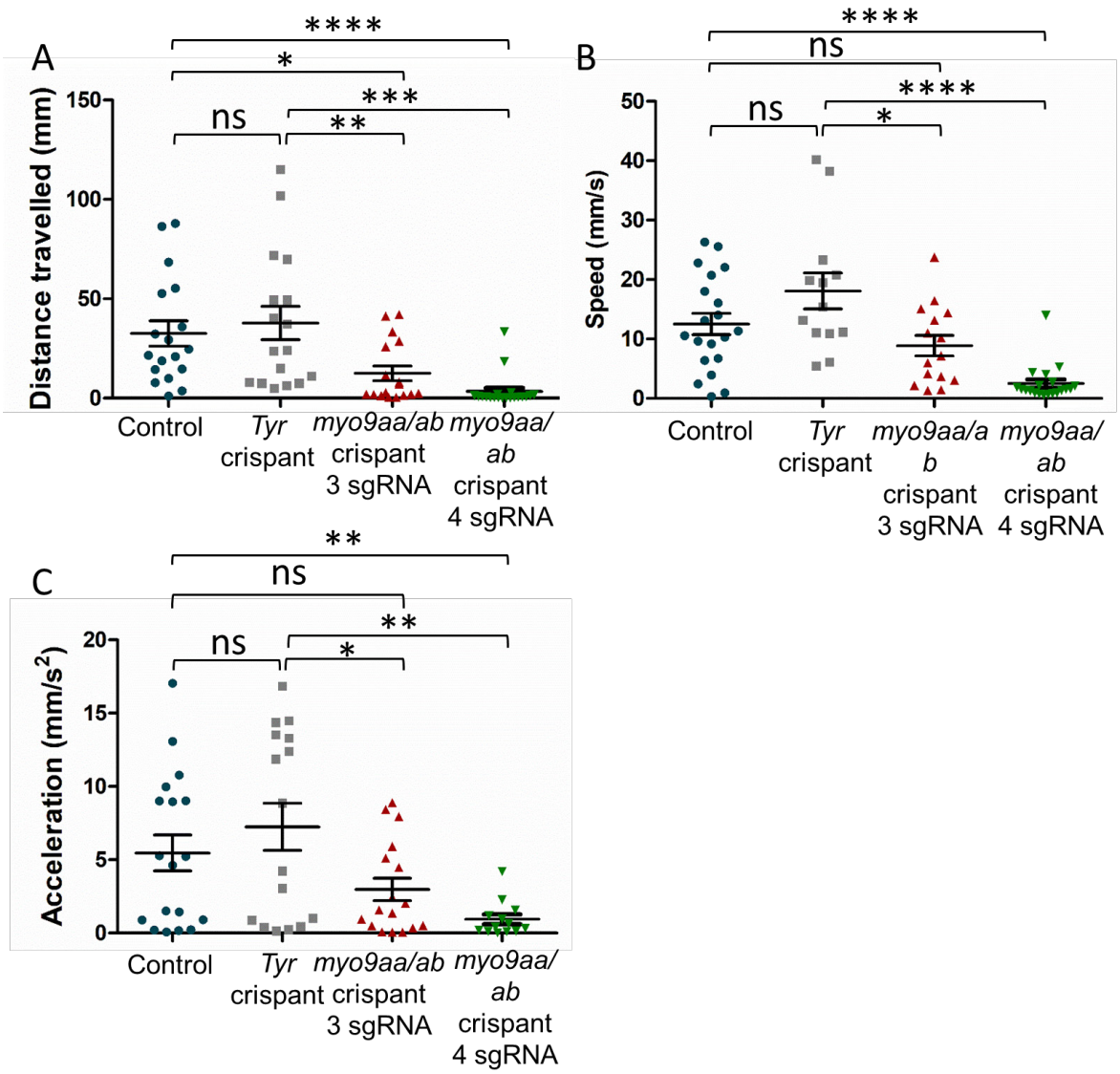

Figure 4.8. Tactile stimulation response of CRISPR/Cas9-mediated *myo9aa/ab* knockdown zebrafish. Uninjected, Tyrosinase (*tyr*) sgRNA injected controls, 3 *myo9aa/ab* sgRNA targeted and 4 *myo9aa/ab* sgRNA targeted fish were subject to a tactile stimulation assay at 48 hpf. The distance travelled (control n=13, *tyr* sgRNA n=15, 3 sgRNA n=17, 4 sgRNA n=20), average speed of movement (control n=18, *tyr* sgRNA n=12, 3 sgRNA n=15, 4 sgRNA n=20) and initial acceleration (control n=13, *tyr* sgRNA n=15, 3 sgRNA n=17, 4 sgRNA n=19) were quantified for each fish. Error bars = mean ± S.E.M. ns = not significant, *p≤0.05, **p≤0.01, ***p≤0.001, ****p<0.0001, Unpaired t-test.

Results obtained from the MO and CRISPR/Cas9-mediated Myo9aa/ab depletion experiments were more similar for the 3 rather than 4 sgRNA-injected fish. Distance travelled in MO fish was 15.5mm, compared to 12.5mm and 3.4mm performed by 3

and 4 sgRNA injected fish, respectively. Speed of swimming responses was 6.8mm/s in MO fish and 8.9mm/s in 3 sgRNA-injected fish, as opposed to just 2.5 mm/s in 4 sgRNA-injected fish. Finally, acceleration was only 0.9mm/s^2 for 4 sgRNA-injected fish, whereas 3 sgRNA and MO-injected fish produced values of 3mm/s^2 and 2.9mm/s^2 respectively. Overall, both methods of depleting *myo9aa/ab* expression affected motor behaviours at 24 and 48 hpf, and as 4 sgRNA-injected fish had a more pronounced phenotype these were used for subsequent NMJ morphology experiments.

4.5 Neuromuscular junctions and muscle fibres in zebrafish models

Earlier analysis of NMJ morphology in 48 hpf Myo9aa/ab morphant zebrafish revealed defects in neuron outgrowth and branching, however, these results were not quantified (O'Connor et al., 2016). Based on these initial findings, and due to the observation that motor behaviours during development are affected by MYO9A orthologue deficiency, a quantitative approach to assessing NMJ morphology was used. Furthermore, as defects in movement could be due to involvement of cranial motor neurons or muscle architecture, these features were also assessed in the *myo9aa/ab* crispant zebrafish, however, no clear gross morphological differences had been identified in the morphant fish. As results in the previous section demonstrated a greater phenotypic severity in 4 sgRNA-injected zebrafish, these were selected for use for the rest of the study and are referred to as '*myo9aa/ab* crispants'.

4.5.1 CNS and muscle gross morphology in zebrafish models

Tg(islet1:GFP) zebrafish express GFP under the control of the islet1 promoter, which drives expression of fluorescence in the cranial motor neurons (as well as the Rohon Beard sensory cells, Higashijima et al., 2000). Visualisation of cranial motor neurons in control and *myo9aa/ab* crispants revealed no gross differences between localisation or network of neurons (Figure 4.9).

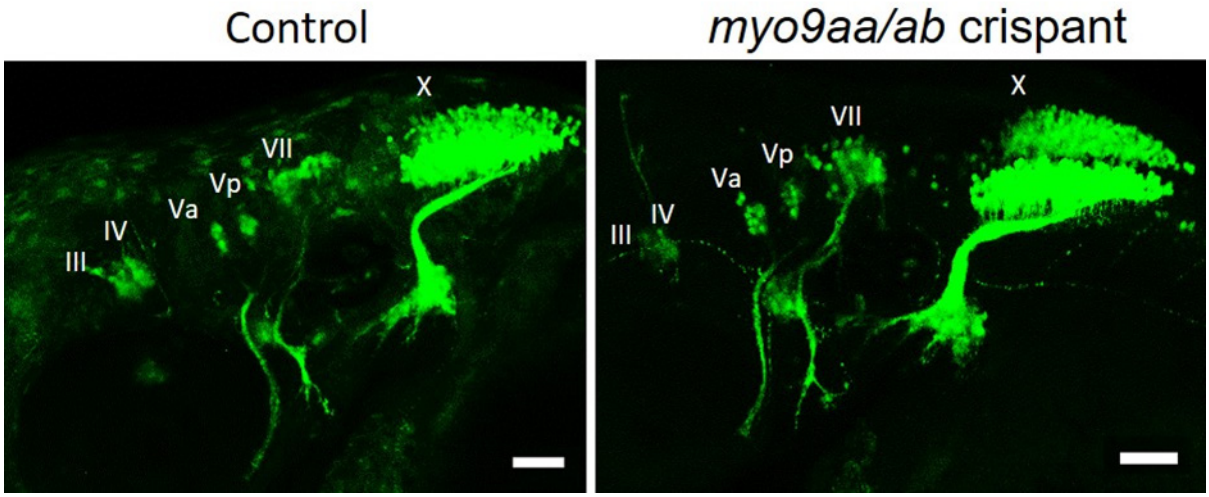

Figure 4.9. Cranial motor neurons in zebrafish. For visualisation of cranial motor neurons, 48 hpf zebrafish expressing GFP under the Islet-1 promoter were analysed. Cranial nerves III, IV, Va, Vp, VII and X are labelled. Scale bar = 50μm, 15 zebrafish screened.

Muscle fibres of 48 hpf fish were stained with fluorophore-conjugated phalloidin which binds to f-actin. In control muscle, somites are clearly delineated with horizontal and vertical myosepta, muscle fibres are organised in the appropriate orientation and no fibres cross over to alternate sides (Figure 4.10). *Myo9aa/ab* crispants have similarly well-structured somites, however, in some cases muscle fibres could be observed crossing the midline.

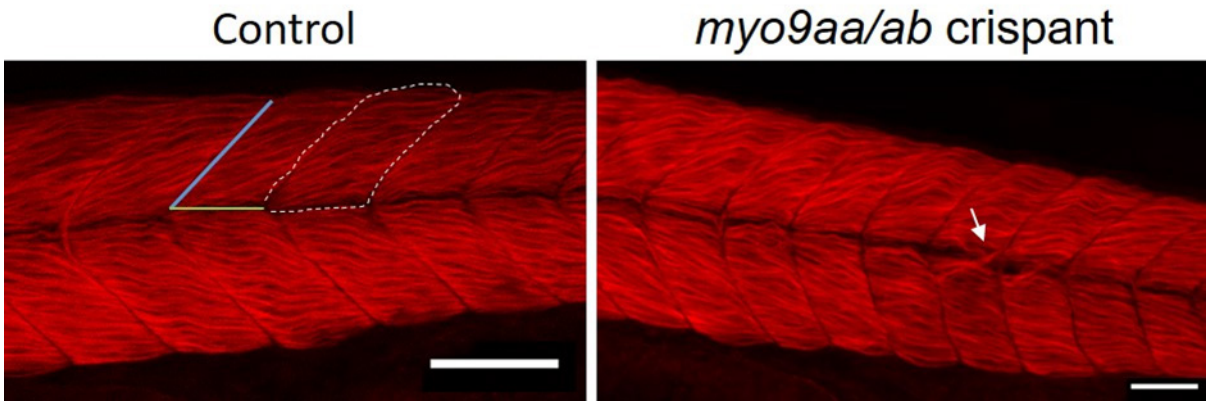

Figure 4.10. Muscle fibre morphology in *myo9aa/ab* crispants. Muscle fibres in control and *myo9aa/ab* crispant fish at 48 hpf were stained with fluorophore-conjugated phalloidin to detect f-actin. The blue line delineates the vertical myosepta, green line is the horizontal myosepta and the white dashed line outlines a myotome (two of which make up a somite). White arrow indicates a muscle fibre crossing over into alternative myotome. Scale bar = 50μm, 15 control and 15 crispant zebrafish were qualitatively assessed.

4.6 NMJ analysis at different time points

A comprehensive morphological characterisation protocol was applied to study the NMJs of *myo9aa/ab* crispant fish at different time points during development. Time

points selected encompass different stages of NMJ maturation: 24 hpf (initial outgrowth of primary motorneurons, synaptogenesis occurring and spontaneous movement), 48 hpf (second and higher order branches of primary motorneurons present, secondary motorneuron outgrowth, response to tactile stimulation) and 5 dpf (innervation territories and coverage representative of adult patterns, larvae behaviours obtained including escape response and spontaneous swimming, maximal swimming rates achieved).

At 24 hpf, zebrafish were fixed and stained with aBTx-conjugated with a fluorophore to detect AChRs and an antibody against SV2 for presynaptic motor neuron vesicles (Figure 4.11, Panzer et al., 2005). At this stage in development, zebrafish have a cluster of AChRs at the horizontal myoseptum and this represents a pathway 'choice point' for extending primary motor neurons. This is clearly visible in control zebrafish, but frequently absent in the *myo9aa/ab* crispants (Figure 4.11).

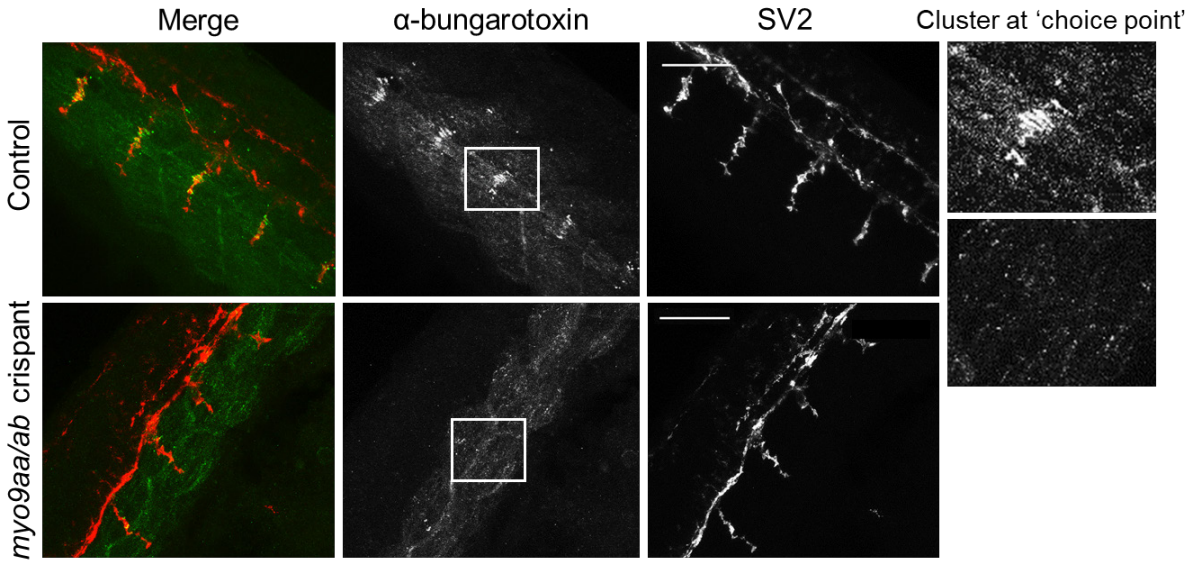

Figure 4.11. NMJ morphology of *myo9aa/ab* crispant zebrafish at 24 hpf. Representative images of NMJs in control and *myo9aa/ab* crispant zebrafish at 24 hpf. Acetylcholine receptors stained with aBTx (green), and motor neurons detected with an antibody against SV2 (red). White boxes demark areas enlarged in the right-hand panel. Scale bar = 50μm.

Various features of NMJs in early development were quantified as shown in Figure 4.12. Measurement of the average area of the AChR clusters revealed a significant decrease in size for *myo9aa/ab* crispants as compared to controls (p= 0.0261, Unpaired t-test). There was no significant change in number of AChR clusters larger than 20μm^2 at this time point, or in the total area of clusters (p=0.3264, p=0.1286 respectively, Unpaired t-test). Proportion of myotomes with a choice point cluster was

significantly decreased in crispants as compared to controls, with almost 100% of controls exhibiting clusters as opposed to only 30% of crispants (p=0.0027, Unpaired t-test). The distance that neurons had extended past the choice point was also measured, revealing that motor neurons in crispants had travelled significantly less than controls, at 17μm and 43μm respectively (p=0.0157, Unpaired t-test). However, overall length of neuron outgrowths was not affected (p=0.3244, Unpaired t-test). Size of myotomes was significantly reduced from 5829μm^2 in controls to 1890μm^2 in crispants (p=0.0013, Unpaired t-test). Overall, both pre and postsynaptic NMJ features are affected in 24 hpf *myo9aa/ab* crispant fish as compared to controls.

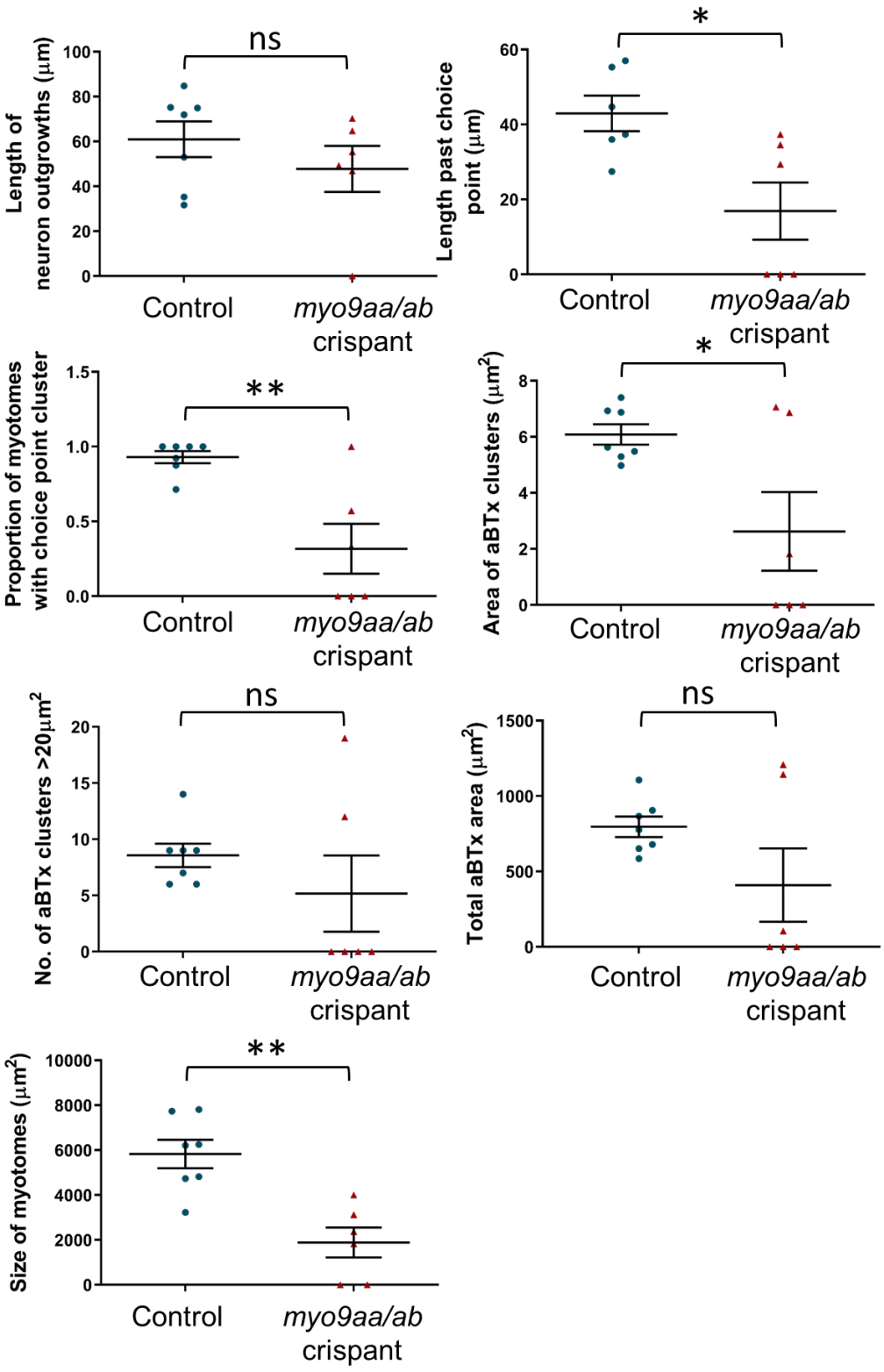

Figure 4.12. Quantification of NMJ morphology in *myo9aa/ab* crispant zebrafish at 24 hpf. Various features of NMJ morphology in control (n=7) and *myo9aa/ab* crispants (n=6) were quantified: average and total area of acetylcholine receptor (aBTx) clusters and number over 20μm^2, size of muscle myotomes, proportion of myotomes with a choice point cluster, number of neurons per myotome and the total

length these neurons had extended, as well as length past the choice point. Error bars = mean ± S.E.M. **p≤0.01, *p≤0.05, ns = not significant, Unpaired t-test.

By 48 hpf motor neurons have extended down the middle of the myotome and started to innervate the vertical myoseptal region. The AChR choice point cluster has dispersed and the majority of prepatterned receptors have been contacted by extending motor axons. An example of a neuron that has not extended as far along the vertical myoseptal in the crispant fish as in the controls is shown in Figure 4.13, along with the presence of uninnervated AChRs.

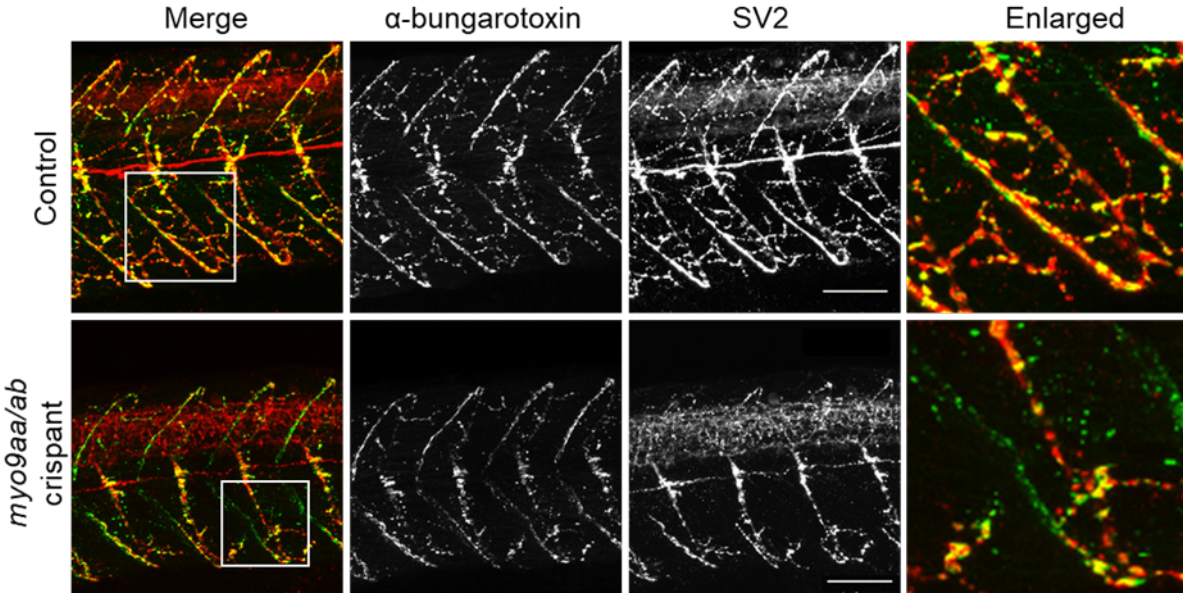

Figure 4.13. NMJ morphology of *myo9aa/ab* crispant zebrafish at 48 hpf. Representative images of NMJs in control and *myo9aa/ab* crispant zebrafish at 48 hpf. Acetylcholine receptors stained with aBTx (green), and motor neurons detected with an antibody against SV2 (red). White boxes demark areas enlarged in the bottom panel. Scale bars = 50μm

A number of presynaptic features were quantified in 48 hpf fish (Figure 4.14), including the number of SV2 clusters per myotome and per 100μm^2. Both measurements revealed significantly less SV2 clusters in crispants as compared to controls (p=0.0031, p=0.0200 respectively, Unpaired t-test). There was no significant difference in the number of SV2 clusters over 20μm^2 in size between controls and crispants (p=0.2193, Unpaired t-test), despite an increase in the average cluster size (p=0.0011, Unpaired t-test). Total cluster area was significantly reduced in crispant fish as opposed to controls (p<0.0001, Unpaired t-test). During development AChRs cluster along the vertical myosepta in preparation for innervation from extending primary motor axons. Therefore, the length of the vertical myosepta in which AChR clusters were present (detected by aBTx fluorescence) was measured, and compared to the distance that the motor axon had extended to give rise to %

innervation. This demonstrated a significant decrease in myoseptal innervation from 80% in controls to 65% in crispants (p=0.0428, Unpaired t-test).

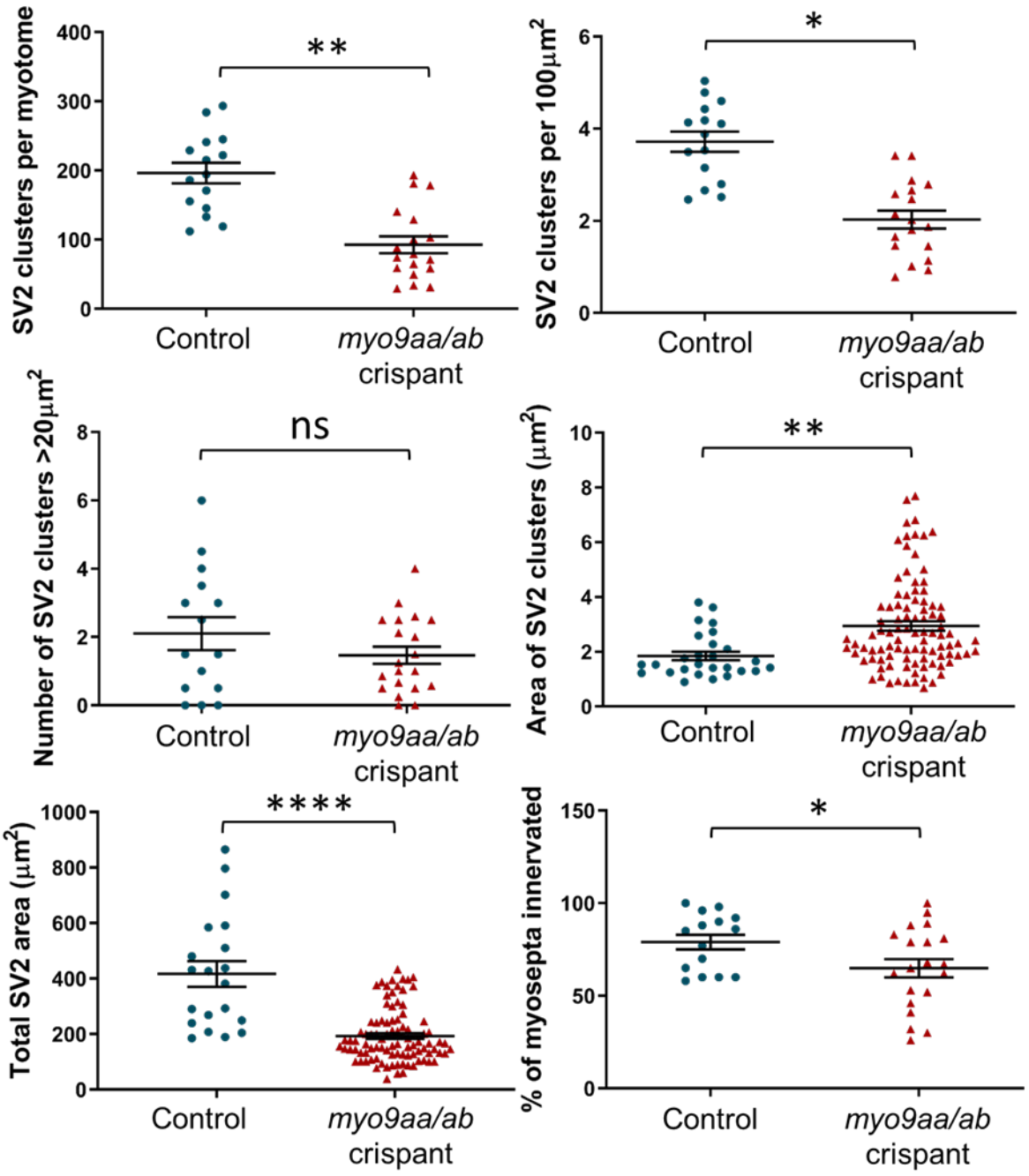

Figure 4.14. Quantification of presynaptic NMJ morphology in *myo9aa/ab* crispant zebrafish at 48 hpf. Various features of NMJ morphology in control (n=15) and *myo9aa/ab* crispant (n=20) were quantified: SV2 clusters per myotome, per 100µm^2 and over 20µm^2 and % innervation of myosepta, as well as average SV2 cluster area and total area. Error bars = mean ± S.E.M. *p≤0.05, **p≤0.01, ****p<0.0001, ns = not significant, Unpaired t-test.

Postsynaptic features of the NMJ were also assessed at 48 hpf, revealing a significant decrease in the number of AChR clusters per myotome and per 100µm^2 (p<0.0001, Unpaired t-test, Figure 4.15). There was no significant difference in the

number of AChR clusters over 20μm^2 in size between controls and crispants ($p=0.0584$, Unpaired t-test), despite an increase in average cluster area in crispants ($p=0.0006$, Unpaired t-test). Total cluster area was significantly decreased in crispants as compared to controls ($p<0.0001$, Unpaired t-test). As opposed to results at 24 hpf, the size of myotomes were no longer significantly smaller in *myo9aa/ab* crispant fish as compared to controls ($p=0.0762$, Unpaired t-test). Overall, the number of pre and postsynaptic clusters were affected in crispant fish, as well as length of motor neuronal innervation of the myosepta, supporting qualitative results obtained previously in Myo9aa/ab morphant fish (O'Connor et al., 2016).

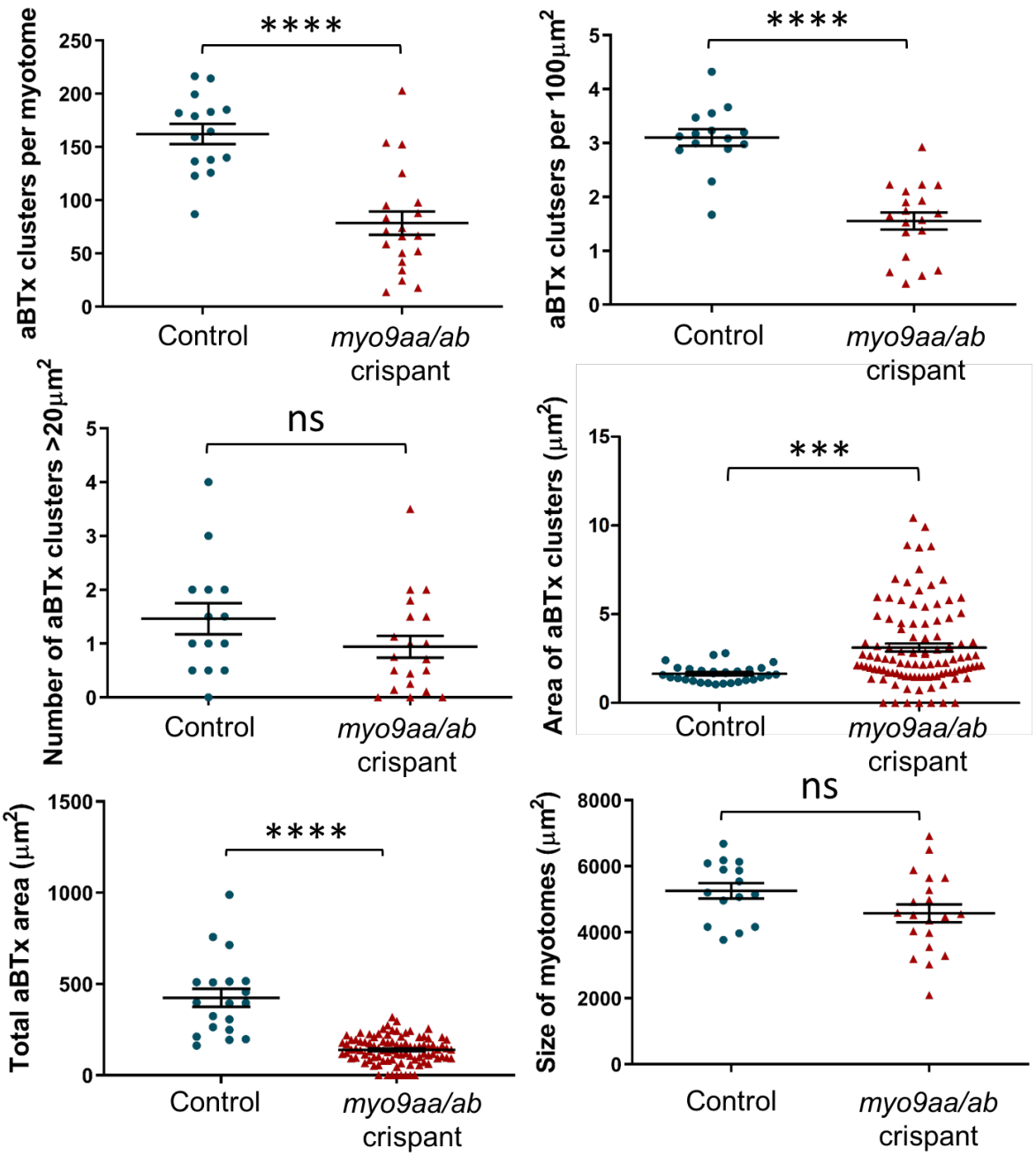

Figure 4.15. Quantification of postsynaptic NMJ morphology in myo9aa/ab crispant zebrafish at 48 hpf. Various features of NMJ morphology in control (n=15) and *myo9aa/ab* crispant (n=20) were quantified: AChR (aBTx) clusters per myotome, per 100µm^2 and over 20µm^2 as well as size of myotomes, average aBTx cluster area and total cluster area. Error bars = mean ± S.E.M. ***p≤0.001, ****p<0.0001, ns = not significant, Unpaired t-test.

In zebrafish at 5 dpf, myotomes have a dense innervation from primary and secondary motor neurons which are in contact with AChRs. In *myo9aa/ab* crispant zebrafish there are examples of sparsely innervated myotomes as shown in Figure 4.16, where branching is less complex than in controls.

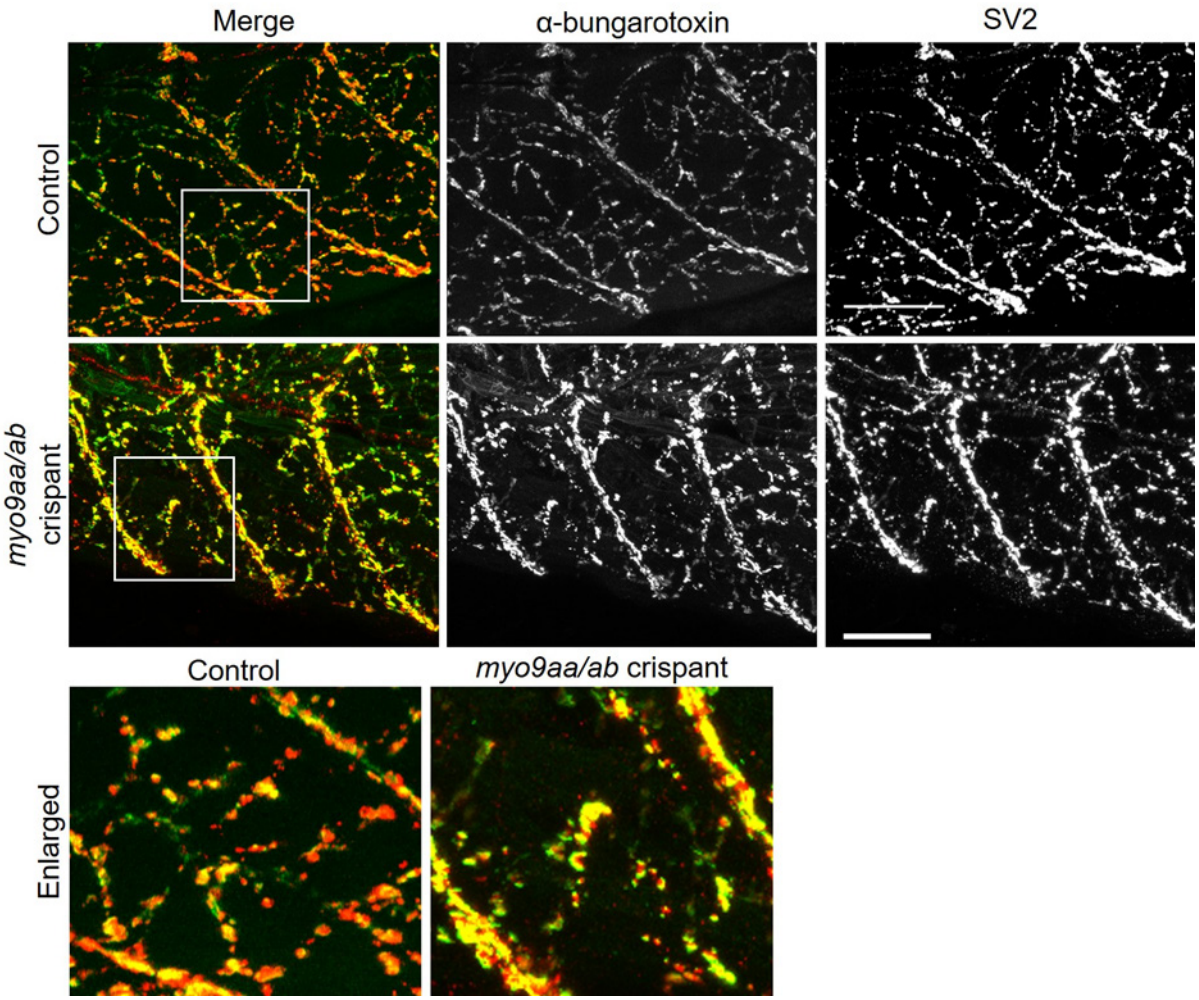

Figure 4.16. NMJ morphology of *myo9aa/ab* crispant zebrafish at 5 dpf. Representative images of NMJs in control and *myo9aa/ab* crispant zebrafish at 5 dpf. Acetylcholine receptors stained with aBTx (green), and motor neurons detected with an antibody against SV2 (red). Scale bars = 50μm.

A number of parameters quantified at 24 and 48 hpf were also measured at 5dpf (Figure 4.17). There was no significant difference in the number of presynaptic clusters per myotome in crispants, however number per 100μm^2 was significantly increased in crispants as compared to controls (p=0.6482, p=0.0095 respectively, Unpaired t-test). The number of SV2-positive clusters over 20μm^2 was not significantly affected, and neither was the average area of clusters (p=0.1995, p=0.1306 respectively, Unpaired t-test). However, there was a decrease in total SV2 cluster area in crispant fish, reflected in the reduced myotomal staining in Figure 4.16 (p=0.0465, Unpaired t-test). The percentage of myoseptal innervation is not significantly affected by depletion of Myo9aa/ab at this time point (p=0.1961, Unpaired t-test).

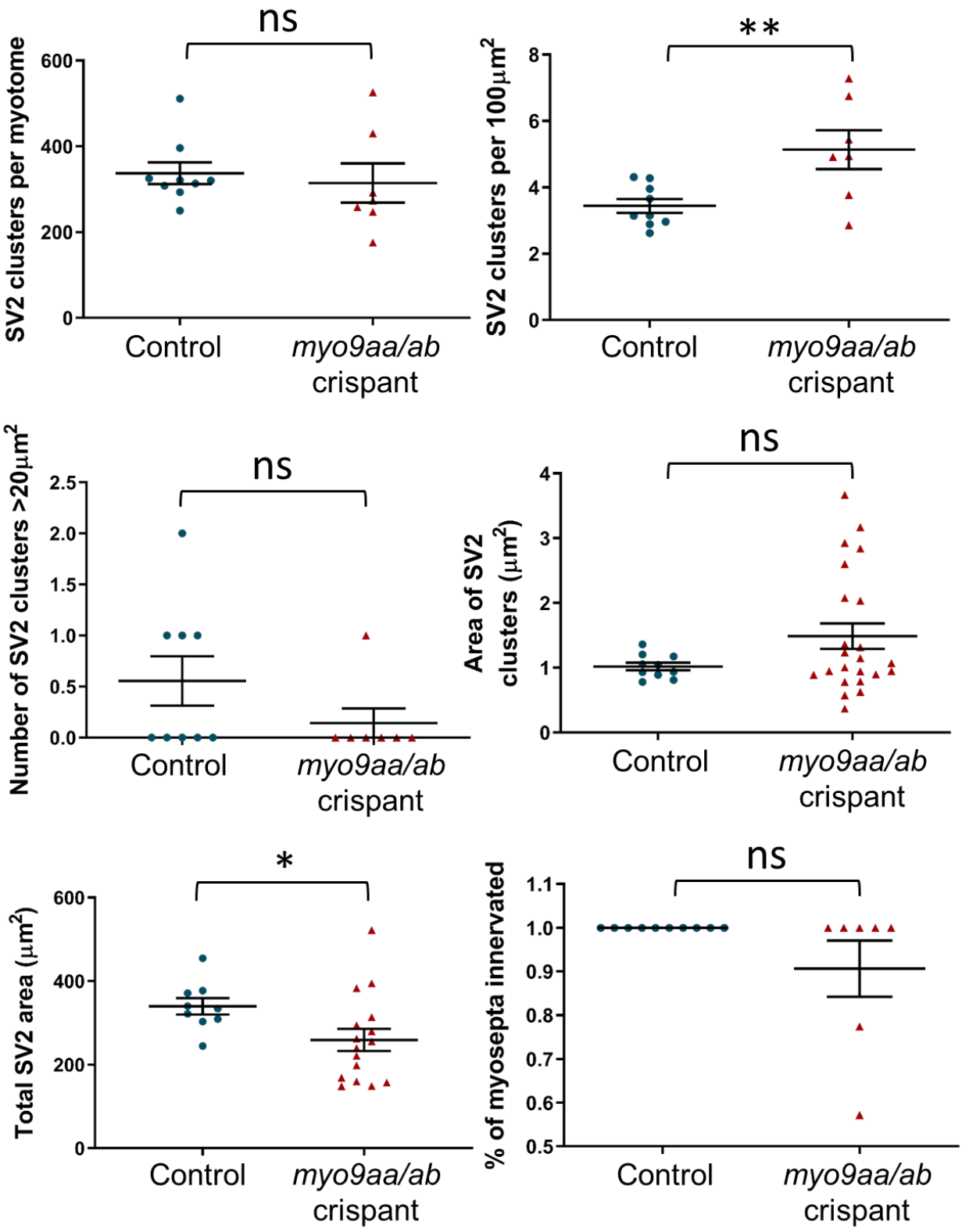

Figure 4.17. Quantification of presynaptic NMJ morphology in *myo9aa/ab* crispant zebrafish at 5 dpf. Various features of presynaptic NMJ morphology in control (n=9) and *myo9aa/ab* crispant (n=7) were quantified: average and total area of SV2-positive clusters, clusters per myotome, per 100µm^2 and over 20µm^2, as well as % myoseptal innervation. Error bars = mean ± S.E.M. **p≤0.01, ns = not significant, Unpaired t-test.

Postsynaptic features of 5dpf zebrafish NMJs were also quantified, and as with presynaptic clusters, there was no significant decrease in the number of AChR clusters per myotome in crispant fish as compared to controls at this time point ($p=0.0862$, Unpaired t-test). Similarly, there was also a significant increase in number of clusters per 100μm^2 in crispant fish, as found with SV2 clusters ($p=0.0424$, Unpaired t-test). The number of large clusters (>20μm^2), as well as total and average area of AChR clusters however, were all significantly reduced in crispant fish as opposed to controls ($p=0.0497$, $p=0.0002$, $p=0.0360$ respectively, Unpaired t-test). As observed at 24 hpf, the size of myotomes in crispant fish were significantly smaller than controls ($p=0.0004$, Unpaired t-test). Overall, there is a general improvement in presynaptic features measured by 5 dpf, except for the total area of SV2 clusters which is decreased and the number of SV2-positive clusters per 100μm^2 which is elevated in crispant fish and reflected also in the increased number of aBTx clusters. Conversely, postsynaptic AChR clusters are more affected at this time point, with area and number of large clusters reduced in crispants, along with the presence of smaller somites.

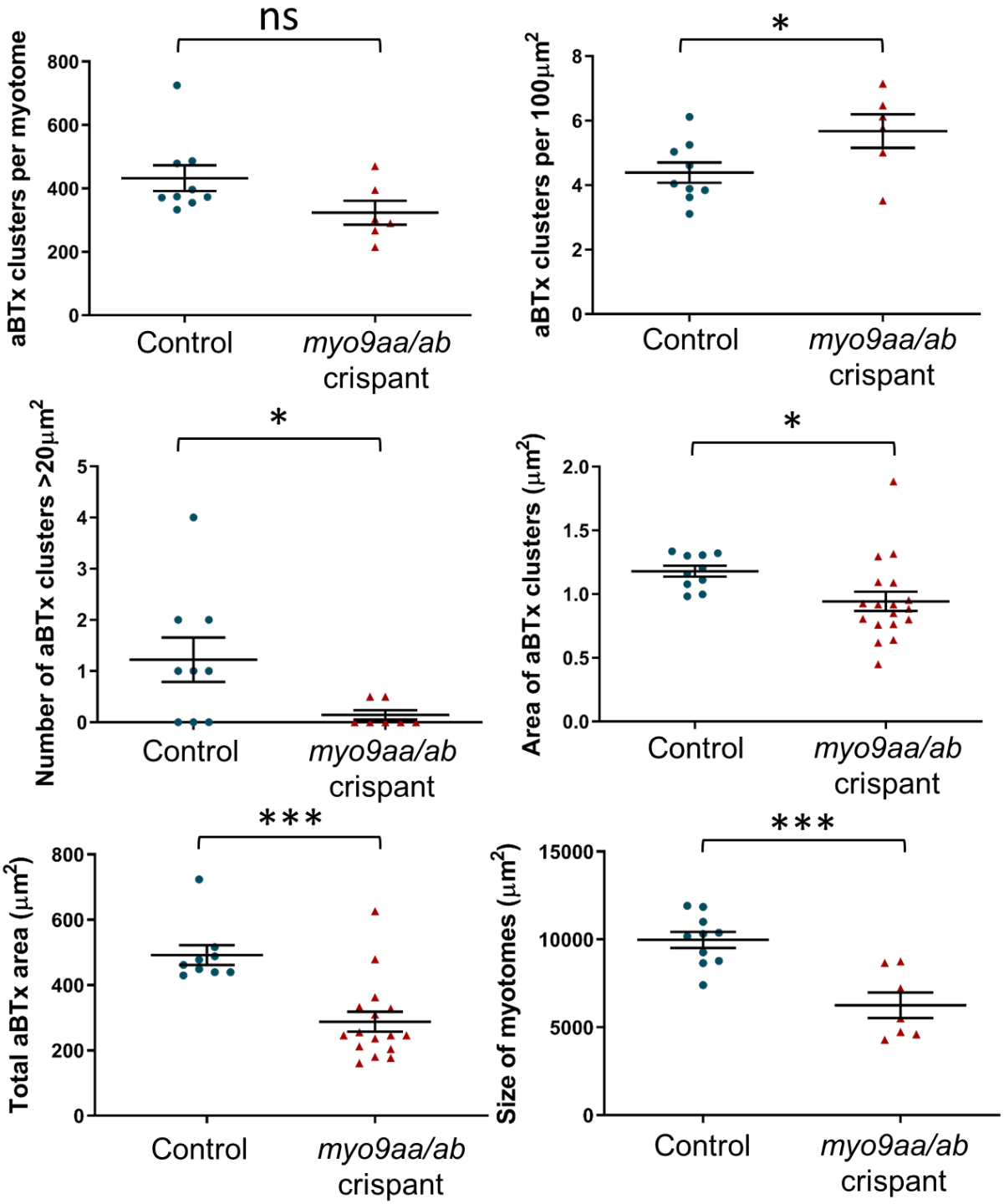

Figure 4.18. Quantification of postsynaptic NMJ morphology in *myo9aa/ab* crispant zebrafish at 5 dpf. Various features of NMJ morphology in control (n=9) and *myo9aa/ab* crispant (n=7) were quantified: Acetylcholine receptor (aBTx) clusters per myotome, per 100µm^2 and over 20µm^2 as well as size of myotomes, average and total area of aBTx clusters. Error bars = mean ± S.E.M. *≤0.05, ***p≤0.001, ns = not significant, Unpaired t-test

AChE is expressed in the CNS, muscle, primary motor and sensory neurons throughout the zebrafish embryo, first appearing around 12 hpf (Bertrand et al., 2001, Behra et al., 2002). Activity of AChE is important as it acts to stop the action of ACh

on AChRs in the synaptic cleft, and in zebrafish the levels of this enzyme have been found to correlate with developmental stage (Koenig et al., 2016). Therefore, this is a useful assay to help address whether the behavioural alterations and NMJ morphology differences are linked to developmental delay/less neuronal and muscle tissue in the crispant fish. AChE activity was calculated using the isolated tails of embryos during the first 5 days of development, to remove the impact of brain AChE from results (Figure 4.19). Expression of AChE is very low at 1 dpf, however, significantly less activity was detected in the *myo9aa/ab* crispants than in controls ($p=0.012$, Mann Whitney test). Activity was also significantly lower at 2 dpf and 5 dpf in crispant fish as compared to controls ($p=0.012$, $p<0.0001$ respectively, Mann Whitney test). There were no significant differences between detected activity at 3 and 4 dpf ($p=0.730$ for both, Mann Whitney test). This suggests that crispant fish have less AChE activity 1,2 and 5 dpf than their control counterparts, and that this could be due to developmental delay, a reduction in neural/muscle tissue or impaired AChE activity.

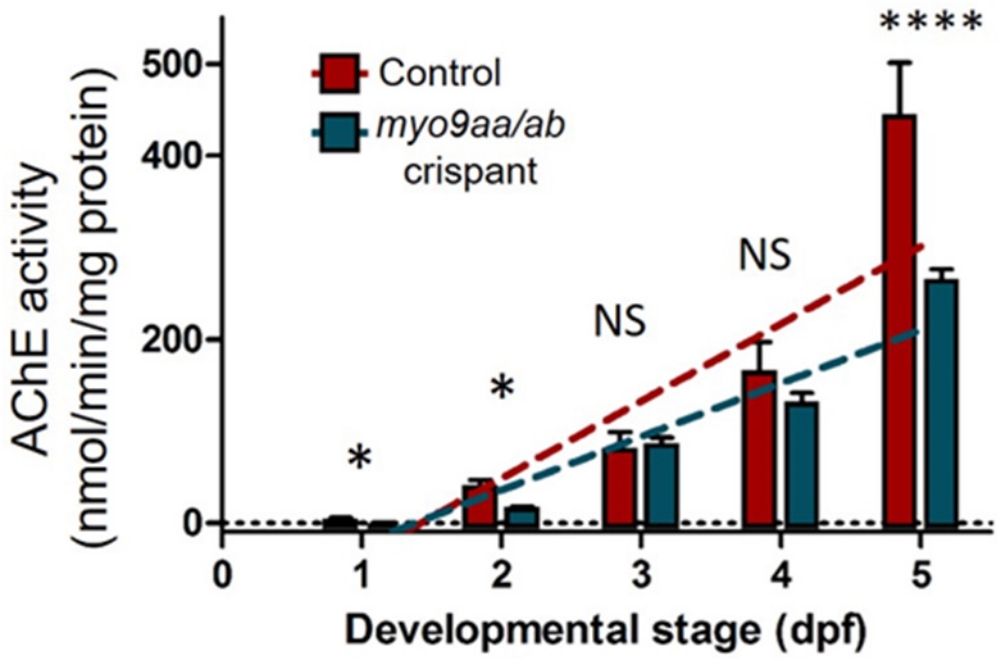

Figure 4.19. AChE activity in tails of *myo9aa/ab* crispant zebrafish during development. Activity of AChE quantified at day 1 – 5 post fertilisation in control and myo9aa/ab crispant fish tails. 10 fish tails pooled per reaction, 5 reactions performed for 1dpf, 2dpf, control 3dpf, myo9aa/ab crispant 4 dpf, 4 reactions for myo9aa/ab crispant 3 dpf, control 4 dpf and 2 reactions for 5 dpf. *p≤0.05, ****p<0.0001, ns = not significant, Mann Whitney test. Error bars = mean + S.E.M. Dpf = days post fertilization

4.6.1 Morphology of MYO9A KO mouse neuromuscular junctions and muscle fibres

The MYO9A KO mouse has not previously been assessed for defects of the NMJ either through behavioural, histological, immunofluorescent or physiological techniques. Therefore, to complement the work performed *in vitro* in a mouse-derived motor neuron cell-line (O'Connor et al., 2016) and patient iNPCs, and *in vivo* in the zebrafish, analysis of NMJ and muscle architecture was performed in the mouse.

4.6.2 Histological assessment of muscle

Muscle from patients was not obtainable and thus the patient muscle phenotype is unknown. As some small, infrequent alterations to muscle fibre organization was observed in the zebrafish, features of muscle in the MYO9A KO mouse were visualized with haematoxylin and eosin staining.

Quadriceps, gastrocnemius and tibialis anterior muscles from MYO9A KO and wildtype mice were analysed and representative images are shown in Figure 4.20. There was no identified fatty infiltration of muscle or fibrosis, neither was there a significant increase in the proportion of rounded muscle fibres (Quadriceps p=0.100, gastrocnemius p=0.229 and tibialis anterior p=0.800, Mann Whitney test). Percentage of fibres (300 per animal per muscle) that had internal nuclei was also quantified. In quadriceps only 1% of wildtype (n=3) muscle fibres had internal nuclei, whereas MYO9A KO had slightly more at 6% (n=3), however this was not significant (p=0.200, Mann Whitney test). In tibialis anterior and gastrocnemius muscles of wildtype animals, 1% had internal nuclei (n=1 tibialis anterior, n=2 gastrocnemius), this was slightly increased to 3% in both muscle types of MYO9A KO animals (n=2, not enough animals to perform statistics).

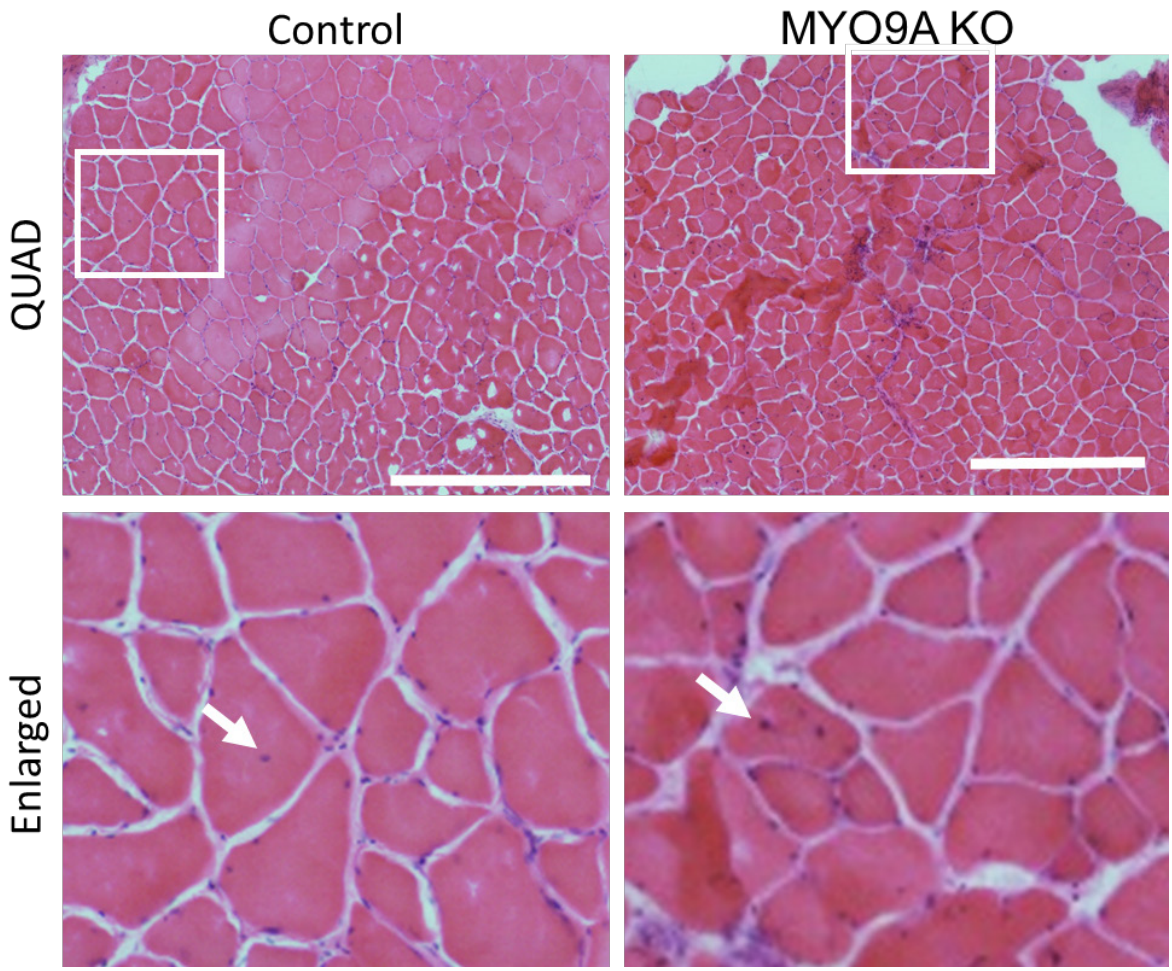

Figure 4.20. Histological features of MYO9A KO mouse muscle. Quadriceps muscle from control and MYO9A KO mouse stained with haematoxylin and eosin. Enlarged regions (white boxes) show presence of internal nuclei (white arrows) in control and MYO9A KO mice. KO = knockout, scale bar = 500μm.

The area of muscle fibres was also measured for comparison between wildtype and MYO9A KO mice. Results were pooled into wildtype and MYO9A KO for easier comparison (Figure 4.21A) and data for individual animals is also shown (Figure 4.21B). In tibialis anterior muscles, wildtype animals had an average fibre area of 3277 ± 1664μm^2 (± standard deviation) whereas mutant muscle had a significantly smaller average fibre area of 2308 ± 986μm^2 ($p<0.0001$, Mann Whitney test). Similarly, quadriceps muscle fibre area was also significantly reduced in MYO9A KO mice as compared to wildtype, from 3065 ± 1121μm^2 to 2579 ± 1312μm^2 ($p<0.0001$, Mann Whitney test). Muscle fibre area was also significantly reduced in gastrocnemius muscles of MYO9A KO mice, from 2428 ± 1172μm^2 in controls to 1721 ± 709μm^2 in MYO9A KOs ($p<0.0001$, Mann Whitney test). Therefore, data demonstrates that mice lacking MYO9A have smaller muscle fibres than wildtypes.

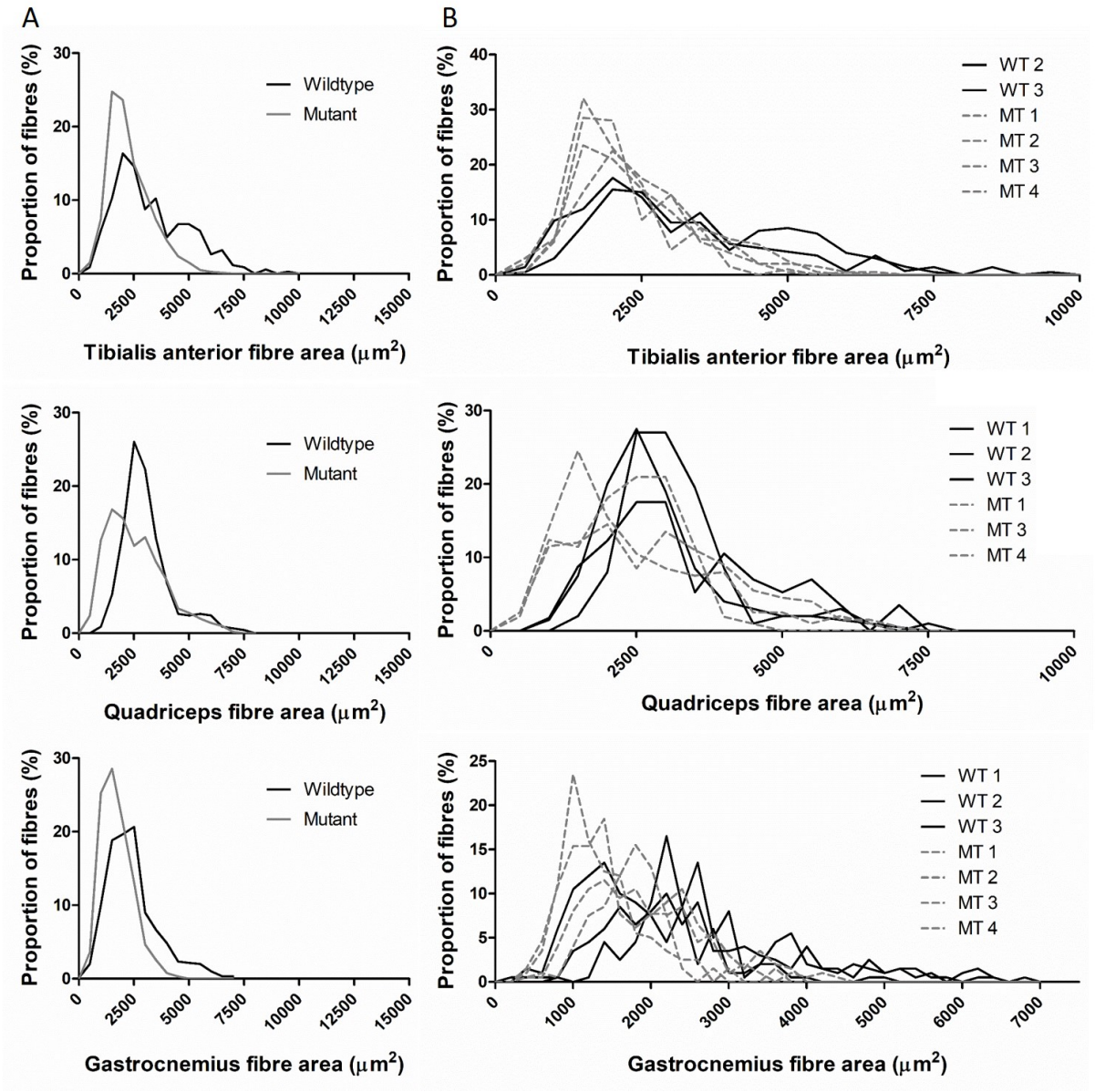

Figure 4.21. Muscle fibre area in wildtype and MYO9A KO mice. A. Frequency distributions of muscle fibre cross sectional area from pooled wildtype (black line) and MYO9A KO (mutant, grey line) mice. B. Muscle fibre area measurements split into individual wildtype (WT, black line) and MYO9A KO (MT, grey dashed line) animals for quadriceps (WT1,3, MT3,4 n=200, WT2 n=57, MT1 n=105 fibres), gastrocnemius (WT1,2,3MT1,3,4 n=200, MT2 n=65) and tibialis anterior (WT2, MT1,2,3,4 n=200, WT3 n=142) muscles. Graphs represent percentage of fibres within each size bin of 500μm^2.

4.6.3 Fibre typing of muscle

Muscle fibre type composition can give an insight as to whether muscles have appropriate proportions of each muscle fibre type, therefore muscles were stained with antibodies against type I, IIa, IIb and IIx MyHC for analysis (Figure 4.23).

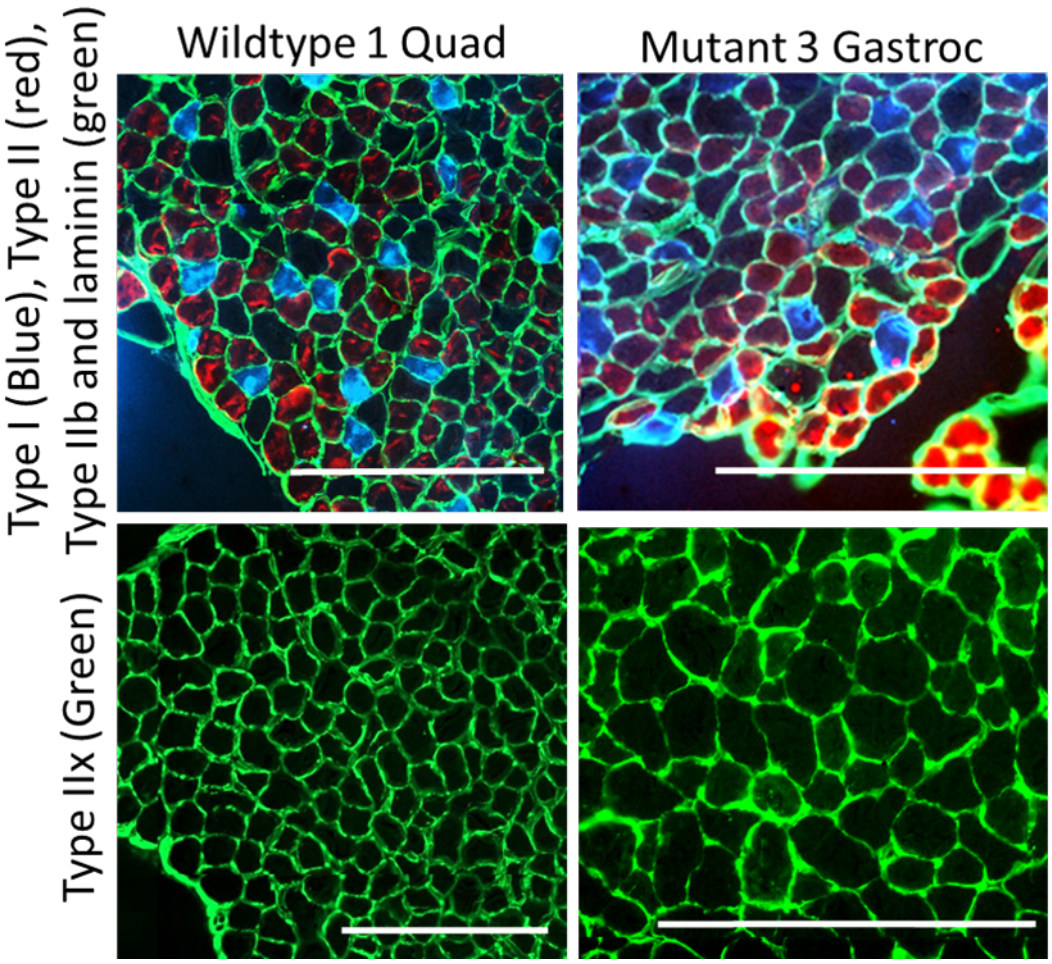

Figure 4.22. Fibre type analysis of wildtype and MYO9A KO mice.
Representative images of fibre type staining in wildtype (quadriceps) and MYO9A KO (gastrocnemius) mice. In the top panel fibres are labelled as follows: type I (blue), type II (red), type IIb (green) and laminin (green). In the bottom panel type IIx fibres and laminin are green. Scale bar = 500μm.

Muscle fibre type quantification was performed by manually categorising each muscle fibre, however, staining for Type IIb and Type IIx fibres was often hard to identify. Nevertheless, there were no significant differences observed for the proportion of muscle fibre types between wildtype and mutant animals ($p>0.05$, Mann Whitney test, Figure 4.24).

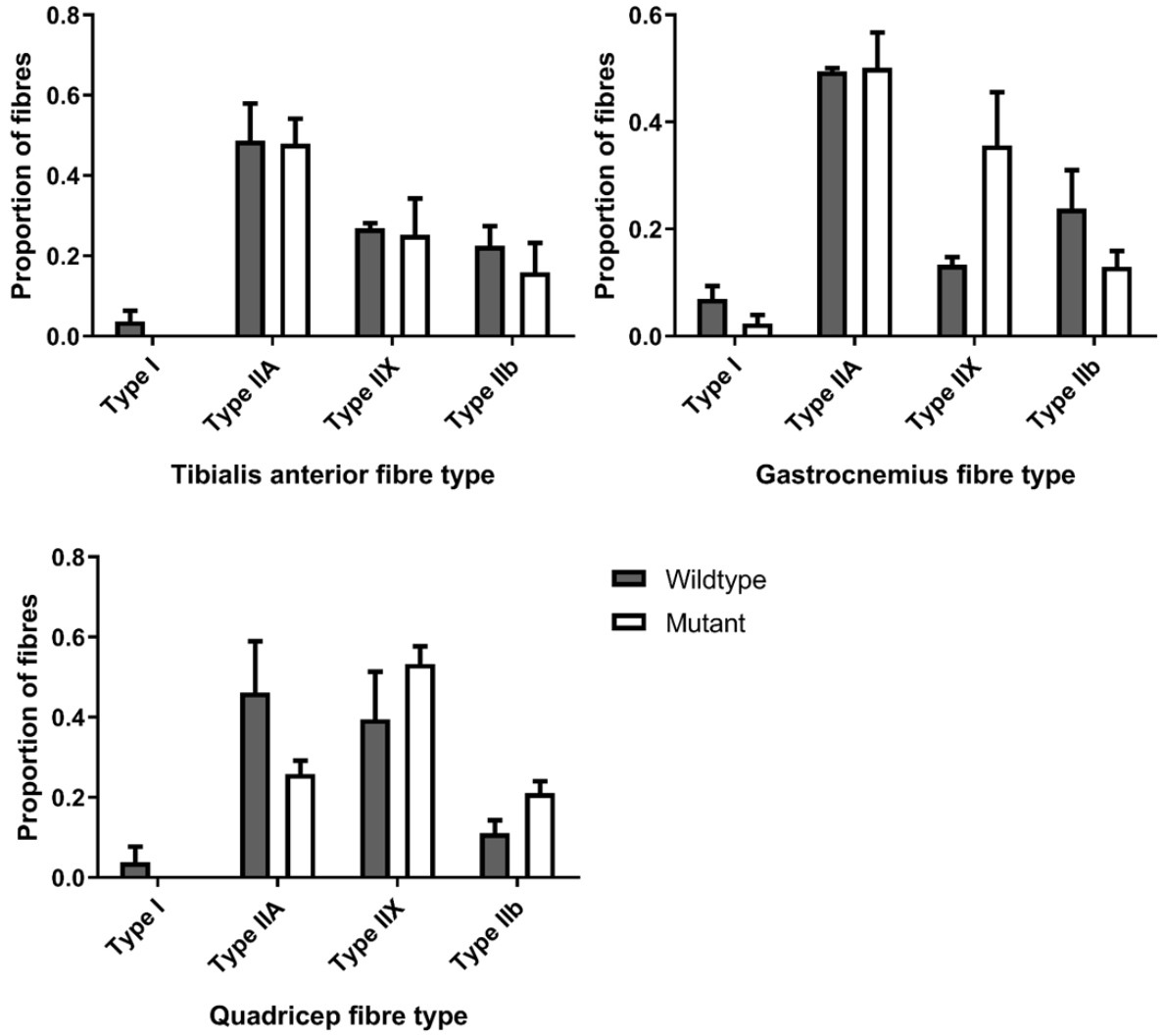

Figure 4.23. Fibre type composition in MYO9A KO mice. Fibre type analysis was performed manually on transverse sections of wildtype and MYO9A KO (mutant) gastrocnemius (wildtype n=3, mutant n=4), tibialis anterior (wildtype n=2, mutant n=4) and quadriceps (wildtype n=3, mutant n=3) muscles. None of the comparisons between wildtype and mutant animals were significant ($p>0.05$, Mann Whitney test). At least 300 fibres analysed per muscle per genotype, error bars = mean + S.E.M.

4.6.4 NMJ morphology

Numerous differences were detected in the analysis of zebrafish NMJs in the absence of MYO9A, therefore MYO9A KO mice were subject to a comprehensive investigation of NMJ morphology. Using the 'NMJmorph' protocol developed by Jones *et al* (2016), a range of presynaptic and postsynaptic features were assessed using whole muscles (tibialis anterior, gastrocnemius, diaphragm and intercostal) stained with aBTx to detect AChRs, and antibodies against neurofilament and synaptophysin for presynaptic axons and nerve terminals, respectively. Representative images are shown in Figure 4.24, highlighting the presence of NMJs

with abnormal structures within mutant animal muscles, however, many mutant NMJs were also normal in appearance.

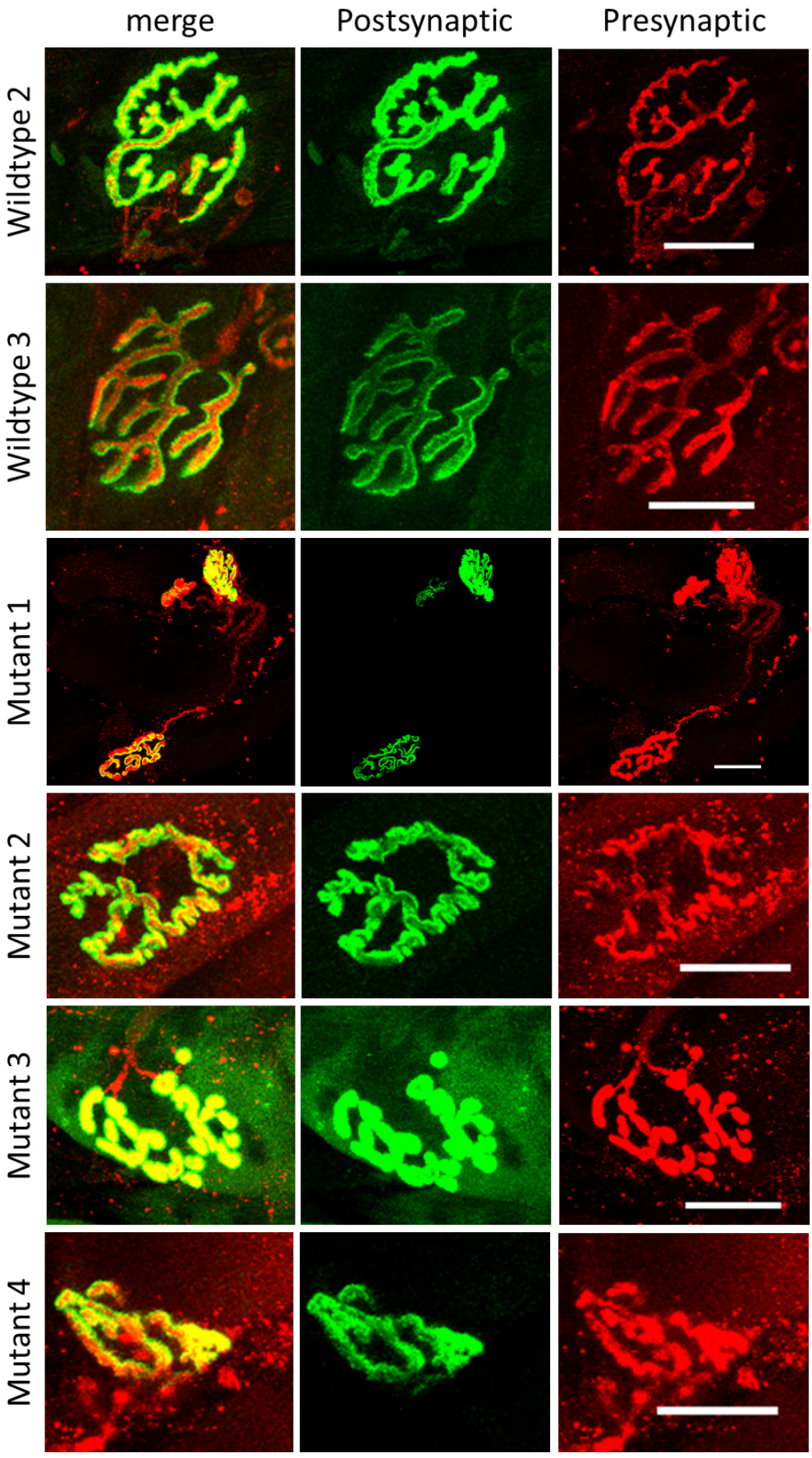

Figure 4.24. Morphology of NMJs in wildtype and MYO9A KO mice.
Representative images of NMJs in wildtype and MYO9A KO mice (mutant 1-4). Presynapse stained with antibody against synaptophysin (red), axon detected with an antibody against neurofilament light chain (red) and postsynaptic AChRs stained with aBTx (green). Scale bar = 25μm.

The NMJ morph protocol provides a comprehensive overview of synaptic morphology, comprising of 21 variables that can be measured. Staining of axons with an antibody against neurofilament was largely unsuccessful in these samples, therefore in this study parameters including axon measurements have been removed. Measurements were performed on tibialis anterior and gastrocnemius muscles, as well as intercostal and diaphragm due to the involvement of a respiratory phenotype in patients (O'Connor et al., 2016). Approximately 30 NMJs per animal per muscle were assessed, exact numbers are provided in Tables 4-1 to 4-4.

The tibialis anterior muscle was the most affected in the NMJ analysis, with a significant reduction in the majority of measured parameters when comparing mutants to wildtype. A summary of results is displayed in Figure 4.25, and full results, including statistics, are shown in Table 4-1. All presynaptic measurements were decreased in mutants, most to between 20 and 40% of wildtype values, including nerve terminal area and number/total length of axon branches. With regards to postsynaptic features, endplate area and average AChR cluster area were most affected in the mutants as compared to controls, whereas % compactness (how compact the endplate is) and fragmentation were relatively unaffected as compared to wildtypes. The final set of measurements cover both pre and postsynaptic features, demonstrating that the % overlap of the nerve and endplate was not affected and thus the two compartments still align with one another, however the average area of synaptic contact was reduced in mutants. When considering the mutants separately, it could be observed that mutant 2 appeared relatively spared, with a significant reduction in only nerve terminal perimeter, area, total length of branches and area of synaptic overlap. However, from the mice available observations suggest an overall reduction in NMJ size in the absence of MYO9A.

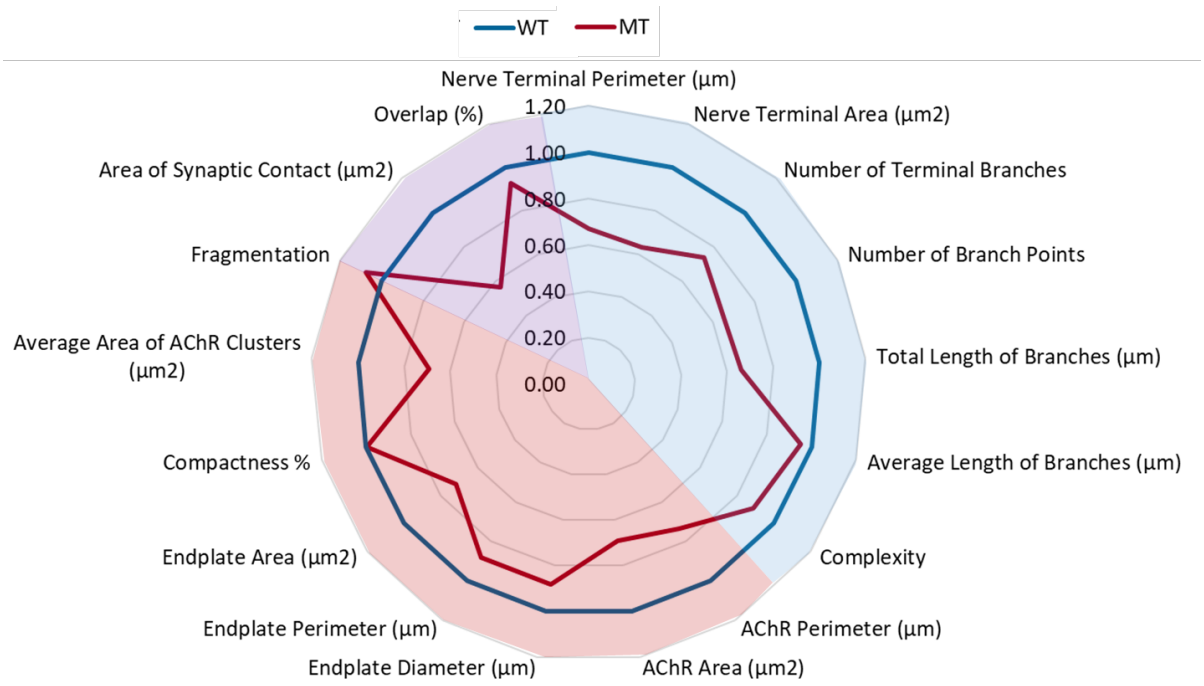

Figure 4.25. Radar plot of NMJ morphology measurements from tibialis anterior muscle. Various features of NMJ morphology measured in mouse tibialis anterior muscle from wildtype (2 mice pooled) and mutant (MYO9A KO, 4 pooled) mice. Values are expressed as a proportion of wildtype. Blue shading = presynaptic features, red shading = postsynaptic features and purple shading = combined features.

The other muscles analysed did not show consistently significant alterations in any of the parameters. Gastrocnemius was relatively unaffected by absence of MYO9A as shown in Table 4-2 and Figure 4.26. Of note is the reduction in nerve terminal area and number of branch points in pooled mutant animals as compared to controls, as found in tibialis anterior muscle. However, there was an increase in the area of synaptic contact and % pre and postsynaptic overlap in mutants. Considering the mutants separately, these values are only elevated in two mutants, whereas they are decreased in the other two, highlighting the variability of results present. Mutant 4 had significantly larger postsynaptic features when compared to the wildtype animals, which was not the case for the other mutants. Overall, there was a general decrease in the presynaptic nerve terminal area and number of branch points, however, the data for this muscle had a higher level of inter-mutant variability.

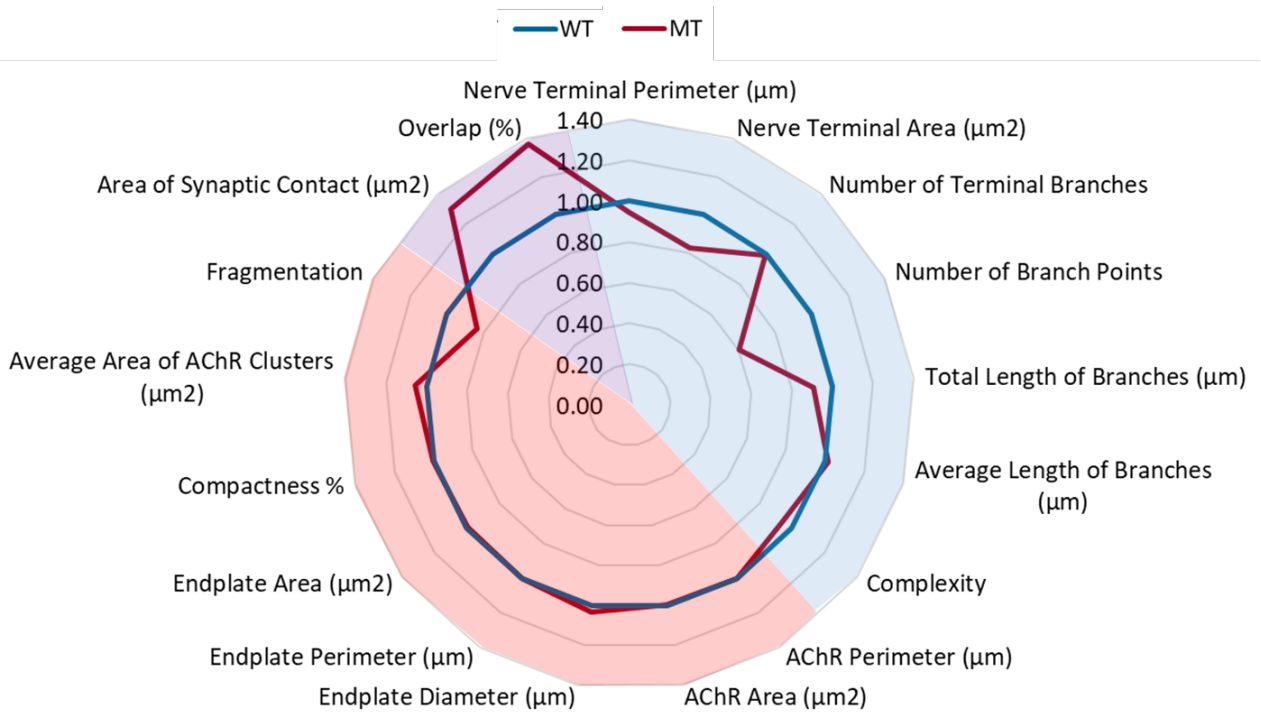

Figure 4.26. Radar plot of NMJ morphology measurements from gastrocnemius muscle. Various features of NMJ morphology measured in mouse gastrocnemius muscle from wildtype (2 mice pooled) and mutant (MYO9A KO, 4 pooled) mice. Values are expressed as a proportion of wildtype. Blue shading = presynaptic features, red shading = postsynaptic features and purple shading = combined features.

As observed in tibialis anterior muscle, NMJs from mutant animals had an overall reduction in the size of presynaptic components in the intercostal muscles (Figure 4.27, Table 4-3). In particular, nerve terminal area and number of branch points were reduced in all mutants as compared to control. However, it should be noted that mutant 1 and 3 had only 3 and 5 NMJs with presynaptic staining present, respectively. With regards to the postsynapse, AChR area, endplate area and average area of AChR clusters were all decreased in mice lacking MYO9A as compared to wildtypes. This was also observed in the tibialis anterior muscle. Analysis of mutants separately revealed a non-significant increase in these features for mutant 4, however this was accompanied by larger standard deviations and a corresponding significant decrease in % compactness, suggesting that endplates are more spread out in this animal (Table 4-3). The area of synaptic contact and % overlap were reduced by 30-50% in mutants as opposed to controls, likely as a reflection of reduced nerve terminal sizes, but also indicating there may be some misalignment of nerve terminals and muscle endplates. Overall for intercostal muscles, as observed in tibialis anterior muscle there is a trend toward smaller NMJs with an emphasis on decreased size of presynaptic components.

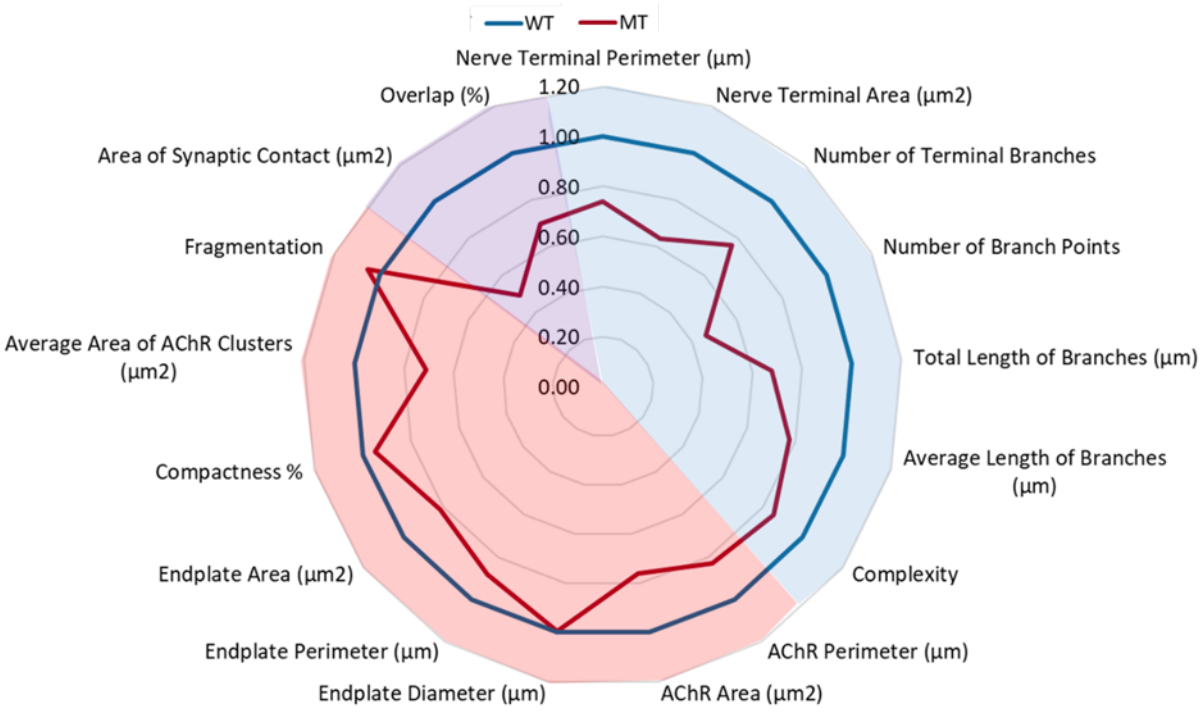

Figure 4.27. Radar plot of NMJ morphology measurements from intercostal muscle. Various features of NMJ morphology measured in mouse intercostal muscles from wildtype (2 mice pooled) and mutant (MYO9A KO, 4 pooled) mice. Values are expressed as a proportion of wildtype. Blue shading = presynaptic features, red shading = postsynaptic features and purple shading = combined features.

NMJ analysis of diaphragm muscle revealed a large decrease in size of presynaptic components for mutants as opposed to wildtype animals (Table 4-4, Figure 4.28). This is in corroboration with tibialis anterior and intercostal muscles. However, it should be noted that presynaptic staining for mutant 1 was not detectable and mutant 3 had only 4 identifiable NMJs, thus the total NMJ number for presynaptic and combined component measurements was only 15. Taking this into account, while there is a considerable decrease in the % overlap and area of synaptic contact in mutants as compared to controls, more NMJs would be required to confirm these observations. The postsynapse is less affected in the diaphragm as opposed to intercostal and tibialis anterior muscles, with a small overall decrease in % compactness and average AChR areas. On the other hand, fragmentation is increased by 20% in mutants in contrast to controls, however none of the mutants have a significantly elevated level of fragmentation as compared to controls when considered separately. Therefore, for diaphragm muscle there is a reduction in size of presynaptic components and some postsynaptic features, however more animals would be required to expand these observations.

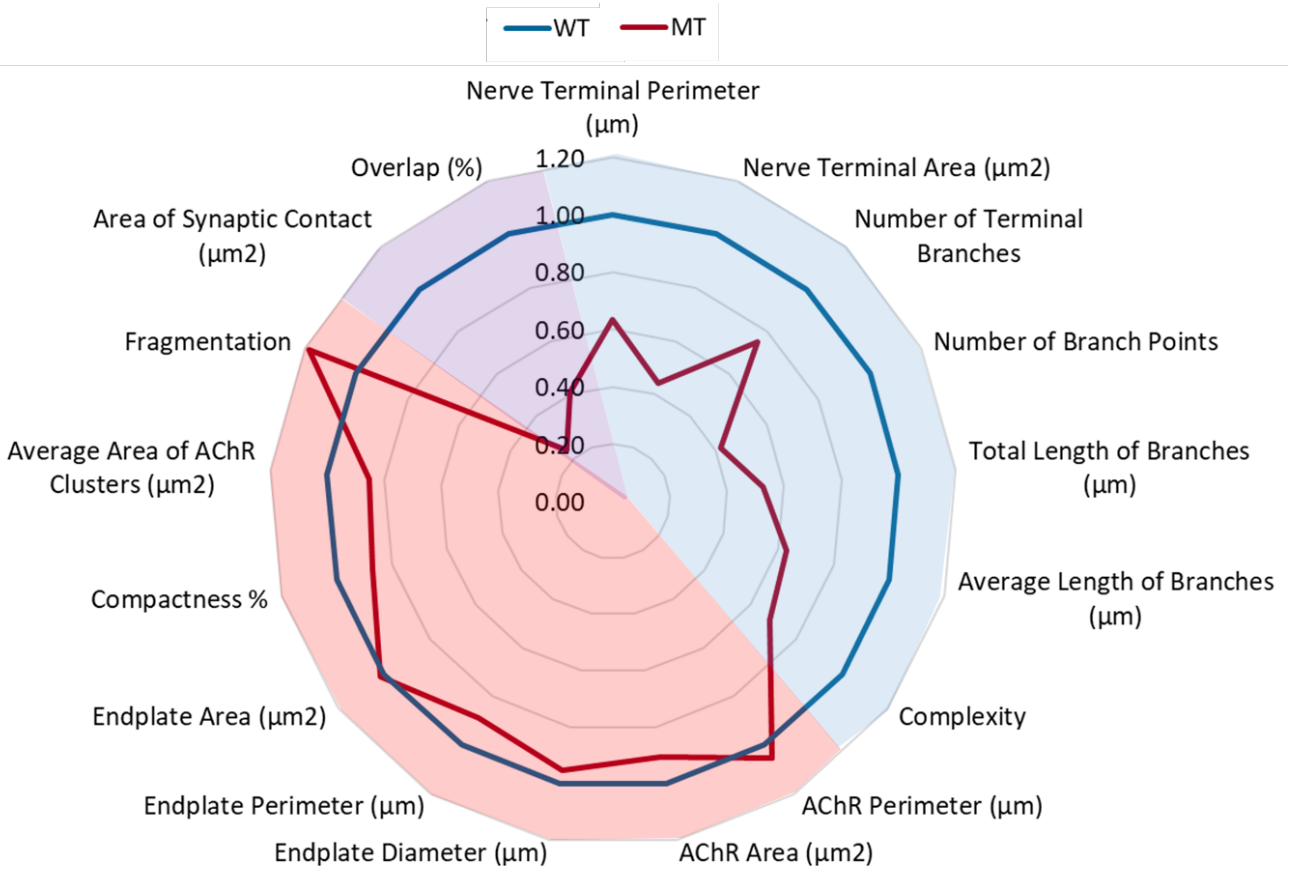

Figure 4.28. Radar plot of NMJ morphology measurements from diaphragm muscle. Various features of NMJ morphology measured in mouse diaphragm muscle from wildtype (2 mice pooled) and mutant (MYO9A KO, 4 pooled) mice. Values are expressed as a proportion of wildtype. Blue shading = presynaptic features, red shading = postsynaptic features and purple shading = combined features.

In summary, presynaptic components assessed in mutant animals were smaller than in controls for tibialis anterior, intercostal and diaphragm muscles, and less affected in gastrocnemius muscle. In tibialis anterior, intercostal and diaphragm muscles there was also a modest decrease in postsynaptic NMJ size, as well as the combined features of % overlap and area of synaptic contact, whereas the latter measurements were increased in gastrocnemius muscles of mutants compared to controls. This highlights a general trend toward smaller NMJ size in some muscles from MYO9A KO mice as compared to wildtype animals.

Tibialis Anterior	WildType			Mutant 1				Mutant 2				Mutant 3				Mutant 4			
Parameter	*Mean*	*SD*	*N*	*Mean*	*SD*	*N*	*P Value*	*Mean*	*SD*	*N*	*P Value*	*Mean*	*SD*	*N*	*P Value*	*Mean*	*SD*	*N*	*P Value*
Nerve Terminal Perimeter (µm)	347.47	128.46	37.00	216.67	75.84	21.00	****	261.21	89.47	15.00	*	248.09	132.44	30.00	**	206.09	64.34	29.00	****
Nerve Terminal Area (µm²)	385.91	134.25	38.00	272.20	70.13	22.00	***	274.20	274.20	16.00	**	219.99	106.02	31.00	****	207.16	77.15	30.00	****
Number of Terminal Branches	32.43	19.53	38.00	19.95	14.15	22.00	*	26.80	14.64	16.00	ns	27.00	20.68	31.00	ns	22.00	11.20	30.00	ns
Number of Branch Points	17.69	10.18	36.00	13.05	8.57	21.00	ns	14.33	6.66	15.00	ns	10.33	6.48	30.00	***	8.38	3.13	29.00	****
Total Length of Branches (µm)	168.02	64.68	38.00	112.00	42.51	22.00	***	127.02	45.81	16.00	*	113.95	59.07	31.00	***	92.47	27.81	30.00	****
Average Length of Branches (µm)	6.75	3.49	38.00	7.58	3.78	22.00	ns	5.57	2.36	16.00	ns	7.57	16.65	31.00	ns	4.96	2.29	30.00	ns
Complexity	4.82	0.60	37.00	4.23	0.68	22.00	**	4.55	0.52	16.00	ns	4.23	0.73	31.00	***	4.13	0.38	30.00	****
AChR Perimeter (µm)	299.28	99.71	52.00	183.89	64.02	31.00	****	265.34	94.43	35.00	ns	229.70	116.43	31.00	*	205.19	87.84	30.00	***
AChR Area (µm²)	437.87	163.31	65.00	257.42	76.93	31.00	****	372.92	125.63	35.00	ns	301.10	141.23	31.00	****	277.07	122.20	30.00	****
Endplate Diameter (µm)	46.47	9.49	65.00	40.12	8.14	31.00	**	44.00	8.15	35.00	ns	42.43	11.16	31.00	ns	37.58	8.96	30.00	****
Endplate Perimeter (µm)	124.50	25.13	65.00	105.80	21.50	31.00	**	117.77	20.44	35.00	ns	109.49	28.22	31.00	*	105.70	27.12	30.00	**
Endplate Area (µm²)	846.47	343.23	65.00	513.71	206.61	31.00	***	737.03	269.24	35.00	ns	606.82	324.75	31.00	**	576.57	274.37	30.00	***
Compactness %	52.27	8.56	65.00	53.11	10.52	31.00	ns	52.46	10.21	35.00	ns	52.28	9.17	31.00	ns	49.99	9.67	30.00	ns
Area of Synaptic Contact (µm²)	282.86	135.38	50.00	144.19	73.32	22.00	****	183.38	101.14	16.00	**	141.54	79.30	28.00	****	171.74	88.45	30.00	***
Overlap (%)	59.48	20.11	38.00	56.16	29.64	22.00	ns	52.75	22.10	16.00	ns	49.53	18.28	28.00	ns	62.89	20.04	30.00	ns
Average Area of AChR Clusters (µm²)	274.68	140.73	52.00	161.24	80.46	31.00	***	229.56	133.36	35.00	ns	173.75	108.95	26.00	**	195.80	115.26	30.00	*
Fragmentation	0.32	0.31	65.00	0.36	0.29	31.00	ns	0.37	0.33	35.00	ns	0.37	0.35	26.00	ns	0.28	0.31	30.00	ns

Table 4-1. NMJ measurements in tibialis anterior muscle. Mean values for each parameter, standard deviation (SD) and number of NMJs assessed (N) are shown. P values for each mutant as compared to the wildtype results (data from 2 wildtypes pooled and averaged) are shown, as calculated using One-way ANOVA, ns=not significant, *p≤0.05, **p≤0.01, ***p≤0.001, ****p<0.0001. AChR=acetylcholine receptor.

Gastrocnemius	WildType			Mutant 1				Mutant 2				Mutant 3				Mutant 4			
Parameter	*Mean*	*SD*	*N*	*Mean*	*SD*	*N*	*P Value*	*Mean*	*SD*	*N*	*P Value*	*Mean*	*SD*	*N*	*P Value*	*Mean*	*SD*	*N*	*P Value*
Nerve Terminal Perimeter (µm)	242.74	105.82	17.00	201.07	85.35	28.00	ns	215.05	95.48	26.00	ns	221.63	68.31	10.00	ns	277.38	86.97	27.00	ns
Nerve Terminal Area (µm²)	275.87	111.93	17.00	194.86	65.68	28.00	*	218.14	94.08	26.00	ns	193.19	86.32	10.00	ns	302.48	95.00	28.00	ns
Number of Terminal Branches	22.71	13.69	17.00	20.75	14.96	28.00	ns	20.73	12.35	26.00	ns	19.20	9.75	10.00	ns	29.39	19.52	28.00	ns
Number of Branch Points	15.00	7.18	4.00	8.11	5.05	28.00	ns	8.38	4.43	26.00	ns	7.90	9.08	10.00	ns	11.84	5.54	28.00	ns
Total Length of Branches (µm)	115.79	50.64	18.00	91.37	35.86	28.00	ns	99.31	42.69	25.00	ns	100.61	43.69	10.00	ns	128.37	39.74	28.00	ns
Average Length of Branches (µm)	5.79	2.45	18.00	5.75	2.52	28.00	ns	5.54	2.01	25.00	ns	6.50	3.14	10.00	ns	5.75	2.64	28.00	ns
Complexity	4.35	0.61	18.00	3.95	0.75	28.00	ns	4.13	0.96	26.00	ns	3.91	0.65	10.00	ns	4.48	0.56	28.00	ns
AChR Perimeter (µm)	229.58	80.20	70.00	204.03	85.88	33.00	ns	210.91	97.95	31.00	ns	229.04	78.79	32.00	ns	274.90	80.67	32.00	*
AChR Area (µm²)	318.46	102.06	70.00	250.49	107.94	33.00	*	265.25	116.45	31.00	ns	360.86	110.34	32.00	ns	392.52	117.19	32.00	**
Endplate Diameter (µm)	39.00	6.05	70.00	37.33	8.33	33.00	ns	36.98	9.09	31.00	ns	38.62	6.58	32.00	ns	48.08	18.17	32.00	***
Endplate Perimeter (µm)	108.92	16.98	70.00	101.03	23.06	33.00	ns	101.23	24.92	31.00	ns	110.34	15.98	32.00	ns	124.75	23.79	32.00	**
Endplate Area (µm²)	657.52	222.93	70.00	529.15	238.55	33.00	ns	558.58	277.04	31.00	ns	697.02	227.98	32.00	ns	836.65	297.02	32.00	**
Compactness %	49.64	10.01	70.00	48.59	8.76	33.00	ns	49.11	8.12	31.00	ns	52.61	8.56	32.00	ns	49.06	10.22	32.00	ns
Area of Synaptic Contact (µm²)	112.77	105.55	16.00	103.09	85.97	28.00	ns	180.88	103.83	26.00	ns	96.38	72.36	9.00	ns	207.29	111.63	28.00	*
Overlap (%)	35.11	42.30	18.00	45.88	30.48	28.00	ns	62.29	19.43	26.00	*	30.54	18.72	9.00	ns	53.88	26.05	28.00	ns
Average Area of AChR Clusters (µm²)	214.59	117.18	70.00	165.40	107.22	32.00	ns	154.36	76.69	31.00	ns	292.71	150.57	32.00	*	293.68	149.56	32.00	*
Fragmentation	0.33	0.30	70.00	0.32	0.31	32.00	ns	0.35	0.31	31.00	ns	0.20	0.30	32.00	ns	0.25	0.27	32.00	ns

Table 4-2. NMJ measurements in gastrocnemius muscle. Mean values for each parameter, standard deviation (SD) and number of NMJs assessed (N) are shown. P values for each mutant as compared to the wildtype results (data from 2 wildtypes pooled and averaged) are shown, as calculated using the one-way ANOVA, ns=not significant, *p≤0.05, **p≤0.01, ***p≤0.001, ****p<0.0001. AChR=acetylcholine receptor.

Intercostal	WildType			Mutant 1				Mutant 2				Mutant 3				Mutant 4			
Parameter	*Mean*	*SD*	*N*	*Mean*	*SD*	*N*	*P Value*	*Mean*	*SD*	*N*	*P Value*	*Mean*	*SD*	*N*	*P Value*	*Mean*	*SD*	*N*	*P Value*
Nerve Terminal Perimeter (µm)	213.48	84.94	29.00	123.44	44.41	3.00	ns	158.22	63.40	23.00	*	146.38	64.01	5.00	ns	202.81	65.38	16.00	ns
Nerve Terminal Area (µm²)	237.98	87.70	29.00	124.49	49.79	3.00	ns	167.54	84.39	23.00	*	122.64	34.67	5.00	**	187.00	56.09	16.00	ns
Number of Terminal Branches	23.93	13.90	29.00	13.00	7.35	3.00	ns	16.04	8.79	23.00	*	19.20	8.84	5.00	ns	24.94	11.58	16.00	ns
Number of Branch Points	12.78	10.82	29.00	4.00	4.24	3.00	ns	6.91	3.63	23.00	*	3.60	1.96	5.00	ns	8.94	6.57	16.00	ns
Total Length of Branches (µm)	102.22	36.85	29.00	56.47	24.40	3.00	ns	72.15	30.47	23.00	**	59.70	26.94	5.00	*	89.43	33.41	16.00	ns
Average Length of Branches (µm)	5.92	4.53	29.00	5.23	1.89	3.00	ns	5.93	4.21	23.00	ns	3.38	1.11	5.00	ns	3.86	1.12	16.00	ns
Complexity	4.27	0.57	29.00	3.09	0.89	3.00	**	3.71	0.58	23.00	**	3.68	0.41	4.00	ns	4.10	0.70	16.00	ns
AChR Perimeter (µm)	177.15	67.01	34.00	88.78	24.39	3.00	ns	147.92	55.05	30.00	ns	153.84	62.69	23.00	ns	197.57	66.42	30.00	ns
AChR Area (µm²)	260.95	85.02	34.00	142.80	40.99	3.00	ns	183.61	77.66	30.00	***	189.10	56.64	23.00	**	276.13	87.28	30.00	ns
Endplate Diameter (µm)	34.79	6.46	34.00	21.15	1.38	3.00	ns	40.25	26.99	28.00	ns	40.71	29.60	23.00	ns	36.07	5.99	30.00	ns
Endplate Perimeter (µm)	95.66	17.12	34.00	62.40	7.08	3.00	**	85.60	17.97	30.00	*	85.54	21.01	23.00	ns	103.62	19.02	30.00	ns
Endplate Area (µm²)	487.37	174.76	34.00	236.01	60.43	3.00	ns	384.67	167.62	30.00	*	388.62	161.15	23.00	ns	583.48	211.86	30.00	ns
Compactness %	54.84	8.73	34.00	60.17	2.91	3.00	ns	48.59	9.23	30.00	**	51.06	7.93	23.00	ns	48.40	6.72	30.00	**
Area of Synaptic Contact (µm²)	113.25	146.65	29.00	37.81	7.32	3.00	ns	82.77	67.61	23.00	ns	16.37	63.10	5.00	ns	87.03	53.28	16.00	ns
Overlap (%)	41.05	65.90	29.00	29.03	11.46	3.00	ns	37.13	21.82	23.00	ns	8.24	34.07	5.00	ns	40.22	23.20	16.00	ns
Average Area of AChR Clusters (µm²)	176.41	99.41	34.00	77.65	18.69	3.00	ns	103.28	52.53	30.00	***	126.09	39.89	23.00	ns	195.03	104.76	30.00	ns
Fragmentation	0.32	0.31	34.00	0.39	0.28	3.00	ns	0.40	0.29	30.00	ns	0.27	0.29	23.00	ns	0.29	0.28	30.00	ns

Table 4-3. NMJ measurements in intercostal muscles. Mean values for each parameter, standard deviation (SD) and number of NMJs assessed (N) are shown. P values for each mutant as compared to the wildtype results (data from 2 wildtypes pooled and averaged) are shown, as calculated using the one-way ANOVA, ns=not significant, *p≤0.05, **p≤0.01, ***p≤0.001, ****p<0.0001. AChR=acetylcholine receptor.

Diaphragm	WildType			Mutant 1				Mutant 2				Mutant 3				Mutant 4			
Parameter	*Mean*	*SD*	*N*	*Mean*	*SD*	*N*	*P Value*	*Mean*	*SD*	*N*	*P Value*	*Mean*	*SD*	*N*	*P Value*	*Mean*	*SD*	*N*	*P Value*
Nerve Terminal Perimeter (µm)	167.02	48.67	29.00	0.00	0.00	0.00		102.87	33.62	3.00	ns	123.66	11.64	4.00	ns	197.17	29.53	8.00	ns
Nerve Terminal Area (µm²)	248.82	123.46	30.00	0.00	0.00	0.00		71.91	33.34	3.00	*	202.75	66.35	4.00	ns	163.00	42.45	8.00	ns
Number of Terminal Branches	15.47	10.53	30.00	0.00	0.00	0.00		14.67	5.19	3.00	ns	6.25	2.95	4.00	ns	25.50	7.12	8.00	*
Number of Branch Points	9.33	11.51	30.00	0.00	0.00	0.00		4.00	1.63	3.00	ns	4.00	1.00	4.00	ns	7.63	3.57	8.00	ns
Total Length of Branches (µm)	86.00	54.75	30.00	0.00	0.00	0.00		42.62	16.63	3.00	ns	56.02	10.32	4.00	ns	82.23	15.89	8.00	ns
Average Length of Branches (µm)	7.40	5.28	30.00	0.00	0.00	0.00		3.30	1.85	3.00	ns	11.83	6.60	4.00	ns	3.54	1.47	8.00	ns
Complexity	3.81	0.70	30.00	0.00	0.00	0.00		3.25	0.26	3.00	ns	3.07	0.21	4.00	ns	4.14	0.28	8.00	ns
AChR Perimeter (µm)	170.14	65.61	87.00	229.33	86.74	37.00	****	183.84	57.37	25.00	ns	133.26	9.28	4.00	ns	170.47	50.45	26.00	ns
AChR Area (µm²)	221.21	73.14	87.00	229.21	93.14	37.00	ns	161.49	39.95	25.00	**	192.35	78.35	4.00	ns	217.71	74.55	26.00	ns
Endplate Diameter (µm)	35.22	21.47	87.00	36.57	14.76	37.00	ns	31.37	4.58	25.00	ns	29.72	2.30	4.00	ns	36.59	25.32	26.00	ns
Endplate Perimeter (µm)	101.35	78.06	87.00	98.89	18.56	37.00	ns	88.40	14.43	25.00	ns	81.46	6.35	4.00	ns	90.91	19.02	26.00	ns
Endplate Area (µm²)	445.19	151.13	87.00	559.81	220.08	37.00	**	428.38	130.24	25.00	ns	366.11	104.74	4.00	ns	454.95	142.60	26.00	ns
Compactness %	52.35	17.39	87.00	42.30	10.11	37.00	**	39.86	10.94	25.00	***	51.23	9.86	4.00	ns	48.77	10.99	26.00	ns
Area of Synaptic Contact (µm²)	112.67	125.03	30.00	0.00	0.00	0.00		51.00	84.00	3.00	ns	52.24	24.77	3.00	ns	5.30	73.35	8.00	ns
Overlap (%)	43.62	50.03	30.00	0.00	0.00	0.00		29.60	46.84	3.00	ns	37.90	33.32	3.00	ns	4.09	39.26	8.00	ns
Average Area of AChR Clusters (µm²)	146.40	93.08	87.00	116.11	88.29	37.00	ns	101.74	73.03	25.00	ns	151.33	109.05	4.00	ns	131.18	85.25	26.00	ns
Fragmentation	0.34	0.32	87.00	0.49	0.36	37.00	ns	0.46	0.34	25.00	ns	0.31	0.32	4.00	ns	0.37	0.34	26.00	ns

Table 4-4. NMJ measurements in diaphragm muscle. Mean values for each parameter, standard deviation (SD) and number of NMJs assessed (N) are shown. Scored out boxes represent measurements that were not obtained for that animal. P values for each mutant as compared to the wildtype results (data from 2 wildtypes pooled and averaged) are shown, as calculated using the one-way ANOVA, ns=not significant, *p≤0.05, **p≤0.01, ***p≤0.001, ****p<0.0001. AChR=acetylcholine receptor

.

4.7 Discussion

The main aim of this chapter was to determine whether loss of MYO9A, or presence of CMS patient mutations, affects the NMJ. This was assessed using an iNPC neurite extension assay, behaviour of zebrafish and zebrafish NMJ morphology, as well as assessment of mouse muscle and NMJ phenotypes.

4.7.1 Neurite phenotype of patient iNPCs

Previous data revealed an increase in neurite extension and branching in NSC-34 cells depleted for MYO9A (O'Connor et al., 2016). Due to our finding that the MYO9A CMS patient fibroblasts did not exhibit a decrease in MYO9A expression at the RNA level, differentiated iNPCs were also subject to a neurite outgrowth assay to determine whether *MYO9A* mutations may cause a similar phenotype. Neurites in MYO9A patient iNPCs were significantly longer than those in control cells, thus corroborating results obtained from the MYO9A KD cell-line. A similar phenotype is also found in dissociated hippocampal neurons from mice lacking another unconventional myosin protein: MYO10, in which excessive extension of neurites is observed (Yu et al., 2015). Furthermore, in hum-7 mutants (*C.elegans* MYO9A homologue) the rate of protrusion formation from epidermal cells in early development is increased as compared to wildtype animals (Wallace et al., 2018), suggesting a common effect of increased RhoA activity on cell extensions.

4.7.2 Assessment of 24 hpf zebrafish movement and NMJ morphology

Zebrafish perform a stereotyped set of locomotive behaviours during early embryonic and larval development stages. These movements can be easily observed in a large number of zebrafish and quantified to reveal abnormalities that may reflect underlying neuronal or muscle defects. The first movement performed is spontaneous twitching in the chorion. Wildtype zebrafish performed a full chorion rotation on average 2.4 times per minute in this study, which is similar to results found elsewhere (Liu et al., 2012). Myo9aa/ab morphant fish were shown to move 30% less than controls at this time point, and it was found that crispant fish injected with either the 3 or 4 sgRNA combinations also displayed reduced movement but to a greater degree (50% and 88% respectively). Loss of an alternative RhoA modulating protein, Ephexin1, from mice also affects motor behaviours demonstrating the importance of RhoA pathway integrity in movement (Shi et al., 2010). The increased severity of the 4 sgRNA injection as compared to the 3 sgRNA could be due to the likelihood of larger deletions induced in *myo9aa* if both target regions are cut at the same time, thus

increasing the chance of disrupting Myo9aa expression. Injected controls receiving sgRNA against the *tyr* gene did not display a reduction in spontaneous movements, suggesting that the injection procedure or CRISPR/Cas9 activity itself does not cause developmental delay or absence of these movements. Furthermore, this behavior is not dependent on supraspinal input and is mediated at the level of the spinal cord (Downes and Granato, 2006). Previous results showed no effect on the distribution or quantity of Rohon Beard sensory cells in the spinal cord during development in the absence of Myo9aa/ab (O'Connor et al., 2016), therefore it is likely an effect of the motor system. The lack of movement observed at this early time point may also underlie the curved tail phenotype exhibited by the 48 hpf zebrafish. It has been shown that embryos raised in anaesthetic (therefore not performing chorion movements), have curved tails upon dechorionation, thus tail straightening may be activity dependent (Saint-Amant and Drapeau, 1998).

In support of these behvioural phenotypes, a number of morphological features were found to be disrupted in 24 hpf *myo9aa/ab* crispants. The average area of AChR clusters was decreased by over 50% in crispants as compared to controls and half of crispant myotomes analysed did not have a choice point cluster present. As this is after the time period expected for prepatterned receptor clusters (primary neurons have already contacted the area), this is unlikely to be a defect in prepatterning but in the incorporation of synaptic AChRs. However, to verify this assumption, earlier time points should be assessed to determine whether prepatterned clusters are ever present. Furthermore, a RhoGDP/GTP nucleotide exchange factor (RhoGEF) protein Ephexin1 has been demonstrated to disperse pre-existing AChR clustering (prior to application of agrin) in C2C12 cells, thus MYO9A as a RhoGAP may also cause early AChR dispersion when absent (Shi et al., 2010).

The size of myotomes was reduced in the crispant zebrafish by 68%. A number of studies in mammals have found muscle fibre diameter to correlate with NMJ size (for example: Wærhaug and Lømo, 1994, Balice-Gordon et al., 1990, Nystrom, 1968, Slater et al., 1992). While muscle fibre diameter wasn’t measured here, as myotome size is reduced more than AChR cluster area it could be that reduced AChR area is a function of reduced muscle size, and Myo9aa/ab may play a role in muscle development. A zebrafish *mlh* mutant also shows evidence of reduced synapse size and smaller somites/muscle fibre diameter (Panzer et al., 2005). However, a recent study challenged the idea that muscle fibre diameter is a predictor for NMJ size due

to a lack of correlation between the two in mouse muscle (Jones et al., 2016). Therefore, further work will be required to determine whether effects on muscle mass or NMJ size are secondary defects to the primary pathology.

Primary motor neurons had also extended further in wildtype fish than crispants at this early time point. As it has been shown that the presence of AChRs are not necessary for motorneuron outgrowth in the fish, this indicated that there may be a defect in axon extension (Westerfield et al., 1990). Other zebrafish models of CMS such as those lacking agrin or GFPT1 homologues also display truncated and abnormal extension of motor neurons during development, thus supporting this finding in the MYO9A-depleted zebrafish (Kim et al., 2007, Senderek et al., 2011). These results are conflicting with the *in vitro* observations that loss of MYO9A causes over-extension of neurites, which could be due to cross-talk with muscle fibres *in vivo* during outgrowth. In order to address this, it would be beneficial to analyse co-cultures in which wildtype/MYO9A KD nerve cells are incubated with wildtype/MYO9A KD muscle cells to observe any effects on neurite extension. Overall, movements of *myo9aa/ab* crispant fish were impaired at 24 hpf and corresponding defects to NMJ morphology were observed.

4.7.3 Assessment of 48 hpf movement and NMJ morphology

As zebrafish development progressed and the ability to respond to tactile stimulation was obtained, it could be observed that fish lacking Myo9aa/ab were less able to perform the response. Corroborating this, ability of CMS zebrafish models to perform appropriate motor activities is impaired in 12 of the 13 studies identified in Table 1-1 (Chapter 1, Section 1.4.2), thus highlighting that impairment of the NMJ in developing embryos due to loss of CMS-associated proteins can impact movement. Of particular interest was the reduction in initial acceleration in morphant and crispant fish, which indicates a reduced force of muscle contraction (Sztal et al., 2016). This could suggest less overall innervation of the myotomes (thus less muscle fibres contracting in response to stimulation), which was supported by the finding that there were less pre- and postsynaptic clusters present at this time point, and the progression of neuronal processes across the myotomes was delayed in crispants. The aforementioned mouse lacking the RhoA-modulating protein, Ephexin1, displays numerous effects on AChR clustering, as well as on formation of postsynaptic specialisations such as junctional folds (Shi et al., 2010). Therefore, the reduced acceleration in crispant fish could also be related to problems with muscle

fibre/endplate architecture which would need a more in depth analysis of muscle at the ultrastructural level. Another study in which acceleration was used as a readout measure for assessment of a muscle disorder in zebrafish identified reduced muscle mass as a cause for decreased force production (Sztal et al., 2018). In *myo9aa/ab* crispants at 48 hpf there is no change in myotome size as compared to controls, thus while muscle mass itself was not measured this implies that it is likely a disorder of transmission rather than amount of muscle tissue. Acceleration impairment could also represent reduced quantal content of presynaptic terminals, as reduced quantal contents have been observed in other CMS zebrafish models that exhibit movement defects (Wen et al., 2016). This is supported by the finding that there is reduced total SV2 cluster area, as area of the presynaptic NMJ has been shown to correlate with QC (Slater, 2015). To assess this electrophysiology recording of activity at individual synapses would be required, such as can be achieved by the paired neuron-muscle recordings performed by Wen *et al* (2010).

4.7.4 Assessment of 5 dpf NMJ morphology, AChE activity and CNS involvement

At 5dpf there was no longer a decrease in pre and postsynaptic cluster number per myotome, and per 100μm^2 there was an increase. For the presynapse, this was accompanied by an increase in average cluster area, however the number of large clusters (over 20μm^2) was not affected and results were variable, ranging from 0.7 to 5.0μm^2 as opposed to 0.8 to 1.4μm^2 in controls. Due to the mosaic genotype of the crispant fish, and not being able to determine which cells were mutant or not, a high level of variability was to be expected. Furthermore, total SV2 cluster area was decreased, suggesting there is still impaired innervation of myotomes at this time point. Reflecting this result, clusters of AChRs remain significantly smaller at 5 dpf, and total cluster area is reduced. This highlights a potential mechanism of MYO9A-loss affecting AChR clustering during development, such as effects on the agrin-LRP4-MuSK pathway. Zebrafish lacking functional proteins involved in this pathway similarly display reduced AChR clustering (Kim et al., 2007, Muller et al., 2010, Remedio et al., 2016, Zhang and Granato, 2000).

The level of AChE activity was quantified in *myo9aa/ab* crispant fish and compared to wildtype controls, revealing a significant reduction in activity at 24 hpf, 48 hpf and 5 dpf. This could reflect developmental delay in the crispant fish as the levels of activity have been shown to correlate with developmental stage (Koenig et al., 2016). This

could also reflect a decrease in expression/action of AChE due to effects of Myo9aa/ab on the enzyme directly. There could also be an indirect effect on AChE through reduced nerve/muscle tissue quantity in crispants and corresponding to this there was a reduction in total AChR/SV2 cluster areas for the time points where reduced AChE activity was observed, which could reflect less NMJs (and thus less AChE expressed). However, whether smaller NMJs lead to less AChE activity or if the effect is converse is not clear, as in a zebrafish AChE mutant AChR clustering and neural input to the axial musculature is also reduced (Behra et al., 2002). Another theory is that reduced AChE activity could influence the amount of ACh present in the synaptic cleft and thus decrease the activation of AChRs, reflected in the abnormal movements observed at 24 and 48 hpf. Defective movements in the AChE mutant zebrafish have similarly been observed, although these fish completely lack enzymatic activity and are paralysed by 3 dpf (Behra et al., 2002). To ascertain whether the reduction in AChE activity in *myo9aa/ab* crispants is sufficient to impair the action of ACh on AChRs, and thus affect depolarisation of the muscle and resulting muscle contractions, it would necessary to perform electrophysiology in the zebrafish.

The question also remains as to whether there is CNS involvement in any phenotypes observed, as previous studies of the MYO9A KO mouse revealed the variable presence of hydrocephalus but also an impairment in CNS glutamatergic signaling (Abouhamed et al., 2009, Folci et al., 2016). One of the MYO9A CMS patients also displayed signs of learning difficulties in early life (O'Connor et al., 2016). While analysis of tg(islet1:GFP) zebrafish didn’t reveal any gross abnormalities, a more in depth characterisation of CNS morphology may be useful, including the cerebellum which is important for movement coordination.

Overall, a number of effects on movement during early development of zebrafish lacking Myo9aa/ab were observed, and supported by a number of defects in NMJ morphology up to 5dpf. Whether these structural changes represent impairment to signal transmission will require further investigation.

4.7.5 Analysis of NMJ morphology in the MYO9A KO mouse

Analysis of NMJ and muscle morphology was performed in the MYO9A KO mouse revealing an overall decrease in NMJ size (for tibialis anterior, diaphragm and intercostal muscle). This included a decrease in presynaptic area, presynaptic branch number, number of branch points, branch length and terminal complexity. There was

also a tendency toward smaller postsynaptic features such as decreased AChR area, endplate area, average AChR cluster area, synaptic contact and % overlap of pre and postsynapse. Analysis of muscle fibre area was also reduced in mutants. The co-occurrence of reduced NMJ size and muscle fibre area could suggest that one is affected as a consequence of the other, however this cannot be determined from the data available and is confounded by the finding that muscle fibre area is also reduced in gastrocnemius muscle which does not exhibit consistent changes in NMJ area. Insight could be gained from measurement of fibre diameters and NMJ morphologies in conjunction, to see whether large NMJs ever appear on small fibres and vice versa. It must be noted that mutant and wildtype mice were not aged matched, with the mutants being approximately 6 months older. As both groups of mice were adults, and it has been shown that little difference is expected to occur in NMJ size until between 14 and 19 months, they were both included in the study (Cheng et al., 2013). Aged matched mice are being analysed in a future project. Furthermore, in the zebrafish experiments using age-matched fish, similar reductions in number of pre and postsynaptic clusters were identified at 48 hpf in fish lacking Myo9aa/ab, as well as a decrease in total SV2 and AChR cluster area at all time points assessed.

In the analysis of mouse NMJs, it was surprising that not all muscles were affected by MYO9A loss in the same way. For example, gastrocnemius NMJs displayed an increase in % overlap of pre and postsynaptic regions as well as an increase in synaptic contact, as opposed to a decrease in these features for the other muscles assessed. However, in other mouse models of CMS such as *agrn*$^{nmf380/nmf380}$, a differential effect on NMJ degeneration was observed in diaphragm, tibialis anterior and soleus muscles, with the rate of degeneration varying between the three muscles (Bogdanik and Burgess, 2011). In the muscle-specific Gfpt1$^{tm1d/tm1d}$ mouse, quantification of AChR cluster area revealed a larger decrease in mutant animals for the tibialis anterior than intercostal muscles, again highlighting the variable susceptibility of muscles to disruption in NMJ-related genes (Issop et al., 2018). It would be interesting to investigate further, using an RNAseq or proteomic-based approach to identify differentially regulated pathways between each of the muscles. Furthermore, as tibialis anterior contains predominantly fast twitch muscle fibres, and gastrocnemius, diaphragm and intercostal muscles are mixed, assessment of a predominantly slow twitch muscle such as soleus should also be performed. This would assist in identifying any fibre-type specific changes to NMJ morphology, as

even in wildtype muscle it has been observed that NMJs have a fibre type-specific morphology (Ogata and Yamasaki, 1985).

4.7.6 Summary

Analysis of NMJs in zebrafish and mice lacking MYO9A, as well as in patient iNPC neurites, reveals some changes regarding morphology that may indicate a role for MYO9A at this synapse. Of particular interest was the discovery that at 24 hpf in zebrafish lacking Myo9aa/ab there is an impairment in AChR cluster formation and neuron growth, and the number of pre and postsynaptic clusters are reduced in 48 hpf zebrafish, as well as less developed innervation patters, which is reflected in the defective movements recorded in morphants and crispants lacking Myo9aa/ab. Similarly, the tibialis anterior muscle in adult MYO9A KO mice had NMJs of a significantly reduced size, as well as less consistent decreases in size for other muscles assessed. Further investigations are required to try and separate the contribution of MYO9A to pre and postsynaptic phenotypes, however, this comprehensive phenotyping provides a basis on which to use modulating compounds or therapeutic targets in an attempt to understand more about the pathways or rescue the phenotype, respectively.

To understand how MYO9A loss is affecting the NMJ and accompanying motor behaviours in the zebrafish, in the next chapter a potential mechanism of action will be explored and contribution of the RhoA pathway to phenotypes assessed.

Chapter 5. Investigation of cytoskeleton and vesicle trafficking in absence of MYO9A

5.1 Introduction

In the previous chapter, a role for MYO9A was identified in nerve cell morphology, as well as in the development of the zebrafish NMJ and in maintenance of adult mouse NMJs. How MYO9A is playing a role at the NMJ is as yet unknown. Due to the interaction of this unconventional myosin with actin and the RhoA pathway, it was hypothesised that MYO9A would affect the cytoskeleton and vesicle trafficking in nerve, and potentially also muscle cells, thus impacting on synaptic organisation.

MYO9A is an actin-based molecular motor, with a RhoGTPase domain in the tail specific to the MYO9 subtype of unconventional myosins. MYO9A has previously been shown to regulate the actin cytoskeleton in a number of studies (Omelchenko and Hall, 2012, Saczko-Brack et al., 2016, Wallace et al., 2018). While the cytoskeleton is critically important for both pre and postsynaptic compartments of the NMJ, here the focus will be on the neuronal cytoskeleton as MYO9A has previously been shown to play a role in neurons (Folci et al., 2016, O'Connor et al., 2016). The neuronal cytoskeleton is a complex structure composed of a series of highly dynamic components, namely microtubules, actin filaments and intermediate filaments, as summarised in Figure 5.1. Throughout neuron migration, neurite extension, synapse formation and maintenance, the cytoskeleton undergoes constant changes in order to accommodate alterations in morphology, protrusion formation, attachment, trafficking of proteins and endo/exocytosing important signaling molecules or receptors. The cytoskeleton is even more critical in neurons as opposed to other cell types, due to the extensive distances that axons have to travel in the body. Therefore, the network of structural and motor proteins must not only maintain cell shape but also transport cargo to and from the cell body and nerve terminals.

The microtubule network is the component primarily responsible for mediating this long-distance axonal transport, and is formed from multiple filaments of α- and β-tubulin that interact to form tubular structures with polarity. A number of proteins associate with microtubules, including the molecular motors that transport cargo between nerve terminals and the soma, proteins that bind to stabilise or destabilise structures and those that provide links to other cytoskeletal components (Kirkpatrick and Brady, 1999).

Actin is also involved in cellular transport processes, as well structural stability of cells and tethering of surface proteins. F-actin is a polar structure composed of globular actin monomers bound to ATP. These filaments are highly dynamic, with constant turnover occurring as monomers are lost and gained, while overall filament length remains the same. Actin binding proteins are able to influence filament dynamics by capping the ends to affect turnover (Kirkpatrick and Brady, 1999, Rottner et al., 2017). Stress-fibres, parallel bundles of actin and myosin, are more stable than other filaments and act to manipulate cell shape and adhesion, influenced by the RhoA/ROCK pathway (Tojkander et al., 2012). Cross-linking proteins are also important in stabilising filaments, and can provide links to important components of the NMJ such α-actinin which may anchor AChRs to the actin network and rapsyn (Dobbins et al., 2008, Mitsui et al., 2000). F-actin utilises a range of motor proteins, such as the myosin superfamily, to facilitate transport within neurons. Myosins can have the ability to respond to important biochemical alterations such as elevated calcium, which in the case of unconventional myosin va causes the binding of syntaxin at active zones and subsequent docking of synaptic vesicles (Watanabe et al., 2005).

Neurofilaments are members of the intermediate filament family and represent the third significant contributor to the neuronal cytoskeleton. These filaments are made up of light, medium and heavy chains and they lack polarity, thus providing predominantly structural support to cells. Peripheral neuropathies including Charcot-Marie-Tooth disease have been shown to be linked to alterations in neurofilament expression (Zhai et al., 2007).

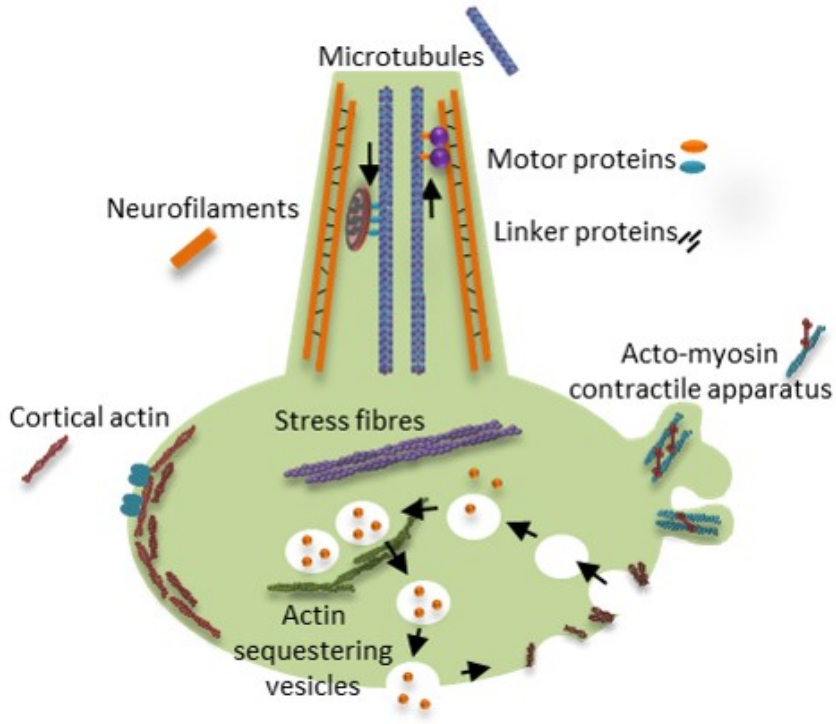

Figure 5.1. Schematic of major cytoskeletal components in neurons. The three main cytoskeletal components of neurons are actin filaments, microtubules and neurofilaments. Microtubules are particularly important for long-distance axonal transport, neurofilaments for stability and various confirmations of actin are shown for stress-fibre formation, acto-myosin contractility, vesicle sequestration and cortical actin for cell morphology. Diagram taken from O'Connor *et al* (2018a).

RhoGAPs and RhoGEFs are important proteins in the dynamic regulation of actin filaments through their interaction with small GTPases such as RhoA. Dysfunction of members of this family, such as FRABIN, have already been reported to impact functioning of the peripheral nervous system, in this case to cause Charcot-Marie-Tooth disease type 4H (Delague et al., 2007). RhoA is of particular interest as MYO9A contains a RhoGAP domain and has been shown to negatively regulate this GTPase (Chieregatti et al., 1998). Rho activity can modulate actin dynamics and affect focal adhesion formation (Ridley and Hall, 1992), thus may provide a link between MYO9A defects and downstream impacts on the filaments to which they bind and traverse. A key effector of RhoA is ROCK, which acts on a number of other molecules. These include activation of LIM kinase which coordinates actin polymerisation, myosin regulatory light chain to promote contractility, and to influence binding of actin to the membrane and intermediate filament proteins such as desmin (Schwartz, 2004). A summary of the main actions of the RhoA/ROCK pathway are shown in Figure 5.2, including the action of the ROCK inhibitor compound: Y-27632, used in this chapter.

Disruption in any of a number of these cytoskeletal components and interacting pathways may lead to disruption in NMJ formation and signal transmission. Therefore, in this chapter the effect of mutations or loss of *MYO9A* expression on the cytoskeleton and RhoA pathway will be examined using the models generated in Chapter 3.

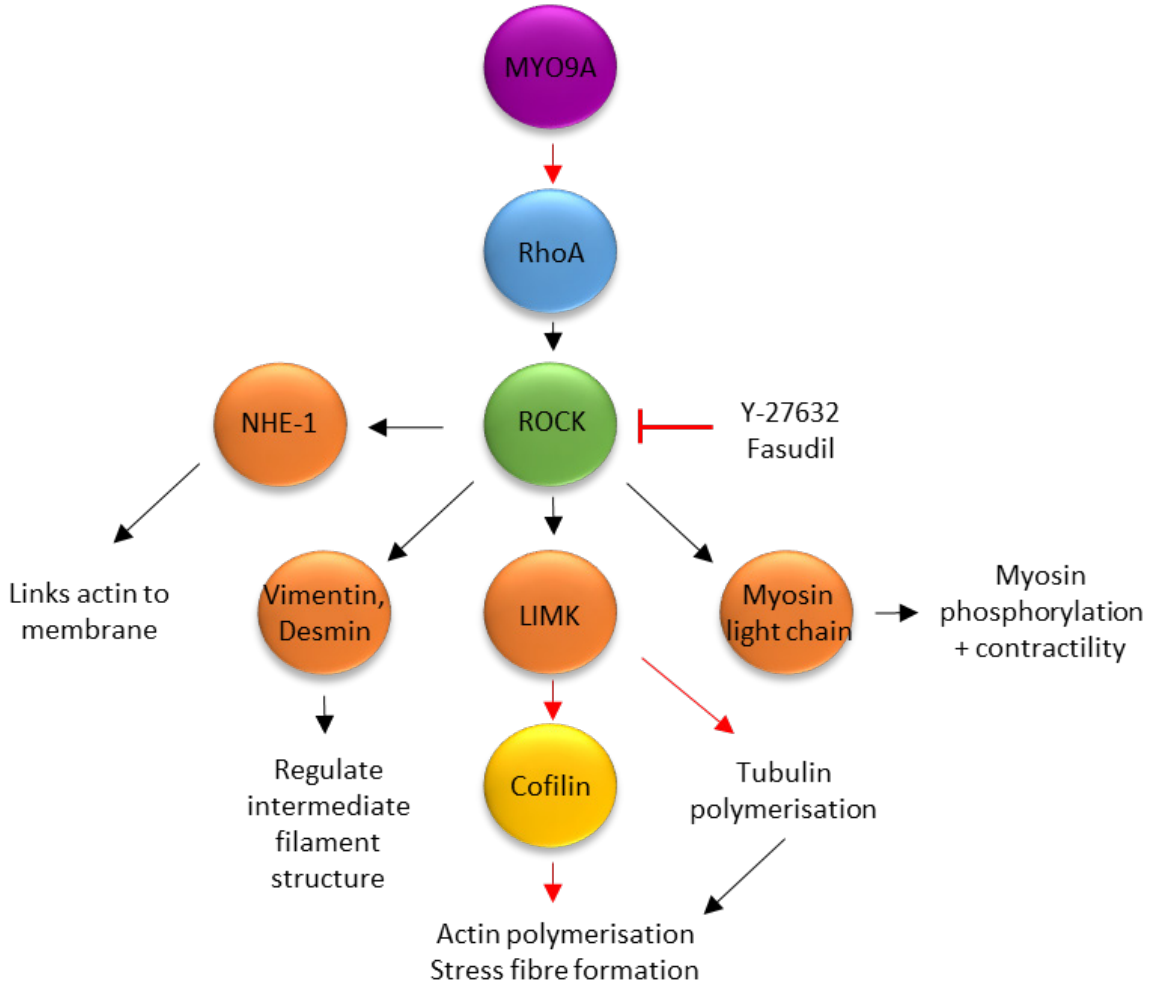

Figure 5.2. Action of MYO9A on the RhoA/ROCK pathway. MYO9A has been shown to negatively regulate the activity of RhoA, an effector of ROCK (among other substrates). Through ROCK signalling, MYO9A may indirectly affect a number of different aspects of neuronal cytoskeleton modulation. Black arrows = activation, red arrows = inhibition. The site of action of two ROCK inhibitors used in this study (Y-27632 and fasudil) is also shown. Figure adapted from: (O'Connor et al., 2018a, Schwartz, 2004).

5.2 Aim of chapter

The aim of this chapter was to determine whether MYO9A influences the structure or function of the NMJ through effects on the cytoskeleton and RhoA pathway.

5.3 Cytoskeletal defects in MYO9A-deficient NSC-34 cells

Based on the aforementioned functions of MYO9A, to assess whether loss of MYO9A impacts the cytoskeleton in nerve cells, immunofluorescence was performed on MYO9A KD NSC-34 cells for 3 of the major cytoskeletal components: β-tubulin, neurofilament (light chain) and F-actin (Figure 5.3A). Observation of protein localisation showed an apparent decrease in perinuclear fluorescence intensity for β-tubulin and neurofilament in MYO9A KD cells. F-actin-positive extensions from the MYO9A KD cells also have a different morphology to those observed in control cells, with a much denser staining pattern and the presence of stress-fibre like structures across the cell body.

Quantification of fluorescence intensity revealed a significant decrease in the amount of β-tubulin in MYO9A KD cells as compared to controls ($p<0.0001$, Mann Whitney test, Figure 5.3B). There was also a decrease in the amount of fluorescently labelled neurofilament light chain detected ($p<0.0001$, Mann Whitney test). Conversely, there was a significant increase in the expression of F-actin in MYO9A KD cells ($p=0.0016$, Mann Whitney test).

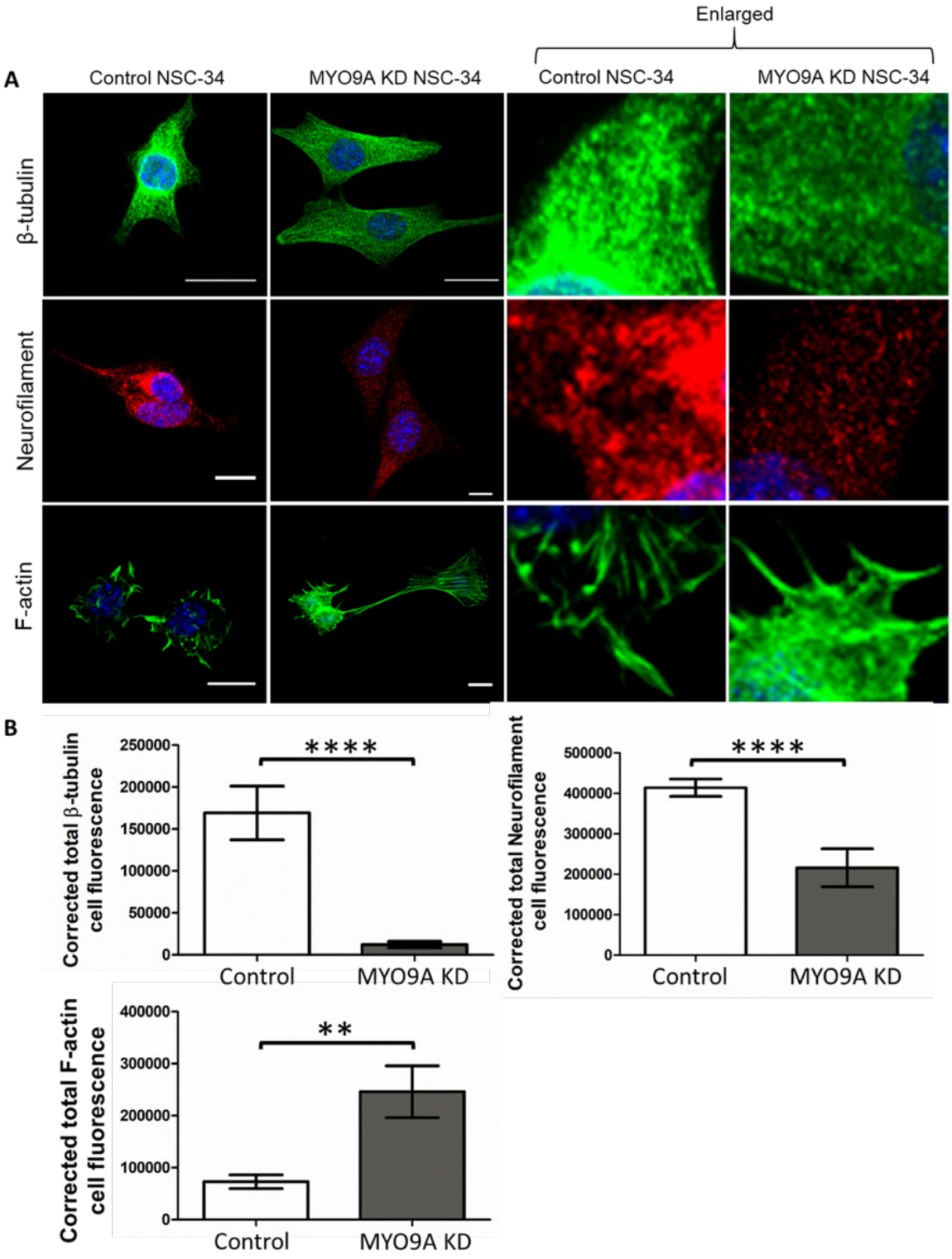

Figure 5.3. Quantification of cytoskeletal protein immunofluorescence in MYO9A KD NSC-34 cells. A. Control and MYO9A KD NSC-34 cells were stained for β-tubulin, neurofilament light chain and F(filamentous)-actin. Enlarged portions of the representative images are shown in the right hand panels. Scale bar = 10μm. B. Corrected total cell fluorescence quantified for each fluorophore in control and MYO9A KD NSC-34 cells: β-tubulin (control n=30, MYO9A KD n=28), neurofilament light chain (control n=130, MYO9A KD n=223) and F-actin (control n=41, MYO9A KD n=34), measurements corrected for cell-size. **p≤0.01, ****p<0.0001, Mann Whitney test. Error bars = mean ± S.E.M.

To confirm the results obtained using fluorescence quantification, western blots were performed for β-actin (ubiquitously expressed actin isoform) and β-tubulin (Figure 5.4). The adjusted β-tubulin density was significantly decreased in MYO9A KD cells as compared to controls (p=0.0286, Mann Whitney test). β-actin on the other hand was significantly increased, as found in the fluorescence experiment (p=0.0286, Mann Whitney test).

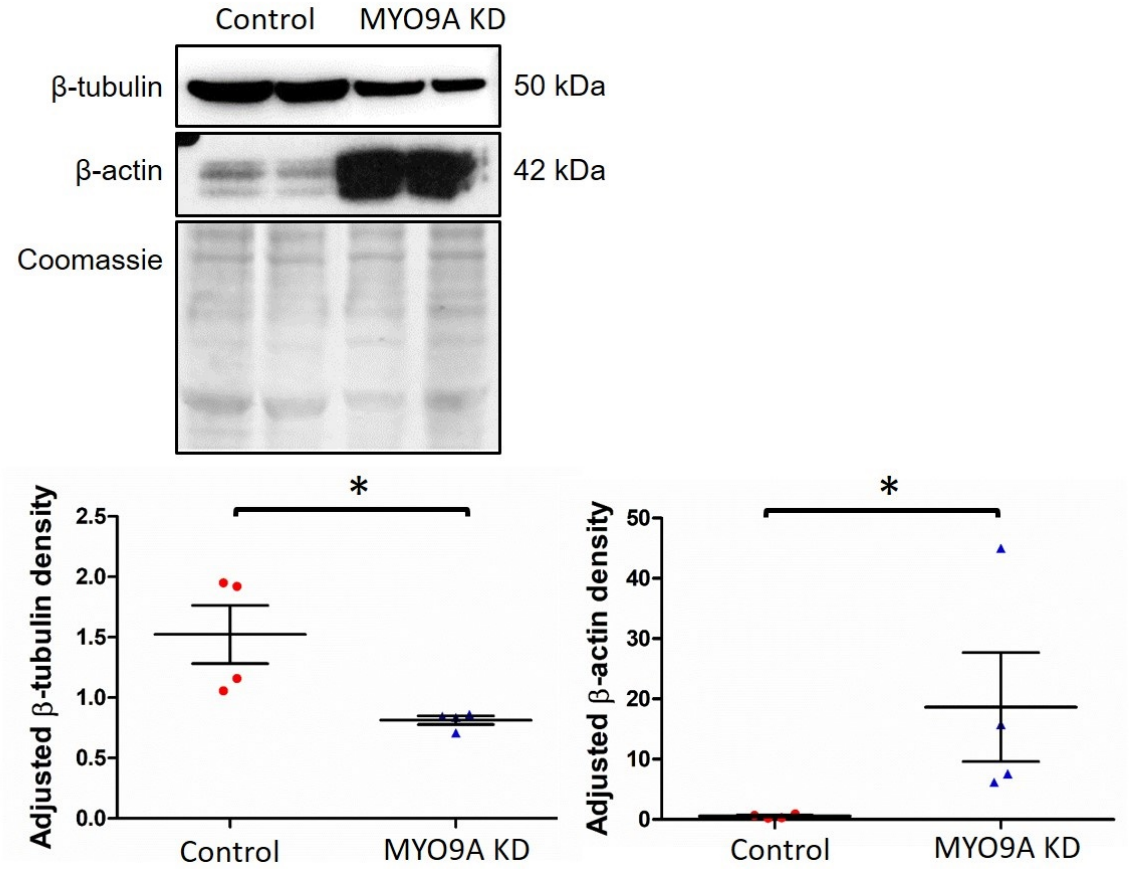

Figure 5.4. Western blot analysis of cytoskeletal proteins in cells depleted for MYO9A. Western blots were performed for β-tubulin and β-actin in control and MYO9A KD NSC-34 cells and a Coomassie used for loading control. Adjusted densities (normalised to loading control) are shown for 4 repeats and MYO9A KD results are expressed as proportion of control. *p≤0.05, Mann Whitney test, error bars = mean ± S.E.M.

Initial observations of the actin cytoskeleton in MYO9A KD cells revealed the presence of actin stress-fibre like structures. Examples of such structures stained with phalloidin are shown in Figure 5.5A. The number of MYO9A KD cells that had actin stress fibre-like bundles present was 67% higher than in control NSC-34 cells (p<0.0001, Mann Whitney test, Figure 5.5B). Using a directionality plugin available on ImageJ, the organisation of actin filaments in the cells was also assessed (Figure 5.5C). The plugin determines the direction that most structures are orientated toward, and from this calculates a degree of dispersion (standard deviation) from this value.

There was significantly less organisation (more dispersion) of actin filaments in control cells as compared to MYO9A KD cells, suggesting that more filaments were arranged into parallel stress fibre-like structures that have a similar orientation in MYO9A KD cells ($p<0.0001$, Mann Whitney test).

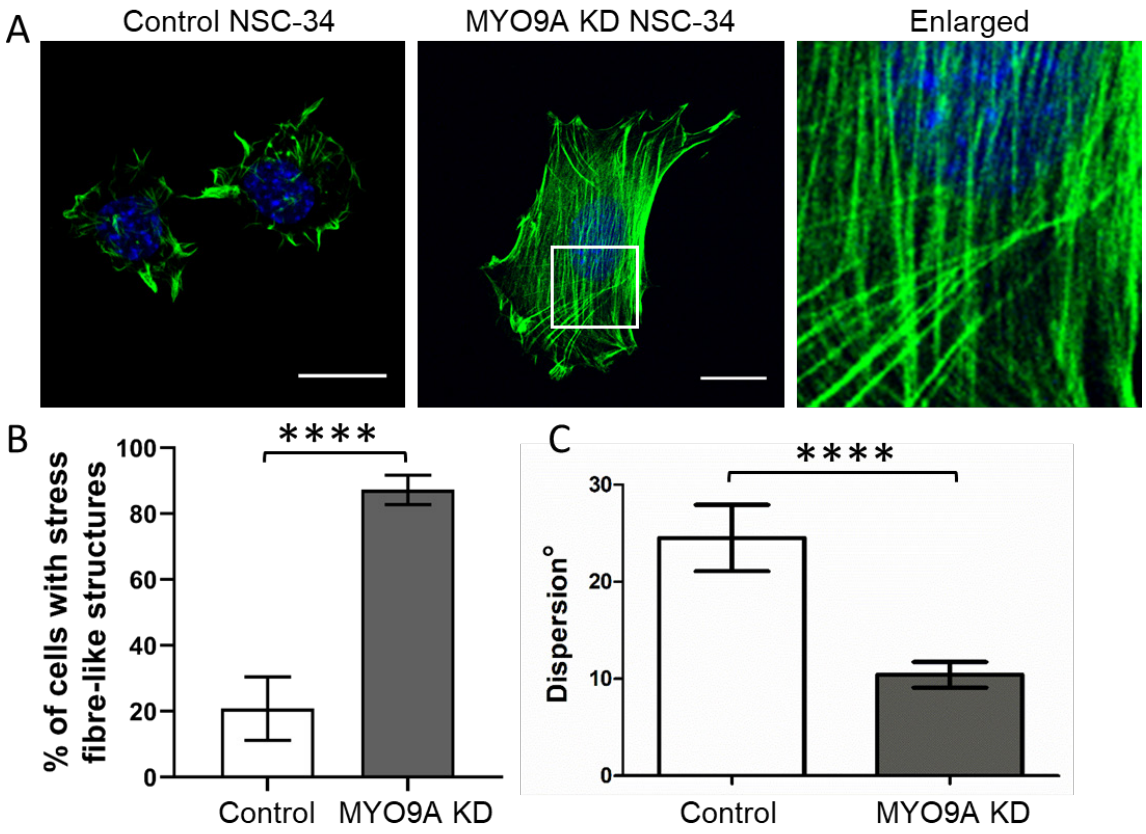

Figure 5.5. Assessment of actin stress fibre-like structures in cells depleted for MYO9A. A: Representative images showing presence of actin stress fibre-like structures in MYO9A KD cells. White box demarks enlarged region of image shown in right-hand panel. Scale bars = 20μm. B. Percentage of control (n=104) and MYO9A-depleted (n=65) NSC-34 cells that have actin stress fibre-like structures present. C: Orientation of actin positive fibres assessed using the ImageJ Directionality plugin. The dispersion of the fibre direction is shown (low dispersion = increased organisation). ****$p<0.0001$, Mann-Whitney test, Control n=75 MYO9A KD n=59, error bars represent mean ± S.E.M.

5.4 Cytoskeleton in MYO9A CMS patient cells

To determine whether the presence of *MYO9A* mutations associated with CMS also cause defects in the cytoskeleton, patient fibroblasts and iNPCs were subject to immunoblot analysis of β-tubulin, β-actin and neurofilament light chain (Figure 5.6A). Following normalisation of β-actin densities to loading control, there was a decrease in detected protein levels in MYO9A patient fibroblasts as compared to control fibroblasts (Figure 5.6B). Conversely, there was a slight increase in expression of β-actin for differentiated MYO9A patient iNPCs. There were no significant differences

between the expression of β-tubulin between patient and control fibroblasts or differentiated iNPCs (Figure 5.6C). Neurofilament light chain levels were decreased in MYO9A patient fibroblasts, as found in immunofluorescence for MYO9A KD NSC-34 cells, however in iNPCs there was a slight increase in average expression as compared to controls (Figure 5.6D). Therefore, the cytoskeleton quantification results do not consistently replicate those observed in NSC-34 cells, however more data would be required to confirm observations.

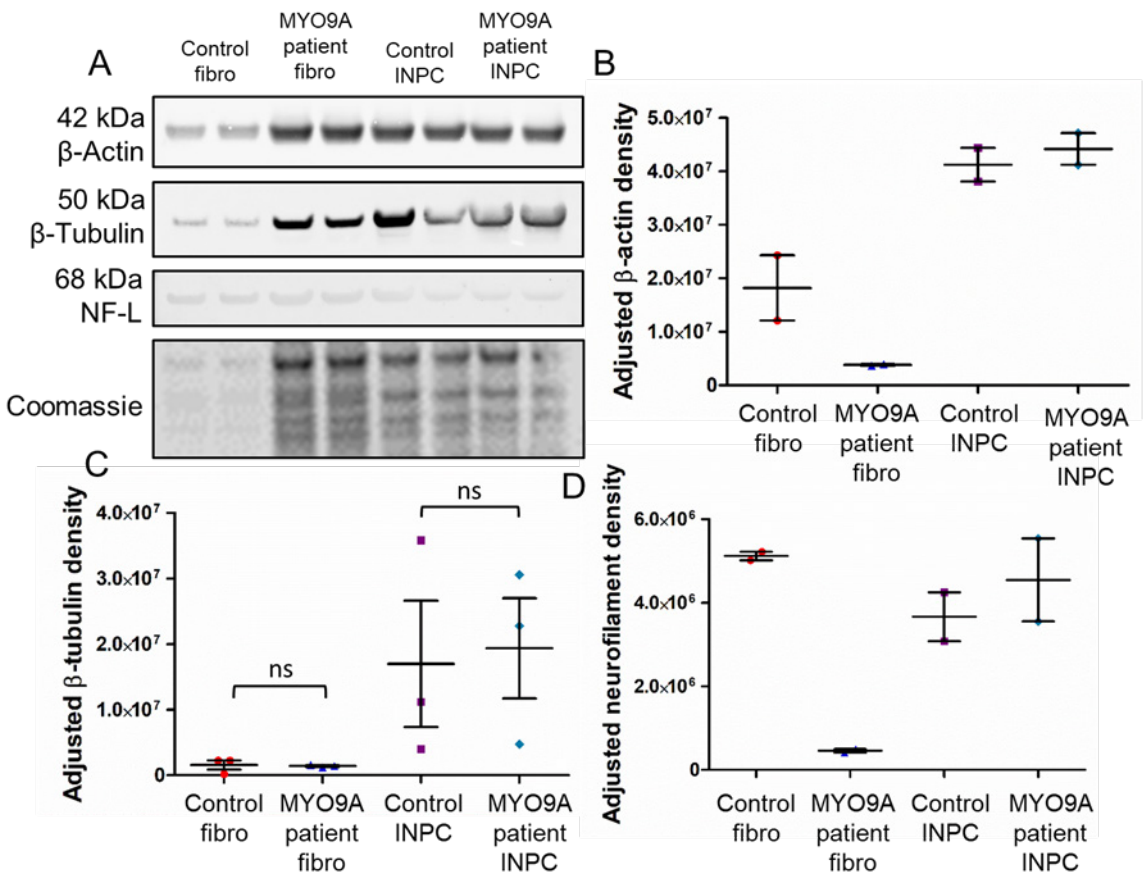

Figure 5.6. Western blot analysis of cytoskeletal proteins in MYO9A patient CMS fibroblasts and iNPCs. (A) Western blots were performed for (B) β-actin (n=2), (C) β-tubulin (n=3) and (D) neurofilament light chain (NF-L, n=2) in control and MYO9A patient fibroblasts and differentiated iNPCs, with Coomassie loading control. Adjusted densities (normalised to loading control) are shown for control and MYO9A CMS patient fibroblasts and iNPCs. ns=not significant, Mann Whitney test, error bars = mean ± S.E.M.

5.5 Cytoskeleton *in vivo*

The levels of cytoskeletal components in zebrafish and mice were also assessed in the absence of MYO9A to determine whether results reflect those obtained *in vitro.* In zebrafish, blots were performed on 48 hpf uninjected, *myo9aa/ab* crispants and *tyr* crispants (Figure 5.7). Following normalisation to loading control, as opposed to results obtained in NSC-34 cells, levels of β-tubulin were significantly increased in

zebrafish lacking Myo9aa/ab as compared to controls or *tyr* crispants (p=0.0027, p=0.0410 respectively, Unpaired t-test). Expression of β-actin, however, corroborates that found in the nerve cell-line, with a significant increase in Myo9aa/ab depleted fish as compared to controls and *tyr* crispants (p<0.0001, p=0.0002 respectively, Unpaired t-test). There was no significant difference in expression of β-tubulin or β-actin between controls and *tyr* crispant fish (p=0.4705, p=0.3613 respectively, Unpaired t-test). Therefore, knockout of MYO9A causes similar effects on amount of β-actin *in vitro* and *in vivo*, whereas β-tubulin quantities differ.

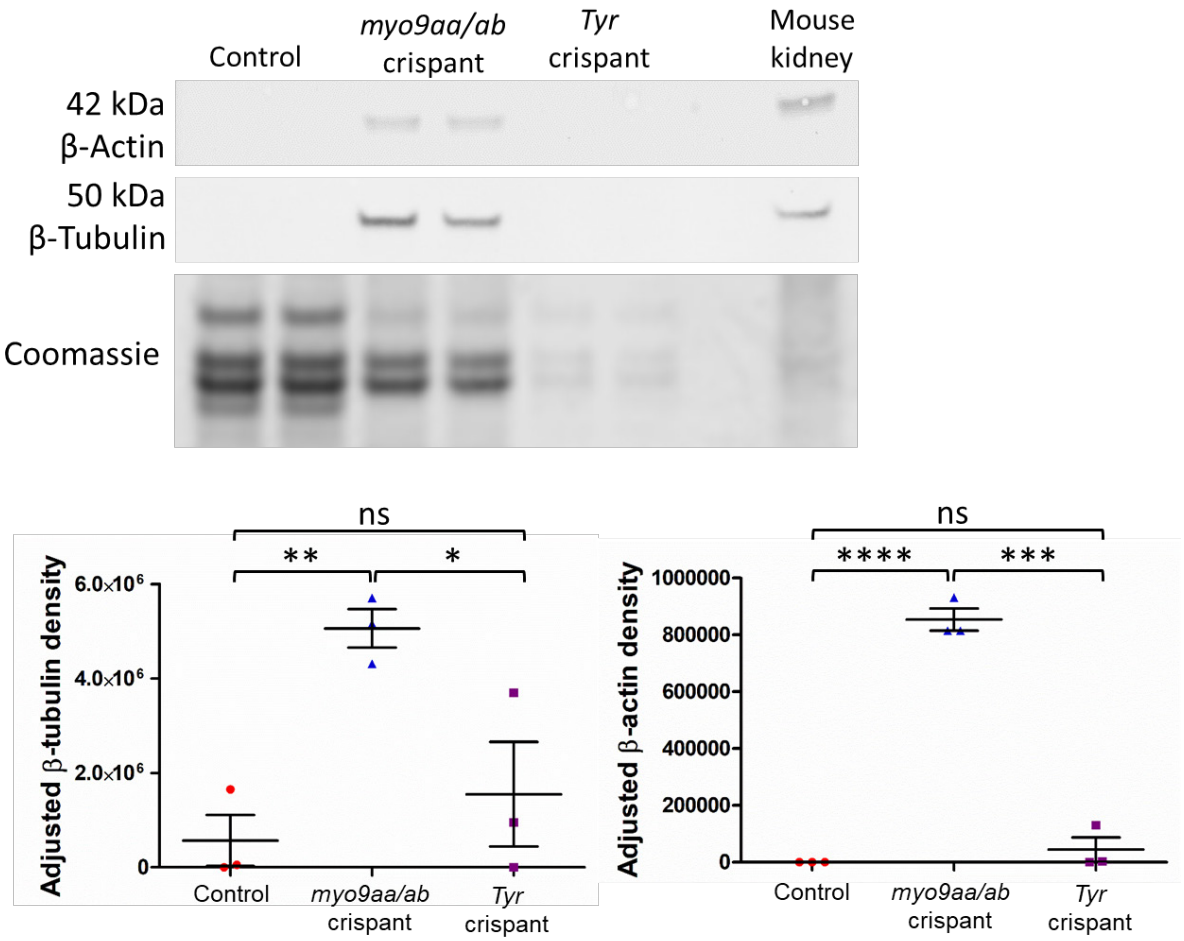

Figure 5.7. Western blot analysis of cytoskeletal proteins in *myo9aa/ab* crispant zebrafish. Western blots were performed for β-tubulin (n=3) and β-actin (n=3) in control, *myo9aa/ab* crispant and *tyr* crispant zebrafish, with a Coomassie loading control. Mouse kidney was included as a positive control. Adjusted densities (normalised to loading control) are shown. NS=not significant, *p≤0.05, **p≤0.01, ***p≤0.001, ****p<0.0001, Mann Whitney test, error bars = mean ± S.E.M.

Wildtype and MYO9A KO mice were also subject to immunoblot analysis for cytoskeletal proteins using gastrocnemius, quadriceps and heart tissues, as well as kidney and tibialis anterior muscle for β-tubulin (Figure 5.8). Levels of β-tubulin after normalisation to loading control were significantly decreased in mutant

gastrocnemius as compared to wildtype ($p<0.0001$, Mann Whitney test). Levels were also reduced in quadriceps muscle but this was not significant ($p=0.1268$, Mann Whitney test), and there was no consistent change in tibialis anterior muscle ($p=0.9338$, Mann Whitney test). Heart and kidney expression of β-tubulin appeared unaffected by absence of MYO9A. Levels of neurofilament or β-actin were not significantly different between wildtype and mutant animals for any tissue measured. Therefore, results obtained in the MYO9A KO mouse for the gastrocnemius muscle reflect those observed in the NSC-34 cells depleted for MYO9A, however, there is a lack of consistent changes for the other cytoskeletal components/tissues.

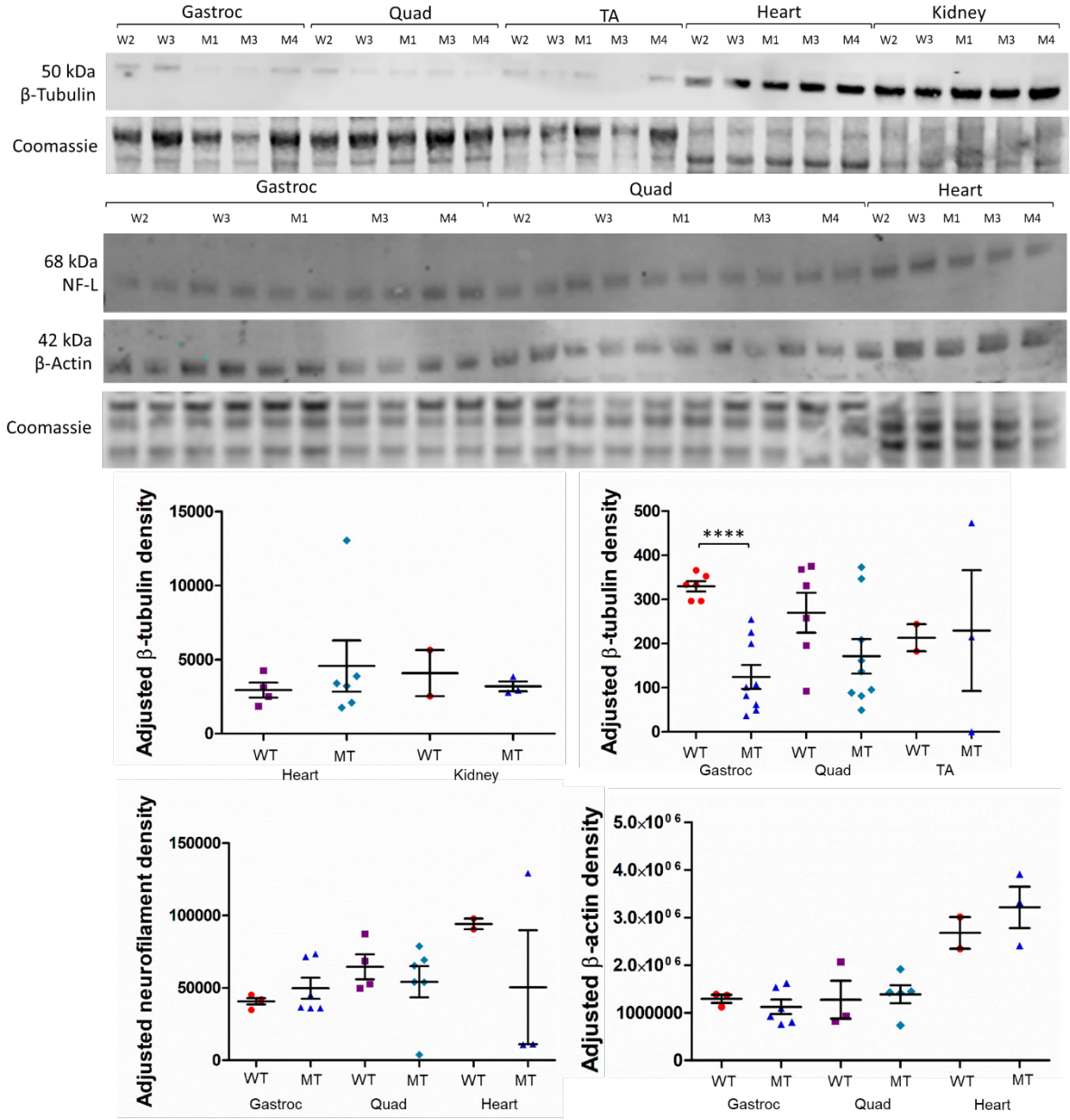

Figure 5.8. Western blot analysis of cytoskeletal proteins in MYO9A KO mice. Western blots were performed for β-tubulin in heart, kidney, gastrocnemius (Gastroc), tibialis anterior (TA) and quadriceps (Quad) muscles of wildtype (WT) and MYO9A KO (MT) mice, with a Coomassie loading control. β-actin and neurofilament (light chain) were also subject to western blot analysis in Gastroc, Quad and Heart tissues. Adjusted densities (normalised to loading control) are shown. ****p<0.0001, Mann Whitney test, unlabelled pairs are not significant. Error bars = mean ± S.E.M. Data from 2 wildtype and 3 mutants pooled for analysis.

5.6 Effects of ROCK inhibitor treatment on cytoskeleton

RhoA mediates the action of a large range of intracellular pathways, including activation of ROCK and subsequent signalling cascades affecting components of the cytoskeleton such as microtubules and actin (Liu et al., 2015). As cytoskeletal protein quantities were found to be altered in NCS-34 cells lacking MYO9A, to determine whether this was due to the action of MYO9A on the RhoA pathway a ROCK inhibitor

(Y-27632) was applied to the cells and the assays repeated. In both control and MYO9A KD cells application of Y-27632 caused neurite extension (Figure 5.9A), as reported in the literature, thus providing evidence of effective treatment conditions (Chen et al., 2013, Gu et al., 2013).

Quantification of fluorescence intensity was performed (Figure 5.9B), revealing that while Y-27632 increased the level of β-tubulin in MYO9A KD cells, it was not significantly improved from the level in untreated cells ($p=0.0590$, Mann Whitney test). The expression of β-tubulin following treatment also remained significantly different to that in controls ($p<0.0001$, Mann Whitney test). Y-27632 application significantly decreased the level of β-tubulin in controls cells as compared to untreated ($p=0.0044$, Mann Whitney test).

Expression of F-actin was significantly reduced in MYO9A KD cells by application of Y-27632 ($p=0.0007$, Mann Whitney test), to a level that was no longer significantly different to control cells ($p=0.4836$, Mann Whitney test). Treatment of control cells did not significantly affect the level of actin present ($p=0.3903$, Mann Whitney test).

Neurofilament levels were decreased in MYO9A KD cells when compared to controls, however, Y-27632 treatment significantly decreased this further ($p=0.0416$, Mann Whitney test). Levels of neurofilament were also significantly decreased in control treated cells as compared to untreated controls ($p<0.0001$, Mann Whitney test). Therefore, application of Y-27632 and thus blockade of ROCK signalling significantly improved levels of F-actin in the MYO9A KD cells but not neurofilament or β-tubulin.

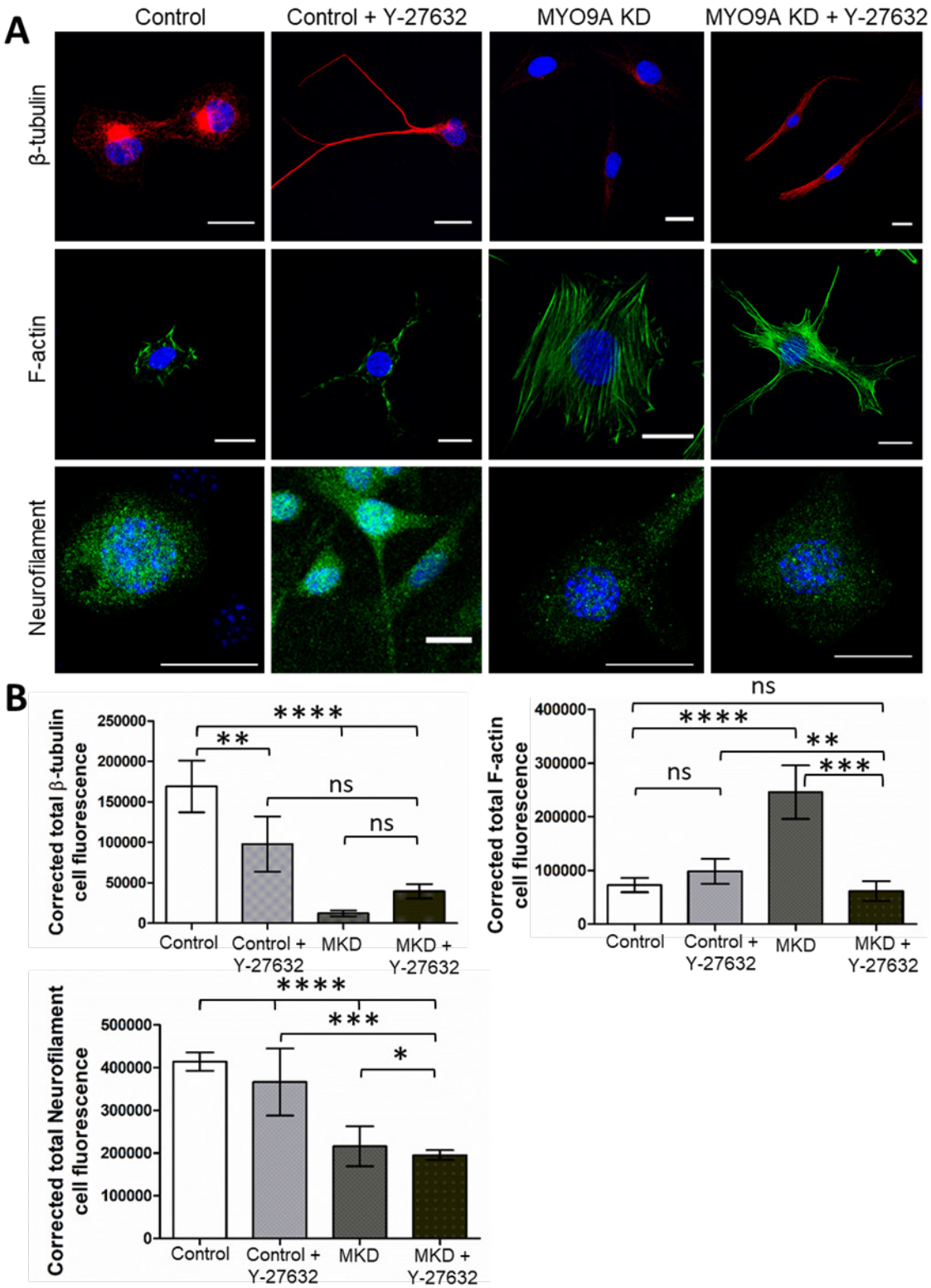

Figure 5.9. Analysis of cytoskeleton in presence of Y-27632. A. Immunofluorescent staining of control and MYO9A-depleted NSC-34 cells with and without over-night treatment of ROCK inhibitor: Y-27632 (10μM). β-tubulin, neurofilament light chain and F-actin were assessed. Scale bars = 20μm. (B) Graphs showing the corrected total cell fluorescence for levels of β-tubulin ($n > 26$), neurofilament ($n > 87$) and F-actin ($n > 33$) in each cell/treatment condition. $p \leq 0.05$, $^{**}p \leq 0.01$, $^{***}p \leq 0.001$, $^{****}p < 0.0001$, ns = not significant, Mann Whitney test. MKD = MYO9A-depleted, error bars = mean ± S.E.M.

Western blot analysis of cells treated with Y-27632 was also performed to confirm fluorescence data (Figure 5.10). Neurofilament levels were decreased in cells lacking MYO9A, and this was increased by application of Y-27632 but not to the same level as in controls. Similarly, treatment also increased levels of neurofilament in control cells. While these trends don't reflect results observed in immunofluorescence, not enough data was obtained to perform statistics.

β-tubulin levels remained unchanged by Y-27632 treatment in MYO9A KD cells ($p=0.4857$, Mann Whitney test), thus expression was still significantly reduced when compared to controls as found in fluorescence analysis ($p=0.0294$, Mann Whitney test). Inhibitor treatment significantly decreased β-tubulin expression in control cells, as also observed using fluorescence quantification ($p=0.0294$, Mann Whitney test).

Reflecting results obtained in the immunofluorescence analysis, application of Y-27632 in MYO9A KD cells was able to reduce the expression of β-actin. However, this still remained higher than in untreated control cells. Control cells treated with the inhibitor displayed a slightly elevated expression of β-actin. Overall, western blot analysis revealed similar effects of Y-27632 treatment on cells for β-actin and β-tubulin expression, but not for neurofilament. A summary of all western blot results is shown in Table 5-1.

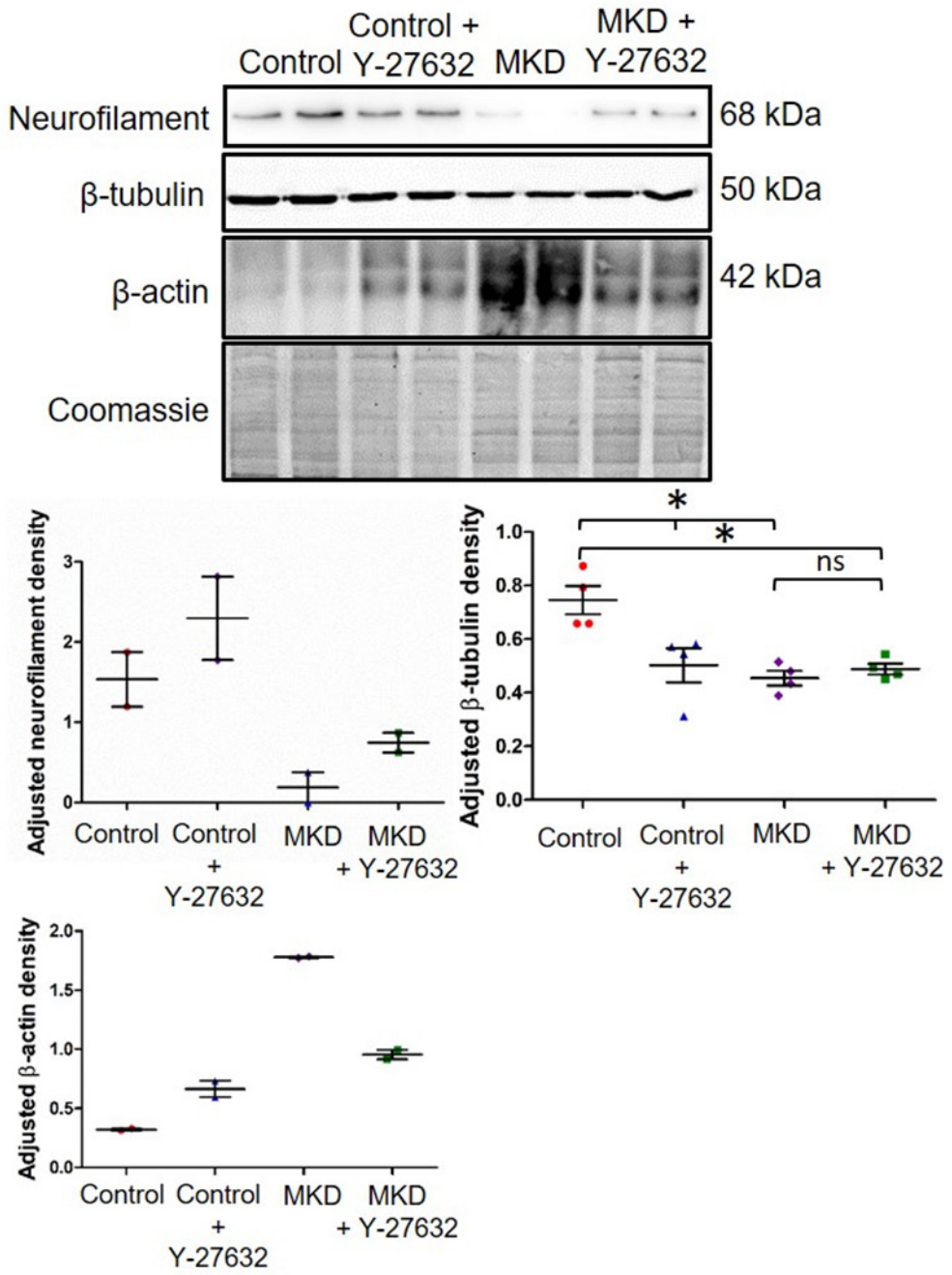

Figure 5.10. Western blot analysis of cytoskeletal proteins in the presence of Y-27632. Control and MYO9A KD (MKD) NSC-34 cells were untreated or subject to Y-27632 treatment overnight before western blot analysis of β-tubulin (n=4), neurofilament light chain (n=2) and β-actin (n=2) quantities. Coomassie used as loading control. Graphs depict the adjusted densities (normalised to loading control). *p≤0.05, ns=not significant, Mann Whitney test for β-tubulin blots. Error bars = mean ± S.E.M.

	Protein analysed by immunoblot	Neurofilament light chain	β-Tubulin	β-Actin
Compared to relevant untreated control	MYO9A KD NSC-34 cells	↓	↓*	↑*
	Control NSC-34 cells + Y-27632	↑	↓*	↑
	MYO9A KD NSC-34 cells + Y-27632	↓	↓*	↑
	MYO9A-patient fibroblasts	↓	↔	↓
	MYO9A-patient iNPCs	↔	↔	↔
	myo9aa/ab crispant		↑**	↑ ****
	tyr crispant		↔	↔
	MYO9A KO mouse TA		↔	
	MYO9A KO mouse Gastroc	↔	↓****	↔
	MYO9A KO mouse Quad	↔	↓	↔
	MYO9A KO mouse heart	↓	↔	↔
	MYO9A KO mouse Kidney		↔	

Table 5-1. Summary of western blot results for MYO9A KD NSC-34 cells, patient fibroblasts and iNPCs and MYO9A KO mouse tissue lysates. Results are shown as compared to the relevant untreated control for each group. Trend of change is indicated by arrows, with no change highlighted by: ↔. Statistically significant results are described elsewhere but are labelled with appropriate number of asterisks. Red = downregulated, blue = no change, green = upregulated.

5.7 Vesicle trafficking

Due to the observed effects of MYO9A-depletion on the cytoskeleton, it was hypothesised that this may lead to a downstream impact on vesicle trafficking, a process highly dependent on the appropriate structure of the cytoskeleton. If vesicle trafficking were impaired, this may provide insight into how MYO9A could cause impaired function of the NMJ, as transport of proteins to the NMJ, out of the terminal and into the cleft and also uptake of proteins from muscle or Schwann cells are crucial for proper function.

5.7.1 FM-dye in NSC-34 cells and iNPCs

In order to test whether there is a global defect in endo/exocytosis from NSC-34 cells depleted for MYO9A, an FM-dye assay was performed using FM 1-43. FM-dyes become brightly fluorescent when taken up into the membrane of endocytosing vesicles, therefore dye was applied to the cells for different time periods to measure its uptake and release over time (Figure 5.11A). Quantification of fluorescence

intensity was performed at times 1, 3, 6, 9 ,12, 15 and 18 mins, to allow time for vesicle internalisation and subsequent spontaneous release (Figure 5.11B, Bertrand et al., 2006, Zefirov et al., 2006). No significant differences in fluorescence intensity were identified at 1 or 3 mins ($p=0.6478$, $p=0.3235$ respectively, Unpaired t-test). At 6 mins, control cells had taken up significantly more dye than MYO9A KD cells ($p=0.0220$, Unpaired t-test), whereas by 9 mins, control cells exocytosed significantly more dye than MYO9A KDs ($p=0.0014$, Unpaired t-test). A significant increase in uptake then occurred in MYO9A KD cells from 12 – 18 mins as compared to controls ($p< 0.0001$, $p=0.0037$, $p< 0.0001$ respectively, Unpaired t-test).

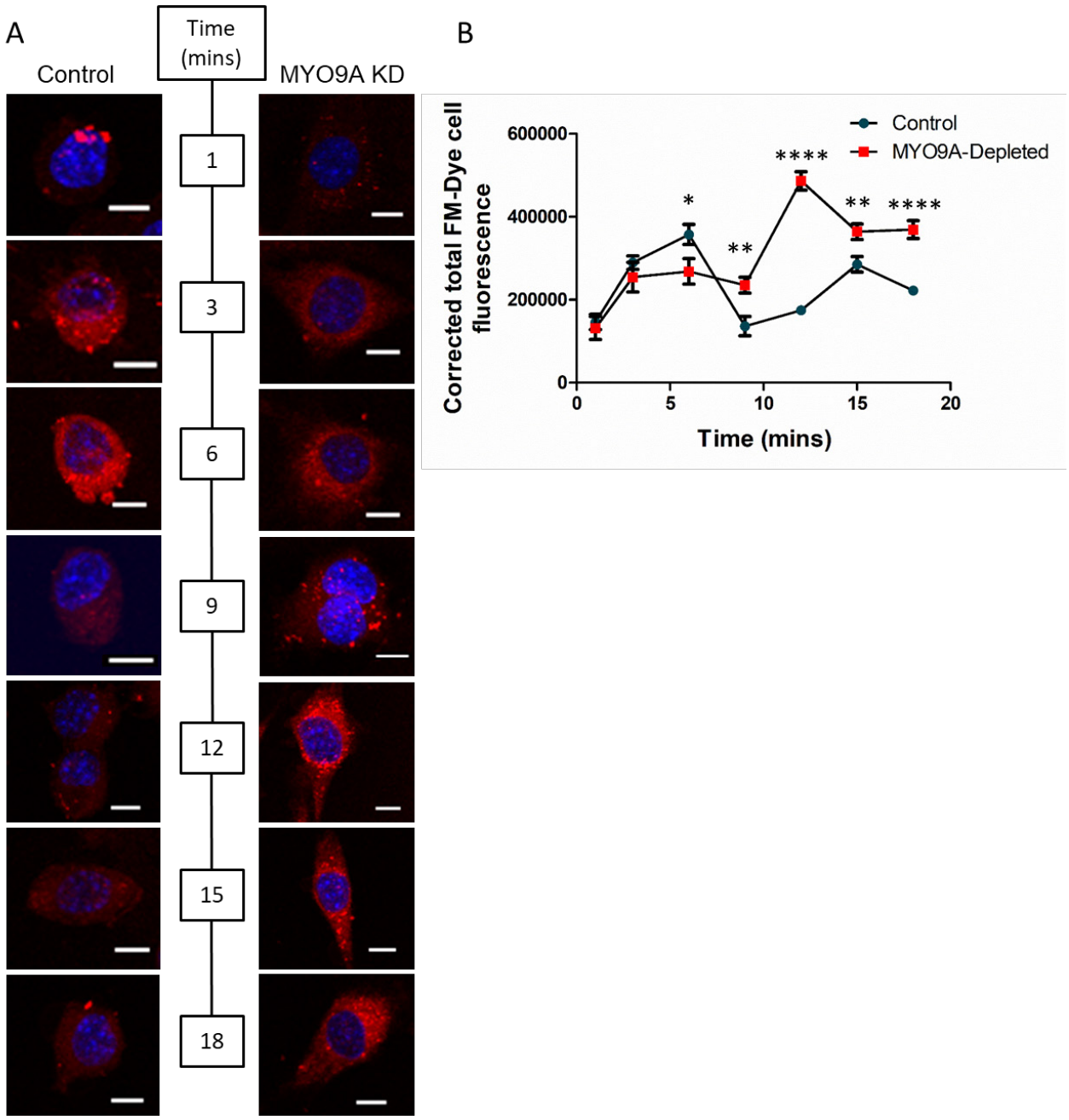

Figure 5.11. Global endo/exocytosis analysis using FM-Dye in MYO9A-depleted cells. A: Control and MYO9A KD NSC-34 cells were exposed to FM 1-43 dye for between 1 and 18 mins before fixation for quantification at different time points. Uptake of dye into membrane of endocytosing vesicles creates a fluorescent signal (red). Scale bar = 10μm. B: Graph displaying the corrected total internal FM-Dye cell fluorescence at different time points, *p≤0.05, **p≤0.01, ***p≤0.001, ****p<0.0001, Unpaired t-test. Error bars = mean ± S.E.M, 1-9 mins n>100, 12-18 mins n>36.

While evidence of disrupted cytoskeleton was not obtained from preliminary western blot analysis in patient fibroblast or iNPCs, samples were limited and thus results not conclusive. In order to determine whether the differentiated iNPCs had similar defects in endo/exocytosis as the MYO9A KD NSC-34 cells, a FM-dye assay was also performed. In this assay cells were incubated with FM 1-43 for 1 minute to allow loading of cells. This was followed by fixation, or by washing for 10 mins then fixation,

or subsequent treatment with a high KCl solution to stimulate vesicle release for 5 or 25 mins before fixation (Figure 5.12A, Iwabuchi et al., 2014). Initial uptake of dye was significantly higher in control subject cells compared to MYO9A patient cells, as identified by increased fluorescence intensity ($p<0.0001$, Mann Whitney test, Figure 5.12B). By 10 mins, uptake had increased in MYO9A iNPCs and was significantly lower in controls ($p<0.0001$, Mann Whitney test), however, this difference was no longer significant by 15 mins ($p=0.3202$, Mann Whitney test). After 25 mins of high KCl treatment, control iNPCs exocytosed the majority of detectable FM 1-43 dye, as expected, however MYO9A KD cells retained the dye within cells and had significantly higher levels of FM 1-43 fluorescence ($p< 0.0001$, Mann Whitney test).

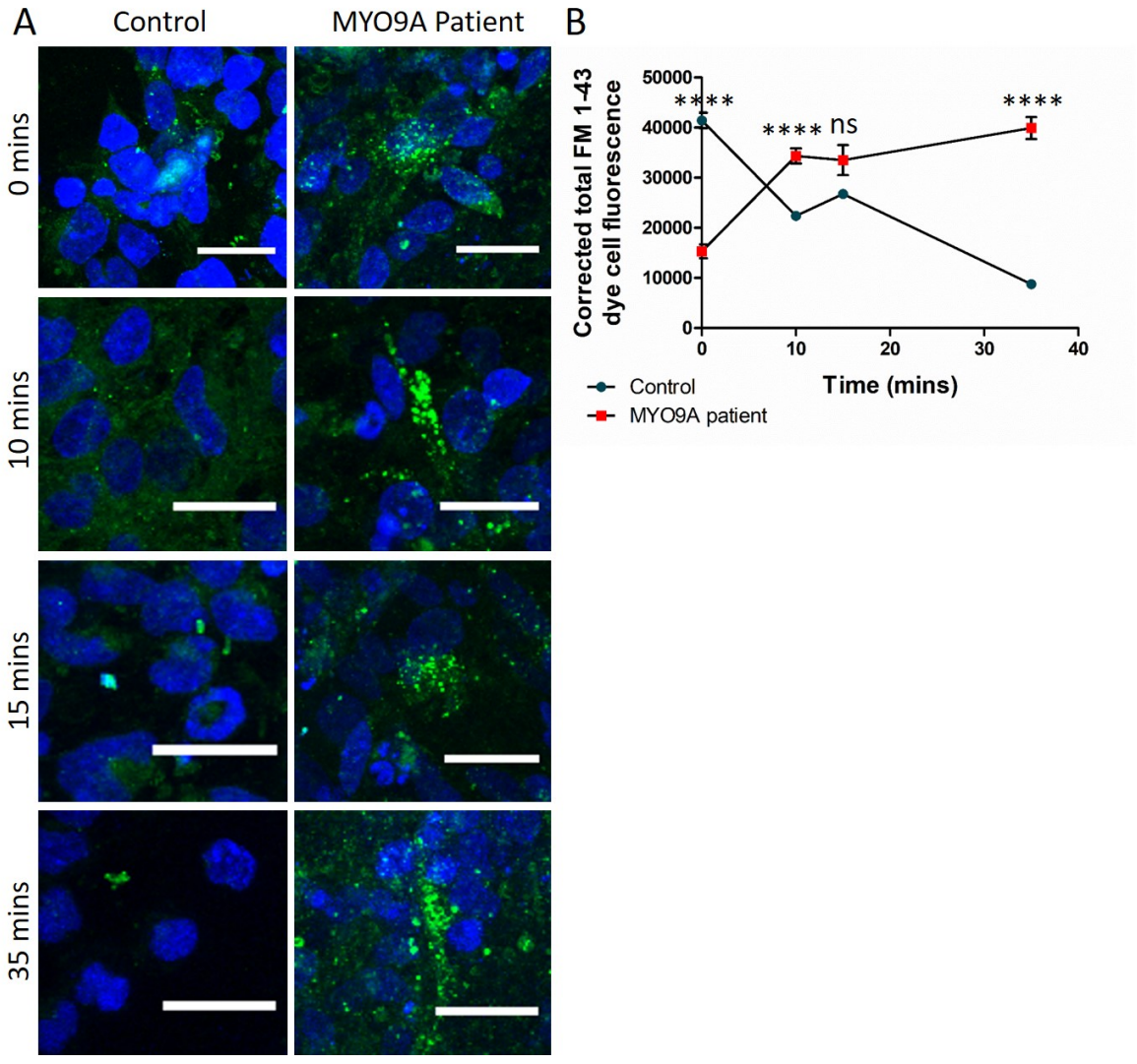

Figure 5.12. Global endo/exocytosis analysis using FM-Dye in MYO9A CMS patient iNPC cells. A: Control and MYO9A CMS patient differentiated iNPC cells were exposed to FM 1-43 dye (green) for 1 minute and then either fixed, washed for 10 mins and fixed, or subject to a further 5 or 25 mins in high KCl solution. Scale bar = 20μm. B: Graph displaying the corrected total FM-Dye cell fluorescence at different time points, ****$p<0.0001$, ns = not significant, Mann Whitney test. Error bars = mean ± S.E.M, $n>147$ per time point.

5.7.2 TrkA receptor dynamics

Following the finding that global endo/exocytosis was impaired in patient and MYO9A KD cells using FM 1-43 dye assays, the internalisation and recycling back to the surface of a paradigmatic receptor was assessed in the NSC-34 cell model. The TrkA receptor was chosen due to the ability to stimulate its internalisation using application of its high affinity ligand: NGF. Transfection of a TrkA-GFP construct was performed in both control and MYO9A KD NSC-34 cells and production of the TrkA protein was confirmed by staining cells with an anti-TrkA antibody (Figure 5.13).

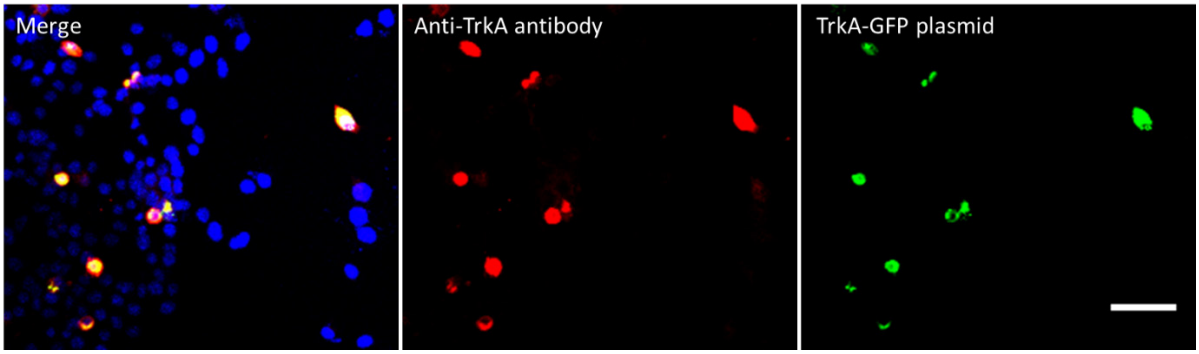

Figure 5.13. Confirmation of TrkA protein production by TrkA-GFP plasmid. Control NSC-34 cells were transfected with a TrkA-GFP (green) plasmid and stained with an anti-TrkA antibody (red) to confirm the antibody colocalises with the GFP-positive signal. Scale bar = 50μm.

After 24 hours the proportion of cells with receptors on the surface or internalised was determined. Example images of receptor position classification are shown in Figure 5.14A. Cells were classified before application of NGF, and then immediately following application and at 10, 30, 60 and 180 minute time points thereafter (Figure 5.14B). An initial decrease in the number of cells expressing surface receptors occurred following application of NGF, as expected, with no significant difference between control and MYO9A KD cells ($p=0.3429$, Mann Whitney test). In control cells almost all receptors had returned to the surface by 60 mins post-NGF application, which was complete by 180 mins. However, MYO9A KD cells had significantly fewer cells with surface receptors at these time points, and did not reach the same level of surface as expression as preNGF within the 180-minute time frame ($p=0.0286$, $p=0.0284$, Mann Whitney test).

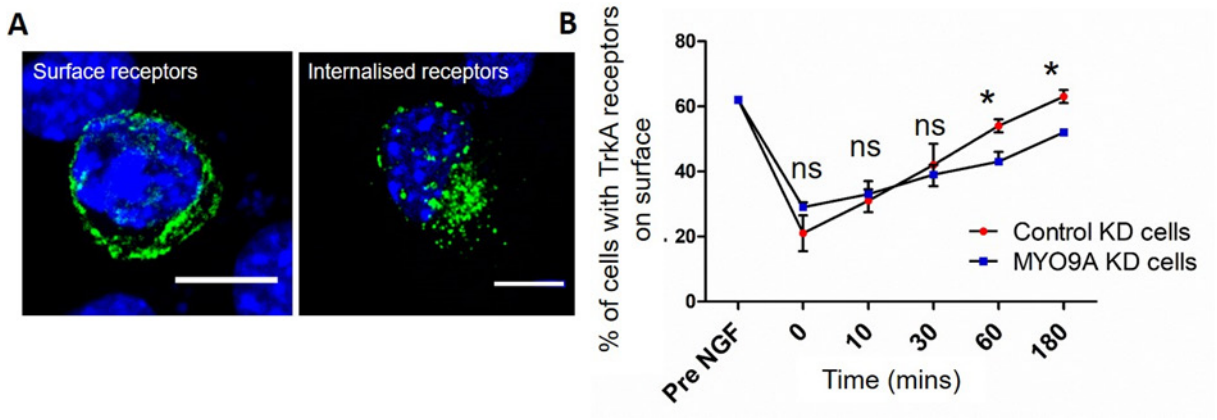

Figure 5.14. Internalisation of paradigmatic receptor in control and MYO9A KD NSC-34 cells. A. Control and MYO9A KD NSC-34 cells were transfected with a TrkA-GFP construct (green). Representative images for classification of surface and internalised TrkA-GFP receptors. Scale bars = 10μm. B. Graph depicting the change in TrkA receptor localisation over-time following NGF application to induce internalisation. Values have been normalised to pre-NGF levels to allow direct comparison at each time point and error bars represent the mean ± S.E.M from 4 repeats, NGF = nerve growth factor, *p≤0.05, ns = not significant, Mann Whitney test, n=200.

A reduction in the number of receptors returning to the surface in MYO9A KD cells could be indicative of disrupted trafficking processes, however it could also be explained by increased degradation of receptors within the cell. To explore this option, the level of TrkA expression over the time period of the experiment was also measured using western blotting. As shown in Figure 5.15, the expression of TrkA decreased over 180 mins in both control and MYO9A KD cells, with no significant difference between the two expression levels (p=0.6428, p=1.000, p=0.700, time 0, 60 and 180 mins respectively, Mann Whitney test). Thus increased protein degradation does not appear to account for the reduced surface expression of TrkA receptors in cells depleted for MYO9A.

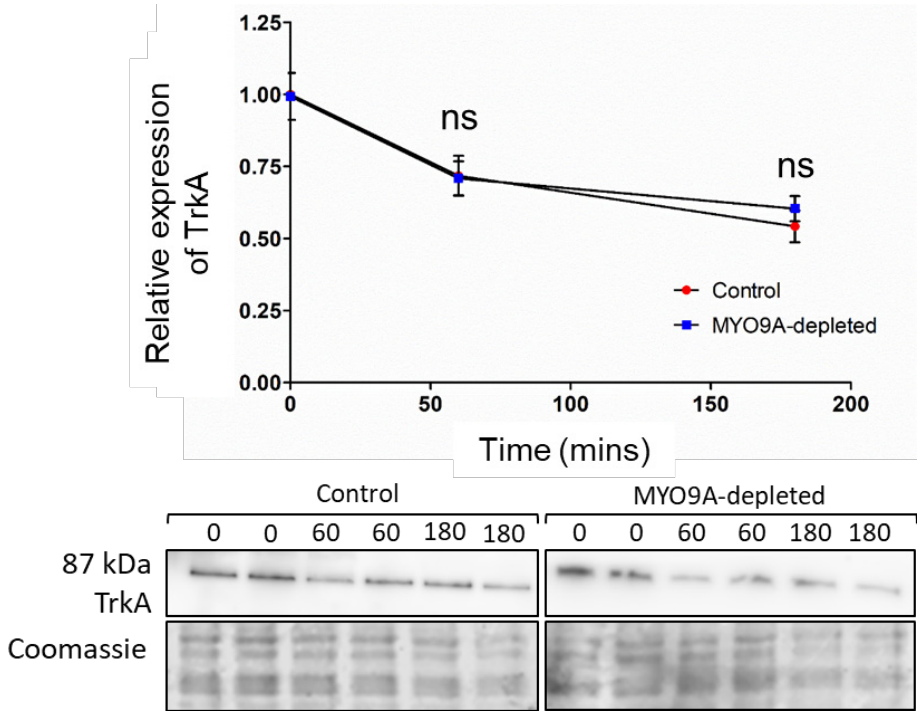

Figure 5.15. Expression of TrkA in control and MYO9A KD cells at time 0, 60 and 180 min, following application of nerve growth factor. Results shown are relative to control cells at time 0 min. Example blots are shown under the graph with Coomassie loading controls. Error bars represent mean ± S.E.M from 3 repeats. ns = not significant, Mann Whitney test.

5.7.3 TrkA trafficking and Y-27632 treatment

Following the observation that there is not increased degradation of TkrA receptors in MYO9A KD cells as compared to controls, a basic tracking experiment was performed to determine whether trafficking of receptors is impaired. Control and MYO9A KD NSC-34 cells were transiently transfected with TrkA-GFP and 24 hours later were subject to live-cell imaging over 10 minute periods (Figure 5.16). The speed of GFP-positive receptors was tracked using IMARIS software (x64 v8.4.0).

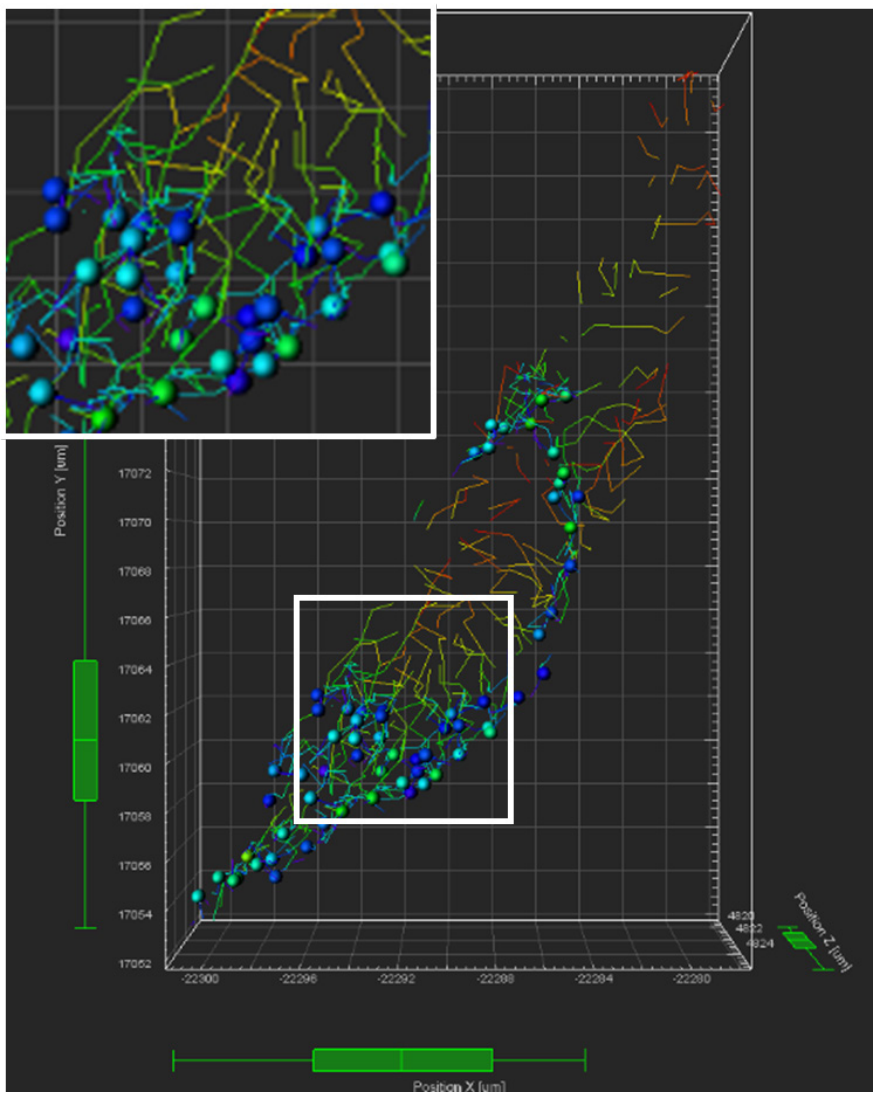

Figure 5.16. IMARIS-based tracking of TrkA-positive vesicles over time. TrkA-GFP clusters were imaged over periods of 10 mins in individual cells and IMARIS used to select and track the movement of individual clusters. Coloured spots represent the cluster/vesicles and the pathways moved are shown as coloured lines. Enlarged region in white box.

In cells depleted for MYO9A, receptors moved significantly slower than in controls ($p<0.0001$, Mann Whitney test, Figure 5.17A). As it was demonstrated that cells have a disrupted cytoskeleton and that expression of some cytoskeletal proteins can be rescued by the application of Y-27632, this was tested to see if blocking the ROCK pathway would improve the speed of intracellular receptor movement. In control cells, overnight treatment with 3nM Y-27632 caused a significant reduction in the speed of TrkA movement ($p<0.0001$, Mann Whitney test), however, in MYO9A KD cells it caused a significant improvement in speed, although not to the same level as untreated controls ($p<0.0001$, Mann Whitney test). As it was hypothesised that transport machinery would be disrupted due to the impact of MYO9A on the cytoskeleton, the result of independent disruption of the cytoskeleton on intracellular

transport was also tested (Figure 5.17A,B). Treatment of control cells with 1µg/ml Cytochalasin-D for 1 hour (disrupts actin cytoskeleton) or 10µM Nocodozole for 5 hours (affects β-tubulin network) caused a significant decrease in the speed of GFP-positive receptor movements within the cells ($p<0.0001$, Mann Whitney test).

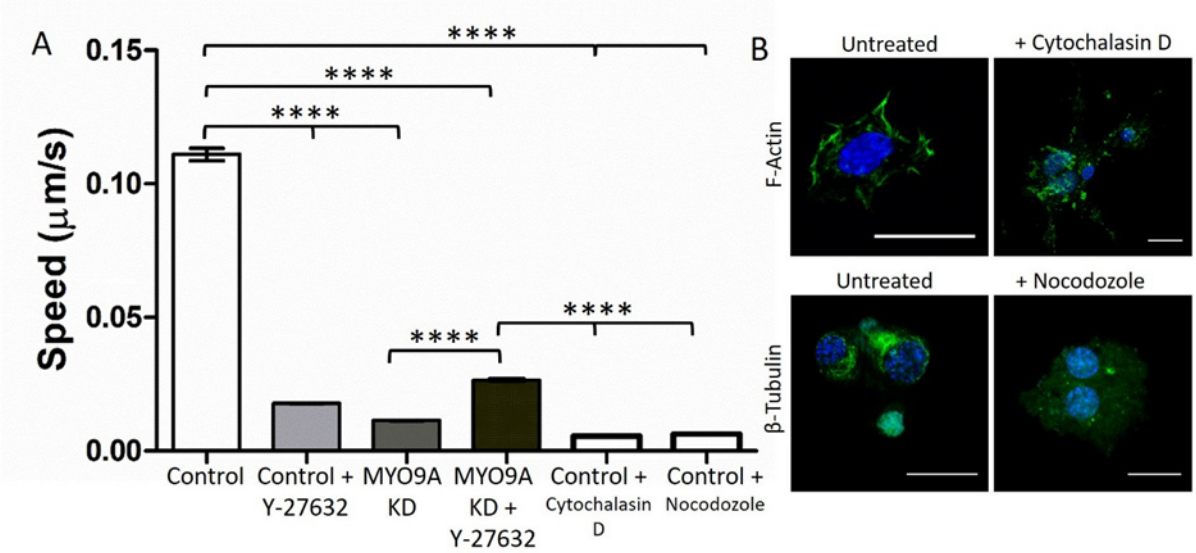

Figure 5.17. Trafficking of TrkA receptors in MYO9A KD NSC-34 cells in presence of Y-27632. A. Speed of internalised TrkA-GFP-positive receptors tracked in live cells imaged over 10 mins. Control and MYO9A KD NSC-34 cells were either untreated or treated with a ROCK inhibitor (Y-27632). Controls cells were also subject to Cytochalasin D (1µg/ml) or Nocodozole (10µM) to disrupt the actin and β-tubulin networks, respectively. Absolute values are shown and error bars represent mean ± S.E.M, ****$p<0.0001$, Mann Whitney test, n=10 cells per condition. B. Representative images of cytoskeletal disruption, identified with fluorescent labelling of β-actin or β-tubulin, are shown for control NSC-34 cells, scale bars = 25µm.

5.8 Rho kinase inhibitor therapy in *myo9aa/ab* crispant zebrafish

In this chapter, evidence has been provided for a beneficial effect of inhibiting the ROCK pathway *in vitro* using the inhibitor Y-27632. Application of this drug to NSC-34 cells depleted for MYO9A revealed a partial restoration of cytoskeletal disruption and defects in the intracellular trafficking of a paradigmatic protein. As Y-27632 was used in an experimental setting, a clinically approved ROCK inhibitor (fasudil) was trialled for effectiveness in the zebrafish crispant model (Okumura et al., 2017). The effects of fasudil on survival rate, motor behaviour and NMJ morphology were assessed, providing insight into whether suppression of an over-active RhoA/ROCK system would be beneficial *in vivo* as well as in the cell model.

5.8.1 Dose-finding experiments for fasudil in zebrafish

Fasudil has been approved for use in humans, and has previously been applied to zebrafish and other animals (Philip et al., 2017, Gunther et al., 2017, Shibuya et al.,

1992). Concentrations in zebrafish that were trialled previously range from 0.01–75μM and an EC50 of 3.85μM was reported, however, the exact treatment regimen and how it was administered was not clear (Philip et al., 2017). Therefore, for this study concentrations from 1nM to 100μM were tested and fasudil was administered in zebrafish E3 medium, as oral administration of the drug is effective in murine systems (Gunther et al., 2017). Wildtype and *myo9aa/ab* crispant fish were treated from 7 hpf until 48 hpf and their survival rates recorded for each concentration (Figure 5.18A). Survival rates were variable throughout the concentration ranges, however, 75% of controls survive without treatment, and this decreases to 66% at 100μM fasudil. Crispant fish have a survival rate of 66%, which increases to a maximum of 92% with treatment at concentrations of 1μM and 10μM fasudil.

These preliminary positive effects on survival in crispant fish were further supported by functional analysis: the effect on motor behaviours during development. In order to find an appropriate dose to use for detailed NMJ analysis, a concentration that improves the movement of the fish was desired. Therefore, crispant fish were subject to chorion movement analysis at 24 hpf, following fasudil treatment from 7hpf at the aforementioned concentrations. Untreated crispants performed on average 0.88 chorion movements per minute (Figure 5.18B), and this improved as concentration was increased, reaching 4.4 movements per minute at 100μM fasudil. While this was the largest number of chorion movements, at this concentration the survival of crispant fish had started to decline. Therefore, based on the positive improvements obtained from 10μM fasudil for both survival and movement, this concentration was selected for the subsequent study.

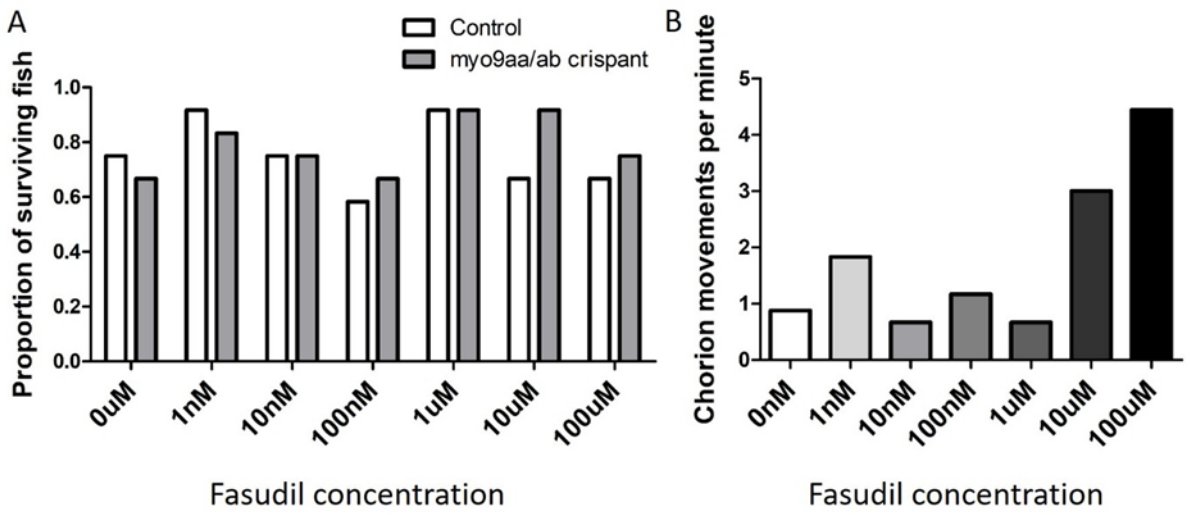

Figure 5.18. Dose-finding experiments for fasudil treatment in zebrafish. A. Control and *myo9aa/ab* crispant zebrafish were treated with fasudil from 7 hpf at concentrations from 1nM to 100μM. Survival rates were assessed at 48 hpf and are expressed as a proportion of treated fish per concentration (12 fish per concentration). B. Fasudil-treated *myo9aa/ab* crispant fish were subject to chorion movement analysis at 24 hpf at varying concentrations of drug from 1nM to 100μM (6 fish per concentration).

Utilising the selected concentration of 10μM fasudil, the survival analysis was repeated on a larger number of fish that were also used for downstream analysis of movement and NMJ morphology (Figure 5.19). In this experiment, 98% of control fish survived to 48 hpf, which decreased to 88% with treatment, however this was not significant (p=0.6634, Kruskal-Wallis test). Crispant fish had a significantly lower survival rate than controls of 63% (p=0.0024, Kruskal-Wallis test), which was significantly increased to 91% with fasudil application (p=0.0009, Kruskal-Wallis test).

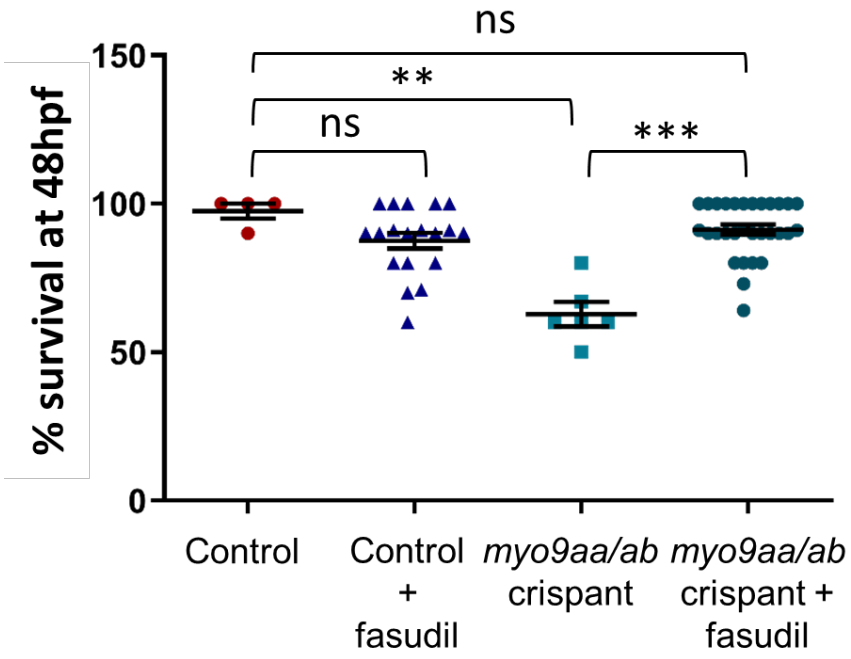

Figure 5.19. Survival rates for fasudil-treated control and *myo9aa/ab* crispant zebrafish. Control (n=4) and *myo9aa/ab* crispant (n=6) fish were treated with 10μM fasudil (control n=19, crispant n=30) at 7 hpf and survival assessed at 48 hpf. Results expressed as percentage of fish survived per condition. **p≤0.01, ***p≤0.001, ns=not significant, Kruskal-Wallis test.

5.8.2 Behavioral analysis

As performed for assessment of Myo9aa/ab depletion, motor behaviors following application of fasudil were also tested to determine whether inhibiting the ROCK pathway leads to functional improvements *in vivo*.

At 24 hpf the chorion movement assay was repeated with 10μM fasudil on control and crispant fish (Figure 5.20). As previously described, there was a significant decrease in the chorion movements performed by *myo9aa/ab* crispants as compared to controls (p=0.0004, Kruskal-Wallis test). Application of fasudil significantly decreased chorion movements in control fish, but improved them in crispants, however, this was not significant (p<0.0001, p>0.9999 respectively, Kruskal-Wallis test).

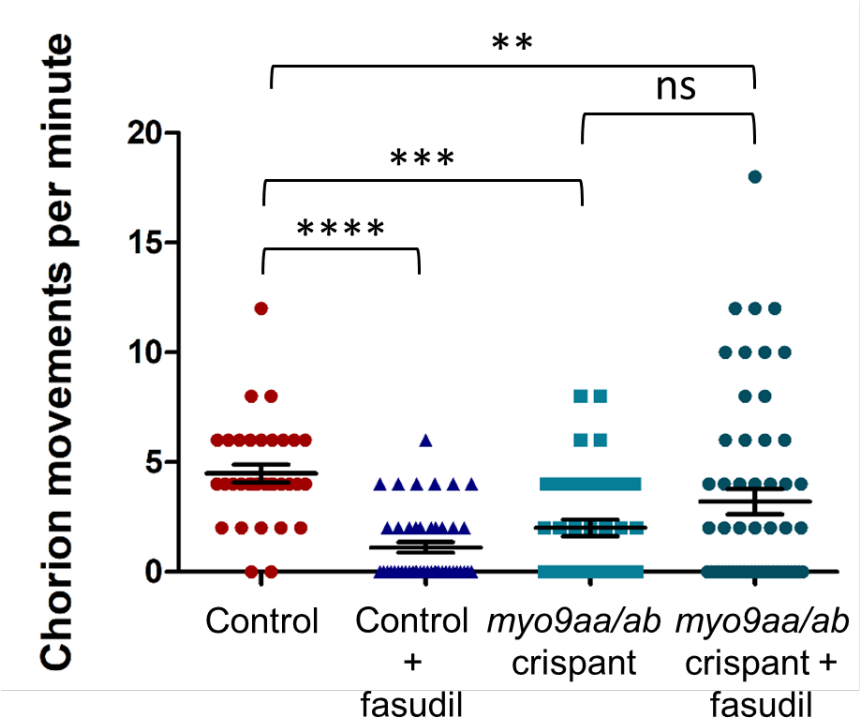

Figure 5.20. Movements performed by fasudil-treated zebrafish within the chorion at 24 hpf. Full chorion movements performed in one minute by control (n=34), *myo9aa/ab* crispant (39), fasudil-treated control (n=45) and fasudil-treated crispant (n=56) zebrafish at 24 hpf. Error bars = mean ± S.E.M. **p≤0.01, ***p≤0.001, ****p<0.0001, ns = not significant, Kruskal-Wallis test.

The response of zebrafish to tactile stimulation at 48 hpf was also recorded and compared after fasudil treatment to determine if modulation of RhoA/ROCK effect the ability of fish to rapidly swim following a stimulus (Figure 5.21). Fasudil was able to significantly improve the distance the crispant fish could swim, how fast they swam and also the acceleration observed at the onset of movement (p<0.0001, p=0.0005, p=0.0025 respectively, Kruskal-Wallis test), to a level comparable with controls. No significant differences in the movement of control fish treated with fasudil were observed for any parameter. Overall, treatment of *myo9aa/ab* crispant fish with 10μM fasudil was able to significantly improve survival rates and motor behaviours.

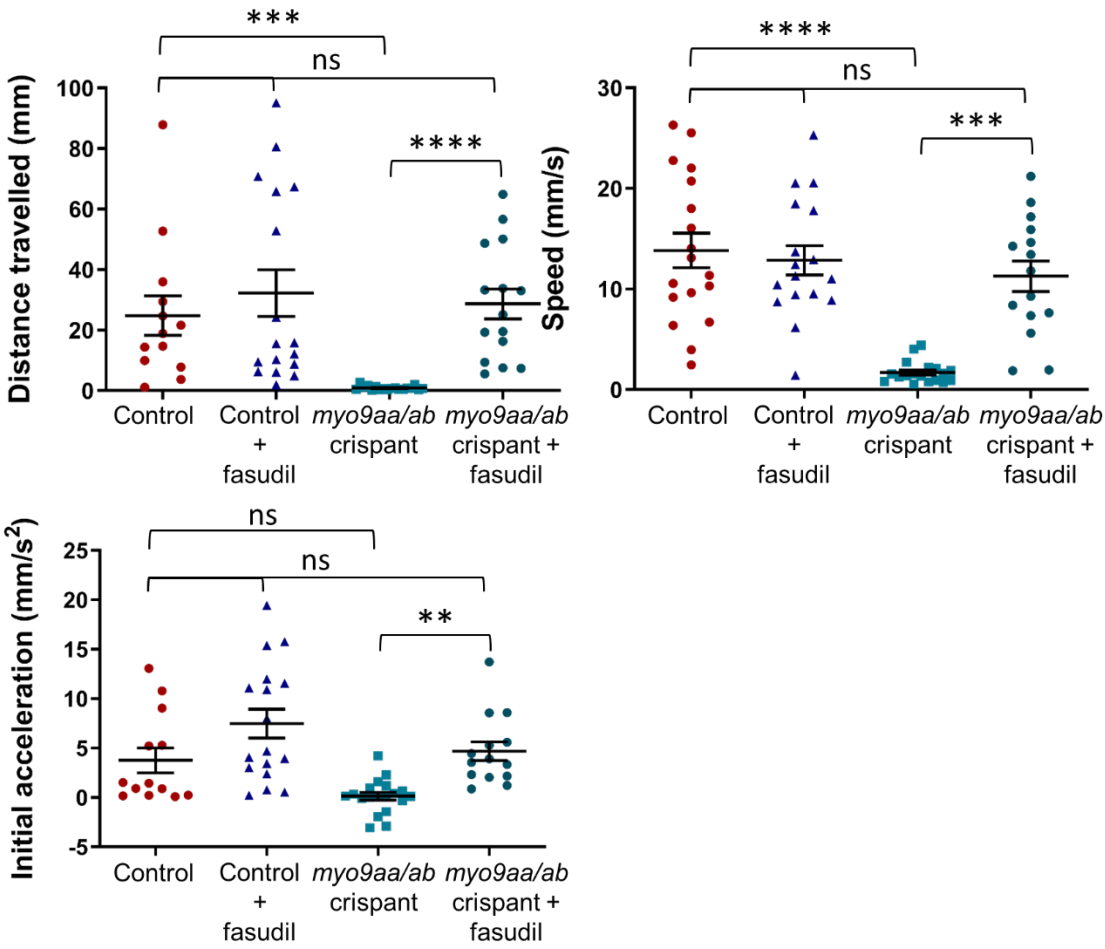

Figure 5.21. Tactile stimulation response of fasudil-treated *myo9aa/ab* crispant zebrafish. Control (n=13), *myo9aa/ab* crispant (20), fasudil-treated control (n=17) and fasudil-treated crispant (n=15) zebrafish were subject to a tactile stimulation assay at 48 hpf. Distance travelled after stimulus applied, average speed of movement and initial acceleration were quantified for each zebrafish. Error bars = mean ± S.E.M. **p≤0.01, ***p≤0.001, ****p<0.0001, ns = not significant, Kruskal-Wallis test.

5.8.3 NMJ analysis

As positive improvements in both survival and motor behaviours were observed following fasudil treatment, whether these changes were reflected at the level of the developing NMJ was also assessed. As representative images for control and *myo9aa/ab* crispants have already been shown in Chapter 4, Section 4.5.2, here only those from fasudil-treated fish are shown (Figure 5.22). Important features are present in the treated crispant fish that had been identified as defective in the untreated crispants, such as the presence of the 'choice point' AChR cluster at 24hpf, myoseptal innervation at 48 hpf and clusters of pre/postsynaptic staining over the myotomal surface at 5dpf.

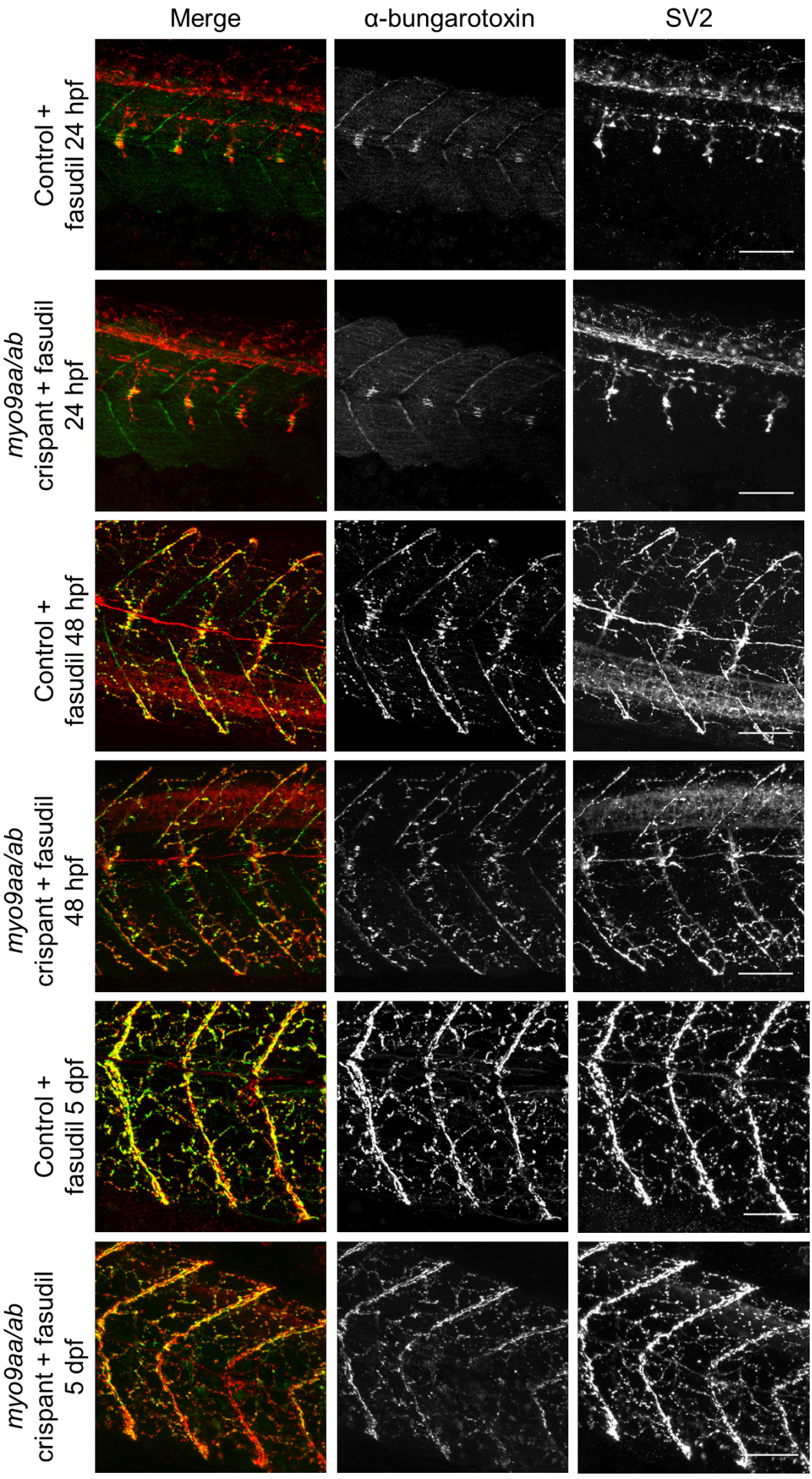
Merge
α-bungarotoxin
SV2
Control + fasudil 24 hpf
myo9aa/ab crispant + fasudil 24 hpf
Control + fasudil 48 hpf
myo9aa/ab crispant + fasudil 48 hpf
Control + fasudil 5 dpf
myo9aa/ab crispant + fasudil 5 dpf

Figure 5.22. NMJ morphology of fasudil-treated zebrafish. NMJs were visualised in control and *myo9aa/ab* crispant zebrafish at 24 hpf, 48 hpf and 5 dpf using an antibody against SV2 (red, presynaptic vesicles) and fluorophore-conjugated aBTx (green, postsynaptic AChRs). Scale bar = 50µm.

As improvements were observed in crispant zebrafish movements at 24 hpf, analysis of NMJ morphology was performed to identify if any of these parameters could be linked to such changes, results are summarised in Table 5-2. Due to variability in data and lower N numbers, the majority of differences observed were not significant (Figure 5.23). The average and total area of AChRs was decreased in *myo9aa/ab* crispant fish as compared to controls, and this rose after fasudil treatment. The same trend was also observed in the number of large AChR clusters over 20µM^2, as well as for the length of motor neuron outgrowths from the spinal cord. The proportion of myotomes exhibiting a 'choice point' cluster of AChRs was significantly decreased in crispant fish as compared to controls and treated controls (p=0.0100, p=0.0147 respectively, Kruskal-Wallis test). While the mean number of myotomes with a cluster increased after fasudil treatment, and there were no longer fish exhibiting no myotomal clustering, this improvement was not significant (p=0.2775, Kruskal-Wallis test). The size of myotomes in the crispant fish were increased following ROCK inhibitor treatment, and this was comparable to the size of control myotomes but was not a significant improvement from untreated crispant fish (p=0.0966, Kruskal-Wallis test). A similar trend also occurred for length of motor neuron extension past the choice point, for which a significant decrease in length was present in crispants but not in treated crispants, despite the improvement between untreated and treated crispants not demonstrating significance (p=0.3696, Kruskal-Wallis test).

		Compared to untreated controls		
	24 hpf NMJ parameters	Control + fasudil	myo9aa/ab crispant	myo9aa/ab crispant + fasudil
Presynaptic	Length of neuron outgrowth			
	Length of axon past choice point			
Postsynaptic	Area of aBTx clusters			
	Total area of aBTx clusters			
	Proportion of myotomes with choice point cluster			
	aBTx clusters >20µm^2			
	Size of myotomes			

Table 5-2. Summary of NMJ morphology results obtained in 24 hpf zebrafish treated with fasudil. Red = significantly less than untreated controls and blue = statistically unchanged from controls as compared to controls.

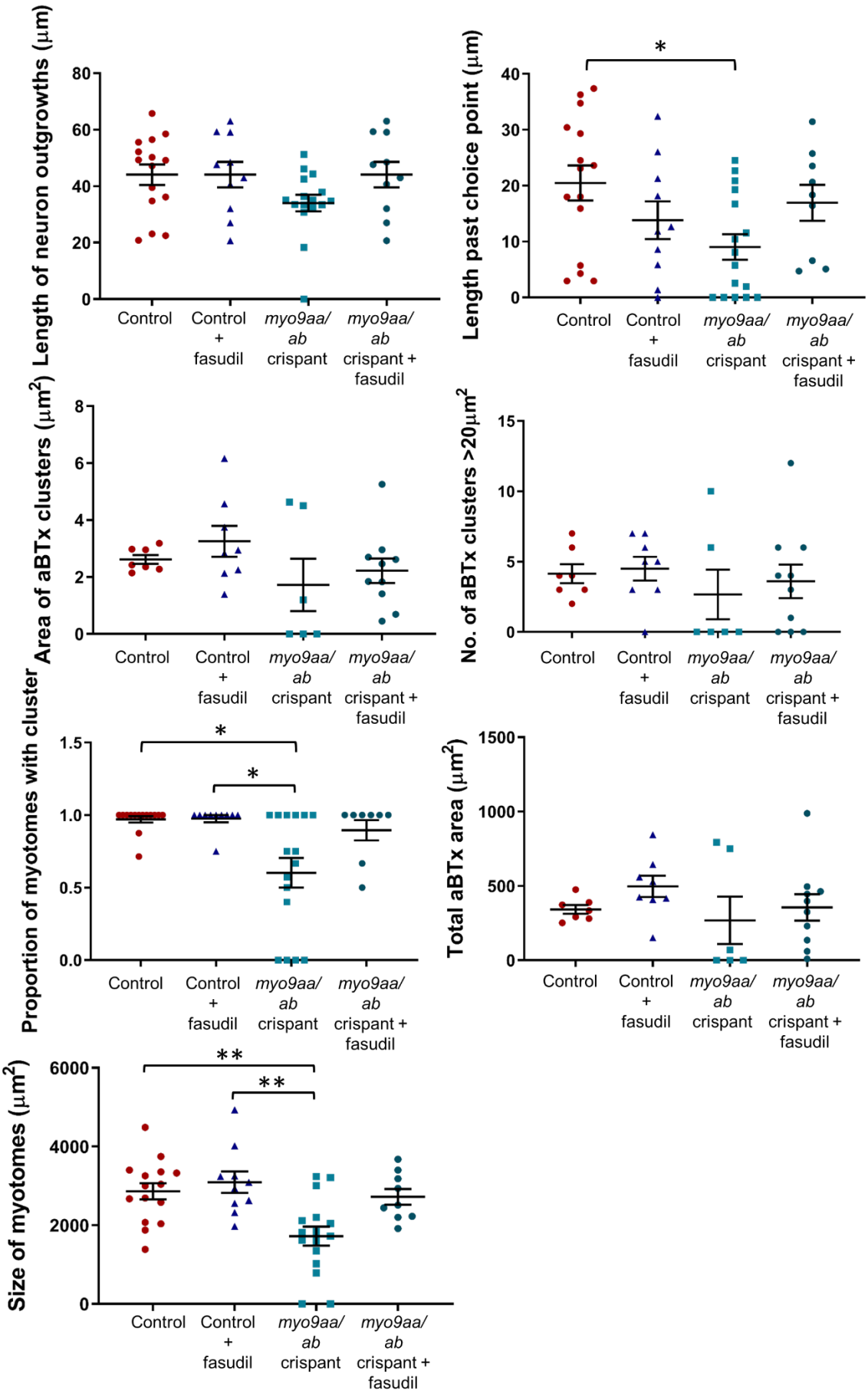

Figure 5.23. Quantification of fasudil-treated *myo9aa/ab* crispant zebrafish NMJ morphology at 24 hpf. Various features of NMJ morphology in control (n=15),

myo9aa/ab crispants (n=16), *myo9aa/ab* crispants + fasudil (n=9) and control + fasudil fish (n=10) were quantified: average and total area of acetylcholine receptor (aBTx) clusters and number over 20μm^2, size of muscle myotomes, proportion of myotomes with a cluster, the length these neurons had extended past the choice point and their overall outgrowth. Error bars = mean ± S.E.M. **p≤0.01, *p≤0.05, no comparison bar = not significant, Kruskal-Wallis test.

Improvements in distance travelled, average speed, and to a lesser extent acceleration, were all improved in fasudil-treated crispant fish at 48 hpf, thus NMJ analysis was repeated at this time point (Figure 5.24), and results are summarised in Table 5-3. There were no significant differences in the number of presynaptic clusters per myotome following fasudil treatment in crispants, however there was a significant reduction in the number of clusters for treated control zebrafish (p=0.1700, p<0.0001 respectively, one-way ANOVA). When accounting for myotome size by analysing number of clusters per 100μm^2, there was a further significant decrease in number of clusters in *myo9aa/ab* crispants following treatment (p=0.0113, one-way ANOVA). No significant differences were observed for the number of presynaptic clusters over 20μm^2, nor was any change found in the % of myoseptal innervation, although slight increases in both parameters were observed in treated crispants as compared to untreated crispants. Quantification of total and average SV2 cluster area similarly revealed no significant differences from 10μM fasudil application.

		Compared to untreated controls		
	48 hpf NMJ parameters	**control + fasudil**	**myo9aa/ab crispant**	**myo9aa/ab crispant + fasudil**
Presynaptic	SV2 clusters per myotome			
	SV2 clusters per 100μm^2			
	SV2 clusters >20μm^2			
	% innervation of myosepta			
	Area SV2 clusters			
	Total area SV2 clusters			
Postsynaptic	aBTx clusters per myotome			
	aBTx clusters per 100μm^2			
	aBTx clusters >20μm^2			
	Area aBTx clusters			
	Total area aBTx clusters			
	Size of myotomes			

Table 5-3. Summary of NMJ morphology results obtained in 48 hpf zebrafish treated with fasudil. Red = significantly less than untreated controls, blue = statistically unchanged from controls and green = significantly increased as compared to controls.

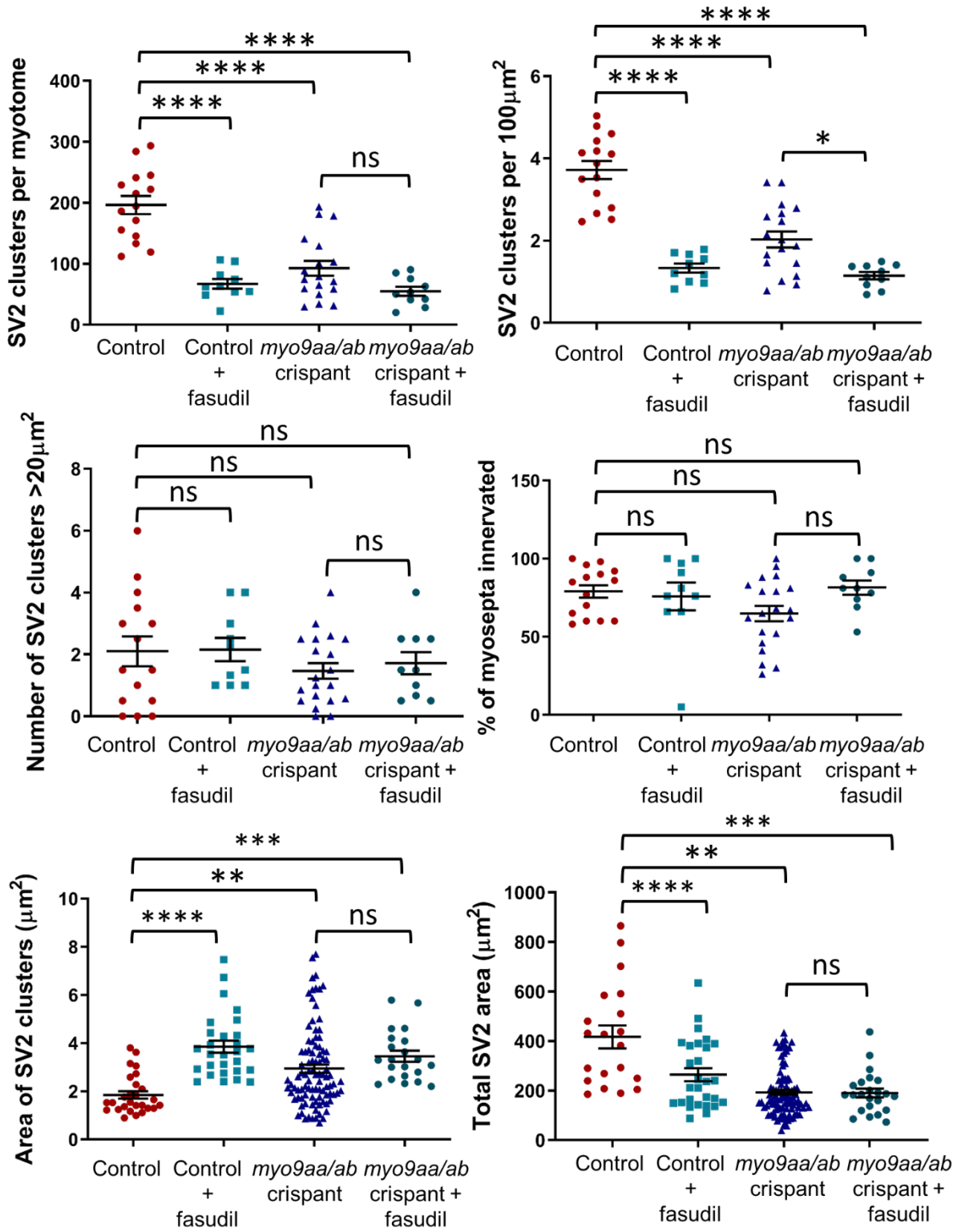

Figure 5.24. Quantification of fasudil-treated *myo9aa/ab* crispant zebrafish presynaptic NMJ morphology at 48 hpf. Various features of presynaptic NMJ morphology in control (n=15), *myo9aa/ab* crispants (n=20), control + fasudil (n=10) and *myo9aa/ab* crispants + fasudil (n=10) were quantified: number of SV2 (presynaptic) clusters per myotome, per 100µm^2 and over 20µm^2, as well as the average and total area of SV2 clusters (expressed as per myotome rather than per fish) and % of myosepta innervation. Error bars = mean ± S.E.M. *p≤0.05, **p≤0.01, ***p*<0.0001, ns = not significant, one-way ANOVA.

Analysis of postsynaptic NMJ features revealed no significant improvements in the number of AChR clusters per myotome or per 100μm^2 in the crispant fish treated with fasudil (Figure 5.25). Size of myotomes and number of large AChR clusters over 20μm^2 in area were not affected by Myo9aa/ab depletion, and fasudil application did not cause any significant alterations to these parameters. Average area of aBTx clusters was significantly increased in crispant fish ($p=0.0005$, one-way ANOVA), which was not rescued by fasudil application. Fasudil significantly increased average aBTx area in control fish ($p=0.0044$, one-way ANOVA). Conversely, total aBTx area was significantly reduced by fasudil application in control fish, and did not rescue the decrease present in crispant fish ($p<0.0001$, $p=0.0716$ respectively, one-way ANOVA).

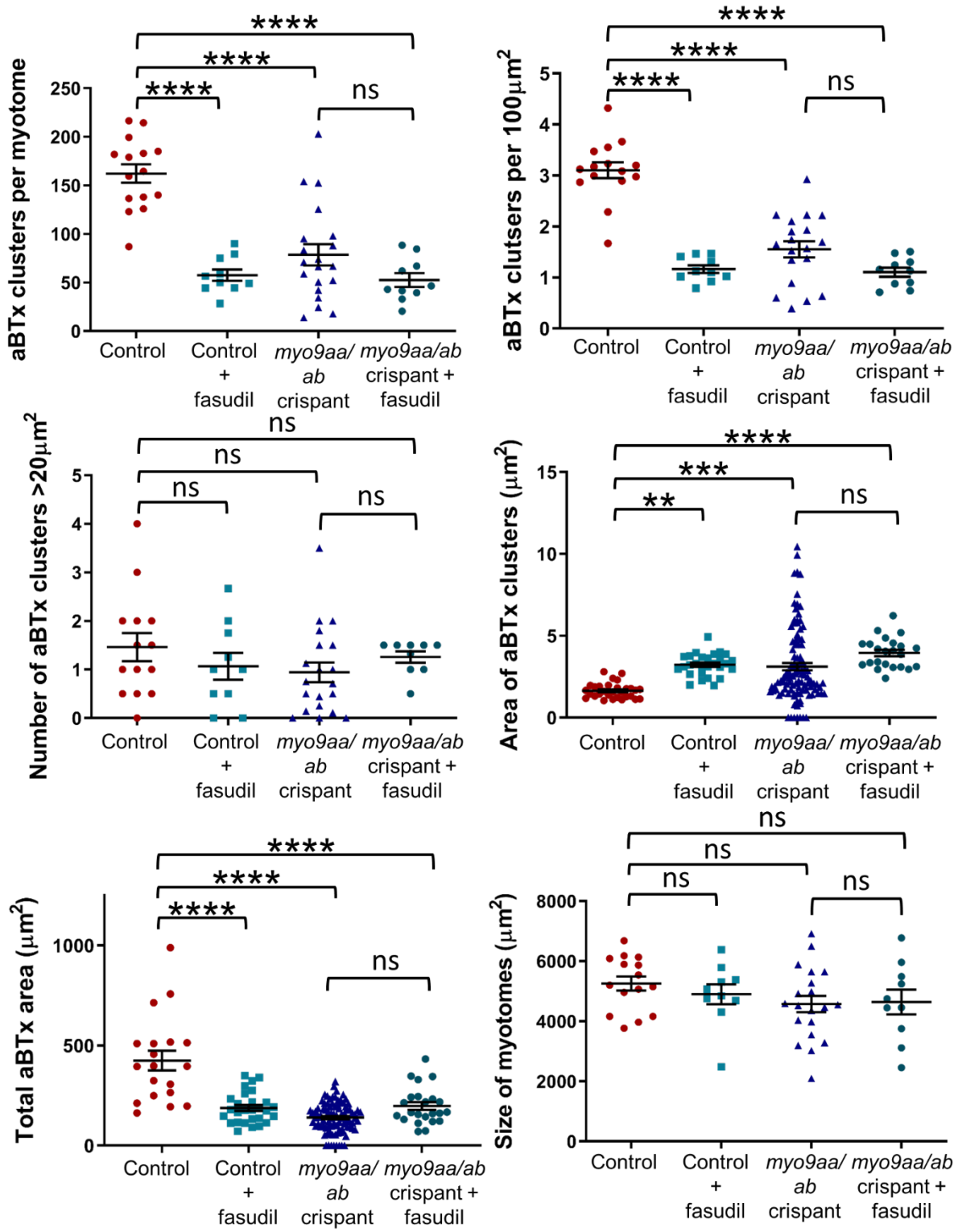

Figure 5.25. Quantification of fasudil-treated *myo9aa/ab* crispant zebrafish postsynaptic NMJ morphology at 48 hpf. Various features of postsynaptic NMJ morphology in control (n=15), *myo9aa/ab* crispants (n=20), control + fasudil (n=10) and *myo9aa/ab* crispants + fasudil (n=10) were quantified: number of aBTx (postsynaptic) clusters per myotome, per 100µm^2 and over 20µm^2, myotome size, as well as average and total aBTx area (expressed as per myotome rather than per fish). Error bars = mean ± S.E.M. *p≤0.05, **p≤0.01, ***p≤0.001****p<0.0001, ns = not significant, one-way ANOVA.

The final analysis performed on fasudil treated fish was at 5dpf, for which motor movement data was not obtained, therefore providing insights into any longer-acting changes induced by blocking the ROCK pathway (Figure 5.26, Figure 5.27). A summary of results is shown in Table 5-4. With regards to presynaptic morphological features of the NMJ, the area of presynaptic clusters was increased in crispant fish following treatment, as compared to untreated crispants and controls ($p<0.0001$, one-way ANOVA). A significant increase in area was also observed in treated control fish ($p=0.0145$, one-way ANOVA). The total area of SV2 clusters also increased in crispants and controls treated with fasudil, as compared to untreated controls ($p=0.0023$, $p=0.0072$ respectively, one-way ANOVA). The number of large clusters (over 20µm^2), was similarly increased following treatment in both control and crispant subgroups as compared to controls ($p=0.0257$, $p=0.0010$ respectively, one-way ANOVA). Following treatment with fasudil, the number of presynaptic clusters per myotome were significantly reduced in crispants as compared to controls and untreated crispants ($p<0.0001$, one-way ANOVA), however no significant change was observed in treated controls. The number of clusters per 100µm^2 had been increased by depletion of Myo9aa/ab, and this was significantly reduced by fasudil, although to a level still significantly different to controls ($p=0.0019$, $p<0.0001$, $p=0.0042$, one-way ANOVA). Percentage of myoseptal innervation was not significantly affected by treatment or depletion of Myo9aa/ab.

		Compared to untreated controls		
	5 dpf NMJ parameters	**control + fasudil**	**myo9aa/ab crispant**	**myo9aa/ab crispant + fasudil**
Presynaptic	Area of SV2 clusters			
	SV2 clusters per myotome			
	SV2 clusters per 100µm^2			
	SV2 clusters >20µm^2			
	Total SV2 area			
	% innervation of myosepta			
Postsynaptic	Area of aBTx clusters			
	aBTx clusters per myotome			
	aBTx clusters per 100µm^2			
	aBTx clusters >20µm^2			
	Total aBTx area			
	Size of myotomes			

Table 5-4. Summary of NMJ morphology results obtained in 5 dpf zebrafish treated with fasudil. Red = significantly less than untreated controls, blue = statistically unchanged from controls and green = significantly increased as compared to controls.

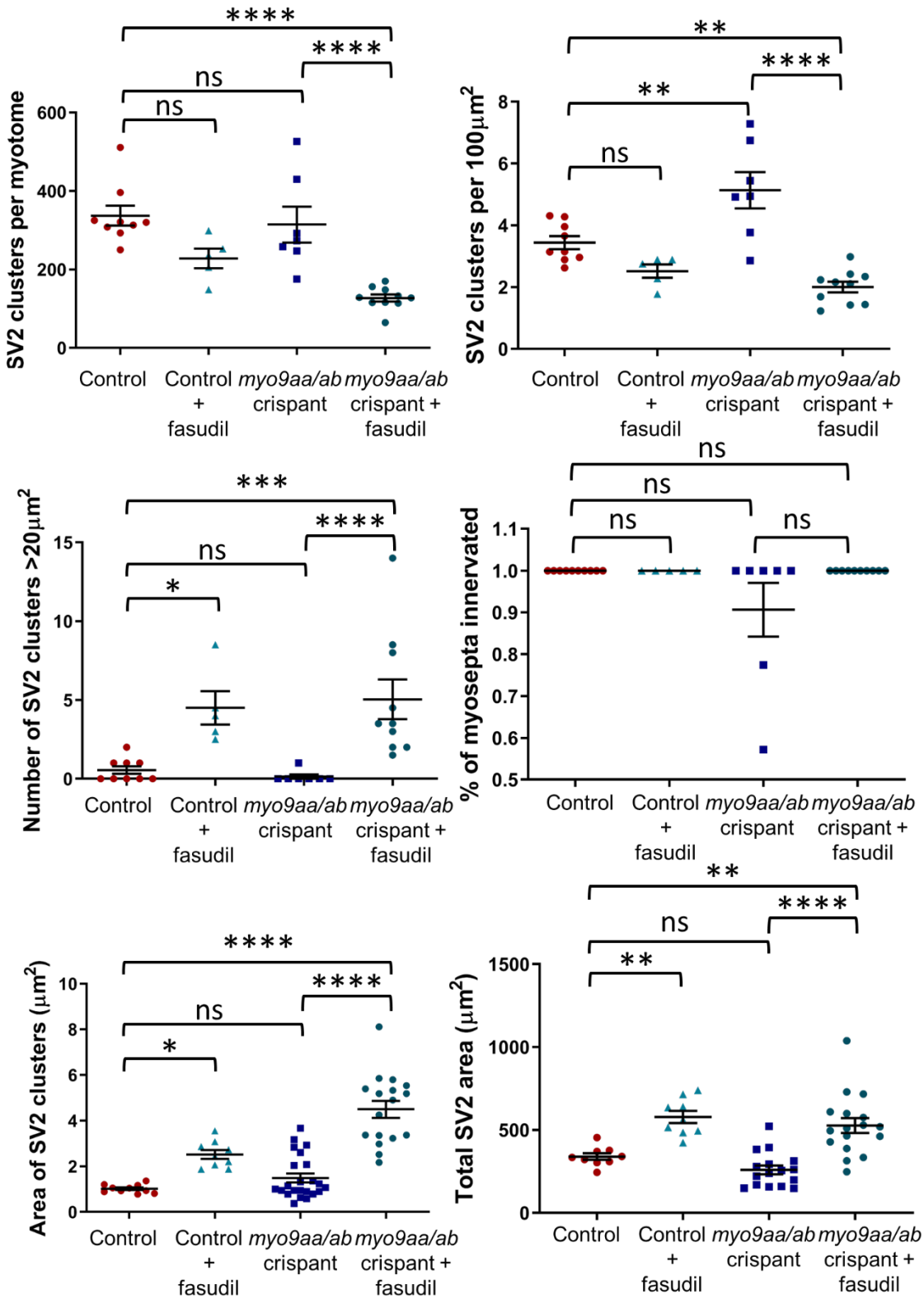

Figure 5.26. Quantification of fasudil-treated *myo9aa/ab* crispant zebrafish presynaptic NMJ morphology at 5 dpf. Various features of presynaptic NMJ morphology in control (n=10), *myo9aa/ab* crispants (n=7), control + fasudil (n=5) and *myo9aa/ab* crispants + fasudil (n=10) were quantified: average and total area of SV2 (presynaptic) clusters (expressed as per myotome rather than per fish), number of clusters per myotome, per 100µm^2 and over 20µm^2, as well as the length of myoseptal innervation and % of myoseptal innervation. Error bars = mean ± S.E.M. *p≤0.05, **p≤0.01, ***p≤0.01, ****p<0.0001, ns = not significant, one-way ANOVA.

As postsynaptic effects of ROCK inhibitor treatment were not assessed *in vitro*, they were also analysed in the zebrafish at 5 dpf (Figure 5.27). The area of postsynaptic receptors was significantly increased in treated crispant fish as compared to controls, as well as in treated controls ($p=0.0112$, $p=0.0028$ respectively, one-way ANOVA). Total aBTx cluster area was not significantly affected in controls treated with fasudil, however, treatment decreased total cluster size further in crispant fish as compared to controls ($p=0.0679$, $p<0.0001$ respectively, one-way ANOVA). The number of larger AChR clusters was only significantly elevated in control zebrafish treated with fasudil, but a slight non-significant elevation was also present in crispants ($p=0.0220$, $p=0.8949$ respectively, one-way ANOVA). No significant differences were observed in the number of AChRs per myotome or per 100μm^2, although a similar trend was observed for both parameters as treatment with fasudil decreased the number of clusters present for control and crispant zebrafish. Crispant fish had smaller myotomes at this time point as compared to controls, and this was slightly improved by application of the ROCK inhibitor ($p=0.0006$, $p=0.0016$ respectively, one-way ANOVA).

Overall, there were numerous changes in NMJ morphology induced by 10μM fasudil during development. The most promising improvements were observed in treated crispant fish at 24 hpf where length of neuron outgrowths, the presence of choice point clusters on myotomes and size of myotomes were rescued. At 5 dpf, a small number of differences in pre and postsynaptic features were observed in treated crispant fish, however, none were fully rescued.

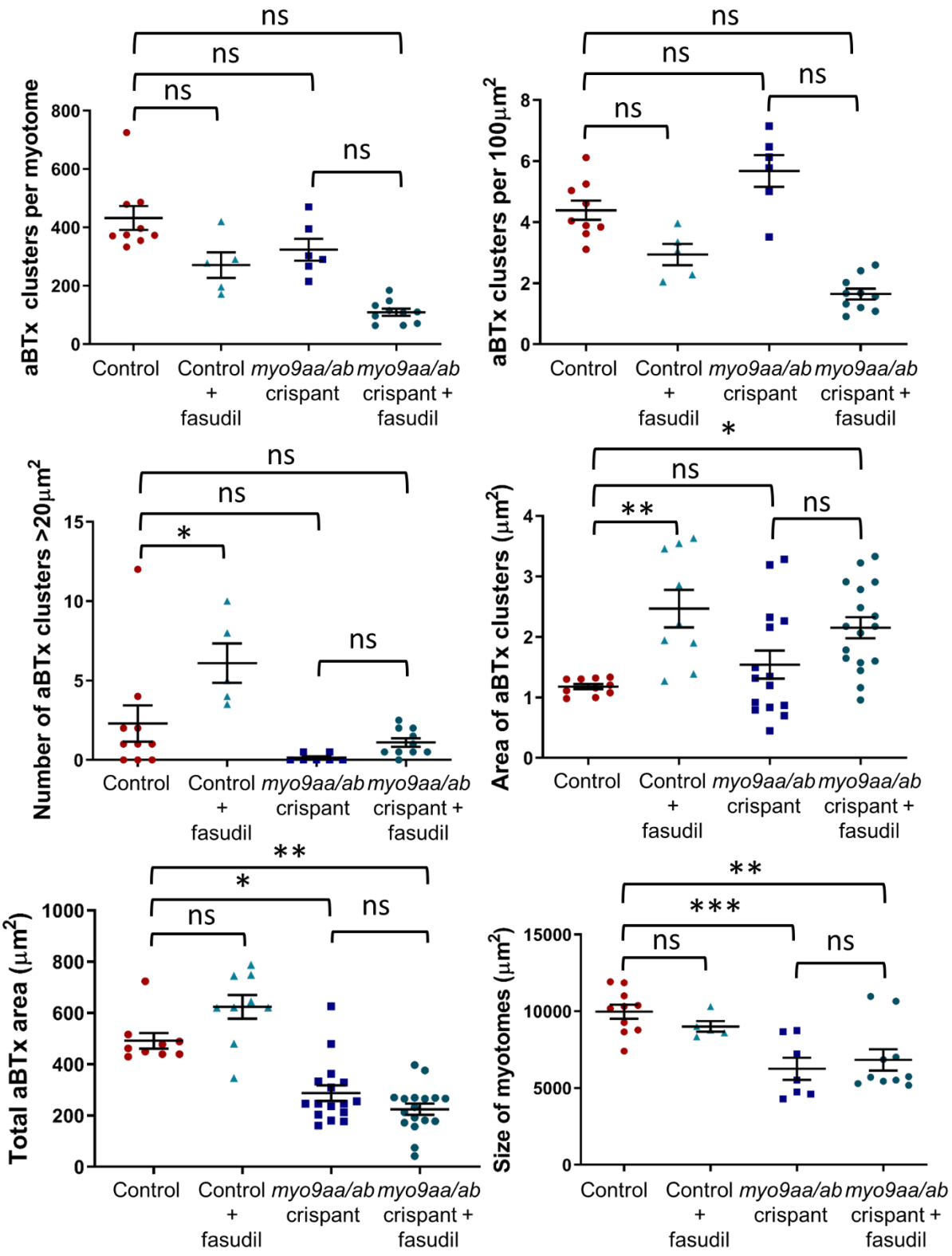

Figure 5.27. Quantification of fasudil-treated *myo9aa/ab* crispant zebrafish postsynaptic NMJ morphology at 5 dpf. Various features of postsynaptic NMJ morphology in control (n=10), *myo9aa/ab* crispants (n=7), control + fasudil (n=5) and *myo9aa/ab* crispants + fasudil (n=10) were quantified: average and total area of aBTx (postsynaptic) clusters (expressed as per myotome rather than per fish), number of clusters per myotome, per 100µm^2 and over 20µm^2, as well as myotome size and myoseptal length. Error bars = mean ± S.E.M. *p≤0.05, **p≤0.01, ***p≤0.01, ****p<0.0001, ns = not significant, one-way ANOVA.

5.9 Discussion

The aim of this chapter was to determine how defective function of MYO9A may contribute to impairment of the NMJ. Unconventional myosin proteins are involved in a diverse range of cellular functions, but primarily they are actin binding molecules that can traverse actin filaments in cells. Association of such proteins with CMS has not previously been reported, however, defects in other proteins associated with the cytoskeleton have been found to cause CMS. These include plectin, an intermediate filament binding protein that also interacts with actin and microtubules (Selcen et al., 2011). Recently, mutations in *MACF1* have also been attributed to CMS, which again has binding sites for microtubules and actin, and plays a role in maintenance of postsynaptic components at the NMJ (Oury et al., 2019). Therefore, the effect of MYO9A on the cytoskeleton and role this may have at the NMJ was investigated *in vitro* and expanded in zebrafish.

5.9.1 Effect of MYO9A loss or patient mutations on cytoskeleton

Analysis of actin, β-tubulin and neurofilament quantities revealed that loss of MYO9A can affect the abundances of important cytoskeletal components. Strikingly, there was a large increase in the presence of actin in NSC-34 cells lacking MYO9A, found in both immunofluorescence and immunoblotting experiments. There was also a significant increase in actin levels for MYO9A KD fish, however, this finding was not reflected in the mouse tissue or patient fibroblasts and only a small increase in expression was found in patient iNPCs. Further western blots would be required to confirm this observation, but it may be that MYO9A is affecting actin abundance specifically in the nerve, thus mouse muscle lysates in which NMJs aren't enriched, and patient fibroblasts, do not offer the best tissue for this assessment. While there is a small increase in actin in the patient iNPCs carrying *MYO9A* missense mutations, it appears that complete loss of MYO9A in our models affects actin levels more significantly. This might be due to loss of the head/neck regions of MYO9A, important for the cross-linking of actin filaments, which are not the same regions holding the mutations for this patient (Saczko-Brack et al., 2016). Loss of this cross-linking ability may cause excessive actin to build-up within cells to compensate, or may disrupt actin cycling dynamics and affect it's break down. Another study demonstrated necessity for the motor (head) domain for targetting of MYO9A to actin bundles, again highlighting why different effects may be observed in the full knockout cell/zebrafish model as compared to patient cells (Omelchenko and Hall, 2012).

MYO9A KD cells were subject to phalloidin staining to allow visualisation of actin cytoskeleton morphology. Actin is important for extending neurites and is enriched at growth cones, where MYO9A was previously shown to be present (O'Connor et al., 2016), and where other unconventional myosins are located (Suter et al., 2000, Yu et al., 2015). In the MYO9A KD NSC-34 cells, actin accumulation was still present in neurite-like protrusions from the cells, and the cells were able to send out extensive projections, however the organisation of actin in these regions appeared disordered. Similarly, in *hum-7* (*C.elegans MYO9A/MYO9B* orthologue) mutants, F-actin still correctly localises to the ventral surface of cells for extension of protrusions important for cell migration (Wallace et al., 2018). Phalloidin staining also revealed the presence of stress-like fibres in the cells, and these were significantly increased in MYO9A KD cells. It should be noted that confirmation of these parallel actin-positive bundles as stress-fibres would require co-staining for the focal adhesion marker, paxillin. Nevertheless, supporting our observation a screen of proteins that show deregulated expression in association with increased actin expression and stress-fibre formation identified MYO9A downregulation (Tavares et al., 2017). Furthermore, overexpression of Myr 7 (MYO9A rat homolog) in HeLa cells was found to cause loss of stress fibres and rounding up of cells, and similar effects were observed for overexpression of the MYO9B homologue (Muller et al., 1997, Chieregatti et al., 1998).

MYO9A is also a negative regulator of the RhoA pathway and the KO models likely effect the RhoGAP domain to a greater extent than the patient mutations. Removal of negative regulation of RhoA could lead to an increase in RhoA activity and thus upregulation of the downstream ROCK pathway. The ROCK pathway can affect the actin, neurofilament and tubulin cytoskeleton through a number of interacting molecules, as highlighted in Figure 5.2. For example, in a SMA mouse model, an increase in RhoA activity was observed in the spinal cord and linked to altered actin cytoskeleton dynamics (Bowerman et al., 2010). In a previous study involving MYO9A, loss of this unconventional myosin was shown to affect bronchial cell migration and ability of cells to form contacts thus leading to cell scattering and this was attributed to local effects on the RhoA pathway and actin organisation (Omelchenko and Hall, 2012).

The action of MYO9A on the RhoA pathway was tested by applying a ROCK inhibitor (Y-27632) to the MYO9A KD cells. This revealed a significant decrease in the

expression of actin to a level similar to control KD cells, thus indicating that at least part of the effect of MYO9A-loss on the cytoskeleton is mediated by the RhoA GTPase domain in the tail region in this study. Although it should be noted that Y-27632 is not a selective inhibitor of ROCK and also inhibits other kinases with similar potency (Davies et al., 2000).

Cytoskeletal analysis also revealed a decrease in the level of neurofilament in the MYO9A KD NSC-34 cells, but no consistent changes in patient cells or mouse tissues. NSC-34 cells expressing mutant SOD1, as a model of the neurodegenerative disease ALS, have also been shown to exhibit lower levels of neurofilament. Whether this phenotype was a protective or injurious occurrence remains unclear (Menzies et al., 2002). There have been no previous reports of MYO9A and neurofilament interactions, however ROCK has been shown to phosphorylate neurofilament, and phosphorylation of neurofilament light chain inhibits fibril formation (Hisanaga et al., 1990, Hashimoto et al., 1998). Activation of the RhoA/ROCK pathway has also been shown to reduce microtubule and neurofilament network assembly, however, the reason for reduced overall expression of these proteins in the knockdown cells remains unclear (Hirose et al., 1998), and addition of the ROCK inhibitor only slightly increased the amount of neurofilament light chain in MYO9A KD cells. Reduced perinuclear staining of neurofilament light chain and β-tubulin can be observed in NSC-34 cells depleted for MYO9A. While localisation of MYO9A in this region has not been reported, Myr 5 (MYO9B rat homologue) has been shown to be localised in the perinuclear region and thus depletion may affect local levels of neurofilament and tubulin through interactions with RhoA (Muller et al., 1997). This would require further investigation and would be assisted by the generation of a cell-line expressing MYO9A with a fluorescent tag. A reduction in β-tubulin network formation has been reported in other cell models of motor neuron-related diseases such as in mutant SOD1 NSC-34 cells (Wen et al., 2010). In absence of MYO9A, β-tubulin was partially rescued by Y-27632 treatment but not to a significant level. An increase in β-tubulin has previously been reported in podocyte cells treated with Y-27632 therefore further improvement may be observed if cells were subject to a dose-response assay (Gao et al., 2004). Mice lacking MYO9A similarly showed a decrease in β-tubulin levels in gastrocnemius and quadriceps muscles, however, in zebrafish a significant upregulation was observed. As tissue from the whole zebrafish were included in lysates, a tissue specific analysis of tubulin expression may provide a better overview of any potential disruptions due

to MYO9A loss. There were no changes in the level of cytoskeletal components in patient iNPCs, however, it should be noted that in order to generate the cells they were treated for a prolonged time period with Y-27632 as part of the conversion protocol (Meyer et al., 2015). This treatment may have affected later results as it could have alleviated some of the phenotype observed from MYO9A disruption, as found in the NSC-34 cells.

Overall, an effect of MYO9A-loss on the actin cytoskeleton was most prominent, and could be partially attributed to the interaction of MYO9A with the RhoA pathway. Some changes to the neurofilament and β-tubulin networks were also observed, although not consistently throughout models, and some improvements to levels of these cytoskeletal components could be achieved with ROCK inhibitor treatment.

5.9.2 A role for MYO9A in intracellular transport and release mechanisms

As disruption of the cytoskeleton was observed, it was hypothesised that this may impact on trafficking within cells and endo/exocytosis, both of which are crucial for the proper functioning of the NMJ. To address this question, FM 1-43 dye assays were performed in MYO9A KD cells and patient iNPCs. In the knockdown cells, a slower uptake of dye was observed. Defective endocytosis was also detected in mouse kidney cells lacking MYO9A, for which it was hypothesised that loss of MYO9A and subsequent increase in Rho activity may increase membrane tension and stall actin dynamics to prevent vesicle internalisation (Thelen et al., 2015). MYO9A has been shown to indirectly regulate activity of mDia1, which plays a role in endosomal trafficking and thus may provide another downstream pathway in which loss of this unconventional myosin acts (Thelen et al., 2015). Furthermore, other unconventional myosins such as myosin Va are also implicated in endocytotic mechanisms (Hasson, 2003). In iNPCs, endocytosis of dye was also slower in patients than in controls. Addition of high KCl solution to stimulate release of vesicles was successful in controls, however, did not stimulate release in the patient cells during the time-frame assessed. Similarly, exocytosis was impaired in NSC-34 cells depleted for MYO9A, highlighting that both patient mutations and MYO9A KD can impair release mechanisms. This may have significant effects at the NMJ as release of proteins such as ACh and agrin from nerve terminals are essential for maintaining the structure and function of the synapse.

Defects in global endo/exocytosis were explored in more detail by employing the use of a GFP-tagged paradigmatic growth factor receptor, TrkA. This receptor was

chosen due to its established internalisation from the cell surface in response to NGF, and the recycling back to the surface of the majority of the internalised population (Chen et al., 2005). However, the use of TrkA is also relevant for synaptic transmission as it has been shown to modulate ACh release from basal forebrain neurons (Auld et al., 2001). Impaired TrkA signaling has also been linked to disturbed neurotransmission and loss of presynaptic and vesicle trafficking proteins in neurons (Latina et al., 2017). Studies have previously been performed using TrkA-GFP dynamics to analyse receptor recycling and internalisation, including the ability to track movements using live-cell confocal microscopy (Chen et al., 2013, Freund-Michel and Frossard, 2008, Jullien et al., 2003). A similar assay has also been performed by Roos *et al.* in which the epidermal growth factor receptor was used as a paradigmatic receptor for analysis of the cytoskeleton and vesicular transport integrity in the neurodegenerative disorder: Marinesco-Sjögren syndrome (2016).

Defective recycling was identified in MYO9A-depleted NSC-34 cells as compared to controls, and this was shown to not be due to increased receptor degradation, thus indicating a likely defect in transport mechanisms. This was supported by live-cell imaging of transfected cells demonstrating slower intracellular movements of TrkA-GFP in MYO9A KD cells. Treatment of cells with Y-27632 was able to significantly improve the speed of receptor movements, therefore both the cytoskeletal and transport defects can at least be partly attributed to effects of MYO9A-loss on the Rho pathway. Others have reported improvements to cell morphology and the cytoskeleton in different cell types lacking MYO9A when treated with Y-27632, although contribution to functional defects such as endocytosis have not previously been investigated (Abouhamed et al., 2009, Omelchenko and Hall, 2012). ROCK inhibitor treatment has also proven successful in rescuing phenotypes observed due to depletion of MYO9B in immune cells and cortical neurons (Hanley et al., 2010, Long et al., 2013). In the future, receptors or surface proteins with direct relevance for NMJ functioning, such as AChRs, MUSK and LRP4, could be assessed for similar defects in recycling/trafficking dynamics using a muscle-cell knockdown model of MYO9A to provide further insights regarding a role for MYO9A at the NMJ. These results collectively implicate a role for MYO9A in regulating intracellular transport and endo/exocytosis *in vitro*, and some aspects such as movement of intracellular receptors was improved by blocking the ROCK pathway.

5.9.3 Fasudil treatment of zebrafish

To provide further evidence regarding the effect of ROCK inhibition on MYO9A-depletion and to explore a potential therapeutic strategy, the *myo9aa/ab* crispant zebrafish model was also treated with a ROCK inhibiting drug. The ROCK inhibitor fasudil was selected for this study as it has already been approved for clinical use in humans, and has previously been used in zebrafish (Shibuya et al., 1992, Suzuki et al., 2007, Philip et al., 2017, Zhou et al., 2018).

Survival of fish treated with increasing concentrations of fasudil varied during the dose optimisation study, which could be due to inconsistent uptake of drug by each fish during incubation as the drug was given in the water and plates containing the fish were not subject to constant agitation. In the future, more accurate dosing could be provided by injecting the drug or if the full CRISPR/Cas9-mediated KO line were generated adults can also be treated by oral gavage (Collymore et al., 2013). Chorion movements were improved in crispant fish in a fasudil dose-dependent manner and survival was also improved, providing support for the mode-of-action of MYO9A-loss leading to increased RhoA pathway activity. The selected fasudil dose of 10μM did not significantly affect survival in control fish, however, there was a detrimental effect to 24 hpf movements. This was to be expected due to the widespread action of the RhoA pathway and thus subsequent impact of reducing its action during development. By 48 hpf, the control zebrafish no longer responded negatively with regards to movement in the presence of fasudil, thus perhaps the dose is less toxic as the fish grow larger, as concentration remained constant throughout the time period of analysis. However, it remained sufficient to significantly improve the response of crispant fish to the tactile stimulation assay. Similarly, in a mouse model of ALS, administration of fasudil after symptom onset was able to improve motor behaviours (Gunther et al., 2017). Overall, movement and survival of zebrafish lacking Myo9aa/ab in development could be improved by application of fasudil to decrease the activity of the ROCK pathway.

Reflecting the changes in movement, NMJ morphology of the crispant fish was similarly improved in some aspects during the time points assessed. Length of motor axon outgrowths past the choice point at 24 hpf were significantly increased by fasudil treatment, corroborating with numerous reports that ROCK inhibition can extend neurites *in vitro* (Govek et al., 2005). The proportion of myotomes expressing a choice point cluster was rescued, which could be linked to the improved neuronal

outgrowth as this time point was beyond that for which prepatterned receptors should be present. This is supported by roles for other RhoA/ROCK modulating proteins, such as Ephexin1, in mediating both prepatterned AChR clustering as well as AChR cluster maturation (Shi et al., 2010). Size of myotomes in the fish were also improved by fasudil treatment, correlating with results demonstrating a positive effect of fasudil application on muscle fibre size in a SMA mouse model (Bowerman et al., 2012).

Surprisingly, despite the improvements to movement observed in 48 hpf crispant fish, no overt rescue of the NMJ parameters assessed was obtained. Fasudil treatment was associated with a further decrease in the number of SV2 and aBTx clusters per 100μm^2 and total area of these clusters, along with a further increase in the average size of SV2 clusters. This suggests that blocking the ROCK pathway caused fewer, larger pre and postsynaptic clusters to form, which could be related to the defects in cytoskeletal arrangement observed *in vitro*. Testing of a range of doses may have better revealed improvements, as well as increasing numbers of animals to account for the variability in data observed due to the mosaicism of the fish. Nevertheless, the movement benefits due to fasudil treatment suggest there may be modest improvements in release/functionality at the NMJ that are not detectable by the morphological changes measured here.

At 5 dpf the average and total areas of SV2 and AChR clusters and number of large SV2 clusters was increased beyond the level observed in controls, while the number of pre and postsynaptic clusters overall decreased. This reflects the results from 48 hpf, with an accumulation of larger pre and postsynaptic regions detected. Analysis of the effects of fasudil in a SMA mouse model revealed that treatment led to an increase in endplate size but had no effect on presynaptic terminal size (Bowerman et al., 2012). To investigate this further, colocalisation analysis would provide insight into whether these larger clusters correctly oppose AChRs, thus still forming synapses. Furthermore, whether this phenotype manifests as functional changes to overall NMJ signalling capacity remains to be determined as neither behavioural testing or electrophysiology have been performed. Size of myotomes is no longer improved by fasudil treatment at this time point. This could suggest different mechanisms contributing to muscle development between embryonic and larval developmental stages, or that the dose of the drug should be increased as the fish grow larger (as concentrations up to 3x higher have been used in zebrafish previously, Zhou et al., 2018). To confirm the effectiveness of doses given, levels of

downstream targets of ROCK could be measured, such as phosphorylated cofilin as performed elsewhere (Bowerman et al., 2012).

Overall, the fasudil treatment ameliorated many of the behavioural deficits observed in zebrafish lacking Myo9aa/ab and this was corroborated by several improvements in NMJ morphology, especially at the earlier stages of development. It is likely that such a treatment would require fine-tuning to optimise the precise dose at each time point, and more detailed longitudinal investigations required to assess for functional changes, as in the aforementioned SMA mice, consistent improvements in NMJ morphology were not observed until 6 months of treatment (Bowerman et al., 2012).

5.9.4 Conclusion

In this chapter a role for MYO9A in organisation and expression of proteins important for the cytoskeleton was demonstrated, including actin, β-tubulin and neurofilament light chain. The extent of defects in the presence of patient mutations required further investigation, however, global endo/exocytosis were shown to be impaired in patient iNPCs, as well as in NSC-34 cells lacking MYO9A. The effects of MYO9A-loss on the cytoskeleton and on intracellular transport could be partly alleviated by blockade of the ROCK-pathway using Y-27632. Treatment of *myo9aa/ab* crispant fish with fasudil also demonstrated some benefits to movement and NMJ development, thus highlighting the involvement of the RhoA/ROCK pathway in the downstream pathophysiology of MYO9A-deficiency.

MYO9A-loss causes defects to the cytoskeleton and therefore disrupts intracellular trafficking mediated by the RhoA pathway. It was demonstrated that this is at least partially the mode of action of MYO9A-depletion in nerve cells, although other factors may contribute to the overall pathophysiology of MYO9A-CMS. These impaired functions may affect secretion and uptake of factors important for NMJ maturation and function, as well for structure of pre/postsynaptic components. The predicted effect on secretion will be explored in the following chapter.

Chapter 6. Deficient agrin secretion as a therapeutic target for MYO9A-related CMS

6.1 Introduction

In the previous chapter defects to the cytoskeleton, intracellular trafficking and endo/exocytosis were identified *in vitro* using MYO9A KD NSC-34 cells and patient iNPCs. The ability to partially modulate these phenotypes was achieved through the use of ROCK inhibitor drugs, both in the nerve cell model as well as in Myo9aa/ab-deficient zebrafish. While this offers preliminary support for a role of MYO9A at the NMJ and a potential therapeutic strategy to investigate, there may be other pathways contributing to the pathological picture of MYO9A-CMS that could be targeted for treatments.

Based on the impact of MYO9A loss on endo/exocytotic mechanisms, it was hypothesised that it may affect secretion of proteins important for the NMJ. Release of growth factors and guidance cues from muscle are important during motor axon extension from the spinal cord to target muscle. Axon growth cones must detect and respond to such environmental stimuli and also release factors attractive to Schwann cells for co-migration. Nerve cells synthesise agrin and it is transported to the nerve terminal for secretion into the synaptic cleft upon reaching the target muscle cell. Agrin acts on its receptor, LRP4, which interacts with MuSK and stimulates a downstream cascade of events culminating in postsynaptic differentiation and appropriate positioning of AChRs at the endplate, as outlined in (Figure 6.1, Tintignac et al., 2015, Wu et al., 2010). Agrin is also important for synaptic maintenance, as depletion from motor neurons in adult mice with normal NMJs causes loss of AChRs, components of the postsynaptic compartment and basal lamina, as well as reduction in size of presynaptic nerve terminals (Samuel et al., 2012).

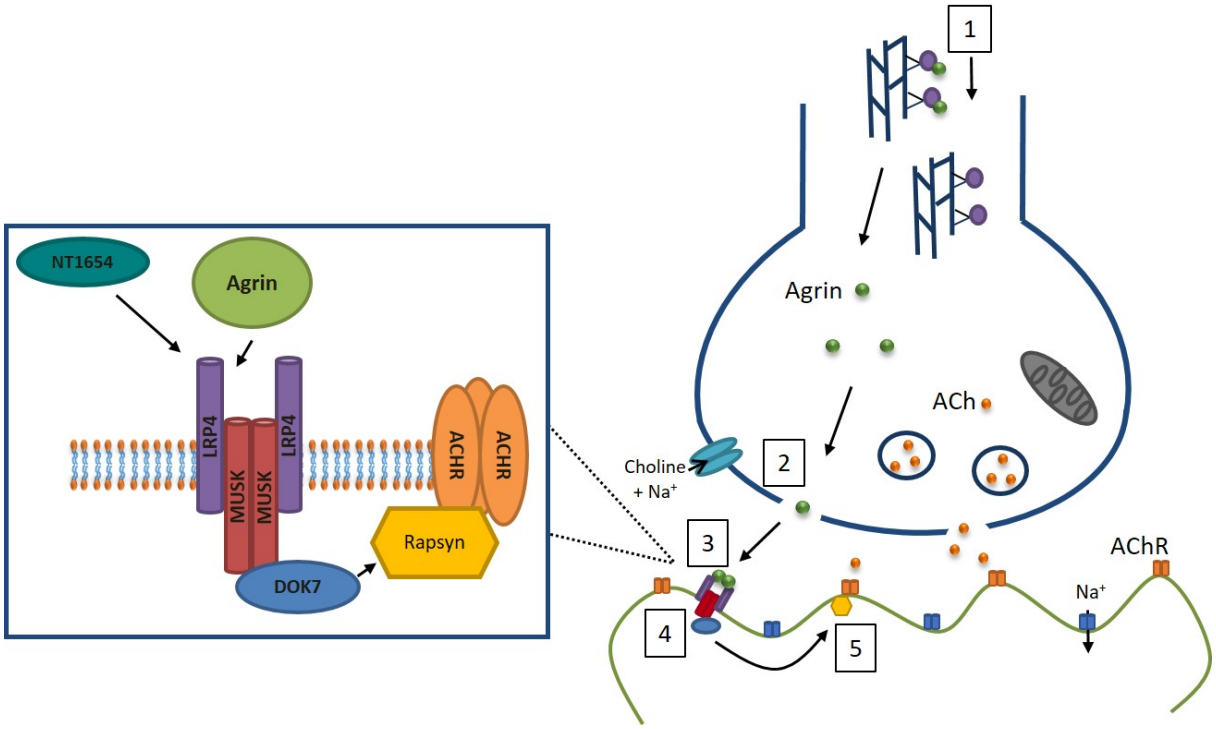

Figure 6.1. Schematic diagram for action of agrin at NMJ. (1) Agrin is synthesised in the cell body of the motor neuron and transported to the nerve terminal, where it is exocytosed (2) into the synaptic cleft. (3) Agrin binds to LRP4 receptors (also the site of action of NT1654, used in this chapter) which stimulates phosphorylation of MuSK and subsequently recruits Dok7 (4). Interaction with Dok7 initiates a number of downstream signalling pathways, including recruitment of Rapsyn to anchor AChRs in clusters at the endplate (5). Figure adapted from Wu *et al* (2010).

Therefore, defective secretion or uptake of factors at the NMJ during development, maintenance or mature function could impact signal transmission through a variety of mechanisms. To determine whether secretory defects underpin the pathology of MYO9A loss at the NMJ, proteomics was performed on the secreted proteins from MYO9A KD NSC-34 cells by collecting cell culture media. Proteomics has been performed on micro-dissected NMJs from mice and human, revealing the protein signature of NMJ-enriched muscle and confirming ability of proteomics to detect proteins associated with nerve-muscle signalling such as agrin, growth factors, axon guidance cues and neurotrophic molecules (Jones et al., 2017). Other studies have analysed the proteomes of nerves, muscle or synaptic fractions from CNS tissue and cultured neural progenitor cells (for example: Cipriani et al., 2018, Phan et al., 2019, Gershoni-Emek et al., 2016, Ibebunjo et al., 2013, Mendes-Pinheiro et al., 2018, Henningsen et al., 2010, Schira et al., 2018), however, the use of secretomics to identify molecular mechanisms and potential drug targets at the NMJ using cultured nerve cells has not been performed previously.

6.2 Aims of chapter

- To identify proteins with altered secretory profiles from MYO9A-deficient NSC-34 cells.
- To test a novel therapeutic strategy based on agrin for MYO9A-deficiency using zebrafish.

6.3 Secretomic analysis of MYO9A-deficient NSC-34 cells

In the previous chapter, a dysregulation of intracellular trafficking and endo/exocytotic functions was identified in cells lacking MYO9A. It was hypothesised that this may cause impairment in the secretion of factors important for NMJ development or function which would provide further insight into the pathophysiology of MYO9A-CMS. To investigate this hypothesis, proteomics was performed on secreted proteins (secretomics) from control and MYO9A KD NSC-34 cells, by Vietxuan Phan (ISAS, Dortmund). This method involves culturing cells to sub-confluence before washing to remove traces of serum that confound proteomic measurements and culturing cells in serum-free media for 3 hours. The medium is then collected and prepared for analysis of secreted proteins.

6.3.1 Analysis of secretomic data

Secretomic data was generated from 3 control and 3 MYO9A KD NSC-34 cell secretion samples and was returned for analysis. Using an unbiased, label-free proteomic approach 1532 proteins were detected in the samples. Of these proteins, those detected by more than one unique peptide, with a fold change greater than 4.06 or lower than -4.44, as well as having significantly different expression between control and KD samples ($p<0.05$, p-ANOVA), were considered dysregulated (n=76). As shown in the volcano plot, 46 of the identified proteins were found to be upregulated in the secretome of MYO9A KD cells as compared to controls, and 30 were downregulated (Figure 6.2).

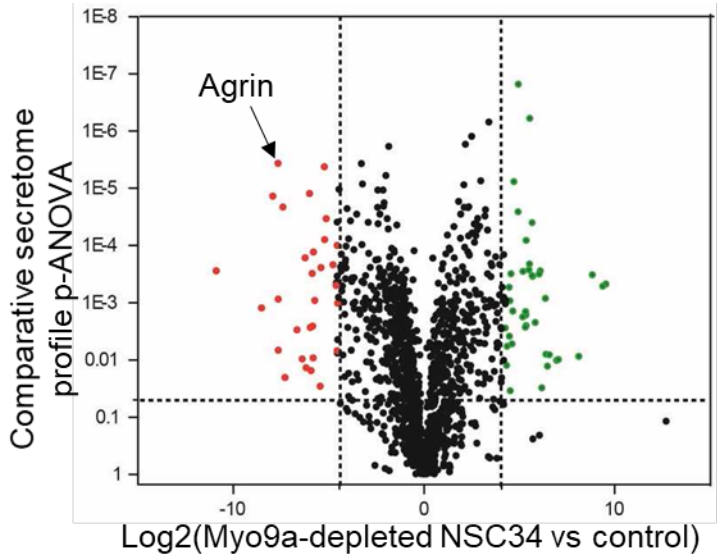

Figure 6.2. Volcano plot of MYO9A KD NSC-34 cell secretome. Secreted proteins from control and MYO9A KD NSC-34 cells were subject to proteomic analysis. Proteins with significantly reduced expression in MYO9A KD cells are shown in red, and upregulated proteins shown in green ($p<0.05$, P-Anova, upregulated>4.06 Log2, downregulated<-4.44 Log2). Volcano plot generated by Vietxuan Phan (ISAS, Dortmund). Agrin data point indicated on graph.

A list of up and downregulated proteins is provided in Table 6-1. Of these 76 proteins, 67 have previously been reported as secreted from a search of Uniprot, Pubmed, LOCATE and MGI databases (Figure 6.3). The remaining 9 proteins have not previously been identified as secreted and include: PDLI1, GAS1, INF2, IGEB, DPYL5, VAT1L, AKA12, EF1A2 and H4. PDLI1 is predicted to play a role in actin stress fibre formation, GAS1 suppresses cell growth, INF2 severs actin filaments, IGEB is related to the immune system, DPYL5 is predicted to play a role in neuron differentiation and axon growth, the function of VAT1L is unknown but it is expressed in the CNS and peripheral nerves, AKA12 localises kinase receptors, EF1A2 is involved in protein synthesis and H4 contributes to the nucleosome (Uniprot https://www.uniprot.org/, last accessed 12/03/2019). Reported disease involvement is also highlighted in the table, with some relevant to the nervous/muscle systems such as ALS (SODE), Charcot-Marie-Tooth disease (NDRG1, INF2), Congenital Muscular dystrophy (CO6A1) and CMS (AGRN). The finding that Agrin (AGRN) secretion was downregulated was of particular importance, as is it is not only an important mediator of NMJ development and structure but also mutations in *AGRN* itself can cause CMS (Huze et al., 2009, Gautam et al., 1996, McMahan, 1990).

Protein	*Accession number*	*Localisation*	*Function*	*Disease involvement*	*Direction of regulation*	*Fold of regulation*
MIME	Q62000	secreted	Bone formation and axonogensis		↑	8.84108552
PPIC	P30412	secreted	Protein folding		↑	8.129945779
HMOX1	P14901	secreted	Cytoprotection	Heme oxygenase 1 deficiency	↑	6.962838522
LPP	Q8BFW7	secreted	Cell shape and motility		↑	6.490882985
MYOF	Q69ZN7	secreted	Plasmalemma repair and endocytic recycling		↑	6.405636168
PDLI1	O70400	cytoskeleton	Cytoskeleton		↑	6.373342417
GAS1	Q01721	cell membrane	Cell growth suppressor		↑	6.178146105
SODE	O09164	secreted	Destroys free radicals	Amyotrophic Lateral Sclerosis 1	↑	6.099830689
CO4A1	P02463	secreted	Interact with laminins, proteoglycans and entactin/nidogen	Brain small vessel disease, Hereditary angiopathy with nephropathy aneurysms and muscle cramps, Porencephaly 1, Intracerebral haemorrhage, Schizencephaly	↑	6.046721552
MMP2	P33434	secreted	Angiogenesis and tissue repair	Multicentric osteolysis, nodulosis, and arthropathy	↑	5.849368216
SRPX2	Q8R054	secreted	Promotes synapse formation	Rolandic epilepsy with speech dyspraxia and mental retardation X-linked	↑	5.70959609

SH3K1	Q8R550	secreted	Endocytosis, lysosomal degradation, cellular stress responses, apoptosis and cytoskeletal organization		↑	5.698131221
NDRG1	Q62433	secreted	Cell growth, differentiation, apoptosis, cell trafficking, myelin sheath, vesicular recycling and regulating microtubule dynamics	Charcot Marie Tooth disease type 4D	↑	5.678838973
CAPG	P24452	secreted	Blocks the barbed ends of actin filaments		↑	5.677222105
CO6A1	Q04857	secreted	Cell-binding protein.	Bethlem myopathy 1 and Ullrich congenital muscular dystrophy 1	↑	5.587756594
ENOB	P21550	secreted	Striated muscle development and regeneration	Glycogen storage disease 13	↑	5.556672165
ANGP1	O08538	secreted	Angiogenesis, endothelial cell survival, proliferation, migration, reorganization of the actin cytoskeleton		↑	5.543351694
S10A4	P07091	secreted			↑	5.524298487
PRELP	Q9JK53	secreted	Anchor basement membrane to connective tissue		↑	5.508115793
OSTP	P10923	secreted	Part of bone mineralized matrix		↑	5.366001405
IBP6	P47880	secreted	Negative regulation of Wnt and cell proliferation		↑	5.353125727
SC65	Q8K2B0	secreted	Cross-linking of collagen		↑	5.34165765
EMIL2	Q8K482	secreted	Anchoring smooth muscle cells to elastic fibres		↑	5.327777219

CO3A1	P08121	secreted	Cortical development, inhibits neuronal migration and activates the RhoA pathway		↑	5.198026478
PLTP	P55065	secreted	Transfer of lipid molecules		↑	5.181661752
LAMA4	P97927	secreted	Attachment, migration and organization of cells into tissues during embryonic development		↑	5.148926308
VIME	P20152	secreted	Intermediate filament, regulates microtubule dynamics	Cataracts	↑	4.949931945
SPB6	Q60854	secreted	Regulation of serine proteinases	Autosomal recessive deafness	↑	4.938047641
RL22L	Q9D7S7	secreted	Structural constituent of ribosome		↑	4.726654112
S10AA	P08207	secreted	Positive regulation of stress fibre assembly		↑	4.673247388
CO5A2	Q3U962	secreted	Connective tissue component	Ehlers-Danlos syndrome, classic type	↑	4.661757006
ANXA3	O35639	secreted	Inhibitor of phospholipase A2		↑	4.62943553
GSTA4	P24472		Conjugation of reduced glutathione to electrophiles		↑	4.585769672
CO1A2	Q01149	secreted	Rho protein signal transduction	Ehlers-Danlos syndrome 7B, Osteogenesis imperfecta 1 and Osteogenesis imperfecta 2	↑	4.572424063
CADH2	P15116	secreted	Calcium-dependent cell adhesion proteins		↑	4.51399316
HTRA1	Q9R118	secreted	Serine protease	Age-related macular degeneration 7, autosomal recessive cerebral arteriopathy	↑	4.483872692
AEBP1	Q640N1	secreted	Enhanced adipocyte proliferation, reduced differentiation, binds calmodulin and is involved in protein processing		↑	4.47579898

PEDF	P97298	secreted	Neurotrophic protein; induces extensive neuronal differentiation, negative regulator of neuronal death	Osteogenesis imperfecta 6	↑	4.423969538
LTBP2	O08999	secreted	Structural role in elastic-fibre organisation	Congenital glaucoma 3 D, Microspherophakia and/or megalocornea and Weill-Marchesani syndrome 3	↑	4.33299379
LYOX	P28301	secreted	Oxidative deamination of peptidyl lysine residues in precursors to fibrous collagen and elastin	Familial thoracic aortic aneurysm 10	↑	4.291993841
INF2	Q0GNC1	cytoplasm	Severs actin filaments and accelerates their polymerization and depolymerisation	Focal segmental glomerulosclerosis 5, Charcot-Marie-Tooth disease, dominant, intermediate type, E	↑	4.273975547
LAMB1	P02469	secreted	Organization of cells into tissues during embryonic development and architecture of cerebral cortex.	Lissencephaly 5	↑	4.191424881
NID1	P10493	secreted	Cell to extracellular matrix interactions		↑	4.186691014
NQO1	Q64669	secreted	Negative regulation of apoptosis		↑	4.186185145
FKB10	Q61576		Accelerate protein folding	Osteogenesis imperfecta 11, Bruck syndrome 1	↑	4.111759089
GMDS	Q8K0C9	secreted	Catalyses the conversion of GDP-D-mannose to GDP-4-dehydro-6-deoxy-D-mannose		↑	4.079698454
IGEB	P03975	cytoplasm			↓	-4.44442495
DOPO	Q64237	secreted	Converts dopamine to noradrenaline	Cardiac Regulation	↓	-4.449643808
IGSF8	Q8R366	secreted	May regulate neurite outgrowth in the adult brain		↓	-4.518081271

MRP	P28667	secreted	Regulates actin cytoskeleton and neuronal migration		↓	-4.520508705
LAT1	Q9Z127	secreted	Involved in cellular amino acid uptake and neurogenesis in the brain		↓	-4.533051028
UCHL1	Q9R0P9	secreted	Processing of ubiquitin precursors and of ubiquitinated proteins	Alzheimer's Disease	↓	-4.538729128
BGLR	P12265	secreted	Degradation of dermatan and keratan sulfates		↓	-4.542954696
COTL1	Q9CQI6	secreted	Binds to F-actin in a calcium-independent manner	Parkinson's Disease	↓	-4.549514023
H4	P62806	nucleus	Core component of nucleosome		↓	-4.549850244
DPYL5	Q9EQF6	cytoplasm	Neuronal differentiation and axon growth		↓	-4.586679792
SCG2	Q03517	secreted	Secretory granule protein	Parkinson's Disease	↓	-4.768512141
SCG3	P47867	secreted	Secretory granule protein	Parkinson's Disease	↓	-5.120730002
VAT1L	Q80TB8	cytoplasm	Secretory granule protein	Parkinson's Disease	↓	-5.205433024
AKA12	Q9WTQ5	cytoplasm			↓	-5.215792684
AGRIN	A2ASQ1	secreted	Formation and the maintenance of the neuromuscular junction	Congenital Myasthenic Syndrome	↓	-5.357776055
GNA13	P27601	secreted	Transmembrane signalling		↓	-5.395246419
TICN2	Q9ER58	secreted	May participate in neurogenesis		↓	-5.636804699
APLP1	Q03157	secreted	Postsynaptic function and regulation of neurite outgrowth		↓	-5.790748164

H2AY	Q9QZQ8	secreted	Represses transcription	↓	-5.833594691
SCG1	P16014	secreted	Mediates the subcellular compartmentation of protein kinase A and C	↓	-5.861864664
MUC18	Q8R2Y2	secreted	Cell adhesion	↓	-5.952142061
CLUS	Q06890	secreted	Prevents aggregation of non-native proteins	↓	-5.993152807
PCSK1	Q9QXV0	secreted	Neuroendocrine secretory pathway	↓	-6.222680148
ELN	P54320	secreted	Structural protein	↓	-6.64445921
DKK1	O54908	secreted	Antagonizes Wnt signalling	↓	-7.281956859
AAAT	P51912	secreted	Amino acid transporter	↓	-7.381076859
LDHB	P16125	secreted	Involved in synthesis of (S)-lactate from pyruvate.	↓	-7.627742699
EF1A2	P62631	nucleus	Promotes binding of aminoacyl-tRNA to ribosomes during protein synthesis	↓	-7.628200738
ITA6	Q61739	secreted	Receptor for laminin on platelets	↓	-7.644407161
CGL	Q8VCN5	secreted	Catalyses the last step in the trans-sulfuration pathway	↓	-7.926937788

Table 6-1. Proteins identified in secretome analysis of MYO9A KD NSC-34 cells. Unbiased, label-free proteomics was performed on secreted proteins from control and MYO9A KD NSC-34 cells. Protein name, Uniprot accession number and fold-change of expression as compared to control cells are shown. Localisation data from Uniprot, Pubmed, LOCATE and MGI and disease involvement data from Uniprot also included.

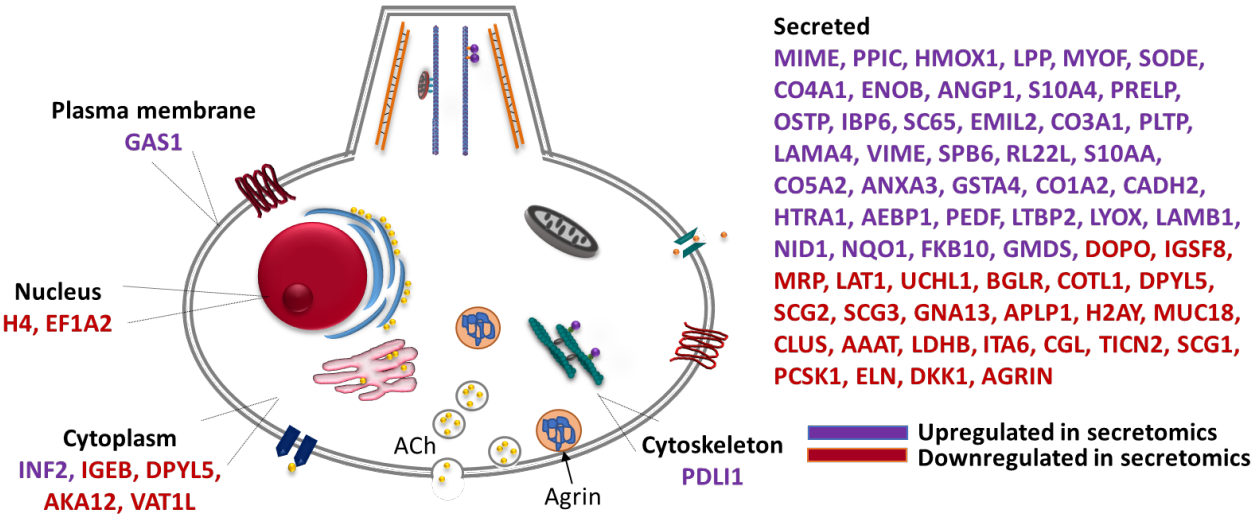

Figure 6.3. Schematic diagram of secretomic protein localisation. Localisation, as identified using Uniprot, MGI, Pubmed and LOCATE, of proteins shown to have dysregulated secretion in MYO9A KD NSC-34 cells as compared to controls. Proteins with upregulated secretion are shown in purple, downregulated are red.

Pathway analysis was performed on the dysregulated proteins to identify any enriched pathways within the dataset that may be particularly affected by loss of MYO9A (Reactome pathways, STRING database v.11, Szklarczyk et al., 2019). For the proteins with increased secretion from KD cells, the top 11 pathways are shown (Figure 6.4A). Extracellular matrix organisation is the most over-represented pathway, with 13 of the 46 proteins displaying involvement in this process. A number of the other pathways contain the same proteins as this first group and are related to collagen dynamics. Of particular relevance to this project, signal transduction, developmental biology and axon guidance pathways are also enriched. Association analysis using the STRING database revealed a large cluster of proteins with predicted interactions (Figure 6.4B). Nodes (proteins) with colour represent those that were included in the enriched pathways and it can also be observed that the majority of these fall within the large cluster.

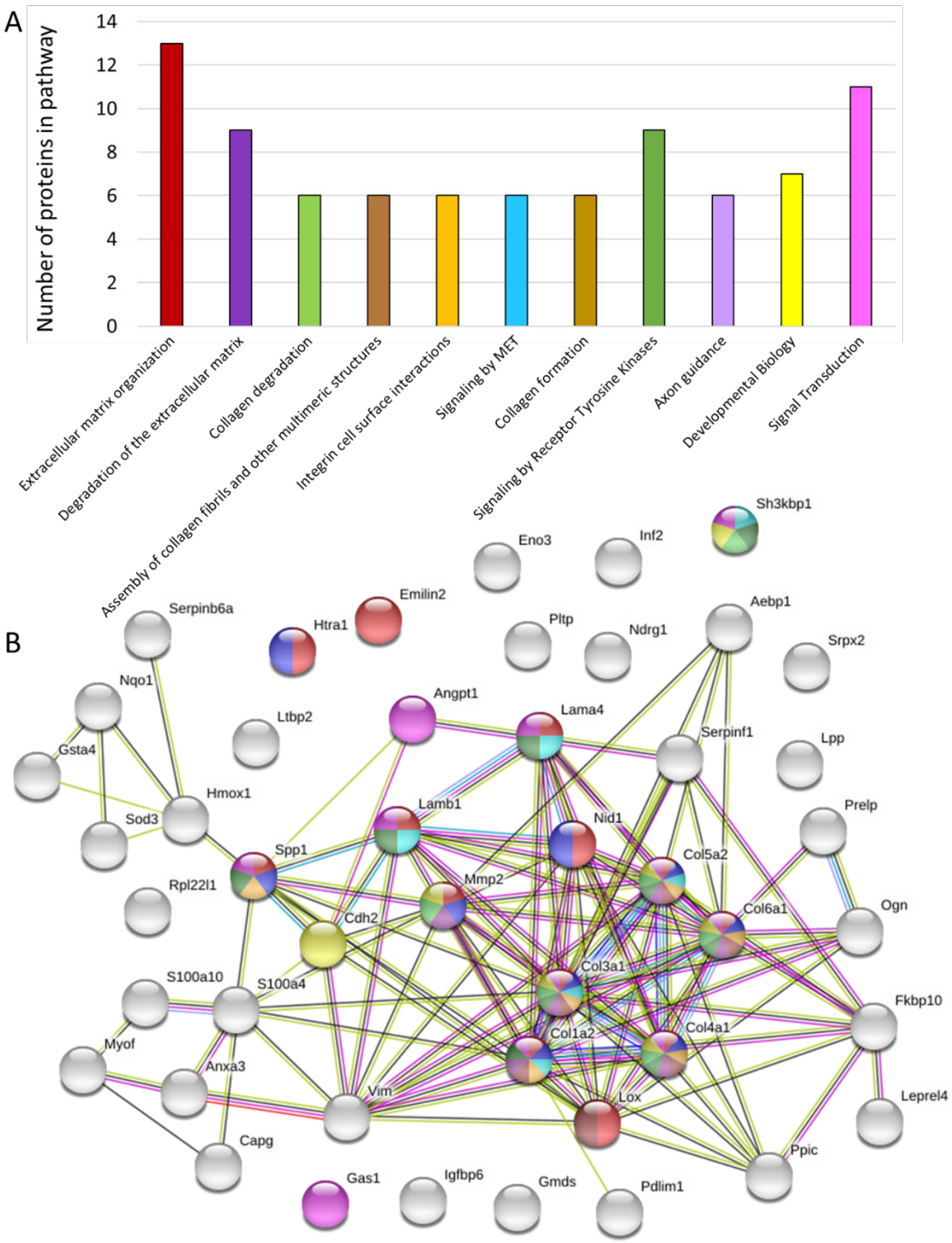

Figure 6.4. Pathway analysis and protein interaction network of upregulated proteins. A. Pathway analysis was performed for upregulated proteins from secretomic data in MYO9A KD and control NSC-34 cells, using STRING software. The top 11 enriched pathways are shown with the number of proteins identified in each. B. STRING interaction network displaying upregulated proteins. Connections represent evidence linking proteins either through co-expression, experimental data and co-occurrence in publications. Coloured nodes indicate presence of protein in enriched pathways shown in the graph.

Pathway analysis was also performed for the proteins found to be less secreted from MYO9A KD NS-34 cells. Only 8 pathways were found to be enriched using Reactome pathways on the STRING database (Figure 6.5A). Presence of proteins involved in protein modification and breakdown appear to be downregulated in the MYO9A KD cell data, including pathways such as heparan sulphate glycosaminoglycan degradation, metabolism of amino acids and post-translational protein phosphorylation. While the enrichment of pathways linked to haemostasis and platelet activation were unexpected, further analysis of the proteins implicated in these pathways revealed they often have other relevant functions. These include a downregulation of clusterin which prevents build-up of non-native proteins, such as blood plasma proteins, but also amyloid fibrils and the secreted isoform protects cells from apoptosis (Uniprot, P10909). GNA13 encodes a RhoA activating protein, and SLC7A5 is implicated in neuronal proliferation (Uniprot, Q14344, Q01650). Association analysis using STRING revealed no distinct clusters of proteins downregulated from secretome of MYO9A KD cells, however, STRING predicts that the network has significantly more interactions than would be expected to occur at random (Figure 6.5B).

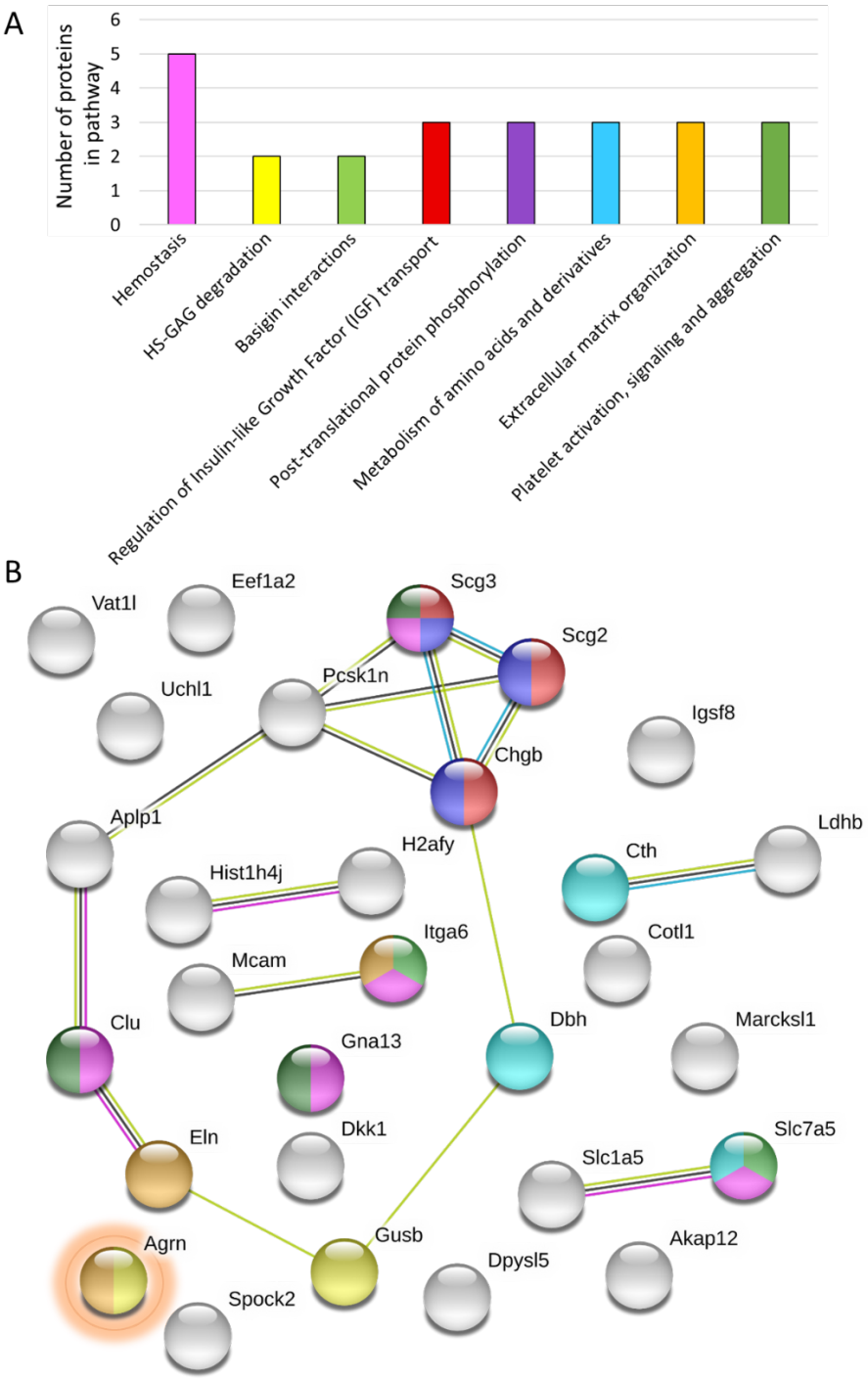

Figure 6.5. Pathway analysis and protein interaction network of downregulated proteins. A. Pathway analysis was performed for downregulated proteins from secretomic data in MYO9A KD and control NSC-34 cells, using STRING software. 8 enriched pathways are shown with the number of proteins identified in each. B. STRING interaction network displaying downregulated proteins. Connections represent evidence linking proteins either through co-expression, experimental data and co-occurrence in publications. Coloured nodes indicate presence of protein in enriched pathways shown in the graph. Agrin highlighted in orange.

6.3.2 Confirmation of secretomic findings

The finding that Agrin secretion was downregulated from NSC-34 cells lacking MYO9A was particularly interesting for this project. Agrin was identified with 8 unique peptides, the identification of one of these peptides in the proteomic screen is shown in Figure 6.6. The absence of this peptide over 3 repeats can be seen in the 3D montage of agrin peaks. Overall there was 5.4-fold less Agrin in the secretome of the KD cells than controls (p=0.0008, pANOVA).

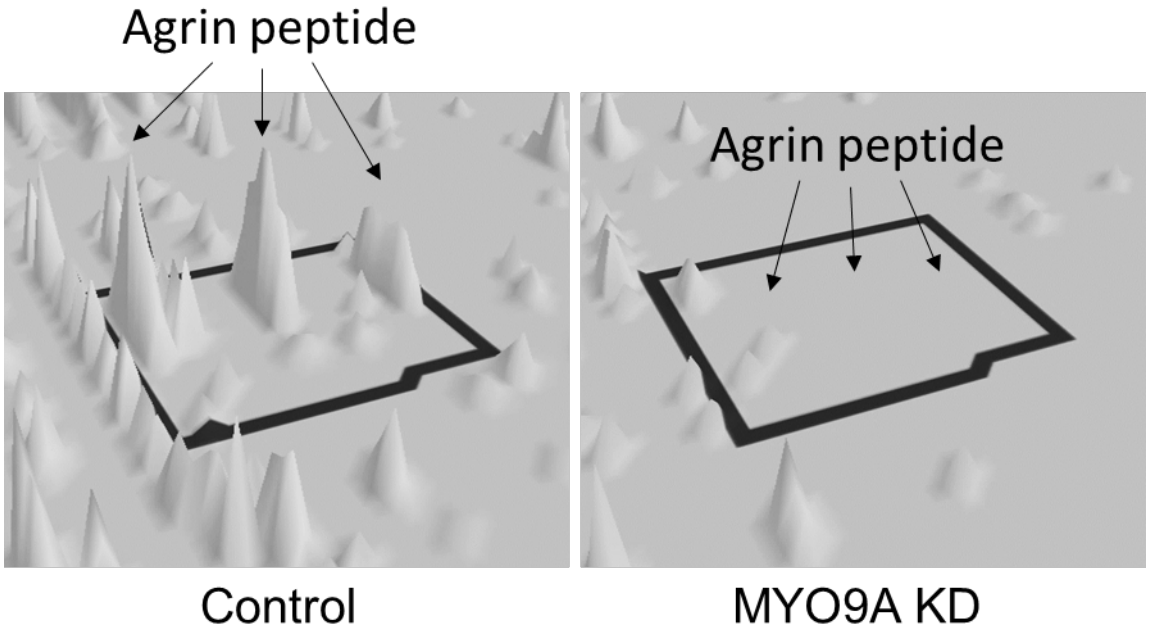

Figure 6.6. 3D montage of agrin peptide peaks. Agrin, as detected using the peptide: LYVGGLPEEQVATVLDR, was identified as dysregulated in the secretomic profile of control and MYO9A KD NSC-34 cells. An Absence of agrin can be observed in the MYO9A KD cells. Image generated by Vietxuan Phan, ISAS, Dortmund.

While detection of a protein by 8 unique peptides, over 3 repeats, is very robust data, this finding was also confirmed using immunofluorescence. Control and MYO9A KD cells were stained with an antibody against agrin and the fluorescence intensity quantified. A large increase in the intracellular presence of agrin can be seen in the MYO9A KD cells as compared to controls (Figure 6.7A). This was confirmed by measurement of the corrected total agrin fluorescence for each cell, in which a significant increase in intracellular agrin was identified in KD cells ($p<0.0001$, Mann Whitney test, Figure 6.7B). In the previous chapter, defects to the cytoskeleton and intracellular trafficking were improved by application of a ROCK inhibitor (Y-27632). It was hypothesised that this significant build-up of intracellular agrin, coupled with the lack of secreted agrin from the MYO9A KD cells could be due to impaired trafficking

or release of the protein from the nerves. Therefore, cells were treated with Y-27632 and then subject to agrin staining, revealing a significant reduction in the level of intracellular agrin in MYO9A-depleted cells ($p<0.0001$, Mann Whitney test), which was still significantly different to that observed in controls ($p<0.0001$, Mann Whitney test). Inhibition of ROCK also lead to a significant increase in intracellular agrin in treated control cells as compared to untreated ($p<0.0001$, Mann Whitney test).

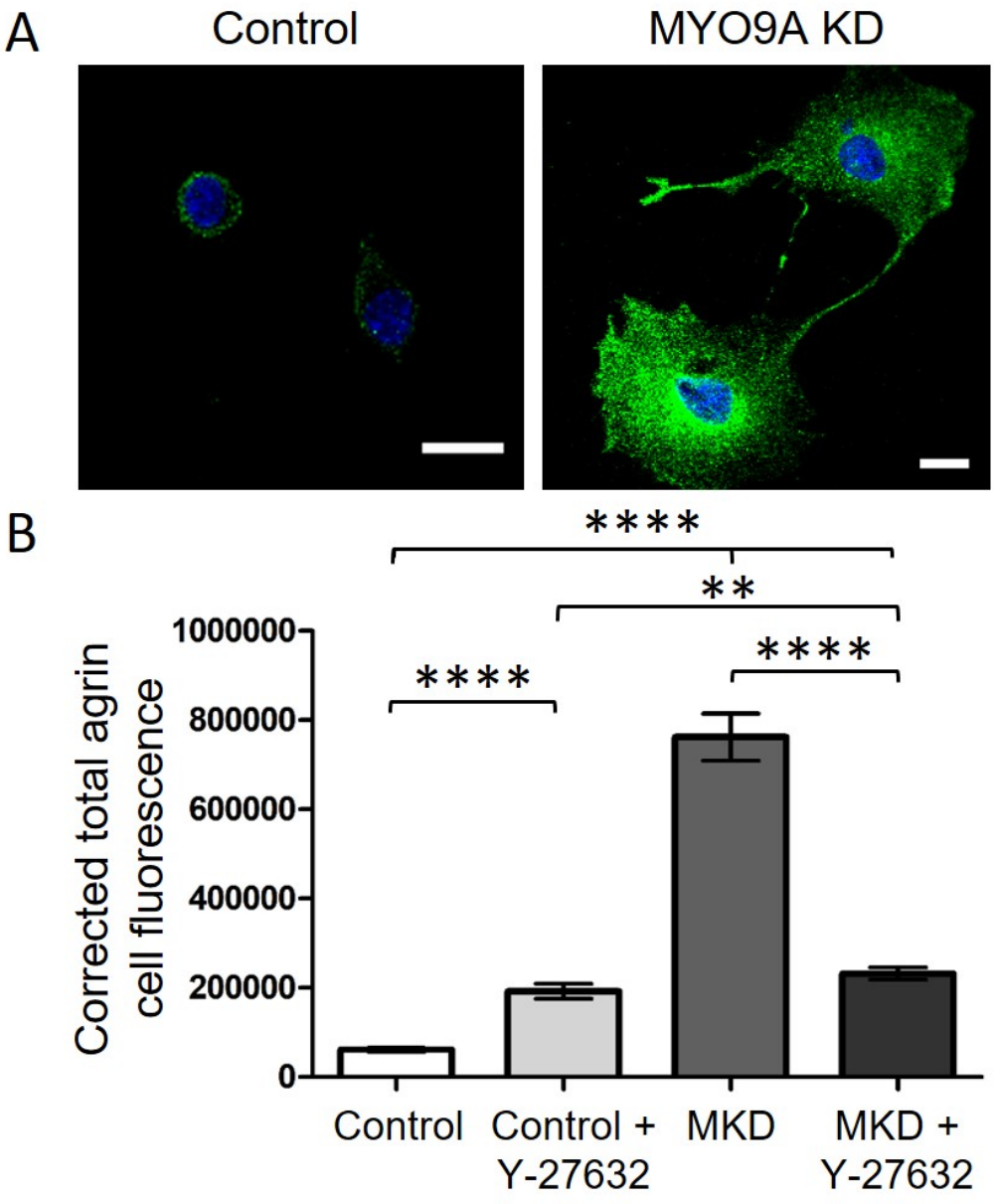

Figure 6.7. Expression of agrin in MYO9A KD cells. A. Immunofluorescent imaging of agrin in control and MYO9A KD NSC-34 cells. Scale bar = 20µm. B. Corrected total agrin fluorescence for control (n=126), MYO9A KD (n=99) and Y-27632-treated cells (control n=92, MYO9A KD n=99). **p<0.01, ****p<0.0001, Mann Whitney test. Error bars = mean ± S.E.M from 3 repeats.

This large increase in intracellular accumulation of agrin was hypothesised to increase the amount of agrin targeted for protein degradation, as secretion appeared impaired. Therefore, to investigate this the co-occurrence of agrin with proteins associated with degradation (P62 and ubiquitin) were investigated using immunofluorescence. IMARIS software was used to subtract background fluorescence from the images and then z-stack images were subject to thresholding to include the brightest 2% of pixels for each channel (Alexa Fluor 488 and 594). This allowed unbiased image analysis that eliminates the issue of differences in exposure time/image brightness between channels (Lorenzen et al., 2010). Colocalisation analysis was performed using Mander's coefficient, as this technique measures co-occurrence independently of the proportion of a signal (Dunn et al., 2011). This revealed a significant increase in the proportion of agrin that colocalised with P62 in MYO9A KD cells as compared with control ($p=0.0022$, Unpaired t-test, Figure 6.8A). The amount of the intracellular P62 population co-occurring with agrin was also significantly increased in cells lacking MYO9A ($p=0.0037$, Unpaired t-test). Representative images demonstrating an increase in pixels containing both green (agrin) and red (p62) for MYO9A KD NSC-34 cells as compared to controls are shown in Figure 6.8B. Similarly, there was a significant increase in the amount of agrin co-occurring with ubiquitin in cells depleted for MYO9A ($p=0.0081$, Unpaired t-test) and of the colocalisation of ubiquitin with agrin ($p=0.0136$, Unpaired t-test, Figure 6.8C). Example images as generated during analysis are shown in Figure 6.8B, including agrin (green) and ubiquitin (red).

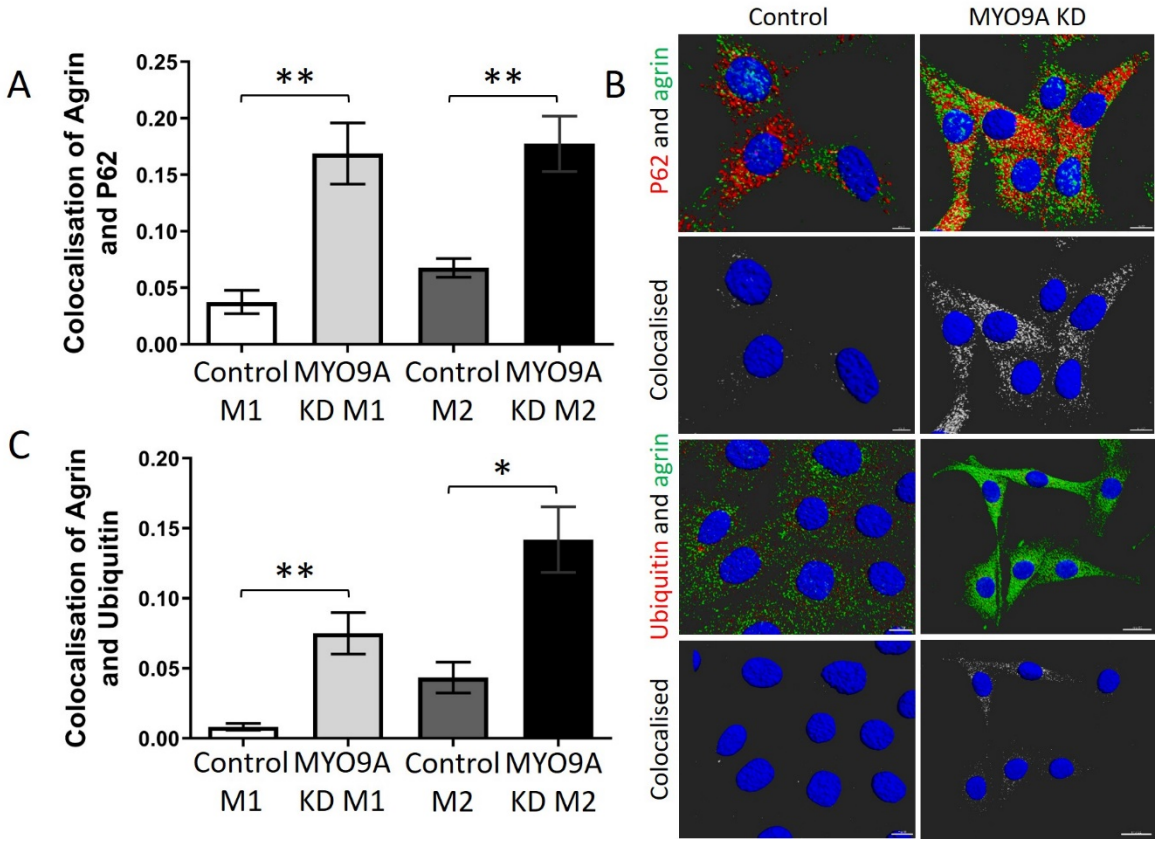

Figure 6.8. Colocalisation analysis of agrin with P62 and ubiquitin. A. Mander's coefficient co-localisation analysis of agrin and p62 in control (n = 6 fields of view) and MYO9A-depleted cells (n = 9 fields of view). M1 = proportion of agrin that co-localises with p62 and M2 = proportion of p62 that co-localises with agrin. B. Representative images of immunofluorescent staining in control and MYO9A KD cells for co-localisation analysis using IMARIS. Images have been subject to thresholding and 3D image projection. White staining represents pixels in which there is co-occurrence of the proteins analysed. Scale bars = 20µm. C. Co-localisation analysis of agrin and ubiquitin in control (n = 5 fields of view) and MYO9A KD cells (n = 10 fields of view). M1 = proportion of agrin that co-localises with ubiquitin and M2 = proportion of ubiquitin that co-localises with agrin. *p≤0.05, **p≤0.01, Mann Whitney test. Error bars represent mean ± S.E.M.

6.4 Agrin replacement therapy in Myo9aa/ab knockdown zebrafish

The decrease in secreted agrin from NSC-34 cells lacking MYO9A was an important finding in this study, and may provide a link between the molecular changes observed using the *in vitro* models to potential dysfunction of the NMJ. Agrin is secreted from the nerve terminal and acts on its receptor, LRP4, on the muscle membrane to stimulate downstream events mediating AChR clustering at the endplate (Kim et al., 2008). If agrin is still being synthesised by nerve cells lacking MYO9A, but is not being released sufficiently, this could impact on the structure of the NMJ and the ability of the muscle to respond to ACh released during synaptic transmission, thus leading to fatigable weakness. To test this hypothesis, the morphant and crispant zebrafish models of MYO9A-deficiency were utilised. As the

defect may be with the secretory process from the nerve, insertion of a plasmid to drive agrin expression would not overcome this problem. Therefore, a compound generated by Neurotune AG was used (Hettwer et al., 2014). This compound, NT1654, is a 44kDa fragment of the c-terminal of mouse agrin (Figure 6.9). It contains an 8 amino acid insert (at the z site), crucial for the ability of agrin to stimulate AChR clustering. NT1654 is also soluble and resistant to neurotrypsin breakdown, thus can be applied systemically and maintain action at the NMJ without inactivation due to trypsin-mediated cleavage. Treating the zebrafish with this compound would bypass the identified issues with secretion, as NT1654 would be present in the synaptic cleft without requiring release from the nerve terminal. Therefore, control and MYO9A-deficient zebrafish were subject to agrin-replacement therapy and effects on NMJ morphology and motor behaviours assessed.

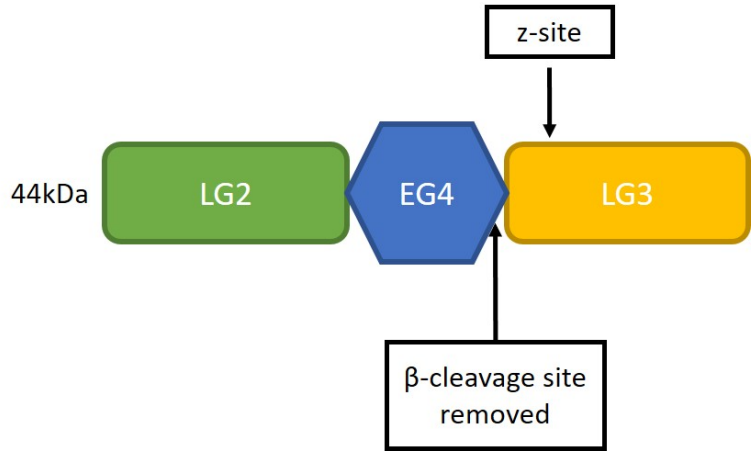

Figure 6.9. Schematic of NT1654. Domains of neural agrin included in the NT1654 compound, including LG2, EG4 and LG3. The β-cleavage site has been removed to prevent breakdown by neurotrypsin and the 8 amino-acid insert at the z-site is present for AchR clustering activity. Figure adapted from(Hettwer et al., 2014).

6.4.1 Dose-finding experiments for NT1654 treatment in zebrafish

NT1654 has not previously been used in zebrafish, therefore a dose-finding experiment was first performed in wildtype fish. Concentrations were trialled from 890pM (0.15ng/4.2nl drop size) to 14.3nM (2.5ng/4.2nl), as *in vitro* analysis of the AChR clustering ability of NT1654 on C2C12 myotubes revealed the ability of the compound to induce clusters between 450pM and 108nM (Hettwer et al., 2014). The molecular weight of NT1654 is 44kDa, therefore it was too large to add to the water of zebrafish and had to be injected into the embryo at the one-cell stage, as performed with MO and sgRNA injections. After 48 hours of development, survival of embryos was assessed, revealing that uninjected zebrafish had a 75% survival rate, while 0.15ng of compound reduced this to 59%. The decline continued in a dose-

dependent manner and amounts over 1.2ng per drop injected reduced survival rates to almost 0% (Figure 6.10).

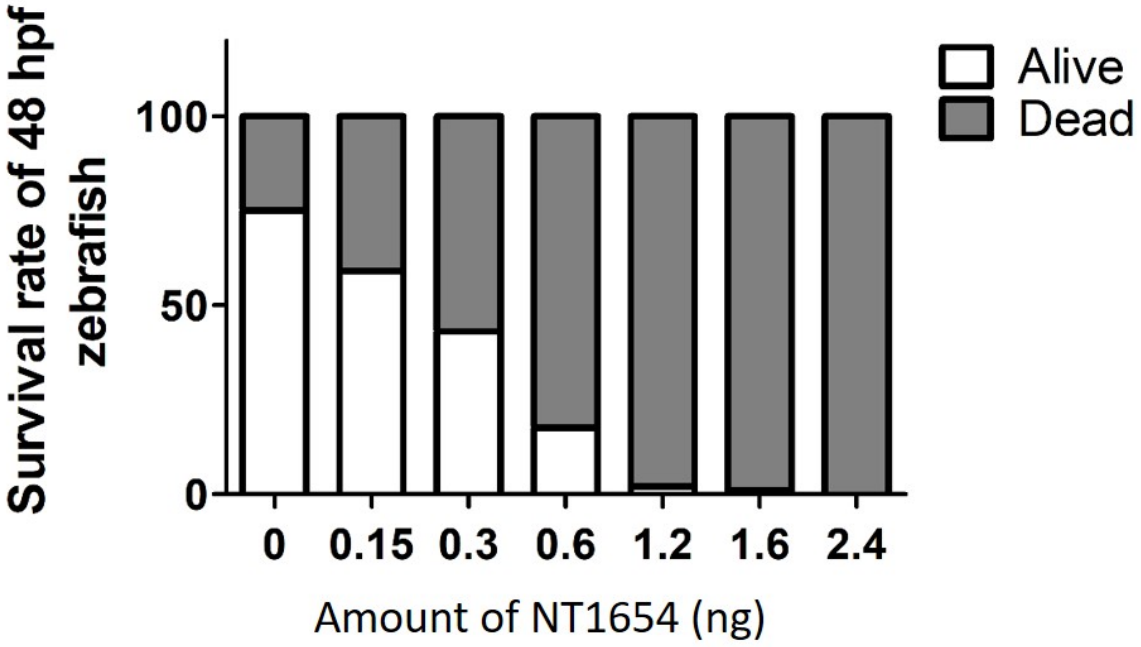

Figure 6.10. Survival rates of zebrafish treated with NT1654. Wildtype zebrafish were injected with different concentrations of NT1654 at the 1-cell stage and survival tracked over 48 hours (0-2.4ng per drop injected). Fish that survived to 48 hpf are shown in white, proportion that died are in grey, n=200 per concentration.

As co-injection of NT1654 with MO or sgRNA/Cas9 is likely to cause increased toxicity in the zebrafish, partly due to injecting larger amounts of foreign material, the lowest two doses assessed for effects on survival were used in the next experiment. As it has been reported that muscles with appropriate innervation are unaffected by NT1654 treatment (Hettwer et al., 2014), here the effect of treatment on motor behaviours in developing zebrafish was tested. As shown in Figure 6.11A, movements performed within the chorion per minute were significantly reduced in fish treated with 0.15ng and 0.3ng of NT1654, as compared with controls ($p=0.0007$, $p<0.0001$ respectively, Mann Whitney test). At 48 hpf, the tactile stimulation assay revealed a significant increase in the distance travelled after application of 0.15ng and 0.3ng NT1654 ($p=0.0284$, $p=0.0039$ respectively, Mann Whitney test, Figure 6.11B). Similarly, this was also reflected in an increase of average speed of movements in response to the stimulus, with speed increasing significantly for both concentrations (0.15ng $p=0.0043$, 0.3ng $p=0.0196$, Mann Whitney test, Figure 6.11C). As toxicity was lower for 0.15ng treatment with NT1654, and effect on

movement in wildtype fish was also less than in 0.3ng-treated, the lower dose was chosen for the subsequent study.

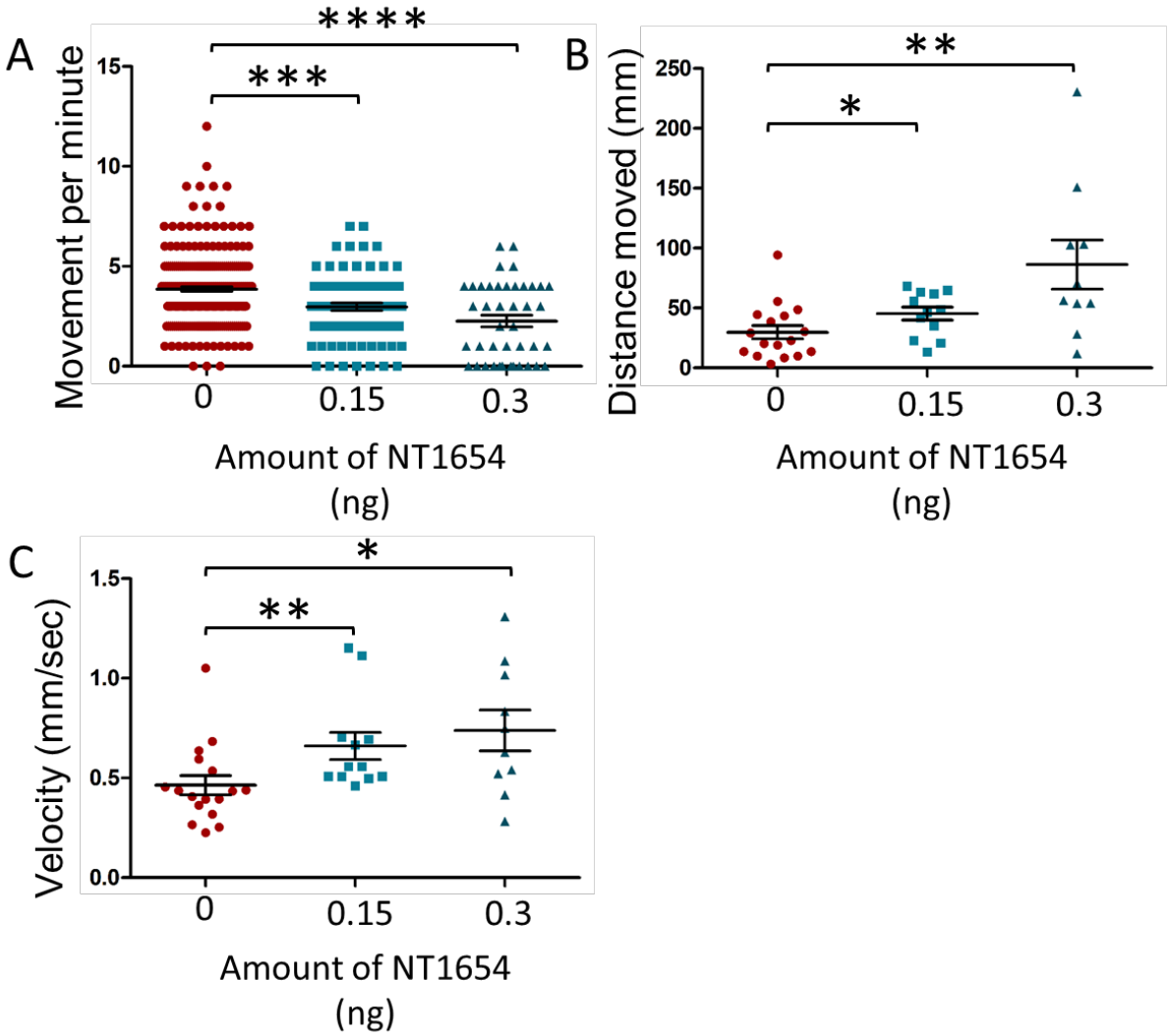

Figure 6.11. Effect of NT1654 on movements during zebrafish development. A. Movements within chorion at 24 hpf by wildtype zebrafish treated with 0ng (n=242), 0.15ng (n=78) and 0.3ng (n=42) NT1654. B. Distance travelled and C. average speed of movement in response to tactile stimulation at 48 hpf of wildtype zebrafish treated with 0ng (n=17), 0.15ng (n=12) and 0.3ng (n=10) NT1654. *p<0.05, **p<0.01, ***p<0.001, ****p<0.0001, Mann Whitney test, error bars = mean ± S.E.M.

6.4.2 Effect of NT1654 on gross morphology and behavioural phenotypes in Myo9aa/ab-depleted zebrafish.

The lowest dose trialled was used for the subsequent study in an attempt to reduce the number of dying zebrafish in early development, as injection of MO and sgRNA to deplete Myo9aa/ab also cause a degree of toxicity. Control (uninjected) and Myo9aa/ab morphant zebrafish were treated with 0.15ng NT1654 at the one-cell stage (NT1654 co-injected with Myo9aa and Myo9ab MOs), as described in O'Connor *et al.* (2018a). After 48 hpf, survival rates were assessed, revealing 11% of

control and 23% of morphant fish had died (p=0.0661, one-way ANOVA, Figure 6.12). Application of NT1654 to control fish caused 29% more to die over 2 days (p<0.0001, one-way ANOVA), and in MO/NT1654 co-injected fish 48% more fish died than in MO-injected alone (p<0.0001, one-way ANOVA).

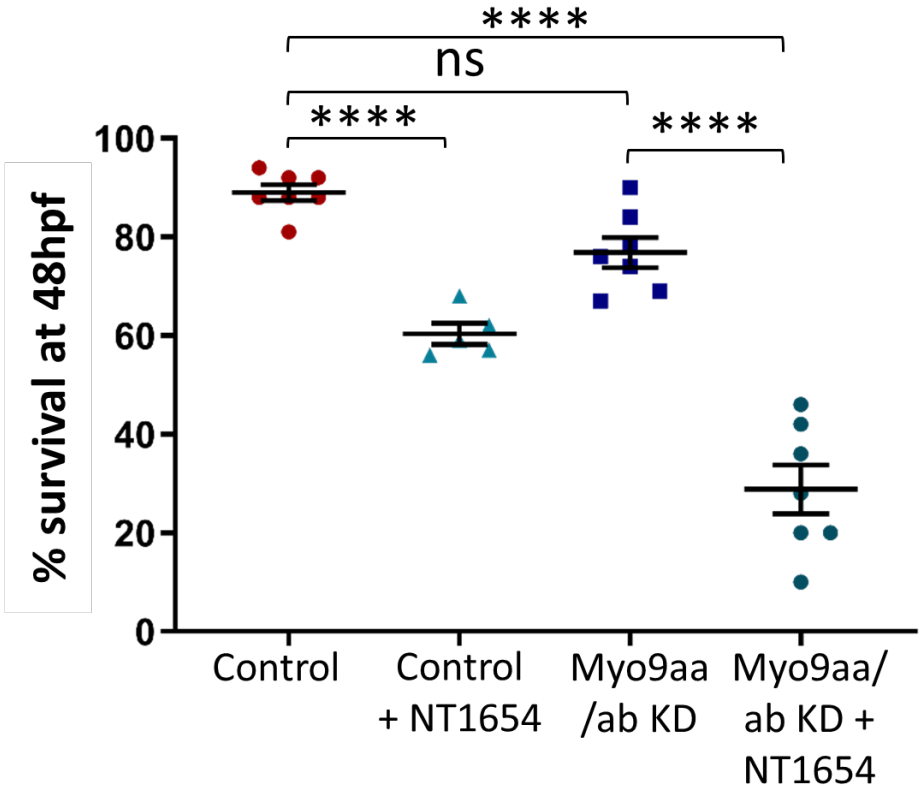

Figure 6.12. Survival rates of Myo9aa/ab morphant zebrafish treated with NT1654. Control and Myo9aa/ab morphant fish were treated with 0.15ng NT1654 and survival at 48 hpf assessed. Control n=354, control + NT1654 n=239, Myo9aa/ab morphant n=319, Myo9aa/ab morphant n=329. ****p<0.0001, ns=not significant, one-way ANOVA. Error bars = mean ± S.E.M.

In order to assess whether application of this concentration of NT1654 was having any observable improvements to the phenotype of Myo9aa/ab-depleted zebrafish (Figure 6.13A), fish were classified according to their gross phenotype at 24 hpf (Figure 6.13B). Phenotypes were classed as ‘normal’, ‘mild/moderate’ and ‘severe’, based on tail lengths, head morphology and overall appearance. In control fish, 93% were normal in phenotype, with 4% mild/moderate and 3% severe. Fish depleted for Myo9aa/ab were 40% normal, 49% mild/moderate and 11% severe, whereas those treated with NT1654 exhibited a 32% improvement in number of normal appearing fish and only 28% were now classed as abnormal.

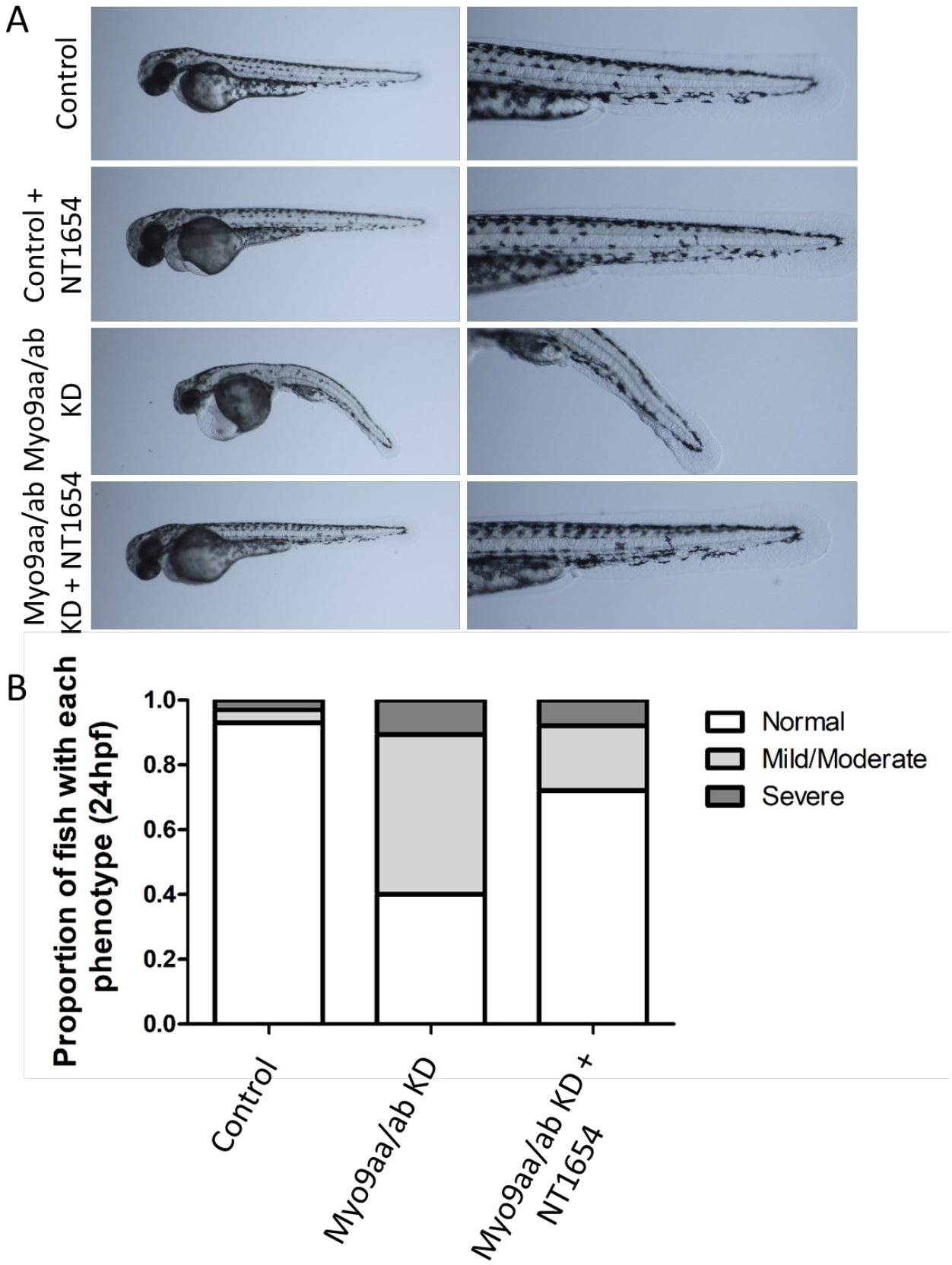

Figure 6.13. Phenotypes of NT1654-treated zebrafish. A. Representative images of control and Myo9aa/ab morphant fish (72 hpf) treated with NT1654. B. Control (n=99), Myo9aa/ab morphant (n=85) and Myo9aa/ab morphant + NT1654-treated (n=50) fish were manually assessed and categorised according to phenotype at 24 hpf. Phenotypes were classed as normal, mild/moderate and severe.

After finding that 0.15ng NT1654 treatment was able to ameliorate some of the gross morphological defects observed in the morphant zebrafish, the effect on motor behaviours was assessed. As shown in Figure 6.14, at 24 hpf a reduction of Myo9aa/ab expression caused a significant reduction in the movements performed in the chorion (p=0.0009, Unpaired t-test). The movement impairment was significantly improved by treatment with NT1654, to a level no longer significantly different to controls (p=0.0079, p=0.6435 respectively, Unpaired t-test).

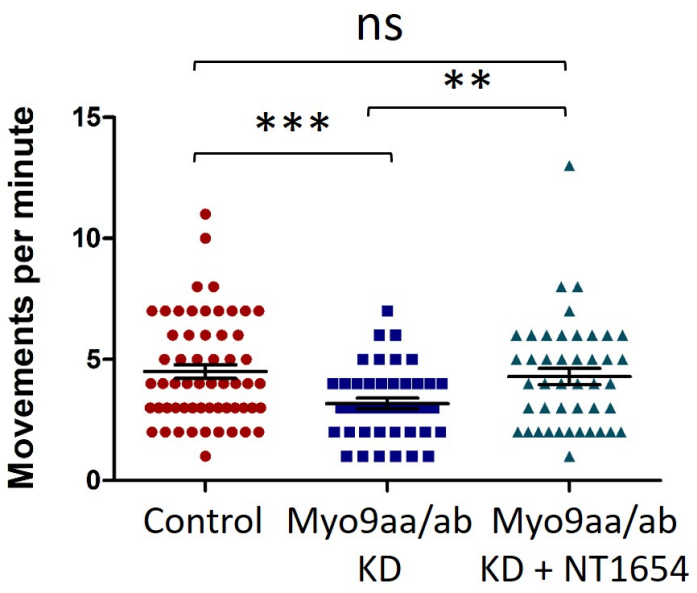

Figure 6.14. Effect of NT1654 on chorion movements of Myo9aa/ab morphant fish. At 24 hpf, control (n=58), Myo9aa/ab morphant (n=43) and Myo9aa/ab morphant + NT1654-treated (n=44) zebrafish were subject chorion movement analysis. Number of full chorion twists performed per minute was assessed. **p≤0.01, ***p≤0.001, ns = not significant, Unpaired t-test.

At 48 hpf, the response of zebrafish depleted for Myo9aa/ab to the tactile stimulation assay was impaired, as described in Chapter 4, Section 4.4.2. To determine whether 0.15ng NT1654 treatment also improved movement at this later time-point, control and Myo9aa/ab morphant fish were tested at 48 hpf. In Figure 6.15, a significant reduction in distance travelled by morphant fish can be observed as compared to controls (p=0.0004, Kruskal-Wallis test). Distance swam in response to tactile stimulation was significantly improved by treatment with NT1654, restoring the response to a level comparable with controls (p=0.0265 and p=0.8769 respectively, Kruskal-Wallis test). No significant difference in the distance travelled was observed in control NT1654-treated fish, as opposed to observations in the dose trial experiment (p=0.3802, Kruskal-Wallis test).

The average speed of the swimming response elicited followed the same trend as the distance travelled, with a significant decrease in the speed of morphant fish as compared to control which was increased by application of NT1654 ($p<0.0001$, Kruskal-Wallis test). Again, control fish treated with NT1654 did not exhibit a significant change in speed and treated morphants were no longer significantly different to controls ($p>0.9999$, Kruskal-Wallis test).

Initial acceleration of zebrafish, indicative of force of muscle contraction, was also significantly impaired in morphant fish ($p<0.0001$, Kruskal-Wallis test). Significant improvements were observed following NT1654-treatment in the morphant fish ($p=0.0037$, Kruskal-Wallis test), to a level comparable with untreated controls. There was no significant effect of NT1654 treatment on the acceleration of control fish ($p>0.9999$, Kruskal-Wallis test).

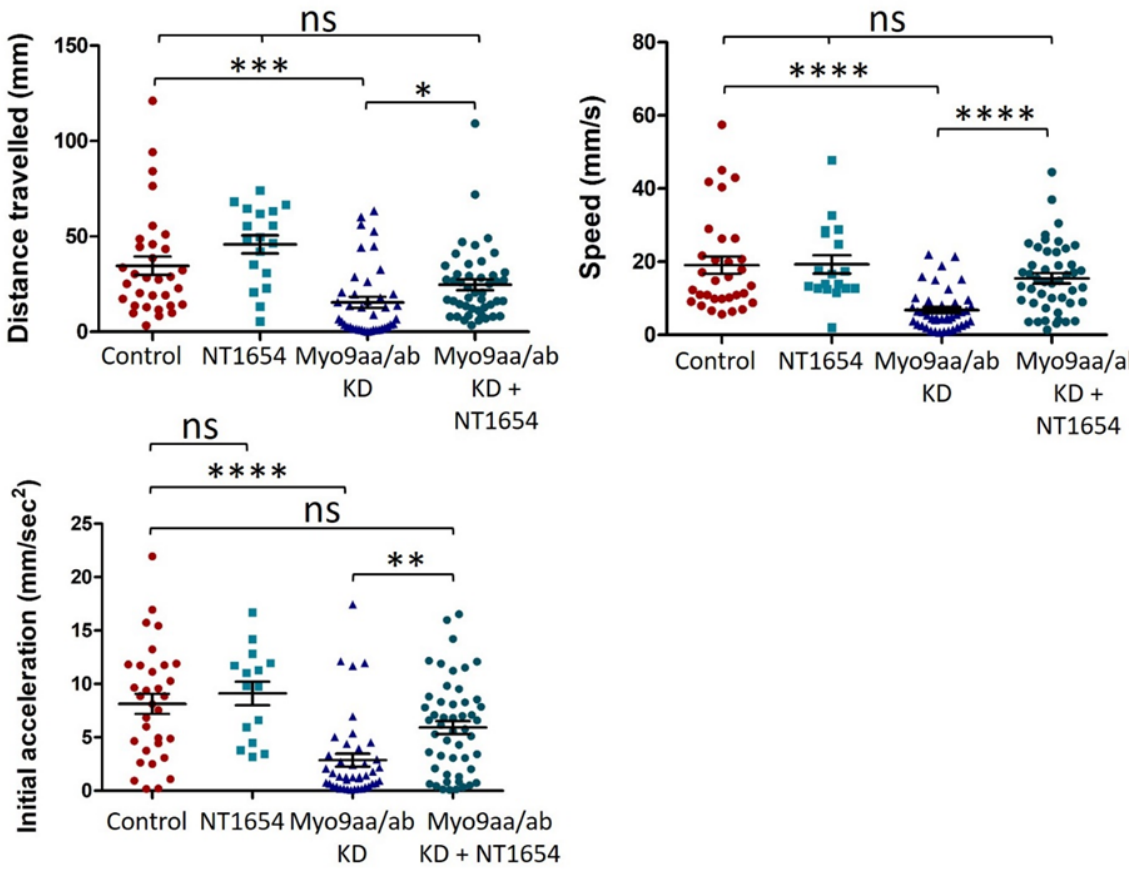

Figure 6.15. Effect of NT1654 on movements of Myo9aa/ab morphant fish at 48 hpf. Distance travelled, average speed and initial acceleration of control, Myo9aa/ab morphant and NT1654-treated zebrafish tactile stimulation responses at 48 hpf as calculated using TrackMate (ImageJ). *P ≤ 0.05, **P ≤ 0.01, ***P ≤ 0.001, ****P ≤ 0.0001, ns=not significant, Kruskal-Wallis test, error bars represent mean ± S.E.M. Control n=32, NT1654 n=18, Myo9aa/ab morphant (KD) n=41, Myo9aa/ab morphant + NT1654 n=46.

While the MO-mediated approach reduces the expression of Myo9aa/ab at the RNA level, the NT1654 treatment was repeated using crispant fish which are genetically mosaic for deletions in *myo9aa/ab.* This was performed to account for the non-specific effects that can be associated with MO-injections that may confound results (Schulte-Merker and Stainier, 2014), and also to remove any potential sampling bias due to higher death rate in co-injected MO+NT1654 fish.

Assessment of survival rates was performed for control (uninjected), *tyr* crispant (injected control) and *myo9aa/ab* crispant, as well as *tyr* and *myo9aa/ab* treated with NT1654 at the time of CRISPR/Cas9 delivery. Results obtained revealed no significant differences in survival rates for any condition (Kruskal-Wallis test, Figure 6.16).

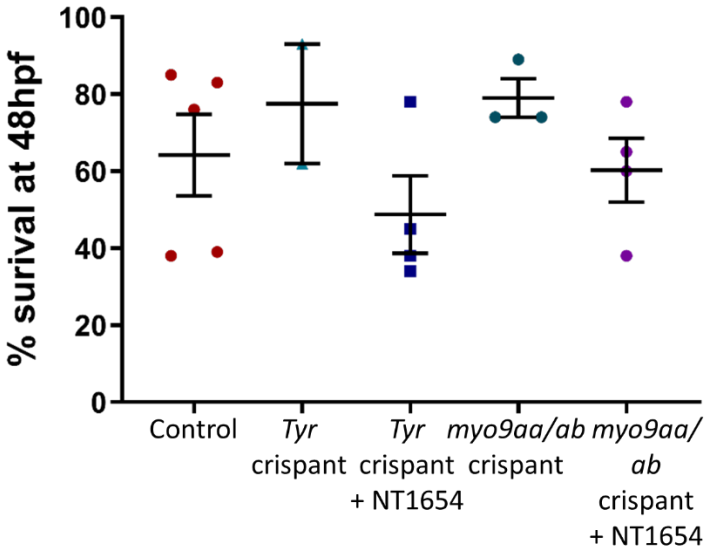

Figure 6.16. Survival rates of *myo9aa/ab* crispant zebrafish treated with NT1654. Control, *tyr* and *myo9aa/ab* crispant fish were treated with 0.15ng NT1654 and survival at 48 hpf assessed. Control n=238, *tyr* n=53, *tyr* + NT1654 n=195, *myo9aa/ab* n=141 and *myo9aa/ab* n=223. No significant differences between any condition, Kruskal-Wallis test. Error bars = mean ± S.E.M.

As survival rates for co-injected crispant and NT1654 fish were not affected, the movement tests that were performed in morphant fish were repeated in crispants to confirm results. At 24 hpf the movements performed in the chorion were significantly reduced by decreasing *myo9aa/ab* expression, and this was significantly improved by treating with NT1654 ($p<0.0001$, Kruskal-Wallis test, Figure 6.17). The improvement in number of movements per minute was still significantly lower than that performed in controls ($p=0.0232$, Kruskal-Wallis test).

In the tactile response assay, distance travelled was significantly reduced after stimulus in *myo9aa/ab* crispants as opposed to controls, and again this was rescued by NT1654 treatment, to a level similar to controls ($p<0.0001$, $p<0.0001$, $p>0.9999$ respectively, Kruskal-Wallis test).

Average speed of crispant fish was decreased significantly as compared with controls ($p=0.0002$, Kruskal-Wallis test). Application of NT1654 able to rescue this decrease to a level comparable with controls ($p<0.0001$, $p>0.9999$ respectively, Kruskal-Wallis test). Acceleration was also significantly decreased in crispants as compared to controls ($p=0404$, Kruskal-Wallis test). The ability of crispant fish to accelerate effectively was improved by treatment, to a level not significantly different from controls ($p=0.0002$, $p=0.8746$ respectively, Kruskal-Wallis test).

Therefore, the restorative effect of NT1654 treatment on movement of zebrafish lacking Myo9aa/ab at 24 hpf and 48 hpf was observed when depletion of Myo9aa/ab was performed using either MO or CRISPR/Cas9 techniques.

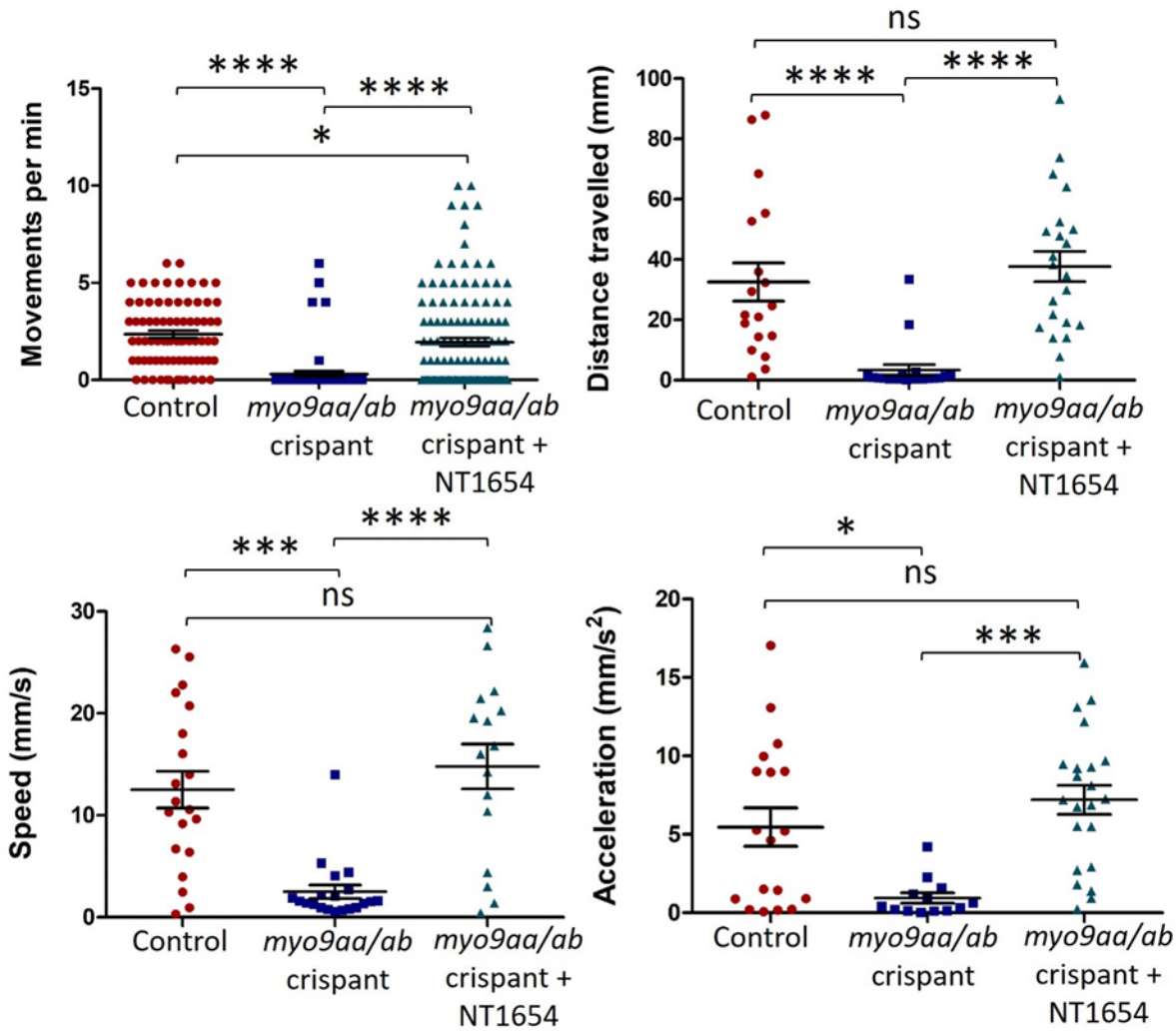

Figure 6.17. Effect of NT1654 on movements of *myo9aa/ab* crispant fish in development. Chorion movements per minute at 24 hpf, as well as distance travelled, average speed and initial acceleration of control, *myo9aa/ab* crispant and 0.15ng NT1654-treated crispant zebrafish in response to tactile stimulation at 48 hpf are shown. *P ≤ 0.05, **P ≤ 0.01, ***P ≤ 0.001, ****P ≤ 0.0001, ns=not significant, Kruskal-Wallis test, error bars represent mean ± S.E.M. Control n=32, NT1654 n=18, *myo9aa/ab* crispant n=41, *myo9aa/ab* crispant + NT1654 n=46. Chorion movements: control n=77, crispant n=65 and NT1654 crispant n=129, 48 hpf movements: control n=18, crispant n=20 and NT1654 crispant n=22.

6.4.3 NMJ analysis after NT1654 application

In Chapter 4, defects to the morphology of the developing NMJ were described in zebrafish, namely an impairment in AChR cluster formation and motor neuron outgrowth in 24hpf crispants, reduced pre and postsynaptic clusters at 48 hpf and less developed innervation patterns which were reflected by the defective movements observed. As motor behaviours show vast improvement after application of the exogenous agrin fragment, whether NT1654 treatment also improved morphology of the developing neuromuscular system was investigated. A screen of MO-injected fish was performed without in-depth morphological analysis (Figure 6.18), which revealed an improvement in the appearance of AChR clusters and motor neuron innervation patterns by 48 hpf after NT1654 treatment (O'Connor et al., 2018a). In the images shown, extension of motor neurons down the myotome and back up the myosepta was observed in the treated morphants but not in the untreated. Furthermore, as expected for the function of NT1654 in clustering AChRs, more prominent AChR staining was present in treated fish as indicated with an arrow-head.

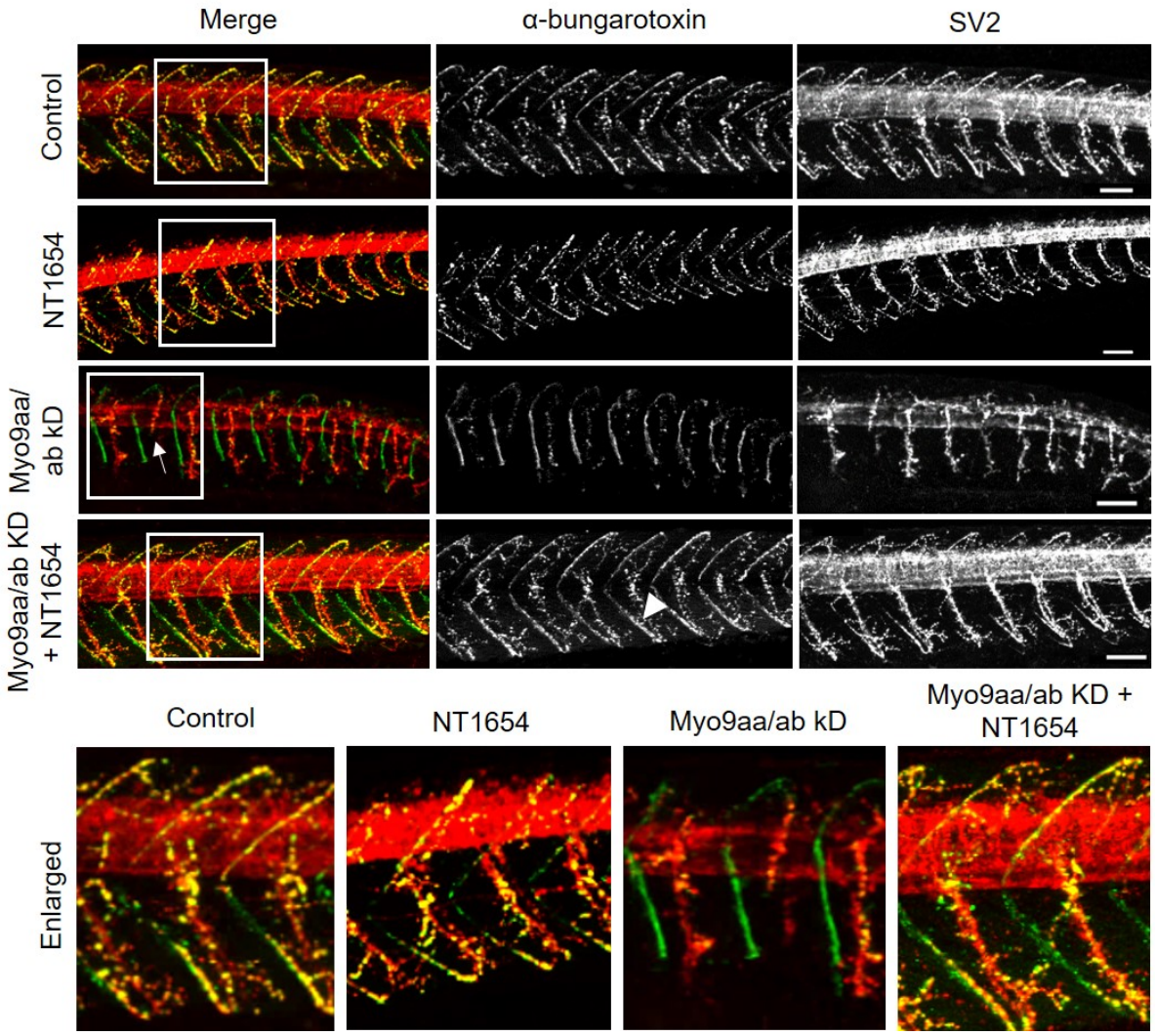

Figure 6.18. Immunofluorescent staining of 48 hpf Myo9aa/ab morphant zebrafish treated with NT1654. Control and Myo9aa/ab morphant (KD) zebrafish were treated with NT1654 and NMJs visualised using an antibody against SV2 (pre-synaptic vesicles, red) and fluorophore-conjugated aBTx (post-synaptic AChRs, green). Example of a shortened motor axon in Myo9aa/ab morphant shown with white arrow. Prominent AChR fluorescence shown with white arrow head. Enlarged regions of images in bottom panel demarcated with white boxes. Scale bars = 50μm.

To expand on the promising observations made in the treated morphant fish, quantitative analysis of NMJs in NT1654-treated crispants was performed at 24 hpf, 48 hpf and 5 dpf. At 24 hpf, the presence of longer motor neurons could be identified, as well as increased presence of the AChR 'choice point' cluster at the horizontal myoseptum (Figure 6.19).

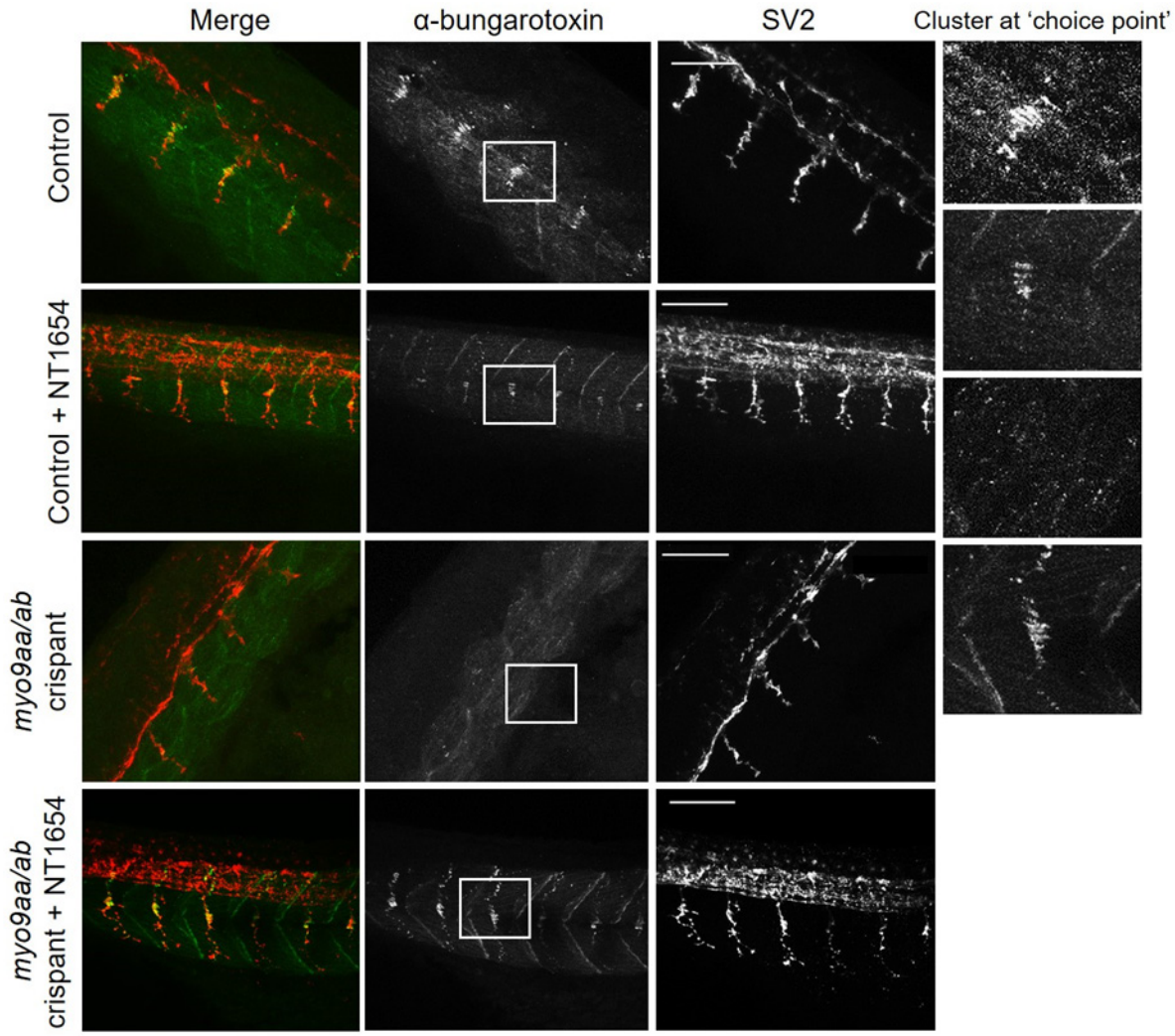

Figure 6.19. NMJ morphology of 24 hpf *myo9aa/ab* crispant zebrafish treated with NT1654. Representative images of NMJs in NT1654-treated control and *myo9aa/ab* crispant zebrafish at 24 hpf. Acetylcholine receptors stained with aBTx (green), and motor neurons detected with an antibody against SV2 (red). White boxes demark areas enlarged in the right-hand panel. Scale bar = 50μm.

Quantification of various features of motor neuron/AChR morphology was also performed at 24 hpf, and compared to data presented in Chapter 4 for control and *myo9aa/ab* crispants (Figure 6.20). A summary of the results are shown in Table 6-2. A significant increase was found in the area of AChR clusters in NT1654-treated crispants as compared to untreated crispants and controls ($p=0.0004$, $p=0.0028$ respectively, one-way ANOVA), corroborating with the observation that there was increased AChR staining at cluster points in Figure 6.19. Total area of AChR clusters was also significantly increased in treated crispant fish as compared to untreated crispants ($p<0.0001$, one-way ANOVA) and controls ($p=0.0025$, one-way ANOVA). The number of AChR clusters over 20μm^2 in size was significantly increased after NT1654 treatment, to a level also significantly higher than in control fish ($p=0.0017$,

p=0.0078 respectively, one-way ANOVA). Reflecting both of these parameters, the proportion of myotomes with a choice point cluster present was also improved, to a similar amount as in controls (p=0.0007, p=0.9649 respectively, one-way ANOVA). Size of myotomes was unaffected by application of NT1654, although the presence of smaller myotomes observed in the crispants were absent in the treated fish and most fish had myotomes of very similar sizes after treatment. With regards to presynaptic features, the length of motor neuron outgrowths past the choice point were not significantly affected by NT1654 treatment, however treatment again reduced variability. The number of neurons expressed as a proportion of somite number at 24 hpf was decreased in *myo9aa/ab* crispants (p=0.0489, one-way ANOVA), and this was significantly increased by application of NT1654 to a level comparable with controls (p=0.0002, one-way ANOVA). Therefore, at 24 hpf treatment of *myo9aa/ab* crispant fish with NT1654 was able to rescue the proportion of myotomes expressing a choice point cluster of AChRs and with a neuron outgrowth, as well as increase the total area covered by AChRs in general and the average cluster size.

Control zebrafish were also treated with NT1654 and NMJ morphology quantified. However, overall at 24 hpf control fish were relatively unaffected by injection of NT1654 and no significant differences were detected for any parameter.

		Compared to untreated controls		
	24 hpf NMJ parameters	**control + NT1654**	**myo9aa/ab crispant**	**myo9aa/ab crispant + NT1654**
Presynaptic	Neurons as proportion of somites			
	Length of axon past choice point			
Postsynaptic	Area of aBTx clusters			
	Total area of aBTx clusters			
	Proportion of myotomes with choice point cluster			
	aBTx clusters >20µm²			
	Size of myotomes			

Table 6-2. Summary of NMJ morphology results obtained in 24 hpf zebrafish treated with NT1654. Red = significantly less than untreated controls, blue = statistically unchanged from controls and green = significantly increased as compared to controls.

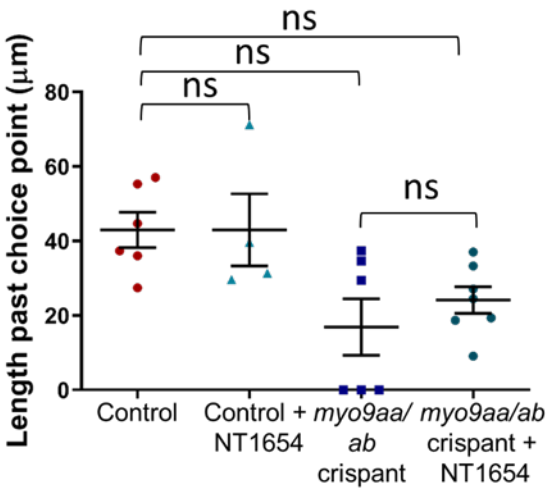
Length past choice point (μm)
ns
ns
ns
ns
Control
Control + NT1654
myo9aa/ab crispant
myo9aa/ab crispant + NT1654

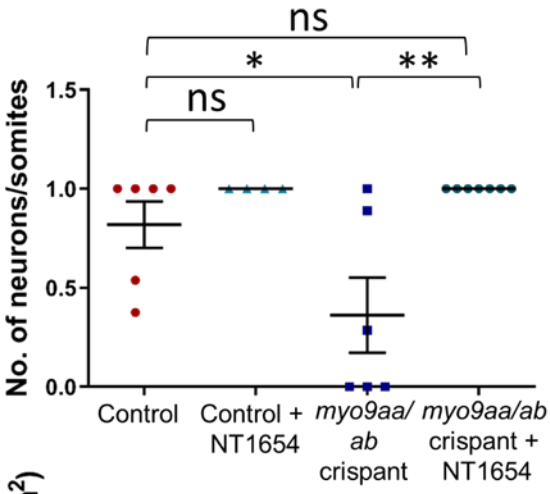
No. of neurons/somites
ns
*
**
ns
Control
Control + NT1654
myo9aa/ab crispant
myo9aa/ab crispant + NT1654

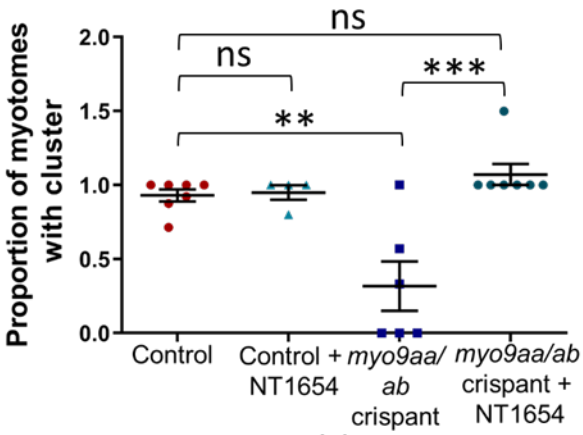
Proportion of myotomes with cluster
ns
ns
**
***
Control
Control + NT1654
myo9aa/ab crispant
myo9aa/ab crispant + NT1654

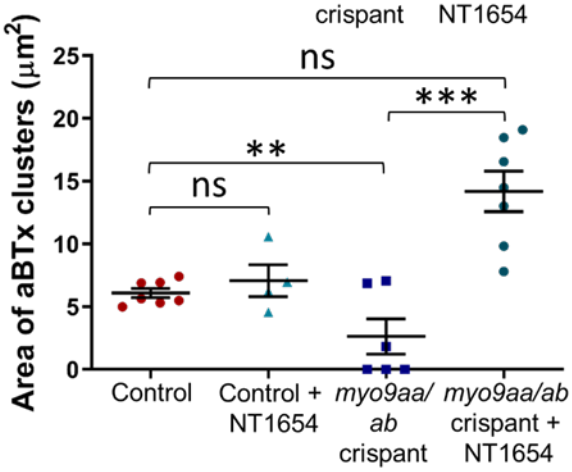
Area of aBTx clusters (μm²)
ns
**
ns
***
Control
Control + NT1654
myo9aa/ab crispant
myo9aa/ab crispant + NT1654

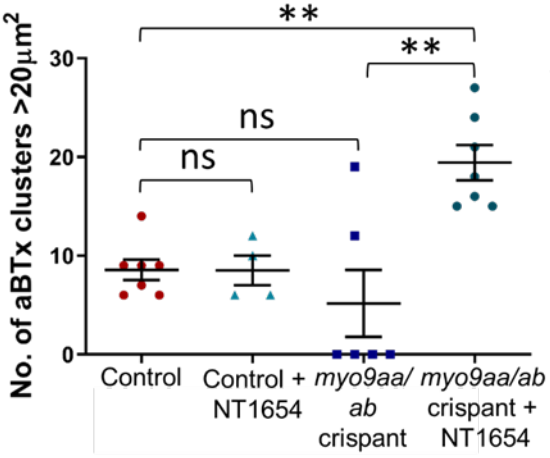
No. of aBTx clusters >20μm²
**
ns
ns
**
Control
Control + NT1654
myo9aa/ab crispant
myo9aa/ab crispant + NT1654

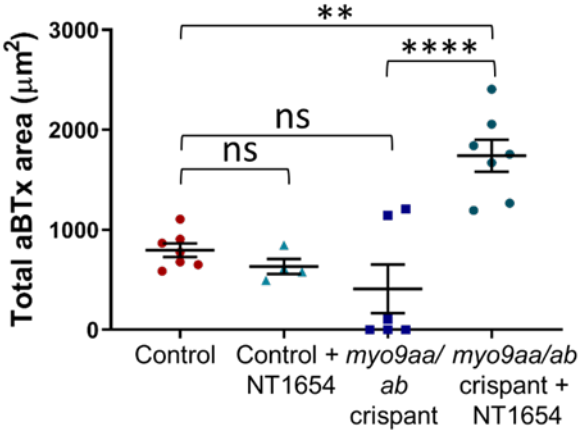
Total aBTx area (μm²)
**
ns
ns
****
Control
Control + NT1654
myo9aa/ab crispant
myo9aa/ab crispant + NT1654

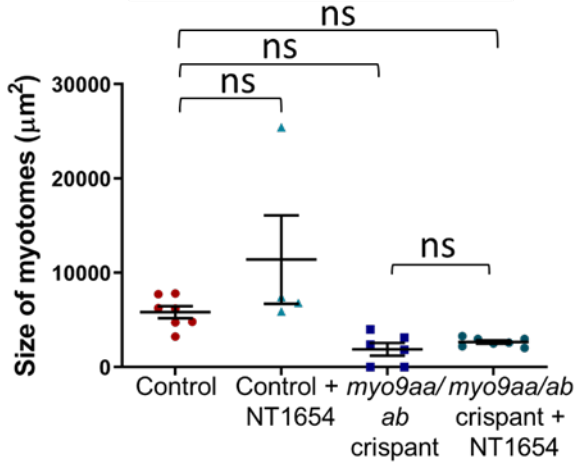
Size of myotomes (μm²)
ns
ns
ns
ns
Control
Control + NT1654
myo9aa/ab crispant
myo9aa/ab crispant + NT1654

Figure 6.20. Quantification of NT1654-treated *myo9aa/ab* crispant zebrafish NMJ morphology at 24 hpf. Various features of NMJ morphology in control (n=7), *myo9aa/ab* crispants (n=6), *myo9aa/ab* crispants + NT1654 (n=6) and control + NT1654 fish (n=4) were quantified: average and total area of acetylcholine receptor (aBTx) clusters and number over 20μm^2, size of muscle myotomes, proportion of myotomes with a cluster, number of neurons per myotome and the length these neurons had extended past the choice point. Error bars = mean ± S.E.M. *p≤0.05, **p≤0.01, ***p≤0.001, ns = not significant, one-way ANOVA.

The effect of NT1654 on 48 hpf NMJs was also assessed, as improvements were found in crispant fish responding to tactile stimulation at this time point. Immunofluorescent imaging revealed a decrease in the presence of pre and postsynaptic clusters across the surface of the myotomes in crispants, which appeared restored in NT1654-treated controls (Figure 6.21). In *myo9aa/ab* crispants the innervation pattern over the surface of the myotome appeared improved after NT1654 treatment as shown in the enlarged image panel, and motor neurons extended further up the myosepta.

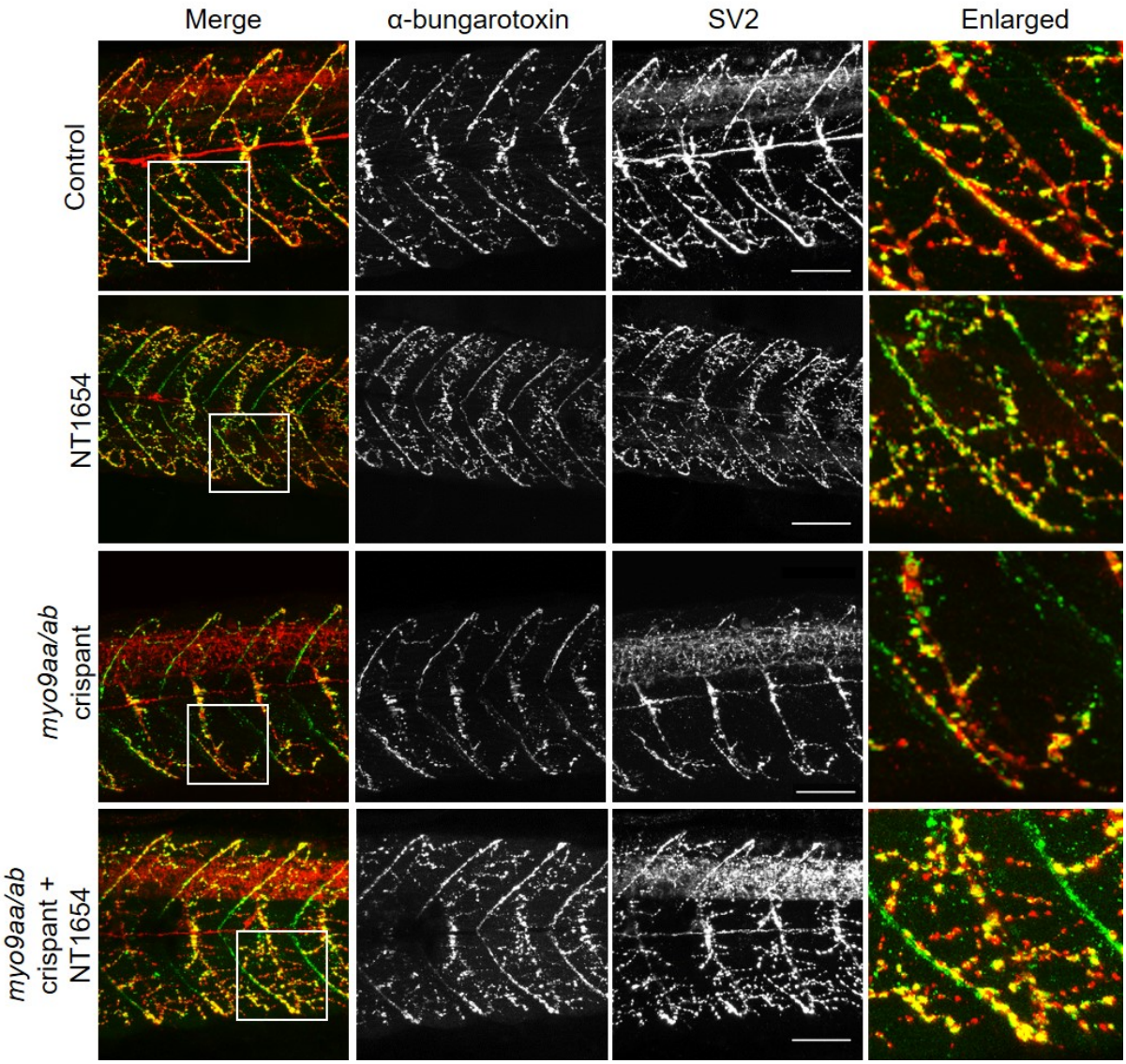

Figure 6.21. NMJ morphology of NT1654-treated *myo9aa/ab* crispant zebrafish at 48 hpf. Representative images of NMJs in untreated or NT1654-treated control and *myo9aa/ab* crispant zebrafish at 48 hpf. AChRs stained with aBTx (green), and motor neurons detected with an antibody against SV2 (red). White boxes demark areas enlarged in the right-hand panel. Scale bars = 50μm.

The effect of NT1654 treatment on control and *myo9aa/ab* crispant fish NMJ morphology was also quantified at 48 hpf (Figure 6.22), and a summary shown in Table 6-3. The number of SV2 (presynaptic) clusters per myotome was significantly improved in crispant fish to a level similar to controls (p=0.0346, Kruskal-Wallis test). The number of clusters per 100μm^2 however, was not significantly changed although there were on average 3.7 clusters in controls, 3.1 in NT1654-treated controls and 2.5 in crispants, which was increased to 4.5 following NT1654 treatment. The number of large clusters, over 20μm^2, was not altered by application of the agrin compound to crispants or controls, and neither was the percentage of myoseptal innervation. The average area of SV2 clusters was significantly elevated in fish lacking

Myo9aa/ab as compared to controls (p=0.0020, Kruskal-Wallis test). The average SV2 cluster area was significantly reduced in crispants treated with NT1654 (p=0.0187, Kruskal-Wallis test), to a level similar to wildtype controls. On the other hand, total area of SV2 clusters was significantly reduced in crispants (p<0.0001, Kruskal-Wallis test), and this was elevated in NT1654 treated fish to a level analogous to controls (p=0.0024, Kruskal-Wallis test). Total SV2 cluster area was the only measured presynaptic parameter that was significantly altered in wildtype fish treated with NT1654, with a reduction in area observed (p=0.0141, Kruskal-Wallis test).

		Compared to untreated controls		
	48 hpf NMJ parameters	**control + NT1654**	**myo9aa/ab crispant**	**myo9aa/ab crispant + NT1654**
Presynaptic	SV2 clusters per myotome			
	SV2 clusters per 100µm²			
	SV2 clusters >20µm²			
	Area of SV2 clusters			
	Total area of SV2 clusters			
	% innervation of myosepta			
Postsynaptic	aBTx clusters per myotome			
	aBTx clusters per 100µm²			
	aBTx clusters >20µm²			
	Area of aBTx clusters			
	Total area of aBTx clusters			
	Size of myotomes			

Table 6-3. Summary of NMJ morphology results obtained in 48 hpf zebrafish treated with NT1654. Red = significantly less than untreated controls, blue = statistically unchanged from controls and green = significantly increased as compared to controls.

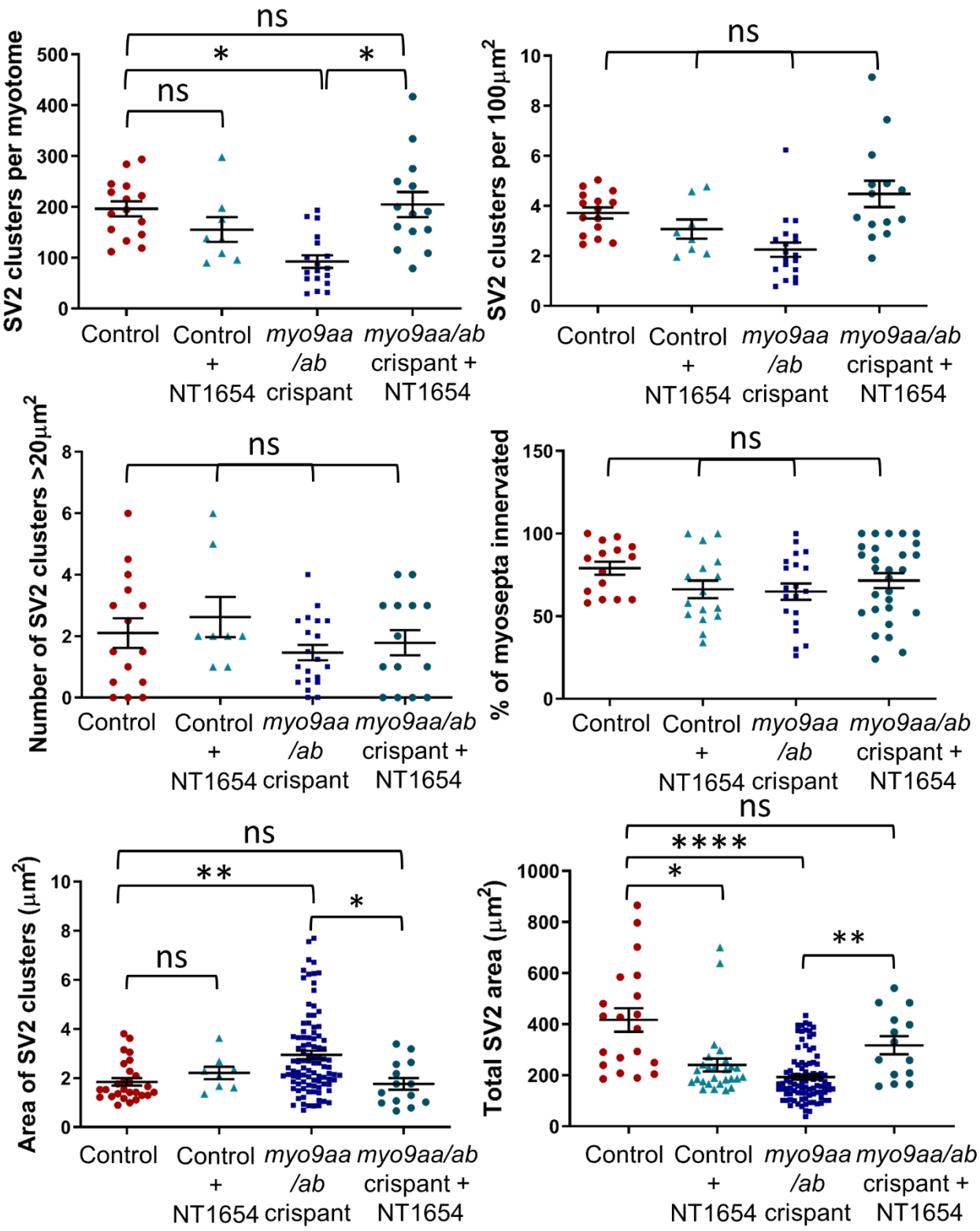

Figure 6.22. Quantification of NT1654-treated *myo9aa/ab* crispant zebrafish presynaptic NMJ morphology at 48 hpf. Various features of presynaptic NMJ morphology in control (n=15), *myo9aa/ab* crispants (n=20), control + NT1654 (n=8) and *myo9aa/ab* crispants + NT1654 (n=8) were quantified: number of SV2 (presynaptic) clusters per myotome, per 100µm^2 and over 20µm^2, as well as the % of myosepta with innervation, average and total SV2 cluster area (expressed as per myotome rather than per fish). Error bars = mean ± S.E.M. *p≤0.05, ns = not significant, Kruskal-Wallis test.

Postsynaptic features of the NMJ were also assessed, revealing that while application of NT1654 to zebrafish depleted for Myo9aa/ab did not significantly improve the number of AChR (aBTx) clusters per myotome when compared to untreated crispants, it did increase the proportion enough that it was no longer significantly different to that observed in controls ($p=0.2101$, Kruskal-Wallis test, Figure 6.23). The number of clusters per 100μm^2 was significantly reduced in crispant fish as compared to controls ($p=0.0004$, Kruskal-Wallis test). While this value was not significantly elevated by NT1654-treatment ($p=0.1501$, Kruskal-Wallis test), cluster number was improved to a level similar to that in controls ($p>0.9999$, Kruskal-Wallis test). No significant changes were observed in myotome size in any condition, and neither were the proportion of large AChR clusters present. Average aBTx cluster area was significantly elevated in crispant fish as compared to controls ($p=0.0009$, Kruskal-Wallis test). The increase in average aBTx area was returned to a level similar to controls after NT1654 treatment ($p=0.0001$, Kruskal-Wallis test). The total area of aBTx clusters was decreased in crispants lacking Myo9aa/ab as compared to controls ($p<0.0001$, Kruskal-Wallis test). NT1654 application did not significantly improve this phenotype ($p>0.9999$, Kruskal-Wallis test), however, the total area was less significantly different to controls ($p=0.0006$, Kruskal-Wallis test). NT1654 did not affect postsynaptic NMJ morphology in control fish treated with the compound, except in the case of total AChR area for which a significant reduction in cluster area was observed ($p<0.0001$, Kruskal-Wallis test).

Overall, the application of NT1654 to *myo9aa/ab* crispant fish was able to rescue the number of SV2 clusters per myotome, average and total area of SV2 clusters, aBTx clusters per 100μm^2 and average area of aBTx clusters, demonstrating both pre and postsynaptic improvements to NMJ morphology at 48hpf.

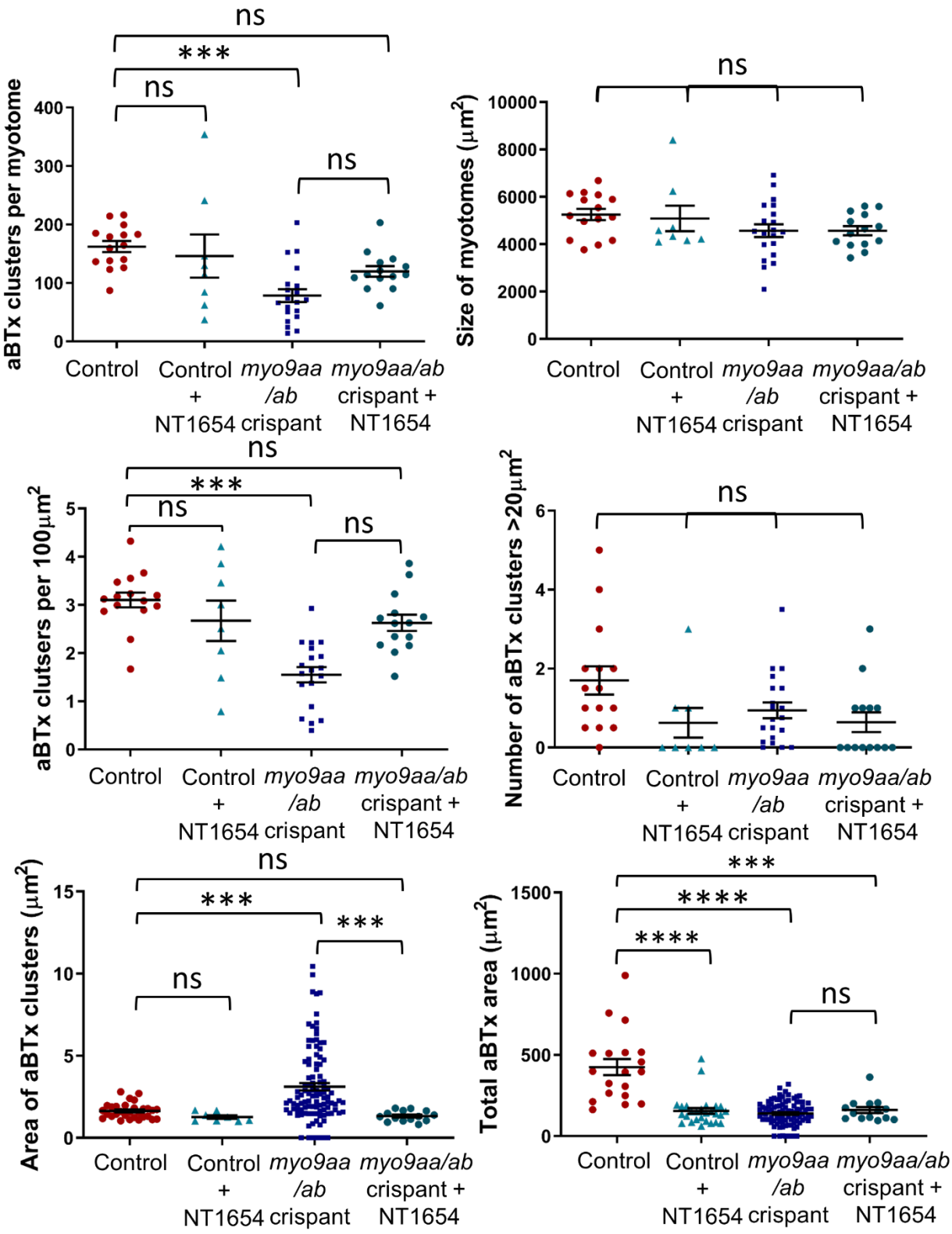

Figure 6.23. Quantification of NT1654-treated *myo9aa/ab* crispant zebrafish postsynaptic NMJ morphology at 48 hpf. Various features of postsynaptic NMJ morphology in control (n=15), *myo9aa/ab* crispants (n=20), control + NT1654 (n=8) and *myo9aa/ab* crispants + NT1654 (n=14) were quantified: number of aBTx (postsynaptic) clusters per myotome, per 100µm^2 and over 20µm^2, as well as myotome size, average and total aBTx cluster area (expressed as per myotome rather than per fish). Error bars = mean ± S.E.M. ***p≤0.001, ns = not significant, Kruskal-Wallis test.

To assess NMJ morphology at a later time-point in order to observe any longer acting effects of NT1654 treatment, the crispants were also subject to staining and analysis at 5dpf (beyond the time for which MO-mediated KDs could be analysed). Crispants had less pre and postsynaptic clusters present across the myotome which was improved in the NT1654-treated fish (Figure 6.24).

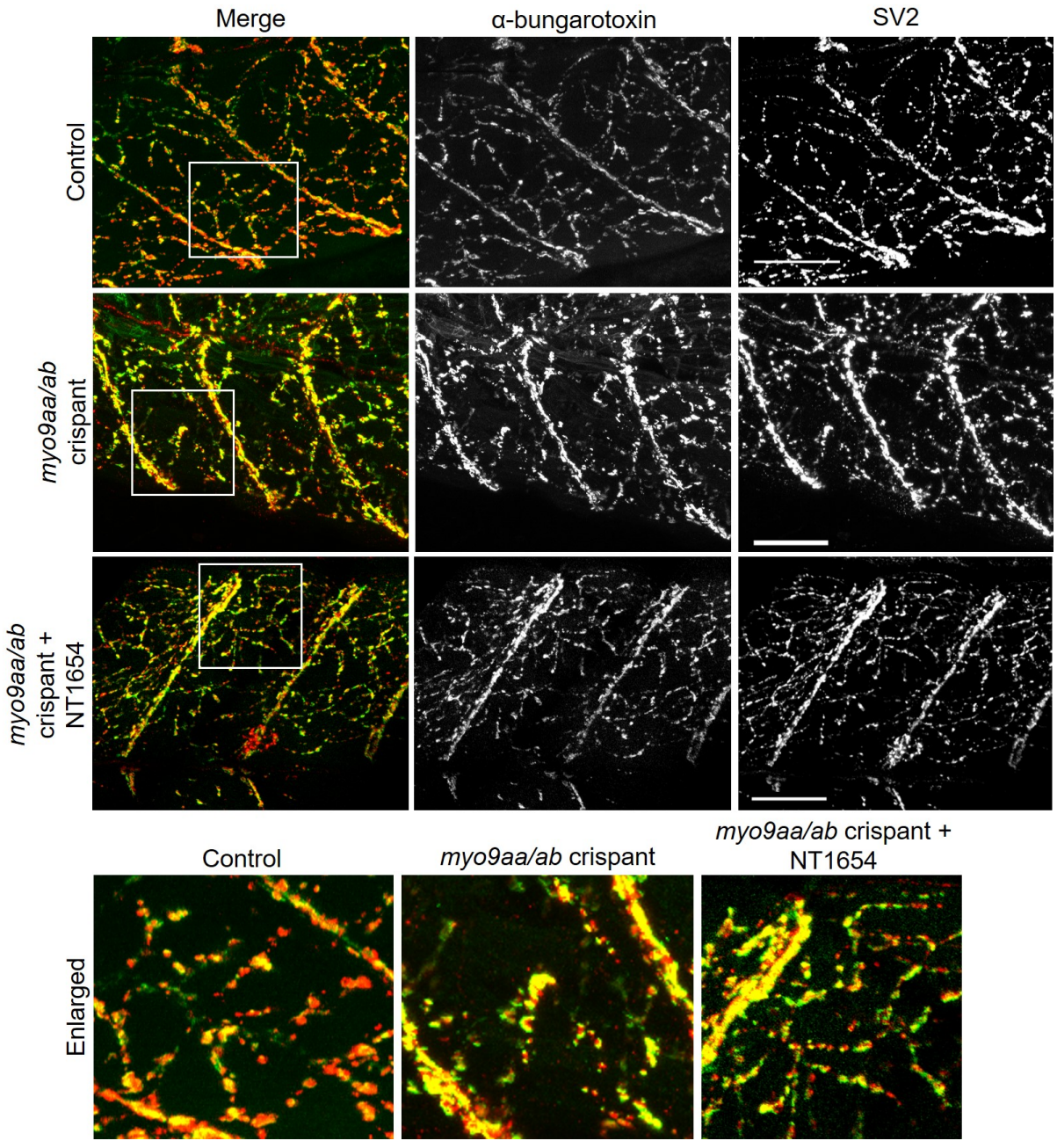

Figure 6.24. NMJ morphology of NT1654-treated *myo9aa/ab* crispant zebrafish at 5dpf pf. Representative images of NMJs in untreated and NT1654-treated control and *myo9aa/ab* crispant zebrafish at 5 dpf. AChRs stained with aBTx (green), and motor neurons detected with an antibody against SV2 (red). White boxes demark areas enlarged in the bottom panel. Scale bars = 50μm.

Quantification of NMJ features in 5dpf fish was performed on control, *myo9aa/ab* crispants and NT1654-treated crispants (Figure 6.25), and a summary of results shown in Table 6-4. Average area of presynaptic (SV2-positive) clusters was not significantly affected in any condition, and neither was the number of clusters per myotome. The number of clusters per 100µm^2, however, was significantly improved by application of NT1654 to the crispants, bringing the number of clusters down to a level comparable with controls (p=0.0035, one-way ANOVA). While the mean number of large presynaptic clusters decreased in crispants from 1.2 to 0.4 and increased after NT1654 to 1.1, these differences were not statistically significant. The total area of SV2-positive clusters was significantly elevated in crispant fish treated with NT1654 as compared to untreated crispants (p=0.0020, one-way ANOVA), however, this remained statistically similar to the total area in control fish (p=0.7580, one-way ANOVA). The percentage of myoseptal innervation was not significantly altered between any of the groups.

		Compared to untreated controls	
	5 dpf NMJ parameters	**myo9aa/ab crispant**	**myo9aa/ab crispant + NT1654**
Presynaptic	Area of SV2 clusters		
	SV2 clusters per myotome		
	SV2 clusters per 100µm^2		
	SV2 clusters >20µm^2		
	Total area of SV2 clusters		
	% innervation of myotome		
Postsynaptic	Area of aBTx clusters		
	aBTx clusters per myotome		
	aBTx clusters per 100µm^2		
	aBTx clusters >20µm^2		
	Total area of aBTx clusters		
	Size of myotomes		

Table 6-4. Summary of NMJ morphology results obtained in 5 dpf zebrafish treated with NT1654. Red = significantly less than untreated controls, blue = statistically unchanged from controls and green = significantly increased as compared to controls.

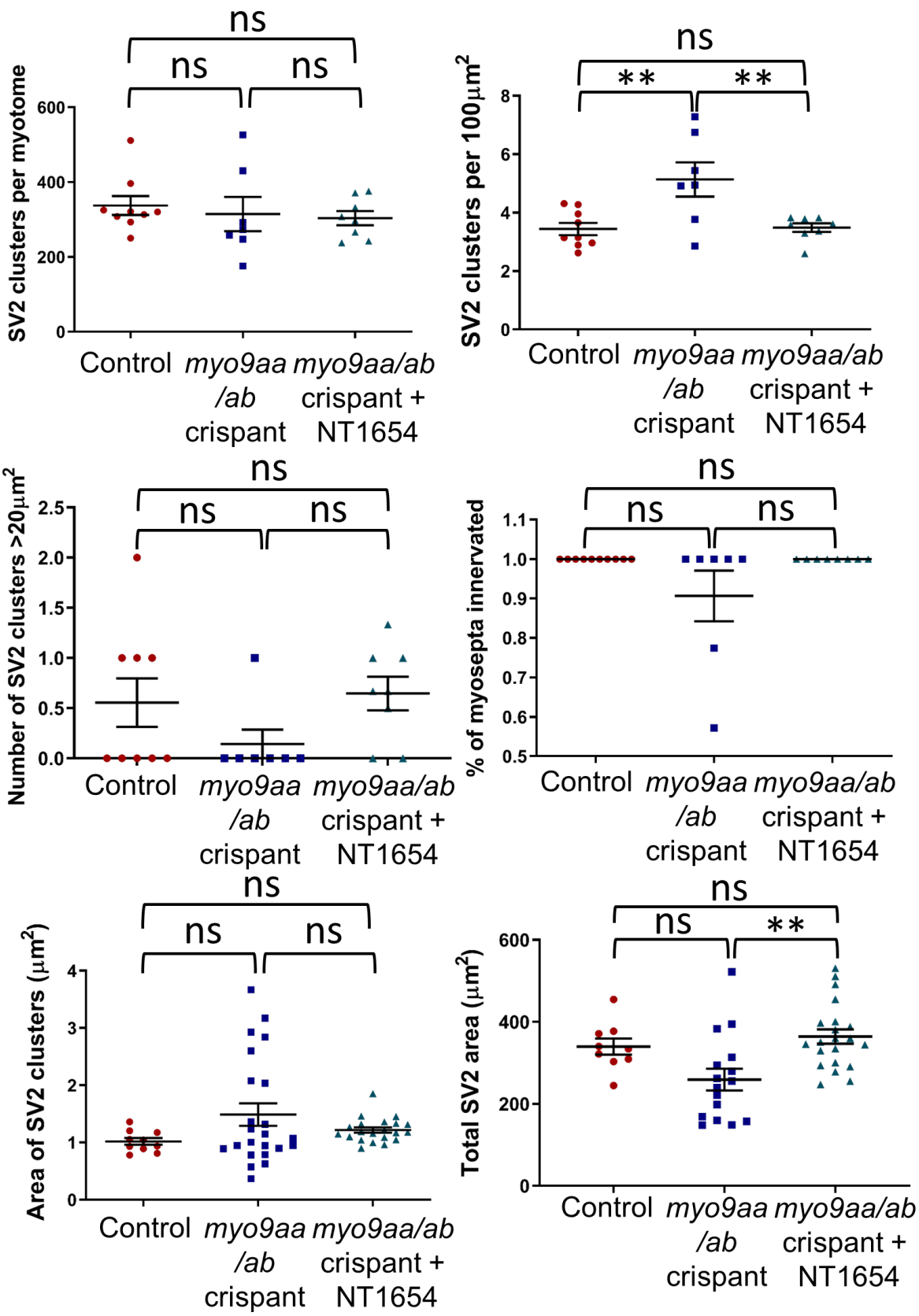

Figure 6.25. Quantification of NT1654-treated *myo9aa/ab* crispant zebrafish presynaptic NMJ morphology at 5 dpf. Various features of presynaptic NMJ morphology in control (n=10), *myo9aa/ab* crispants (n=7) and *myo9aa/ab* crispants + NT1654 (n=8) were quantified: average and total area of SV2 (presynaptic) clusters (expressed as per myotome rather than per fish), number of clusters per myotome,

per 100μm^2 and over 20μm^2, as well as the length of myoseptal innervation and % of myoseptal innervation. Error bars = mean ± S.E.M. **p≤0.01, ns = not significant, one-way ANOVA.

Postsynaptic NMJ analysis in 5dpf fish revealed a significant decrease in the average area of AChR clusters in NT1654-treated crispants as compared to control fish (p=0.0421, one-way ANOVA, Figure 6.26). Considering the total area of AChR clusters, loss of Myo9aa/ab led to a significant reduction in area (p=0.0010, one-way ANOVA), and this was significantly improved by addition of NT1654, to a level similar to controls (p=0.0119, one-way ANOVA). The number of clusters per myotome in crispant fish was also significantly increased by NT1654 treatment, as compared to both crispants and controls (p=0.0141, p=0.0214 respectively, one-way ANOVA). While size of myotomes was reduced in fish lacking Myo9aa/ab (p=0.0006, one-way ANOVA), this was improved by application of NT1654, to a level comparable with controls (p=0.0459, p=0.5702 respectively, one-way ANOVA). To determine whether total AChR area is altered in relation to somite size, the percentage change between each treatment condition was calculated. This revealed that while somite size is on average 37% decreased in crispants as compared to controls, the total AChR cluster area is 41% decreased. The increase in somite size following NT1654 treatment is 40%, and for total AChR area is 44%, thus there may be a link between the two measurements. However, when considering the earlier time points measured, these changes are not consistent. For example, at 48hpf somite size is only 13% reduced in crispant fish as compared to controls, however, total postsynaptic cluster area is decreased by 67%. Following NT1654 treatment average somite size is unchanged, whereas total AChR area per somite increases by 15%. The number of postsynaptic clusters per 100μm^2 was significantly elevated by NT1654 treatment of crispant fish, as compared to untreated controls (p=0.0120, one-way ANOVA). Finally, the proportion of large receptor clusters over 20μm^2 in size was decreased from 1.2 per myotome in controls to 0.1 in crispants, which was increased to 1.1 by NT1654-treatment, although these changes were not statistically significant.

Overall, at 5dpf there was a restoration of SV2 cluster number per 100μm^2, total AChR cluster area and size of myotomes in NT1654 treated crispants as compared to the untreated fish depleted for Myo9aa/ab.

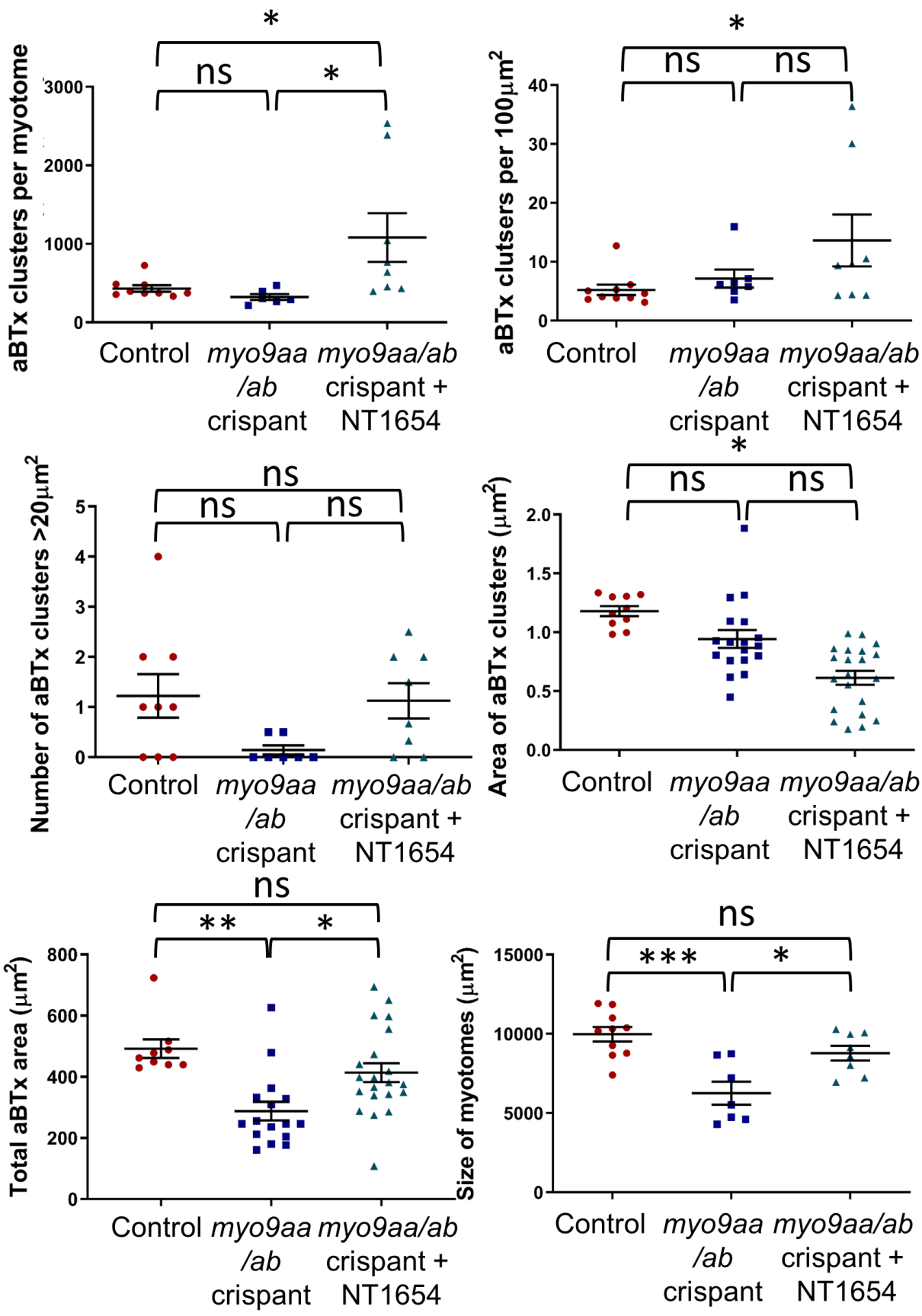

Figure 6.26. Quantification of NT1654-treated *myo9aa/ab* crispant zebrafish postsynaptic NMJ morphology at 5 dpf. Various features of postsynaptic NMJ morphology in control (n=10), *myo9aa/ab* crispants (n=7) and *myo9aa/ab* crispants + NT1654 (n=8) were quantified: average and total area of aBTx (postsynaptic) clusters

(expressed as per myotome rather than per fish), number of clusters per myotome, per 100μm^2 and over 20μm^2, as well as myotome size and myoseptal length. Error bars = mean ± S.E.M. *p≤0.05, ***p≤0.001, ns = not significant, one-way ANOVA.

6.5 Discussion

In this chapter, the effect of MYO9A-depletion on secretion of proteins from nerves was investigated based on the observation that loss of this unconventional myosin protein impacted on trafficking and uptake/release mechanisms. To address this, a secretomic approach was used to quantify the abundances of proteins secreted from control and MYO9A KD NCS-34 cells. While a number of proteins were identified as dysregulated, perhaps the most important finding was the downregulated secretion of agrin from NSC-34 cells lacking MYO9A. As agrin has a critical role at the NMJ as a protein secreted from the nerve terminal that acts to modulate AChR clustering at the postsynapse, application of a novel agrin compound to zebrafish was tested in an attempt to rescue some features associated with Myo9aa/ab-loss.

6.5.1 Analysis of MYO9A KD NSC-34 cell secretomic profile

In the secretomic analysis of NSC-34 cells depleted for MYO9A, 76 proteins of 1532 detected were identified as dysregulated. There were 46 proteins with upregulated secretion, and 30 downregulated. Whether these findings represent increased/decreased expression or effects on secretion is not known, however this could be investigated by performing RNAseq on the cells to look at the expression of identified proteins. Investigation into reported localisation of the dysregulated proteins revealed that 9 of the 76 proteins were not previously identified as secreted. Included in this subset are those related to the cytoskeleton and neuron extension such as PDL1, INF2 and DPYL5 (Brot et al., 2014, Chen et al., 2009, Schnepp et al., 2005, Sia et al., 2013), with VAT1L also displaying peripheral nerve expression (Thul et al., 2017, https://www.proteinatlas.org/ENSG00000171724-VAT1L/tissue). Furthermore, INF2, a Charcot-Marie-Tooth associated protein, is involved in the acceleration of actin cycling (Boyer et al., 2011, Chhabra and Higgs, 2006) and thus its increase may be associated with the increase in actin expression in cells lacking MYO9A. Dysregulation of other proteins involved in diseases affecting the nerve and muscle, such as ALS, congenital muscular dystrophy and CMS, were also identified and thus provide a link between MYO9A-related pathology and other disorders causing motor deficits, suggesting converging pathways and molecular mechanism between many of these diseases.

A number of the proteins that have been reported as secreted previously may also be important for the pathophysiology of MYO9A CMS, including the neuronal ubiquitin hydrolase, UCHL1. The UCHL1 KO mouse exhibits defective accumulation of vesicles at nerve terminals and have signal transmission defects at the NMJ (Chen et al., 2010). Mutations in *UCHL1* are also associated with a motor neuropathy (Bilguvar et al., 2013). Alterations in the secretion of proteins may also reflect the activation of protective pathways, for example upregulation of pigment epithelium-derived factor (PEDF), which is a neurotrophic factor (Houenou et al., 1999, Taniwaki et al., 1995).

Pathway analysis performed on the secreted proteins was automated, using the STRING database, rather than manually curated, thus removing bias. However, this method may have missed numerous secondary pathways that could be relevant to the pathology of MYO9A-loss. An example of this was the surprising enrichment of haemostasis-related pathways in the downregulated proteins from KD cells. However, investigation of the proteins reported in this pathway revealed a number of secondary functions including preventing protein aggregation, RhoA activation and neuronal proliferation, which are likely more relevant that haemostatic processes. Another unexpected finding was the upregulation of extracellular matrix proteins, mainly collagens, in the secretome of MYO9A KD cells. As there has been no reported interaction between MYO9A and collagens, it could be that this is a stress response of the cells as collagen secretion has been shown to be upregulated after nerve injury (Koopmans et al., 2009). Proteomic profiling of sciatic nerves from SH3TC2-deficient mice also displayed increased collagens, which was hypothesised to be a protective action to maintain degenerating NMJs (Cipriani et al., 2018). The extracellular matrix is linked to the cytoskeleton via integrin signalling (also upregulated), thus providing an association between the defective cytoskeleton and extracellular matrix (Wu and Reddy, 2012). Furthermore, in our data there was dysregulated secretion of laminins, such as LAMA4, which is associated with mislocalisation of synaptic specialisations at the NMJ as reported in the *Lama4* KO mice, and mutations in another laminin subunit gene (*LAMA5)* can cause CMS (Patton et al., 2001, Maselli et al., 2018). To determine if a similar synaptic phenotype occurs in absence of MYO9A as in Lama4, it would be interesting to perform electron microscopy of NMJs in MYO9A KO mice. In zebrafish, loss of Lamb1a, another identified laminin in the secretomics, affects muscle cell elongation during development (Snow et al., 2008). This could be linked to the small somite size

observed in Myo9aa/ab-depleted zebrafish. There was also an enrichment of proteins involved in axon guidance, signal transduction and developmental biology pathways in the secretomic dataset, thus providing support for a role for MYO9A at the NMJ.

6.5.2 Decreased secretion of agrin

The downregulation of agrin secretion from cells lacking MYO9A was considered one of the most important findings from the secretomic analysis. Agrin is secreted from nerves and acts on the Lrp4/Musk complex on the postsynaptic membrane in order to stimulate AChR clustering at the endplate (Maselli et al., 2012, Nicole et al., 2014, McMahan, 1990). CMS can also be caused by mutations in *AGRN* (Huze et al., 2009, Karakaya et al., 2017, Nicole et al., 2014). The decrease in agrin secretion was associated with an increase in intracellular staining of agrin, supporting evidence obtained that exocytosis was affected in cells lacking MYO9A and in patient iNPCs. In the future, secretomics of iNPCs from patients and controls would be beneficial to confirm whether downregulation of agrin also occurs in the presence of patient mutations.

Thus far 9 CMS patients with mutations in *AGRN* have been reported, whereas there are only 3 *MYO9A* patients. Analysis of phenotypic overlaps reveal presence of proximal and distal muscle weakness with respiratory involvement (Huze et al., 2009, Karakaya et al., 2017, Nicole et al., 2014, O'Connor et al., 2016). However, not all phenotypes are found in both subtypes, including the presence of hypotonia, delayed motor milestones and ocular/bulbar involvement in MYO9A-CMS patients, highlighting that there are further factors influencing MYO9A pathophysiology. Nevertheless, a treatment such as NT1654 to ameliorate at least an agrin-mediated aspect of the disease may provide valuable improvement of symptoms and of NMJ signalling. Replacement of agrin has also shown benefit in a mouse model of severe SMA, in which a reduction in agrin was also identified, thus demonstrating the wider ranging appeal for such a treatment (Kim et al., 2017). In the SMA mouse, agrin was rescued by expression of a motor neuron-specific transgene, however, if secretion is impaired in the case of MYO9A this would not be of therapeutic benefit. One of the most promising features of the NT1654 treatment lies in the ability to administer the drug systemically, removing the need for complex gene therapy in patients. Therefore, the exogenous agrin fragment can act directly on the postsynapse without relying on transport and release machinery in the nerve.

6.5.3 Agrin-replacement therapy as a therapeutic strategy for MYO9A-CMS

NT1654 treatment was tested in zebrafish to determine whether agrin replacement showed any therapeutic promise *in vivo*. Zebrafish express agrin from 2hpf (maternal transcripts) with a large increase by 24 hpf. Localisation to the brain, spinal cord and motor neurons has been shown (Kim et al., 2007). Zebrafish agrin has a 54% homology with mouse neural agrin, increasing to 60% when considering only the domains included within the NT1654 compound (Laminin G-like 2, EGF-like 4 and Laminin G-like 3). As the compound had not previously been tested in zebrafish, only in mice and cells, a range of concentrations were trialed using wildtype fish. The range tested fell within those shown to induce AChR clusters *in vitro* on C2C12 cells (450pM to 108nM) and a concentration of 890pM was selected for use based on minimising toxicity and effects on movement in controls (Hettwer et al., 2014). As survival of zebrafish co-injected with MO and NT1654 was considerably reduced, in the future a lower dose of NT1654 could be trialed in an effort to determine whether beneficial NMJ effects can still be obtained without impacting survival. However, co-injection of Cas9/sgRNA with NT1654 did not affect survival rates, and thus it is likely that the toxicity was related to the combined delivery of the compound with morpholinos.

Zebrafish depleted for Myo9aa/ab have curved tails, and in crispant fish tails curve dorsally or ventrally. Tails of fish lacking agrin have also been shown to curve in the same way and they exhibit abnormal swimming patterns (Kim et al., 2007). The rescue of this phenotype was obtained in many of the NT1654-treated morphant fish, thus corroborating a role for agrin in developing zebrafish morphology.

Application of NT1654 also improved the motor behaviours of the morphant and crispant fish. At 24 hpf fish lacking Myo9aa/ab (mediated by either editing technique) displayed reduced chorion movements and they had impaired responses to tactile stimulation by 48 hpf. Mice lacking agrin ($Agrn^{nmf380/nmf380}$) similarly display poor motor control phenotypes, thus reflecting the importance of agrin in performing tasks relying on NMJ integrity (Bogdanik and Burgess, 2011). Highlighting this point, the chorion movements were improved in both morphants and crispants lacking Myo9aa/ab when treated with NT1654. At 48 hpf consistent improvements were seen for all parameters measured as part of the tactile response assay (distance travelled, velocity and initial acceleration), for both crispants and morphants treated with NT1654. Of particular interest was the improvement in acceleration, which at this

time point has been shown to be indicative of muscle contraction force (Sztal et al., 2016). In a sarcopenia mouse model in which a reduced grip strength was observed, treatment with NT1654 was able to ameliorate the grip strength deficits (Hettwer et al., 2014). Similarly, in a mouse model of SMA, NT1654 significantly improved the ability of mice to perform a range of behavioural tests including the hind-limb suspension test (Boido et al., 2018), thus reflecting observations obtained in the fish. No significant differences to the movement of control fish treated with NT1654 were observed, again supported by findings in mice that no detrimental effects were observed on healthy muscles (Hettwer et al., 2014). In the future, it would be beneficial to identify Myo9aa/ab-depleted zebrafish with movement defects during development and then to administer the NT1654 and monitor any subsequent changes in behaviour. This would require an alternative delivery method, for example pericardial injection of the drug which can be performed from around 3dpf (Smith et al., 2015).

In the sarcopenia mouse model on which NT1654 was initially tested, vast improvements to NMJ morphology and muscle fibre composition were observed in soleus and diaphragm muscles, after onset of the sarcopenic phenotype (Hettwer et al., 2014). Myo9aa/ab-deficient zebrafish treated with NT1654 from the one-cell stage exhibited increases in the number of large AChR clusters and overall area of clusters, as well as the number of neurons extending from each somitic region and somites with a choice point cluster at 24 hpf. The increases in the presence of large AChR clusters and overall AChR fluorescence was expected, based on the interaction of NT1654 with the LRP4-MuSK signalling pathway (Hettwer et al., 2014). In agrin deficient zebrafish, the converse effect is observed, in which a decrease in myotomal AChR clusters can be observed during development (Kim et al., 2007). In the agrin-deficient fish, prepatterned AChR clusters and the presence of the choice point cluster occur normally, highlighting that these processes are not agrin-dependent in the fish, as in mice (Lin et al., 2001). However, at 24hpf the *myo9aa/ab* crispant fish display reduced choice point clusters, which is improved by NT1654 application. There are a number of potential explanations for this observation which require further investigation. For example, the choice point clusters assessed in this study are present after the motor neuron has already contacted that area in the majority of cases, therefore no longer represent prepatterned clusters and may be those incorporated in an agrin-dependent manner. To determine whether this is the case fish could be analysed at earlier time points of development when prepatterned

receptors are present, before the outgrowth of motor axons. Another option is that this represents an unexplored role of MYO9A in the muscle, potentially affecting AChR insertion at this early time point, which is then restored by NT1654 application.

The effect of NT1654 on neurons extending from the spinal cord was unexpected, however application of agrin to *in vitro* cultures of PC12 cells and chick retinal neurons has been shown to mediate FGF2-induced neurite extension (Kim et al., 2003). Furthermore, in the opposite scenario removal of agrin from zebrafish has been shown to cause truncated primary motor axons during development, as well as erratic trajectories of these axons across the myotome, corroborating our findings (Kim et al., 2007). Similar effects of abnormal axonal extensions are also observed in the diaphragm muscle of a murine model of agrin deficiency (AGZ) (Gautam et al., 1996).

The identified increase in total aBTx fluorescence at 24hpf was also observed at 48hpf and 5dpf. This response to NT1654 was expected due to the demonstrated ability of this compound in previous studies to increase AChR density at NMJs and to induce AChR clustering *in vitro* (Li et al., 2018, Hettwer et al., 2014). Furthermore, agrin-deficient zebrafish show the converse, with reduced AChR clustering across the myotomes (Kim et al., 2007). This also supports evidence from the secretomic data which highlighted a lack of agrin secretion from the MYO9A KD NSC-34 cells, rather than defective functioning of the agrin pathway. Replacement of agrin, by the exogenous application of NT1654, was able to increase total AChRs on the myotome in the crispant fish, and thus the pathway between agrin and AChR clustering appears functional.

There was also a decrease in the average size of aBTx clusters at 48hpf and 5dpf in crispant fish treated with NT1654, which may represent a removal of extra-synaptic receptors next to the NMJs or condensation of diffuse endplate clusters into mature synaptic form. Conversely, in Agrin-deficient mice (AGZ) there are smaller AChR clusters and increased scattered receptors (Gautam et al., 1996, Lin et al., 2001). As individual NMJs are difficult to identify at this stage in zebrafish development, to determine whether the reduced cluster sizes quantified apply to size of NMJs, older fish could be examined in the future. Furthermore, the contribution of such changes in cluster size to synaptic function should be analysed using electrophysiology, as in mammalian systems it has been reported that a loss or blockade of 80% of AChRs at the NMJ would be required to reduce the mEPP amplitude by half, highlighting the

high safety factor of the NMJ (Pennefather and Quastel, 1981). The presynaptic SV2 clusters were similarly reduced in size at 48hpf in NT1654 treated crispants. This could highlight a return to normal function as terminals in zebrafish decrease in size during early development (Drapeau et al., 2001). Thus the significantly larger SV2 clusters observed in untreated crispants may signify a delay in NMJ maturation, corroborating with the reduced AChE activity observed in Chapter 4, Section 4.5.2. These effects on nerve terminal size are further supported by observations from a conditional agrin KO mouse, in which atrophy and swelling of nerve terminals has been reported (Samuel et al., 2012).

Agrin has been shown to induce ectopic, fully differentiated postsynaptic compartments anywhere on the muscle, including insertion of AChRs (Tintignac et al., 2015). While there is an increase in cluster number per 100μm^2 at 48 hpf in NT1654-treated crispants, this is only to the level observed in controls. However, at 5dpf, there is a further increase in cluster number which may represent ectopic AChRs. Colocalisation analysis should be performed in the future to determine whether clusters are correctly opposed with presynaptic terminals or not. From the data available, there is in fact a decrease in SV2 cluster number per 100μm^2 by 5dpf highlighting that there may be non-synaptic AChR clusters present due to the NT1654 application, although no clear lack of SV2 staining overlying aBTx clusters can be visualised in the immunofluorescence images.

At 5dpf *myo9aa/ab* crispant fish had significantly smaller muscle myotomes in the tail, and this was improved by NT1654 treatment. In the sarcopenia mouse, as well as in a rat model of autoimmune myasthenia gravis, NT1654 was able to restore the body weights of animals to the same level as controls (Hettwer et al., 2014, Li et al., 2018). Furthermore, in the myasthenia gravis rat and the SMA mouse model, a rescue of muscle atrophy was also achieved, thus supporting the observations in zebrafish (Boido et al., 2018, Li et al., 2018).

Agrin deficient zebrafish exhibit CNS defects, including truncated branchiomotor axons. However, in analysis of Myo9aa/ab-deficient zebrafish no gross morphological differences were observed in cranial motor neurons. Detailed analysis of CNS morphology could be performed in the future, including staining of all axons using a zn-5 antibody. MYO9A KO mice have been reported to display CNS defects, although these were related to structure of ventricles and insertion of receptors at the postsynaptic density in dendrites of excitatory neurons and not in axon extension

(Abouhamed et al., 2009, Folci et al., 2016). Sensory neurons were also impaired in agrin deficient zebrafish, however this has not been observed in MYO9A KO mice, as well as in the zebrafish models, and patients have not reported any sensory abnormalities.

6.5.4 Conclusion

In this chapter, proteomic profiling of secreted proteins from MYO9A KD NSC-34 cells was performed. Analysis of this data revealed a number of secreted proteins with dysregulated quantities in MYO9A KD cells as compared to controls, and their potential relation to pathology discussed. While many avenues to explore remain, of particular interest was the finding of downregulated agrin secretion from MYO9A-deficient cells. This provided a novel therapeutic strategy that could be used as a starting point for the development of a non-invasive treatment for any condition in which agrin is decreased or dysfunctional at the NMJ, including MYO9A-CMS.

Chapter 7. General discussion and future directions

The NMJ plays a critical role in generation of movement by the skeletal system, by transmitting signals from motor axons to muscles to induce contraction. This highly specialised synapse is present in animals from humans to small invertebrates, allowing a range of motor activities to be performed with precision and in response to rapidly changing stimuli. The safety factor of the NMJ, present due to the numerous specialisations that occur during development, maintains synaptic activity unless dysfunction impairs it enough to lead to failure of reliable NMJ signalling and disease. Defects in genes encoding proteins involved in maintaining this safety factor, thus causing CMS, are becoming increasingly identified using genetic techniques such as whole exome or genome sequencing. However, such studies are impeded by the rarity of the genetic subtypes of CMS and the absence of large cohorts of patients with the same mutations, or even mutations in the same gene. This renders the study of the pathophysiology of such genetic alterations difficult, and access to human material to aide this process is not always possible. In this study, investigations were based on a previous identification of missense mutations in *MYO9A* in 3 patients with CMS from 2 unrelated families (O'Connor et al., 2016). To overcome the problem of lack of patient muscle biopsies, or previous studies of MYO9A at the NMJ, a range of *in vitro* and *in vivo* models were successfully generated to investigate the role for this unconventional myosin protein at the NMJ.

The initial hypothesis was that defects in MYO9A cause a presynaptic CMS, due to interactions with the cytoskeleton and RhoA pathway within motor neurons. To address this, the main aim of this project was to determine whether MYO9A contributes to the development and integrity of the NMJ.

The main findings of this study were a role for MYO9A in extension of neurites in patient iNPCs, as well as morphology of developing zebrafish and adult mouse NMJs. An effect of MYO9A-loss was also found on the nerve cell cytoskeleton, intracellular transport and endo/exocytosis. These features of MYO9A-pathophysiology could be partially ameliorated by inhibition of the ROCK pathway, and similarly a ROCK inhibitor was able to improve some early developmental defects in zebrafish NMJs. Furthermore, lack of agrin secretion from nerve cells lacking MYO9A was identified, and application of an artificial agrin fragment rescued some features of NMJ morphology disruption in zebrafish. Overall, the initial

hypothesis has been addressed, demonstrating a role for MYO9A at the NMJ and linking this with cytoskeletal and RhoA dynamics.

7.1 Hypothesis for MYO9A-CMS pathomechanism

Based on investigations carried out in this project, it is further hypothesised that MYO9A-CMS is caused by reduced agrin secretion from the nerve terminal. This is consistent with the known roles of agrin in NMJ development and maintenance (Butikofer et al., 2011, Samuel et al., 2012, Tintignac et al., 2015, Wu et al., 2010). Furthermore, mutations in *AGRN* itself can also cause CMS (Huze et al., 2009, Karakaya et al., 2017, Nicole et al., 2014). The evidence supporting this hypothesis, and areas identified that require clarification and further investigation will be highlighted in this discussion.

7.2 Reduced agrin secretion

The main evidence supporting the proposed pathomechanism for MYO9A-CMS arose from the finding that NSC-34 cells depleted for MYO9A secrete 5.4-fold less agrin than their control KO counterparts. While numerous other proteins of potential importance to the phenotype were also identified as dysregulated in the proteomic profile, agrin is a key player in NMJ development and in stability of the synapse throughout life (Tintignac et al., 2015). Immunofluorescence analysis of intracellular agrin revealed a corresponding build-up of this proteoglycan within cells lacking MYO9A, supporting the idea that secretion, rather than agrin expression, is impaired.

The identification of 76 proteins with altered abundances in the media from MYO9A KD NSC-34 cells also highlights a general effect on release processes, rather than a specific loss of agrin secretion. This was supported by an impairment in uptake and release of the FM 1-43 dye from the medium of cultured MYO9A-deficient NSC-34 cells and MYO9A-CMS patient differentiated iNPCs.

A reduction of agrin release may drastically impair the development of the NMJ, and could coincide with the early onset of phenotypes observed in the MYO9A-CMS patients. Agrin KO mice do not survive after birth due to an inability to inflate their lungs, and analysis of NMJs reveals a marked reduction in AChR cluster area and presynaptic nerve branching and differentiation (Gautam et al., 1996). Conversely, CMS patients with *AGRN* mutations have not been reported to present with symptoms in the neonatal or early postnatal periods, but can exhibit a progressive worsening of symptoms and often have respiratory involvement (Huze et al., 2009, Karakaya et al., 2017, Nicole et al., 2014). Agrin is cleaved by a neuron-derived

serine protease; neurotrypsin, which removes the c-terminal portion of the protein important for the clustering of synaptic AChRs (Reif et al., 2007). Overexpression of neurotrypsin in mice causes a reduction in agrin activity at the NMJ due to increased cleavage, and causes numerous phenotypes associated with sarcopenia in aging, including fragmentation of the NMJ (Butikofer et al., 2011). MYO9A KO mice and zebrafish also show disrupted NMJs. Therefore, if there were a reduction in agrin secretion in the absence of MYO9A, it would be consistent with a negative effect on the NMJ as observed in other conditions in which agrin is depleted.

To support this data, obtaining evidence for impaired agrin secretion *in vivo* is an important objective. This could be achieved by culturing motor neurons from MYO9A KO mice and performing secretomic analysis (Gingras et al., 2007), or through the visualisation of agrin *in vivo* at nerve terminals using a fluorescently-tagged construct, such as that used in rats by Bezekova *et al* (2001). Confirming the downregulation of agrin secretion should also be performed using the patient iNPCs and as only cells from one patient are available, fibroblasts that have the other patient's mutations introduced and then subsequently converted to iNPCs would be beneficial. Although, to date the secretion of agrin from iNPCs differentiated toward the neuronal lineage has not be demonstrated, if agrin were secreted this would provide support that not only loss of MYO9A, but the identified missense mutations, can also lead to impaired secretion.

7.3 Increased RhoA activity impedes agrin secretion

Previous studies of MYO9A function have not reported an association between this unconventional myosin and agrin. Based on findings in this project, it is hypothesised that the decreased agrin secretion observed in cells lacking MYO9A is due to the corresponding increase in RhoA activity. This is demonstrated by the decrease in intracellular build-up of agrin in MYO9A-KO cells treated with the ROCK inhibitor Y-27632, which decreases downstream RhoA pathway activity. Furthermore, effects on intracellular movement of the TrkA receptor were also improved following Y-27632 treatment.

As many RhoGAPs are expressed in neurons and therefore influence RhoA activity (Govek et al., 2005), it is likely that MYO9A affects local RhoA activity rather than having a global effect within the cell. MYO9A co-localises with f-actin and we have previously identified expression at the growth cones of neurons, where other unconventional myosins have also been reported (Raines et al., 2012, Suter et al.,

2000, O'Connor et al., 2016). This may indicate that MYO9A-loss affects RhoA activity and actin dynamics in the nerve terminal of motor neurons, thus affecting secretion of proteins such as agrin. In order to address this, in the future MYO9A KO cells could be treated with the ROCK inhibitor and subject to secretomics to determine whether this rescues secretion of agrin. Additionally, evidence regarding impaired endo/exocytosis should be obtained *in vivo* which could be performed using FM 1-43 dye assays in zebrafish to assess efficiency of uptake and release at the NMJ (Li et al., 2003).

While a number of studies have identified RhoA as an important mediator of postsynaptic differentiation through its effects on agrin-induced AChR clustering, there is limited research into roles at the presynapse. The C. elegans homolog of RhoA, RHO-1, has been shown to increase the levels of diacyglycerol, an UNC-13 interacting protein, at the plasma membrane (McMullan et al., 2006, Momboisse et al., 2011). This action recruits UNC-13 (also a CMS-related protein) to the membrane where it is involved in vesicle exocytosis (Momboisse et al., 2011, Lackner et al., 1999, Xu et al., 2017). In PC12 cells, RhoA has also been shown to inhibit exocytosis, related to the formation of peripheral actin filament dynamics (Bader et al., 2004). Therefore, if similar processes also occur in human nerve terminals, RhoA over-activity may affect the local actin cytoskeleton and recruitment of UNC-13, impairing release of vesicles including those containing agrin. Further research would be required to investigate this hypothesis, such as detailed structural analysis of the actin cytoskeleton in nerve terminals of cells lacking MYO9A, and examination of UNC-13 localisation to determine whether appropriate levels are present at the active zone.

7.4 Treatment with NT1654 improves NMJ morphology in zebrafish lacking Myo9aa/ab

The development of the NMJ and associated motor behaviours were assessed in zebrafish depleted for Myo9aa/ab using both MO and CRISPR/Cas9-mediated techniques. Use of both techniques revealed impaired movement of zebrafish at 24 and 48 hpf, similar to those reported for zebrafish lacking agrin (Kim et al., 2007), thus providing support for reduced agrin secretion contributing to the pathomechanism of MYO9A-CMS. As impaired movements in zebrafish are not restricted to MYO9A or agrin knockdown and are present in a number of other zebrafish models of CMS, further evidence was obtained by the improvement of these behaviours by the application of NT1654 (a modified form of agrin). To support

this observation, in the future other zebrafish models of CMS in which agrin dysfunction is not implicated could be treated with NT1654, to ascertain whether the compound provides a general improvement to motor behaviours rather than a specific effect due to reduced agrin.

Agrin secretion from the motor neuron during NMJ synaptogenesis is a critical step, without which AChR clusters do not form correctly (Gautam et al., 1996). In the *myo9aa/ab* crispant fish, there are fewer, larger AChR and SV2 clusters, but an overall decrease in pre/postsynaptic staining at 48hpf. This corroborates with observations of reduced myotomal AChR clustering in agrin-deficient zebrafish (Kim et al., 2007). By 5dpf, zebrafish lacking Myo9aa/ab exhibit decreased AChR and SV2 cluster sizes, as well as an increase in cluster number as compared to wildtype fish. This reflects observations in the *AGRN* KO mouse, which exhibited a number of small AChR clusters opposing nerve terminals during development *in utero*, as well as an increase in presence of un-innervated clusters (Gautam et al., 1996). As it is difficult to interpret cluster size in zebrafish in a comparable way to NMJs in human or mouse due to the lack of distinct NMJ clusters at this period of development and at the resolution obtained, it would be beneficial to also analyse the adult homozygous *myo9aa/ab* KO zebrafish. Furthermore, observations of developing NMJs could be performed using zebrafish with fluorescent motor neurons and AChRs in a time-lapse experiment (Epley et al., 2008, Flanagan-Steet et al., 2005), to determine whether clusters decrease in size over-time, or if there is a lack of growth of clusters between 48hpf and 5dpf and the insertion of new clusters at distinct points to increase cluster number. Nevertheless, reduced MYO9A affects the formation of appropriately distributed and proportioned NMJs across the tail musculature of zebrafish to at least 5dpf.

In support of the hypothesis that MYO9A-CMS is based on a reduction in agrin secretion, a number of the defects in NMJ morphology can be rescued by NT1654 treatment. For example, an increase in total AChR cluster area was observed at all time points assessed, presence of a choice point cluster of AChRs at 24hpf was improved, number of SV2-positive clusters was rescued at 5dpf, as well as an improvement in myotome size. Many of these improvements corroborate with reported benefits of this compound in a mouse model of sarcopenia, induced by increased cleavage of agrin at the NMJ (Hettwer et al., 2014). The use of this exogenous agrin fragment bypasses the proposed impairment of secretion. However,

to confirm that mechanisms related to secretion rather than expression were the cause of reduced agrin in the MYO9A KD cell secretome, the *myo9aa/ab* crispants could be injected with an agrin construct to drive expression in motor neurons. This would determine whether similar improvements could be obtained, or whether no effect would be observed due to lack of ability to secrete the agrin. A further confirmatory study that would provide insight into the zebrafish phenotype would be electron microscope imaging of the NMJs in developing fish. This could be used to assess for both appropriately formed pre/postsynaptic apparatus, and a build-up of dense core vesicles that may contain agrin, reflecting observations in MYO9A KO NSC-34 cells at the light microscope level. While improvements in movement were obtained in the zebrafish, the contribution of morphological alterations at the NMJ to function is widely debated (Slater, 2008, Willadt et al., 2016). This is partly due to the safety factor of the NMJ, for example it has been suggested that a decrease of 80% of functional AChRs would be required at the murine NMJ to reduce the amplitude of an mEPP by 50% (Pennefather and Quastel, 1981). Therefore, it would also be beneficial to analyse both aspects in conjunction as performed in zebrafish by the laboratory of Prof. Paul Brehm (Ono et al., 2001, Wen et al., 2016). In the future, using a full *myo9aa/ab* CRISPR-mediated knockout model, fish could be subject to electrophysiological recording of postsynaptic activity in individual muscle cells in response to stimulation of presynaptic motor neurons in a paired patch clamp configuration (Wen and Brehm, 2010). This powerful technique would address whether important aspects of synaptic transmission such as QC are affected in the mutant fish and could be coupled with subsequent NMJ morphology analysis before and after NT1654 treatment.

Analysis of mature NMJ morphology was performed using MYO9A KO mice, and this revealed further features compatible with a reduction in agrin secretion. For example, there was a decrease in AChR/endplate area in all but one mutant for the tibialis anterior muscle, and in certain mutants for gastrocnemius, intercostal and diaphragm muscles (correlating with the decreased cluster size observed in 5dpf fish). This was accompanied by a decrease in presynaptic nerve terminal area and reduced branching complexity in all but gastrocnemius muscle, similarly the zebrafish lacking MYO9A homologs showed abnormal motor neuron outgrowth during development. These features are consistent with observations of the conditional agrin KO mouse, whereby loss of agrin from adult NMJs revealed a decrease in AChR cluster area and atrophy of nerve terminals (Samuel et al., 2012). There was also a reduction in

myofibre cross-sectional area in MYO9A KO mouse as compared to controls. This reflects the phenotype of neurotrypsin overexpressing mice, in which there is a reduction in neural agrin activity at the NMJ. These mice have smaller muscle fibres, as well as a reduction in total fibre number, among other features not assessed in this study such as fibre-type grouping (Butikofer et al., 2011). Therefore, these characteristics are all compatible with a reduction in agrin from the nerve in the absence of MYO9A. It was unfortunate that treatment of the mice with NT1654 was not possible, as this would have confirmed whether the NMJ phenotype of the mice could similarly be improved by application of an exogenous agrin fragment. In the future, MYO9A KO mice could also be crossed with neurotrypsin KO mice (Reif et al., 2007, Stephan et al., 2008), to ascertain whether preventing the cleavage of the agrin that is secreted is sufficient to improve the NMJ phenotype. Furthermore, analysis of gene expression for components of the agrin-LRP4-MuSK pathway could be performed as it would be expected that components may be downregulated in the MYO9A KO mouse and zebrafish, especially the activated, phosphorylated form of MuSK (Glass et al., 1996, Zong and Jin, 2013).

7.5 Other pathways of potential importance to MYO9A-deficient phenotype

While the main hypothesis for the mode of action for MYO9A loss is a reduction in agrin secretion from the nerve, a number of other scenarios may also contribute to impaired NMJ signalling. For example, both the *in vitro* and *in vivo* models studied exhibit effects on nerve and presynaptic nerve terminal morphology. This could be related to cytoskeletal disruption due to RhoA over-activity, as application of Y-27632 was able to ameliorate some cytoskeletal defects in NSC-34 cells, and therefore improve intracellular trafficking. Furthermore, treatment of zebrafish with the ROCK inhibitor, fasudil, was found to provide some improvements to the NMJ, including neurite extension, somite size and choice point AChR clustering in early development. However, it is possible that the improvements observed due to fasudil *in vivo* were acting upstream of agrin release, and thus not due to distinct effects of MYO9A on the cytoskeleton (outlined in Figure 1.1). MYO9A has also been shown to act directly on the cytoskeleton, through cross-linking of actin-filaments (Saczko-Brack et al., 2016). Loss of this action, as in the case of the KO models used in this project, may have implications for vesicle transport within nerves, as well as structure of the nerve terminal. However, patient mutations are not in the myosin motor domain which is the region crucial for the actin binding ability of this protein and the patient iNPCs still exhibited neurite extension defects and impaired FM dye uptake/release.

Investigation of such features would require ultrastructural analysis of actin filament morphology in both MYO9A KO mouse or zebrafish NMJs, as well as differentiated patient iNPCs. It is likely that disruption of intracellular trafficking or nerve cell morphology due to direct actin interaction or mediated via the RhoA pathway would similarly reduce agrin secretion, rather than these mechanisms being separate.

It is also possible that MYO9A plays a role in the muscle, where its downstream target RhoA has been shown to be important for agrin-mediated AChR clustering (Weston et al., 2003). Conversion of fibroblasts to myoblasts and subsequent differentiation into myotubes would allow clustering of AChRs in the presence of MYO9A-CMS patient mutations to be analysed *in vitro*. Furthermore, generation of tissue-specific MYO9A KO mice such as nerve and muscle KOs would allow the contribution of this unconventional myosin to the NMJ and other phenotypes that have been associated with MYO9A-loss to be elucidated, as performed recently for another ubiquitously expressed CMS gene: *GFPT1* (Issop et al., 2018).

7.6 Conclusion

In conclusion, evidence has been presented supporting a role for MYO9A at the NMJ, and its absence or dysfunction being compatible with causing CMS. The proposed working model for MYO9A-CMS is shown in Figure 7.1. While many avenues for exploration of the precise function of MYO9A at the NMJ remain open, an action on RhoA and the cytoskeleton have been demonstrated, with a downstream effect on agrin secretion. This is supported by a role in NMJ development in zebrafish, with impaired clustering of AChRs and motor neuron extension. Mature NMJs in mice also show disruption in the absence of MYO9A with smaller NMJs present and reduced myofibre areas. The identification of MYO9A as a protein important for NMJ morphology and motor behaviours supports the identification of *MYO9A* as a CMS gene and broadens the involvement of ubiquitously expressed proteins implicated in the disease. In the future, other genes within the unconventional myosin family or within the RhoA pathway may be considered as potential candidates for neuromuscular disease or in roles for NMJ function. A novel therapeutic strategy based on application of NT1654, an agrin fragment, was also tested in this study and phenotypic improvements obtained from treatment. This may provide support for future use of this compound in clinical trial for patients in which reduced presence of agrin at the NMJ is implicated, including MYO9A-CMS.

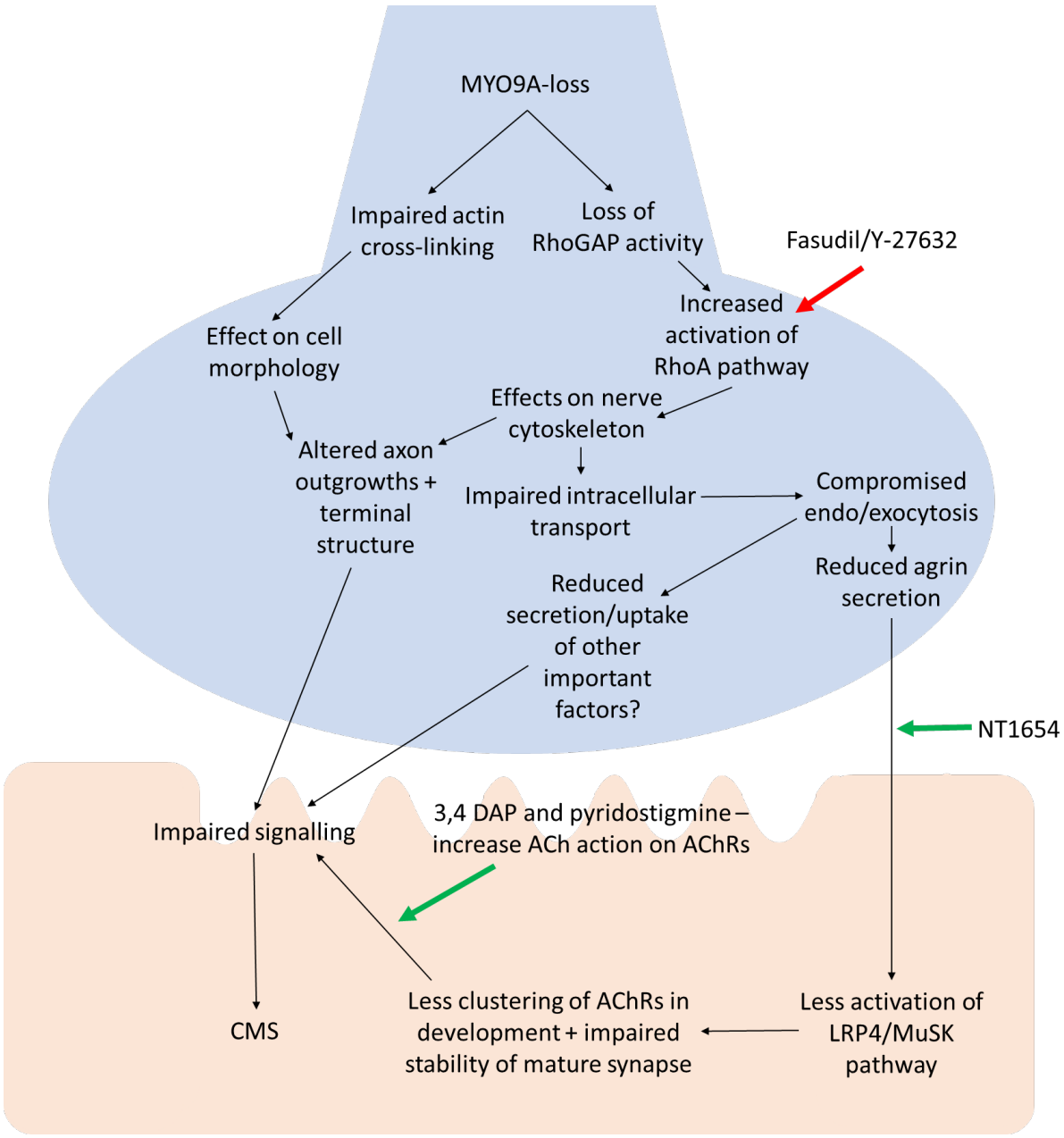

Figure 7.1. Proposed pathway of action for MYO9A-dysfunction at the NMJ. The pathway begins with loss or dysfunction of MYO9A and the predicted effect of this on a number of downstream processes, culminating in impaired neuromuscular transmission and CMS. The points of action for fasudil/Y-27632, NT1654 and 3,4-DAP/Pyridostigmine as used with some efficacy in the patients are shown. Green arrow = positive action, red arrow = inhibits action.

References

Abouhamed, M., Grobe, K., San, I. V., Thelen, S., Honnert, U., Balda, M. S., Matter, K. & Bahler, M. 2009. Myosin IXa regulates epithelial differentiation and its deficiency results in hydrocephalus. *Mol Biol Cell,* 20**,** 5074-85.

Ackermann, F., Waites, C. L. & Garner, C. C. 2015. Presynaptic active zones in invertebrates and vertebrates. *EMBO Rep,* 16**,** 923-38.

Acsadi, G., Lee, I., Li, X., Khaidakov, M., Pecinova, A., Parker, G. C. & Huttemann, M. 2009. Mitochondrial dysfunction in a neural cell model of spinal muscular atrophy. *J Neurosci Res,* 87**,** 2748-56.

Al-Ali, H., Beckerman, S. R., Bixby, J. L. & Lemmon, V. P. 2017. In vitro models of axon regeneration. *Exp Neurol,* 287**,** 423-434.

Anderson, M. J. & Cohen, M. W. 1974. Fluorescent staining of acetylcholine receptors in vertebrate skeletal muscle. *J Physiol,* 237**,** 385-400.

Aran, A., Segel, R., Kaneshige, K., Gulsuner, S., Renbaum, P., Oliphant, S., Meirson, T., Weinberg-Shukron, A., Hershkovitz, Y., Zeligson, S., Lee, M. K., Samson, A. O.*, et al.* 2017. Vesicular acetylcholine transporter defect underlies devastating congenital myasthenia syndrome. *Neurology,* 88**,** 1021-1028.

Auld, D. S., Mennicken, F. & Quirion, R. 2001. Nerve growth factor rapidly induces prolonged acetylcholine release from cultured basal forebrain neurons: differentiation between neuromodulatory and neurotrophic influences. *J Neurosci,* 21**,** 3375-82.

Azuma, Y., Topf, A., Evangelista, T., Lorenzoni, P. J., Roos, A., Viana, P., Inagaki, H., Kurahashi, H. & Lochmuller, H. 2017. Intragenic DOK7 deletion detected by whole-genome sequencing in congenital myasthenic syndromes. *Neurol Genet,* 3**,** e152.

Babin, P. J., Goizet, C. & Raldua, D. 2014. Zebrafish models of human motor neuron diseases: advantages and limitations. *Prog Neurobiol,* 118**,** 36-58.

Bader, M. F., Doussau, F., Chasserot-Golaz, S., Vitale, N. & Gasman, S. 2004. Coupling actin and membrane dynamics during calcium-regulated exocytosis: a role for Rho and ARF GTPases. *Biochim Biophys Acta,* 1742**,** 37-49.

Bahler, M. 2000. Are class III and class IX myosins motorized signalling molecules? *Biochim Biophys Acta,* 1496**,** 52-9.

Bahler, M., Elfrink, K., Hanley, P. J., Thelen, S. & Xu, Y. 2011. Cellular functions of class IX myosins in epithelia and immune cells. *Biochem Soc Trans,* 39**,** 1166-8.

Balice-Gordon, R. J., Breedlove, S. M., Bernstein, S. & Lichtman, J. W. 1990. Neuromuscular junctions shrink and expand as muscle fiber size is manipulated: in vivo observations in the androgen-sensitive bulbocavernosus muscle of mice. *J Neurosci,* 10**,** 2660-71.

Barik, A., Lu, Y., Sathyamurthy, A., Bowman, A., Shen, C., Li, L., Xiong, W. C. & Mei, L. 2014. LRP4 is critical for neuromuscular junction maintenance. *J Neurosci,* 34**,** 13892-905.

Bartsakoulia, M., Pyle, A., Troncoso-Chandia, D., Vial-Brizzi, J., Paz-Fiblas, M. V., Duff, J., Griffin, H., Boczonadi, V., Lochmuller, H., Kleinle, S., Chinnery, P. F., Grunert, S.*, et al.* 2018. A novel mechanism causing imbalance of mitochondrial fusion and fission in human myopathies. *Hum Mol Genet,* 27**,** 1186-1195.

Bassett, D. I., Bryson-Richardson, R. J., Daggett, D. F., Gautier, P., Keenan, D. G. & Currie, P. D. 2003. Dystrophin is required for the formation of stable muscle attachments in the zebrafish embryo. *Development,* 130**,** 5851-60.

Batters, C. & Veigel, C. 2016. Mechanics and Activation of Unconventional Myosins. *Traffic,* 17**,** 860-71.

Bayram, Y., Karaca, E., Coban Akdemir, Z., Yilmaz, E. O., Tayfun, G. A., Aydin, H., Torun, D., Bozdogan, S. T., Gezdirici, A., Isikay, S., Atik, M. M., Gambin, T.*, et al.* 2016. Molecular etiology of arthrogryposis in multiple families of mostly Turkish origin. *J Clin Invest,* 126**,** 762-78.

Behra, M., Cousin, X., Bertrand, C., Vonesch, J. L., Biellmann, D., Chatonnet, A. & Strahle, U. 2002. Acetylcholinesterase is required for neuronal and muscular development in the zebrafish embryo. *Nat Neurosci,* 5**,** 111-8.

Belaya, K., Finlayson, S., Slater, C. R., Cossins, J., Liu, W. W., Maxwell, S., Mcgowan, S. J., Maslau, S., Twigg, S. R., Walls, T. J., Pascual Pascual, S. I., Palace, J.*, et al.* 2012. Mutations in DPAGT1 cause a limb-girdle congenital myasthenic syndrome with tubular aggregates. *Am J Hum Genet,* 91**,** 193-201.

Bergamin, E., Hallock, P. T., Burden, S. J. & Hubbard, S. R. 2010. The cytoplasmic adaptor protein Dok7 activates the receptor tyrosine kinase MuSK via dimerization. *Mol Cell,* 39**,** 100-9.

Bertrand, C., Chatonnet, A., Takke, C., Yan, Y. L., Postlethwait, J., Toutant, J. P. & Cousin, X. 2001. Zebrafish acetylcholinesterase is encoded by a single gene localized on linkage group 7. Gene structure and polymorphism; molecular forms and expression pattern during development. *J Biol Chem,* 276**,** 464-74.

Bertrand, C. A., Laboisse, C., Hopfer, U., Bridges, R. J. & Frizzell, R. A. 2006. Methods for detecting internalized, FM 1-43 stained particles in epithelial cells and monolayers. *Biophys J,* 91**,** 3872-83.

Betts, M. J. & Russell, R. B. 2003. Amino-Acid Properties and Consequences of Substitutions. *Bioinformatics for Geneticists.*

Bezakova, G., Rabben, I., Sefland, I., Fumagalli, G. & Lomo, T. 2001. Neural agrin controls acetylcholine receptor stability in skeletal muscle fibers. *Proc Natl Acad Sci U S A,* 98**,** 9924-9.

Bilguvar, K., Tyagi, N. K., Ozkara, C., Tuysuz, B., Bakircioglu, M., Choi, M., Delil, S., Caglayan, A. O., Baranoski, J. F., Erturk, O., Yalcinkaya, C., Karacorlu, M.*, et al.* 2013. Recessive loss of function of the neuronal ubiquitin hydrolase UCHL1 leads to early-onset progressive neurodegeneration. *Proc Natl Acad Sci U S A,* 110**,** 3489-94.

Boda, E., Pini, A., Hoxha, E., Parolisi, R. & Tempia, F. 2009. Selection of reference genes for quantitative real-time RT-PCR studies in mouse brain. *J Mol Neurosci,* 37**,** 238-53.

Bogdanik, L. P. & Burgess, R. W. 2011. A valid mouse model of AGRIN-associated congenital myasthenic syndrome. *Hum Mol Genet,* 20**,** 4617-33.

Boido, M., De Amicis, E., Valsecchi, V., Trevisan, M., Ala, U., Ruegg, M. A., Hettwer, S. & Vercelli, A. 2018. Increasing Agrin Function Antagonizes Muscle Atrophy and Motor Impairment in Spinal Muscular Atrophy. *Front Cell Neurosci,* 12**,** 17.

Bond, L. M., Brandstaetter, H., Sellers, J. R., Kendrick-Jones, J. & Buss, F. 2011. Myosin motor proteins are involved in the final stages of the secretory pathways. *Biochem Soc Trans,* 39**,** 1115-9.

Boon, K. L., Xiao, S., Mcwhorter, M. L., Donn, T., Wolf-Saxon, E., Bohnsack, M. T., Moens, C. B. & Beattie, C. E. 2009. Zebrafish survival motor neuron mutants exhibit presynaptic neuromuscular junction defects. *Hum Mol Genet,* 18**,** 3615-25.

Bowerman, M., Beauvais, A., Anderson, C. L. & Kothary, R. 2010. Rho-kinase inactivation prolongs survival of an intermediate SMA mouse model. *Hum Mol Genet,* 19**,** 1468-78.

Bowerman, M., Murray, L. M., Boyer, J. G., Anderson, C. L. & Kothary, R. 2012. Fasudil improves survival and promotes skeletal muscle development in a mouse model of spinal muscular atrophy. *BMC Med,* 10**,** 24.
Boyer, O., Nevo, F., Plaisier, E., Funalot, B., Gribouval, O., Benoit, G., Huynh Cong, E., Arrondel, C., Tete, M. J., Montjean, R., Richard, L., Karras, A.*, et al.* 2011. INF2 mutations in Charcot-Marie-Tooth disease with glomerulopathy. *N Engl J Med,* 365**,** 2377-88.
Brose, N., Petrenko, A. G., Sudhof, T. C. & Jahn, R. 1992. Synaptotagmin: a calcium sensor on the synaptic vesicle surface. *Science,* 256**,** 1021-5.
Brot, S., Smaoune, H., Youssef-Issa, M., Malleval, C., Benetollo, C., Besancon, R., Auger, C., Moradi-Ameli, M. & Honnorat, J. 2014. Collapsin response-mediator protein 5 (CRMP5) phosphorylation at threonine 516 regulates neurite outgrowth inhibition. *Eur J Neurosci,* 40**,** 3010-20.
Brown, M. E. & Bridgman, P. C. 2004. Myosin function in nervous and sensory systems. *J Neurobiol,* 58**,** 118-30.
Brownlow, S., Webster, R., Croxen, R., Brydson, M., Neville, B., Lin, J. P., Vincent, A., Newsom-Davis, J. & Beeson, D. 2001. Acetylcholine receptor delta subunit mutations underlie a fast-channel myasthenic syndrome and arthrogryposis multiplex congenita. *J Clin Invest,* 108**,** 125-30.
Bruneau, E., Sutter, D., Hume, R. I. & Akaaboune, M. 2005. Identification of nicotinic acetylcholine receptor recycling and its role in maintaining receptor density at the neuromuscular junction in vivo. *J Neurosci,* 25**,** 9949-59.
Bruses, J. L. 2011. N-cadherin regulates primary motor axon growth and branching during zebrafish embryonic development. *J Comp Neurol,* 519**,** 1797-815.
Budick, S. A. & O'malley, D. M. 2000. Locomotor repertoire of the larval zebrafish: swimming, turning and prey capture. *J Exp Biol,* 203**,** 2565-79.
Burden, S. 1977. Acetylcholine receptors at the neuromuscular junction: Developmental change in receptor turnover. *Developmental Biology,* 61**,** 79-85.
Burger, A., Lindsay, H., Felker, A., Hess, C., Anders, C., Chiavacci, E., Zaugg, J., Weber, L. M., Catena, R., Jinek, M., Robinson, M. D. & Mosimann, C. 2016. Maximizing mutagenesis with solubilized CRISPR-Cas9 ribonucleoprotein complexes. *Development,* 143**,** 2025-37.
Buss, R. R. & Drapeau, P. 2001. Synaptic drive to motoneurons during fictive swimming in the developing zebrafish. *J Neurophysiol,* 86**,** 197-210.
Butikofer, L., Zurlinden, A., Bolliger, M. F., Kunz, B. & Sonderegger, P. 2011. Destabilization of the neuromuscular junction by proteolytic cleavage of agrin results in precocious sarcopenia. *FASEB J,* 25**,** 4378-93.
Cabrera, J. R., Viejo-Borbolla, A., Martinez-Martin, N., Blanco, S., Wandosell, F. & Alcami, A. 2015. Secreted herpes simplex virus-2 glycoprotein G modifies NGF-TrkA signaling to attract free nerve endings to the site of infection. *PLoS Pathog,* 11**,** e1004571.
Cappello, V. & Francolini, M. 2017. Neuromuscular Junction Dismantling in Amyotrophic Lateral Sclerosis. *Int J Mol Sci,* 18.
Cashman, N. R., Durham, H. D., Blusztajn, J. K., Oda, K., Tabira, T., Shaw, I. T., Dahrouge, S. & Antel, J. P. 1992. Neuroblastoma x spinal cord (NSC) hybrid cell lines resemble developing motor neurons. *Dev Dyn,* 194**,** 209-21.
Chaouch, A., Muller, J. S., Guergueltcheva, V., Dusl, M., Schara, U., Rakocevic-Stojanovic, V., Lindberg, C., Scola, R. H., Werneck, L. C., Colomer, J., Nascimento, A., Vilchez, J. J.*, et al.* 2012. A retrospective clinical study of the treatment of slow-channel congenital myasthenic syndrome. *J Neurol,* 259**,** 474-81.

Chaouch, A., Porcelli, V., Cox, D., Edvardson, S., Scarcia, P., De Grassi, A., Pierri, C. L., Cossins, J., Laval, S. H., Griffin, H., Muller, J. S., Evangelista, T.*, et al.* 2014. Mutations in the Mitochondrial Citrate Carrier SLC25A1 are Associated with Impaired Neuromuscular Transmission. *J Neuromuscul Dis,* 1**,** 75-90.

Chen, F., Sugiura, Y., Myers, K. G., Liu, Y. & Lin, W. 2010. Ubiquitin carboxyl-terminal hydrolase L1 is required for maintaining the structure and function of the neuromuscular junction. *Proc Natl Acad Sci U S A,* 107**,** 1636-41.

Chen, K., Zhang, W., Chen, J., Li, S. & Guo, G. 2013. Rho-associated protein kinase modulates neurite extension by regulating microtubule remodeling and vinculin distribution. *Neural Regen Res,* 8**,** 3027-35.

Chen, Q., Muller, J. S., Pang, P. C., Laval, S. H., Haslam, S. M., Lochmuller, H. & Dell, A. 2015. Global N-linked Glycosylation is Not Significantly Impaired in Myoblasts in Congenital Myasthenic Syndromes Caused by Defective Glutamine-Fructose-6-Phosphate Transaminase 1 (GFPT1). *Biomolecules,* 5**,** 2758-81.

Chen, X., Fu, W., Tung, C. E. & Ward, N. L. 2009. Angiopoietin-1 induces neurite outgrowth of PC12 cells in a Tie2-independent, beta1-integrin-dependent manner. *Neurosci Res,* 64**,** 348-54.

Chen, Z. Y., Ieraci, A., Tanowitz, M. & Lee, F. S. 2005. A novel endocytic recycling signal distinguishes biological responses of Trk neurotrophin receptors. *Mol Biol Cell,* 16**,** 5761-72.

Cheng, A., Morsch, M., Murata, Y., Ghazanfari, N., Reddel, S. W. & Phillips, W. D. 2013. Sequence of age-associated changes to the mouse neuromuscular junction and the protective effects of voluntary exercise. *PLoS One,* 8**,** e67970.

Chhabra, E. S. & Higgs, H. N. 2006. INF2 Is a WASP homology 2 motif-containing formin that severs actin filaments and accelerates both polymerization and depolymerization. *J Biol Chem,* 281**,** 26754-67.

Chieregatti, E., Gartner, A., Stoffler, H. E. & Bahler, M. 1998. Myr 7 is a novel myosin IX-RhoGAP expressed in rat brain. *J Cell Sci,* 111 (Pt 24)**,** 3597-608.

Cipriani, S., Phan, V., Medard, J. J., Horvath, R., Lochmuller, H., Chrast, R., Roos, A. & Spendiff, S. 2018. Neuromuscular Junction Changes in a Mouse Model of Charcot-Marie-Tooth Disease Type 4C. *Int J Mol Sci,* 19.

Clausen, L., Cossins, J. & Beeson, D. 2018. Beta-2 Adrenergic Receptor Agonists Enhance AChR Clustering in C2C12 Myotubes: Implications for Therapy of Myasthenic Disorders. *J Neuromuscul Dis,* 5**,** 231-240.

Cohen, M. W., Frair, P. F., Cantin, C. & Hebert, G. 1990. Developmental changes in the half-life of acetylcholine receptors in the myotomal muscle of Xenopus laevis. *J Physiol,* 426**,** 281-96.

Colasante, C., Brouard, M. O. & Pecot-Dechavassine, M. 1993. Synaptophysin (p38) immunolabelling at the mouse neuromuscular junction. *Neuromuscul Disord,* 3**,** 395-400.

Collymore, C., Rasmussen, S. & Tolwani, R. J. 2013. Gavaging adult zebrafish. *J Vis Exp*.

Cossins, J., Belaya, K., Hicks, D., Salih, M. A., Finlayson, S., Carboni, N., Liu, W. W., Maxwell, S., Zoltowska, K., Farsani, G. T., Laval, S., Seidhamed, M. Z.*, et al.* 2013. Congenital myasthenic syndromes due to mutations in ALG2 and ALG14. *Brain,* 136**,** 944-56.

Court, F. A., Gillingwater, T. H., Melrose, S., Sherman, D. L., Greenshields, K. N., Morton, A. J., Harris, J. B., Willison, H. J. & Ribchester, R. R. 2008. Identity, developmental restriction and reactivity of extralaminar cells capping mammalian neuromuscular junctions. *J Cell Sci,* 121**,** 3901-11.

Davies, S. P., Reddy, H., Caivano, M. & Cohen, P. 2000. Specificity and mechanism of action of some commonly used protein kinase inhibitors. *Biochem J,* 351**,** 95-105.
Delague, V., Jacquier, A., Hamadouche, T., Poitelon, Y., Baudot, C., Boccaccio, I., Chouery, E., Chaouch, M., Kassouri, N., Jabbour, R., Grid, D., Megarbane, A.*, et al.* 2007. Mutations in FGD4 encoding the Rho GDP/GTP exchange factor FRABIN cause autosomal recessive Charcot-Marie-Tooth type 4H. *Am J Hum Genet,* 81**,** 1-16.
Desmet, F. O., Hamroun, D., Lalande, M., Collod-Beroud, G., Claustres, M. & Beroud, C. 2009. Human Splicing Finder: an online bioinformatics tool to predict splicing signals. *Nucleic Acids Res,* 37**,** e67.
Dobbins, G. C., Luo, S., Yang, Z., Xiong, W. C. & Mei, L. 2008. alpha-Actinin interacts with rapsyn in agrin-stimulated AChR clustering. *Mol Brain,* 1**,** 18.
Downes, G. B. & Granato, M. 2006. Supraspinal input is dispensable to generate glycine-mediated locomotive behaviors in the zebrafish embryo. *J Neurobiol,* 66**,** 437-51.
Drapeau, P., Buss, R. R., Ali, D. W., Legendre, P. & Rotundo, R. L. 2001. Limits to the development of fast neuromuscular transmission in zebrafish. *J Neurophysiol,* 86**,** 2951-6.
Dunn, K. W., Kamocka, M. M. & Mcdonald, J. H. 2011. A practical guide to evaluating colocalization in biological microscopy. *Am J Physiol Cell Physiol,* 300**,** C723-42.
Dusl, M., Senderek, J., Muller, J. S., Vogel, J. G., Pertl, A., Stucka, R., Lochmuller, H., David, R. & Abicht, A. 2015. A 3'-UTR mutation creates a microRNA target site in the GFPT1 gene of patients with congenital myasthenic syndrome. *Hum Mol Genet,* 24**,** 3418-26.
Egashira, Y., Zempo, B., Sakata, S. & Ono, F. 2018. Recent advances in neuromuscular junction research prompted by the zebrafish model. *Current Opinion in Physiology,* 4**,** 70-75.
Eisen, J. S., Myers, P. Z. & Westerfield, M. 1986. Pathway selection by growth cones of identified motoneurones in live zebra fish embryos. *Nature,* 320**,** 269-71.
Elfrink, K., Liao, W., Pieper, U., Oeding, S. J. & Bahler, M. 2014. The loop2 insertion of type IX myosin acts as an electrostatic actin tether that permits processive movement. *PLoS One,* 9**,** e84874.
Engel, A. G. 2007. The therapy of congenital myasthenic syndromes. *Neurotherapeutics,* 4**,** 252-7.
Engel, A. G. 2018. Congenital Myasthenic Syndromes in 2018. *Curr Neurol Neurosci Rep,* 18**,** 46.
Engel, A. G., Shen, X. M., Selcen, D. & Sine, S. M. 2015. Congenital myasthenic syndromes: pathogenesis, diagnosis, and treatment.
Epley, K. E., Urban, J. M., Ikenaga, T. & Ono, F. 2008. A modified acetylcholine receptor delta-subunit enables a null mutant to survive beyond sexual maturation. *J Neurosci,* 28**,** 13223-31.
Escobar-Aguirre, M., Zhang, H., Jamieson-Lucy, A. & Mullins, M. C. 2017. Microtubule-actin crosslinking factor 1 (Macf1) domain function in Balbiani body dissociation and nuclear positioning. *PLoS Genet,* 13**,** e1006983.
Fagerlund, M. J. & Eriksson, L. I. 2009. Current concepts in neuromuscular transmission. *Br J Anaesth,* 103**,** 108-14.
Felsenfeld, A. L., Curry, M. & Kimmel, C. B. 1991. The fub-1 mutation blocks initial myofibril formation in zebrafish muscle pioneer cells. *Dev Biol,* 148**,** 23-30.

Ferns, M., Deiner, M. & Hall, Z. 1996. Agrin-induced acetylcholine receptor clustering in mammalian muscle requires tyrosine phosphorylation. *J Cell Biol,* 132**,** 937-44.
Finsterer, J. 2019. Congenital myasthenic syndromes. *Orphanet J Rare Dis,* 14**,** 57.
Flanagan-Steet, H., Fox, M. A., Meyer, D. & Sanes, J. R. 2005. Neuromuscular synapses can form in vivo by incorporation of initially aneural postsynaptic specializations. *Development,* 132**,** 4471-81.
Flucher, B. E. & Daniels, M. P. 1989. Distribution of Na+ channels and ankyrin in neuromuscular junctions is complementary to that of acetylcholine receptors and the 43 kd protein. *Neuron,* 3**,** 163-75.
Folci, A., Murru, L., Vezzoli, E., Ponzoni, L., Gerosa, L., Moretto, E., Longo, F., Zapata, J., Braida, D., Pistillo, F., Bahler, M., Francolini, M*., et al.* 2016. Myosin IXa Binds AMPAR and Regulates Synaptic Structure, LTP, and Cognitive Function. *Front Mol Neurosci,* 9**,** 1.
Folker, E. S. & Baylies, M. K. 2013. Nuclear positioning in muscle development and disease. *Front Physiol,* 4**,** 363.
Foth, B. J., Goedecke, M. C. & Soldati, D. 2006. New insights into myosin evolution and classification. *Proc Natl Acad Sci U S A,* 103**,** 3681-6.
Francis, M. M., Evans, S. P., Jensen, M., Madsen, D. M., Mancuso, J., Norman, K. R. & Maricq, A. V. 2005. The Ror receptor tyrosine kinase CAM-1 is required for ACR-16-mediated synaptic transmission at the C. elegans neuromuscular junction. *Neuron,* 46**,** 581-94.
Freund-Michel, V. & Frossard, N. 2008. Overexpression of functional TrkA receptors after internalisation in human airway smooth muscle cells. *Biochim Biophys Acta,* 1783**,** 1964-71.
Furman, B. L. 2018. Alpha Bungarotxin. *Reference Module in Biomedical Sciences.* Elsevier.
Fusaki, N., Ban, H., Nishiyama, A., Saeki, K. & Hasegawa, M. 2009. Efficient induction of transgene-free human pluripotent stem cells using a vector based on Sendai virus, an RNA virus that does not integrate into the host genome. *Proc Jpn Acad Ser B Phys Biol Sci,* 85**,** 348-62.
Gan, W. B. & Lichtman, J. W. 1998. Synaptic segregation at the developing neuromuscular junction. *Science,* 282**,** 1508-11.
Gao, S. Y., Li, C. Y., Chen, J., Pan, L., Saito, S., Terashita, T., Saito, K., Miyawaki, K., Shigemoto, K., Mominoki, K., Matsuda, S. & Kobayashi, N. 2004. Rho-ROCK signal pathway regulates microtubule-based process formation of cultured podocytes--inhibition of ROCK promoted process elongation. *Nephron Exp Nephrol,* 97**,** e49-61.
Gautam, M., Noakes, P. G., Moscoso, L., Rupp, F., Scheller, R. H., Merlie, J. P. & Sanes, J. R. 1996. Defective neuromuscular synaptogenesis in agrin-deficient mutant mice. *Cell,* 85**,** 525-35.
Gautam, M., Noakes, P. G., Mudd, J., Nichol, M., Chu, G. C., Sanes, J. R. & Merlie, J. P. 1995. Failure of postsynaptic specialization to develop at neuromuscular junctions of rapsyn-deficient mice. *Nature,* 377**,** 232-6.
Gershoni-Emek, N., Mazza, A., Chein, M., Gradus-Pery, T., Xiang, X., Li, K. W., Sharan, R. & Perlson, E. 2016. Proteomic Analysis of Dynein-Interacting Proteins in Amyotrophic Lateral Sclerosis Synaptosomes Reveals Alterations in the RNA-Binding Protein Staufen1. *Mol Cell Proteomics,* 15**,** 506-22.
Gervasio, O. L., Armson, P. F. & Phillips, W. D. 2007. Developmental increase in the amount of rapsyn per acetylcholine receptor promotes postsynaptic receptor packing and stability. *Dev Biol,* 305**,** 262-75.

Gesemann, M., Denzer, A. J. & Ruegg, M. A. 1995. Acetylcholine receptor-aggregating activity of agrin isoforms and mapping of the active site. *J Cell Biol,* 128**,** 625-36.
Gingras, M., Gagnon, V., Minotti, S., Durham, H. D. & Berthod, F. 2007. Optimized protocols for isolation of primary motor neurons, astrocytes and microglia from embryonic mouse spinal cord. *J Neurosci Methods,* 163**,** 111-8.
Glass, D. J., Bowen, D. C., Stitt, T. N., Radziejewski, C., Bruno, J., Ryan, T. E., Gies, D. R., Shah, S., Mattsson, K., Burden, S. J., Distefano, P. S., Valenzuela, D. M.*, et al.* 1996. Agrin acts via a MuSK receptor complex. *Cell,* 85**,** 513-23.
Godfrey, E. W., Nitkin, R. M., Wallace, B. G., Rubin, L. L. & Mcmahan, U. J. 1984. Components of Torpedo electric organ and muscle that cause aggregation of acetylcholine receptors on cultured muscle cells. *J Cell Biol,* 99**,** 615-27.
Gomez, C. M. & Gammack, J. T. 1995. A leucine-to-phenylalanine substitution in the acetylcholine receptor ion channel in a family with the slow-channel syndrome. *Neurology,* 45**,** 982-5.
Gorman, S. W., Haider, N. B., Grieshammer, U., Swiderski, R. E., Kim, E., Welch, J. W., Searby, C., Leng, S., Carmi, R., Sheffield, V. C. & Duhl, D. M. 1999. The cloning and developmental expression of unconventional myosin IXA (MYO9A) a gene in the Bardet-Biedl syndrome (BBS4) region at chromosome 15q22-q23. *Genomics,* 59**,** 150-60.
Govek, E. E., Newey, S. E. & Van Aelst, L. 2005. The role of the Rho GTPases in neuronal development. *Genes Dev,* 19**,** 1-49.
Gu, H., Yu, S. P., Gutekunst, C. A., Gross, R. E. & Wei, L. 2013. Inhibition of the Rho signaling pathway improves neurite outgrowth and neuronal differentiation of mouse neural stem cells. *Int J Physiol Pathophysiol Pharmacol,* 5**,** 11-20.
Guilluy, C., Dubash, A. D. & Garcia-Mata, R. 2011. Analysis of RhoA and Rho GEF activity in whole cells and the cell nucleus. *Nat Protoc,* 6**,** 2050-60.
Gunther, R., Balck, A., Koch, J. C., Nientiedt, T., Sereda, M., Bahr, M., Lingor, P. & Tonges, L. 2017. Rho Kinase Inhibition with Fasudil in the SOD1(G93A) Mouse Model of Amyotrophic Lateral Sclerosis-Symptomatic Treatment Potential after Disease Onset. *Front Pharmacol,* 8**,** 17.
Gupta, V. A., Kawahara, G., Myers, J. A., Chen, A. T., Hall, T. E., Manzini, M. C., Currie, P. D., Zhou, Y., Zon, L. I., Kunkel, L. M. & Beggs, A. H. 2012. A splice site mutation in laminin-alpha2 results in a severe muscular dystrophy and growth abnormalities in zebrafish. *PLoS One,* 7**,** e43794.
Hall, A. 1998. Rho GTPases and the actin cytoskeleton. *Science,* 279**,** 509-14.
Handa, Y., Durkin, C. H., Dodding, M. P. & Way, M. 2013. Vaccinia virus F11 promotes viral spread by acting as a PDZ-containing scaffolding protein to bind myosin-9A and inhibit RhoA signaling. *Cell Host Microbe,* 14**,** 51-62.
Hanley, P. J., Xu, Y., Kronlage, M., Grobe, K., Schon, P., Song, J., Sorokin, L., Schwab, A. & Bahler, M. 2010. Motorized RhoGAP myosin IXb (Myo9b) controls cell shape and motility. *Proc Natl Acad Sci U S A,* 107**,** 12145-50.
Harlow, M. L., Szule, J. A., Xu, J., Jung, J. H., Marshall, R. M. & Mcmahan, U. J. 2013. Alignment of synaptic vesicle macromolecules with the macromolecules in active zone material that direct vesicle docking. *PLoS One,* 8**,** e69410.
Hashimoto, R., Nakamura, Y., Goto, H., Wada, Y., Sakoda, S., Kaibuchi, K., Inagaki, M. & Takeda, M. 1998. Domain- and site-specific phosphorylation of bovine NF-L by Rho-associated kinase. *Biochem Biophys Res Commun,* 245**,** 407-11.
Hasson, T. 2003. Myosin VI: two distinct roles in endocytosis. *J Cell Sci,* 116**,** 3453-61.
Helmprobst, F., Frank, M. & Stigloher, C. 2015. Presynaptic architecture of the larval zebrafish neuromuscular junction. *J Comp Neurol,* 523**,** 1984-97.

Henningsen, J., Rigbolt, K. T., Blagoev, B., Pedersen, B. K. & Kratchmarova, I. 2010. Dynamics of the skeletal muscle secretome during myoblast differentiation. *Mol Cell Proteomics,* 9**,** 2482-96.

Hesser, B. A., Henschel, O. & Witzemann, V. 2006. Synapse disassembly and formation of new synapses in postnatal muscle upon conditional inactivation of MuSK. *Mol Cell Neurosci,* 31**,** 470-80.

Hettwer, S., Lin, S., Kucsera, S., Haubitz, M., Oliveri, F., Fariello, R. G., Ruegg, M. A. & Vrijbloed, J. W. 2014. Injection of a soluble fragment of neural agrin (NT-1654) considerably improves the muscle pathology caused by the disassembly of the neuromuscular junction. *PLoS One,* 9**,** e88739.

Higashijima, S., Hotta, Y. & Okamoto, H. 2000. Visualization of cranial motor neurons in live transgenic zebrafish expressing green fluorescent protein under the control of the islet-1 promoter/enhancer. *J Neurosci,* 20**,** 206-18.

Hirose, M., Ishizaki, T., Watanabe, N., Uehata, M., Kranenburg, O., Moolenaar, W. H., Matsumura, F., Maekawa, M., Bito, H. & Narumiya, S. 1998. Molecular dissection of the Rho-associated protein kinase (p160ROCK)-regulated neurite remodeling in neuroblastoma N1E-115 cells. *J Cell Biol,* 141**,** 1625-36.

Hisanaga, S., Gonda, Y., Inagaki, M., Ikai, A. & Hirokawa, N. 1990. Effects of phosphorylation of the neurofilament L protein on filamentous structures. *Cell Regul,* 1**,** 237-48.

Houenou, L. J., D'costa, A. P., Li, L., Turgeon, V. L., Enyadike, C., Alberdi, E. & Becerra, S. P. 1999. Pigment epithelium-derived factor promotes the survival and differentiation of developing spinal motor neurons. *J Comp Neurol,* 412**,** 506-14.

Howard, J. F., Jr. 2013. Electrodiagnosis of disorders of neuromuscular transmission. *Phys Med Rehabil Clin N Am,* 24**,** 169-92.

Howe, K., Clark, M. D., Torroja, C. F., Torrance, J., Berthelot, C., Muffato, M., Collins, J. E., Humphray, S., Mclaren, K., Matthews, L., Mclaren, S., Sealy, I.*, et al.* 2013. The zebrafish reference genome sequence and its relationship to the human genome. *Nature,* 496**,** 498-503.

Huze, C., Bauche, S., Richard, P., Chevessier, F., Goillot, E., Gaudon, K., Ben Ammar, A., Chaboud, A., Grosjean, I., Lecuyer, H. A., Bernard, V., Rouche, A.*, et al.* 2009. Identification of an agrin mutation that causes congenital myasthenia and affects synapse function. *Am J Hum Genet,* 85**,** 155-67.

Hwang, W. Y., Fu, Y., Reyon, D., Maeder, M. L., Kaini, P., Sander, J. D., Joung, J. K., Peterson, R. T. & Yeh, J. R. 2013. Heritable and precise zebrafish genome editing using a CRISPR-Cas system. *PLoS One,* 8**,** e68708.

Ibebunjo, C., Chick, J. M., Kendall, T., Eash, J. K., Li, C., Zhang, Y., Vickers, C., Wu, Z., Clarke, B. A., Shi, J., Cruz, J., Fournier, B.*, et al.* 2013. Genomic and proteomic profiling reveals reduced mitochondrial function and disruption of the neuromuscular junction driving rat sarcopenia. *Mol Cell Biol,* 33**,** 194-212.

Inoue, A., Setoguchi, K., Matsubara, Y., Okada, K., Sato, N., Iwakura, Y., Higuchi, O. & Yamanashi, Y. 2009. Dok-7 activates the muscle receptor kinase MuSK and shapes synapse formation. *Sci Signal,* 2**,** ra7.

Issop, Y., Hathazi, D., Khan, M. M., Rudolf, R., Weis, J., Spendiff, S., Slater, C. R., Roos, A. & Lochmuller, H. 2018. GFPT1 deficiency in muscle leads to myasthenia and myopathy in mice. *Hum Mol Genet,* 27**,** 3218-3232.

Iwabuchi, S., Kakazu, Y., Koh, J. Y., Goodman, K. M. & Harata, N. C. 2014. Examination of synaptic vesicle recycling using FM dyes during evoked, spontaneous, and miniature synaptic activities. *J Vis Exp*.

Jaffe, A. B. & Hall, A. 2005. Rho GTPases: biochemistry and biology. *Annu Rev Cell Dev Biol,* 21**,** 247-69.

Jagtap, S. A., Abraham, K., Sarada, C. & Nair, M. D. 2013. Congenital myasthenic syndromes: Natural history and long-term prognosis. *Annals of Indian Academy of Neurology,* 16**,** 338-341.
Jao, L. E., Wente, S. R. & Chen, W. 2013. Efficient multiplex biallelic zebrafish genome editing using a CRISPR nuclease system. *Proc Natl Acad Sci U S A,* 110**,** 13904-9.
Jing, L., Lefebvre, J. L., Gordon, L. R. & Granato, M. 2009. Wnt signals organize synaptic prepattern and axon guidance through the zebrafish unplugged/MuSK receptor. *Neuron,* 61**,** 721-33.
Jones, R. A., Harrison, C., Eaton, S. L., Llavero Hurtado, M., Graham, L. C., Alkhammash, L., Oladiran, O. A., Gale, A., Lamont, D. J., Simpson, H., Simmen, M. W., Soeller, C.*, et al.* 2017. Cellular and Molecular Anatomy of the Human Neuromuscular Junction. *Cell Rep,* 21**,** 2348-2356.
Jones, R. A., Reich, C. D., Dissanayake, K. N., Kristmundsdottir, F., Findlater, G. S., Ribchester, R. R., Simmen, M. W. & Gillingwater, T. H. 2016. NMJ-morph reveals principal components of synaptic morphology influencing structure-function relationships at the neuromuscular junction. *Open Biol,* 6.
Jullien, J., Guili, V., Derrington, E. A., Darlix, J. L., Reichardt, L. F. & Rudkin, B. B. 2003. Trafficking of TrkA-green fluorescent protein chimerae during nerve growth factor-induced differentiation. *J Biol Chem,* 278**,** 8706-16.
Jung, J. H., Szule, J. A., Stouder, K., Marshall, R. M. & Mcmahan, U. J. 2018. Active Zone Material-Directed Orientation, Docking, and Fusion of Dense Core Vesicles Alongside Synaptic Vesicles at Neuromuscular Junctions. *Front Neuroanat,* 12**,** 72.
Kalhammer, G., Bahler, M., Schmitz, F., Jockel, J. & Block, C. 1997. Ras-binding domains: predicting function versus folding. *FEBS Lett,* 414**,** 599-602.
Karakaya, M., Ceyhan-Birsoy, O., Beggs, A. H. & Topaloglu, H. 2017. A Novel Missense Variant in the AGRN Gene; Congenital Myasthenic Syndrome Presenting With Head Drop. *J Clin Neuromuscul Dis,* 18**,** 147-151.
Kent, W. J., Sugnet, C. W., Furey, T. S., Roskin, K. M., Pringle, T. H., Zahler, A. M. & Haussler, D. 2002. The human genome browser at UCSC. *Genome Res,* 12**,** 996-1006.
Khan, M. M., Lustrino, D., Silveira, W. A., Wild, F., Straka, T., Issop, Y., O'connor, E., Cox, D., Reischl, M., Marquardt, T., Labeit, D., Labeit, S.*, et al.* 2016. Sympathetic innervation controls homeostasis of neuromuscular junctions in health and disease. *Proc Natl Acad Sci U S A,* 113**,** 746-50.
Kim, J. K., Caine, C., Awano, T., Herbst, R. & Monani, U. R. 2017. Motor neuronal repletion of the NMJ organizer, Agrin, modulates the severity of the spinal muscular atrophy disease phenotype in model mice. *Hum Mol Genet,* 26**,** 2377-2385.
Kim, M. J., Cotman, S. L., Halfter, W. & Cole, G. J. 2003. The heparan sulfate proteoglycan agrin modulates neurite outgrowth mediated by FGF-2. *J Neurobiol,* 55**,** 261-77.
Kim, M. J., Liu, I. H., Song, Y., Lee, J. A., Halfter, W., Balice-Gordon, R. J., Linney, E. & Cole, G. J. 2007. Agrin is required for posterior development and motor axon outgrowth and branching in embryonic zebrafish. *Glycobiology,* 17**,** 231-47.
Kim, N., Stiegler, A. L., Cameron, T. O., Hallock, P. T., Gomez, A. M., Huang, J. H., Hubbard, S. R., Dustin, M. L. & Burden, S. J. 2008. Lrp4 is a receptor for Agrin and forms a complex with MuSK. *Cell,* 135**,** 334-42.
Kimmel, C. B., Ballard, W. W., Kimmel, S. R., Ullmann, B. & Schilling, T. F. 1995. Stages of embryonic development of the zebrafish. *Dev Dyn,* 203**,** 253-310.

Kimmel, C. B., Patterson, J. & Kimmel, R. O. 1974. The development and behavioral characteristics of the startle response in the zebra fish. *Dev Psychobiol,* 7**,** 47-60.
Kirkpatrick, L. L. & Brady, S. T. 1999. Molecular Components of the Neuronal Cytoskeleton. *In:* SIEGEL, G. J., AGRANOFF, B. W., ALBERS, R. W. & AL., E. (eds.) *Basic Neurochemistry: Molecular, Cellular and Medical Aspects.* 6 ed. Philadelphia: Lippincott-Raven.
Knight, D., Tolley, L. K., Kim, D. K., Lavidis, N. A. & Noakes, P. G. 2003. Functional analysis of neurotransmission at beta2-laminin deficient terminals. *J Physiol,* 546**,** 789-800.
Koenig, J. A., Dao, T. L., Kan, R. K. & Shih, T. M. 2016. Zebrafish as a model for acetylcholinesterase-inhibiting organophosphorus agent exposure and oxime reactivation. *Ann N Y Acad Sci,* 1374**,** 68-77.
Kok, F. O., Shin, M., Ni, C. W., Gupta, A., Grosse, A. S., Van Impel, A., Kirchmaier, B. C., Peterson-Maduro, J., Kourkoulis, G., Male, I., Desantis, D. F., Sheppard-Tindell, S.*, et al.* 2015. Reverse genetic screening reveals poor correlation between morpholino-induced and mutant phenotypes in zebrafish. *Dev Cell,* 32**,** 97-108.
Koopmans, G., Hasse, B. & Sinis, N. 2009. Chapter 19: The role of collagen in peripheral nerve repair. *Int Rev Neurobiol,* 87**,** 363-79.
Kranenburg, O., Poland, M., Van Horck, F. P., Drechsel, D., Hall, A. & Moolenaar, W. H. 1999. Activation of RhoA by lysophosphatidic acid and Galpha12/13 subunits in neuronal cells: induction of neurite retraction. *Mol Biol Cell,* 10**,** 1851-7.
Krendel, M. & Mooseker, M. S. 2005. Myosins: tails (and heads) of functional diversity. *Physiology (Bethesda),* 20**,** 239-51.
Lackner, M. R., Nurrish, S. J. & Kaplan, J. M. 1999. Facilitation of synaptic transmission by EGL-30 Gqalpha and EGL-8 PLCbeta: DAG binding to UNC-13 is required to stimulate acetylcholine release. *Neuron,* 24**,** 335-46.
Langheinrich, U., Hennen, E., Stott, G. & Vacun, G. 2002. Zebrafish as a model organism for the identification and characterization of drugs and genes affecting p53 signaling. *Curr Biol,* 12**,** 2023-8.
Latina, V., Caioli, S., Zona, C., Ciotti, M. T., Amadoro, G. & Calissano, P. 2017. Impaired NGF/TrkA Signaling Causes Early AD-Linked Presynaptic Dysfunction in Cholinergic Primary Neurons. *Front Cell Neurosci,* 11**,** 68.
Legay, C. & Mei, L. 2017. Moving forward with the neuromuscular junction. *J Neurochem,* 142 Suppl 2**,** 59-63.
Lek, M., Karczewski, K. J., Minikel, E. V., Samocha, K. E., Banks, E., Fennell, T., O'donnell-Luria, A. H., Ware, J. S., Hill, A. J., Cummings, B. B., Tukiainen, T., Birnbaum, D. P.*, et al.* 2016. Analysis of protein-coding genetic variation in 60,706 humans. *Nature,* 536**,** 285-91.
Li, J., Chen, Y., Deng, Y., Unarta, I. C., Lu, Q., Huang, X. & Zhang, M. 2017. Ca(2+)-Induced Rigidity Change of the Myosin VIIa IQ Motif-Single alpha Helix Lever Arm Extension. *Structure,* 25**,** 579-591 e4.
Li, L., Cao, Y., Wu, H., Ye, X., Zhu, Z., Xing, G., Shen, C., Barik, A., Zhang, B., Xie, X., Zhi, W., Gan, L.*, et al.* 2016. Enzymatic Activity of the Scaffold Protein Rapsyn for Synapse Formation. *Neuron,* 92**,** 1007-1019.
Li, W., Ono, F. & Brehm, P. 2003. Optical measurements of presynaptic release in mutant zebrafish lacking postsynaptic receptors. *J Neurosci,* 23**,** 10467-74.
Li, Z., Li, M., Wood, K., Hettwer, S., Muley, S. A., Shi, F. D., Liu, Q. & Ladha, S. S. 2018. Engineered agrin attenuates the severity of experimental autoimmune myasthenia gravis. *Muscle Nerve,* 57**,** 814-820.

Liao, W., Elfrink, K. & Bahler, M. 2010. Head of myosin IX binds calmodulin and moves processively toward the plus-end of actin filaments. *J Biol Chem,* 285**,** 24933-42.
Lin, W., Burgess, R. W., Dominguez, B., Pfaff, S. L., Sanes, J. R. & Lee, K. F. 2001. Distinct roles of nerve and muscle in postsynaptic differentiation of the neuromuscular synapse. *Nature,* 410**,** 1057-64.
Liu, C., Ma, W., Su, W. & Zhang, J. 2012. Prdm14 acts upstream of islet2 transcription to regulate axon growth of primary motoneurons in zebrafish. *Development,* 139**,** 4591-600.
Liu, H., Xi, Y., Liu, G., Zhao, Y., Li, J. & Lei, M. 2018. Comparative transcriptomic analysis of skeletal muscle tissue during prenatal stages in Tongcheng and Yorkshire pig using RNA-seq. *Funct Integr Genomics,* 18**,** 195-209.
Liu, J., Gao, H. Y. & Wang, X. F. 2015. The role of the Rho/ROCK signaling pathway in inhibiting axonal regeneration in the central nervous system. *Neural Regen Res,* 10**,** 1892-6.
Liu, R., Li, B., Flanagan, S. W., Oberley, L. W., Gozal, D. & Qiu, M. 2002. Increased mitochondrial antioxidative activity or decreased oxygen free radical propagation prevent mutant SOD1-mediated motor neuron cell death and increase amyotrophic lateral sclerosis-like transgenic mouse survival. *J Neurochem,* 80**,** 488-500.
Logan, C. V., Cossins, J., Rodriguez Cruz, P. M., Parry, D. A., Maxwell, S., Martinez-Martinez, P., Riepsaame, J., Abdelhamed, Z. A., Lake, A. V., Moran, M., Robb, S., Chow, G.*, et al.* 2015. Congenital Myasthenic Syndrome Type 19 Is Caused by Mutations in COL13A1, Encoding the Atypical Non-fibrillar Collagen Type XIII alpha1 Chain. *Am J Hum Genet,* 97**,** 878-85.
Long, H., Zhu, X., Yang, P., Gao, Q., Chen, Y. & Ma, L. 2013. Myo9b and RICS modulate dendritic morphology of cortical neurons. *Cereb Cortex,* 23**,** 71-9.
Lorenzen, A., Samosh, J., Vandewark, K., Anborgh, P. H., Seah, C., Magalhaes, A. C., Cregan, S. P., Ferguson, S. S. & Pasternak, S. H. 2010. Rapid and direct transport of cell surface APP to the lysosome defines a novel selective pathway. *Mol Brain,* 3**,** 11.
Luna, V. M., Daikoku, E. & Ono, F. 2015. "Slow" skeletal muscles across vertebrate species. *Cell Biosci,* 5**,** 62.
Maddirevula, S., Alzahrani, F., Al-Owain, M., Al Muhaizea, M. A., Kayyali, H. R., Alhashem, A., Rahbeeni, Z., Al-Otaibi, M., Alzaidan, H. I., Balobaid, A., El Khashab, H. Y., Bubshait, D. K.*, et al.* 2019. Autozygome and high throughput confirmation of disease genes candidacy. *Genet Med,* 21**,** 736-742.
Magill-Solc, C. & Mcmahan, U. J. 1988. Motor neurons contain agrin-like molecules. *J Cell Biol,* 107**,** 1825-33.
Maselli, R. A., Arredondo, J., Vazquez, J., Chong, J. X., Bamshad, M. J., Nickerson, D. A., Lara, M., Ng, F., Lo, V. L., Pytel, P. & Mcdonald, C. M. 2018. A presynaptic congenital myasthenic syndrome attributed to a homozygous sequence variant in LAMA5. *Ann N Y Acad Sci,* 1413**,** 119-125.
Maselli, R. A., Fernandez, J. M., Arredondo, J., Navarro, C., Ngo, M., Beeson, D., Cagney, O., Williams, D. C., Wollmann, R. L., Yarov-Yarovoy, V. & Ferns, M. J. 2012. LG2 agrin mutation causing severe congenital myasthenic syndrome mimics functional characteristics of non-neural (z-) agrin. *Hum Genet,* 131**,** 1123-35.
Matthews-Bellinger, J. A. & Salpeter, M. M. 1983. Fine structural distribution of acetylcholine receptors at developing mouse neuromuscular junctions. *J Neurosci,* 3**,** 644-57.

Mccallie, B. R., Parks, J. C., Patton, A. L., Griffin, D. K., Schoolcraft, W. B. & Katz-Jaffe, M. G. 2016. Hypomethylation and Genetic Instability in Monosomy Blastocysts May Contribute to Decreased Implantation Potential. *PLoS One,* 11**,** e0159507.
Mcelvany, K. D. 2009. FDA requirements for preclinical studies. *Front Neurol Neurosci,* 25**,** 46-9.
Mcmacken, G., Cox, D., Roos, A., Muller, J., Whittaker, R. & Lochmuller, H. 2018a. The beta-adrenergic agonist salbutamol modulates neuromuscular junction formation in zebrafish models of human myasthenic syndromes. *Hum Mol Genet,* 27**,** 1556-1564.
Mcmacken, G., Whittaker, R. G., Evangelista, T., Abicht, A., Dusl, M. & Lochmuller, H. 2018b. Congenital myasthenic syndrome with episodic apnoea: clinical, neurophysiological and genetic features in the long-term follow-up of 19 patients. *J Neurol,* 265**,** 194-203.
Mcmacken, G. M., Spendiff, S., Whittaker, R. G., O'connor, E., Howarth, R. M., Boczonadi, V., Horvath, R., Slater, C. R. & Lochmüller, H. 2019. Salbutamol modifies the neuromuscular junction in a mouse model of ColQ myasthenic syndrome.
Mcmahan, U. J. 1990. The agrin hypothesis. *Cold Spring Harb Symp Quant Biol,* 55**,** 407-18.
Mcmullan, R., Hiley, E., Morrison, P. & Nurrish, S. J. 2006. Rho is a presynaptic activator of neurotransmitter release at pre-existing synapses in C. elegans. *Genes Dev,* 20**,** 65-76.
Melancon, E., Liu, D. W., Westerfield, M. & Eisen, J. S. 1997. Pathfinding by identified zebrafish motoneurons in the absence of muscle pioneers. *J Neurosci,* 17**,** 7796-804.
Mendell, L. M. 2005. The size principle: a rule describing the recruitment of motoneurons. *J Neurophysiol,* 93**,** 3024-6.
Mendes-Pinheiro, B., Teixeira, F. G., Anjo, S. I., Manadas, B., Behie, L. A. & Salgado, A. J. 2018. Secretome of Undifferentiated Neural Progenitor Cells Induces Histological and Motor Improvements in a Rat Model of Parkinson's Disease. *Stem Cells Transl Med,* 7**,** 829-838.
Menzies, F. M., Grierson, A. J., Cookson, M. R., Heath, P. R., Tomkins, J., Figlewicz, D. A., Ince, P. G. & Shaw, P. J. 2002. Selective loss of neurofilament expression in Cu/Zn superoxide dismutase (SOD1) linked amyotrophic lateral sclerosis. *J Neurochem,* 82**,** 1118-28.
Meriggioli, M. N. & Sanders, D. B. 2009. Autoimmune myasthenia gravis: emerging clinical and biological heterogeneity. *Lancet Neurol,* 8**,** 475-90.
Meyer, A. & Schartl, M. 1999. Gene and genome duplications in vertebrates: the one-to-four (-to-eight in fish) rule and the evolution of novel gene functions. *Curr Opin Cell Biol,* 11**,** 699-704.
Meyer, S., Worsdorfer, P., Gunther, K., Thier, M. & Edenhofer, F. 2015. Derivation of Adult Human Fibroblasts and their Direct Conversion into Expandable Neural Progenitor Cells. *J Vis Exp***,** e52831.
Mishina, M., Takai, T., Imoto, K., Noda, M., Takahashi, T., Numa, S., Methfessel, C. & Sakmann, B. 1986. Molecular distinction between fetal and adult forms of muscle acetylcholine receptor. *Nature,* 321**,** 406-11.
Mitsui, T., Kawajiri, M., Kunishige, M., Endo, T., Akaike, M., Aki, K. & Matsumoto, T. 2000. Functional association between nicotinic acetylcholine receptor and sarcomeric proteins via actin and desmin filaments. *J Cell Biochem,* 77**,** 584-95.

Momboisse, F., Houy, S., Ory, S., Calco, V., Bader, M. F. & Gasman, S. 2011. How important are Rho GTPases in neurosecretion? *J Neurochem,* 117**,** 623-31.
Mongeon, R., Walogorsky, M., Urban, J., Mandel, G., Ono, F. & Brehm, P. 2011. An acetylcholine receptor lacking both gamma and epsilon subunits mediates transmission in zebrafish slow muscle synapses. *J Gen Physiol,* 138**,** 353-66.
Moreno-Mateos, M. A., Vejnar, C. E., Beaudoin, J. D., Fernandez, J. P., Mis, E. K., Khokha, M. K. & Giraldez, A. J. 2015. CRISPRscan: designing highly efficient sgRNAs for CRISPR-Cas9 targeting in vivo. *Nat Methods,* 12**,** 982-8.
Mosca, T. J., Luginbuhl, D. J., Wang, I. E. & Luo, L. 2017. Presynaptic LRP4 promotes synapse number and function of excitatory CNS neurons. *Elife,* 6.
Muller, J. S., Jepson, C. D., Laval, S. H., Bushby, K., Straub, V. & Lochmuller, H. 2010. Dok-7 promotes slow muscle integrity as well as neuromuscular junction formation in a zebrafish model of congenital myasthenic syndromes. *Hum Mol Genet,* 19**,** 1726-40.
Muller, R. T., Honnert, U., Reinhard, J. & Bahler, M. 1997. The rat myosin myr 5 is a GTPase-activating protein for Rho in vivo: essential role of arginine 1695. *Mol Biol Cell,* 8**,** 2039-53.
Myers, P. Z., Eisen, J. S. & Westerfield, M. 1986. Development and axonal outgrowth of identified motoneurons in the zebrafish. *J Neurosci,* 6**,** 2278-89.
Nguyen, P. V., Aniksztejn, L., Catarsi, S. & Drapeau, P. 1999. Maturation of neuromuscular transmission during early development in zebrafish. *J Neurophysiol,* 81**,** 2852-61.
Nicole, S., Chaouch, A., Torbergsen, T., Bauche, S., De Bruyckere, E., Fontenille, M. J., Horn, M. A., Van Ghelue, M., Loseth, S., Issop, Y., Cox, D., Muller, J. S.*, et al.* 2014. Agrin mutations lead to a congenital myasthenic syndrome with distal muscle weakness and atrophy. *Brain,* 137**,** 2429-43.
Nishimune, H., Numata, T., Chen, J., Aoki, Y., Wang, Y., Starr, M. P., Mori, Y. & Stanford, J. A. 2012. Active zone protein Bassoon co-localizes with presynaptic calcium channel, modifies channel function, and recovers from aging related loss by exercise. *PLoS One,* 7**,** e38029.
Noakes, P. G., Gautam, M., Mudd, J., Sanes, J. R. & Merlie, J. P. 1995. Aberrant differentiation of neuromuscular junctions in mice lacking s-laminin/laminin beta 2. *Nature,* 374**,** 258-62.
Nystrom, B. 1968. Postnatal development of motor nerve terminals in "slow-red" and "fast-white" cat muscles. *Acta Neurol Scand,* 44**,** 363-83.
O'connor, E., Phan, V., Cordts, I., Cairns, G., Hettwer, S., Cox, D., Lochmuller, H. & Roos, A. 2018a. MYO9A deficiency in motor neurons is associated with reduced neuromuscular agrin secretion. *Hum Mol Genet,* 27**,** 1434-1446.
O'connor, E., Topf, A., Muller, J. S., Cox, D., Evangelista, T., Colomer, J., Abicht, A., Senderek, J., Hasselmann, O., Yaramis, A., Laval, S. H. & Lochmuller, H. 2016. Identification of mutations in the MYO9A gene in patients with congenital myasthenic syndrome. *Brain,* 139**,** 2143-53.
O'connor, E., Topf, A., Zahedi, R. P., Spendiff, S., Cox, D., Roos, A. & Lochmuller, H. 2018b. Clinical and research strategies for limb-girdle congenital myasthenic syndromes. *Ann N Y Acad Sci,* 1412**,** 102-112.
Ogata, T. & Yamasaki, Y. 1985. The three-dimensional structure of motor endplates in different fiber types of rat intercostal muscle. A scanning electron-microscopic study. *Cell Tissue Res,* 241**,** 465-72.
Ohno, K., Fau, H. D., Milone, M., Brengman, J. M., Bouzat, C., Sine, S. M. & Engel, A. G. 1995. Congenital myasthenic syndrome caused by prolonged acetylcholine receptor channel openings due to a mutation in the M2 domain of the epsilon subunit.

Okada, K., Inoue, A., Okada, M., Murata, Y., Kakuta, S., Jigami, T., Kubo, S., Shiraishi, H., Eguchi, K., Motomura, M., Akiyama, T., Iwakura, Y., *et al.* 2006. The muscle protein Dok-7 is essential for neuromuscular synaptogenesis. *Science,* 312**,** 1802-5.

Okumura, N., Kinoshita, S. & Koizumi, N. 2017. Application of Rho Kinase Inhibitors for the Treatment of Corneal Endothelial Diseases. *J Ophthalmol,* 2017**,** 2646904.

Omelchenko, T. & Hall, A. 2012. Myosin-IXA regulates collective epithelial cell migration by targeting RhoGAP activity to cell-cell junctions. *Curr Biol,* 22**,** 278-88.

Ono, F., Higashijima, S., Shcherbatko, A., Fetcho, J. R. & Brehm, P. 2001. Paralytic zebrafish lacking acetylcholine receptors fail to localize rapsyn clusters to the synapse. *J Neurosci,* 21**,** 5439-48.

Ota, S., Hisano, Y., Ikawa, Y. & Kawahara, A. 2014. Multiple genome modifications by the CRISPR/Cas9 system in zebrafish. *Genes Cells,* 19**,** 555-64.

Oury, J., Liu, Y., Topf, A., Todorovic, S., Hoedt, E., Preethish-Kumar, V., Neubert, T. A., Lin, W., Lochmuller, H. & Burden, S. J. 2019. MACF1 links Rapsyn to microtubule- and actin-binding proteins to maintain neuromuscular synapses. *J Cell Biol*.

Panzer, J. A., Gibbs, S. M., Dosch, R., Wagner, D., Mullins, M. C., Granato, M. & Balice-Gordon, R. J. 2005. Neuromuscular synaptogenesis in wild-type and mutant zebrafish. *Dev Biol,* 285**,** 340-57.

Park, J. Y., Mott, M., Williams, T., Ikeda, H., Wen, H., Linhoff, M. & Ono, F. 2014. A single mutation in the acetylcholine receptor delta-subunit causes distinct effects in two types of neuromuscular synapses. *J Neurosci,* 34**,** 10211-8.

Patel, K. G., Liu, C., Cameron, P. L. & Cameron, R. S. 2001. Myr 8, a novel unconventional myosin expressed during brain development associates with the protein phosphatase catalytic subunits 1alpha and 1gamma1. *J Neurosci,* 21**,** 7954-68.

Patton, B. L., Cunningham, J. M., Thyboll, J., Kortesmaa, J., Westerblad, H., Edstrom, L., Tryggvason, K. & Sanes, J. R. 2001. Properly formed but improperly localized synaptic specializations in the absence of laminin alpha4. *Nat Neurosci,* 4**,** 597-604.

Pelka, K. E., Henn, K., Keck, A., Sapel, B. & Braunbeck, T. 2017. Size does matter - Determination of the critical molecular size for the uptake of chemicals across the chorion of zebrafish (Danio rerio) embryos. *Aquat Toxicol,* 185**,** 1-10.

Pennefather, P. & Quastel, D. M. 1981. Relation between subsynaptic receptor blockade and response to quantal transmitter at the mouse neuromuscular junction. *J Gen Physiol,* 78**,** 313-44.

Perez, M. J., Ponce, D. P., Osorio-Fuentealba, C., Behrens, M. I. & Quintanilla, R. A. 2017. Mitochondrial Bioenergetics Is Altered in Fibroblasts from Patients with Sporadic Alzheimer's Disease. *Front Neurosci,* 11**,** 553.

Personius, K. E., Slusher, B. S. & Udin, S. B. 2016. Neuromuscular NMDA Receptors Modulate Developmental Synapse Elimination. *J Neurosci,* 36**,** 8783-9.

Phan, V., Cox, D., Cipriani, S., Spendiff, S., Buchkremer, S., O'connor, E., Horvath, R., Goebel, H. H., Hathazi, D., Lochmuller, H., Straka, T., Rudolf, R., *et al.* 2019. SIL1 deficiency causes degenerative changes of peripheral nerves and neuromuscular junctions in fish, mice and human. *Neurobiol Dis,* 124**,** 218-229.

Philip, A. M., Wang, Y., Mauro, A., El-Rass, S., Marshall, J. C., Lee, W. L., Slutsky, A. S., Dossantos, C. C. & Wen, X. Y. 2017. Development of a zebrafish sepsis model for high-throughput drug discovery. *Mol Med,* 23**,** 134-148.

Pitt, M. 2018. Neurophysiological Assessment of Abnormalities of the Neuromuscular Junction in Children. *Int J Mol Sci,* 19.
Plantman, S., Zelano, J., Novikova, L. N., Novikov, L. N. & Cullheim, S. 2013. Neuronal myosin-X is upregulated after peripheral nerve injury and mediates laminin-induced growth of neurites. *Mol Cell Neurosci,* 56**,** 96-101.
Post, P. L., Bokoch, G. M. & Mooseker, M. S. 1998. Human myosin-IXb is a mechanochemically active motor and a GAP for rho. *J Cell Sci,* 111 (Pt 7)**,** 941-50.
Raines, A. N., Nagdas, S., Kerber, M. L. & Cheney, R. E. 2012. Headless Myo10 is a negative regulator of full-length Myo10 and inhibits axon outgrowth in cortical neurons. *J Biol Chem,* 287**,** 24873-83.
Regal, L., Shen, X. M., Selcen, D., Verhille, C., Meulemans, S., Creemers, J. W. & Engel, A. G. 2014. PREPL deficiency with or without cystinuria causes a novel myasthenic syndrome. *Neurology,* 82**,** 1254-60.
Reif, R., Sales, S., Hettwer, S., Dreier, B., Gisler, C., Wolfel, J., Luscher, D., Zurlinden, A., Stephan, A., Ahmed, S., Baici, A., Ledermann, B.*, et al.* 2007. Specific cleavage of agrin by neurotrypsin, a synaptic protease linked to mental retardation. *FASEB J,* 21**,** 3468-78.
Remedio, L., Gribble, K. D., Lee, J. K., Kim, N., Hallock, P. T., Delestree, N., Mentis, G. Z., Froemke, R. C., Granato, M. & Burden, S. J. 2016. Diverging roles for Lrp4 and Wnt signaling in neuromuscular synapse development during evolution. *Genes Dev,* 30**,** 1058-69.
Ridley, A. J. & Hall, A. 1992. The small GTP-binding protein rho regulates the assembly of focal adhesions and actin stress fibers in response to growth factors. *Cell,* 70**,** 389-99.
Rizzardini, M., Mangolini, A., Lupi, M., Ubezio, P., Bendotti, C. & Cantoni, L. 2005. Low levels of ALS-linked Cu/Zn superoxide dismutase increase the production of reactive oxygen species and cause mitochondrial damage and death in motor neuron-like cells. *J Neurol Sci,* 232**,** 95-103.
Robu, M. E., Larson, J. D., Nasevicius, A., Beiraghi, S., Brenner, C., Farber, S. A. & Ekker, S. C. 2007. p53 activation by knockdown technologies. *PLoS Genet,* 3**,** e78.
Roder, I. V., Petersen, Y., Choi, K. R., Witzemann, V., Hammer, J. A., 3rd & Rudolf, R. 2008. Role of Myosin Va in the plasticity of the vertebrate neuromuscular junction in vivo. *PLoS One,* 3**,** e3871.
Roder, I. V., Strack, S., Reischl, M., Dahley, O., Khan, M. M., Kassel, O., Zaccolo, M. & Rudolf, R. 2012. Participation of myosin Va and Pka type I in the regeneration of neuromuscular junctions. *PLoS One,* 7**,** e40860.
Rodrigues, A. C. Z., Messi, M. L., Wang, Z. M., Abba, M. C., Pereyra, A., Birbrair, A., Zhang, T., O'meara, M., Kwan, P., Lopez, E. I. S., Willis, M. S., Mintz, A.*, et al.* 2019. The sympathetic nervous system regulates skeletal muscle motor innervation and acetylcholine receptor stability. *Acta Physiol (Oxf),* 225**,** e13195.
Rodriguez Cruz, P. M., Palace, J. & Beeson, D. 2018. The Neuromuscular Junction and Wide Heterogeneity of Congenital Myasthenic Syndromes. *Int J Mol Sci,* 19.
Roos, A., Kollipara, L., Buchkremer, S., Labisch, T., Brauers, E., Gatz, C., Lentz, C., Gerardo-Nava, J., Weis, J. & Zahedi, R. P. 2016. Cellular Signature of SIL1 Depletion: Disease Pathogenesis due to Alterations in Protein Composition Beyond the ER Machinery. *Mol Neurobiol,* 53**,** 5527-41.
Rottner, K., Faix, J., Bogdan, S., Linder, S. & Kerkhoff, E. 2017. Actin assembly mechanisms at a glance. *J Cell Sci,* 130**,** 3427-3435.

Ruegg, M. A. & Bixby, J. L. 1998. Agrin orchestrates synaptic differentiation at the vertebrate neuromuscular junction. *Trends Neurosci,* 21**,** 22-7.
Saczko-Brack, D., Warchol, E., Rogez, B., Kross, M., Heissler, S. M., Sellers, J. R., Batters, C. & Veigel, C. 2016. Self-organization of actin networks by a monomeric myosin. *Proc Natl Acad Sci U S A,* 113**,** E8387-E8395.
Saint-Amant, L. & Drapeau, P. 1998. Time course of the development of motor behaviors in the zebrafish embryo. *J Neurobiol,* 37**,** 622-32.
Samuel, M. A., Valdez, G., Tapia, J. C., Lichtman, J. W. & Sanes, J. R. 2012. Agrin and synaptic laminin are required to maintain adult neuromuscular junctions. *PLoS One,* 7**,** e46663.
Sanes, J. R. & Lichtman, J. W. 2001. Induction, assembly, maturation and maintenance of a postsynaptic apparatus. *Nat Rev Neurosci,* 2**,** 791-805.
Schiaffino, S. & Reggiani, C. 2011. Fiber types in mammalian skeletal muscles. *Physiol Rev,* 91**,** 1447-531.
Schira, J., Heinen, A., Poschmann, G., Ziegler, B., Hartung, H. P., Stuhler, K. & Kury, P. 2018. Secretome analysis of nerve repair mediating Schwann cells reveals Smad-dependent trophism. *FASEB J***,** fj201801799R.
Schnepp, A., Komp Lindgren, P., Hulsmann, H., Kroger, S., Paulsson, M. & Hartmann, U. 2005. Mouse testican-2. Expression, glycosylation, and effects on neurite outgrowth. *J Biol Chem,* 280**,** 11274-80.
Schubert, S., Keddig, N., Hanel, R. & Kammann, U. 2014. Microinjection into zebrafish embryos (Danio rerio) - a useful tool in aquatic toxicity testing? *Environmental Sciences Europe,* 26**,** 32.
Schulte-Merker, S. & Stainier, D. Y. 2014. Out with the old, in with the new: reassessing morpholino knockdowns in light of genome editing technology. *Development,* 141**,** 3103-4.
Schwartz, M. 2004. Rho signalling at a glance. *J Cell Sci,* 117**,** 5457-8.
Schwarz, J. M., Cooper, D. N., Schuelke, M. & Seelow, D. 2014. MutationTaster2: mutation prediction for the deep-sequencing age. *Nat Methods,* 11**,** 361-2.
Selcen, D., Juel, V. C., Hobson-Webb, L. D., Smith, E. C., Stickler, D. E., Bite, A. V., Ohno, K. & Engel, A. G. 2011. Myasthenic syndrome caused by plectinopathy. *Neurology,* 76**,** 327-36.
Selcen, D., Shen, X. M., Brengman, J., Li, Y., Stans, A. A., Wieben, E. & Engel, A. G. 2014. DPAGT1 myasthenia and myopathy: genetic, phenotypic, and expression studies. *Neurology,* 82**,** 1822-30.
Selvan, V. A. 2011. Single-fiber EMG: A review. *Ann Indian Acad Neurol,* 14**,** 64-7.
Senderek, J., Muller, J. S., Dusl, M., Strom, T. M., Guergueltcheva, V., Diepolder, I., Laval, S. H., Maxwell, S., Cossins, J., Krause, S., Muelas, N., Vilchez, J. J.*, et al.* 2011. Hexosamine biosynthetic pathway mutations cause neuromuscular transmission defect. *Am J Hum Genet,* 88**,** 162-72.
Shen, C., Li, L., Zhao, K., Bai, L., Wang, A., Shu, X., Xiao, Y., Zhang, J., Zhang, K., Hui, T., Chen, W., Zhang, B.*, et al.* 2018. Motoneuron Wnts regulate neuromuscular junction development. *Elife,* 7.
Shi, L., Butt, B., Ip, F. C., Dai, Y., Jiang, L., Yung, W. H., Greenberg, M. E., Fu, A. K. & Ip, N. Y. 2010. Ephexin1 is required for structural maturation and neurotransmission at the neuromuscular junction. *Neuron,* 65**,** 204-16.
Shibuya, M., Suzuki, Y., Sugita, K., Saito, I., Sasaki, T., Takakura, K., Nagata, I., Kikuchi, H., Takemae, T., Hidaka, H. & Et Al. 1992. Effect of AT877 on cerebral vasospasm after aneurysmal subarachnoid hemorrhage. Results of a prospective placebo-controlled double-blind trial. *J Neurosurg,* 76**,** 571-7.

Sia, G. M., Clem, R. L. & Huganir, R. L. 2013. The human language-associated gene SRPX2 regulates synapse formation and vocalization in mice. *Science,* 342**,** 987-91.
Slater, C. R. 1982. Postnatal maturation of nerve-muscle junctions in hindlimb muscles of the mouse. *Dev Biol,* 94**,** 11-22.
Slater, C. R. 2008. Structural factors influencing the efficacy of neuromuscular transmission. *Ann N Y Acad Sci,* 1132**,** 1-12.
Slater, C. R. 2015. The functional organization of motor nerve terminals. *Prog Neurobiol,* 134**,** 55-103.
Slater, C. R. 2017. The Structure of Human Neuromuscular Junctions: Some Unanswered Molecular Questions. *Int J Mol Sci,* 18.
Slater, C. R., Fawcett, P. R., Walls, T. J., Lyons, P. R., Bailey, S. J., Beeson, D., Young, C. & Gardner-Medwin, D. 2006. Pre- and post-synaptic abnormalities associated with impaired neuromuscular transmission in a group of patients with 'limb-girdle myasthenia'. *Brain,* 129**,** 2061-76.
Slater, C. R., Lyons, P. R., Walls, T. J., Fawcett, P. R. & Young, C. 1992. Structure and function of neuromuscular junctions in the vastus lateralis of man. A motor point biopsy study of two groups of patients. *Brain,* 115 (Pt 2)**,** 451-78.
Smith, S. J., Horstick, E. J., Davidson, A. E. & Dowling, J. 2015. Analysis of Zebrafish Larvae Skeletal Muscle Integrity with Evans Blue Dye. *J Vis Exp*.
Snow, C. J., Goody, M., Kelly, M. W., Oster, E. C., Jones, R., Khalil, A. & Henry, C. A. 2008. Time-lapse analysis and mathematical characterization elucidate novel mechanisms underlying muscle morphogenesis. *PLoS Genet,* 4**,** e1000219.
Sorlien, E. L., Witucki, M. A. & Ogas, J. 2018. Efficient Production and Identification of CRISPR/Cas9-generated Gene Knockouts in the Model System Danio rerio. *J Vis Exp*.
Stainier, D. Y. R., Raz, E., Lawson, N. D., Ekker, S. C., Burdine, R. D., Eisen, J. S., Ingham, P. W., Schulte-Merker, S., Yelon, D., Weinstein, B. M., Mullins, M. C., Wilson, S. W*., et al.* 2017. Guidelines for morpholino use in zebrafish. *PLoS Genet,* 13**,** e1007000.
Stephan, A., Mateos, J. M., Kozlov, S. V., Cinelli, P., Kistler, A. D., Hettwer, S., Rulicke, T., Streit, P., Kunz, B. & Sonderegger, P. 2008. Neurotrypsin cleaves agrin locally at the synapse. *FASEB J,* 22**,** 1861-73.
Straka, T., Vita, V., Prokshi, K., Horner, S. J., Khan, M. M., Pirazzini, M., Williams, M. P. I., Hafner, M., Zaglia, T. & Rudolf, R. 2018. Postnatal Development and Distribution of Sympathetic Innervation in Mouse Skeletal Muscle. *Int J Mol Sci,* 19.
Sundaramoorthy, V., Walker, A. K., Tan, V., Fifita, J. A., Mccann, E. P., Williams, K. L., Blair, I. P., Guillemin, G. J., Farg, M. A. & Atkin, J. D. 2015. Defects in optineurin- and myosin VI-mediated cellular trafficking in amyotrophic lateral sclerosis. *Hum Mol Genet,* 24**,** 3830-46.
Suter, D. M., Espindola, F. S., Lin, C. H., Forscher, P. & Mooseker, M. S. 2000. Localization of unconventional myosins V and VI in neuronal growth cones. *J Neurobiol,* 42**,** 370-82.
Suzuki, Y., Shibuya, M., Satoh, S., Sugimoto, Y. & Takakura, K. 2007. A postmarketing surveillance study of fasudil treatment after aneurysmal subarachnoid hemorrhage. *Surg Neurol,* 68**,** 126-31; discussion 131-2.
Szklarczyk, D., Gable, A. L., Lyon, D., Junge, A., Wyder, S., Huerta-Cepas, J., Simonovic, M., Doncheva, N. T., Morris, J. H., Bork, P., Jensen, L. J. & Mering, C. V. 2019. STRING v11: protein-protein association networks with

increased coverage, supporting functional discovery in genome-wide experimental datasets. *Nucleic Acids Res,* 47**,** D607-D613.
Sztal, T. E., Mckaige, E. A., Williams, C., Oorschot, V., Ramm, G. & Bryson-Richardson, R. J. 2018. Testing of therapies in a novel nebulin nemaline myopathy model demonstrate a lack of efficacy. *Acta Neuropathol Commun,* 6**,** 40.
Sztal, T. E., Ruparelia, A. A., Williams, C. & Bryson-Richardson, R. J. 2016. Using Touch-evoked Response and Locomotion Assays to Assess Muscle Performance and Function in Zebrafish. *J Vis Exp*.
Taniwaki, T., Becerra, S. P., Chader, G. J. & Schwartz, J. P. 1995. Pigment epithelium-derived factor is a survival factor for cerebellar granule cells in culture. *J Neurochem,* 64**,** 2509-17.
Tapia, J. C., Wylie, J. D., Kasthuri, N., Hayworth, K. J., Schalek, R., Berger, D. R., Guatimosim, C., Seung, H. S. & Lichtman, J. W. 2012. Pervasive synaptic branch removal in the mammalian neuromuscular system at birth. *Neuron,* 74**,** 816-29.
Tavares, S., Vieira, A. F., Taubenberger, A. V., Araujo, M., Martins, N. P., Bras-Pereira, C., Polonia, A., Herbig, M., Barreto, C., Otto, O., Cardoso, J., Pereira-Leal, J. B.*, et al.* 2017. Actin stress fiber organization promotes cell stiffening and proliferation of pre-invasive breast cancer cells. *Nat Commun,* 8**,** 15237.
Taylor, P. & Brown, J. H. 1999. Synthesis, Storage and Release of Acetylcholine. *In:* SIEGEL G.J., A. B. W., ALBERS R.W., ET AL. (ed.) *Basic Neurochemistry: Molecular, Cellular and Medical Aspects.* 6th ed. Philadelphia: Lippincott-Raven.
Teixido, E., Pique, E., Gomez-Catalan, J. & Llobet, J. M. 2013. Assessment of developmental delay in the zebrafish embryo teratogenicity assay. *Toxicol In Vitro,* 27**,** 469-78.
Thelen, S., Abouhamed, M., Ciarimboli, G., Edemir, B. & Bahler, M. 2015. Rho GAP myosin IXa is a regulator of kidney tubule function. *Am J Physiol Renal Physiol,* 309**,** F501-13.
Thierry-Mieg, D. & Thierry-Mieg, J. 2006. AceView: a comprehensive cDNA-supported gene and transcripts annotation. *Genome Biol,* 7 Suppl 1**,** S12 1-14.
Thompson, R., Bonne, G., Missier, P. & Lochmüller, H. 2019. Targeted therapies for congenital myasthenic syndromes: systematic review and steps towards a treatabolome. *Emerging Topics in Life Sciences***,** ETLS20180100.
Thul, P. J., Akesson, L., Wiking, M., Mahdessian, D., Geladaki, A., Ait Blal, H., Alm, T., Asplund, A., Bjork, L., Breckels, L. M., Backstrom, A., Danielsson, F.*, et al.* 2017. A subcellular map of the human proteome. *Science,* 356.
Tintignac, L. A., Brenner, H. R. & Ruegg, M. A. 2015. Mechanisms Regulating Neuromuscular Junction Development and Function and Causes of Muscle Wasting. *Physiol Rev,* 95**,** 809-52.
Tojkander, S., Gateva, G. & Lappalainen, P. 2012. Actin stress fibers--assembly, dynamics and biological roles. *J Cell Sci,* 125**,** 1855-64.
Uhlen, M., Fagerberg, L., Hallstrom, B. M., Lindskog, C., Oksvold, P., Mardinoglu, A., Sivertsson, A., Kampf, C., Sjostedt, E., Asplund, A., Olsson, I., Edlund, K.*, et al.* 2015. Proteomics. Tissue-based map of the human proteome. *Science,* 347**,** 1260419.
Vajsar, J., Sloane, A., Macgregor, D. L., Ronen, G. M., Becker, L. E. & Jay, V. 1995. Arthrogryposis multiplex congenita due to congenital myasthenic syndrome. *Pediatr Neurol,* 12**,** 237-41.
Van Der Pijl, E. M., Van Putten, M., Niks, E. H., Verschuuren, J. J., Aartsma-Rus, A. & Plomp, J. J. 2016. Characterization of neuromuscular synapse function

abnormalities in multiple Duchenne muscular dystrophy mouse models. *Eur J Neurosci,* 43**,** 1623-35.
Van Raamsdonk, W., Pool, C. W. & Te Kronnie, G. 1978. Differentiation of muscle fiber types in the teleost Brachydanio rerio. *Anat Embryol (Berl),* 153**,** 137-55.
Varshney, G. K., Carrington, B., Pei, W., Bishop, K., Chen, Z., Fan, C., Xu, L., Jones, M., Lafave, M. C., Ledin, J., Sood, R. & Burgess, S. M. 2016. A high-throughput functional genomics workflow based on CRISPR/Cas9-mediated targeted mutagenesis in zebrafish. *Nat Protoc,* 11**,** 2357-2375.
Villarroel, A. & Sakmann, B. 1996. Calcium permeability increase of endplate channels in rat muscle during postnatal development. *J Physiol,* 496 (Pt 2)**,** 331-8.
Vishavkarma, R., Raghavan, S., Kuyyamudi, C., Majumder, A., Dhawan, J. & Pullarkat, P. A. 2014. Role of actin filaments in correlating nuclear shape and cell spreading. *PLoS One,* 9**,** e107895.
Wærhaug, O. & Lømo, T. 1994. Factors causing different properties at neuromuscular junctions in fast and slow rat skeletal muscles. *Anatomy and Embryology,* 190**,** 113-125.
Wakao, J., Kishida, T., Fumino, S., Kimura, K., Yamamoto, K., Kotani, S. I., Mizushima, K., Naito, Y., Yoshikawa, T., Tajiri, T. & Mazda, O. 2017. Efficient direct conversion of human fibroblasts into myogenic lineage induced by co-transduction with MYCL and MYOD1. *Biochem Biophys Res Commun,* 488**,** 368-373.
Wallace, A. G., Raduwan, H., Carlet, J. & Soto, M. C. 2018. The RhoGAP HUM-7/Myo9 integrates signals to modulate RHO-1/RhoA during embryonic morphogenesis in Caenorhabditis elegans. *Development,* 145.
Walsh, M. K. & Lichtman, J. W. 2003. In vivo time-lapse imaging of synaptic takeover associated with naturally occurring synapse elimination. *Neuron,* 37**,** 67-73.
Wang, S., Reuveny, A. & Volk, T. 2015. Nesprin provides elastic properties to muscle nuclei by cooperating with spectraplakin and EB1. *J Cell Biol,* 209**,** 529-38.
Wang, W. C. & Brehm, P. 2017. A Gradient in Synaptic Strength and Plasticity among Motoneurons Provides a Peripheral Mechanism for Locomotor Control. *Curr Biol,* 27**,** 415-422.
Watanabe, M., Nomura, K., Ohyama, A., Ishikawa, R., Komiya, Y., Hosaka, K., Yamauchi, E., Taniguchi, H., Sasakawa, N., Kumakura, K., Ushiki, T., Sato, O.*, et al.* 2005. Myosin-Va regulates exocytosis through the submicromolar Ca2+-dependent binding of syntaxin-1A. *Mol Biol Cell,* 16**,** 4519-30.
Webster, R. G. 2018. Animal Models of the Neuromuscular Junction, Vitally Informative for Understanding Function and the Molecular Mechanisms of Congenital Myasthenic Syndromes. *Int J Mol Sci,* 19.
Webster, R. G., Cossins, J., Lashley, D., Maxwell, S., Liu, W. W., Wickens, J. R., Martinez-Martinez, P., De Baets, M. & Beeson, D. 2013. A mouse model of the slow channel myasthenic syndrome: Neuromuscular physiology and effects of ephedrine treatment. *Exp Neurol,* 248**,** 286-98.
Wells, A. L., Lin, A. W., Chen, L. Q., Safer, D., Cain, S. M., Hasson, T., Carragher, B. O., Milligan, R. A. & Sweeney, H. L. 1999. Myosin VI is an actin-based motor that moves backwards. *Nature,* 401**,** 505-8.
Wen, H. & Brehm, P. 2005. Paired motor neuron-muscle recordings in zebrafish test the receptor blockade model for shaping synaptic current. *J Neurosci,* 25**,** 8104-11.
Wen, H. & Brehm, P. 2010. Paired patch clamp recordings from motor-neuron and target skeletal muscle in zebrafish. *J Vis Exp*.

Wen, H., Hubbard, J. M., Wang, W. C. & Brehm, P. 2016. Fatigue in Rapsyn-Deficient Zebrafish Reflects Defective Transmitter Release. *J Neurosci,* 36**,** 10870-10882.
Wen, H. L., Lin, Y. T., Ting, C. H., Lin-Chao, S., Li, H. & Hsieh-Li, H. M. 2010. Stathmin, a microtubule-destabilizing protein, is dysregulated in spinal muscular atrophy. *Hum Mol Genet,* 19**,** 1766-78.
Westerfield, M., Liu, D. W., Kimmel, C. B. & Walker, C. 1990. Pathfinding and synapse formation in a zebrafish mutant lacking functional acetylcholine receptors. *Neuron,* 4**,** 867-74.
Westerfield, M., Mcmurray, J. V. & Eisen, J. S. 1986. Identified motoneurons and their innervation of axial muscles in the zebrafish. *J Neurosci,* 6**,** 2267-77.
Weston, C., Gordon, C., Teressa, G., Hod, E., Ren, X. D. & Prives, J. 2003. Cooperative regulation by Rac and Rho of agrin-induced acetylcholine receptor clustering in muscle cells. *J Biol Chem,* 278**,** 6450-5.
Willadt, S., Nash, M. & Slater, C. R. 2016. Age-related fragmentation of the motor endplate is not associated with impaired neuromuscular transmission in the mouse diaphragm. *Sci Rep,* 6**,** 24849.
Wilson, C. 2012. Aspects of larval rearing. *ILAR J,* 53**,** 169-78.
Wirtz, P. W., Titulaer, M. J., Gerven, J. M. & Verschuuren, J. J. 2010. 3,4-diaminopyridine for the treatment of Lambert-Eaton myasthenic syndrome. *Expert Rev Clin Immunol,* 6**,** 867-74.
Wood, S. J. & Slater, C. R. 2001. Safety factor at the neuromuscular junction. *Prog Neurobiol,* 64**,** 393-429.
Wu, H., Xiong, W. C. & Mei, L. 2010. To build a synapse: signaling pathways in neuromuscular junction assembly. *Development,* 137**,** 1017-33.
Wu, X. & Reddy, D. S. 2012. Integrins as receptor targets for neurological disorders. *Pharmacol Ther,* 134**,** 68-81.
Xu, J., Camacho, M., Xu, Y., Esser, V., Liu, X., Trimbuch, T., Pan, Y.-Z., Ma, C., Tomchick, D. R., Rosenmund, C. & Rizo, J. 2017. Mechanistic insights into neurotransmitter release and presynaptic plasticity from the crystal structure of Munc13-1 C1C2BMUN. *eLife,* 6**,** e22567.
Yampolsky, P., Pacifici, P. G., Lomb, L., Giese, G., Rudolf, R., Roder, I. V. & Witzemann, V. 2010. Time lapse in vivo visualization of developmental stabilization of synaptic receptors at neuromuscular junctions. *J Biol Chem,* 285**,** 34589-96.
Yang, H., Hong, D., Cho, S. Y., Park, Y. S., Ko, W. R., Kim, J. H., Hur, H., Lee, J., Kim, S. J., Kwon, S. Y., Lee, J. H., Park, D. Y.*, et al.* 2018. RhoGAP domain-containing fusions and PPAPDC1A fusions are recurrent and prognostic in diffuse gastric cancer. *Nat Commun,* 9**,** 4439.
Yang, X., Arber, S., William, C., Li, L., Tanabe, Y., Jessell, T. M., Birchmeier, C. & Burden, S. J. 2001. Patterning of muscle acetylcholine receptor gene expression in the absence of motor innervation. *Neuron,* 30**,** 399-410.
Yu, H., Sun, D., Wang, N., Wang, M., Lan, Y., Fan, W., Zhao, Y., Guo, W. & Zhu, X. 2015. Headless Myo10 is a regulator of microtubule stability during neuronal development. *J Neurochem,* 135**,** 261-73.
Zefirov, A. L., Abdrakhmanov, M. M., Mukhamedyarov, M. A. & Grigoryev, P. N. 2006. The role of extracellular calcium in exo- and endocytosis of synaptic vesicles at the frog motor nerve terminals. *Neuroscience,* 143**,** 905-10.
Zhai, J., Lin, H., Julien, J. P. & Schlaepfer, W. W. 2007. Disruption of neurofilament network with aggregation of light neurofilament protein: a common pathway leading to motor neuron degeneration due to Charcot-Marie-Tooth disease-linked mutations in NFL and HSPB1. *Hum Mol Genet,* 16**,** 3103-16.

Zhang, H., Wang, S. Z., Wang, Z. P., Da, Y., Wang, N., Hu, X. X., Zhang, Y. D., Wang, Y. X., Leng, L., Tang, Z. Q. & Li, H. 2012. A genome-wide scan of selective sweeps in two broiler chicken lines divergently selected for abdominal fat content. *BMC Genomics,* 13**,** 704.

Zhang, J. & Granato, M. 2000. The zebrafish unplugged gene controls motor axon pathway selection. *Development,* 127**,** 2099-111.

Zhang, J., Lefebvre, J. L., Zhao, S. & Granato, M. 2004. Zebrafish unplugged reveals a role for muscle-specific kinase homologs in axonal pathway choice. *Nat Neurosci,* 7**,** 1303-9.

Zhang, J., Malayaman, S., Davis, C. & Granato, M. 2001. A dual role for the zebrafish unplugged gene in motor axon pathfinding and pharyngeal development. *Dev Biol,* 240**,** 560-73.

Zhang, W., Coldefy, A. S., Hubbard, S. R. & Burden, S. J. 2011. Agrin binds to the N-terminal region of Lrp4 protein and stimulates association between Lrp4 and the first immunoglobulin-like domain in muscle-specific kinase (MuSK). *J Biol Chem,* 286**,** 40624-30.

Zhou, Z. Y., Huang, B., Li, S., Huang, X. H., Tang, J. Y., Kwan, Y. W., Hoi, P. M. & Lee, S. M. 2018. Sodium tanshinone IIA sulfonate promotes endothelial integrity via regulating VE-cadherin dynamics and RhoA/ROCK-mediated cellular contractility and prevents atorvastatin-induced intracerebral hemorrhage in zebrafish. *Toxicol Appl Pharmacol,* 350**,** 32-42.

Zhu, X. J., Wang, C. Z., Dai, P. G., Xie, Y., Song, N. N., Liu, Y., Du, Q. S., Mei, L., Ding, Y. Q. & Xiong, W. C. 2007. Myosin X regulates netrin receptors and functions in axonal path-finding. *Nat Cell Biol,* 9**,** 184-92.

Zong, Y. & Jin, R. 2013. Structural mechanisms of the agrin-LRP4-MuSK signaling pathway in neuromuscular junction differentiation. *Cell Mol Life Sci,* 70**,** 3077-88.